

DESIGN OF
FATIGUE AND FRACTURE
RESISTANT STRUCTURES

Abelkis/Hudson, editors



DESIGN OF FATIGUE AND FRACTURE RESISTANT STRUCTURES

A symposium
sponsored by ASTM
Committees E-9 on Fatigue
and E-24 on Fracture Testing
Bal Harbour, Fla., 10-11 Nov. 1980

ASTM SPECIAL TECHNICAL PUBLICATION 761
P. R. Abelkis, Douglas Aircraft Company,
McDonnell Douglas Corporation,
and C. M. Hudson, NASA-Langley Research
Center, editors

ASTM Publication Code Number (PCN)
04-761000-30



1916 Race Street, Philadelphia, Pa. 19103

Copyright © by AMERICAN SOCIETY FOR TESTING AND MATERIALS 1982
Library of Congress Catalog Card Number: 81-68806

NOTE

The Society is not responsible, as a body,
for the statements and opinions
advanced in this publication.

Printed in Baltimore, Md.
February 1982

Foreword

This publication contains papers presented at the ASTM Symposium on the Design of Fatigue and Fracture Resistant Structures, Bal Harbour, Florida, 10-11 Nov. 1980, and other submitted papers. The symposium was co-sponsored by ASTM Committees E-9 on Fatigue and E-24 on Fracture Testing. Paul R. Abelkis, Douglas Aircraft Company, and Dr. C. Michael Hudson, NASA-Langley Research Center, presided as symposium co-chairmen and served as co-editors of this publication.

Related ASTM Publications

Fractography and Materials Science, STP 733 (1981), 04-733000-30

Fatigue Crack Growth Measurement and Data Analysis, STP 738 (1981),
04-738000-30

Fracture Mechanics, STP 700 (1980), 04-700000-30

Statistical Analysis of Fatigue Data, STP 744 (1981), 04-744000-30

Methods and Models for Predicting Fatigue Crack Growth under Random
Loading, STP 748 (1981), 04-748000-30

Crack Arrest Methodology and Applications, STP 711 (1980),
04-711000-30

Computer Automation of Materials Testing, STP 710 (1980),
04-710000-32

A Note of Appreciation to Reviewers

This publication is made possible by the authors and, also, the unheralded efforts of the reviewers. This body of technical experts whose dedication, sacrifice of time and effort, and collective wisdom in reviewing the papers must be acknowledged. The quality level of ASTM publications is a direct function of their respected opinions. On behalf of ASTM we acknowledge with appreciation their contribution.

ASTM Committee on Publications

Editorial Staff

Jane B. Wheeler, *Managing Editor*

Helen M. Hoersch, *Senior Associate Editor*

Helen P. Mahy, *Senior Assistant Editor*

Allan S. Kleinberg, *Assistant Editor*

Virginia M. Barishek, *Assistant Editor*

Contents

Introduction	1
---------------------	----------

OVERVIEW

Fatigue Life Assessment of Ground Vehicle Components—P. WATSON AND S. J. HILL	5
Applications of Fatigue and Fracture Tolerant Design Concepts in the Nuclear Power Industry—R. L. JONES, T. U. MARSTON, S. W. TAGART, D. M. NORRIS, AND R. E. NICKELL	28
Long-Life Damage Tolerant Jet Transport Structures— U. G. GORANSON, J. HALL, J. R. MACLIN, AND R. T. WATANABE	47

DESIGN AND CRITERIA

Selected Aspects of the Design of Offshore Structures for Fatigue Resistance—W. H. HARTT	91
Crack Initiation and Propagation Approaches to Fatigue Analysis— D. V. NELSON AND D. F. SOCIE	110
Durability Design Requirements and Analysis for Metallic Airframes— J. L. RUDD, J. N. YANG, S. D. MANNING, AND W. R. GARVER	133
Experimental Evaluation of Initial Flaw Criticality and Analysis Methods for Damage Tolerant Air Force Aircraft—J. L. RUDD, T. R. BRUSSAT, S. T. CHIU, AND M. CREAGER	152
Maintenance Scheduling Based on Accumulated Crack Growth— A. P. BERENS AND J. P. GALLAGHER	172

CRACK GROWTH

An Investigation of Initial Fatigue Quality—D. Y. WANG	191
Factors Influencing Propagation of Mode III Fatigue Cracks under Torsional Loading—N. J. HURD AND P. E. IRVING	212

Load-Environment Interaction Effects on Crack Growth in Landing Gear Steels—C. R. SAFF AND M. S. ROSENFELD	234
---	------------

ANALYSIS METHODOLOGY

Prediction of Fatigue Crack Growth under Variable-Amplitude and Spectrum Loading Using a Closure Model—J. C. NEWMAN, JR.	255
---	------------

Application of an Improved Crack Growth Prediction Methodology on Structure Preliminary Design—J. B. CHANG, R. M. ENGLE, AND R. M. HIYAMA	278
--	------------

Fatigue-Life Prediction for Spotweld Using Neuber's Rule—H. L. OH	296
--	------------

Critical Failure Modes in Cracked Mechanically Fastened Stiffened Panels—C. K. GUNTHER AND J. T. WOZUMI	310
Discussion	326

Methodology for Evaluating Weight Savings from Basic Material Properties—J. C. EKVALL, J. E. RHODES, AND G. G. WALD	328
--	------------

EXPERIMENTAL AND ANALYTICAL EVALUATION OF STRUCTURES

Fatigue Crack Growth in Stiffened Panels under Pressure Loading—H. P. CHU, J. A. HAUSER, AND J. P. SIKORA	345
--	------------

Durability and Damage Tolerance Behavior of Adhesively Bonded Primary Structure—D. L. POTTER	373
---	------------

Residual Life Prediction of Jet Engine Rotor Disks—M. ZAKO, T. KAWASHIMA, H. AONO, K. JIMBOH, H. OHNABE, AND T. MIYOSHI	408
--	------------

Fatigue and Fracture Tolerance Evaluation of Tall Loran Tower Eyebolts—R. C. RICE AND C. E. SMITH	424
--	------------

Fracture Tolerance Analysis of the Solid Rocket Booster Servo-Actuator for the Space Shuttle—S. H. SMITH, N. D. GHADIALI, AKRAM ZAHOR, AND M. R. WILSON	445
--	------------

SUMMARY

Summary	477
----------------	------------

Index	483
--------------	------------

Introduction

The constant quest for more efficient structures has prompted the development of improved materials, stress analysis, fabrication, and inspection techniques. Higher allowable stresses frequently result from the use of these improved materials and techniques. From the standpoint of static strength, these higher stresses are perfectly acceptable. However, when these stresses are cyclic in nature, fatigue failures may occur. Fortunately, testing and analysis techniques are being developed which can predict, with reasonable accuracy, the fatigue and fracture behavior of various structures. These techniques are now being incorporated into the design procedures for such diverse structures as (1) pressure vessels in nuclear power plants (Section III of the ASME Boiler and Pressure Vessel Code), and (2) aircraft for military applications (Specification MIL-A-83444).

In order to review the latest developments in dealing with fatigue and fracture behavior, a symposium was held in Bal Harbour, Florida, on November 10 and 11, 1980. This symposium was specifically concerned with the design of fatigue and fracture resistant structures. The symposium was originally divided into three sessions: ground transportation structures, aircraft structures, and nuclear structures. (Invited keynote speakers provided general status reviews for each of these three topics.) However, many good papers dealing with other types of structures were submitted for consideration. Consequently, the scope of the symposium was expanded to include all types of structures.

This volume, which resulted from the Bal Harbour symposium, contains the text of all the papers presented, plus the texts of other submitted papers. These papers deal with fatigue and fracture prevention in ground transportation, aircraft, nuclear and offshore structures, rotor disks, and loran tower eyebolts. The wide variety of structures discussed in this symposium is a potent indication that fatigue and fracture behavior are receiving considerable scrutiny in the design of all types of structures.

A large number of people contributed their time and energy to make the Bal Harbour symposium a success. Special thanks are due: (1) the speakers, for the time and effort spent in preparing their presentations; (2) the reviewers, for their careful editing of the manuscripts; (3) the organizing committee, Harvey Eidinoff, Bryant Leis, Tom Orange, John Potter, Darrell Socie, and Roy Watanabe, for its efforts in selecting the fine papers which were presented; (4) the chairmen of ASTM Committees E-9 and E-24, Harold Reem-snyder and Gil Kaufman, for their dedicated efforts in bringing their com-

2 DESIGN OF FATIGUE AND FRACTURE RESISTANT STRUCTURES

mittees into a harmonious working relationship; and (5) the ASTM staff, for its help in organizing and completing the symposium.

P. R. Abelkis

Douglas Aircraft Company, McDonnell Douglas Corporation, Long Beach, California;
co-chairman and co-editor

C. M. Hudson

NASA-Langley Research Center, Hampton, Virginia; co-chairman and co-editor

Overview

Fatigue Life Assessment of Ground Vehicle Components

REFERENCE: Watson, P. and Hill, S. J., "Fatigue Life Assessment of Ground Vehicle Components," *Design of Fatigue and Fracture Resistant Structures, ASTM STP 761*, P. R. Abelkis and C. M. Hudson, Eds., American Society for Testing and Materials, 1982, pp. 5-27.

ABSTRACT: Fatigue has been a major problem in ground vehicle components for more than 130 years. This paper considers why our increasing knowledge of fatigue has now significantly reduced its importance. A historical review of past work in a wide range of vehicle components is presented. The different aspects of durability assessment—namely, service load measurement, materials testing, stress analysis, and component testing—are concentrated on in turn. The work is brought up to the present by use of examples of how modern methods of fatigue analysis are being applied to contemporary problems.

KEY WORDS: fatigue, ground vehicle components, historical review, life prediction methods, cycle counting, component testing, load measurement, materials testing, stress analysis

Since the expansion of transportation in the first half of the nineteenth century, fatigue has been of major importance in determining the durability of ground vehicles, and hence considerable effort has been devoted to the subject. Even prior to 1850 it had been identified by railway engineers, and their researches culminated in the intensive studies of Wöhler. Despite these and subsequent efforts, the problem was not resolved, as illustrated by a quotation from the March 1920 issue of *Scientific American Monthly*: "Metal parts of machines, such as springs, shafts, crankpins and axles, occasionally fail suddenly when only subjected to conditions of ordinary service. Not only does failure occur suddenly, but the part about to fail shows no ordinary evidence of weakness." This statement is made more pointed in that a further 60 years of even more concentrated effort have not rendered it any less true.

One of the reasons for this apparent lack of progress is the ever-increasing restraints facing the designer. The twin challenges of fuel economy and prod-

¹Materials Engineering Department, GKN Technology Ltd., Wolverhampton, England.

uct liability are particularly relevant today. However, it is also true that lessons have been forgotten, old ground has been re-covered, and effort has not been directed most effectively. This paper seeks to illustrate this by an historical review of past work on a wide range of vehicle components. It concentrates in turn on different aspects of durability assessment, namely, service load measurement, stress analysis, materials testing, life prediction, and component testing. It brings the work up to the present by giving examples of how modern methods of fatigue analysis are being applied to contemporary problems.

Service Load Measurement

Reference to Fig. 1 shows that service load measurement is a necessary input to fatigue life assessment by both analytical and experimental methods. Notwithstanding this importance, it has over the years often been paid only scant attention despite the insight of a number of individuals. An excellent example of this insight dates back to the early work on railway axles, when it was observed in 1879 by Beaumont [1]² that: "When a train was running, the wheels were lifted up and down again on the very many irregularities of the line at a velocity which induced severe shocks. The velocity at which impact shocks were transmitted through the wheels to the axle was not simply that of gravity and that of the velocity of the train, but very many of the shocks were thus transmitted at the velocity of recoil of a loaded spring, which was probably as much as 1300 feet per second."

Although some notice was taken of this observation in 1895 by Andrews [2], the railway axle soon entered folklore as something to be designed with the nominal stress under a fatigue limit (for example, Ref 3). This attitude

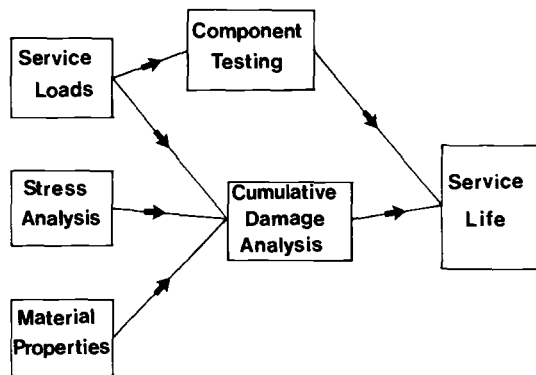


FIG. 1—Fatigue life assessment.

²The italic numbers in brackets refer to the list of references appended to this paper.

provided much of the justification for the tremendous volume of work between the two World Wars on studying fatigue almost exclusively as an endurance limit problem, and still lingers on despite publications by people who have actually measured operating loads and strains. Of direct relevance, Moreau and Peterson in 1955 published a paper [4] with remarkable insight into "Field Testing of Diesel Locomotive Axles." It is well worth repeating some of their comments in full:

It is now possible to predict, with reasonable accuracy, what stresses will be induced in a specific axle design by a certain load and the relation between the stress and the number of stress applications which will cause a failure is also fairly well established . . . There is, however, very little information available about the loads an axle is actually exposed to in service. To determine whether a part of a structure or a machine is strong enough, the engineer must know the type of loading to which it will be exposed. If he does not, he has no other choice than to make a guess and see if it fails. It is too expensive to learn about weaknesses in axles from failures and it is also too expensive to make them so heavy that they are bound to be strong enough in spite of the designers' ignorance about the loads . . . To study axles under service conditions it is necessary to study axles in high speed passenger service and in slow freight service, on curves and on tangent track, on good track and on bad. The axles might be damaged under conditions which occur only occasionally. To make sure that no such conditions are overlooked the behaviour of the axles must be observed over long periods.

They observed in the course of their investigation that about once every 1000 miles a stress of nearly four times the normal value occurred with a full spectrum of loads in between, which was very different from the view held by the majority at that time.

One of the major reasons for the state of affairs until about 1940 was the lack of a suitable transducer to make the measurements. In the late 1930s, the development of the bonded wire resistance strain gage by Ruge and De Forest at MIT and Simmons and Clark at the California Institute of Technology revolutionized the technique of service load measurement. Until that time, with the exception of a brief period of use of magnetic strain gages and carbon strip gages (for example, Ref 5), only mechanical means had been available. These were best suited to stationary objects such as bridge beams and rails, and were direct descendents of the method reported by the 1857 Commission into the Application of Iron to Railway Structures [6]: "... and a pencil was fixed to the underside of one of the girders of the bridge, so that when the latter was deflected by the weight of the engine or train either placed at rest or passing over it, the pencil traced the extent of the deflection upon a drawing board attached to the scaffold." Although as stated earlier this and subsequent developments were generally used for bridge structures, Hill [7] reported their use in 1935 on a dragline boom and 1937 on the structure of a bus.

Despite these belated successes of the mechanical gages, the resistance strain gages were seized upon with great enthusiasm for application directly relevant to ground vehicles. Thus in 1943 Tucker [8] reported on dynamic

strain measurements on cylinder slides and cylinder barrel flanges, and in 1944 Meier [9] reported on slip rings, special calibrated links or load cells, and suggested a potentiometer system to measure the deflection of rubber or shock absorbers. In the same year, Goloff [10] wrote about the determination of operating loads and stresses in crankshafts. The more complex subject of measuring strains in con-rods and pistons was treated in 1946 by Wallace and Cassler [11]. Only the problem of mobility prevented the wide-scale application to automotive components in service, and this was overcome in 1953 when Colwell [12] presented a paper on "Mobile Instrumentation for Automotive Equipment." Although some of the means of implementation seem a little old fashioned nearly 30 years later, the basic concepts are remarkably like those used widely today by many automotive companies. A power supply (generator) was mounted on the back of the test vehicle and an instrumentation pack was mounted on the door. In later developments batteries to provide power were accommodated in a passenger car. This can be compared directly with work carried out by GKN about 25 years later where the same basic elements can be identified (Fig. 2). More important than the details of the system is the care Colwell took to obtain good signals. Such techniques as identifying and replacing electric components susceptible to vibration, shock mounting equipment on foam, checking the frequency content of the signal, assessing the suitability in terms of response of the recording medium, and driving with a dummy balanced input over bumps to try to generate spurious data were all employed.



FIG. 2—Conventional instrumentation system.

One year later, Polzin [13] reported on the "Performance Evaluation of the Magnesium Alloy Truck Wheel." He used a similar technique to Colwell's with the following two exceptions: (1) because he was working with rotating components he had to use slip rings; and (2) in order to site his gages he used the brittle lacquer technique. The latter is perhaps of more significance in that guidance can be drawn from this example even today. He used multiple coatings to cope with varying temperature and humidity and also to provide some strain level segregation. More fundamentally, he took care to observe the effects of wheel mounting, tire inflation, and various driving maneuvers. His comments that "... It was evident that the final analysis of life expectancy and design efficiency would have to come purely from strain gage readings. It was felt that locating these gages by judgment alone was pure folly ..." are still generally applicable.

One final development remained to make the techniques of the early 1950s fully equivalent to those in widespread use today. This was a means of recording the signal so that it could be played back at will for analysis, rather than relying solely on paper or film hard copies. About five more years were to pass before researchers such as MIRA (The Motor Industry Research Association, U.K.) were able to interface FM tape recorders for use over many miles of roads. The use of a discrete instrumentation pack for easy fitting into a range of vehicles [14] has been widely adopted and used in a wide variety of environments. The instrumentation has been fitted to passenger cars, buses, lorries, and military vehicles and a number of off-highway vehicles, and has proved equal to the job in all cases. As such it is a standard method of data acquisition at this time.

That is not to say that the system is without serious disadvantages. The equipment is heavy, inconvenient to operate, bulky, very expensive, and will only operate off its own batteries for a relatively short period of time. One of the methods proposed to circumvent some of these problems is to divorce the recorder from the test vehicle. "Umbilical cords" have been used for the job, particularly on test tracks. However, it is readily apparent that for general service this scheme is severely impractical, although it has been used successfully on slow moving off-highway vehicles (Fig. 3).

A more practical scheme is to use long-range telemetry. This should not be confused with short-range telemetry, which is used to obtain signals from rotating components such as propshafts and acts as a direct replacement for slip rings. Long-range telemetry has been used for a considerable time in the aerospace industry to obtain data from radio sondes and guided missiles. Its application for ground vehicles is rather more recent, with the strongest proponents being Deere and Company, who have been using the technique since 1967 [15]. Other manufacturers have reported on its use rather more recently, and GKN has successfully used long-range telemetry not only in its usual role with a stationary recording center but also with a moving one in pursuit of a test vehicle. In this last more general role some deficiencies of the method have become apparent, principally in identifying the effects of loss of cou-



FIG. 3—*"Umbilical Cord" method.*

pling, eliminating them in subsequent analysis, and keeping contact with a service vehicle. It is fair to say that in this role, the method is still in its infancy, and many of the problems could be reduced if more liberal licensing arrangements could be made to boost the signal power.

Also of recent interest to the ground vehicle industry is the technique of High Density Digital Recording, more popularly known as Pulse Code Modulation (PCM). By encoding the various channels of information and incorporating synchronization data, improved signal-to-noise ratios can be obtained and many more data channels can be recorded. This system is being actively investigated by GKN, although to date no completely suitable system has been identified. Problems exist owing to the cost of further developments to meet particular requirements and the task of converting or replacing existing hardware.

Finally, the option exists to remove the tape recorder completely and analyze the data on board. This is by no means a new concept. Moreau and Peterson [4] reported the use of a level crossing counter. They used it principally as a warning device to investigate aspects of service operation more closely. Unfortunately this type of device continued in use for a considerable time owing to its convenience, despite the fact that the "cycles" it counted were based purely on the convenience of a mechanical or electromechanical device rather than on the characteristics of the material under load. Fortunately microprocessor-based devices using the "rainflow" algorithm are now available, and have been in use for nearly three years with considerable suc-

cess. One example of an installation is given in Fig. 4. This should be contrasted with Fig. 2 which shows the earlier tape recorder based system. This microprocessor-based system has now been used successfully for over 30 000 miles in a wide variety of service operations.

The data generated can be sorted to investigate the effects of different drivers, or the effects of different service operations can be studied in detail. It should be noted, however, that the data must be of the highest quality, since the analysis proceeds with no discrimination between genuine signal and noise. The devices are probably best used as a "follow up" to full-scale recording exercises where the mechanics of the loading can be observed and the quality of the data checked. The comments made by MIRA [14] on an early on-board data analyzer are still valid: "The type of testing carried out was what we now call "complex routes" and whilst the data was, for its intended purpose, quite satisfactory, it was difficult to understand the reasons for, and the significance of variation in sets of data."

Stress Analysis

In general, stress analysis has a dual role to play in fatigue life assessments. The first part is to determine the critical locations, the areas most at risk in the component, so that subsequent service load measuring can be made most effectively. The extent of the stress analysis required can range from simple



FIG. 4—Microprocessor-based recording and analysis.

examination of a failed component through techniques such as brittle lacquer methods to finite-element stress analysis. The importance of carrying out this stage properly cannot be conveyed better than by the suggestion by Polzin [13] quoted earlier that "... locating these gages by judgment alone was pure folly ..."

The second role of stress analysis is to overcome the very localized nature of fatigue. It is often impossible in engineering components to locate a strain gage at the critical site. The latter is generally at a stress concentration such as a fillet radius or a hole where the strain gradient can be very steep. Fortunately by measuring nominal loads, in the vicinity of the critical location, stress analysis can be used to derive the local conditions. This has the further advantage that the effects of changing materials or local geometry can be assessed rapidly by analytical means without recourse to a further measuring exercise.

The importance of stress concentrations was understood at a very early stage in the development of fatigue life prediction techniques. Whilst the argument was raging in 1850 as to whether or not railway axles "crystallized" during fatigue, Ramsbottom [16] had the insight to point out that since failures always occurred in the same place at the shoulders of the axle, it was more important to reconsider the design. It is surprising that the point had to be remade since, in 1843, Rankine [17] had delivered a paper to the Institute of Civil Engineers attributing the failure of a large number of axles to the journal fillet radius.

At the time, no means were available to provide a quantitative assessment of the degree of stress concentration. It was left to good engineering practice to specify transitions as gradual as possible. The case of a circular hole in an infinite plate was considered first and solved in 1898 by Kirsch [18]; an elastic stress concentration factor of 3 was obtained. Inglis [19] in 1913 extended the analysis to elliptic holes, which he used to consider the behavior of cracks. The 1920s brought another paper on holed plates, this time of finite width [20], and saw the emergence of experimental techniques. Baud [21] in 1928 provided early work on photo-elasticity, and Jacobsen [22] used electrical analog techniques. This experimental work is not to be confused with fatigue testing of specimens with stress concentrations, which included a multiplicity of effects including the use of elastic analysis despite the presence of plasticity, the development of nonpropagating cracks, and generation of a multi-axial stress state. This logic became further confused by the sterile concept of "notch fatigue" where arbitrary notches were used, which unfortunately lingers on today. However, studies of the effects solely of notch geometry continued, and by 1930 Peterson [23] could review the subject of "Stress Concentration and Fatigue Strength" and reference 46 sources. He continued to maintain an active interest in the subject, and any reader requiring a rapid assessment of a stress concentration factor is recommended to at least start with his excellent review *Stress Concentration Factors* [24]. Often if an exact

analysis cannot be found, a case closely approaching the problem can be utilized, and therein lies a major but often unappreciated facet of the work. The user is forced into considering the sensitivity of the solution to a variety of parameters and by so doing accumulates a useful background in the design of components.

This is not the case for a more recent development, the technique of finite-element stress analysis. The technique will provide only specific answers, is often expensive and time consuming, and is sensitive to the boundary conditions imposed. This last is particularly important for items where the area of greatest interest is adjacent to the interface, for example, near the bearing caps of universal joints. Despite these problems the method is of great utility, particularly for complex structures at the early stages of design. Perhaps because of its cost and association with computers there is a tendency to view finite-element analysis as the only tool necessary in the assessment of durability. This is generally *not* the case and care must be taken to ensure that it still forms an integrated part of the fatigue life analysis package.

The final development of stress analysis methods to be considered is the consideration of plasticity. Although most components used in the ground vehicle industry remain nominally elastic, at the critical location where failure will take place a plastic analysis has to be utilized. Although the finite-element method has been extended to use nonlinear stress-strain relationships, the cost and time at present involved in its use are prohibitive for all but a very few specialized components. Fortunately, the elastic stress concentration factor, K_T , has been combined with cyclic stress strain information to generate information about the stress concentration factor, K_σ , and the strain concentration factor, K_ϵ . Peterson [24] touches briefly upon this in mentioning the rules devised by Stowell [25]. A more popular rule, owing to its greater ease of manipulation, is based on the observations of Neuber [26] and extended by Topper and his co-workers into the field of fatigue (for example, Ref 27). Neuber's Rule is now an essential part of most modern computer-based methods of fatigue life prediction.

Material Testing

The first systematic investigations of metal fatigue failure were carried out by Wöhler [28] from about 1850. Since then, the continued interest in cyclic material testing can be divided into three broad activities. First and by far the most prolific has been the attempt to quantify the relationships between applied load, stress or strain, and fatigue resistance. This resistance can be expressed in terms of crack initiation or propagation or an often unspecified mixture of both. The importance of Wöhler's work can be reflected in the fact that the $S-N$ or Wöhler curve is still widely used today as one of the methods of quantifying fatigue resistance. Other notable early contributors to this area were Gerber [29] and Goodman [30] who considered the effect of mean

stress and Basquin [31] who introduced the exponential relationship between stress and fatigue life.

The second activity based on material testing has been the search for fundamental understanding of the fatigue damage process. Despite the splendid beginnings by such researchers as Ewing and Humfrey [32], we are still a long way from complete understanding, and hence have to rely on the empirical approach first established in the last century.

An astute comment, quoted by Peterson [33] was made by an English reporter in an account of the 1867 Paris Exhibition. He wrote of Wöhler's display [34]:

Wöhler's modest exhibition may have been overlooked by 99 out of every 100 visitors to the Exhibition yet we believe that his patient experiments will be referred to long after the majority of those things which have drawn a shower of medals and ribbons will have been forgotten.

Wöhler's work was initiated because of the many failures of locomotive axles reported and discussed in the mid-nineteenth century. He began his work by running full-scale tests. These were eventually replaced by model axles and then by laboratory specimens in his famous rotating bending testing machine. The range of topics he covered included bending, torsion, residual stresses, stress concentrations, stress-life curves, recording of service histories, and the relationship between monotonic and fatigue strengths. This last topic became the subject of some outstanding work by Bauschinger in the 1880s [35]. His work was the starting point for the final area of activity, the search for a quantitative understanding of how the metals behave under cyclic conditions. Bauschinger's attention was drawn to one of Wöhler's conclusions; that is, when a bar was subjected to equal tension and compression it broke at a stress lower than its original elastic limit. As a result of extensive, careful experiments, Bauschinger explained this by stating that the primitive elastic limits of many materials are artificially raised. He also found that cyclic loads had the effect of raising an artificially lowered limit or lowering an artificially raised limit. This major conclusion from his work was published in England and strongly supported by Unwin [36] who wrote:

By subjecting a bar to a few alterations of equal stresses which are equal to or somewhat exceed the elastic limits they tend towards a fixed position which Bauschinger calls the natural elastic limit. The range of stress for which a bar is perfectly elastic after a few repetitions of such alternating stresses appears to agree very closely with Wöhler's range of stress for unlimited repetitions of alternating stresses.

Out of this arises a very important practical suggestion. To determine the safe range of stress by Wöhler's method requires experiments extending over a period counted by years. If Bauschinger is right, a bar can be subjected to alternating stresses in an ordinary testing machine perhaps a dozen times and the elastic limits determined. Those elastic limits will define the safe range of alternating stresses. Such experiments are not easy and measurements must be made as accurately as Bauschinger makes them (e.g. to 1/125,000th of an inch). But they are far easier than experiments by Wöhler's method. Yet further. If the ultimate static strength is known and the range of stress

for repeated tensions and compressions, the Gerber parabola can be drawn, and the safe range of stress for any other limits of loading determined.

Despite the importance of such work and despite Unwin's very strong recommendations, the work of Bauschinger has been largely ignored. Even the "effect" which is attributed to him is often ignored in fatigue calculations.

The next important link in this pioneering work was that of Bairstow at the National Physical Laboratory [37,38]. His 1909 paper [38] contains the earliest published hysteresis loops. This work indicates that the phenomenon of cyclic softening was known to Bairstow. He also demonstrated that "... the maximum width of any loop measured parallel to the axis of extension added to the elastic extension of the specimen is the total change of length in each cycle."

Extensive studies of stress-strain loops in two low-carbon steels were published by Smith and Wedgewood [39] in 1915. This monumental paper contains many results and figures remarkably similar to the results of cyclic stress-strain studies conducted during the last fifteen years.

From these very strong beginnings we have moved forward fitfully to our present level of knowledge. Many subjects have arisen and much time has been wasted. Perhaps the worst example of misdirected effort was the period during the 1920s which has been described by Frost [40] in an entertaining review as: "... the golden age for devising quick methods of determining the fatigue limit." He also states that such activities: "... provided the raw material for scientific papers but were of little direct use to designers."

This wasted opportunity may well be repeated, as indicated by the comments of Morrow [41] in 1978:

A number of us have tried to eliminate the concept of an endurance limit from our thinking and from the thinking of people who have to design parts to last under service conditions. I am disappointed, frankly, that some of you backslide to thinking of a safe stress below which fatigue will never be a problem and a threshold stress below which cracks will not propagate. I think that is a mistake and certainly has no place in the design philosophy of engineers who try to make parts that last a safe period of time.

Since 1950, however, three major contributions have been made. They start with the work of Coffin [42] and Manson [43] who have independently established the relationship between plastic strain and fatigue life. Next, Paris, and his co-workers (for example, Ref 44) in opening up the field of crack growth and Linear Elastic Fracture Mechanics have considerably extended our ability to design and assess components. Finally, the work of Morrow and his many colleagues has made a major contribution, particularly in the ground vehicle industry, to our understanding of fatigue and of how we can assess the durability of products. Based on these contributions and many others, we can now assess the fatigue life of a component or structure based on strain-life data, crack growth data, and the use of the stress-strain relationships which are relevant to the cyclic condition.

Component Testing

A technique which is often presented as an alternative to the analytical methods mentioned above and described in later sections is component testing. This suggestion of competition is not strictly true, since in many cases the problem can best be solved using the two methods to complement each other. In those cases where the analytical methods are not developed, however, component testing has to be carried out exclusively. The attendant penalties are increased cost, slower response time to problem solving, and a loss of generality and flexibility.

The term as considered in this section is used in its most general sense. Tests can take many forms, ranging from operation in service or simulated service on rigs, through accelerated testing on proving grounds or test machines, to constant-amplitude testing of subassemblies. It is apparent that the further the testing becomes removed from direct reproduction of service, the greater becomes the analytical input requirement. In all cases, a detailed knowledge of service loads is required.

The concept of component testing is by no means a new one. One of the earliest papers on fatigue by Albert [45] in 1838 is a report of tests on mine cables. The testing method is reproduced in Fig. 5. Although the idea of component testing remained popular with civil engineers, as shown by the work of Fairbairn [6] and Hopkinson [6], its extension into the ground vehicle industry was far more tentative. The trend is well illustrated by the example of Wöhler [28], who initially utilized full-sized axles in his tests but soon

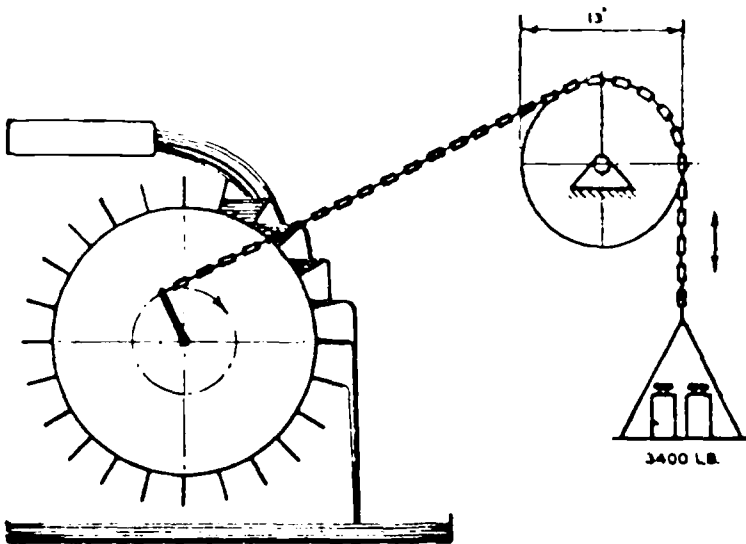


FIG. 5—Albert's machine for testing chains (1829).

turned to smaller specimens. Component testing soon became considered of value only for proof testing as described by Andrews [2] for railway axles:

The axles are to be tested by a weight of 1 ton falling through a space of 30 feet, the axle resting upon solid iron bearings about four feet apart. It must receive at least two blows without showing any signs of fracture.

The axles are to be capable of standing without fracture five blows from a weight of 2000 lbs. falling from a height of 20 feet upon the axle, which shall be placed upon bearings three feet six inches apart, and shall be turned after each blow.

The axles to be placed upon supports three feet six inches apart, and to stand a weight of 1800 lbs. falling a distance of 19 feet.

The axle to be placed upon supports three feet six inches apart, and to stand two blows from a weight of 1 ton falling 20 feet; axle to be turned after each blow.

The axle to be placed upon supports three feet six inches apart, and to stand four blows from a weight of 2369 lbs. (21 cwt. 0 qr 17 lbs.) falling a distance of 17 feet six inches on the centre of the axle; the axle to be turned over after each blow.

The axle to be placed upon supports three feet six inches apart, and to stand four or five blows from a tup of 2300 lbs. (20 cwt. 2 qrs. 4 lbs.) falling a distance of 18 feet; axle to be turned over after each blow.

The tests were requirements of the various railway companies, and Andrews agreed with his audience that, although shock loading was inflicted upon his axles in service, the tests were unrealistic in their severity. This is an early example where the requirements for a rapid test supplanted the need to relate to service operations. This need to accelerate tests at all costs unfortunately is still with us today.

With only a few isolated examples, component testing went into a virtual lull until the 1930s. This reflects the attitude prevalent at the time that a detailed study of the fatigue limit in isolation would provide answers to all of the problems.

One area where at least some component testing was carried out was the proving ground. The Dodge Brothers built an early example in 1915, consisting of an oval track with a test hill. The construction was interesting, being of split logs, thus introducing a form of surface now known as corrugations. This of course provided a severe test for the suspension, and this form of accelerated testing is a feature of all proving-ground tests today. Present day proving-ground requirements run the whole gamut from the very simple and straightforward, with perhaps a week's testing, to much more complex requirements.

The crudest criterion is based on surviving a given distance, usually 1000 miles, traveling over Belgian pavé. More sophisticated requirements are formed from a mixture of high-speed track operations, driving over rough surfaces and violent maneuvers. When attention is paid to maintaining test track failures of the same nature as service failures, this last form of operation is reasonably useful in assessing the durability of components developed by a gradual evolutionary process. Where the component is novel in con-

struction or material, all of the test criteria become arbitrary and possibly seriously misleading.

In the 1930s, it became apparent that in many cases the design of automotive components need not be based on endurance limit concepts, but rather on the use of finite life techniques. Perhaps the leading figure was Almen who, in 1935 [46], published details of experimental work on the fatigue strength of spiral bevel gears in back axles. He was able to debunk the myth of impact loadings, in addition to demonstrating the inadequacies of the 40-year-old gear design formulae still in use at the time, and pointing out that the endurance of the gears was determined by the short period of the time the vehicle was in bottom gear. His analysis of the problem concluded that the vast majority of the fatigue damage arose from only some 30 miles of operation. Thus he proposed that fatigue tests on specimens should concentrate on the finite life region, about 100 000 cycles in this particular case, rather than the endurance limit. The testing of components for the ground vehicle industry continued in this still fairly low-key fashion until well after World War II. During this time, few service load measurements were available and testing machines were unsophisticated. Some full-scale testing was carried out on railway axles (for example, Refs 47 and 48); sections of crankshafts were tested in torsion [49] and bending [50], and gear teeth were loaded using a hydraulic pulsator by Mansion [51].

A major contributor in the early 1950s was Gassner [52], who recognized the complex nature of service loading. To overcome the pitfalls of constant-amplitude testing, he suggested that variable-loading tests be carried out for both ground vehicles and aircraft. He proposed the use of block programming, where the service data are analyzed and broken down into blocks of loading to be applied sequentially. The idea was taken up enthusiastically and is still common today, particularly in the aircraft industry. The principal weakness of this approach is demonstrated by the ensuing discussions over the need to randomize the order of the blocks, the number of the blocks, etc. Unfortunately, the validity of each test depends critically upon the analysis used to process the complex loading data. If the analysis method is correct, the question should be asked why testing has to be undertaken in the first place. Despite these inconsistencies the method is still popular. In the case of ground vehicles this is particularly true of acceptance tests of components. Often the requirements are based on supposition or guesswork, but have a peculiar charisma owing to the apparent scientific basis, in the same way that proving-ground tests frequently become almost deified. Perhaps the most perverse use of block program tests is the "reproduction" of proving-ground operations in the laboratory.

As stated previously, the block program form of testing still remains popular despite the widespread availability of servo-hydraulic actuators that can accurately reproduce service loads. Apparatus is now available to test components ranging from simple welded joint specimens [53] to complete

vehicles [54]. Argument as to whether the frequency content, as, say, measured by the PSD of the signal, or the cycle-by-cycle content should be reproduced are being swept aside by the addition of computer control to test rigs. In these cases, service loads can be reproduced directly, satisfying both criteria.

The advantage of such systems is readily apparent: the component can be observed during fully reproducible tests conducted safely and, perhaps, more rapidly than real service. The disadvantages are equally apparent: complex systems are expensive both to buy and operate, and tests are almost inevitably of long duration. It is to be hoped that the opportunity is taken to develop a better understanding of the mechanisms of failure and hence better analytical techniques, and that the temptation to accelerate the tests or base them on fallacious criteria is resisted.

Cumulative Damage Analysis

Fatigue failure has almost always occurred in ground vehicle components as a result of a complex series of loadings. Hence it has always been necessary to assess the cumulative effect of such different loads. This is seen nowadays as a two-stage process. The initial step is to break down the local history into its constituent events, and then the damaging effects of these events must be added together. Paradoxically it is this second stage which has received the most attention, with the classic papers of Palmgren [55] in 1924 and Miner [56] in 1945 the major contributions. Of more interest nowadays, however, is the process of extracting from the local history the damaging events and using fatigue life data and stress analysis information to predict life.

The methods used to assess variable-amplitude load histories can be placed in two groups. They are (1) continuous load or PSD analysis, and (2) cycle counting. In (1) the history is considered as a whole, whereas in (2) it is broken down into discrete events, generally cycles of load, stress, or strain, which are immediately compatible with basic fatigue data. PSD analysis has only limited application to the wide variety of problems facing the ground vehicle engineer and such methods are rarely used.

Cycle counting is thus the first stage of most of the cumulative damage analysis methods used today. There are many counting methods in general use [57,58]. Unfortunately most of them have flaws which severely limit their general application. Two broad approaches have been developed. The first consists of methods which identify and count single events which are not necessarily related to cyclic damage accumulation in any simple fashion; for example, peaks, peak distribution, and level crossing counting have been used. These and other methods are described in many papers (for example, Ref 59). Their success has been limited to very special classes of signals, and hence they should be eliminated from serious consideration for more general use.

The second group consists of methods that are based on the ranges of stress or strain which occur. These techniques are preferred because it is known that fatigue damage is closely related to such ranges. They include range counting, range mean analysis, range-pair counting, and the rainflow method [60]. With the exception of range counting, these techniques also identify the mean levels in each range. Unfortunately range-mean counting suffers from the well-known [61] hysteresis or gate-level effect and can be discounted. Therefore, after several decades of development, we have two almost identical counting methods, rainflow and range-pair, which are consistent with modern views of fatigue damage accumulation.

The recent development of computer-based analytical methods (for example, Refs 62, 63, and 64) depends upon successful mathematical modeling of cyclic material behavior. The first publication of a cyclic material model was by Martin et al in 1971 [65], and this has been considerably extended and improved by Jhansale [66], Wetzel [67], Conle [68], and many others.

Surprisingly the first material models were described 60 years ago by Jenkin [69]. His models, which consisted of springs and sliders, were developed in order to explain the experimental observations from the fundamental research of the 1920s. The springs and slider combinations were used by Jenkin to explain such phenomena as fatigue limits, cyclic yield, mean stress effects, cyclic hardening, overload effects, and coxing. He concluded one of his papers [70] with the following paragraphs:

Perhaps you wish to know the practical end of all these researches, and may feel inclined to say: What is the use of your pretty models and fine theories?

We hope before long to be able to put figures into designers' hands which will be a sure basis for all their strength calculations, figures which will not need factors of safety to allow for our ignorance of the strength of the materials. We hope to introduce fatigue limits into steel specifications so that you will buy your materials on the basis of their useful strengths. We hope to have methods of fatigue testing as simple as tensile tests. We hope to be able to issue instructions which will save endless failures of engines. All these things are already possible. We have now only to verify and confirm before issuing our reports.

Despite such optimism we have had to wait until the last decade to approach his objective.

Material models and rainflow cycle counting can now be combined in the computer. The additional process of stress analysis can also be included for many applications. Material behavior is easily quantified and stored. As a result, it is now possible by processing measured or predicted load histories to predict the durability at the critical regions in components. The methods used will be illustrated in the next section.

Modern Fatigue Analysis

Several efficient and reliable methods now exist to perform fatigue analysis of complex components using data generated from simple constant-amplitude

tests on simple specimens. Assuming that a critical region in a component has been identified by analysis or experiment, one of the most common procedures used is shown in Fig. 6. This consists of five closely interrelated steps:

- (1) Description of the service environment in terms of a nominal load/strain history experienced at a point related to, but remote from, the critical area.
- (2) Determination of the stress-strain response of the material at the critical area.
- (3) Identification in this response of cyclic events in a manner consistent with basic material behavior using the rainflow method of cycle counting.
- (4) Calculation of the damage contribution of these individual events by comparison with conventional cyclic fatigue data.
- (5) Summation of the damage caused by each event to give a total damage for the particular service history.

Extensive software routines have now been developed and implemented to exploit the techniques described previously. The programs are designed to be user orientated, requiring no detailed knowledge of either the computer software or hardware. The programming option selected depends on the problem under consideration and the available data. Communication with the computer is via a visual display unit (output) and keyboard (input). Software operating instructions are displayed to the user at relevant stages in the process.

The fundamental input to all life assessment routines is the service load history. Initially the original analogue field recordings of the data are digitized and stored in a service load history databank, under individual file-names, on computer disk. These digitized sequences representing specific operations (for example, digging, dumping, carrying, etc., for a loader) can be linked together to create appropriate duty cycles (Fig. 7) for subsequent analysis.

The analysis combines this history with relevant material data, an estimated K_T -value possibly from Ref 24, and Neuber's rule. Combining the loads shown in Fig. 7 with data for nodular iron from Ref 71 and at K_T of 3.0 results in the local stress-strain response and life estimate shown in Fig. 8. Reducing the severity of the local stress concentration (that is, the K_T from 3.0 to 2.2) for the same application results in the stress-strain response in Fig. 9. This reduction in concentration factor has led to a life increase of 33 times.

This process of changing the basic parameters can be continued endlessly. The strength of this approach is based on this facility. Many materials can be considered, local geometry changes assessed, and the effects of variations in load history or service duty cycles can be quantified. Hence many problems can be forecast and forestalled before expensive prototype or service trials are undertaken.

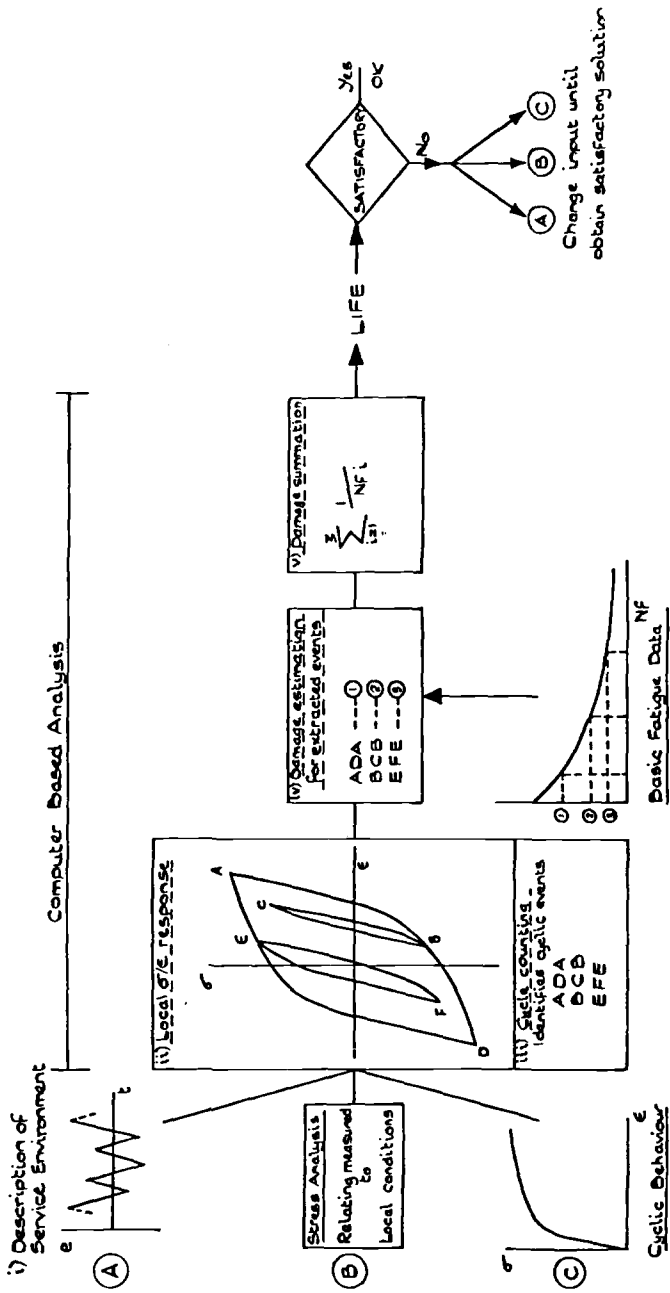
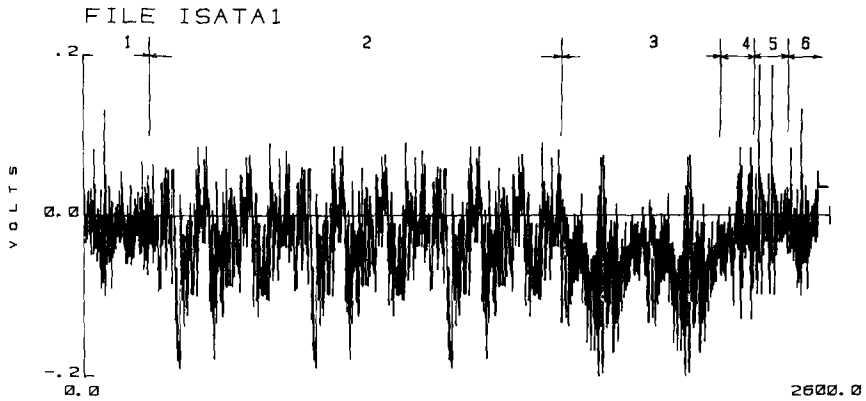


FIG. 6—Elements of fatigue life prediction procedure.



- 1 ... Empty running across quarry
- 2 ... 3 x Load & dump sequences
- 3 ... 2 x Load carrying across quarry sequences
- 4 ... 2 x Carrying load up grade sequences
- 5 ... 2 x Carrying load down grade with severe brake
- 6 ... Empty running across quarry

FIG. 7—Sample of digitized load history.

LOADER - FRONT AXLE - AREA 1 - RUN 112

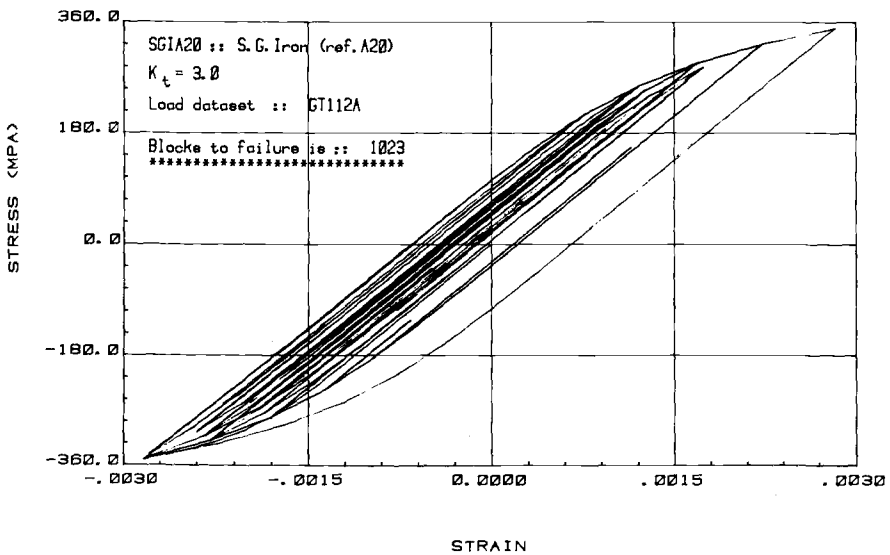


FIG. 8—Local stress-strain response and predicted life.

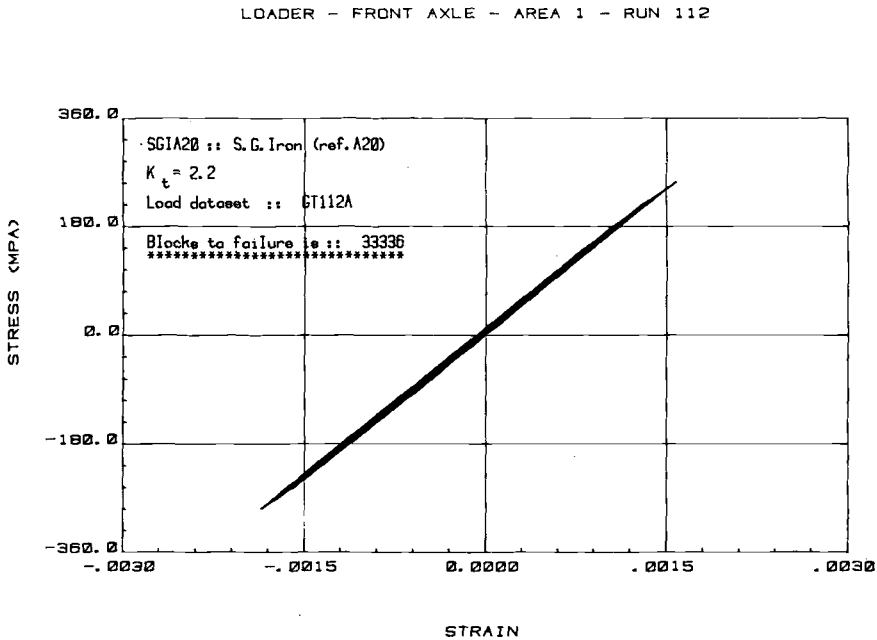


FIG. 9—Local stress-strain response and predicted life.

Routines have been developed (for example, Refs 72 and 53) that use component test data. Thus the vast store of fatigue data, stress analysis knowledge, and material properties that have been generated over the past century can be utilized by such methods.

Concluding Remarks

Fatigue has always been a problem in ground vehicles and it is difficult to take an optimistic view of its future role. However, methods are available which could significantly reduce its importance and allow more efficient designs. The lessons of the past must not be forgotten nor must the vast store of fatigue data. Many current problems have been studied before. Many recent innovations could have been introduced previously. Modern computers can be the basis of new methods, but they also can be used as a means of utilizing the results of more than a century of research into the phenomenon of metal fatigue in ground vehicle components.

Acknowledgments

The authors would like to thank Dr. T. L. Johnston, Corporate Director of Technology, GKN, for permission to publish this paper. We would also like

to acknowledge the debt we owe to J. Y. Mann, Aeronautical Research Laboratories, Melbourne, Australia, whose two magnificent books [73,74] have made it possible to learn from the past.

References

- [1] Beaumont, W. Worley, discussion to "The Strength of Wrought-Iron Railway Axles" by T. Andrews, *Transactions of the Society of Engineers*, Oct. 1879, pp. 143-178.
- [2] Andrews, T., "The Effect of Strain on Railway Axles and the Minimum Flexion Resistance Point in Axles," *Transactions of the Society of Engineers*, Nov. 1895, pp. 181-234.
- [3] "Fatigue Phenomena in Metals," *Scientific American Monthly*, Vol. 1, No. 3, March 1920, pp. 221-226.
- [4] Moreau, R. A. and Peterson, L., "Field Testing of Diesel Locomotive Axles," in *Proceedings*, Society for Experimental Stress Analysis, Vol. XIII, No. 2, 1955, pp. 27-38.
- [5] Magee, G. M. and Ferguson, Rondon, "Applications of Electric Measuring Equipment in Railroad Research," in *Proceedings*, Society of Experimental Stress Analysis, Vol. II, No. 1, 1944, pp. 1-8.
- [6] "Report of the Commissioners Appointed to Inquire into the Applications of Iron to Railway Structures," William Clowes and Sons, London, 1847.
- [7] Hill, H. N., "Some Experience in Experimental Stress Determined at the Aluminum Research Laboratories," in *Proceedings*, Society for Experimental Stress Analysis, Vol. II, No. 1, 1944, pp. 18-33.
- [8] Tucker, M., "Vibratory Stress Measurement in Aircraft Engine Parts," in *Proceedings*, Society for Experimental Stress Analysis, Vol. I, No. 1, 1943, pp. 37-40.
- [9] Meier, J. H., "Some Aspects of Observing the Performance of Large Machinery under Operating Conditions," in *Proceedings*, Society for Experimental Stress Analysis, Vol. I, No. 2, 1944, pp. 11-17.
- [10] Goloff, A., "Determination of Operating Loads and Stresses in Crankshafts," in *Proceedings*, Society for Experimental Stress Analysis, Vol. II, No. 2, 1944, pp. 139-149.
- [11] Wallace, W. A. and Cassler, W. A., "Device for Maintaining Continuous Electrical Connections with Reciprocating Engine Parts," in *Proceedings*, Society for Experimental Stress Analysis, Vol. IX, No. 1, 1952, pp. 65-76.
- [12] Colwell, A. W., "Mobile Instrumentation for Automotive Equipment," in *Proceedings*, Society for Experimental Stress Analysis, Vol. IX, No. 1, 1952, pp. 65-76.
- [13] Polzin, M. H., "Performance Evaluation of a Magnesium Alloy Truck Wheel," in *Proceedings*, Society for Experimental Stress Analysis, Vol. XI, No. 1, 1953, pp. 65-80.
- [14] Motor Industry Research Association, "Vehicle Service Loads-Development of Instrumentation and Test Techniques," MIRA Report No. 1967/4, May 1967.
- [15] Orme, R. W., Penfold, G. F., and Thomas, K. R., "Telemetry System for Data Acquisition from Test Vehicles," Paper 690727, presented at SAE Mississippi Valley Section, Davenport, Iowa, May 1969.
- [16] Parsons, R. H., "A History of the Institution of Mechanical Engineers, 1847-1947," Institution of Mechanical Engineers, 1947, p. 97.
- [17] Rankine, W. J. M., "On the Causes of the Unexpected Breakage of the Journals of Railway Axles; and on the Means of Preventing Such Accidents by Observing the Law of Continuity in their Construction," in *Proceedings*, Institute of Civil Engineers, Vol. 2, 1943, pp. 105-108.
- [18] Kirsch, B., *Z. VDI*, 16 July 1898, p. 797.
- [19] Inglis, C. E., "Stresses in a Plate due to the Presence of Cracks and Sharp Corners," *Transactions of the Institution of Naval Architects*, Vol. 55, 1913, pp. 219-242.
- [20] Howland, R. C. J., "On the Stresses in the Neighbourhood of a Circular Hole in a Strip Under Tension," *Philosophical Transactions of the Royal Society (London) A*, Vol. 229, 1929-30, p. 67.
- [21] Baud, R. V., "Study of Stresses by Means of Polarised Light and Transparencies," in *Proceedings*, Engineers Society of Western Pennsylvania, Vol. 44, 1928, p. 199.
- [22] Jacobsen, L. S., "Torsional Stress Concentration in Shafts of Circular Cross-Section and

- Variable Diameter," in *Transactions of the American Society of Mechanical Engineers*, Vol. 47, 1925, p. 219.
- [23] Peterson, R. E., "Stress Concentrations and Fatigue Strength," Appendix to the Report of the Research Committee, in *Proceedings*, American Society for Testing and Materials, Vol. 30, Part 1, 1930, pp. 298-310.
 - [24] Peterson, R. E., *Stress Concentration Factors*, Wiley, New York, 1974.
 - [25] Stowell, E. Z., "Stress and Strain Concentration at a Circular Hole in an Infinite Plate," Technical Note 2073, National Advisory Committee for Aeronautics, 1950.
 - [26] Neuber, H., "Theory of Stress Concentration for Shear Strained Prismatic Bodies with Arbitrary Non-Linear Stress-Strain Law," *Transactions of the American Society of Mechanical Engineers*, Series E, Vol. 28, Dec. 1961, pp. 544-550.
 - [27] Topper, T. H., Wetzel, R. M., and Morrow, J., "Neuber's Rule Applied to Fatigue of Notched Specimens," *Journal of Materials*, Vol. 4, No. 1, March 1969.
 - [28] Wohler, A., "Versuche zur Ermittlung der auf die Eisenbahnwagen-Achsen einwirkenden Kräfte und der Widerstandsfähigkeit der Wagen-Achsen," *Zeitschrift fuer Bauwesen*, Vol. 10, 1860, pp. 583-616.
 - [29] Gerber, W., "Bestimmung der Zulässigen Spannungen in Eisen Konstruktionen," *Zeitschrift des Bayerischen*, Ver. 6, 1874, pp. 101.
 - [30] Goodman, J., *Mechanics Applied to Engineering*, Longmans, Green and Company, London, 1899.
 - [31] Basquin, O. H., "The Exponential Law of Endurance Tests," in *Proceedings*, American Society for Testing and Materials, No. 10, 1910, pp. 625-630.
 - [32] Ewing, J. A. and Humfrey, J. C. W., "The Fracture of Metals under Repeated Alterations of Stress," *Philosophical Transactions (A)*, Vol. 200, 1902, pp. 241-250.
 - [33] Peterson, R. E., "Fatigue of Metals-Part 3-Engineering and Design Aspects," *Materials Research and Standards*, American Society for Testing and Materials, Feb. 1963, pp. 122-139.
 - [34] *Engineering (London)*, 23 Aug. 1867, p. 160.
 - [35] Bauschinger, J., "Mittheilungen aus dem Mechanisch-technischen Laboratorium," *Technischen Hochschule in München*, Vol. 13, No. 8, 1886, pp. 1-115.
 - [36] Unwin, W. C., "A New View of the Nature of the Resistance of Materials to Repeated Loads," *Engineering (London)*, Vol. 62, 10 Dec. 1886, p. 457.
 - [37] Stanton, T. E. and Bairstow, L., "The Resistance of Materials to Impact," in *Proceedings*, Institute of Mechanical Engineers (London), Parts 3/4, 1908, pp. 889-919.
 - [38] Bairstow, L., "The Elastic Limits of Iron and Steel under Cyclical Variations of Stress," *Philosophical Transactions (A)*, Vol. 210, 1909-1910, pp. 35-55.
 - [39] Smith, J. H. and Wedgewood, G. A., "Stress-Strain Loops for Steel in the Cyclic State," *Journal of the Iron and Steel Institute*, Vol. 91, No. 1, 1915, pp. 365-397.
 - [40] Frost, N. E., "The Current State of the Art of Fatigue: Its Development and Interaction with Design," presented at Society of Environmental Engineers Fatigue Group Conference, Oct. 1974, London.
 - [41] Morrow, JoDean in *Fatigue Mechanisms*, ASTM STP 675, American Society for Testing and Materials, 1978, pp. 891-892.
 - [42] Coffin, L. F., "A Study of the Effects of Cyclic Thermal Stresses on a Ductile Metal," *Transactions of the American Society for Testing and Materials*, Vol. 76, 1954, pp. 931-950.
 - [43] Manson, S. S., "Behaviour of Materials under Conditions of Thermal Stress," *Heat Transfer Symposium*, University of Michigan Engineering Research Institute, 1953, pp. 9-75.
 - [44] Paris, P. C., Gomez, M. P., and Anderson, W. E., "A Rational Analytic Theory of Fatigue," *The Trend in Engineering*, 1961, Vol. 13, p. 9.
 - [45] Albert, W. A. J., "Über Treibseile am Harz," *Archiv für Mineralogie, Geognosie, Bergbau und Hüttenkunde*, Vol. 10, 1838, pp. 215-234.
 - [46] Almen, J. O. and Boergehold, A. C., "Rear Axle Gears: Factors which Influence their Life," in *Proceedings*, American Society for Testing and Materials, Vol. 35, Part 2, 1935, pp. 99-146.
 - [47] "Passenger Car Axle Tests, 5½" × 10" Journals," First Progress Report, Association of American Railroad Operations and Maintenance Department, Mechanical Division, May 1938, p. 22.
 - [48] Buckwalter, T. V., Horger, O. J., and Sanders, W. C., "Locomotive Axle Testing," *Trans-*

- actions of the American Society of Mechanical Engineers, Vol. 60, No. 4, May 1938, pp. 335-345.
- [49] Bardour, K., "Dauerhaltbarkeit von Stahl-und Gusskurbelwellen," *Deutsche Krallfahrt Jorschung*, No. 14, 1938.
 - [50] Love, R. J., "Fatigue in Automobiles," in *Proceedings*, International Conference on Fatigue of Metals, Institution of Mechanical Engineers, 1956.
 - [51] Mansion, H. D., "The Failure of Gears by Pitting: A Comparison of some Typical Gear Steels," MIRA Report No. 1951/8, 1951.
 - [52] Gassner, E., "Betriebsfestigkeit, eine Bemessungsgrundlage für Konstruktionsteile mit statistisch Wechselnden Betriebsbeanspruchungen Konstruktion, Vol. 6, No. 3, 1954, pp. 97-104.
 - [53] Dabell, B. J. and Watson, P. in *Proceedings*, International Conference on Fatigue Testing and Design, Society of Environmental Engineers, London, April 1976, pp. 2.1-2.50.
 - [54] Marsh, K. J., "Full-Scale Testing of Components and Structures," in *Proceedings*, International Conference on Fatigue Testing and Design, Society of Environmental Engineers, London, April 1976, pp. 22.1-22.11.
 - [55] Palmgren, A., "Die Lebensdauer von Kugellagern," *ADVL* 68, 1924, p. 339.
 - [56] Miner, M. A., "Cumulative Damage in Fatigue," *Journal of Applied Mechanics*, Vol. 12, 1945, pp. 1-159.
 - [57] Schijve, J. in *Fatigue of Aircraft Structures*, Pergamon Press, London, 1963, pp. 115-150.
 - [58] Weber, D., "Working Stresses Related to Fatigue in Military Bridges," *Stresses in Service*, I.C.E., London, 1966, pp. 237-247.
 - [59] Haas, T., "Load Statistics as a Basis of Structural and Mechanical Design," *The Engineer's Digest*, Vol. 23, No. 3, March 1962, pp. 79-83.
 - [60] Matsuisaki, M. and Endo, T., "Fatigue of Metals Subjected to Varying Stress," paper presented at Kyushu District Meeting of Japan Society of Mechanical Engineers, March 1968.
 - [61] Watson, P. and Dabell, B. J., "Cycle Counting and Fatigue Damage," *Journal of the Society of Environmental Engineers*, Vol. 15-3, Sept. 1976.
 - [62] Landgraf, R. W. and Lapointe, N. R., "Cyclic Stress-Strain Concepts Applied to Component Fatigue Life Prediction," Paper No. 740280, Society of Automotive Engineers, Feb. 1974.
 - [63] Dabell, B. J., Hill, S. J., Eaton, D. E., and Watson, P., "Fatigue Life Prediction for Notched Components," *Journal of the Society of Environmental Engineers*, Dec. 1977.
 - [64] Dabell, B. J. and Hill, S. J., "The Use of Computers in Fatigue Design and Development," *International Journal of Fatigue*, Vol. 1, No. 1, 1979, pp. 29-35.
 - [65] Martin, J. F., Topper, T. H., and Sinclair, G. M., "Computer Based Simulation of Cyclic Stress-Strain Behaviour," *Materials Research and Standards*, ASTM, Vol. 11, No. 2, Feb. 1971, pp. 23-28.
 - [66] Jhansale, H. R., "A New Parameter for the Hysteretic Stress-Strain Behaviour of Metals," *Journal of Engineering Materials and Technology*, ASME, Jan. 1975, pp. 33-38.
 - [67] Wetzel, R. M., "A Method of Fatigue Damage Analysis," Ph.D. thesis, University of Waterloo, Canada, Sept. 1971.
 - [68] Topper, T. H. and Conle, A., "An Approach to the Analysis of the Non-Linear Deformation and Fatigue Response of Components Subjected to Complex Load Histories," *International Symposium on Experimental Mechanics*, University of Waterloo, June 1972.
 - [69] Jenkin, C. F., "A Mechanical Model Illustrating the Behaviour of Metals under Static and Alternating Loads," *Engineering (London)*, Vol. 114, 17 Nov. 1922, p. 603.
 - [70] Jenkin, C. F., "Fatigue of Metals," *Engineering (London)*, Vol. 134, 8 Dec. 1922, pp. 612-614.
 - [71] Watson, P. and Dabell, B. J., "A Realistic Computer-Based Fatigue Comparison of Spheroidal Graphite Cast Iron and Cast Steel," *International Journal of Fatigue*, Vol. 1, No. 2, April 1979, pp. 69-80.
 - [72] Haibach, E., "The Influence of Cyclic Material Properties on Fatigue Life Prediction by Amplitude Transformation," *International Journal of Fatigue*, Vol. 1, No. 1, Jan. 1979, pp. 7-16.
 - [73] Mann, J. Y., "Bibliography on the Fatigue of Materials, Components and Structures, Vol. 1, 1838-1950," Pergamon Press, London, 1970.
 - [74] Mann, J. Y., "Bibliography on the Fatigue of Materials, Components and Structures, Vol. 2, 1951-1960," Pergamon Press, London, 1978.

R. L. Jones,¹ T. U. Marston,¹ S. W. Tagart,¹
D. M. Norris,¹ and R. E. Nickell¹

Applications of Fatigue and Fracture Tolerant Design Concepts in the Nuclear Power Industry

REFERENCE: Jones, R. L., Marston, T. U., Tagart, S. W., Norris, D. M., and Nickell, R. E., "Applications of Fatigue and Fracture Tolerant Design Concepts in the Nuclear Power Industry," *Design of Fatigue and Fracture Resistant Structures. ASTM STP 761*, P. R. Abelkis and C. M. Hudson, Eds., American Society for Testing and Materials, 1982, pp. 28-46.

ABSTRACT: To assure the integrity of nuclear power plant components, fatigue and fracture tolerant design concepts have been incorporated into Sections III and XI of the ASME Code; these contain requirements for nuclear power plant design, construction, and in-service inspection. The methods used in the Code to design against fatigue and brittle fracture are described together with the fracture mechanics based procedure suggested in Section XI for the evaluation of flaws detected by in-service inspections. Some aspects of the present Code methods that could probably be improved are identified.

KEY WORDS: nuclear power reactor, design, operation, in-service inspection, flaw, fatigue, fracture, evaluation

In the United States, the design of nuclear power plants is governed by Federal law (for example, Title 10 of the Code of Federal Regulations, Part 50), and by voluntary consensus standards [for example, Sections III and XI of the American Society of Mechanical Engineers (ASME) Boiler and Pressure Vessel Code] supplemented by ASME Code cases and by guidelines issued by the U.S. Nuclear Regulatory Commission (NRC). In essence, the ASME Code, the NRC regulations, and Federal law together are intended to provide a conservative basis for the safe design of nuclear plants.

Fatigue and fracture tolerant design, in the sense of assuring resistance to sudden and catastrophic component failure, has been the central objective of

¹Program Manager, Program Manager, Technical Specialist, Technical Manager, and Technical Specialist, respectively, Electric Power Research Institute, Palo Alto, Calif.

the ASME Code since its inception in 1914. This objective is especially important in Sections III and XI, since attaining and maintaining the integrity of the pressure boundary components has a crucial role in ensuring the safe and reliable operation of nuclear power plants. Currently, these sections include conservative procedures for designing against fatigue and for structural integrity and flaw evaluation analyses. This paper reviews some of the key elements in these procedures, with particular emphasis on those aspects that have recently undergone revision or are believed to be likely to be revised in the near future. For an excellent review of the historical development of the ASME Code approach to structural integrity assurance, the reader is referred to the paper by Yukawa [1].²

The ASME Boiler and Pressure Vessel Code (hereafter called the Code) was originally developed, and has continued to evolve, on an empirical basis; that is, the fundamental premise is the ability to identify, either from service experience or laboratory simulation, the potential failure modes of the mechanical components, and then to develop design and inspection rules that assure that each of these potential failure modes is prevented. In the early years of Code development, the relatively large number of boiler failures provided the practitioners with a straightforward means of distinguishing reliable design practice from unsafe practice, with the result that "design by formula" became the standard for boilers. The thicknesses obtained from such formulas, and the limits thus implied for pressure stresses, provided safety margin against ductile failure.

For structures of high reliability, ductile rupture becomes a rare event. During the past three decades, the need to identify less common failure modes for nuclear power plant equipment and to codify standards for prevention of these failure modes has dominated the ASME Code evolution. Section III of the Code, which governs the materials, design, fabrication, and pre-service inspection of nuclear power plant structures, is similar to its fossil plant counterpart—Section VIII, Division 2—in that design by analysis (as opposed to design by rule) is required. A difference, however, is the greater emphasis in Section III on fatigue as a failure mode. Also in Section III are rules for the prevention of brittle fracture and time-independent buckling. Time-dependent failure modes, such as those associated with elevated temperature operation—creep rupture, creep buckling, and creep-fatigue interaction—are considered in recent Nuclear Code Cases. With the exception of one reference curve in Section XI (discussed later), failure modes that are caused or influenced by environmental effects are not dealt with explicitly by the current Code; the designer is merely advised to take such effects into account. It is not entirely surprising, therefore, that corrosion-related failure modes are currently by far the most prevalent cause of component failures in nuclear power plants.

²The italic numbers in brackets refer to the list of references appended to this paper.

For the purposes of this discussion, the issues of concern are the rules governing design against fatigue failure, brittle fracture, and environmentally assisted crack growth. In the following sections we discuss the present state of development of the rules for Class 1 nuclear construction relative to each of these failure modes. The results of recent research that appear likely to lead to changes in the Code rules are also briefly summarized.

Fatigue Tolerant Design: ASME Code Section III

Fatigue failure is handled in Section III of the Code by requiring that cyclic strain be evaluated at all strain concentrating points in the component. This strain is usually evaluated on the basis of an elastic theory where strain is assumed to be linearly proportional to stress. The Code requires that a fatigue design $S-N$ curve be satisfied at all strain concentrating locations using a linear cumulative damage theory and a shear stress rule to provide an equivalent uniaxial stress. The major elements in the fatigue analysis are given in the Appendix. All of the anticipated cyclic loadings must be identified in the certified design specification for normal and upset loading conditions. Some provision for low-probability cyclic loading such as earthquake-induced cycling is usually also included in application of the Code fatigue analysis. The fatigue design $S-N$ curve is developed for each Code-acceptable base material by first performing uniaxial strain-controlled fatigue tests on small-size polished bar specimens in an air environment. Next, two types of correction (a mean stress correction and a temperature effect correction) are applied to the mean of this specimen data so that the modified polished bar data represent a realistic or conservative evaluation of the number of cycles required to initiate a fatigue crack at temperatures up to 644 or 700 K (700 or 800°F), depending on the type of material. The modified polished bar specimen data (represented by a mean smooth curve) are then converted into design fatigue curves (Fig. 1) by applying a reduction factor of 2 to the mean strain amplitude or 20 to the mean cycles, whichever factor leads to the greater conservatism.

A number of important assumptions are both explicit and implicit in the process of converting strain-controlled fatigue data to the Code design fatigue curves. These include the following:

1. The fatigue design curve is based on test data which measure chiefly fatigue crack initiation in smooth base material bars. Therefore additional Code rules are necessary to apply this design curve to cases where notches are present, where material is welded, or where strains are not accurately predicted from elastic stress analysis.
2. Environmental effects such as corrosion-assisted fatigue, stress corrosion cracking, or radiation damage are not accounted for in the present Code $S-N$ curves. Designers are assigned the responsibility for accounting for such environmental effects.

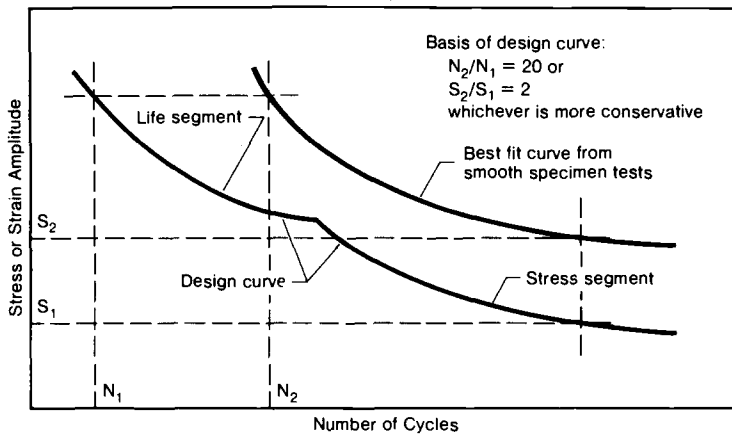


FIG. 1—The fatigue design curves of the ASME Code are obtained from the best-fit life curves for uniaxially loaded smooth specimens by applying a safety factor of 2 on stress or 20 on life, whichever is the more conservative at each point. The design curve therefore consists of two segments, as shown.

3. No credit is explicitly permitted in the Code to account for the crack growth stage that follows fatigue crack initiation and precedes failure in an actual component. An implicit credit is permitted for some sharply notched configurations where there is likely to be no significant crack initiation stage, such as at Code acceptable fillet welds or flaws missed by nondestructive evaluation (NDE).

4. Since the safety factors of 2 and 20 are applied to the mean of smooth bar data, it cannot be inferred that crack initiation in components will have a 2 and 20 safety factor. The reasons why the 2 and 20 factors do not translate to actual components are due to environmental effects, specimen data scatter, and surface finish effects as well as to inaccuracies in the Code rules that account for biaxial strain effects, cumulative damage, notch effects, and welding effects. As a consequence, the fatigue life to crack initiation of a component designed in accordance with ASME Section III does not have a well-defined safety margin.

5. The ASME Section III fatigue design curves presently extend from low to intermediate cycle ranges up to 10^6 cycles. The question of high-cycle fatigue design, involving stress reversals up to 10^{11} to 10^{12} cycles, is not explicitly covered by the Code.

6. Section III suggests rules for preventing plastic cycle ratcheting. Code Case N-196-1 provides rules for situations in which plastic ratcheting cannot be avoided that permit up to 5 percent localized strains to accumulate throughout the design fatigue life.

The basic fatigue design procedure which is in the ASME Code today appeared in the first issue of the Nuclear Vessel Code in 1961. Although nu-

merous interpretations and refinements have taken place over the years, the main aspects of the procedure have remained essentially unchanged. The philosophy which originally led to these Code fatigue rules recognized that a complete understanding of metal fatigue would not be achieved in the near future. (By complete understanding we mean deterministic forecasting of actual fatigue life without significant uncertainty.) Therefore careful judgment was necessary to account for the uncertainties that exist with any fatigue design procedure. Ongoing research and field experience were expected to indicate the need and provide the basis for evolutionary changes in the Code fatigue rules. A significant amount of information now suggests that chemical environmental effects not covered by the Code cause the majority of field failures. Therefore it would be highly desirable to develop an environmental fatigue procedure which would have sufficient generality to propose for Code adoption. Along with such a major step, it would seem prudent to consider other Code fatigue rule improvements to take advantage of the improved understanding of fatigue life that has developed over the past 20 years. For example, the cyclic crack growth stage that follows crack initiation and precedes component failure could now be explicitly accounted for (at least for inert environments). Specific acknowledgment of the crack growth stage would also permit a more rational treatment of fatigue by providing a means of dealing with flaws which escape detection in pre-service inspection.

The Electric Power Research Institute (EPRI) has sponsored research [2] to evaluate the Code treatment of biaxial loading effects. That work was completed recently and the results indicate that up to a 15 percent nonconservative effect (in terms of allowable strain range) is present in the Code rules. In addition, EPRI is currently sponsoring research [3] to broadly examine the fatigue behavior of carbon steel piping with emphasis on the potential environmental effects of reactor coolants. This research program is also examining notch effects, environmental crack growth behavior, and possible improvements to the ASME fatigue design procedure for carbon steel piping. Other EPRI projects are generating crack growth data for pressure vessel steels [4], stainless steels [5,6], and other nuclear plant structural materials.

In summary, we believe that serious consideration should be given in the near future to major improvements in the ASME Code fatigue design procedures; EPRI research activities in support of such revisions have already been initiated.

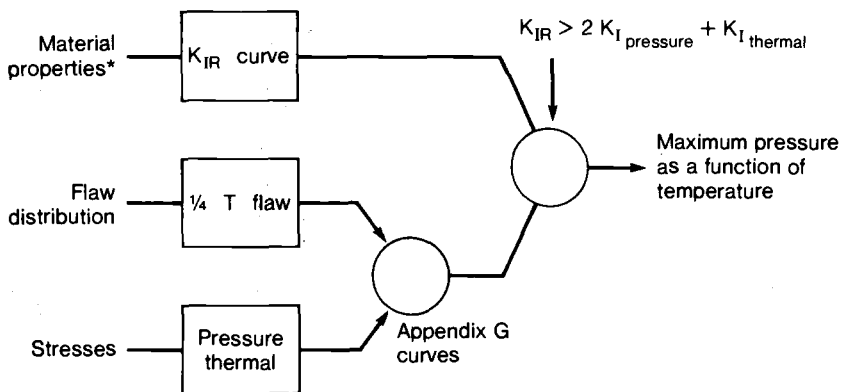
Fracture Tolerant Design: ASME Code Sections III and XI and 10 CFR Part 50

As previously stated, ductile failure or collapse of nuclear components is avoided by assuring that the primary stresses are small compared with the strengths of the construction materials. Nonductile or brittle fracture can oc-

cur at these small stress levels if the material is sufficiently brittle, but Section III (NB 2300) specifies minimum toughness (Charpy) properties for construction materials and therefore ensures ductile behavior through material selection. With the general acceptance of linear elastic fracture mechanics (LEFM) in the 1960s, the Code adopted additional procedures to further reduce the likelihood of nonductile failure. The first area of LEFM application is in Section III, the design portion of the Code, where fracture mechanics concepts are used to establish the allowable pressure-temperature limits for operation of a nuclear installation. The procedure is schematically presented in Fig. 2 and originally appeared in the form of a nonmandatory appendix, Appendix G. A virtually identical procedure appears in 10 CFR Part 50, thus making the procedure no longer optional, but part of Federal law. LEFM is also utilized in Section XI of the Code, the in-service inspection portion, as the basis for evaluating flaws discovered during reactor service. This procedure is described in the next section of this paper.

The fracture mechanics analyses of Sections III and XI use reference curves to estimate the available fracture toughness of pressure vessel steels as a function of temperature. The Code reference curves (and supporting data) appear in Figs. 3 and 4. The reference toughness curves K_{Ia} (Section XI) and K_{IR} (Section III) are identical. Note that these curves are referenced to a temperature called " RT_{NDT} ," The Reference Temperature for the Nil Ductility Transition. The RT_{NDT} -concept is supposed to remove the heat-to-heat and material-to-material variability of pressure vessel steels. The RT_{NDT} of a material is determined from a combination of Charpy impact and drop weight testing. The details of the procedure are contained in paragraph NB 2331 of Section III of the ASME Code.

Although the intent of the RT_{NDT} -approach is to remove variability, recent



*Includes RT_{NDT} shift due to irradiation

FIG. 2—ASME Code Section III structural integrity analysis.

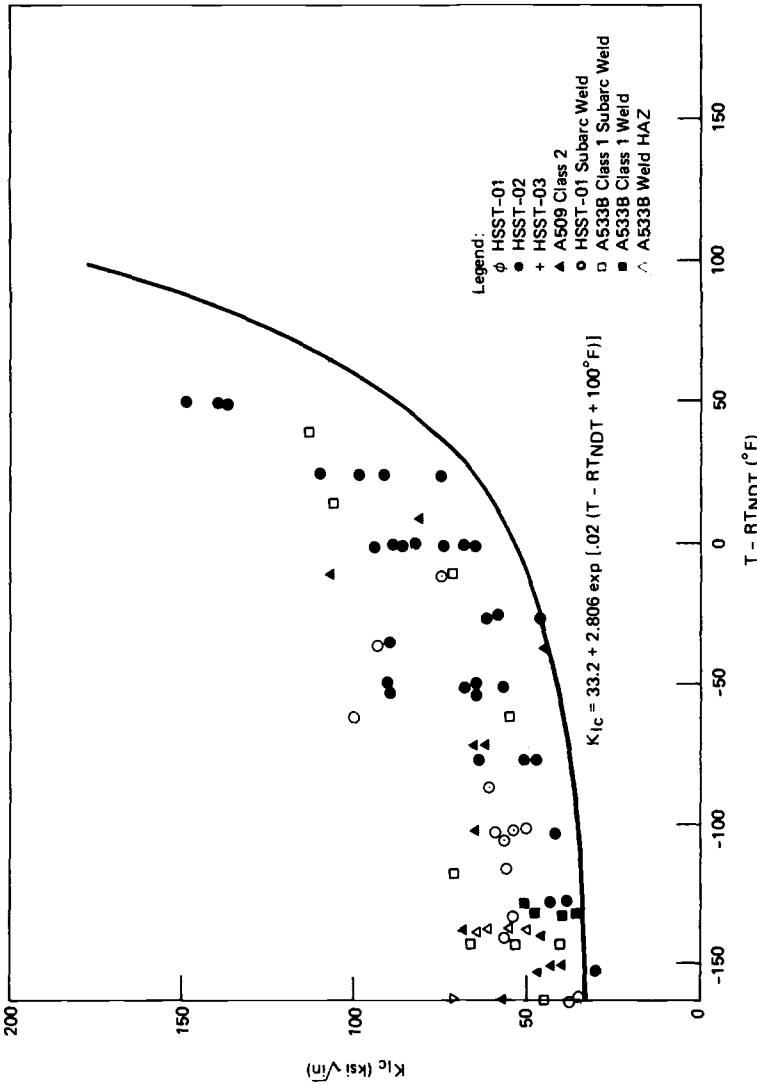


FIG. 3— K_{Ic} reference toughness curve with supporting data (conversion factors: $1 \text{ ksi}\cdot\text{in.}^{1/2} \approx 1.098 \text{ MPa}\cdot\text{m}^{1/2}$; $T_K = (5/9)(T_F + 459.67)$).

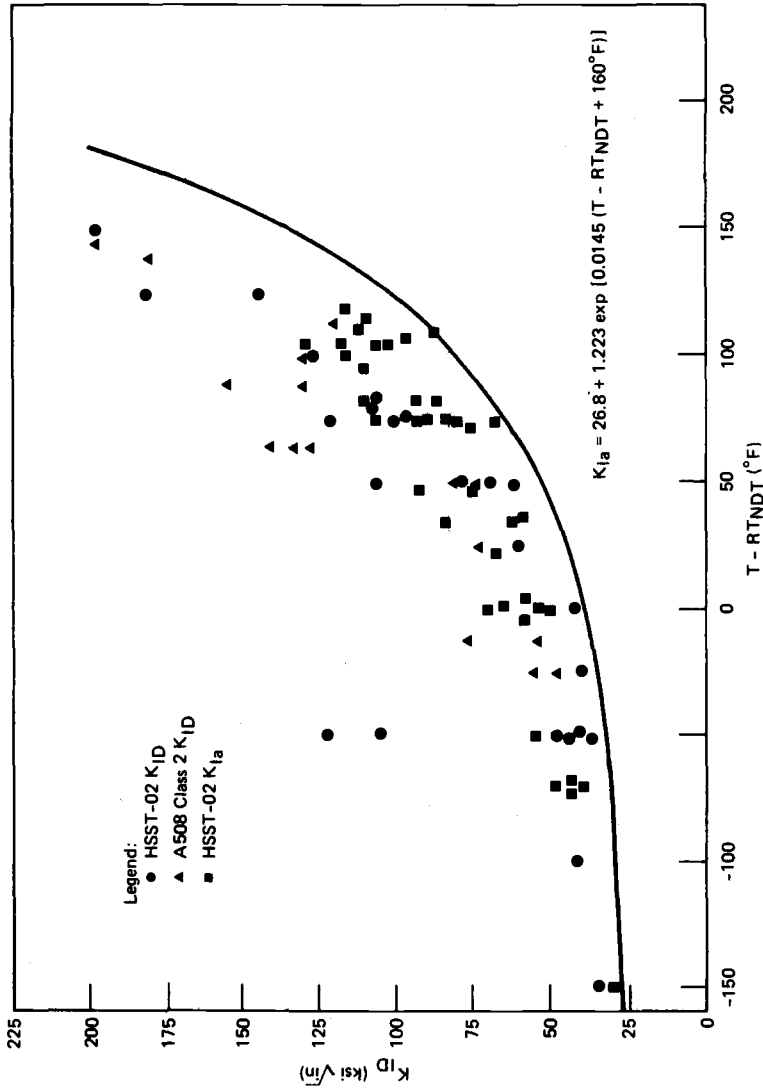


FIG. 4— K_{Ia} reference toughness curve with supporting data (conversion factors: $1 \text{ ksi} \cdot \text{in.}^{1/2} = 1.098 \text{ MPa} \cdot \text{m}^{1/2}$; $T_K = (T_F)/T_F = 459.67$).

results [7] indicate this goal is not in fact achieved. For a large base of fracture toughness data, the scatter has been shown to be greater when the data are plotted against RT_{NDT} than when they are plotted against test temperature. In addition, the present method assumes that the shape of the toughness curve is constant for all applicable materials and the upper shelf (or maximum) toughness level is not defined. Additional problems arise when one estimates irradiated fracture toughness by simply translating the reference curves by the radiation-induced shift in the Charpy impact properties.

An alternative approach to the K_{IR} and K_{Ia} procedure is presently being evaluated for incorporation into the ASME Code. This method, developed by Oldfield [8], uses statistical techniques to transform Charpy impact data to fracture toughness. The procedure is illustrated in Fig. 5. The toughness-temperature data for a number of typical reactor vessel materials are fitted to a hyperbolic tangent function that approximates the physical behavior. Charpy data from the same heats of material are then statistically analyzed and, with reasonable probabilistic assumptions, conversion factors are generated to transform the coefficients of the Charpy fit to corresponding coefficients for fracture toughness-temperature curve. The fracture toughness-temperature response of any given vessel material can then be estimated from its measured Charpy transition curve using these conversion factors. Conversion factors are now available to provide average toughness estimates, as well as to develop fracture toughness-temperature curves to specified confidence or tolerance levels.

This procedure is being evaluated by the industry technical committee responsible for the development of improved reference toughness curves for the ASME flaw evaluation procedures. Work is also progressing to assess the use of this method for predicting the fracture toughness of irradiated materials from a knowledge of their irradiated Charpy impact behavior.

Fatigue Crack Growth Analysis: ASME Code Section XI

Section XI of the Code specifies in-service inspection (ISI) requirements for nuclear power plant components and contains acceptance standards for evaluation of any flaws detected in such inspections. The technical basis underlying these acceptance standards is described in Ref. 9. In establishing the standards, primary consideration was given to satisfying the Code provisions for protection against brittle fracture contained in Appendix G to Section III, which were described in the previous section and are illustrated in Fig. 2.

If ISI reveals the presence of a flaw that exceeds the Section XI acceptance limits, the component must either be retired or repaired (using one of five prescribed procedures), or an analysis must be performed to demonstrate that an adequate safety margin exists for continued operation. Appendix A to Section XI describes a nonmandatory analysis procedure suitable for

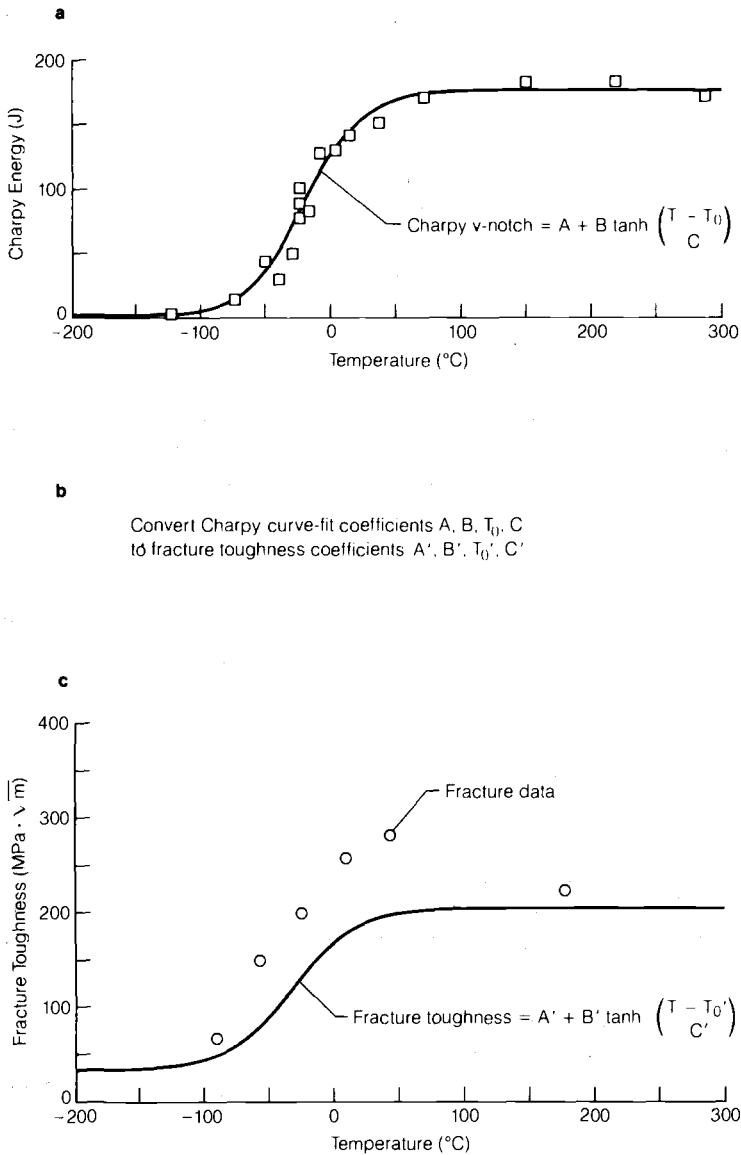


FIG. 5—Schematic for the fracture toughness estimation scheme. Charpy impact data are fitted with an analytic function (a) and corresponding coefficients are determined (A, B, T_0, C). These coefficients are adjusted (b) by statistical functions developed in this research. These adjusted coefficients then describe an estimated fracture toughness curve (c) for the same material. Actual fracture toughness data are plotted to indicate the accuracy of the estimated curve. The curve indicated in (c) is a tolerance bound (limit) indicating that with 90 percent confidence, 90 percent of the fracture toughness data lie above the curve (conversion factor: $T_K = T_C + 273.15$).

detailed evaluation of flaws in heavy-section steel components such as the reactor vessel, and an equivalent analysis procedure suitable for piping is currently under development. The Appendix A procedure is illustrated schematically in Fig. 6. In essence Appendix A is a simple structural integrity analysis based on linear elastic fracture mechanics that includes consideration of flaw growth due to fatigue and uses the reference toughness curves discussed earlier to assess the acceptability of the margin to fracture for the end-of-life flaw predicted by the growth analysis. Sample problems showing the use of the Appendix A procedure can be found in Ref 10. In this section of the paper we will focus on the fatigue crack growth prediction part of the procedure.

The fatigue crack growth analysis procedure in Appendix A can be summarized as follows:

1. The flaw is assumed to be of a simple elliptical shape and to lie in a plane perpendicular to the line of action of the principal tensile stress.
2. The cyclic stresses at the flaw are calculated for each anticipated normal, upset, and test transient.
3. The range of the stress intensity factor, ΔK , at the crack tip due to the first transient is calculated.
4. The incremental flaw growth, Δa , corresponding to one cycle at the stress intensity range, ΔK , is calculated from a crack growth equation:

$$\Delta a = C (\Delta K)^m$$

where C and m are constants given in the Code in the form of reference curves for both subsurface flaws (inert environment) and internal surface flaws (water reactor environment).

5. The crack depth is updated to $a + \Delta a$. The procedure then returns to Step 3 for the second transient and so on until all the transients expected to occur during the remaining reactor life are completed and the end-of-life crack depth is obtained.

This analysis procedure is expected to substantially overpredict fatigue crack growth in real components due to the use of conservative flaw shapes, loads, and stress intensity factor solutions in the first three steps. Moreover, the simple additive summation of crack growth increments employed in Step 5 ignores the crack growth retardation effects that are expected to follow the larger load transients. However, it is difficult to quantify the conservatism of the procedure, particularly for the surface flaw case, because of uncertainties associated with the crack growth reference curves used in Step 4.

The fatigue crack growth reference curves were formulated in 1972 using all pertinent data available at that time. Considerable data were available for an air environment (Fig. 7). An upper-bound line was drawn above these data and became the Section XI fatigue crack growth reference curve for a

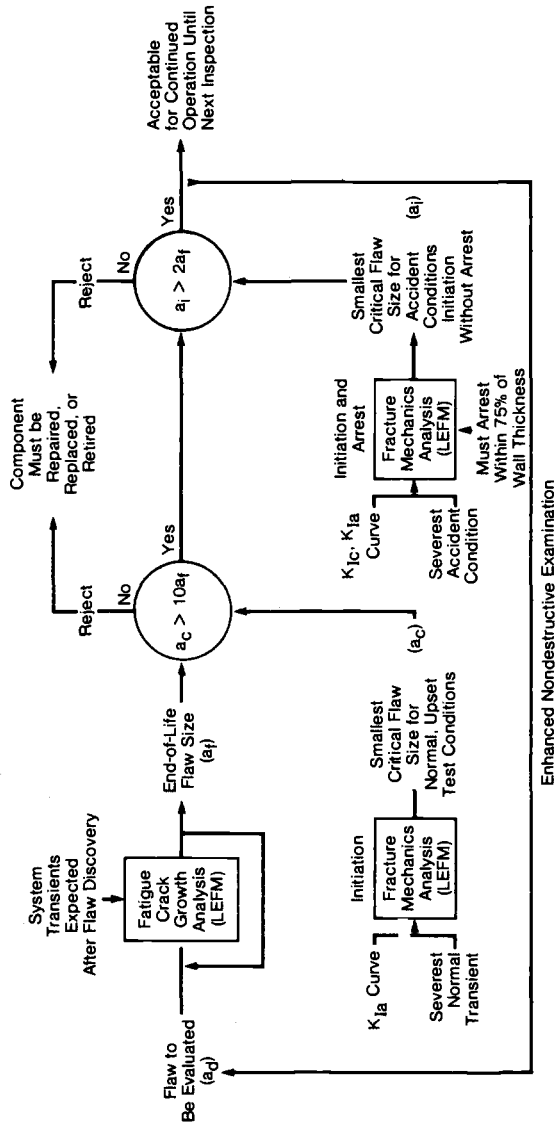


FIG. 6—Schematic representation of Appendix A flaw evaluation process.

subsurface flaw. The curve was based on data from Refs 11 and 12. Recent data obtained by Dowling [13] and others have shown that the air environment curve remains a good representation. The effect of a water environment on fatigue crack growth had been studied by Paris et al [12] and Mager and McLaughlin [14]. These investigations were conducted at frequencies of 1 Hz or greater, and indicated no significant effects of environment, R -ratio (K_{\min}/K_{\max}), or material type. However, in early 1972, Kondo et al [15] reported data showing that crack growth rates for reactor pressure vessel steels in high-temperature aqueous environments increased significantly at lower test frequencies. Further testing conducted by Legge and Mager [16] at a frequency of 0.0167 Hz verified this effect. As shown in Fig. 7, very few low-frequency data were available at the time of the formulation of the Appendix A reference curve. Consequently, as an interim step, a crack growth curve was drawn parallel to the air environment curve, which was a bound to the available low-frequency water environment data and predicted that surface flaws would grow ten times as fast as subsurface flaws for equivalent loading conditions. Data obtained subsequently at low cyclic frequencies [17,18] have shown that this interim crack growth curve does not represent an upper bound to the crack growth behavior at high values of R -ratio for a water environment.³ Furthermore, the more recent crack growth data display a bi-linear form (Fig. 8) which is in contrast to the single slope displayed by the air data in a log-log plot (Fig. 7).

As a consequence of the new data, the crack growth reference curve for surface flaws is currently undergoing revision. The proposed revision is shown in Fig. 9. The form is bi-linear and two curves are used to explicitly account for the effect of R -ratio. Unlike the previous bounding curve approach, the new reference curves are based on 95 percent global confidence limits on the mean of the currently available data.

It is likely that the treatment of environmentally assisted fatigue crack growth now embodied in Appendix A will undergo further revision in the future as our understanding of the processes involved improves. The effects of R -ratio and frequency are not quantitatively understood at present, and it is therefore of concern that many of the reactor transients of interest lead to loadings that combine high R -ratios, low frequencies, and small ΔK 's, which is the most difficult regime to access in laboratory tests. Predictions of crack rates in this regime involve substantial extrapolations of the laboratory data that are of questionable validity in view of our present inability to explain some aspects of the behavior observed in the laboratory tests. For example, in very recent work [19] it has been convincingly demonstrated that a given combination of ΔK , R , frequency, temperature, and water chemistry is *not*

³A note was added to Appendix A in the summer 1977 addendum to the ASME Code to reflect this information.

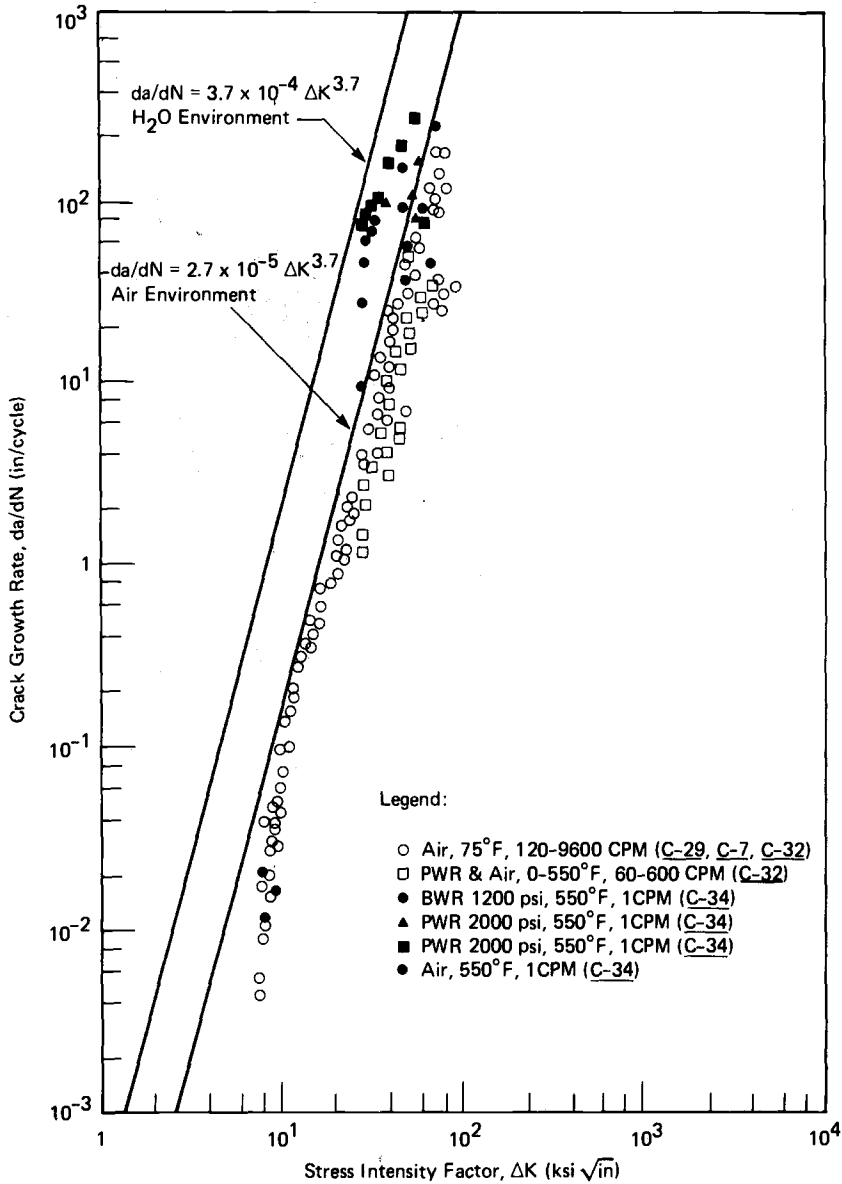


FIG. 7—Fatigue crack growth of A533B steel (ASME Code, Section XI) (conversion factors: 1 ksi·in.^{1/2} = 1.098 MPa·m^{1/2}; 1 in. = 25.4 mm).

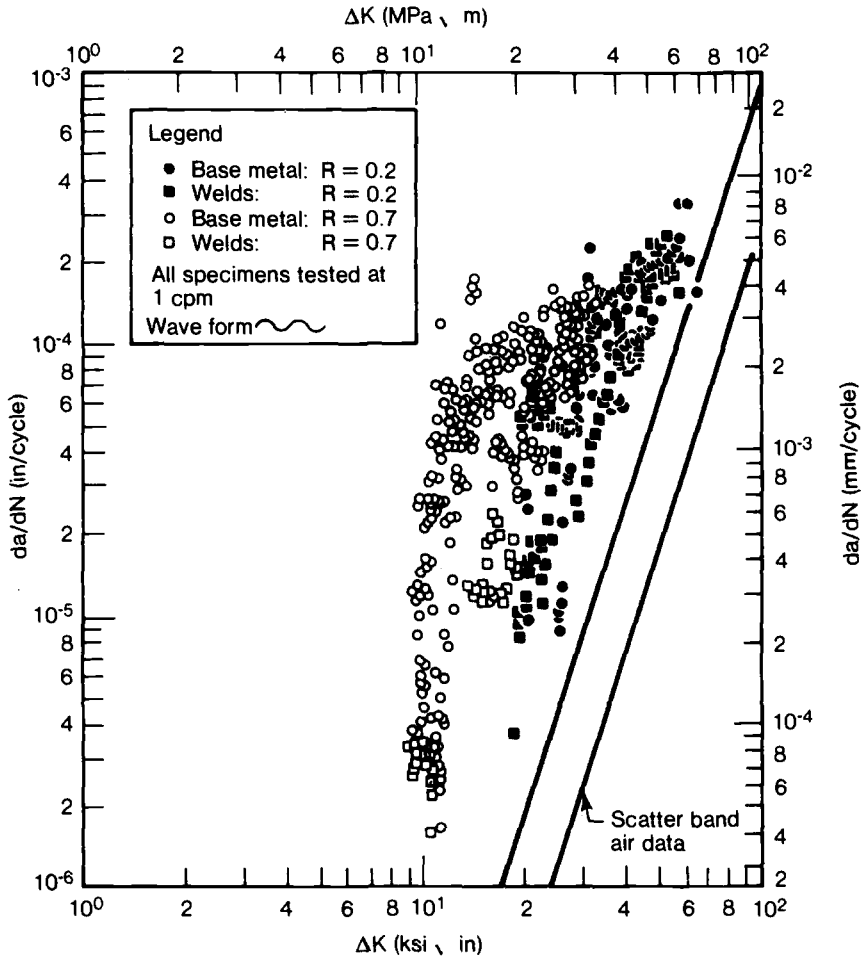


FIG. 8—Effect of R -ratio on crack growth rate—base metal and welds in a PWR environment.

associated with a unique value of crack growth rate: in the course of a test in which ΔK , R , frequency, temperature, and water chemistry were all held constant, a range of crack growth rates spanning an order of magnitude was observed. Thus at least one variable in addition to those already known to be important can exert a major influence on the rate of environmentally assisted crack growth in pressure vessel steels exposed to reactor coolant. We expect that the results of ongoing NRC- and EPRI-sponsored programs on cyclic crack growth will identify the additional variable(s) and also will generate further information on other areas of current uncertainty, such as the effect of neutron irradiation.

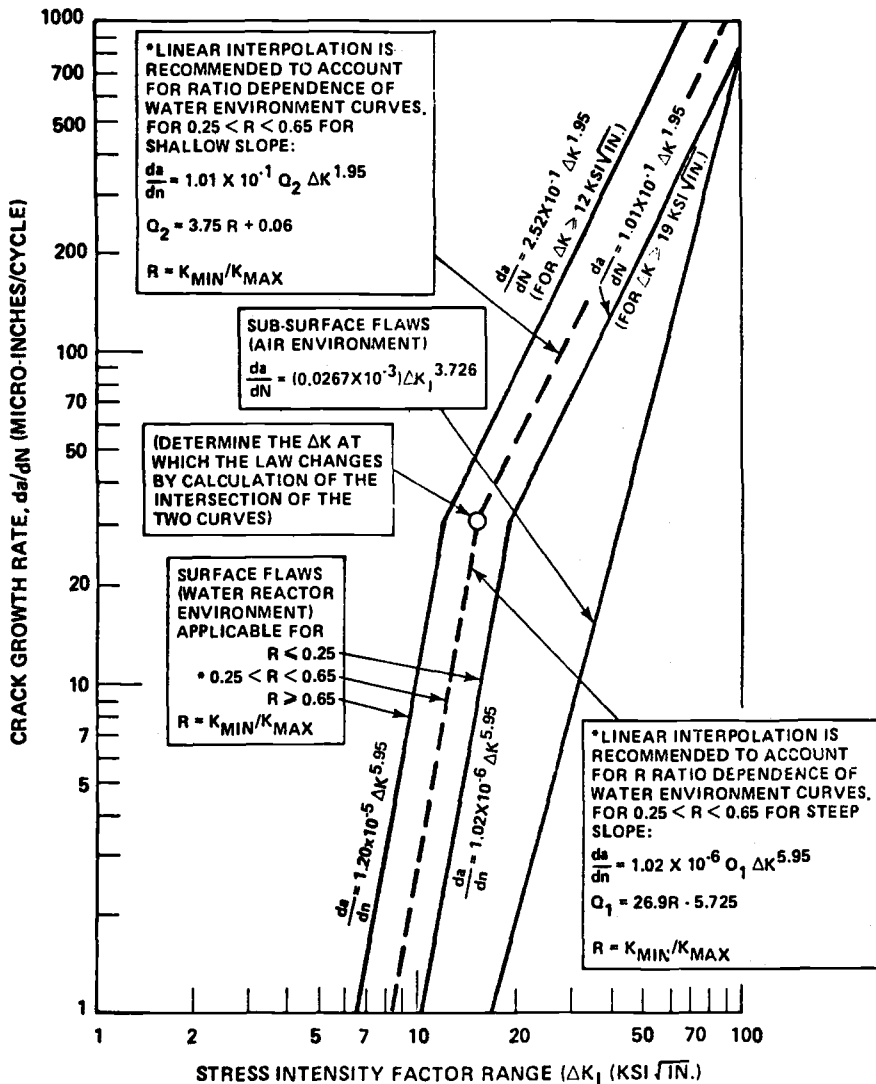


FIG. 9—Proposed reference fatigue crack growth curves for carbon and low-alloy ferritic steels (conversion factors: $1 \text{ ksi} \cdot \text{in.}^{1/2} = 1.098 \text{ MPa} \cdot \text{m}^{1/2}$; $1 \text{ in.} = 25.4 \text{ mm}$).

Summary

To assure the integrity of pressure-retaining components in nuclear power plants, fatigue and fracture tolerant design concepts have been incorporated into Sections III and XI of the ASME Code which, in conjunction with the Code of Federal Regulations and NRC guidelines, specify requirements for plant design, materials, construction, operation and in-service inspection.

The treatments of fatigue and fracture currently used by the nuclear industry are expected to be conservative, but the margins against failure provided by today's design practices are often poorly defined. Accordingly, it is anticipated that future developments will emphasize refinements that allow safety factors to be estimated more exactly.

Design against fatigue is considered in Section III of the ASME Code. Rules are provided for assessing fatigue damage at strain concentrating locations and for comparing the total damage accumulated at a given location during component life with the tolerance of the material expressed in the form of a design curve that shows allowable combinations of strain range and number of stress reversals. These material-specific design curves are derived from smooth specimen fatigue life data and include large safety margins to account for factors not explicitly treated in the fatigue analysis, such as surface finish and life reduction due to material-environment interactions. The fatigue design procedure is now nearly 20 years old and could probably be improved. In particular, it would seem desirable to develop and incorporate an environmental fatigue procedure because chemical environmental effects appear to be involved in the majority of recent field failures.

The basic philosophy of the Code is to avoid brittle fracture through careful selection of materials of construction. For heavy-section steel components added assurance of margin against brittle fracture is provided by the inclusion of structural integrity analysis procedures in Sections III and XI that are based on linear elastic fracture mechanics concepts. Conservative assumptions of flaw shape, orientation, and loading are used to obtain higher than expected estimates of the driving force for brittle fracture which are compared with lower than expected estimates of the material's resistance, obtained from reference curves of fracture toughness versus temperature. An easily determined reference temperature (RT_{NDT}) is used to position the reference curve for any particular heat of material, but recent results have revealed some deficiencies in this approach. A new procedure is currently under consideration that shows promise of providing toughness estimates having less uncertainty than values obtained using the current Code-accepted method.

Flaw growth due to fatigue loading of heavy-section steel components is considered in Appendix A of Section XI for evaluation of flaws discovered by in-service inspection. The material property input to the analysis is in the form of curves relating crack growth rate in low-alloy steels to stress intensity range. Two curves are provided in Appendix A, one for surface flaws (water environment), the other for buried flaws (inert environment). Data generated in the eight years since the curves were formulated have lent additional support to the inert environment curve, but have indicated the need for the development of more complex treatment for the surface flaw case. New reference curves have been proposed for surface flaws that explicitly account for the ratio of the minimum to maximum stress in the loading cycle (R -ratio),

but the results of laboratory studies suggest that further revision of the Code treatment of environmentally assisted cyclic crack growth will probably be necessary in the future.

APPENDIX

Major Elements in the ASME Code Section III Fatigue Analysis

- Evaluate primary stresses, P , and secondary stresses, Q , and compare with Sm , $1.5 Sm$, and $3 Sm$.
- Evaluate cyclic ratcheting.
- Determine the apparent alternating stress amplitudes (actually strains) for each cyclic condition (n_1, n_2, \dots, n_i):

$$S_{a1} = \frac{K_{e1}K_t(P + Q)_1}{2} \quad \text{for } n_1 \text{ cycles}$$

$$S_{a2} = \frac{K_{e2}K_t(P + Q)_2}{2} \quad \text{for } n_2 \text{ cycles}$$

$$\vdots \quad \quad \quad \vdots \quad \quad \quad \vdots$$

$$S_{ai} = \frac{K_{ei}K_t(P + Q)_i}{2} \quad \text{for } n_i \text{ cycles}$$

- Use Code design fatigue S - N curve to determine allowable cycles, N_i , at each value of S_{ai} .
- Satisfy cumulative fatigue rule:

$$\frac{n_1}{N_1} + \frac{n_2}{N_2} + \dots \leq 1.0$$

where

Sm = tabulated allowable stress value in ASME Section III,

P = primary equivalent stress,

$(P + Q)_i$ = primary plus secondary equivalent stress range for cyclic condition n_i ,

$K_t(P + Q)_i$ = elastic calculated peak equivalent stress range for cyclic condition n_i , and

K_{ei} = elastic-plastic strain correction factor ≥ 1.0 and is assumed to be 1.0 if $P + Q \leq 3 Sm$.

References

- [1] Yukawa, S. in *Proceedings, Conference on Structural Integrity Technology*, American Society of Mechanical Engineers, 1979, pp. 29-38.

- [2] Garud, Y. S. in *Methods for Predicting Material Life in Fatigue*, American Society of Mechanical Engineers, 1979, pp. 247-263.
- [3] Ranganath, S., Kass, J., and Heald, J., "Fatigue Behavior of Carbon Steel Components in High-Temperature Water Environments," presented at International Symposium on Low-Cycle Fatigue and Life Prediction, Firminy, France, 23-25 Sept. 1980, to be published in *Low-Cycle Fatigue and Life Prediction, ASTM STP 770*.
- [4] Van Der Sluys, W. A., "Corrosion Fatigue Characterization of Reactor Pressure Vessel Steels," Second Semi-Annual Report on EPRI RP1325-1, Babcock and Wilcox Company, Alliance, Ohio, March 1980.
- [5] Ford, F. P. and Silverman, M., "Mechanisms of Environmentally-Enhanced Cracking," Second Semi-Annual Report on EPRI RP1332-1, General Electric Corporate Research and Development, Schenectady, New York, July 1979.
- [6] Horn, R. M., "Growth and Stability of Stress Corrosion Cracks in Large Diameter BWR Piping," Second Semi-Annual Report on EPRI RPT118-1, General Electric Nuclear Engineering Division, San Jose, Calif., July 1980.
- [7] Oldfield, W., "Fracture Toughness Correlations and Reference Curves," First Annual Report on EPRI RP1021-4, Materials Research and Computer Simulation, Goleta, Calif., April 1980.
- [8] Oldfield, W., *Journal of Testing and Evaluation*, Vol. 7, No. 6, 1979, pp. 326-333.
- [9] Maccray, R. R. and Quinn, J. R., "Nondestructive Examination Acceptance Standards," EPRI NP1406-SR, Electric Power Research Institute, May 1980.
- [10] Marston, T. U., Ed., "Flaw Evaluation Procedures: ASME Section XI," EPRI NP719-SR, Electric Power Research Institute, Aug. 1978.
- [11] Clark, W. G., Jr., *Journal of Materials*, Vol. 16, 1971, pp. 134-149.
- [12] Paris, P. C., Bucci, R. J., Wessel, E. T., Clark, W. G., Jr., and Mager, T. R. in *Stress Analysis and Growth of Cracks, ASTM STP 513*, American Society for Testing and Materials, 1972, pp. 141-176.
- [13] Dowling, N. E. in *Cracks and Fracture, ASTM STP 601*, American Society for Testing and Materials, 1976, pp. 19-32.
- [14] Mager, T. R. and McLaughlin, V. J., "The Effect of an Environment of High Temperature Primary Grade Nuclear Reactor Water on the Fatigue Crack Growth Characteristics of A533, Grade-B, Class 1 Plate and Weldment Material," HSST Technical Report 16, WCAP-7776, Oct., 1971.
- [15] Kondo et al, "Fatigue Crack Propagation Behavior of ASTM A533B and A302B Steel in High Temperature Aqueous Environment," HSST 6th Annual Information Meeting, Paper No. 6, 1972.
- [16] Legge, S. A. and Mager, T. R., "Effects of High Temperature Primary Reactor Water on the Subcritical Crack Growth of Reactor Vessel Steel, 1 Heavy Section Steel Technology Program Progress Report for Period Ending August 31, 1972," ORNL-4855, April 1973.
- [17] Bamford, W. H., "Effects of Reactor Vessel Fatigue Loading Cycles on Crack Growth," paper presented at 3rd Water Reactor Safety Information Meeting, Gaithersburg, Md., Oct. 1975.
- [18] Bamford, W. H., Moon, D. M., and Scott, K. V., "Evaluation of Critical Factors in Crack Growth Rate Studies of LWR Steels," paper presented at 4th Water Reactor Safety Information Meeting, Gaithersburg, Md., Oct. 1976.
- [19] Jones, R. L., "Cyclic Crack Growth in High Temperature Water—Results of a Testing Round Robin," paper presented at IAEA Specialists Meeting on Subcritical Crack Growth, Freiburg, West Germany, 13-15 May 1981.

Long-Life Damage Tolerant Jet Transport Structures

REFERENCE: Goranson, U. G., Hall, J., Maclin, J. R., and Watanabe, R. T., "Long-Life Damage Tolerant Jet Transport Structures," *Design of Fatigue and Fracture Resistant Structures*, ASTM STP 761, P. R. Abelkis and C. M. Hudson, Eds., American Society for Testing and Materials, 1982, pp. 47-87.

ABSTRACT: Criteria and procedures used in commercial aircraft design over the last two decades have produced long-life damage tolerant structures with a credible safety record. This has been achieved through diligent attention to detail design, manufacturing, maintenance, and inspection procedures. Recent updates of federal regulations governing fatigue and fail-safe strength evaluation of transport category airplane structures and advancements in the capability to analyze damaged structure have spurred new technological developments. Adaptation of traditional fatigue and fracture mechanics technologies plus a large test and service experience data base have led to development of technology control methods suitable for nonspecialist engineers.

Detection of damage before it becomes dangerous is the ultimate control in ensuring damage tolerance throughout the economic service life of the structure. Traditional damage growth and residual strength evaluations fail to incorporate damage detection parameters which influence maintenance planning. New technology is under development for proper recognition of damage detection opportunities in a fleet of aircraft with possible multiple cracking events and subjected to a multitude of inspections. Emerging damage tolerance rating systems provide efficient measurements of inspection activities and permit coordinated manufacturer/operator/certifying agency actions necessary to ensure continued structural airworthiness of existing and future jet transport fleets.

KEY WORDS: crack growth, damage detection, durability, fatigue, fracture, inspection, maintenance, residual strength

Federal regulations for fatigue and fail-safe certification of large commercial aircraft have recently been updated. This has accelerated development of more rational methods of assuring structural safety in the presence of unexpected fatigue, environmental deterioration, or accidental damage.

Engineering methods used in the design process of long-life damage tolerant aircraft structures have evolved over a long period of time and have been

¹Structural Damage Technology Staff, Boeing Commercial Airplane Company, Seattle, Wash. 98124.

supported by extensive testing and service experience. Major Boeing efforts during the last decade have been devoted to providing nonspecialist designers and stress engineers with durability and damage tolerance analysis methods similar to traditional strength checking procedures. Recognition of damage growth and consideration of damage at multiple sites is included in damage tolerance assessments of new and maturing transports, along with their impact on operator maintenance programs. Emerging new technology will provide more quantitative assessments of damage detection opportunities in a fleet of aircraft with possible multiple cracking events and subjected to a multitude of inspections.

Overview

A multitude of design considerations are involved in achieving structural integrity in commercial aircraft (Fig. 1). This overview is focused on structural damage tolerance and durability characteristics and their relationship to the maintenance and inspection program required to achieve a safe and economic operating life.

The damage tolerance design approach in the 1950s and 1960s was essentially based on multistructural member concepts, with established strength requirements for the failure or obvious partial failure of a single structural element. These fail-safe design concepts, supported by considerable testing, have worked well in the past and required diligent performance by the designer/manufacturer, operators, and regulatory agencies for continued safe operation (Fig. 2). Fatigue analyses and tests provided early indications of unexpected cracking requiring modifications to assure a long economic operating life. It is imperative for operators to provide continuous surveillance of airplane structure to detect and report damage and perform prompt repairs as required. Knowledge of damage that is occurring in the fleet is essential to the manufacturer so that timely advice through service bulletins or other publications can be provided to all operators.

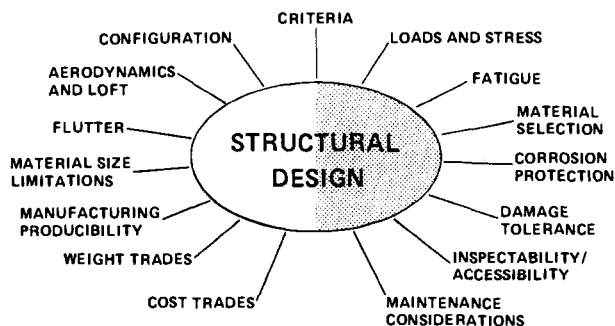


FIG. 1—Structural design considerations.

SERVICE EXPERIENCE SUMMARY, 1958-1978

- 37 aircraft models and derivatives certificated
- 8,000 aircraft manufactured
- 2,300 aircraft now in U.S. domestic air carrier service
- 100 million U.S. domestic air carrier flight hours
- Present system has performed well in hundreds of cases:
 - Fatigue cracking to the extent of depressurization
 - Fatigue damage to the extent of fuel leakage
 - Multiple fatigue damage sites
 - Turbine disk and blade penetration of primary structure
- Present system has failed in a few limited cases

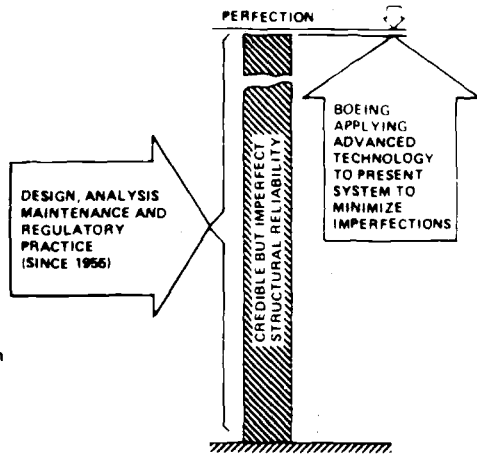


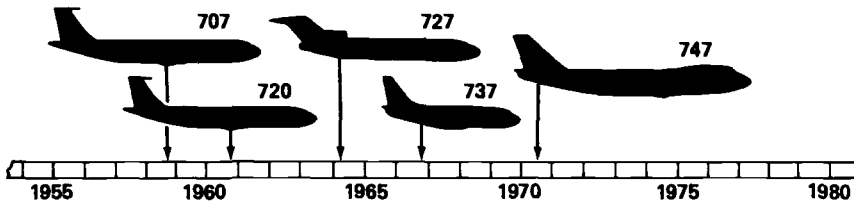
FIG. 2—Present damage tolerance system record.

Continued airworthiness of aging transport airplanes currently in service has been debated among experts in the industry in recent years. The question has been raised whether the inspection programs supporting fail-safe design practices used in the 1950s and 1960s are adequate as airplanes designed in this era exceed their design life objectives. The need for re-evaluation or recertification after some period of operation has recently been proposed. High-time Boeing 707 airplanes have exceeded their original design life objectives, and models 727 and 737 are rapidly approaching theirs (Fig. 3). Supplemental Inspection Documents (SIDs), calling for special directed inspections, have been released for the 707/720 and 727 based on a reassessment of structural integrity. Similar activities are now progressing for models 737 and 747. These SIDs, which enhance normally scheduled maintenance and inspection actions, will permit continued safe operation of aging aircraft until economics dictate retirement.

Design Principles

Modern aircraft operate in a complex combination of external load sources, environments, human elements, and economic requirements. The primary airframe components are designed to specific static and dynamic loading conditions, deformation and functional criteria, and basic service loading criteria.

The structural strength in the absence of any deterioration such as fatigue, corrosion, or accidental damage is founded on design criteria that have evolved



Model	Delivered airplanes	Design objectives		High-time airplanes*	
		Flights	Hours	High flights	High hours
707	785	—	60,000	33,700	67,600
720	154	—	60,000	52,500	62,500
727	1,692	50,000	60,000	49,700	50,000
737	715	75,000	51,000	60,800	41,100
747	487	20,000	60,000	14,900	48,900

*Different airplanes in high flights and high hours.

FIG. 3—Boeing jet fleet summary.

since the infancy of aviation. The design limit load for maneuvers, gust velocities, take-off, and landing conditions are based on millions of commercial aircraft hours and flights. Ultimate design loads exceed envelope-type limit load conditions by 50 percent. The overall capability of the aircraft to meet static strength requirements is demonstrated by analysis and supported by test evidence. Because it is impractical to conduct ultimate load tests of all critical conditions and portions of the structure, certification is substantiated by analysis. Literally hundreds of analyses of the structure are conducted on thousands of details. Limit load capability is demonstrated by full-scale testing, while testing to failure is mainly conducted to establish gross weight growth potential.

Commercial aviation experience shows the undamaged structure has a high level of structural integrity with regard to the design operational loads. Significant developments in the ability to analyze damaged structure have occurred since inception of the fail-safe design concept in the 1950s. The primary emphasis at that time was on a multistructural member concept with established strength requirements for a failure of a single structural element or an obvious partial failure. Considerable testing was conducted to verify design concepts. These envelope criteria were intended to represent more critical conditions than would normally be encountered in service. In addition, such structure has generally possessed desirable crack growth features permitting timely detection and repair. The relationship between static ultimate design requirements for undamaged structure and limit load requirements for damaged structure is illustrated schematically in Fig. 4. Note that the safe damage detection period is governed by damage growth and residual

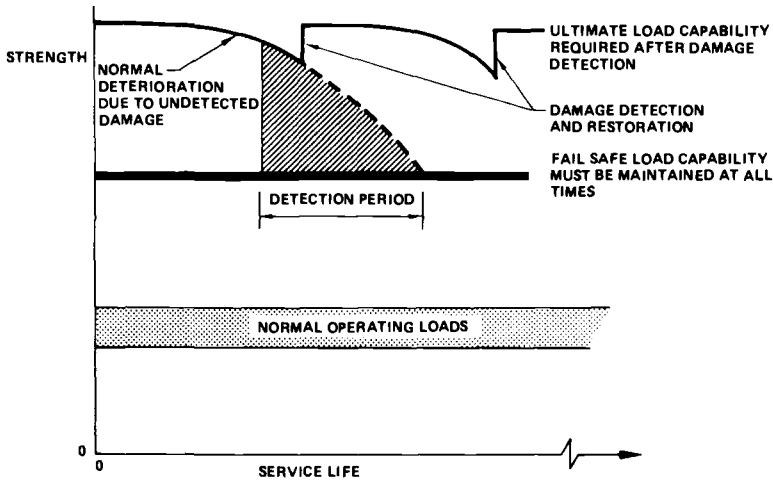


FIG. 4—Strength criteria for damage tolerant structure.

strength characteristics as well as by maintenance and inspection procedures determining damage detection thresholds and number of detection opportunities. Once damage has been detected, strength must be restored to the design ultimate level.

Planning for continued structural integrity is an evolutionary process blending increased understanding of the parameters affecting durability and damage tolerance with service experience. Current certification requirements have evolved with advancements in durability and damage tolerance evaluations, but they also attempt to reflect the equally important role of timely detection of structural damage by the operators. Certification of commercial jet transports requires damage tolerant designs in all instances where it can be used without unreasonable penalty. The technical capability now exists to relate inspection requirements to damage growth which, in the past, were based on service experience. In addition, appropriate multiple-site damage is now considered. Future analysis refinements are likely to focus more on probabilistic considerations, since the joint likelihood of significant undetected damage and high loads are extremely remote and may unjustly penalize design concepts based on the envelope type of criteria relied upon today.

Design Considerations

Characteristics required to achieve current structural design objectives must be satisfied jointly by:

Durability—Ability of the structure to sustain degradation from such sources as fatigue, accidental damage, and environmental deterioration to

the extent that they can be controlled by economically acceptable maintenance programs.

Damage Tolerance—Ability of structure to sustain anticipated loads in the presence of fatigue, corrosion, or accidental damage until such damage is detected through inspections or malfunctions and repaired.

Interaction between structural damage tolerance and durability characteristics must be recognized in design, manufacturing, and operation of modern jet transports. Design evolution and maintenance requirements are motivated by both safety and economic concerns. While these aspects are difficult to separate entirely, damage tolerance is primarily governed by minimum certification requirements jointly developed by the manufacturer, operator, and the regulating agency. Durability characteristics of damage tolerant structures mainly influence the economics of in-service operation, maintenance, and repair, and are dictated by the requirements of a competitive international market.

Inspectability and accessibility characteristics of the structure must be such that general visual methods of damage detection can be confidently employed for the majority of the structure. Directed inspections involving sophisticated damage detection equipment may be acceptable in areas where inaccessibility dictates infrequent inspections.

The key element of damage tolerance is the ability to detect damage (shown schematically as detection windows in Fig. 5). A short crack growth period with high detectability can provide as many opportunities for damage detection as a long crack growth period with low detectability. Damage tolerance comprises three distinct elements of equal importance for achieving the desired level of safety:

Allowable Damage—The maximum damage, including multiple secondary cracks that the structure can sustain under fail-safe load conditions.

Damage Growth Period—The interval in which damage progresses from a

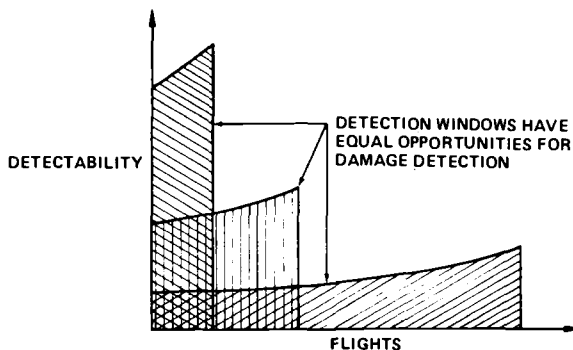


FIG. 5—Opportunities for damage detection.

detectable threshold to maximum allowable based on proper recognition of operating service loads, load sequencing, and environmental effects.

Inspection Program—A sequence of inspections in a fleet of aircraft with methods and frequencies aimed at timely damage detection.

Adequate contributions from all elements are usually required to achieve the desired level of damage tolerance. The best design has safety provided by structural characteristics and requires only a small contribution from inspections (Fig. 6). In extreme cases, where these elements combined provide insufficient contributions, a safe life classification is the only alternative.

It is important to recognize that all structure, whether classified as safe life or damage tolerant, has a limited period of safe performance. Several combinations of the primary damage tolerance parameters can provide safety beyond this initial service period. If allowable damage is obvious in terms of detection prior to flight or permits safe operation for the remainder of a flight, there is no need for additional damage growth substantiation and inspection program analysis. Example of this case would be foreign object impact with the fuselage resulting in controlled decompression or splice-to-splice wing skin damage with extensive fuel leakage.

Technology Control Methods

Interacting technologies employed in the evaluation of long-life jet transport structures have been available in various degrees for 25 or more years, but have generally been applied to aircraft analysis by a limited number of specialists using nonuniform methods. Performance demands, increasing structural complexity, aging fleets, and multiple aircraft programs have required the development and documentation of disciplined technology methods (Fig. 7) with the following principal advantages: (1) application of ad-

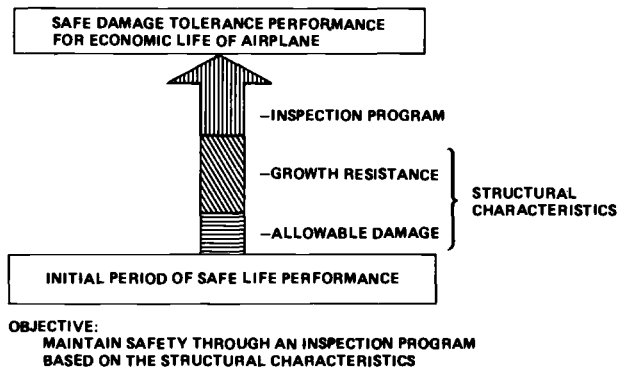


FIG. 6—Elements required to provide safe operation of damage tolerant structures.

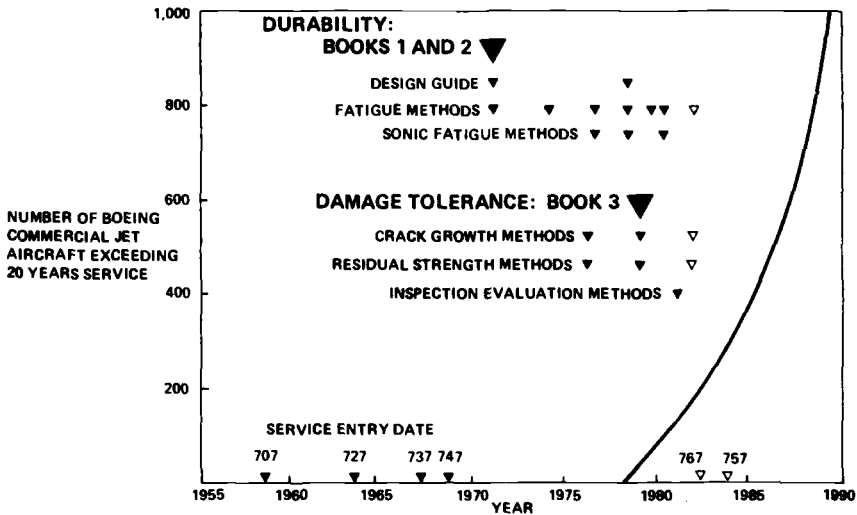


FIG. 7—Boeing structural damage technology development.

vanced technology by large teams of nonspecialist engineers: (2) consistency between multiple airplane programs, sometimes involving great geographic distances; and (3) visibility and control of key design and maintenance parameters.

Fatigue evaluations of early Boeing commercial jet transports depended heavily on experience, engineering judgment, and tests during the design and analysis process. As technology progressed and competitive pressures for long-life economic structures increased, fatigue specialists were forced to apply more sophisticated analysis methods. However, the timing of such evaluations was often incompatible with the detail design and drawing release process, since fatigue evaluations involved time-consuming analyses and lacked visibility of key parameters. Logistics involved in managing large teams of engineers to effectively utilize cumulative design experience and to apply disciplined fatigue methods prompted development of a Durability System in the early 1970s.

Fracture problems have effectively been resolved in the design of commercial jet transports by designing structures to selected fail-safe load conditions under assumed structural damage conditions. Significant advancements have been made in recent years in the ability to analyze damaged structure. Recognition of damage growth and consideration of damage at multiple sites are now included in the damage tolerance assessment of structures. Residual strength and crack growth characteristics are necessary ingredients for evaluation of inspection programs necessary to maintain safety of damage tolerant structure. The ability to use the emerging state-of-the-art technological advancements has been confined to relatively few specialists in the fields of

fracture mechanics and structural maintenance. Boeing has developed standardized damage tolerance and inspection evaluation methods suitable for engineers with varying levels of familiarity with these technical disciplines.

Durability

Successful design of long-life structure requires balancing detail design practices with operating stress environment. Ninety million commercial flight hours of accumulated fatigue design experience have supported this by showing that incompatible operating stresses and fatigue allowables cause 85 percent of the fatigue problems encountered. By properly recognizing and evaluating the key variables illustrated in Fig. 8, each designer and analyst can balance required and actual fatigue qualities. The most significant item in standardizing the fatigue analysis process is the damage model which allows the requirement analysis to be conducted independently and prior to the capability analysis and benefit the design process in the following ways: (1) early attention can be directed toward fatigue; (2) fatigue methods and allowables are available to all structural engineers; (3) emphasis on improving detail design to achieve life goal objectives; and (4) trade studies lead to efficient weight/cost design improvements.

Design for durability involves proper recognition of accidental damage, environmental deterioration such as corrosion and stress corrosion, in addition to fatigue damage. Accidental damage is considered in the design and analysis process by applying equivalent minimum stress concentration factors to represent scratches and nicks anticipated during the economic service life. Corrosion damage cannot be tolerated in a fleet of aircraft; every effort must be made by the operator and the manufacturer to eliminate any problem at the first sign of distress. Experience has shown that certain materials

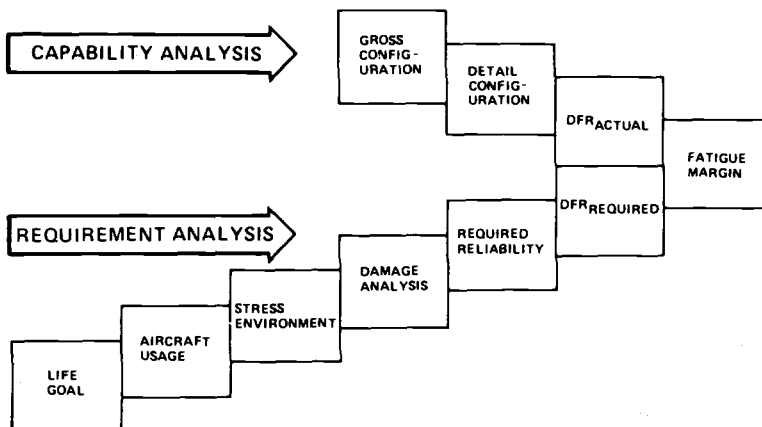


FIG. 8—Fatigue check procedure.

or material forms are prone to stress corrosion problems, and that certain structural locations, details, and assemblies are prone to environmental corrosion problems. The design process for selecting material, configuration, and protective finish is continually updated based on service experience and technological advancements and reflected in durability design guides. Control of corrosion and stress corrosion in the fleet also requires diligent efforts by the manufacturer, operator, and regulator to jointly develop efficient maintenance programs such as described later.

Fatigue Ratings and Allowables

Flight-by-flight fatigue damage calculations are based on linear damage models representing known test and service experience. The nomenclature "damage model" will be used here to relate it to the function performed while avoiding confusion with direct SN -data. A limited range of the stress-life regime is similar in shape to traditional SN -curves, which retains the advantage of basic fatigue quality determinations from such testing (Fig. 9). The selected damage model accounts for low amplitude stresses and load sequencing effects previously addressed by Smith and Goranson and by Craig and Goranson.^{2,3} The focal point in the damage model is defined by a Detail Fatigue Rating (DFR) for structural fatigue and Detail Sonic Rating (DSR) for sonic fatigue. A comprehensive inventory of service and test-proven design details was developed based on this family of damage curves and repre-

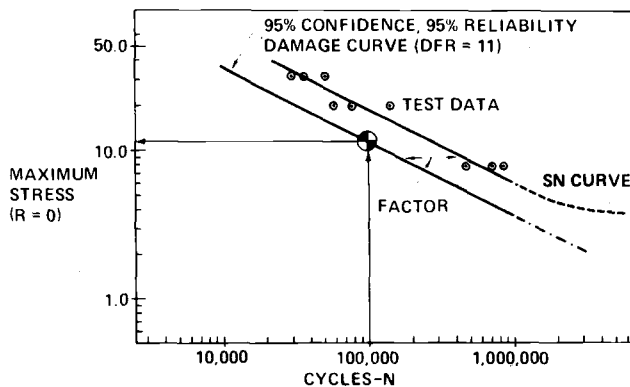


FIG. 9—Test data reduction to match damage model.

²Smith, H. W. and Goranson, U. G., "Spectrum Loading in Relation to Aircraft Design," 8th International Committee on Aeronautical Fatigue Symposium, Lausanne, Switzerland, June 1975.

³Craig, L. E. and Goranson, U. G., "Airworthiness Assessment of Boeing Jet Transport Structures," 10th International Committee on Aeronautical Fatigue Symposium, Brussels, May 1979.

sensation of various mean and alternating stress combinations uniquely defined by given DFR or DSR values. Such Detail Fatigue Ratings permit quantitative compilation of the cumulative fatigue and design experience (Fig. 10). All stress analysts and designers have Durability Design manuals which show inactive and acceptable design concepts based on historical data. Figure 11 illustrates the format used to convey attention to durability design considerations. In many cases, new design considerations are provided and relative cost comparisons are given for design alternatives.

Structural configuration in terms of material, type of structure, panel division, load paths, and operating stresses is selected to meet the design life goal objectives. This implies that a minimum fatigue quality must be achieved with the desired level of confidence and reliability. A two-parameter Weibull distribution is assumed with shape parameters based on over 2000 test samples of several duplicate specimens. Standard test representation, confidence, and reliability factors are employed to obtain airplane reliability levels of 95 percent with 95 percent confidence. These factors are selected to achieve competitive economic structures with very limited cracking during the anticipated service life. Additional fatigue reliability factors are applied to the design life goals to recognize economic consequences of cracking in unique areas, and thus effectively increase the reliability levels to well above 95 percent.

Analytical fatigue allowables complementing the durability design guides are also available to all designers and stress analysts to modify existing configurations proven by test and fleet experience, or to derive fatigue ratings for a completely new design. The type of detail, amount of load transfer, fastening system, surface finish, and other specific properties for test or service data have been used to derive empirical fatigue rating solutions.³

Fatigue Analysis Methods

Boeing jet transports are designed to achieve a minimum of 20 years of service life without cracking causing an undue economic maintenance burden. Design life goals are based on the most critical combinations of flight length and number of flights (shown schematically in Fig. 12). A high degree of operational flexibility is therefore provided to the airlines, since the selected discrete short, medium, and long flight profiles represent both typical and extreme usage during the projected service life.

Operating load conditions and spectra are standardized to allow efficient and timely derivation of operating stresses for discrete flight profiles applicable to different models. A concept of equivalent load cycles is used to facilitate hand fatigue checking of discrete items. Computer analyses with interactive graphics permit full spectra analyses to be conducted and summarized for each load condition. This facilitates surveillance of large-scale analyses by simple examination of amplitude and frequency of equivalent gust and man-

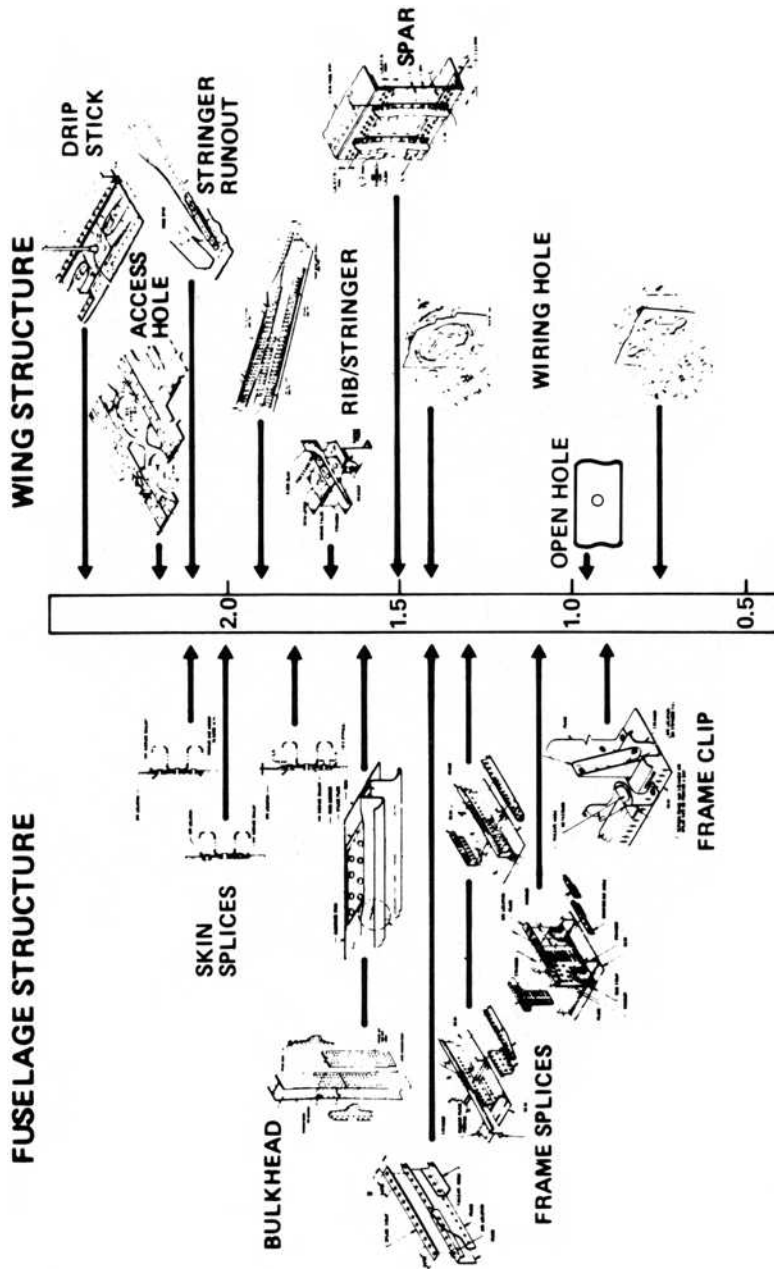


FIG. 10—Relative fatigue ratings.

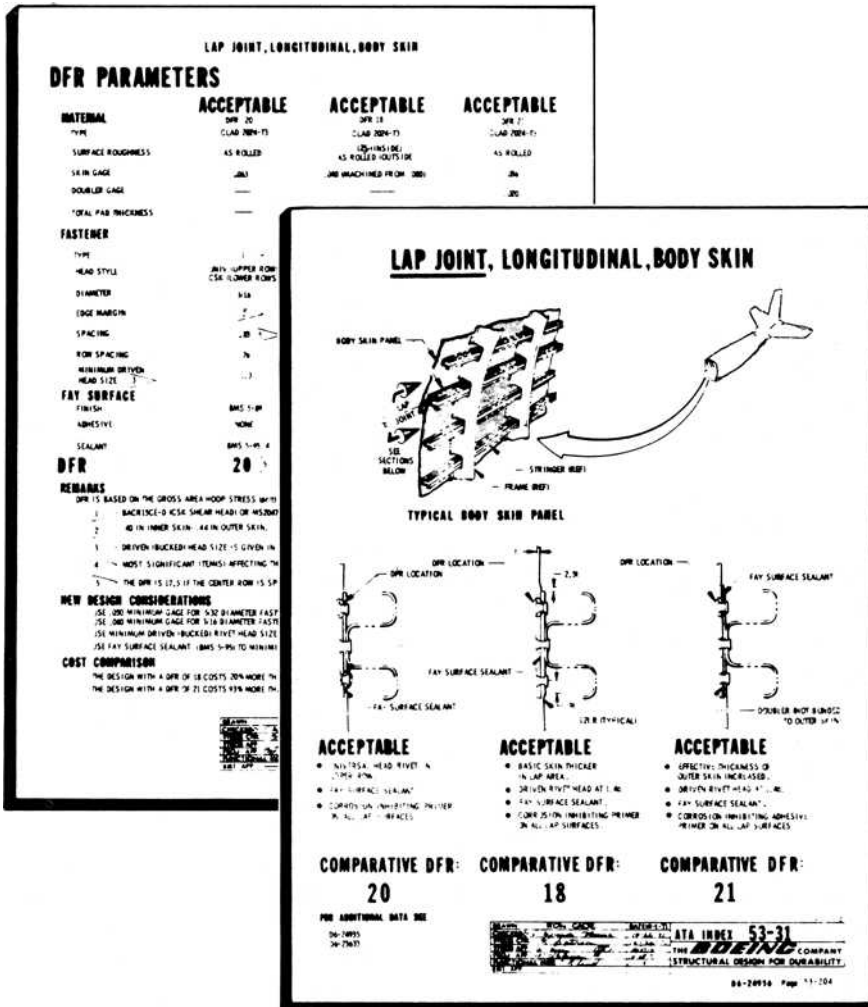


FIG. 11—Durability design guide example.

euver cycles. Flight-by-flight fatigue analyses are based on the damage models discussed earlier. Load sequencing effects are verified by comparison with fleet experience in terms of demonstrated characteristic lives. By providing contour plots as shown in Fig. 13 for wing panels, the designer is able to focus attention on detail design considerations without repetitive, complex evaluations of required fatigue ratings on a detail-by-detail basis.

The structural capability and requirement analyses are compared with a fatigue margin paralleling the static margin of safety. The fatigue analysis

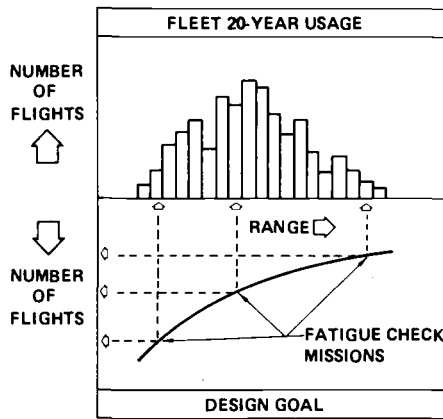


FIG. 12—Design life goal variable.

system is summarized by a check form displaying key parameters (Fig. 14). These forms are often generated as part of computerized large-scale structural analyses, but can also be completed quickly by hand for single details. Related service experience, source of fatigue ratings, and corrosion control must be addressed prior to final design approval. It is important to recognize that detail design improvements can eliminate a negative margin without decreasing operating stress and increasing weight. The required fatigue quality can be determined independently of detail configuration early in the design process by solving for zero fatigue margin.

Sonic fatigue is a phenomenon whereby noise forces structure to vibrate and develop cracks. The primary source of noise in aircraft is the engines, although aerodynamic noise can be significant in some cases. Sonic fatigue methods and allowables are similar to those described previously with the following significant features: (1) various noise spectrum shapes can be accommodated without complex analyses; (2) structural response frequency expressions define the sonic fatigue damage accumulation rate for different structural configurations; (3) unit stress solutions define panel response characteristics; (4) fatigue quality is defined by Detail Sonic Ratings (DSR); and (5) a sonic fatigue margin is used to describe fatigue performance relative to design life goals.

Comparative Analyses

Although fatigue tests of components and the entire airframe are extremely valuable in the early life of a given model, the proof-of-quality stems from accumulated experience of maturing fleets. Boeing uses comparative analysis methods to verify fatigue analysis systems and to provide a basis for timely and efficient maintenance planning actions. The operational Boeing jet fleet

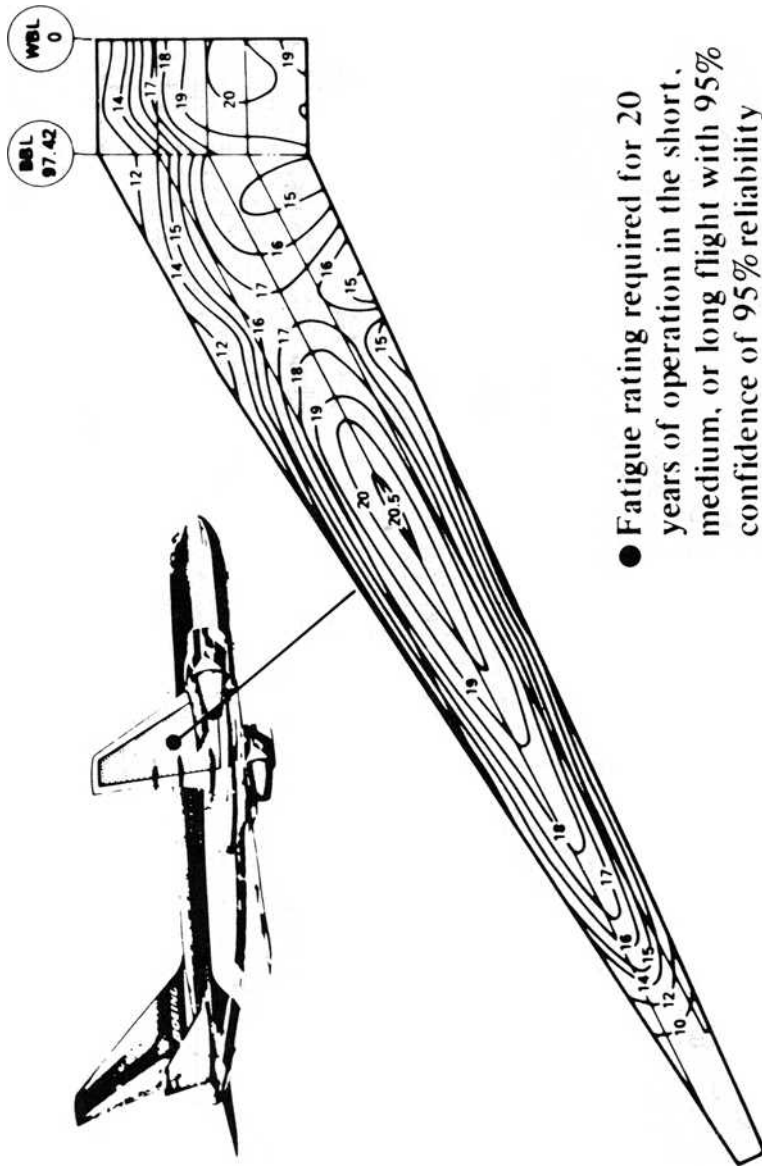


FIG. 13—Required DFR contours.

FATIGUE CHECK FORM									
FLIGHT LENGTH 17 HRS		2 FRR		57 HRS		SHEET & LOCATION OF DETAIL SECTION NO. 212.2.1			
LIFE GOAL 30 000		25 000		18 000		STRAIGHT SPARE MAINTENANCE LOG-11			
FRF		1.5		1.5		SACRIFICIAL BOLTS			
FRR		-6.9		-8.9		-9.4		FRR	
GAG STRESSES		FRR		FRR		FRR		FRR	
CRITICAL CORRS.		FRR		FRR		FRR		FRR	
GAG		FRR		FRR		FRR		FRR	
DAMAGE RATIO		.59		.62		.65		DAMAGE	
EQUIVALENT GAG CYCLES		36 000		60 400		28 000		EQUIVALENT	
DFR		19		19		19		DFR	
FRR		14.1		16.3		19.9		FRR	
FATIGUE MARGIN		.07		.08		.06		FATIGUE MARGIN	
REQUIRED DFR		17.9		17.6		18.0		REQUIRED DFR	
<p>① SEE DETAIL SHEET NO. 212.2.1 FOR DETAIL DESCRIPTION</p> <p>② SEE DETAIL SHEET NO. 212.2.1 FOR DETAIL DESCRIPTION</p> <p>③ SEE DETAIL SHEET NO. 212.2.1 FOR DETAIL DESCRIPTION</p>									
<p>④ SEE DETAIL SHEET NO. 212.2.1 FOR DETAIL DESCRIPTION</p> <p>⑤ SEE DETAIL SHEET NO. 212.2.1 FOR DETAIL DESCRIPTION</p> <p>⑥ SEE DETAIL SHEET NO. 212.2.1 FOR DETAIL DESCRIPTION</p>									
<p>⑦ SEE DETAIL SHEET NO. 212.2.1 FOR DETAIL DESCRIPTION</p> <p>⑧ SEE DETAIL SHEET NO. 212.2.1 FOR DETAIL DESCRIPTION</p> <p>⑨ SEE DETAIL SHEET NO. 212.2.1 FOR DETAIL DESCRIPTION</p>									
<p>⑩ SEE DETAIL SHEET NO. 212.2.1 FOR DETAIL DESCRIPTION</p> <p>⑪ SEE DETAIL SHEET NO. 212.2.1 FOR DETAIL DESCRIPTION</p> <p>⑫ SEE DETAIL SHEET NO. 212.2.1 FOR DETAIL DESCRIPTION</p>									
<p>⑬ SEE DETAIL SHEET NO. 212.2.1 FOR DETAIL DESCRIPTION</p> <p>⑭ SEE DETAIL SHEET NO. 212.2.1 FOR DETAIL DESCRIPTION</p> <p>⑮ SEE DETAIL SHEET NO. 212.2.1 FOR DETAIL DESCRIPTION</p>									
<p>⑯ SEE DETAIL SHEET NO. 212.2.1 FOR DETAIL DESCRIPTION</p> <p>⑰ SEE DETAIL SHEET NO. 212.2.1 FOR DETAIL DESCRIPTION</p> <p>⑱ SEE DETAIL SHEET NO. 212.2.1 FOR DETAIL DESCRIPTION</p>									
<p>⑲ SEE DETAIL SHEET NO. 212.2.1 FOR DETAIL DESCRIPTION</p> <p>⑳ SEE DETAIL SHEET NO. 212.2.1 FOR DETAIL DESCRIPTION</p> <p>㉑ SEE DETAIL SHEET NO. 212.2.1 FOR DETAIL DESCRIPTION</p>									
<p>⑳ SEE DETAIL SHEET NO. 212.2.1 FOR DETAIL DESCRIPTION</p> <p>㉒ SEE DETAIL SHEET NO. 212.2.1 FOR DETAIL DESCRIPTION</p> <p>㉓ SEE DETAIL SHEET NO. 212.2.1 FOR DETAIL DESCRIPTION</p>									
<p>㉓ SEE DETAIL SHEET NO. 212.2.1 FOR DETAIL DESCRIPTION</p> <p>㉔ SEE DETAIL SHEET NO. 212.2.1 FOR DETAIL DESCRIPTION</p> <p>㉕ SEE DETAIL SHEET NO. 212.2.1 FOR DETAIL DESCRIPTION</p>									
<p>㉕ SEE DETAIL SHEET NO. 212.2.1 FOR DETAIL DESCRIPTION</p> <p>㉖ SEE DETAIL SHEET NO. 212.2.1 FOR DETAIL DESCRIPTION</p> <p>㉗ SEE DETAIL SHEET NO. 212.2.1 FOR DETAIL DESCRIPTION</p>									
<p>㉗ SEE DETAIL SHEET NO. 212.2.1 FOR DETAIL DESCRIPTION</p> <p>㉘ SEE DETAIL SHEET NO. 212.2.1 FOR DETAIL DESCRIPTION</p> <p>㉙ SEE DETAIL SHEET NO. 212.2.1 FOR DETAIL DESCRIPTION</p>									
<p>㉙ SEE DETAIL SHEET NO. 212.2.1 FOR DETAIL DESCRIPTION</p> <p>㉚ SEE DETAIL SHEET NO. 212.2.1 FOR DETAIL DESCRIPTION</p> <p>㉛ SEE DETAIL SHEET NO. 212.2.1 FOR DETAIL DESCRIPTION</p>									
<p>㉛ SEE DETAIL SHEET NO. 212.2.1 FOR DETAIL DESCRIPTION</p> <p>㉜ SEE DETAIL SHEET NO. 212.2.1 FOR DETAIL DESCRIPTION</p> <p>㉝ SEE DETAIL SHEET NO. 212.2.1 FOR DETAIL DESCRIPTION</p>									
<p>㉝ SEE DETAIL SHEET NO. 212.2.1 FOR DETAIL DESCRIPTION</p> <p>㉞ SEE DETAIL SHEET NO. 212.2.1 FOR DETAIL DESCRIPTION</p> <p>㉟ SEE DETAIL SHEET NO. 212.2.1 FOR DETAIL DESCRIPTION</p>									
<p>㉟ SEE DETAIL SHEET NO. 212.2.1 FOR DETAIL DESCRIPTION</p> <p>㊱ SEE DETAIL SHEET NO. 212.2.1 FOR DETAIL DESCRIPTION</p> <p>㊲ SEE DETAIL SHEET NO. 212.2.1 FOR DETAIL DESCRIPTION</p>									
<p>㊲ SEE DETAIL SHEET NO. 212.2.1 FOR DETAIL DESCRIPTION</p> <p>㊳ SEE DETAIL SHEET NO. 212.2.1 FOR DETAIL DESCRIPTION</p> <p>㊴ SEE DETAIL SHEET NO. 212.2.1 FOR DETAIL DESCRIPTION</p>									
<p>㊴ SEE DETAIL SHEET NO. 212.2.1 FOR DETAIL DESCRIPTION</p> <p>㊵ SEE DETAIL SHEET NO. 212.2.1 FOR DETAIL DESCRIPTION</p> <p>㊶ SEE DETAIL SHEET NO. 212.2.1 FOR DETAIL DESCRIPTION</p>									
<p>㊶ SEE DETAIL SHEET NO. 212.2.1 FOR DETAIL DESCRIPTION</p> <p>㊷ SEE DETAIL SHEET NO. 212.2.1 FOR DETAIL DESCRIPTION</p> <p>㊸ SEE DETAIL SHEET NO. 212.2.1 FOR DETAIL DESCRIPTION</p>									
<p>㊸ SEE DETAIL SHEET NO. 212.2.1 FOR DETAIL DESCRIPTION</p> <p>㊹ SEE DETAIL SHEET NO. 212.2.1 FOR DETAIL DESCRIPTION</p> <p>㊺ SEE DETAIL SHEET NO. 212.2.1 FOR DETAIL DESCRIPTION</p>									
<p>㊺ SEE DETAIL SHEET NO. 212.2.1 FOR DETAIL DESCRIPTION</p> <p>㊻ SEE DETAIL SHEET NO. 212.2.1 FOR DETAIL DESCRIPTION</p> <p>㊼ SEE DETAIL SHEET NO. 212.2.1 FOR DETAIL DESCRIPTION</p>									
<p>㊼ SEE DETAIL SHEET NO. 212.2.1 FOR DETAIL DESCRIPTION</p> <p>㊽ SEE DETAIL SHEET NO. 212.2.1 FOR DETAIL DESCRIPTION</p> <p>㊾ SEE DETAIL SHEET NO. 212.2.1 FOR DETAIL DESCRIPTION</p>									
<p>㊾ SEE DETAIL SHEET NO. 212.2.1 FOR DETAIL DESCRIPTION</p> <p>㊿ SEE DETAIL SHEET NO. 212.2.1 FOR DETAIL DESCRIPTION</p> <p>1 SEE DETAIL SHEET NO. 212.2.1 FOR DETAIL DESCRIPTION</p>									

FIG. 14—Fatigue check forms.

is used as a large group of test specimens loaded in real life environment to demonstrate service-demonstrated fatigue life and to predict future fatigue performance.

The techniques used to perform the fleet-demonstrated life calculations have been described by Craig and Goranson.³ The status of the Boeing fleet is surveyed continuously in terms of operating statistics, and this information is summarized for all designers and analysts for each model and series combination. Some relevant statistics are (1) data base represents over 3000 active aircraft; (2) total fleet experience exceeds 60 million flight cycles; and (3) daily utilization exceeds 17 000 flights.

Two techniques are employed to derive fleet demonstrated lives. Where a statistically significant number of small fatigue cracks have been reported, a two-parameter Weibull distribution is assumed, and maximum-likelihood estimates of the shape parameter and central tendency lives are determined. These estimates are used to determine fleet demonstrated DFR values, thus providing a means of relating service experience for one model to other models with different utilization characteristics (Fig. 15). Significant fleet findings, often augmented by extensive teardown inspections, are also used to update fatigue methods and allowables described previously. Correlation between predicted probable damage locations and fleet inspection/teardown findings is illustrated in Fig. 16.

Damage Tolerance

The key objective for aircraft structure designed to the damage tolerance concept has always been to minimize the risk of catastrophic failure resulting

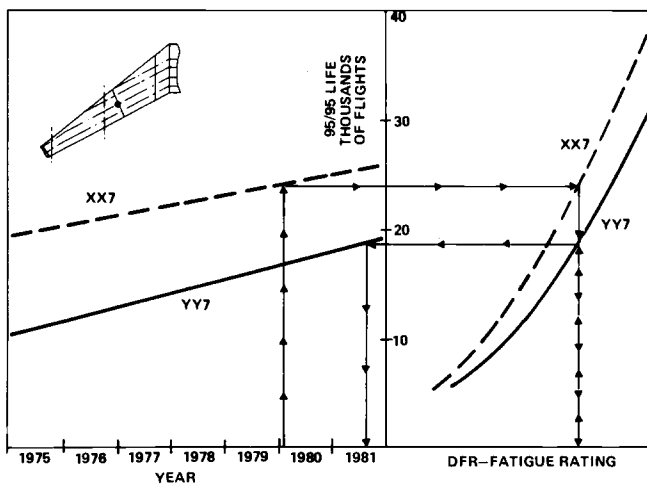


FIG. 15—Comparative fatigue analysis example.

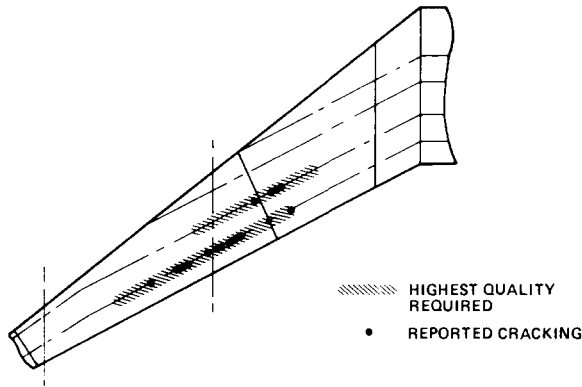


FIG. 16—Correlation between prediction and service findings.

from fatigue cracks, corrosion, manufacturing defects, or accidental damage occurring in service. The damage tolerance design approach in the 1950s and 1960s was essentially focused on multistructural member concepts, with established strength requirements for the failure or obvious partial failure of a single structural element. Considerable testing was conducted to verify design concepts (Fig. 17).

Damage tolerance and safe-life are the two methods of achieving structural operating safety (Fig. 18). Up to three separate but related technologies are involved in the damage tolerance assessments as shown for Category 3. Only landing gear structures are qualified under Category 4 for Boeing jet transports, since required damage detection sizes are very small for the high strength alloys used.

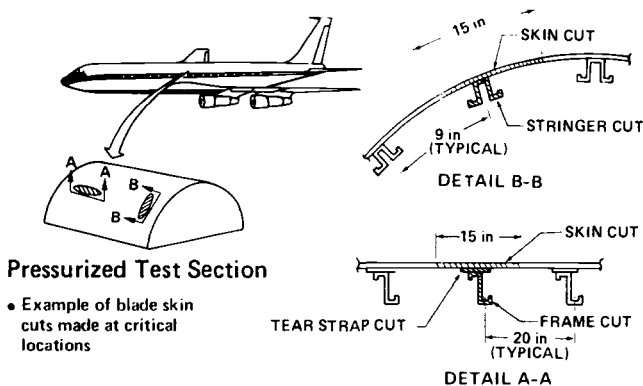


FIG. 17—Fail-safe test verification examples.

SAFETY ANALYSIS REQUIREMENTS				
STRUCTURAL CATEGORY			TECHNIQUE OF ASSURING SAFETY	TECHNOLOGY CONTROL METHOD
SECONDARY STRUCTURE	DAMAGE TOLERANCE DESIGN	① SECONDARY STRUCTURE	DESIGN FOR LOSS OF COMPONENT OR SAFE SEPARATION	CONTINUED SAFE FLIGHT
		② DAMAGE OBVIOUS OR MALFUNCTION EVIDENT	ADEQUATE RESIDUAL STRENGTH WITH EXTENSIVE DAMAGE THAT IS OBVIOUS	• RESIDUAL STRENGTH
		③ DAMAGE DETECTION BY PLANNED INSPECTION PROGRAM	INSPECTION PROGRAM MATCHED TO STRUCTURAL CHARACTERISTICS	• RESIDUAL STRENGTH • CRACK GROWTH • INSPECTION PROGRAM
	SAFE-LIFE DESIGN	④ SAFE-LIFE	CONSERVATIVE FATIGUE LIFE	• FATIGUE

FIG. 18—Safety analysis requirements for damage tolerant and safe-life structure.

Residual Strength

The maximum allowable damage that a structure can sustain at critical fail-safe load is a key to the level of damage growth and inspections needed to assure damage detection. Monolithic, and particularly brittle, structures tend to conform closely to the engineering theory of fracture mechanics. Built-up aircraft structures consist of sheet elements reinforced by stiffening elements joined together by fasteners. Interaction between these cracked and uncracked elements cause significant redistribution of stresses. Failures are precipitated by local exhaustion of plastic strain capability of the most critical elements and/or net section failures involving a mixture of fracture mechanics and transitional behavior in some elements. Ductile aluminum alloys frequently used in commercial transports are difficult to characterize by fracture toughness values alone and special allowables are necessary in many instances.

Failure Modes and Criteria—The residual strength of the structure has to equal or exceed the regulatory fail-safe loads. This determines the increasing amount of damage that can be sustained and is a key element of the Inspection Analysis described later. Several failure modes are illustrated in Fig. 19 for a broken central stiffener case as follows: (A) dynamic extension of short skin crack, possible crack arrest at splice stiffeners; (B) unstable skin crack extension followed by crack arrest at adjacent stiffeners; (C) adjacent stiffener/fastener failures after skin crack arrest; (D) unstable skin crack extension, arrested at splice stiffeners; and (E) splice stiffener/fastener failures.

To minimize inspection requirements for damage-tolerant structures, obvious damage-containment capability such as splice-to-splice wing panel

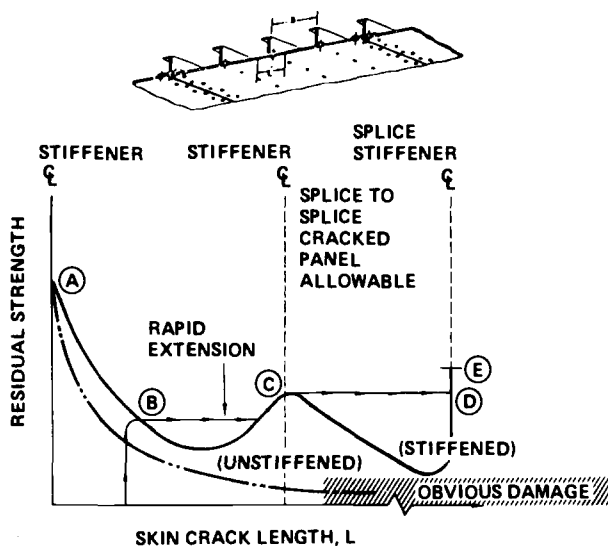


FIG. 19—Potential failure modes for stiffened panels.

failure with massive fuel leakage or large fuselage cracks resulting in safe decompression are desirable design objectives.

Some of these failure conditions can be determined by stress intensity factor and/or *R*-curve methods, depending on material ductility and fracture toughness characteristics. Interaction between net section failure behavior and elasto-plastic element deflection constraints tend to limit traditional fracture mechanics applications. Configuration factors reflecting element deflections and load distributions can be applied for less ductile alloys for which fracture toughness properties tend to govern the failure behavior.

In addition to primary cracking, multiple damage considerations require assessment of cracking in adjacent structure. These configurations comprise part-through or through-the-thickness crack fronts for which different failure criteria apply. Analysis of test data from a variety of sources indicates that failure of cracked elements may be precipitated by two potential failure mechanisms (modes):

Fracture Mechanics Modes—Classic principles of linear elastic fracture mechanics (LEFM) can predict failure below 90 percent of yield strength (through-thickness cracks) or ultimate strength (part-through cracks).

Transition Mode—The effects of yield and ultimate strength on net section stress must be considered if LEFM predicts higher than 90 percent of yield or ultimate strength, respectively.

These failure modes are illustrated in Fig. 20 for through-the-thickness cracks. Tests have verified the convergence to yield strength for through-the-thickness cracks approaching infinitesimal sizes. It should further be noted

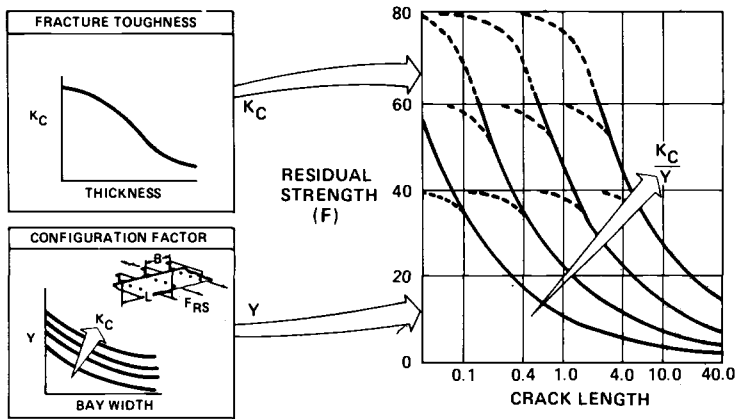


FIG. 20—Residual strength parameters.

that part-through cracks in structures may arrest at a larger through-the-thickness crack length under certain plane stress conditions.

Material Allowables—Fracture toughness properties define the ability of a material to resist rapid fracture in the presence of fatigue cracks or other flaws. The stress intensity, K , derived from linear elastic stress analysis is normally used for material characterization. The fracture toughness levels are influenced by stress-strain states along the crack front, strain rates, and temperature. Material properties and thickness essentially determine whether plane stress or plane strain conditions prevail. Characterization of fracture toughness in the plane stress or transitional stress conditions is complicated by the degree of crack-tip plasticity and the associated stable crack extension manifested prior to final fracture. Consideration of these characteristics is essential for realistic residual strength assessments. Typical aircraft panels of ductile materials tend to exhibit net section failure stresses near yield. Development of fracture toughness parameters for such alloys requires large test panels to validate complex structural design. Recent advancements in the crack resistance concept offer promising solutions for ductile alloys by obtaining R -curves from test and avoiding use of empirical K_c -values to match test data. Figure 21 illustrates solutions for a stiffened wing panel with substantial stable skin crack growth prior to dynamic extension at approximately two bays.

Built-up panels loaded to fail-safe levels tend to exhibit substantial local deformations of critical elements. Failure analyses are thus dependent on elasto-plastic deflection allowables for both fastener and skin/stringer elements. Traditionally available static strength property data often fail to include such ultimate deflections which tend to govern failure sequences of complex structures.

Configuration Factors, Y —Configuration factors, Y , used for damage

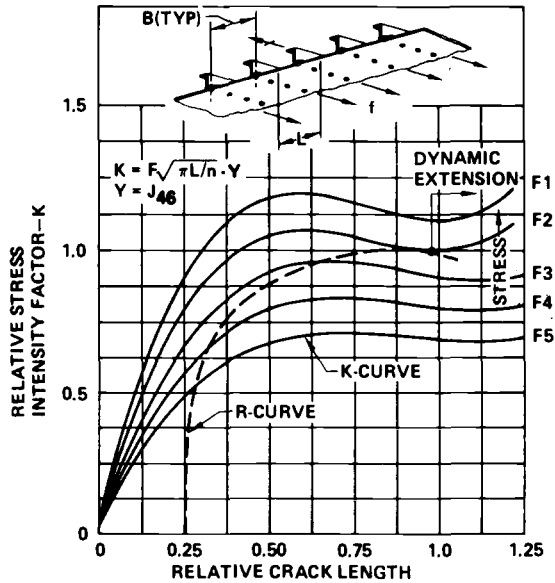


FIG. 21—Resistance curve analysis.

growth evaluations and residual strength checking of monolithic structures are often based on linear elastic fracture mechanics principles. The failure modes of complex structures may need to be evaluated differently, because several elements may experience large deflections and stresses beyond yield. Failure criteria must therefore recognize the transition into static-strength-type failures for small cracks. Elastic failure analysis of a stiffened panel indicates fastener elements are most critical, while elasto-plastic analysis indicates skin material criticality. In addition to configuration factors, Y , load redistribution factors, C , are often required for evaluation of critical elements. These factors define local stress fields resulting from a given amount of cracking—that is, a cracked stringer across a partly or fully broken skin bay—and are applied to the gross area stress. Figure 22 shows detailed configuration factors, Y , and load redistribution factors, C , for one of the typical analysis configurations shown in Fig. 23.

Crack Growth

The rate of damage propagation is a function of material properties, structural configuration, environment, crack length, and operating stress levels. Damage detection assessments require crack growth data from detectable lengths to the critical damage defined by residual strength analyses. Recognition of multiple damage is a key ingredient in such evaluations. Boeing has developed dependent and independent crack size criteria in relation to the

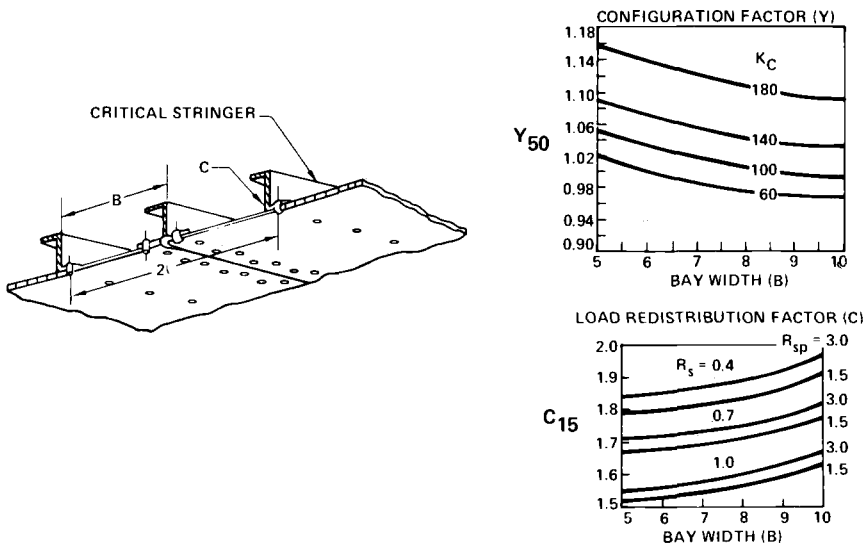


FIG. 22—Configuration load redistribution factor—wing.

detectable lead crack, as shown schematically in Fig. 24. These guidelines have been established by detailed evaluations of typical configurations and verified by teardown inspections of test panels. This procedure eliminates the need for time consuming evaluations of initial secondary crack growth periods—for example, skin crack size associated with a detectable stringer crack.

Efficient use of normalized damage models and calculation of relative growth per flight, including load sequencing effects, permits separation of the material, stress, and geometry parameters. Significant features of the Boeing damage growth analysis system are shown in Fig. 25. Solution of the G -integral for typical configurations in combination with material ratings, M , and crack stress ratings, S , provides the basic ingredient for rapid damage growth evaluations.

Material Crack Growth Ratings, M —Crack-tip stress intensity has proven to be the most relevant parameter for prediction of growth rates with any combination of stress, geometry, and crack length. The majority of relevant crack growth rate data, for crack lengths between detectable and critical, falls in the intermediate linear portion, and damage growth models have evolved based on extensive experimental test evidence (Fig. 26). The minimum stress factor, Z , collapses the family of growth rate curves for different stress ratios into a single curve. The focal point, M , represents the maximum stress intensity at a selected standard crack-tip growth rate and serves as a fundamental material parameter. Design data for different environments have been established in terms of M -values reflecting effects of temperature, humidity, loading frequency, etc. The slope parameter, p , is dependent on

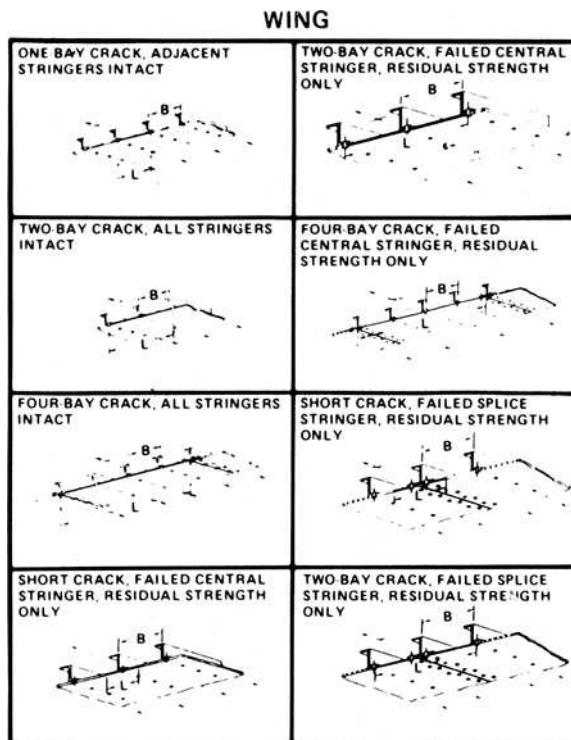


FIG. 23—Typical wing residual strength configuration.

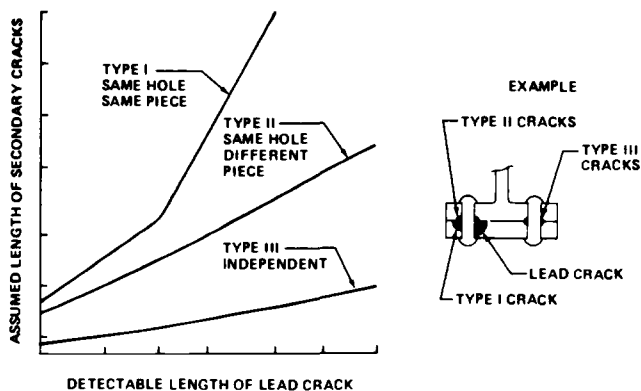


FIG. 24—Multiple-site damage criteria.

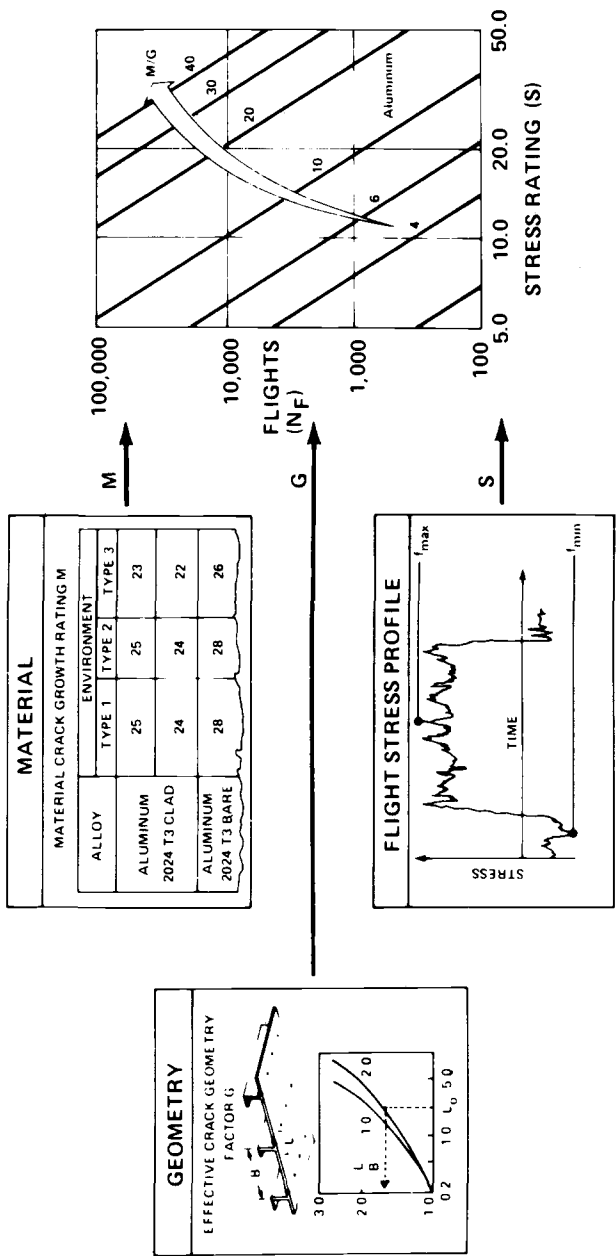
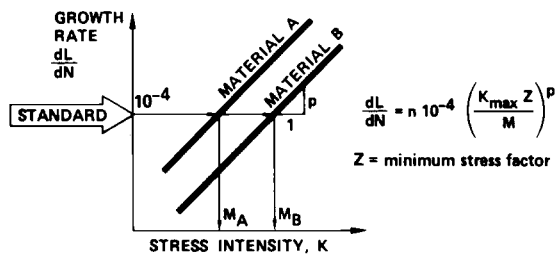


FIG. 25—Key crack growth parameters.



M MEASURES RELATIVE MATERIAL RESISTANCE TO CRACK GROWTH

FIG. 26—Material crack growth rating.

material characteristics. A representative value of p is established for a group of alloys to facilitate large-scale analyses. This allows calculation of relative growth per flight and the derivation of geometry factors for typical structure.

Geometry Factors, G—Efficient evaluation of the multitude of geometries encountered in aircraft structure requires separation of geometry and stress related parameters affecting the crack-tip stress intensity. A technique involving unit stress solutions is used to obtain equivalent stress intensities between initial and final crack lengths (Fig. 27). Geometry factors are based on an extensive library of stress intensity solutions for both simple and complex structure. Configuration component factors, J , account for parameters such as edge margins, crack eccentricity, crack-tip proximity to stress concentrations, other active crack-tips, and stress redistribution in stiffened structures dependent on stiffening ratios, fastener pitch and flexibility, etc. The configuration factor, Y , is then obtained by combining one or several linearly independent J -factors: $Y = J_1 \cdot J_2 \cdot J_3 \dots$

Two- or three-dimensional finite element solutions incorporating isoparametric, quadrilateral singularity elements are often required to obtain solutions for structures with interacting cracks in several members. Figure 28

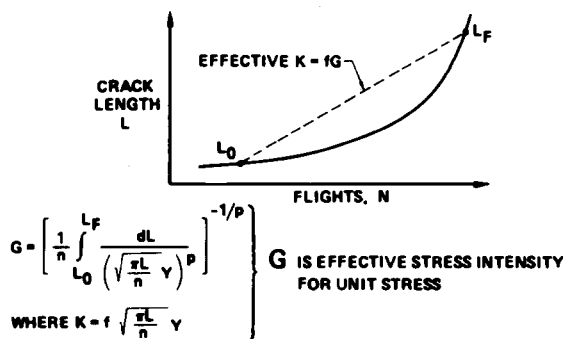


FIG. 27—Geometry factor concept.

Y FACTOR—SHEAR TIED FRAME

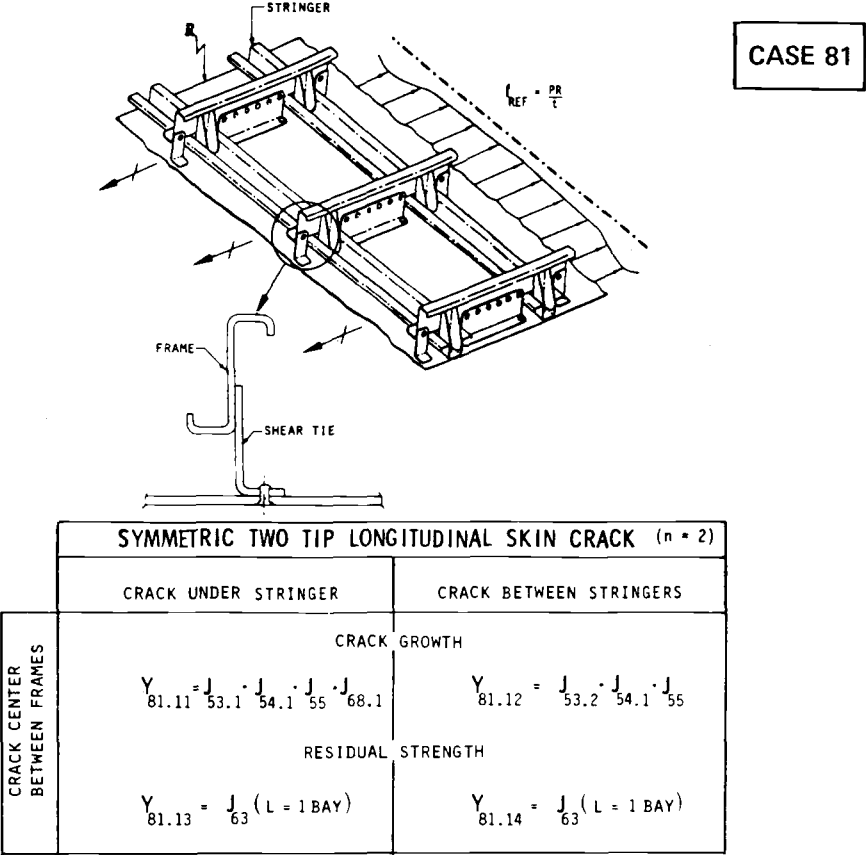


FIG. 28—Configuration factor example—shear tied frame.

shows the combination of *J*-factors for determining the configuration factor, *Y*, for a longitudinal skin crack between fuselage shear tied frames. The individual *J*-factors are illustrated in Fig. 29.

It is apparent that such complex combinations are not readily usable by engineers engaged in strength checking. Computerized routines with libraries of *Y*-factors have therefore been established to derive *G*-charts for typical configurations and to provide solutions for special configurations and material.

Figure 30 shows a typical *G*-chart for several final crack lengths, *L_F*, and stiffening ratios, *R_s*. The total geometry factor, *G*, can be obtained by combining different stages of crack growth for through-the-thickness growth, followed by growth to a free edge then to the critical or final crack length; that is, $G = G_1^{-p} + G_2^{-p} + G_3^{-p}$. Similarly, *G*, can be obtained for crack growth through a stringer, followed by skin crack growth to critical length.

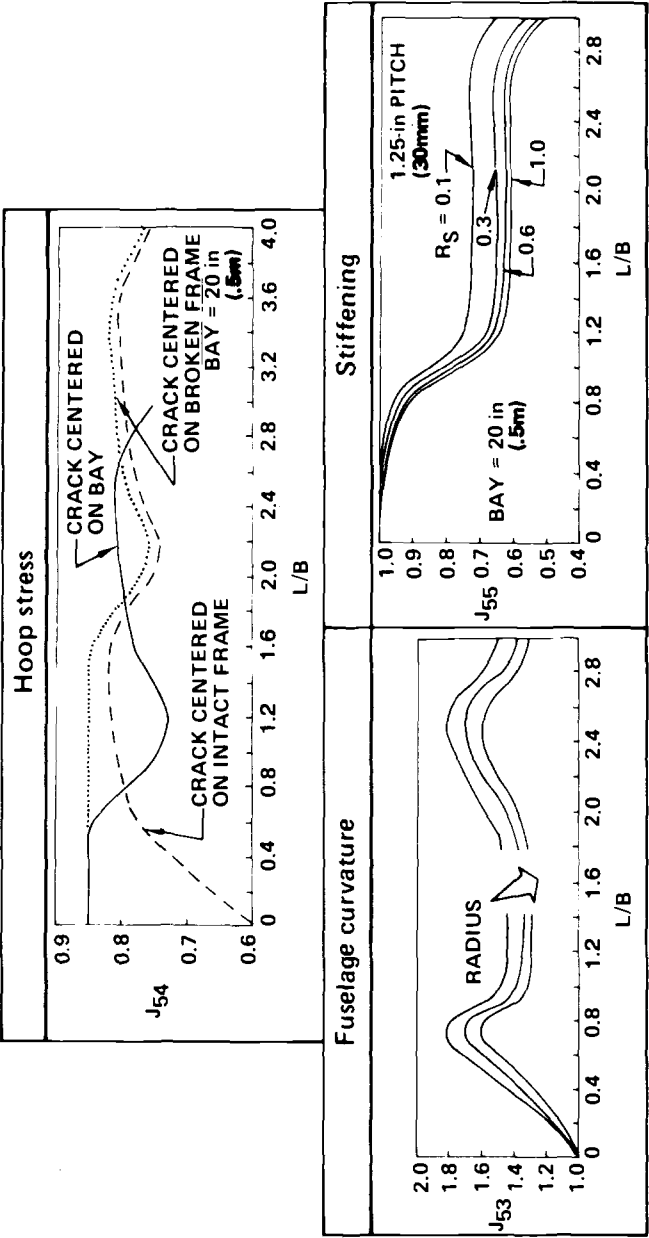


FIG. 29—Configuration/load redistribution factors—fuselage.

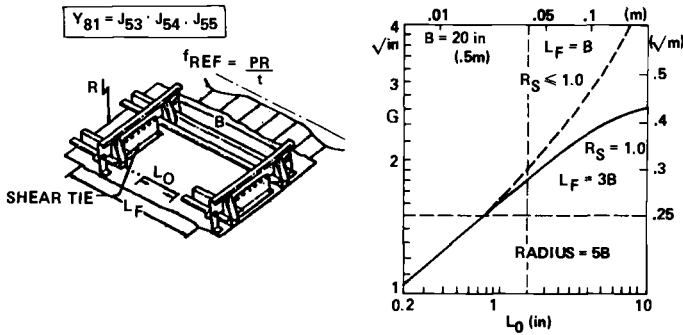


FIG. 30—G-factor for fuselage panel.

Crack Stress Ratings, S—Operating load conditions and spectra defined for durability analyses are also used for crack growth evaluations. Normalized spectrum crack growth evaluations can be performed on a flight-by-flight basis for fixed M/G values based on models reflecting growth rates at different combinations of alternating and steady-state crack-tip stress intensities. This eliminates repetitive cycle-by-cycle calculations for each combination of structural configuration, material, and crack length. The normalized damage analyses incorporate load sequencing effects to accommodate retardation-acceleration phenomena peculiar to jet transport loading spectra. The crack stress rating, S , collapses both spectrum and load sequencing effects into a single parameter reflecting damage growth per flight (Fig. 31).

Damage Detection

Detection of damage before it becomes dangerous is the ultimate control in ensuring damage tolerance throughout the economic life of the structure. It is important to note that for a specific detail the basic objective is the detec-

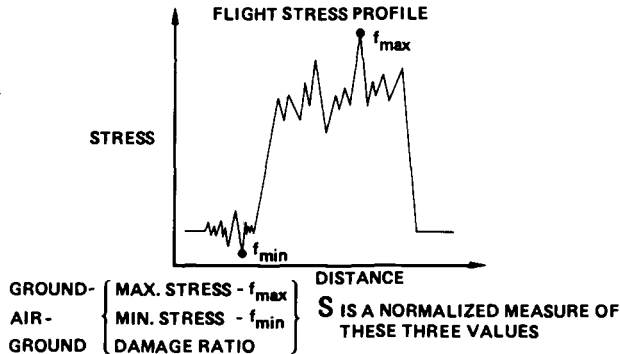


FIG. 31—Stress environment rating (S).

tion of “any” damage in the fleet, and not necessarily the most critical. It is then standard industry practice to investigate the damage circumstances and, when necessary, to call for inspection of all aircraft in the fleet at a detectable damage threshold, and to take other appropriate action. There are three principal sources of damage to aircraft structure; these must be considered independently (Fig. 32). Rating systems for these three primary damage sources provide a direct quantitative means of determining inspection requirements for maintaining structural integrity in a fleet of aircraft. Successful past practice and manufacturer and operator experience is used to determine the minimum inspection requirements. Full maintenance flexibility, which is essential for economic operation of the fleet, is retained without compromising safety.

Environmental Deterioration Rating (EDR) and Accidental Damage Rating (ADR) Systems—Environmental deterioration, which may or may not be time dependent, is characterized by structural deterioration caused by an adverse environment. For example, deterioration resulting from a breakdown in surface protection is more probable as the calendar age increases; conversely, corrosion due to galley spillage is a randomly occurring discrete event.

Maintenance programs must provide assurance of timely detection of corrosion or stress corrosion, that is, before the damage exceeds applicable regulatory requirements. Requirements to achieve this are based on an evaluation of susceptibility to and timely detection of this type of damage (Fig. 33). Susceptibility is assessed on the basis of probable exposure to an adverse environment and the adequacy of the protective system. Timely detection is assessed on the basis of sensitivity to relative size of damage and accessibility and visibility of the structure for inspection. Manufacturer and operator experience is a key ingredient for this type of evaluation. Inspection requirements from this evaluation are applicable to all aircraft in the fleet for both

DAMAGE PHASE	PRINCIPAL PARAMETERS CONTROLLING GIVEN SOURCE OF DAMAGE AND DAMAGE PHASE		
	FATIGUE	ENVIRONMENTAL DETERIORATION	ACCIDENTAL
INITIATION	<ul style="list-style-type: none"> ● QUALITY (DFR) ● CYCLIC STRESS ● OPERATING ENVIRONMENT ● FLIGHT CYCLES/HOURS 	<ul style="list-style-type: none"> ● CORROSION <ul style="list-style-type: none"> —OPERATING ENVIRONMENT —PROTECTIVE SYSTEM ● STRESS CORROSION <ul style="list-style-type: none"> —MATERIAL SENSITIVITY —LEVEL OF SUSTAINED TENSILE STRESS 	<ul style="list-style-type: none"> ● RANDOM DISCRETE EVENT FROM A CAUSE NOT NORMALLY ENCOUNTERED DURING FLEET OPERATIONS
GROWTH	<ul style="list-style-type: none"> ● MATERIAL ● GEOMETRY ● CYCLIC STRESS ● ENVIRONMENT ● FLIGHT CYCLES/HOURS 	<ul style="list-style-type: none"> ● EXTENT OF CONDITIONS THAT CAUSED DAMAGE INITIATION ● MAY RESULT IN SUBSEQUENT CRACK GROWTH IF NOT DETECTED AND REPAIRED 	<ul style="list-style-type: none"> ● MAY RESULT IN SUBSEQUENT CRACK GROWTH IF NOT DETECTED AND REPAIRED

FIG. 32—Principal damage sources.

• **EDR = SUSCEPTABILITY INDEX + TIMELY DETECTION INDEX**

SUSCEPTIBILITY INDEX		EXPOSURE TO ADVERSE ENVIRONMENT		
		ABOVE AVERAGE	AVERAGE	BELOW AVERAGE
ENVIRONMENTAL PROTECTION	STANDARD	0	1	2
	IMPROVED	1	2	3
	SPECIAL ATTENTION	2	3	4

TIMELY DETECTION INDEX		SENSITIVITY TO DAMAGE SIZE		
		HIGH	MEDIUM	LOW
VISIBILITY OF THE SSI FOR INSPECTION DURING SCHEDULED MAINTENANCE CHECKS	BELOW AVERAGE	0	1	2
	AVERAGE	1	2	3
	ABOVE AVERAGE	2	3	4

FIG. 33—*Environmental Deterioration Rating (EDR) system.*

damage tolerant and safe life structure. A fleet leader inspection program can be used to protect the fleet from time or age dependent sources of environmental deterioration.

Accidental damage is characterized by the occurrence of a random discrete event that reduces the inherent level of residual strength. Sources of such damage include ground and cargo handling equipment; manufacturing imperfections, foreign objects, erosion from rain, hail, lightning, etc.; runway debris; spillage; and human error during assembly, operation and maintenance.

Large-size accidental damage, such as that caused by engine disintegration, bird strike, and major collision with ground equipment, is considered as obvious. This type of damage is covered by specific regulations that require evaluation of residual strength capability for a short period of time. The maintenance program for all other types of accidental damage must provide assurance of timely detection of the damage before it exceeds applicable regulatory requirements.

Maintenance requirements to achieve this are based on an evaluation of susceptibility to residual strength after, and timely detection of, this type of damage (Fig. 34). Susceptibility is based on the likelihood of the structure receiving accidental damage. Residual strength is considered on the basis of the probable size of accidental damage, relative to critical damage size. Timely detection is considered on the basis of rate of growth after accidental damage and the accessibility and visibility of the structure for inspection. Inspection requirements from this evaluation are applicable to all aircraft in the fleet for both damage tolerant and safe life structure.

• **ADR = SUSCEPTIBILITY INDEX + TIMELY DETECTION INDEX**

SUSCEPTIBILITY AND RESIDUAL STRENGTH INDEX		LIKELIHOOD OF ACCIDENTAL DAMAGE		
		ABOVE AVERAGE	AVERAGE	BELOW AVERAGE
ESTIMATED RESIDUAL STRENGTH AFTER ACCIDENTAL DAMAGE	LOW	0	1	2
	MEDIUM	1	2	3
	HIGH	2	3	4

TIMELY DETECTION INDEX		SENSITIVITY TO DAMAGE GROWTH		
		HIGH	MEDIUM	LOW
VISIBILITY OF THE SSI FOR INSPEC- TION DURING SCHEDULED MAINTENANCE CHECKS	BELOW AVERAGE	0	1	2
	AVERAGE	1	2	3
	ABOVE AVERAGE	2	3	4

FIG. 34—Accidental Damage Rating (ADR) system.

Several parameters used to determine EDRs and ADRs stem from the same basic considerations. Many of the decisions used to determine these ratings are based on previous experience. In some cases, the operators have most of the background knowledge for determining relative values, and in other cases, it is the manufacturer. The primary responsibility for determining the relative values is shown in Fig. 35, based on inputs from both the operators and Boeing.

Worksheets are used to determine the EDRs and ADRs for all the Structurally Significant Items (SSIs) in the same general location and to allow convenient overviews of ratings so that appropriate inspection tasks can be defined for the SSIs. Since the rating assessments are relative to a given zone, no specific rating versus inspection interval can be established. Each zone will have a service proven acceptable level for external or internal surveillance. For example, external inspections of C or 2C, and internal at 4C, are used in many locations. These typical surveillance levels, which will generally be defined by the operators, should be related to the midportion of the rating scale. A zero rating is unacceptable, and added protection, or redesign, is required. The lowest acceptable rating, one, is generally related to the minimum interval the operators will use for inspecting a few critical details in the zone. Accessibility of these details is obviously a prime consideration.

Both the EDR and ADR systems are primarily subjective, relying heavily on past operator and manufacturer experience. To account for damage from unforeseen circumstances, a maximum interval for general surveillance should be determined for each zone. These intervals are generally quite short, for a new airplane model, until experience is gained in the fleet. Typical intervals used are 1C or 2C for external inspections and 4C for internal inspections.

RATING CATEGORY	APPLICATION		PRIMARY RESPONSIBILITY		KEY CONSIDERATIONS
	EDR	ADR	OPERATOR	BOEING	
VISIBILITY	•	•	•		VISIBILITY FOR INSPECTION AFTER ACCESS
SENSITIVITY TO DAMAGE SIZE OR GROWTH	•	•		•	<ul style="list-style-type: none"> • RELATIVE SENSITIVITY WITHIN ZONE CONSIDERED • EXTERNAL: MULTIPLE ELEMENT DAMAGE • INTERNAL: SINGLE ELEMENT DAMAGE
ENVIRONMENTAL PROTECTION	•		•	•	COMPARISON WITH PREVIOUS PROTECTION SYSTEMS AND RECENT SERVICE HISTORY
EXPOSURE TO ADVERSE ENVIRONMENT	•		•		CORROSION EXPERIENCE IN SAME ZONE
				•	MATERIAL SUSCEPTIBILITY TO STRESS CORROSION AND POTENTIAL FOR PRELOAD
LIKELIHOOD OF ACCIDENTAL DAMAGE		•	•		OPERATOR EXPERIENCE IN THE SAME ZONE
STRENGTH AFTER ACCIDENTAL DAMAGE		•		•	LIKELY SIZE OF DAMAGE RELATIVE TO CRITICAL DAMAGE SIZE

FIG. 35—Summary of key considerations and responsibilities for EDR and ADR evaluations.

On the new airplane models, reasonable access has generally been provided to all internal areas where previous experience has shown structural damage may occur. In other internal areas with a lower than average rating, but difficult access, an age exploration program is generally used. This means that at the maximum interval prescribed for internal inspections, each operator will inspect some part of their fleet on a rotational basis. The sample sizes used for age exploration are generally $\frac{1}{5}$ for tension loaded structure and $\frac{1}{10}$ for compression loaded structure.

Having established minimum, average, and maximum inspection intervals for each zone, the EDR and ADR system values can be evenly distributed between the known values. The resulting inspection program will have shown general surveillance proven adequate by previous service experience and a clear indication of structure requiring special consideration within each zone (Fig. 36).

Fatigue Damage Detection Rating System—Damage detection is normally considered in terms of the damage size at the time of an inspection, and the inspection method or procedure used. While this is still the basis for evaluating damage detection, there is a multiplicity of events which significantly increase the probability of detecting fatigue damage in aircraft structure (Fig. 37). The probability of detecting fatigue damage that has occurred on a specific detail in a fleet of aircraft is a function of three independent probabilities previously addressed by Goranson and Hall (Fig. 38).⁴

⁴Goranson, U. G. and Hall, John, "Airworthiness of Long-Life Jet Transport Structures," The Royal Aeronautical Society Spring Convention on Long-Life Aircraft Structures, London, May 1980.

RATING	GROUND RULES FOR ESTABLISHING STRUCTURAL INSPECTION INTERVALS
1	LOWEST PRACTICAL INTERVAL FOR INSPECTING A FEW CRITICAL SSI's IN THE ZONE CONSIDERED
2	INTERMEDIATE INTERVALS EQUALLY SPACED BETWEEN INTERVALS ESTABLISHED FOR 1 AND 4
3	
4	SERVICE PROVEN ACCEPTABLE INTERVALS FOR EXTERNAL OR INTERNAL SURVEILLANCE OF THE ZONE CONSIDERED
5	INTERMEDIATE INTERVALS EQUALLY SPACED BETWEEN INTERVALS ESTABLISHED FOR 4 AND 7/8
6	
7	MAXIMUM INTERVAL CONSIDERED ADEQUATE FOR DETECTING DAMAGE FROM UNFORESEEN CIRCUMSTANCES. THE INTERVALS ARE GENERALLY BASED ON ECONOMIC CONSIDERATIONS FOR ACCESSIBILITY AND REPAIR. AN AGE EXPLORATION PROGRAM IS USED FOR INTERNAL STRUCTURE WITH DIFFICULT ACCESS
8	

FIG. 36—Relationship between ED/AD ratings and inspection intervals.

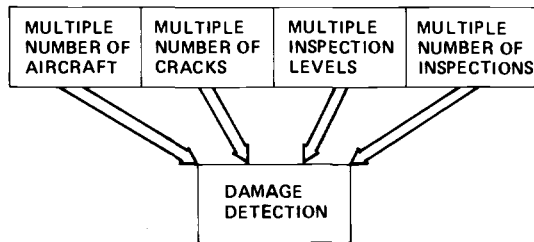


FIG. 37—Damage detection in a fleet of aircraft.

The probability of inspecting an aircraft with a damaged detail, P_1 , is a function of the number of aircraft inspected and their position in the fleet relative to a given fatigue life. With the assumption that damage has occurred, $P_1 = 1$ when the full fleet is inspected. The influence of inspection sampling procedure on P_1 is shown in Fig. 39. The fleet leader and selected high-time curves show the advantages of supplemental inspections on fleet leader aircraft. These curves will vary in shape with fleet size and use. Values of P_2 , the probability of inspecting the detail considered, will generally be one or zero for an individual airline. This value determines which maintenance levels are used to inspect the detail. Typical fleet values are used for design checking purposes. For a single inspection of the detail considered ($P_2 = 1$) on an aircraft with damage ($P_1 = 1$), the probability of detecting damage \hat{P}_3 , is a function of crack length, inspection check level, and detection method (for example, visual, ultrasonic). It is considered in terms of a three-parameter Weibull distribution:

$$\hat{P}_3 = 1 - \text{EXP} \left[- \left(\frac{L - L_0}{\lambda - L_0} \right)^\alpha \right]$$

in which the three parameters are: L_0 , the threshold below which cracks are assumed undetectable; λ , the characteristic crack length of the distribution; and α , the shape function. \hat{P}_3 is derived from service cracking data, taking due account of the inspections that failed to detect a known crack (Fig. 40).

A large data base of reported service cracking is used to determine individual aircraft crack sizes at previous inspections. The total number of non-detection events is usually 20 to 50 times larger than the detection events and influence the detecting probabilities significantly (Fig. 41). Data bases are continuously updated and provide a viable link to operator maintenance practice in terms of damage detection statistics.

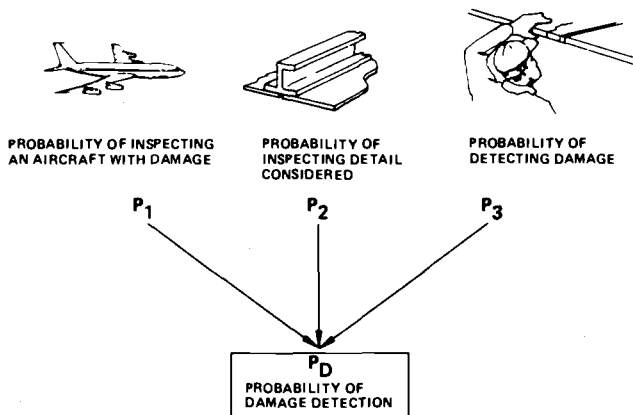


FIG. 38—Probability of damage detection (P_D).

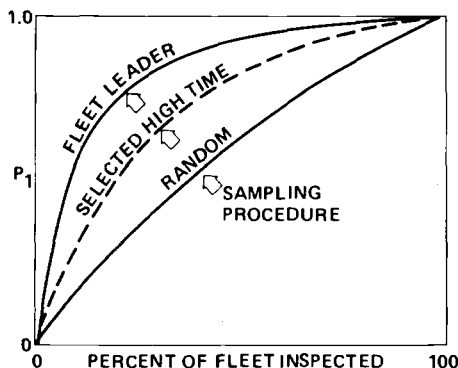


FIG. 39—Probability of inspecting an aircraft with damage (P_1).

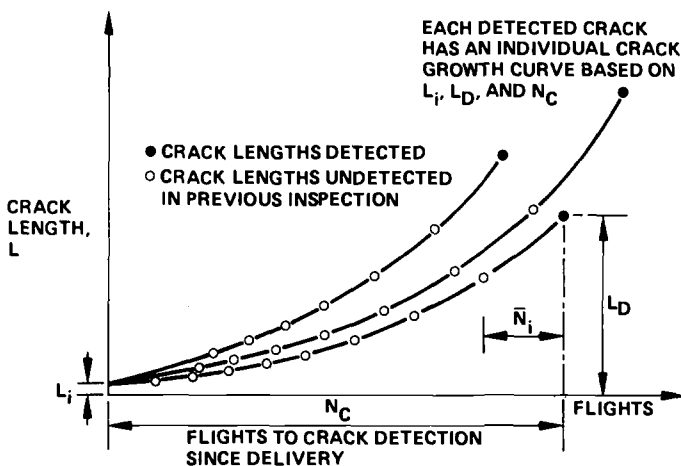


FIG. 40—Detection and nondetection events.

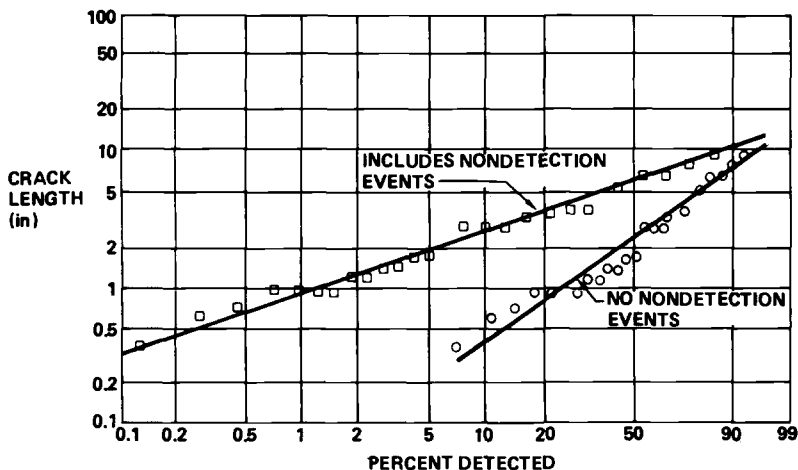
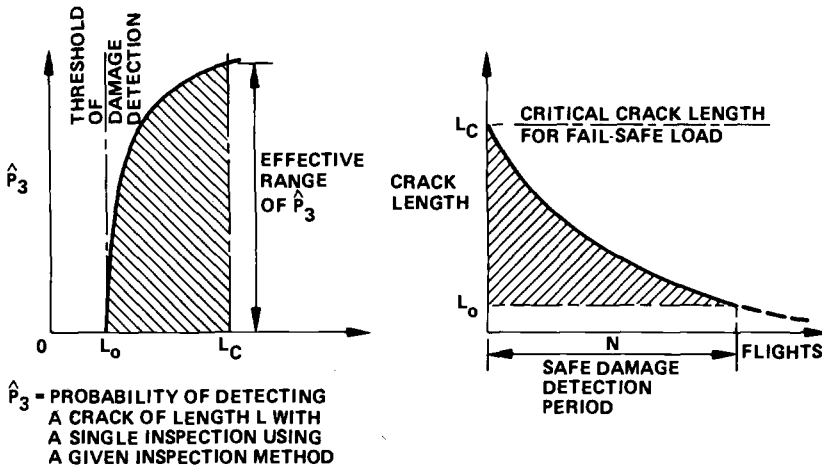


FIG. 41—Effect of nondetection events.

To ensure continued safe operation, it must be shown that there is a high probability of detecting fatigue damage in the fleet before any damage exceeds the applicable regulatory requirements. The safe damage detection period, therefore, ranges from a detectable crack threshold to critical damage size for fail-safe load (Fig. 42). It is important to note that failure to detect damage before exceeding the critical size does not automatically mean loss of an aircraft. Catastrophic failure will only occur if the damaged aircraft experiences the design fail-safe load while the critical size crack remains undetected, an extremely unlikely event.


 FIG. 42—Safe damage detection period (N).

Crack length at the time of an inspection is random. The last inspection during the damage detection period, N , occurs at some point during the final inspection interval, \bar{N} (Fig. 43). A typical location for the final inspection corresponds to the average \hat{P}_3 -value during the interval \bar{N} . With the position of the final inspection established, the previous inspections are spaced at intervals of \bar{N} , prior to this. A crack length and hence \hat{P}_3 -value can now be associated with each inspection. Assuming $P_1 = P_2 = 1.0$, the cumulative probability of detection for a *single airplane* during the period N is derived by considering the product of the nondetections in the equation

$$P_3 = 1 - \prod_{i=1}^n (1 - \hat{P}_{3i})$$

where n is the number of inspections (integer).

In some cases the inspection interval \bar{N} is equal to or greater than the damage detection period. For these cases, the location of the inspection is derived by considering $\bar{N} = N$. The probability that this inspection will occur during the period N is accounted for by the equation

$$P_3 = \hat{P}_3 \cdot N/\bar{N}$$

Experience has shown that when damage is detected in the fleet, further inspections generally reveal additional damage in the same detail on other aircraft and/or a similar detail at another location. Additional damage in the fleet increases the probability of detecting at least one crack. The number of flights between damage occurrences in the fleet of the same detail, ΔN , can

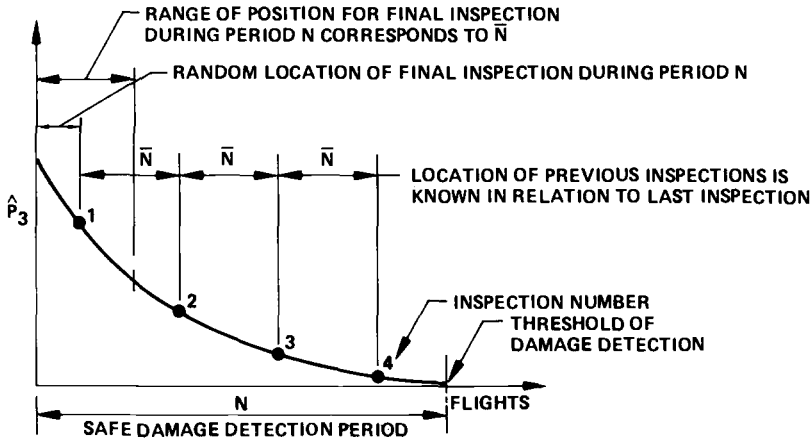


FIG. 43—Multiple inspections.

be derived from actual fleet cracking statistics or from fleet utilization and fatigue life distribution. If the first damage is detectable at N_1 -flights, the second damage will reach the same level of detectability at $N_1 + \Delta N$, and the third at $N_1 + 2 \Delta N$ (Fig. 44).

Each successive crack occurring during the period N has a reduced interval for detection and final crack length. Taking this into consideration, the cumulative probability of detection can be determined for each crack using the same procedure. From this the probability of crack detection *in the fleet*, using a given inspection method and frequency, is given by

$$P_3 = 1 - \prod_{j=1}^m \prod_{i=1}^n (1 - \hat{P}_{3ij})$$

where the \hat{P}_{3ij} are the probabilities of detection on the i th inspection on the j th cracked airplane. During the damage detection period N , m is the number of cracked aircraft, and n is the number of inspections performed on the j th cracked airplane.

For convenience an equivalent constant probability of detection for each inspection can be defined by

$$\bar{P}_3 = 1 - (1 - P_3)^{\bar{N}/N}$$

Considering all levels of inspection in the fleet, the cumulative probability of damage detection is given by

$$P_D = 1 - \prod (1 - P_{di})$$

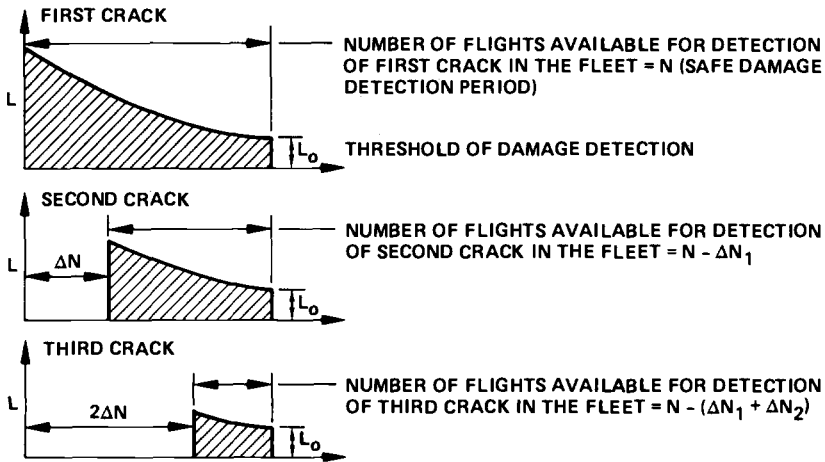


FIG. 44—Multiple cracking in the fleet.

where

$$P_d = P_1 \cdot P_2 \cdot P_3, \text{ and}$$

i = applicable inspection (A, B, C, D, or S).

Values of P_D such as 0.999 and 0.998 appear to be very close. If the probability of not detecting damage ($1 - P_D$) is considered, it can be seen that there is actually a two to one difference in these values. This provides a better comparison between P_D -levels. To provide a direct qualitative measure of design and/or maintenance planning actions, an equivalent number of 50/50 opportunities of detection is used to define a Damage Tolerance Rating (DTR) (Fig. 45).

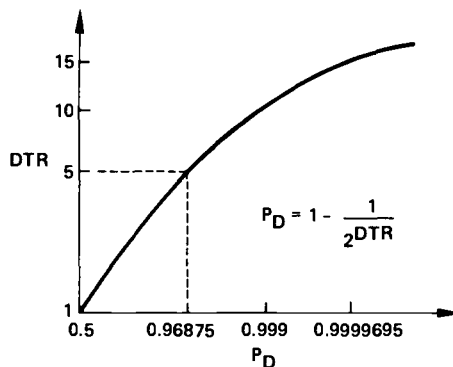


FIG. 45—Damage Tolerance Rating (DTR) definition.

The DTR system uses the principal random variables that influence damage detection in the fleet and is the most suitable for comparative analysis of similar structural details. The procedure for using the DTR system for a quantitative comparative detectability evaluation is outlined in Fig. 46. The most realistic and reliable method for establishing acceptable damage detection characteristics is to evaluate previous service cracking history. In some cases the design configuration or damage detection circumstances are considered inadequate and the service data should only be used indirectly or not at all. For most cases the design and/or the damage detection circumstances are adequate and can then be used with the corresponding maintenance history to establish demonstrated acceptable DTRs.

The maintenance planning requirements for new design, or existing structure where damage has not been detected, can be evaluated by the DTR system. The calculated DTR for a maintenance plan is derived by considering fleet demonstrated detectability standards in conjunction with typical crack growth/residual strength characteristics. The detectability margin is adequate if the calculated DTR is equal to or greater than the demonstrated acceptable DTR.

Conclusions

This paper has outlined the criteria and procedures used to design long-life damage tolerant commercial aircraft structures. New durability and damage tolerance technology development has been spurred by revisions to federal airworthiness regulations and the desire to maintain the present credible safety record in the aging fleets.

Assurance of continuing airworthiness requires adequate durability and

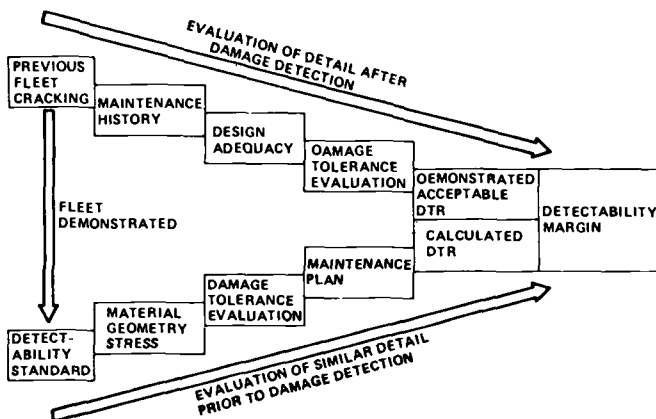


FIG. 46—Comparative detectability evaluation.

damage tolerance design of all primary airframe structure. This leads to development of technology control methods suitable for use by large teams of nonspecialist engineers. These methods are adapted from traditional fatigue and fracture mechanics technologies supported by a large test and service experience data base.

Damage tolerance rating systems are being developed to allow proper recognition of damage detection opportunities in a fleet of aircraft with possible multiple cracking events and subjected to a multitude of inspections. These systems provide efficiency measurements of flexible manufacturer/operator/certifying agency actions to ensure continuing structural airworthiness.

The next generation of Boeing commercial jet transports will incorporate these technological advancements from the outset, assuring continuing airworthiness and economic operation throughout their service life. Improvements in the design process and efficient surveillance of operating aircraft will continue to produce one of the world's safest transportation systems.

Design and Criteria

Selected Aspects of the Design of Offshore Structures for Fatigue Resistance

REFERENCE: Hartt, W. H., "Selected Aspects of the Design of Offshore Structures for Fatigue Resistance," *Design of Fatigue and Fracture Resistant Structures*, ASTM STP 761, P. R. Abelkis and C. M. Hudson, Eds., American Society for Testing and Materials, 1982, pp. 91-109.

ABSTRACT: The problem of fatigue of welded steel connections in sea water is reviewed, and it is demonstrated that this failure mode is most troublesome in deep water or rough sea locations where 10^7 to 10^8 relatively low-stress range load excursions must be anticipated during a typical design life. Mechanical, material, and environmental variables which influence this fatigue are discussed; and attention is focused upon the effects of cathodic protection, where existing data appear contradictory. The appropriateness of a design procedure which integrates $S-N$ and $(da/dN)-\Delta K$ data is discussed, and examples of its applicability to welded specimens and connections in sea water are presented.

KEY WORDS: fatigue, sea water, offshore structures, cathodic protection, welded steel, fracture mechanics

Nomenclature

a	Crack depth
E	Young's modulus
$\Delta\epsilon$	Strain range per fatigue cycle
ΔK	Stress intensity range
ΔK_0	Threshold stress intensity range
M_s	Free surface stress correction factor
M_t	Finite thickness stress correction factor
M_p	Plasticity stress correction factor
M_k	Stress concentration due to geometry of weld reinforcement
N	Cycles of loading, cycles to failure, or cycles of crack growth

¹Professor and Director of the Center for Marine Materials, Department of Ocean Engineering, Florida Atlantic University, Boca Raton, Fla. 33431.

- R Ratio of minimum stress to maximum stress per cycle
 S Stress per fatigue cycle
 ϕ Complete elliptical integral

Fatigue has been judged to be an important factor with regard to the integrity of offshore structures [1-4].² Historically, marine engineering activity such as petroleum production has taken place in relatively shallow, calm waters (near-shore Gulf of Mexico, for example). For this type of exposure, failure due to fatigue is typically of lesser consequence than damage from occasional severe storms, the latter being readily accounted for in terms of existing design criteria [3]. On the other hand, weather and sea-state conditions in frontier-type areas, such as the North Sea and Gulf of Alaska, are more severe. Figure 1 illustrates that during a 50 year period this latter type service may result in several orders of magnitude more stress cycles in the 70 to 140 MPa (10 to 20 ksi) stress range than for the former (near-shore Gulf of Mexico). A similar situation arises for deep-water structures, even in relatively calm waters, due to the fact that the period of small waves is close to the first mode period of the structure [3].

Based upon this rationale it is apparent that design of offshore structures for service in deep water or rough seas requires that occurrence of 10^7 to 10^8 cycles of relatively low stress amplitude and frequency in the range of 0.05 to 0.5 Hz be considered. Development of realistic test data for these specific conditions requires unduly long test times, however; and so accelerated ex-

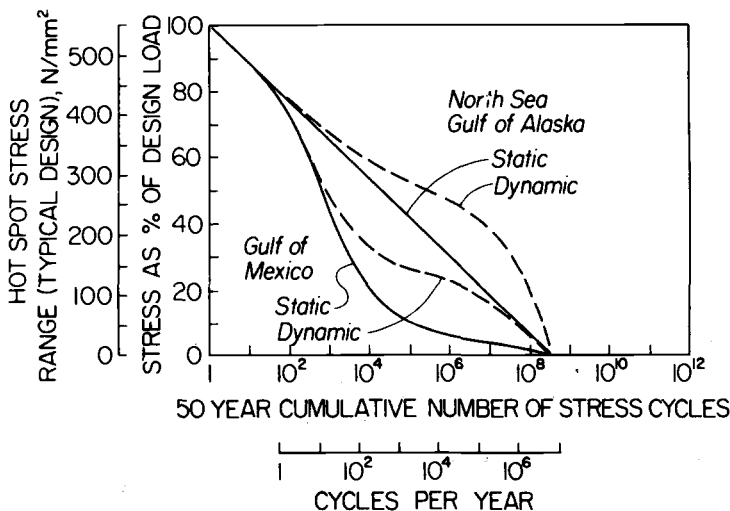


FIG. 1—Projected long-term stress distribution for several different global locations [3].

²The italic numbers in brackets refer to the list of references appended to this paper.

periments have historically been employed for the purpose of developing information from which design criteria are developed. Figure 2 illustrates that the intermediate portion of the AWS fatigue design curves [5] represents a lower bound to test data available as of several years ago [6]. The results included here are for tubular joint and similar as-welded specimens from various investigations. In all instances the welds conformed to a Class C profile, where the weld metal merges smoothly with the parent plate. Note that there are actually two curves beyond 2×10^6 cycles. The AWS-X considers that the $S-N$ curve levels off in the high-cycle regime, perhaps due to a beneficial influence of cathodic protection. Design based upon this curve has more recently been judged as lacking appropriate conservatism [7], as will be discussed subsequently. Alternatively, the AWS-X Modified represents a straight-line extension of the lower cycles curve, possibly reflecting concern on the part of its formulators for corrosion and for the presence of notches.

The point of emphasis here, however, is that the choice and justification of these or any other design curve beyond about 10^6 cycles is difficult based upon past experimental information. On the one hand, designers must incorporate adequate conservatism into their plan; alternatively, the economic penalties for overdesign may be enormous.

The purpose of the present paper is to discuss various important aspects of the high-cycle fatigue problem for welded steel in sea water and to evaluate applicable data that have recently become available. Also considered is a new, potentially useful approach to this problem which could lead to enhanced confidence in design procedures and to better certainty regarding scheduling of inspection and repair operations.

Fatigue Variables

While the lack of relevant high-cycle fatigue data, as apparent from Fig. 2, is due in part to the fact that we are dealing with large numbers of relatively low amplitude stress cycles which are applied at a slow rate, the difficulty in establishing a confident design curve in the high-cycle region is compounded by the complex nature of fatigue of welded steel in sea water and by the large number of significant variables. These include (1) a complex service stress history, (2) the variable structure and properties of welds, and (3) influences from sea water and cathodic protection.

Service Stress History

To accomplish fatigue design calculations a Miner's rule type procedure is specified, where the long-term sea state is divided into an appropriate number of sub-states. Thus, the damage which results from the significant stress range of each, when applied for the appropriate number of cycles, is determined; and the net damage, D , is then determined by summing the contri-

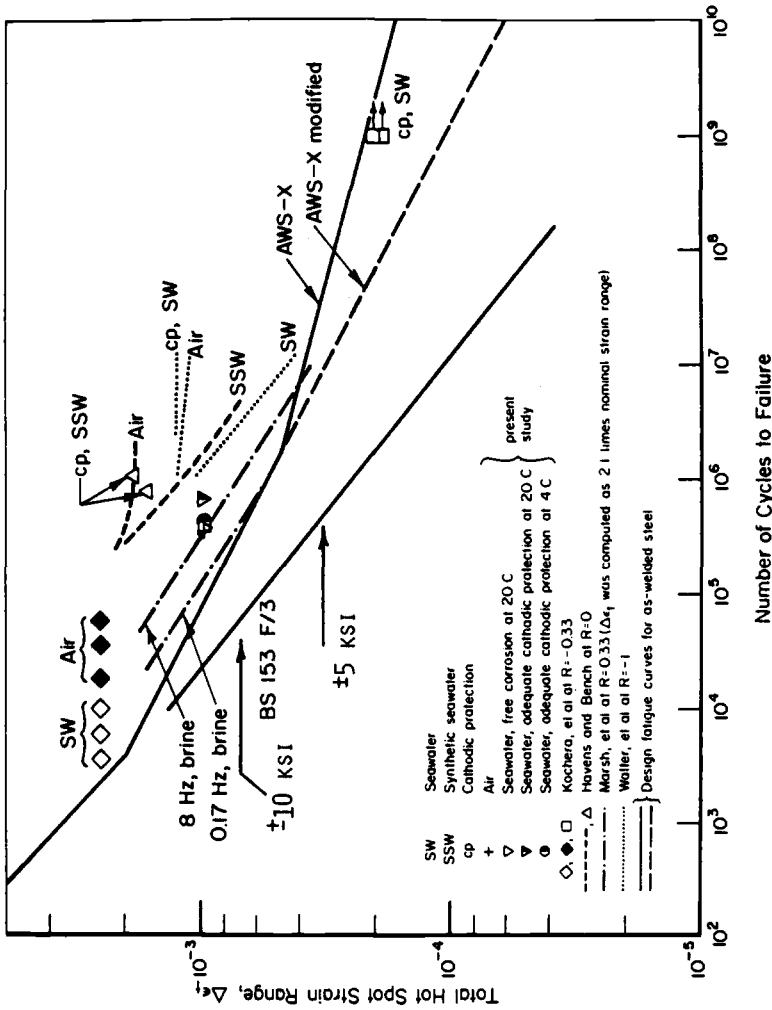


FIG. 2—AWS fatigue design curves and related test data for welded specimens and tubular connections.

bution from all sub-states. Such a technique is generally recognized as being an approximation only because firstly, it neglects interactive effects and, secondly, it considers stress cycles below the endurance to be nondamaging.

The aircraft and automotive industries have developed standardized load spectra for the purpose of overcoming the aforementioned difficulty. However, activity in the offshore fatigue community has not yet advanced to this same extent, although recently several spectra have been proposed which might ultimately achieve this [8-11]. Little fatigue data based upon these are yet available, however.

Structure and Properties of Welds

While it is generally recognized that numerous types of defects influence mechanical properties of welded members, the weld profile and the stress concentration that results are considered to be particularly important with regard to tubular connections of offshore structures [6]. Analytical investigations have addressed the significance of weld height, angle, and toe radius, as illustrated in Fig. 3, upon the stress concentration that results at welds [12]; and tests have shown that fatigue life increases with decreasing weld height [13] and with increasing included angle [13,14]. While decreasing toe radius increases the stress concentration factor, the significance of this variable is apparently less than for the other two factors (weld height and angle) [13].

The offshore industry generally specifies that connections conform to a Class C weld, which requires that weld metal merge smoothly with the adjoining base metal. Concerns regarding whether or not such weld quality is universally realized on actual structures, along with recent test results employing specimens without profile control, have prompted a more conservative set of design curves [15]. These are illustrated in Fig. 4, where it is apparent that

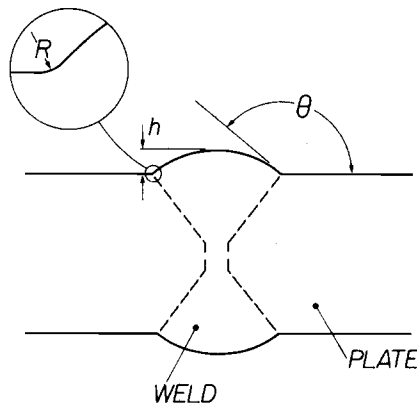


FIG. 3—Schematic representation of a butt weld in terms of weld height, h , weld angle, θ , and toe radius, R .

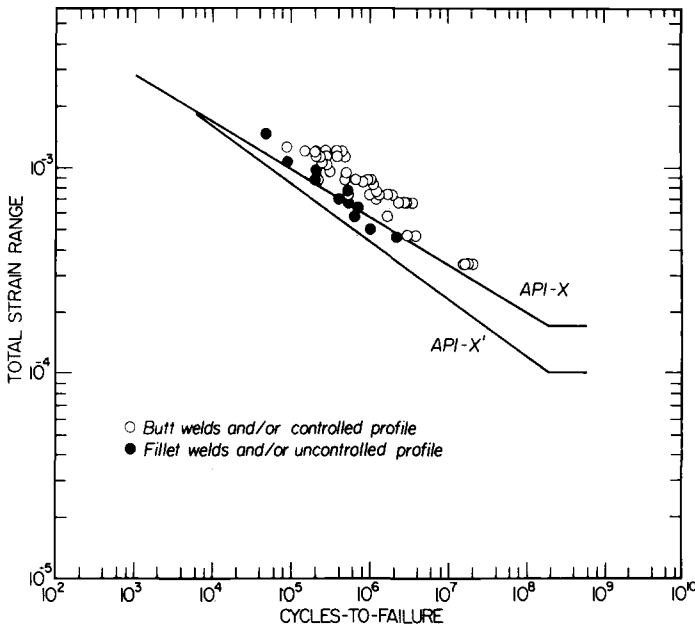


FIG. 4—Fatigue data from various investigations as referenced to the API-X and API-X' design curves.

recent data for specimens with profile control [16–18] fall to the safe side of the API-X (alternatively, AWS-X Modified) curve. Similarly, the API-X' curve is conservative with regard to the data from specimens without profile control [19,20].

Electrochemical (Corrosion) Factors

It is generally recognized that the presence of an aqueous corrosion environment reduces fatigue resistance of steel compared with exposure in air [21]. This corrosion component of the net damage is generally more significant the lower the cyclic stress amplitude [22] and the less the frequency [23]. Hence it is in the high-cycle region of the S - N curve where corrosion is likely to be most influential.

Numerous fatigue investigations employing smooth structural steel specimens have demonstrated that any corrosion prevention technique which reduces the rate of uniform attack enhances fatigue resistance. For example, it has been shown that reducing the uniform corrosion rate to a sufficiently low value, either by deaeration [23] or by cathodic polarization [24], restored the air endurance limit of 1018 steel specimens in a sodium chloride (NaCl) solution. Similarly, several investigations have demonstrated that the endurance limit of notched steel specimens in sea water and synthetic sea water can be

increased to above the air value provided potential is sufficiently negative [25-27]. This result could be directly important to welded steel members, since the weld toe region represents, in effect, a notch. Figure 5 presents results of recent fatigue experiments where 25.4 mm thick by 152 mm wide welded ABS DH 32 steel specimens were fatigued in flowing sea water at 3 Hz [16]. With the exception of the single cathodically protected specimen which failed at 27×10^6 cycles, all welds conformed to a Class C profile. Consistent with projections made above with regard to Figure 4, the data all lie to the safe or conservative side of the API-X design curve. The data also illustrate a beneficial influence upon fatigue resistance of cathodically polarizing the steel from the freely corroding potential [≈ -0.65 V, saturated calomel electrode (SCE)] to -0.78 V. Improvement is even greater for polarization to -0.93 V, at least at the higher stress investigated (138 MPa). Since cathodic protection is the primary corrosion prevention technique which is employed to mitigate corrosion in submerged marine situations, these results may be directly applicable to design of offshore structures in the high-cycle regime.

It has been suggested [28] that the fracture mechanics approach to design for fatigue prevention is particularly appropriate in the case of welded components, such as tubular joints of offshore structures, since defects in the size range 0.1 to 0.5 mm are typically present from the welding process [29]. Hence it may be reasoned that fatigue life of the member or structure is the number of cycles for such an initial crack-like defect to grow to critical size.

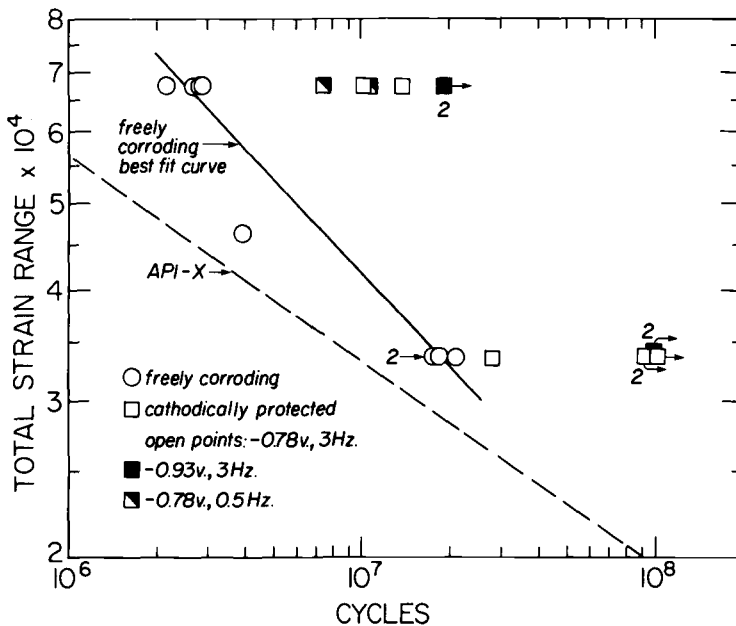


FIG. 5—Results of recent fatigue tests with respect to the API-X design curve.

Analyses based on this rationale, where the accepted relationship between stress intensity range and crack growth rate,

$$da/dN = C(\Delta K - \Delta K_0)^m \quad (1)$$

has been integrated between appropriate limits, have claimed good agreement of the results with experimentally determined $S-N$ curves [28,30]. A problem with $S-N$ curve prediction based upon fracture mechanics analysis becomes apparent, however, when the influence of environment and cathodic protection upon ordering of the crack growth rate curves is considered. For example, Scott and Silvester [31,32] have performed comprehensive fatigue crack growth rate (FCGR) determinations upon BS 4360 Grade 50D steel under cyclic stress and environment conditions comparable to those which occur at welded tubular connections of offshore structures. Figure 6 illustrates their results for the freely corroding situation, where for $\Delta K \leq 18 \text{ MN m}^{-3/2}$ crack growth rate in sea water was equal to or less than in air. This is

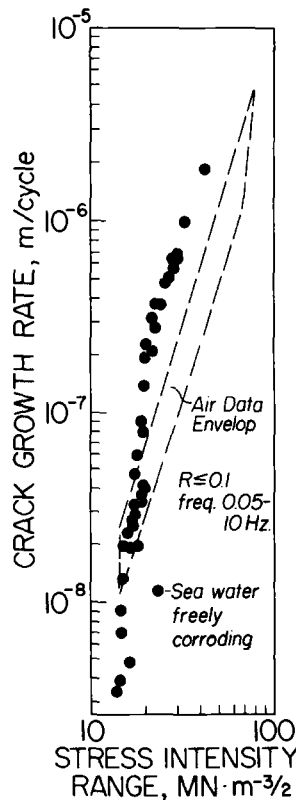


FIG. 6—FCGR versus stress intensity range data for freely corroding specimens under test conditions applicable to marine structures.

in qualitative agreement with data of Vosikovsky [33], who fatigued X-65 line pipe steel in a 3.5 percent NaCl-distilled water solution. If one considers, though, that the major portion of life of a welded member fatigued in the high-cycle regime occurs with the crack small, such that stress intensity range is low ($< 18 \text{ MN m}^{-3/2}$), then the fracture mechanics approach predicts life in sea water to be greater than or equal to that in air. It is in the low-stress region of the S - N curve, however, where corrosion reactions have been found to have the most compromising influence upon fatigue life.

Scott and Silvester [31] further observed that for the same experimental conditions as in Fig. 6 and for $20 < \Delta K < 40 \text{ MN m}^{-3/2}$ small amounts of cathodic polarization ($\approx 0.07 \text{ V}$) reduced crack growth rate relative to the freely corroding value by a factor of 0.3 to 0.4, but the rate increased with further polarization and at -1.00 V (Ag/AgCl) was in excess of that with no polarization. For $\Delta K < 20 \text{ MN m}^{-3/2}$, cracks propagated at about the same rate in both freely corroding and cathodically protected specimens. It is difficult, however, to project trends for this latter experimental condition, first, because data are limited and, second, because crack growth is highly sensitive here to variations in stress intensity range.

In the case of welded members it can be reasoned that crack growth rate at high mean stress intensities should be considered. Figure 7 presents data for this situation and shows crack growth rate under freely corroding conditions to be greater than in air down to 10^{-8} m/cycle . Thus in this case the approach does allow a correct prediction of the S - N curve order. However, the same does not hold true for conditions of cathodic protection, since at low ΔK potential has little influence upon crack growth rate and for $10 < \Delta K < 20 \text{ MN m}^{-3/2}$ polarization to -0.85 V enhances crack growth rate relative to the freely corroding value (Fig. 7). This result contrasts with the accepted influence of potential upon ordering of S - N curves, as discussed previously in conjunction with Fig. 5. Based upon these comparisons it may be argued that an approach to fatigue design of welded components and structures for submerged offshore service involving small-amplitude stresses which considers life to be comprised solely of the time for small defects to propagate to critical size is inappropriate.

A possible explanation for this apparent lack of correspondence between the S - N and (da/dN) - ΔK approaches to fatigue life prediction is that corrosion and cathodic polarization have contrasting influences upon fatigue crack nucleation and crack propagation. Thus, in the high-cycle regime of the S - N curve the cycles for crack nucleation (alternatively, cycles for crack nucleation and initial growth) may be significantly reduced by corrosion and enhanced by cathodic polarization. The influence of potential upon crack growth is often opposite to this, however, as discussed in conjunction with Figs. 6 and 7. On the other hand, it may be that the interactive influence of sea water and cathodic polarization upon fatigue crack growth is not yet adequately characterized in the low ΔK (threshold) regime. The added possi-

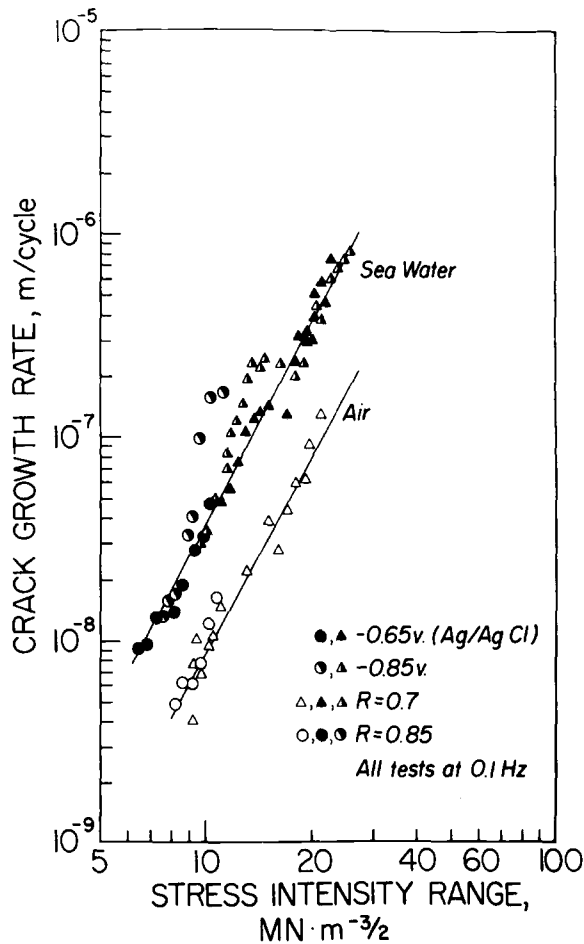


FIG. 7—FCGR versus stress intensity range data for freely corroding and cathodically polarized specimens under test conditions applicable to marine structures and for high R-values.

bility that growth characteristics of cracks of the size of weld defects (several millimetres and less) might be different from larger cracks, as observed by Bardal et al [34,35], should be considered.

A factor which additionally complicates quantification of fatigue crack growth rates in sea water under conditions of cathodic polarization is formation of calcareous deposits [36,37] within the crack. These deposits are comprised principally of CaCO_3 and $\text{Mg}(\text{OH})_2$ which precipitate on or near the metal surface as a consequence of the cathodic current and the resultant increase in pH of the electrolyte in this region [36]. Deposits have been observed to form preferentially within cracks [31], presumably because of greater alkalinity here, and to affect a reduction in crack growth rate or com-

plete arrestment [26,27]. This has been attributed to a lowering of the effective stress intensity range due to interference on the part of the deposits with crack closure [38].

The specimen in Fig. 5 which was cathodically polarized to -0.78 V and which failed at 27×10^6 cycles requires special comment. Post-test sectioning disclosed an undercut approximately 0.35 mm deep at the weld toe (Fig. 8). Despite this, fatigue life was still about 50 percent greater than for comparable tests on freely corroding specimens without undercuts. This may be attributed to a significant benefit of cathodic polarization to -0.78 V upon fatigue crack growth during that period when the crack was small.

Interface of $S-N$ and $(da/dN)-\Delta K$ Approaches

A potentially useful interface of fracture mechanics with existing design criteria for offshore construction may be proposed, based upon a modification of the representation developed by Sprowls et al [39]. The approach is consistent with the aforementioned consideration that different factors may control the corrosion fatigue process in the nucleation and small crack stage compared with after the crack is developed. A generalized, sequential illustration of this is projected in Fig. 9. On the left side the procedure involves (1) characterization of the joint *per se* and of the weld according to its geometrical severity and the resultant hot spot stress (Fig. 9a), (2) development of a fatigue design curve for this particular type of weld, based upon experimental data or theoretical analysis or both (Fig. 9b), and (3) selection of a design strain range, based upon projected life (Fig. 9b). In principle, this technique is identical to the present AWS and API procedures.

Consider now a plot of strain range versus crack size (Fig. 9c), where the design strain range from (3) above appears as a horizontal line. From $(da/dN)-\Delta K$ data (Fig. 9d), where material, fatigue, and environmental variables have been appropriately selected for the application in question, the threshold value for fatigue crack growth is determined. From the fundamental relationship

$$\Delta K = E \Delta \epsilon (\pi a)^{1/2} \quad (2)$$

the second curve (sloping) in Fig. 9c is calculated. If the state of the member or joint is such that it falls within the lower left region or "safe zone," then neither fatigue crack initiation or growth of any existing crack should occur within the design life. The crack size designated as "significant" indicates the minimum size flaw which should propagate due to cyclic stressing of magnitude equal to the design strain range. If this "significant crack size" (SCS) is greater than the size of crack-like defects from welding or elsewhere, then crack growth should not occur.

The nature of a surface crack emanating from a weld toe is such that quan-

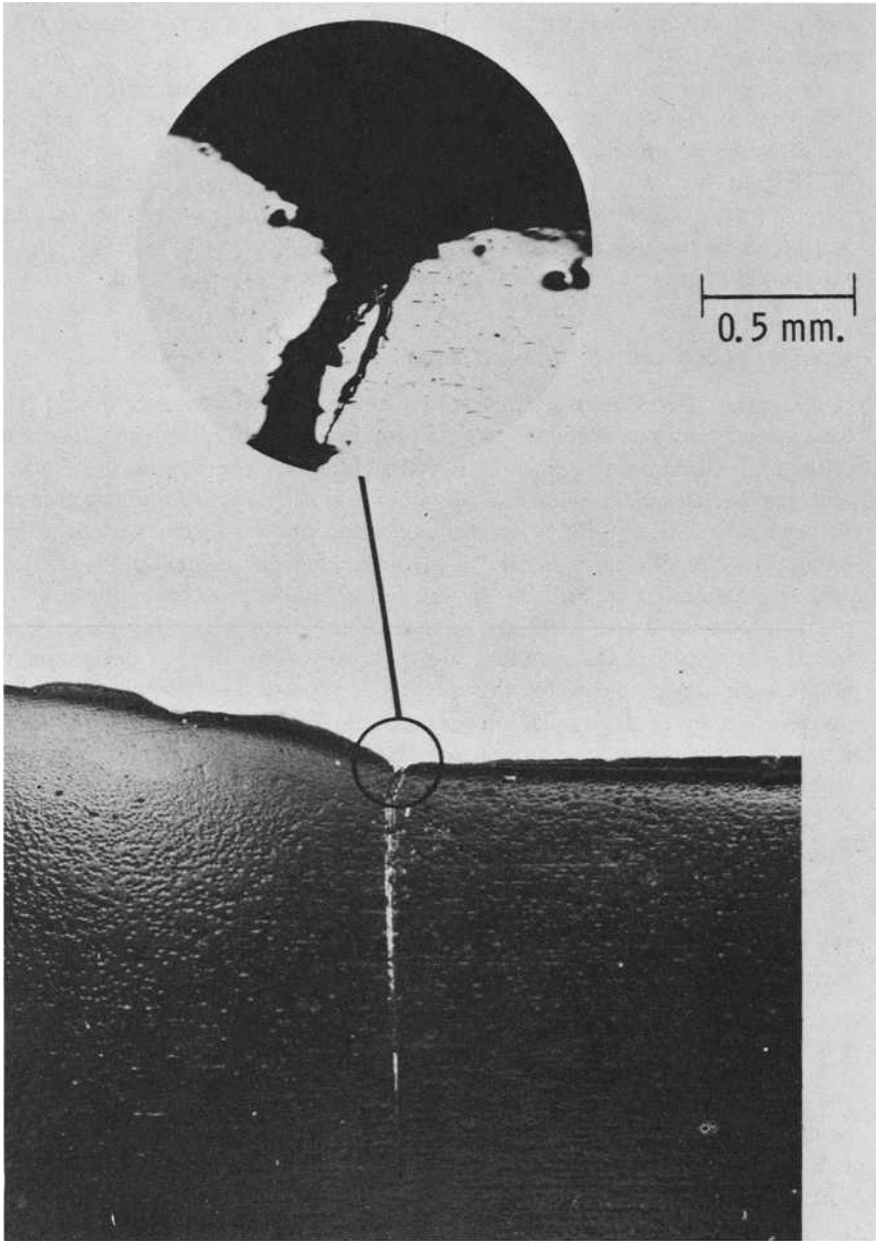


FIG. 8—*Appearance of typical section through cracked portion of the specimen which failed at 27×10^6 cycles. Note undercutting at weld toe.*

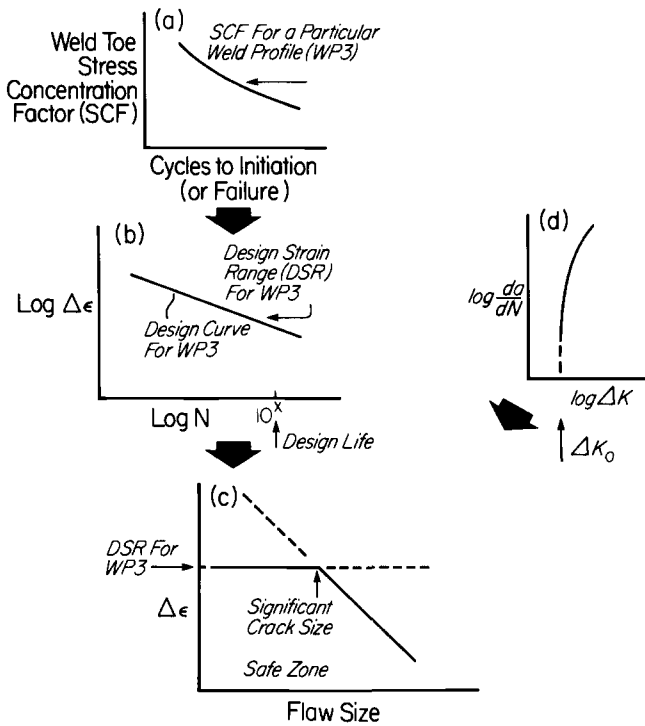


FIG. 9—Generalized representation of proposed design rationale.

titative development of Fig. 9c requires a more comprehensive statement of the stress intensity range. Thus, by the development of Maddox [40],

$$\Delta K = \frac{M_s M_t M_p M_k}{\phi} E \Delta \epsilon (\pi a)^{1/2} \quad (3)$$

Based upon evaluation of the influence of various weld, crack, and plate dimension and shape parameters upon M_k by Gurney [41] and assuming $\Delta K_0 = 3 \text{ MN m}^{-3/2}$, Fig. 10 illustrates this approach for the case of a butt weld. Curves for two weld angles are included, showing that the more the safe zone area is reduced the more severe the weld geometry. The effect of weld angle is greater the smaller the crack. Strain ranges corresponding to the API-X (alternatively, AWS-X Modified) and API-X' curves at $N = 2 \times 10^8$ cycles are illustrated. For design to the latter situation (API-X' at 2×10^8 cycles) $SCS = 6 \text{ mm}$, irrespective of the two weld angles considered. In the former case (API-X strain range at 2×10^8 cycles) the corresponding crack size is 2.2 mm for the 135 deg weld and 2.6 mm for the 160 deg weld. Note that in this region below about 2×10^{-4} , SCS is highly sensitive to the total strain range value.

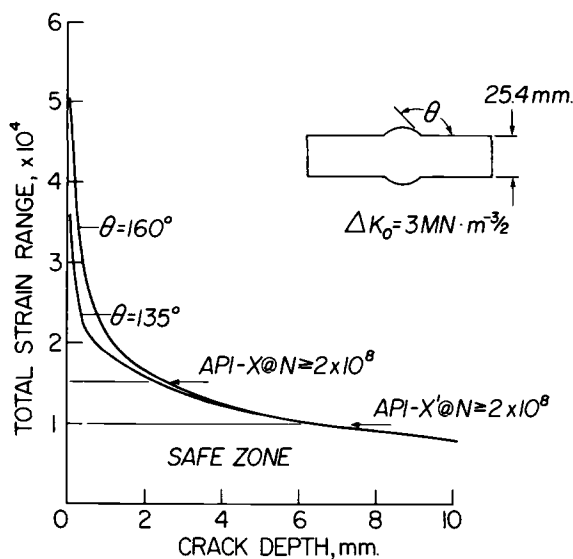


FIG. 10—Strain range versus crack depth for a butt weld illustrating various aspects of this rationale for the geometry considered.

Increasing plate thickness is generally considered to result in reduced fatigue resistance, and applicability of this point with regard to tubular connections of offshore structures has recently been discussed [7,42]. Figure 11 compares $\Delta\epsilon$ - a curves for 25.4- and 152-mm-thick butt welded members and illustrates that the safe zone area and SCS are reduced in the case of the thicker plate. This presumes a scale-up not only of the base plate thickness but also of the weld metal, in which case a crack of particular depth in a thick plate experiences greater stress concentration from the weld toe irregularity compared with an identical crack in a thinner member.

The assumed value of threshold stress intensity range in Figs. 10 and 11 ($3 \text{ MN m}^{-3/2}$) is near the lower bound of values reported in the literature for structural steel [31,43]. Figure 12 illustrates $\Delta\epsilon$ - a curves for several different ΔK_0 -values. It is apparent from this that SCS is sensitive to ΔK_0 . For example, the strain range corresponding to API-X' at 2×10^8 cycles yields a SCS of 0.4 mm for $\Delta K_0 = 2 \text{ MN m}^{-3/2}$, 1.6 mm for a threshold of $3 \text{ MN m}^{-3/2}$, and $>10 \text{ mm}$ for $5 \text{ MN m}^{-3/2}$.

Determination of threshold ΔK -values under conditions applicable to offshore structures is a difficult experimental problem. Based upon the aforementioned analysis, however, it is not unrealistic that whether or not a pre-existing weld defect propagates as a fatigue crack depends quite sensitively upon ΔK_0 . The situation is complicated, first, by the low stressing rates which must be employed and, second, by the fact that ΔK_0 is a function of mean stress intensity [34]. Also, as a consequence of residual stress effects this latter parameter (mean stress intensity) is expected to change as the

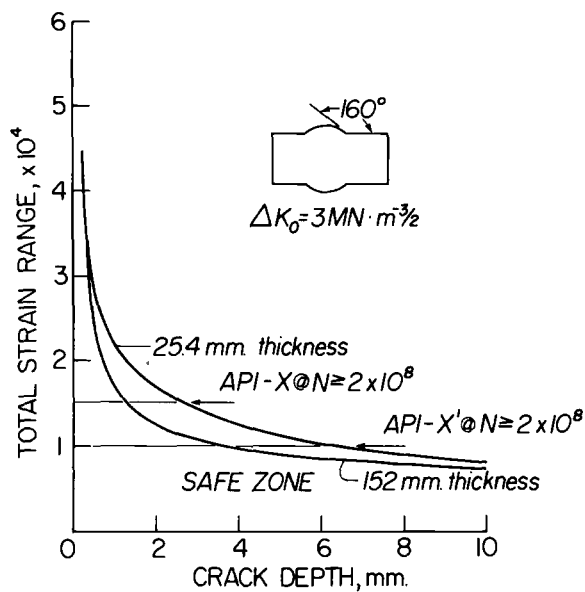


FIG. 11—Strain range versus crack depth plots for a butt weld of two different thicknesses.

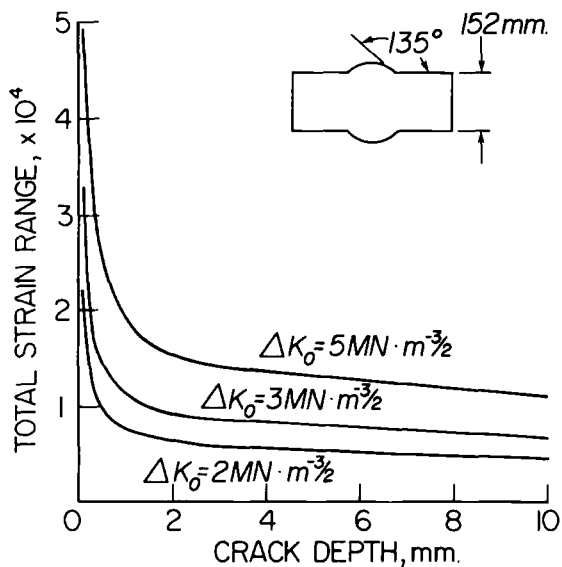


FIG. 12—Strain range versus crack depth plots for three different values of threshold stress intensity range.

crack propagates from the weld toe into the parent plate. Further difficulties must be anticipated for test conditions involving cathodic polarization, due to precipitation of calcareous deposits within the crack, as discussed previously.

Figure 13 reproduces Fig. 10 such that the small crack region ($0 < a < 2$ mm) is expanded. Illustrated also are data for the specimen in Figs. 5 and 8 with strain range 3.33×10^{-4} which failed at 27×10^6 cycles. The weld profile in this case was estimated to form an angle of 150° , which is intermediate to that for the two $\Delta\epsilon$ - a curves in Fig. 13. Assuming that the 0.35-mm-deep undercut which was apparent for this specimen constituted a crack, then the state of this specimen was such that it was to the unsafe or fail side of the growth threshold curve for this stress range. This is consistent with the fact that this specimen failed and that three specimens without detectable undercuts which were tested under identical conditions survived 10^8 cycles.

Data and analysis are available for a welded tubular tee connection which permits a sample evaluation by the aforementioned technique. Specifically, Tomkins and Scott [44] have calculated S - N curves for this type of member employing applicable stress intensity information with crack growth data for the freely corroding condition and assuming various sizes for the initial surface crack. Based upon their results, Fig. 14 illustrates the $\Delta\epsilon$ - a curve for failure of the tee connection at 10^7 and 10^8 cycles. The assumed ΔK_0 is $2 \text{ MN m}^{-3/2}$. As should be anticipated, the safe zone area expands as one designs to a decreasing number of cycles-to-failure. Thus, in terms of the API-X cri-

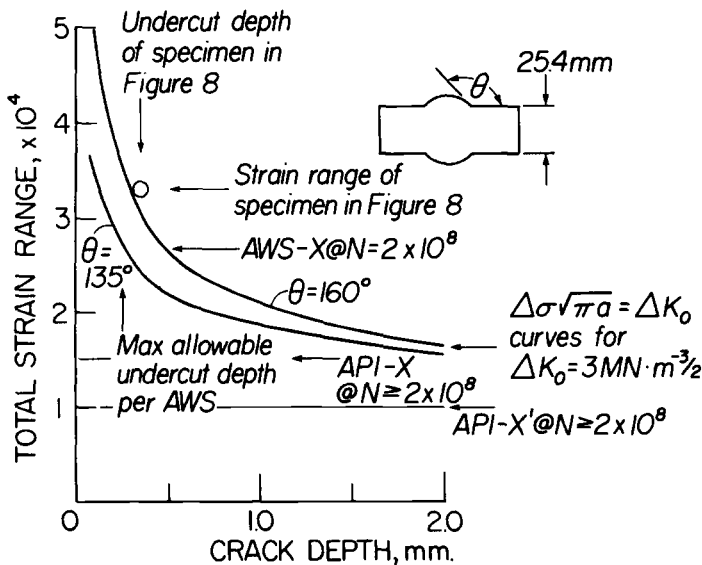


FIG. 13—Strain range versus crack depth plot as applicable to evaluation of the effect of undercutting upon fatigue failure.

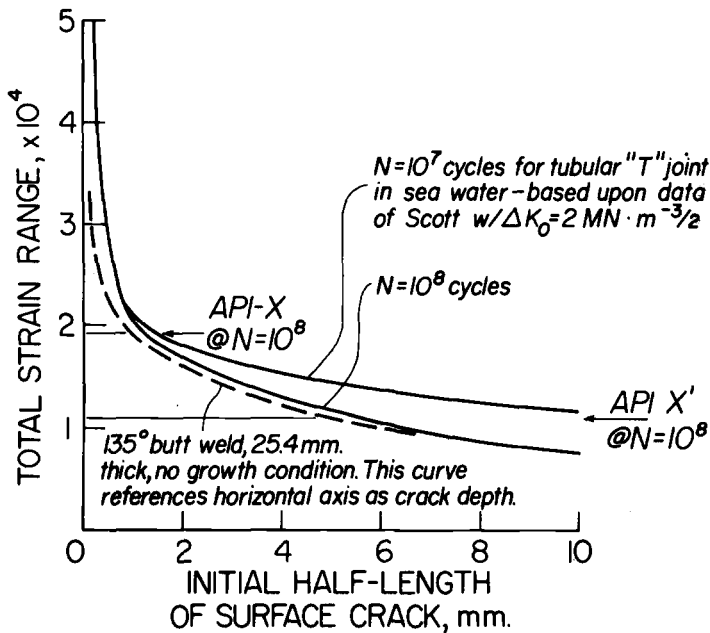


FIG. 14—Strain range versus crack length plot for a tubular T-joint.

terion at 10^8 cycles, the significant crack length is 3.2 mm, whereas for the API-X' it is 10.8 mm. The $\Delta\epsilon$ - a curve for a butt weld (Fig. 8) in 25.4-mm-thick plate and assuming $\Delta K_0 = 3 \text{ MN m}^{-3/2}$ is included for comparison.

The rationale discussed in conjunction with Figs. 8 to 14 offers to enhance the confidence with which welded components and structures can be designed. In particular, the approach allows the influence of various crack-like defects from welding to be better quantified. What we presently lack, however, are crack growth rate data for small cracks fatigued near the threshold stress intensity range under both freely corroding and cathodically protected conditions. It is projected that development of this type of datum is a logical next step in the attempt to establish material property information directly applicable to prevention of fatigue in offshore structures.

Acknowledgments

The author is indebted to the American Petroleum Institute and to the Sea Grant Program of NOAA Grant No. 04-8-MO1-76 for financial support of this research. The continued involvement of the API Technical Advisory Committee on Corrosion Fatigue and the many helpful comments and suggestions made by its members are also gratefully acknowledged.

References

- [1] Hicks, J. G. in *Proceedings of Conference on Welding in Offshore Constructions*, 1974, p. 1.
- [2] Wintermark, H., "Materials and Welding in Offshore Constructions," 1975 Portevin Lecture, International Institute of Welding.
- [3] Marshall, P. W., "Problems in Long-Life Fatigue Assessment for Fixed Offshore Structures," Pre-print 2638, ASCE National Water Resources and Ocean Engineering Conference, San Diego, April 1976.
- [4] Jaske, C. E., Slater, J. E., Brock, D., Leis, B. N., Anderson, W. E., Turn, J. C., and Omar T., "Corrosion Fatigue of Welded Carbon Steel for Application to Offshore Structures," Interpretative Report submitted to American Petroleum Institute by Battelle Columbus Laboratories, 1 Feb. 1977.
- [5] "Section 10. Design of New Tubular Structures," in *Structural Welding Code*, AWS D1.1-79, American Welding Society, 1978, p. 145.
- [6] Marshall, P. W., "Basic Considerations for Tubular Joint Design in Offshore Construction," Welding Research Council Bulletin No. 193, April 1974.
- [7] Wyld, J. G. and McDonald, A., "The Influence of Joint Dimensions on the Fatigue Strength of Welded Tubular Joints," Paper No. 42 presented at Second International Conference on Behavior of Offshore Structures, 28-31 Aug. 1979.
- [8] Pook, L. P., *Journal of the Society of Environmental Engineers*, Vol. 171, 1978, p. 22.
- [9] Holmes, R., "Fatigue and Corrosion Fatigue of Welded Joints under Random Load Conditions," Paper No. 11 presented at Select Seminar, European Offshore Steels Research, U.K. Department of Energy, 27-29 Nov. 1978, Cambridge, England.
- [10] Holmes, R., "The Fatigue Behavior of Welded Joints under North Sea Environmental and Random Loading Conditions," Paper No. 3700, presented at 12th Annual Offshore Technology Conference, 5-8 May, 1980, Houston.
- [11] Wirsching, P. H., *International Journal of Fatigue*, Vol. 2, 1980, p. 77.
- [12] Mattos, R. J. and Lawrence, F. V., "Estimation of the Fatigue Crack Initiation Life in Welds Using Low Cycle Fatigue Concepts," FCP Report No. 19, University of Illinois, Oct. 1975.
- [13] Williams, H. E., Ottosen, H., Lawrence, F. V., and Munse, W. H., "The Effects of Weld Geometry on the Fatigue Behavior of Welded Connections," Interim Report, IHR-64 Behavior of Welded Highway Structures, University of Illinois, Aug. 1970.
- [14] Newman, R. P. and Gurney, T. R., *British Welding Journal*, Vol. 6, 1959, p. 567.
- [15] "API Recommended Practice for Planning, Designing and Constructing Fixed Offshore Platforms," API RP 2A, 11th ed., 1980.
- [16] Hartt, W. H., Henke, T. E., and Martin, P. E., "Influence of Sea Water and Cathodic Protection upon Fatigue of Welded Steel Plates, As Applicable to Offshore Structures," EIES Report No. TR-OE-80-1, Florida Atlantic University, Boca Raton, Fla., 20 March 1980.
- [17] Solli, O., "Corrosion Fatigue of Welded Joint in Structural Steels and the Effect of Cathodic Protection," Paper No. 10, presented at Select Seminar, European Offshore Steels Research, U.K. Department of Energy, 27-29 Nov. 1980, Cambridge, England.
- [18] Berge, S., "Constant Amplitude Fatigue Strength of Welds in Sea Water Drip," Paper No. 12, presented at Select Seminar, European Offshore Steels Research, U.K. Department of Energy, 27-29 Nov. 1980, Cambridge, England.
- [19] Booth, G. S., "Constant Amplitude Fatigue Tests Performed on Welded Steel Joints in Sea Water," Paper No. 9, presented at Select Seminar, European Offshore Steels Research, U.K. Department of Energy, 27-29 Nov. 1980, Cambridge, England.
- [20] de Back, J., Dortland, W., and Wildschut, H., "Fatigue Behavior of Welded Joints in Air and Sea Water," Paper No. 5, presented at Select Seminar, European Offshore Steels Research, U.K. Department of Energy, 27-29 Nov. 1980, Cambridge, England.
- [21] McAdams, D., *Proceedings*, American Society for Testing and Materials, Vol. 26, Part II, 1926, p. 224.
- [22] Gough, H. J. and Sopwith, D. G., *Journal of the Iron and Steel Institute*, Vol. 127, 1933, p. 301.
- [23] Endo, K. and Miyao, Y., *Bulletin of the Japan Society of Mechanical Engineers*, Vol. 1, 1958, p. 374.

- [24] Duquette, D. J. and Uhlig, H. H., *Transactions of the American Society of Metals*, Vol. 61, 1968, p. 449.
- [25] Lyashchenko, A. E., Glikman, L. A., and Zobachev, Yu. E., *Soviet Materials Science*, Vol. 9, 1975, p. 496.
- [26] Hooper, W. C. and Hartt, W. H., *Corrosion Journal*, Vol. 34, 1978, p. 320.
- [27] Hartt, W. H. and Hooper, W. C., *Corrosion Journal*, Vol. 36, 1980, p. 107.
- [28] Maddox, S. J., *Welding Research International*, Vol. 6, 1976, p. 1.
- [29] Signes, E. G., *British Welding Journal*, Vol. 14, 1967, p. 108.
- [30] Lohne, Per W., *Metal Construction*, Aug. 1979, p. 382.
- [31] Scott, P. M. and Silvester, D. R. V., "The Influence of Mean Tensile Stress on Corrosion Fatigue Crack Growth in Structural Steel Immersed in Sea Water," Interim Technical Report 3/02, Department of Energy, United Kingdom Offshore Steels Research Project, 25 May 1977.
- [32] Scott, P. M. and Silvester, D. R. V., "The Influence of Sea Water on Fatigue Crack Propagation Rates in Structural Steel," Interim Technical Report 3/03, Department of Energy, United Kingdom Offshore Steels Research Project, 19 Dec. 1977.
- [33] Vosikovskiy, O., *Closed Loop*, Vol. 6, 1976, p. 3.
- [34] Bardal, E., "The Effect of Corrosion and Cathodic Protection on Fatigue Crack Growth in Structural Steel at Low Stress Ranges and Low Loading Frequencies in Artificial Sea Water," Paper No. 121, presented at 7th International Congress on Metallic Corrosion, Rio de Janeiro, 4-11 Oct. 1978.
- [35] Bardal, E., Sondentor, J. M., and Gartland, P. O., "Slow Corrosion Fatigue Crack Growth in a Structural Steel in Artificial Sea Water at Different Potentials, Crack Depths and Loading Frequencies," Paper No. 16, presented at Select Seminar, European Offshore Steels Research, U.K. Department of Energy, 27-29 Nov. 1980, Cambridge, England.
- [36] Humble, R. A., *Corrosion Journal*, Vol. 4, 1948, p. 358.
- [37] Hartt, W. H. and Wolfson, S. L., *Corrosion Journal*, Vol. 37, 1981, p. 70.
- [38] Scott, P. M., Harwell Corrosion Service, Materials Development Division, Atomic Energy Research Establishment, Harwell, England, private communication.
- [39] Sprowls, D. O., Shumaker, M. B., and Walsh, J. D., "Evaluation of Stress Corrosion Cracking Susceptibility Using Fracture Mechanics Techniques," Final Report, Part 1, G. C. Marshall Space Flight Center, Contract No. NAS 8-21487, 31 May 1973, pp. 93-100.
- [40] Maddox, S. J., *International Journal of Fracture*, Vol. 11, 1975, p. 221.
- [41] Gurney, T. R., *Welding Research International*, Vol. 6, 1976, p. 40.
- [42] Gurney, T. R., "The Influence of Thickness on the Fatigue Strength of Welded Joints," Paper No. 41, presented at Second International Conference on Behavior of Offshore Structures, 28-31 Aug. 1979.
- [43] Ritchie, R. O., *International Metals Reviews*, Vol. 24, 1979, p. 205.
- [44] Tomkins, B. and Scott, P. M., "An Analysis of the Fatigue Endurance of Tubular 'T'-Joints by Linear Elastic Fracture Mechanics," Interim Technical Report UKOSRP 4/01, Department of Energy, United Kingdom Offshore Steels Research Project, 15 June 1977.

Crack Initiation and Propagation Approaches to Fatigue Analysis

REFERENCE: Nelson, D. V. and Socie, D. F., "Crack Initiation and Propagation Approaches to Fatigue Analysis," *Design of Fatigue and Fracture Resistant Structures, ASTM STP 761*, P. R. Abelkis and C. M. Hudson, Eds., American Society for Testing and Materials, 1982, pp. 110-132.

ABSTRACT: Commonly used analysis methods for predicting "uniaxial" crack initiation and propagation lives in notched structural components are summarized. Experimental trends in the crack initiation and propagation behavior of notched laboratory specimens are presented and discussed in terms of the influence of such factors as notch stress concentration and stress gradient, nature of the loading, residual stress, etc. Conditions for which fatigue life tends to be governed by crack growth considerations are identified. A criterion for nonpropagating cracks is examined. Examples showing how design factors influence the selection of crack initiation or propagation approaches are given. Potential advantages of a better understanding of small crack behavior at notches are noted.

KEY WORDS: fatigue of metals, notches, crack initiation, crack propagation, residual stress, mean stress, nonpropagating cracks, fracture mechanics, small cracks, fatigue design, life prediction, stress concentration, stress gradient

Several different analysis procedures are currently available for use in uniaxial fatigue life evaluations (that is, where maximum principal stress or strain is assumed to govern behavior). The procedures can be broadly classified as either "crack initiation" or "crack propagation" approaches and will be summarized in the next section. Many papers have been published on the computational details of the procedures. However, little has been written on factors which influence when a particular approach, or approaches, seem most suitable for use.

This paper has two main purposes. The first is to review and discuss how crack initiation and propagation behavior in notched laboratory specimens is influenced by notch geometry, presence of residual stress, etc. The ability of

¹Assistant Professor, Mechanical Engineering Department, Stanford University, Stanford, Calif. 94305.

²Associate Professor, Department of Mechanical and Industrial Engineering, University of Illinois, Urbana, Ill. 61801.

the different analysis approaches to account for such influences will also be discussed. A second purpose is to show by example how practical considerations in various industries strongly influence the type of approach taken. It is hoped that these discussions will be of use to designers in selecting approaches best suited to the analysis situations they face. Effects of thermal or aggressive environments on fatigue behavior will not be considered in this paper.

Crack Initiation Approaches

Current "crack initiation" fatigue analysis procedures generally use stress amplitude versus cycles to fracture ($S-N$) data or strain amplitude versus cycles ($\epsilon-N$) data from small, smooth laboratory specimens to predict life to occurrence of a crack at a critical location in a structure, which is usually a notch. It is assumed that if a notch experiences the same maximum principal stresses or strains as a smooth specimen, it will develop in the same life a crack of a size comparable to that which causes fracture in the laboratory specimen. This size is typically on the order of 0.3 to 3 mm, depending on the metal and stress or strain level. The following two analysis methods are commonly used to estimate crack initiation lives of notched specimens.

Stress-Life Method

Maximum principal stress histories at a notch are computed elastically, generally by applying a stress concentration factor, K_t , to nominal stresses. Empirical fatigue notch factors, K_f , are sometimes used instead of K_t in an attempt to account for effects of notch size, stress gradient, etc. Methods for estimating fatigue lives from notch stress histories are given, for example, in Ref 1.

The stress-life method is best suited for long-life fatigue evaluations, where notch strains are predominantly elastic. When significant localized inelastic straining does occur, this method cannot properly keep track of changes in notch mean or residual stresses. Lack of ability to account for notch inelastic stress-strain behavior also means that the stress-life method cannot account for load sequence effects, such as the increase in crack initiation life caused by a high tensile load which produces compressive residual stresses at a notch. In spite of such shortcomings, this method, or ones similar to it, are widely used in fatigue analyses. (For many service loadings, sequence and mean stress effects may be small.)

Strain-Life Method

Maximum principal strain histories at a notch are either measured, or computed by inelastic finite-element analysis, or estimated by simplified inelastic methods such as Neuber's rule adapted to cyclic stress-strain behavior

[2].³ Fatigue life evaluations are made using notch strain amplitude and notch mean stress in conjunction with smooth specimen ϵ - N data. Computational details of this method can also be found in Ref 1.

When inelastic analysis is conducted, it is possible to estimate notch cyclic stress-strain behavior, thereby allowing changes in local mean and residual stresses to be computed over the course of a loading history. The strain-life method also has the apparent ability to assess sequence effects attributable to notch surface residual stresses [3]. The method can be used over the entire range of fatigue lives, but does require a somewhat more sophisticated analysis than the stress-life method.

Neither the stress-life method nor the strain-life method has the ability to account for the effects of notch stress/strain gradient on the crack growth which occurs before a "crack initiation" size of 0.3 to 3 mm is reached, except through the use of empirical K_f -factors. Neither can they assess the influence in depth of residual stresses on small crack growth since both methods are concerned only with notch root *surface* stress or strain behavior.

Crack Propagation Approach

This analysis approach assumes the existence of a initial flaw and then predicts the life spent in growing the flaw to some final size. Final sizes may be the critical size for unstable growth, or a size which can be readily detected by in-service inspection, etc. Initial sizes may be those determined, for example, by nondestructive testing.

Crack growth life prediction methods based on linear elastic fracture mechanics are described thoroughly in the literature. See, for example, Refs 4 to 7, which also discuss the effects of mean stress, residual stress, and load sequence on growth behavior. These effects are often more significant for propagation than for initiation.

At present, no widely accepted analysis methods are available for predicting small crack growth within the influence of notch inelastic straining; however, approaches to the problem have recently been proposed [8-10].

Laboratory Data Trends

In this section, data on the crack initiation and propagation behavior of notched specimens will be reviewed to provide insight into the influence of factors such as notch severity, mean stress, etc. Particular attention will be given to those situations in which the fatigue behavior is dominated by crack growth considerations.

³The italic numbers in brackets refer to the list of references appended to this paper.

Long-Life Regime

It has been known for several decades that loadings sufficient to start a crack at a notch will not necessarily cause the crack to grow catastrophically. Small, nonpropagating cracks may form, depending on a number of factors, including notch severity and stress gradient, the resistance of the metal to crack growth, the presence of notch residual stresses and the nature of the loading itself (for example, tensile versus compressive mean bias), etc. Crack initiation life prediction methods cannot, of course, evaluate the potential for crack propagation and will produce unduly conservative estimates of life if nonpropagating or slowly propagating cracks occur.

Frost [11,12] and Nisitani [13] investigated the influence of notch severity on the uniaxial, fully reversed crack initiation and propagation behavior of mild steel specimens at the fatigue limit. Circumferentially notched round bars were tested in both rotating bending and tension, while edge-notched sheets were tested only in tension. As shown in Fig. 1, the long-life crack initiation fatigue strength (net section) of notched specimens, σ_n , under tension loading follows the smooth specimen fatigue strength, σ_s , divided by the elastic stress concentration factor, K_t . For K_t below about four, values of (σ_n/σ_s) for initiation and fracture are so close that only the data for fracture are plotted. For sharper notches, nonpropagating cracks occurred for (σ_n/σ_s) values within the region shown in Fig. 1. The lower bound of this region is the demarcation between no crack formation and the existence of small nonpropagating cracks, while the upper bound indicates the transition between non-

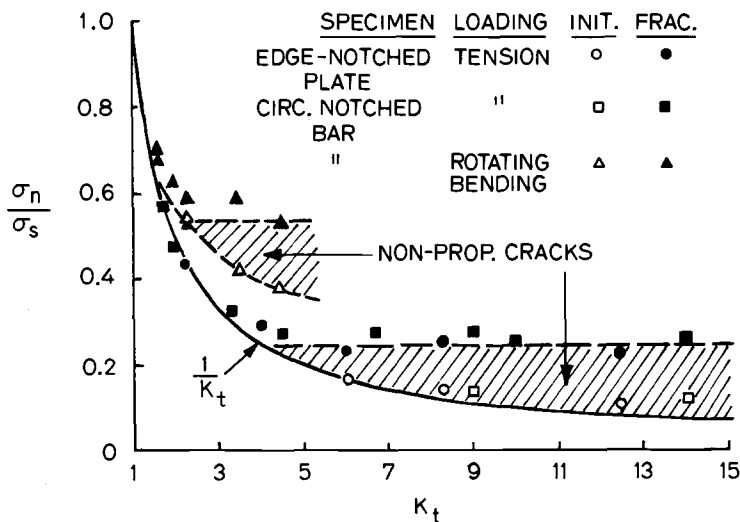


FIG. 1—Ratio of long-life, notched-to-smooth specimen fatigue strength versus stress concentration factor for mild steel specimens.

propagating cracks and those which grew to fracture. These data suggest that for sharper notches, long-life fatigue strength is governed by crack growth considerations and is independent of increases in K_t .

Tests conducted in *rotating bending* showed that nonpropagating cracks occurred at even lower values of K_t , on the order of two (Fig. 1). Thus K_t alone is not sufficient to characterize the potential for nonpropagating cracks. The steeper stress gradient at the notch and support by material adjacent to the notch influence the potential as well. It is also interesting to note that the crack initiation fatigue strength is somewhat higher in rotating bending than would be predicted by $\sigma_n = \sigma_s/K_t$.

The effect of notch severity on the behavior of nonpropagating cracks in a high-strength aluminum alloy was also studied by Frost [12] using the same types of specimens as in the tests of mild steel. As shown in Fig. 2, a considerably higher K_t was required for nonpropagating cracks in both tension and rotating bending than in corresponding tests of steel. For extremely sharp notches, the upper bound for nonpropagating cracks (as well as the crack initiation strength) actually increased over that for somewhat less sharp notches. Frost notes that this may have been due to compressive residual stresses introduced at the notch by the sharp cutting tool.

Additional data from Nisitani and Kawano [14,15] for rotating bending, fatigue limit tests of specimens with circumferential V-notches, shoulders, and diametral holes are shown in Fig. 3. All specimens were made of a 0.40 percent carbon steel with yield and ultimate strengths of 325 and 560 MPa, respectively. Nonpropagating cracks were observed at K_t -values between

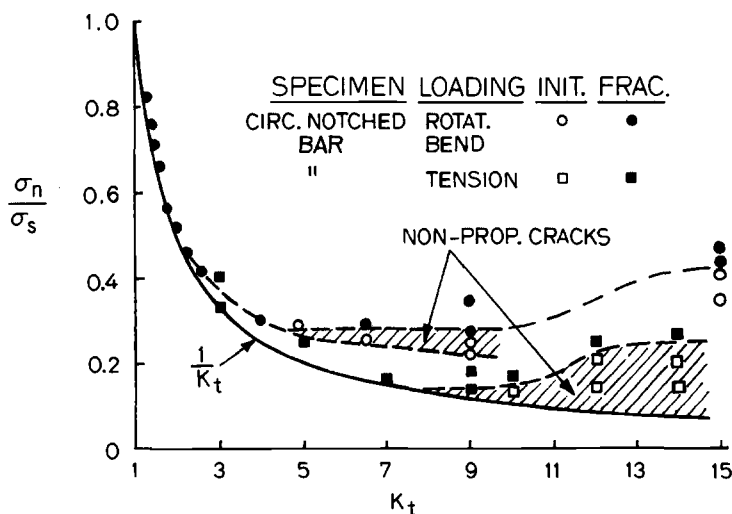


FIG. 2—Ratio of long-life, notched-to-smooth specimen fatigue strength versus stress concentration factor for aluminum specimens.

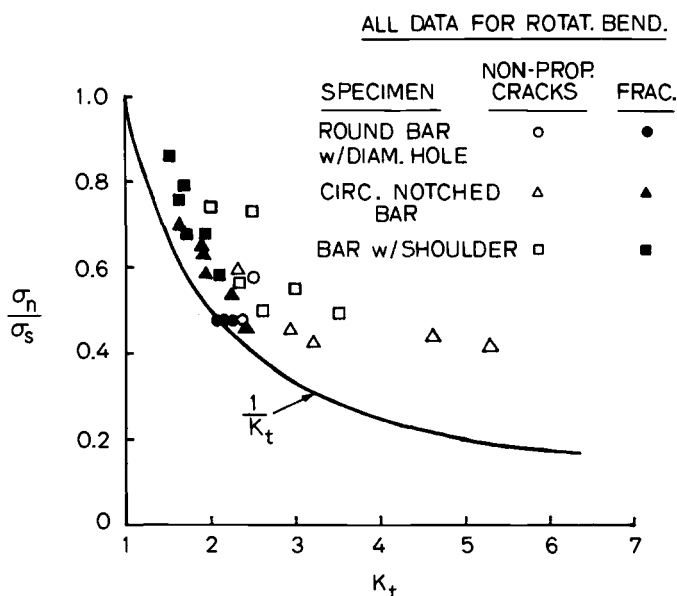


FIG. 3—Ratio of long life, notched-to-smooth specimen fatigue strength versus stress concentration factor for medium-strength steel specimens.

about 2 and 2.5, depending on size and type of both specimen and notch. For a given K_t , shouldered specimens had both the highest crack initiation and nonpropagating crack fatigue strengths.

As suggested by Dowling [16] and Hammouda and Miller [8], the potential for nonpropagating cracks may be estimated using linear elastic fracture mechanics, at least for deeply notched specimens. If the stress intensity range, ΔK_I , of a small crack which has formed at a notch is less than the threshold value for growth, ΔK_{th} , then crack arrest is expected. An attempt was made to see if such an approach could predict conditions for nonpropagating cracks for both the rotating bending and tension data of Figs. 1 to 3. (No attempt, however, was made to apply the approach to the data for specimens with diametral holes or shoulders owing to lack of appropriate K_I -factors.)

Since the size of nonpropagating cracks will often be small relative to the depth of the notch, the effective crack length for K_I can be taken approximately as notch depth, giving:

$$\Delta K_I = F \sigma_g \sqrt{\pi d} \quad (1)$$

where

F = dimensionless factor depending on crack geometry, loading,
 σ_g = remote (gross) stress amplitude, and
 d = notch depth.

The value of σ_g for fully reversed stressing is computed from the local stress amplitude ($\sigma_n = \sigma_s/K_t$) and the differences between net and gross section areas or bending moduli, as appropriate. (It is necessary to use σ_g rather than σ_n since K_t -solutions are generally expressed in terms of remote (gross) stress.) By setting Eq 1 equal to ΔK_{th} , a critical value of K_t for nonpropagating cracks can be estimated. This was done assuming $\Delta K_{th} \approx 2 \text{ MPa } \sqrt{\text{m}}$ for aluminum and $\Delta K_{th} \approx 5 \text{ MPa } \sqrt{\text{m}}$ for mild steel. Although the nonpropagating crack tests were conducted under $R = -1$ loading, it was assumed that values of ΔK_{th} for $R = 0$ would apply. The K_t -values for the different specimen geometries and types of loading were computed using solutions given by Tada et al [17]. It was also assumed that the circumferentially notched round bars could be represented by K_t -solutions for uniform depth cracking, and that cracking in the edge-notched sheets could be represented by through-thickness solutions.

A comparison between estimated critical K_t and observed values is given in Table 1.

In view of the assumptions made in estimating critical K_t , agreement with observed values is reasonably good. The estimated values tend to be low, but would be closer to observed values if the actual depth of the nonpropagating crack were added to the notch depth in computing ΔK_t . It must also be noted that in the fully reversed tension tests, the notch depth was 5 mm in all cases, while in the rotating bending tests, depths ranging from 1.3 to as little as 0.1 mm were used. The above approach did not work well for the shallower notches. It predicted K_t -values for nonpropagating cracks much lower than what was observed experimentally.

The effect of mean stress on the behavior of nonpropagating cracks in notched specimens was also investigated by Frost [12]. He found that tensile mean stress reduced the nominal stress amplitude at which such cracks would occur, while compressive mean stress had the opposite effect. Viewed

TABLE 1—Estimated and observed stress concentration values for nonpropagating cracks.

Metal	Specimen Type	Loading	Critical K_t	
			Estimated	Observed
Mild steel	edge-notched sheet	tension (fully reversed)	4.5	≈ 4
Mild steel	circumferentially notched round bar	tension (fully reversed)	3.2	≈ 4
Mild steel	circumferentially notched round bar	rotating bending	1.3 to 2.9 ^a	≈ 2 to 2.5
Aluminum	circumferentially notched round bar	tension (fully reversed)	5.8	≈ 7
Aluminum	circumferentially notched round bar	rotating bending	2.8	≈ 4

^aDepending on specimen size and notch size.

in another way, compressive mean stress permits nonpropagating cracks at blunter notches and vice versa for tensile mean stress, for a fixed value of nominal stress amplitude. Frost observed that crack growth could be correlated with that portion of the loading cycle when the crack is open, which he took to be zero load. Thus, for a given stress amplitude, tensile mean stress increases this portion, while compressive mean stress reduces it.

Hubbard [18] and Saal [19] investigated fatigue crack growth behavior in notched sheet specimens subjected to cyclic compressive loading. The tensile residual stresses introduced at the notch by unloading from peak compression were sufficient to cause cracks to grow, but only to a depth where the influence of the tensile residual stress vanished. Thereafter, the cracks were nonpropagating since they experienced only nominal compressive loading. By comparing crack growth rate in the zone of tensile residual stress with the rate from standard $R = 0$ tests, Hubbard was able to estimate the "effective" ΔK_I as a function of crack length from the notch, as shown in Fig. 4. Cracks arrested at "effective" ΔK_I -values of approximately 1.5 to 2 $\text{MPa} \sqrt{\text{m}}$, which are close to ΔK_{th} for the aluminum alloy 7075-T6 he tested. Both Saal and Hubbard were able to estimate the depth of crack arrest by superposing the K_I -solutions for the applied loading and for the residual tensile stresses.

Gerber and Fuchs [20] reported the effects of applied compressive mean stress on the crack growth behavior in circumferentially notched round bars. Nonpropagating cracks were found when the loading was entirely compres-

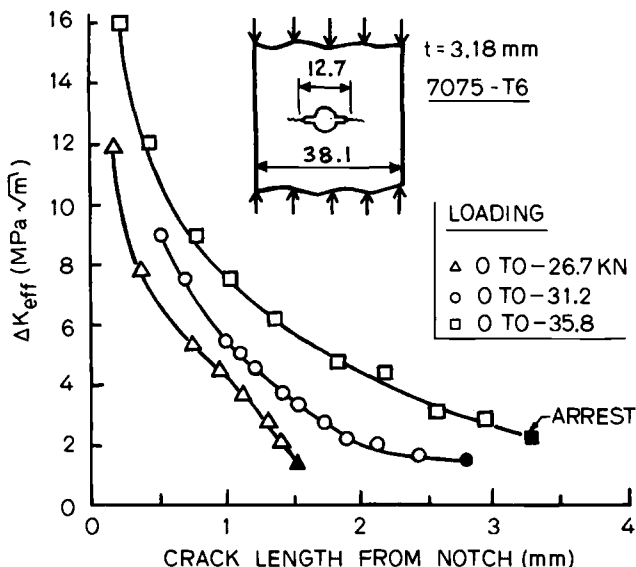


FIG. 4—Effective stress intensity range for crack growth in the zone of tensile residual stress at a notch in a specimen experiencing compression loading.

sive. In tests where the compressive mean stress level was reduced such that significant portions of the load cycle were above zero, cracks grew to fracture. Using the condition that cracks should not grow when the tensile stress at the tip (due to the sum of applied and notch tensile residual stress) vanishes, they were able to estimate the depth of crack arrest. Presumably, a fracture mechanics analysis could also predict that depth, but would require a K_I -expression for cracks growing in a tensile residual stress field of a circumferentially notched bar.

If the nominal loading is entirely compressive, nonpropagating cracks will occur. If the loading contains portions above zero, cracks may or may not grow to fracture, depending on ΔK_{th} and on ΔK_I for the crack after it has left the influence of notch residual stresses.

Nonpropagating or slowly propagating cracks may also occur when compressive residual stress fields of sufficient magnitude and depth are present below a notch root. Cold-working of fastener holes, rolling of threads, tensile preloading, shot-peening, etc., produce such stresses.

Rosenthal and Sines [21] studied the effect on fatigue strength of tensile preloading of notched aluminum sheets. A significant increase (up to 50 percent) in high-cycle strength was found in precipitation-hardened specimens, while little effect was observed in specimens annealed prior to preloading. Cracks propagated in both cases. X-ray diffraction measurement of surface residual stress showed cyclic relaxation, especially in the softer metal condition. The influence of surface residual stress was treated as a mean stress effect on crack initiation. Increases in fatigue strength were most pronounced for lives above 10^6 cycles, and progressively diminished at lower lives owing to increased relaxation by cyclic plastic straining. Similar results were found by Taira and Murakami [22] for notched sheets made of a medium carbon steel.

Dugdale [23] investigated the influence of tensile preloading on circumferentially notched round bars and found increases in long-life fatigue strength ranging between about 50 and 270 percent, depending on the metal and amount of preload. He observed that fatigue strength increased with both notch severity and yield strength. No attempt was made to measure or calculate residual stresses.

In the aforementioned studies, attempts to quantitatively relate the effect of notch residual stress on fatigue behavior were hampered by difficulties in either measuring or computing (1) residual stress distributions, and (2) how they may be altered by the applied loading and crack growth through them. The measurement difficulty still persists. Elastic-plastic finite-element analysis offers the potential for computing such distributions and changes in them, but is expensive and time-consuming.

Gerber and Fuchs [24] reported the effect of tensile preloading on the long-life fatigue strength of circumferentially notched round bars tested in rotating bending. Increases in strength of up to 300 percent were found in 4340 steel, with the increase being more pronounced for harder conditions of

the steel at a given preload. They found that nonpropagating cracks were responsible for the increased strength, and were able to estimate the depth at crack arrest using an approximate, closed form elastic-plastic analysis.

The ability of notch compressive residual stresses to arrest, or at least retard, crack growth depends very much on (1) the distribution in depth of both the residual stresses and the cyclic stresses from the applied loading, and (2) the ability of the applied cyclic stresses to relax the residual stresses *in depth*. For example, consider the two hypothetical residual stress distributions shown in Fig. 5, with equal values of surface residual stress, σ_r , but different distributions in depth. The distributions might result from applying different tensile preloads to a plate with a mild edge-notch. Suppose the load history causes only a very small plastic zone below the notch surface such that relaxation and redistribution of residual stresses in depth can be neglected. The residual stress field of Fig. 5b will be far more likely to retard or arrest growth than that of Fig. 5a. This can be seen through the "residual stress intensity factors," K_{res} , for growth through the respective fields, as also illustrated in Fig. 5. These K_{res} -expressions apply to uniform depth edge cracks. Case (a) is from Ref 25 and (b) from Ref 26. The use of effective stress intensities based on the superposition of K_{res} and $K_{applied}$ to predict the rate of fatigue crack growth through compressive residual stress fields at notches [27,28] has proven quite successful, as have similar approaches [29] based on crack closure considerations.

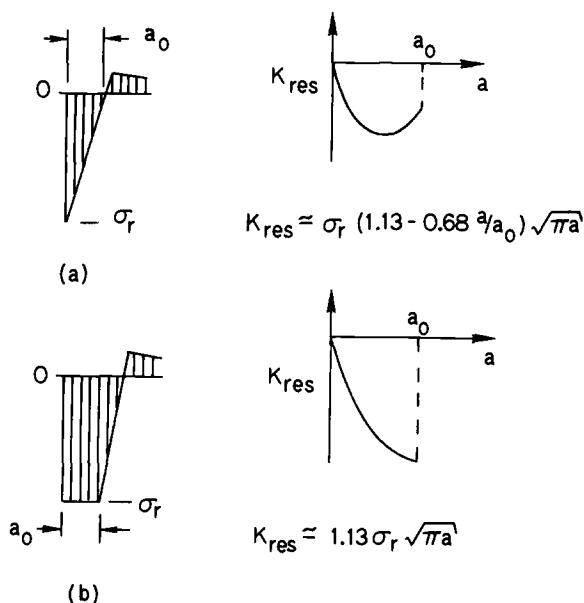


FIG. 5—Hypothetical notch residual stress fields and corresponding "residual" stress intensity factors.

The influence of gradient of applied stress at a notch with compressive residual stresses is also important. The largest increase in long-life fatigue strength of tension-preloaded, notched specimens occurs when they are tested in rotating bending. This empirical observation can also be rationalized, at least qualitatively, by fracture mechanics. For the same notch configuration and nominal stress amplitude, the K_{applied} in bending will always be less severe *in depth* than for uniform tension loading. Thus the effective $K = (K_{\text{applied}} - K_{\text{res}})$ will be smaller at a given depth below the notch surface, leading to a greater likelihood of nonpropagating cracks or slower growth.

The constraint on plastic flow of a given notch configuration also influences crack growth behavior. A circumferentially notched round bar subjected to a tensile preload which causes reversed yielding to the same depth as in a bluntly notched plate will have a higher axial compressive residual stress in depth due to the elevation of the yield condition by constraint of surrounding elastic material. This will, in turn, cause a higher K_{res} as a crack penetrates the compressive residual stress distribution. As noted previously, the greatest effect of compressive residual stress in producing nonpropagating cracks has been observed in notched round bar tests.

When a load history is applied at a higher level, or a lower strength metal is used, or when there is less constraint on plastic flow at a notch (for example, a blunt notch in plane stress), the zone of cyclic plastic straining will be larger, causing a greater relaxation and redistribution in depth of residual stress, thereby reducing the ability of compressive residual stresses to retard or arrest crack growth. This is consistent with the empirical observations cited previously. Under these conditions, the use of a linear elastic fracture mechanics approach for estimating the effect of residual stress on crack growth also becomes doubtful. Compressive residual stresses at a notch will thus be most beneficial in higher strength metals, for long-life loadings and at notches where the plastic straining is constrained. These conditions are also those for which linear elastic fracture mechanics approaches are best suited for taking into account the effect of residual stress on crack growth.

To this point, all of the data and discussion concerning nonpropagating cracks have been for uniaxial loading. Very little is known about the behavior of such cracks in notched specimens under multiaxial fatigue loadings. However, Kawano and Nisitani [30] have investigated nonpropagating cracks in fully reversed, long-life torsional fatigue of circumferentially notched and shoulder notched round bars made of a 0.40 percent carbon steel. Their results are replotted in terms of the notched torsional fatigue limit, τ_s , versus K_t (shear) in Fig. 6. In the shouldered specimens, nonpropagating cracks were not observed until a K_t of about two, which corresponds to a rather sharp shoulder. In circumferentially notched specimens, a zig-zag pattern of nonpropagating cracks occurred at considerably lower values of K_t , on the order of only 1.3. Thus, in notched torsion, the influence of crack propagation behavior on total life may actually be more important than in uniaxial

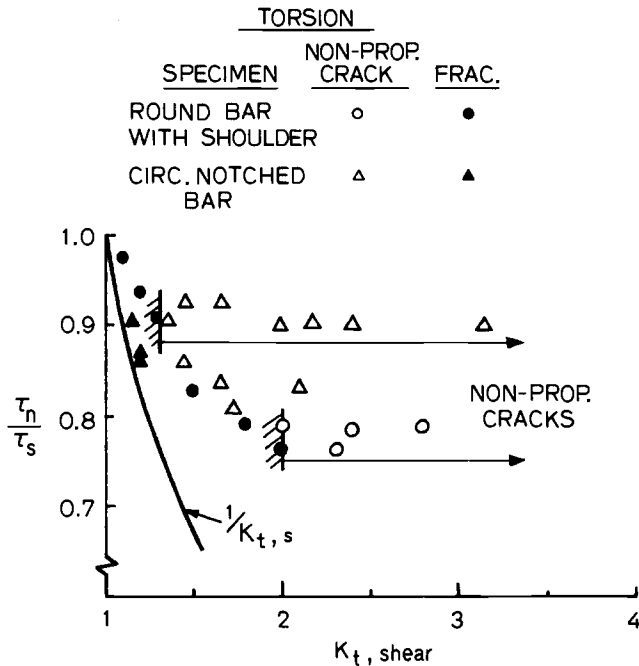


FIG. 6—Ratio of long-life, notched-to-smooth torsional fatigue strength (fully reversed) versus torsional stress concentration factor.

fatigue. The data of Kawano and Nisitani also show that the stress distribution in the minimum cross section is not sufficient to estimate conditions for nonpropagating cracks, as it may be for tension or rotating bending. Crack growth also depends on the geometry of and stresses in the material surrounding the notch. No attempt has been made to reconcile conditions for crack arrest in notched torsion using a fracture mechanics approach because of analytical difficulties in trying to estimate K_I for crack growth out of a circumferential notch. The existence of nonpropagating cracks in circumferentially notched round bars at such relatively low values of K_t may also help to explain why the long-life torsional τ_n -strength approaches the bending σ_n -strength in such specimens.

Finite-Life Regime

Historically, laboratory fatigue data from small specimen tests have been reported almost exclusively in terms of life to fracture. Relatively few studies have been made which try to distinguish the life spent in “crack initiation” and that spent in propagation. Hunter and Fricke [31] did perform such a study in rotating bending tests of both smooth and notched specimens of aluminum 6061-T6. Crack initiation was defined as first detection by surface

replicas. Their results are replotted as the ratio of initiation-to-total life, (N_I/N_T) , versus N_T in Fig. 7. Also shown in this figure are data from Manson and Hirschberg [32] for notched aluminum 7075-T6 specimens tested in low-cycle, fully reversed uniaxial tension; in this case, crack initiation was taken as a surface length of 150 to 250 microns. Several trends are apparent in Fig. 7. First of all, most of the life of small laboratory specimens is spent in crack growth at shorter lives. In notched specimens, cracks start very quickly and even more of the life is spent in propagation. This tendency increases with notch severity.

Schijve [33] and Dowling [34] reported results of smooth specimen fatigue tests of aluminum 2024-T3 and A533B steel, respectively, in which life to various crack surface lengths was observed. Both of their sets of data are replotted in terms of (N_I/N_T) versus N_T in Fig. 8 (to save space and not to suggest any relative comparison between the two sets.) The fraction of life spent in propagation depends very much, of course, on the crack size considered to be "initiation." Results of similar tests by Dowling [16] of both smooth and notched specimens of 4340 steel are given in Fig. 9. Again, progressively more of the life is spent in crack initiation at longer lives, but increased notch severity reduces this trend. Most of the test results cited above were generated under fully reversed, uniaxial loading. Test data on the effect of mean stress on constant amplitude (N_I/N_T) are difficult to locate in the literature, if they exist at all.

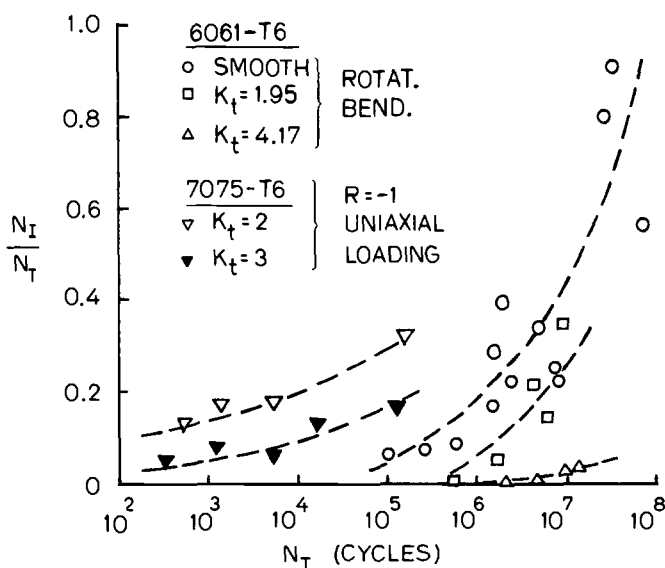


FIG. 7—Effect of stress concentration on the ratio of crack initiation-to-total life for two aluminum alloys.

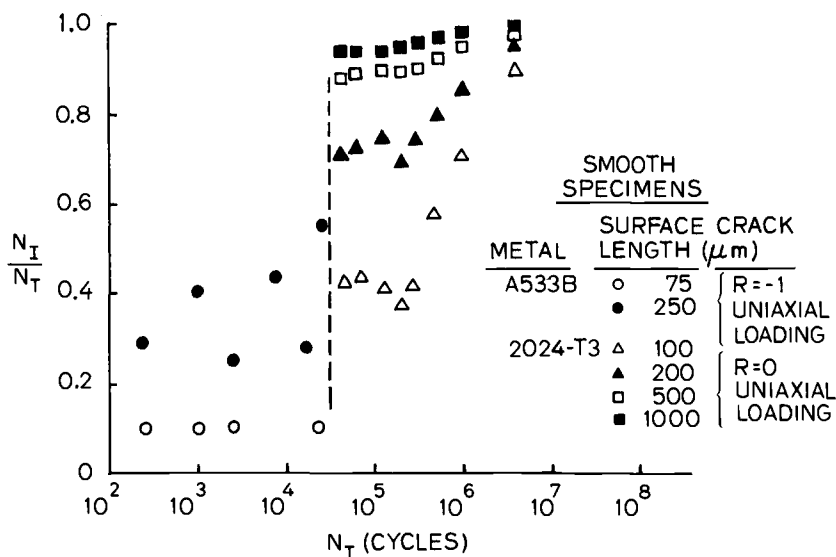


FIG. 8—Effect of crack size on the ratio of crack initiation-to-total life for a pressure vessel steel and an aluminum alloy.

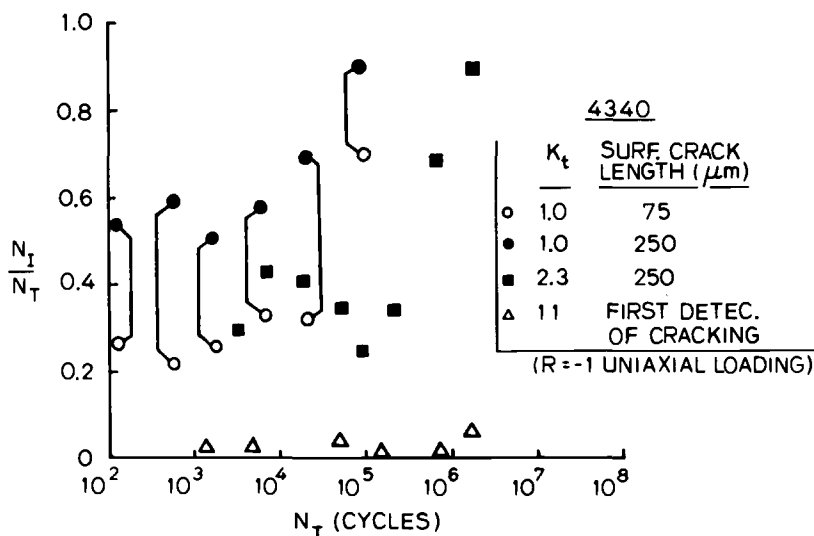


FIG. 9—Effect of crack size and stress concentration on the ratio of crack initiation-to-total life.

The previous test results were also all for small laboratory specimens. Several years ago, the lives spent in crack initiation and propagation were observed in tests of a bluntly notched ($K_t \approx 2.7$), compact tension specimen as part of a well-documented SAE cooperative research program [1]. In these tests, initiation was taken as a through crack 2.5 mm deep in a specimen with a net section of about 70 mm width. For fully reversed, constant-amplitude loading, most of the life was spent in growing a crack to that length, as shown in Fig. 10.

Tests conducted under irregular block loading produced different trends than those seen in Fig. 10. Three contrasting histories, consisting of simulated service loadings, were used in the tests. The "Transmission" block had a strong tensile mean bias, the "Suspension" block a strong compressive mean bias, and the "Bracket" block, little or no bias. Each block had several thousand reversals.

As shown in Fig. 11, by the time a crack of 2.5 mm had formed under the Transmission history loading, most of the life had been expended, regardless of load level and total life. Since this history had most of its load ranges applied at a high mean level, as depicted schematically in Fig. 12, the effective ΔK for growth was also high in accordance with the crack closure concept [35]. (The occasional high tensile peaks were repeated so often that crack growth retardation did not occur.) Also, the crack length at fracture was relatively small. On the other hand, a significant portion of total life was spent in propagation for the Bracket and Suspension histories, even when a crack as large as 2.5 mm was taken as the definition of "initiation". For these histories, the effective ΔK is considerably lower, especially for the Sus-

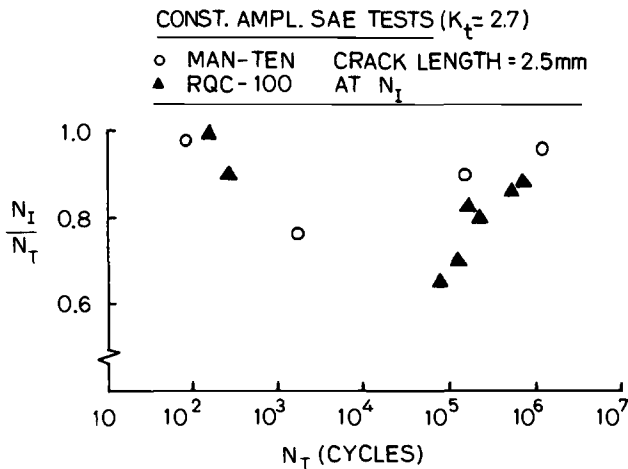


FIG. 10—Ratio of crack initiation-to-total life in a keyhole notched ($K_t = 2.7$) compact tension specimen under fully reversed loading.

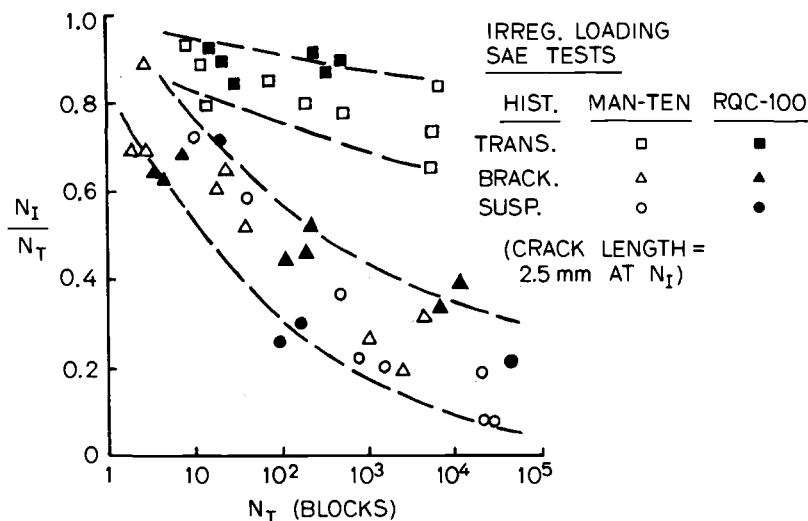


FIG. 11—Ratio of crack initiation-to-total life for the same specimen considered in Fig. 10 subjected to repeated irregular loading blocks.

pension (Fig. 12). Nonpropagating cracks were found in several of the Suspension history tests conducted at lower load levels.

The data in Fig. 11 suggest that life becomes increasingly dominated by crack propagation at higher numbers of cycles, just the opposite of what was observed in the tests of small laboratory specimens. Part of the reason for this is that the crack length at fracture was not much larger than 2.5 mm in the higher load level tests, giving a very short remaining propagation life. At lower load levels, the critical crack length for fracture increased substantially, making the crack growth portion of life more significant. Had crack initiation been detected much earlier (for example, 100 μm size) in the SAE tests, it is quite probable that crack propagation dominance would have been observed at all load levels, particularly for the Suspension and Bracket histories.

Summary of Trends from Laboratory Data

The following summary pertains to uniaxial fatigue of small laboratory specimens.

Increasing notch severity causes progressively larger portions of total life to be spent in propagation and, in some cases, may cause nonpropagating cracks to occur.

Applied loadings with a tensile mean bias promote faster crack propagation, thereby reducing the portion of life spent in propagation or the chances for nonpropagating cracks. An exception is when occasional high tensile peaks retard growth by creating notch compressive residual stresses.

Applied loadings with a compressive mean bias produce long propagation

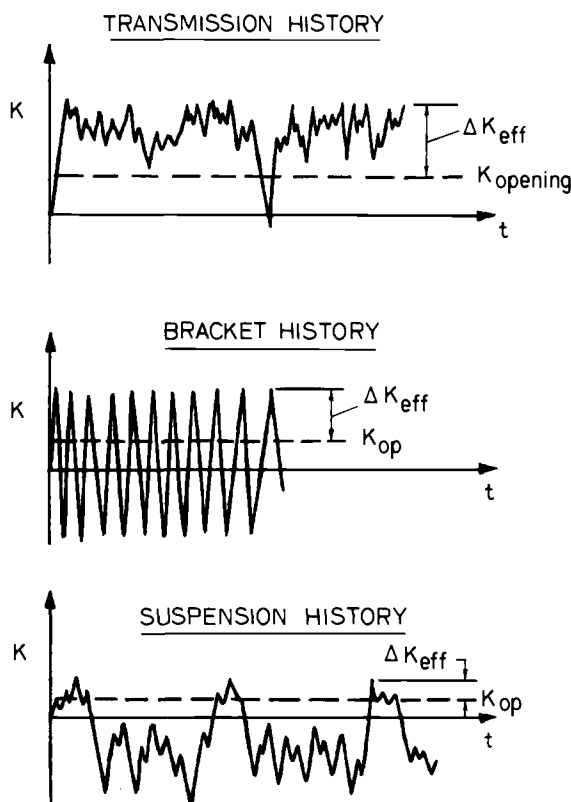


FIG. 12—Schematic of the likely variation of effective stress intensity range (based on crack closure) for three irregular loadings.

lives or nonpropagating cracks, thereby causing total life to be controlled by crack growth considerations.

Compressive residual stress fields of sufficient magnitude and depth below a notch can cause nonpropagating or slowly propagating cracks, thus causing life to be dominated by crack growth considerations. However, the effects are reduced at blunter notches, in lower strength metals and at lives below about 10^6 cycles, owing to cyclic relaxation by plastic straining. Also, large compressive loads may diminish notch compressive residual stresses or even create tensile residual stresses, thereby accelerating growth.

It is not possible, of course, to predict in advance of analysis or testing the relative proportions of life spent in initiation and propagation for variable amplitude loadings. The aforementioned trends do, however, point to certain cases in which crack growth analyses seem necessary to properly assess component fatigue life. In other cases (for example, blunt notches and loadings

with a tensile mean bias), crack initiation analyses alone may be adequate, depending on specific design objectives.

Design Factors

The previous discussion was based on the behavior of laboratory specimens. There are, of course, many other practical considerations which influence the selection of an analysis approach, such as (1) size and type of structural components, (2) volume of production, (3) opportunities for in-service inspection and repair, (4) consequences of structural failure, (5) nature and knowledge of expected service loadings, (6) prototype testing opportunities, (7) ease with which a crack propagation analysis can be done, and so forth. Examples of how such design factors can affect the choice of analysis approach follow.

Crack Propagation Approach

The aircraft industry pioneered and continues to lead in the use of crack propagation analysis for fatigue design evaluation. In fact, such analysis is mandatory for USAF aircraft. Initial, undetected flaws are assumed to exist in structural components from beginning of life. Structure is designed to "contain" the growth of such flaws (or those which may be introduced in-service) for specified periods of service, while maintaining an acceptable level of residual strength. Detailed descriptions of crack growth fatigue analysis procedures are given by Walker et al [36] for large commercial aircraft and by Wood and Engle [7] for USAF aircraft.

Key factors which make an entirely crack growth based approach practical in aircraft fatigue design are the opportunities for periodic in-service inspection and maintenance and the use of damage tolerant structure [5]. Components are generally large enough to permit substantial crack growth which can be detected well before a critical crack size is reached. Also, aircraft structure lends itself to the use of multiple load paths and crack arresting devices to "contain" damage.

Crack propagation analysis is also used extensively for aircraft because the industry has expended the effort and resources to develop comprehensive crack growth rate data and stress intensity relations for relevant flaw-structural configurations. The validity of aircraft crack growth prediction methods can be checked by coupon, component, and even full-scale prototype tests using simulated service loadings. In addition, the service records of loading and of cracking behavior of past and current aircraft provide feedback for assessing crack growth analyses and also permit corrective action to be taken in-service.

A major concern in any fatigue design analysis is the ability to forecast ex-

pected loadings. For aircraft, comparatively large amounts of service data on previous aircraft as well as extensive model and prototype testing are available to help guide estimation of probable service loadings for new designs. For example, USAF Standard MIL-A-8866B provides typical load spectra for different military aircraft and types of service ("mission segments"), and Ref 7 furnishes guidelines on how to construct flight histories from such information.

It is well known that load sequence can have a strong effect on crack growth behavior, particularly when a load history contains periodic high tensile loads interspersed among many smaller loads. Analytical models to account for sequence effects are given in Ref 7, and recommendations provided for sequencing loads in simulated histories.

The initial flaw sizes used in aircraft crack growth evaluations vary widely, depending on type of flaw, location, method of inspection, etc. For example, Ref 7 prescribes sizes ranging from about 0.5 to 50 mm. Actual initial size are, of course, likely to be much smaller than these assumed values, so that considerable conservatism is thus built into fatigue evaluations. In effect, any "crack initiation" life is neglected. Efforts [37] are now underway to develop the technology for predicting the growth behavior of much smaller flaws (that is, on the order of 0.02 to 0.2 mm), while also taking into account the probabilistic nature of initial flaw populations.

Stress-Life Crack Initiation Approach

The fatigue design evaluation of freight car structural components [38] is concerned with life to occurrence of cracks which can be detected by the unaided eye. The analysis approach used is similar to the stress-life method.

Representative loading spectra for various types of cars are provided in Ref 38. The spectra were derived from range-mean cycle counting of loads recorded on instrumented cars travelling over several hundred miles of track. Nominal stress cycles are computed from the load spectra and, except in the case of welded structure, multiplied by K_t (or K_f if available) to obtain elastic notch stress cycles. Damage is computed from S_{\max} versus N data and modified Goodman diagrams, which range from $R(=S_{\min}/S_{\max}) = +1$ to -1 and which are cut off at S_y . For welded structure, the effect of stress concentration is built into the Goodman diagrams furnished the design analyst for commonly encountered weld details. Load sequence effects are neglected. Compressive stresses are treated in the following manner. If nominal S_{\max} is positive, S_{\min} negative and $|S_{\min}|$ larger than S_{\max} , a cycle is treated as fully reversed with $S_{\max} = 1/2 |S_{\min} + S_{\max}|$. If both S_{\min} and S_{\max} are negative, no damage is computed.

A number of factors which can influence fatigue design and evaluation of both aircraft and freight car structural components are similar. There are, of course, several important differences. Similar factors include (1) severe con-

sequences if structural failure causes a crash or derailment, (2) structural components of roughly comparable size in many instances, and (3) an incentive to reduce structural weight. Major differences are as follows. The volume of production of freight cars is considerably larger than for aircraft, and it is generally difficult to monitor the movements and service experienced by any particular car. Thus periodic, scheduled in-service inspection of freight cars would indeed be difficult, if not infeasible. Although Ref 38 furnishes some "typical" load spectra, the actual spectra experienced by a freight car operating throughout the country is difficult to define, and the spectra may vary substantially from car to car. It would be impractical to keep a log of service loadings experienced by each car, as is possible for each aircraft in a fleet. Also, the fabrication quality of freight cars has an inherently greater variability than in aircraft due to the use of welded joint construction and to unit costs several orders of magnitude lower than aircraft, which makes expensive quality control programs difficult to justify for freight cars. In view of these considerations, the type of analysis used in freight car fatigue evaluations thus tends to match the level of uncertainty in knowledge of service loadings, fabrication variability, etc.

Fatigue crack propagation analysis is not part of the procedure recommended in Ref 38, but the possibility of its future inclusion is noted in that report. Considerable progress has been made over the past few years in development of crack growth based methods for predicting weldment fatigue behavior [39-43].

Strain-Life Crack Initiation Approach

Automotive vehicle structural components are designed and tested to preclude the occurrence of fatigue cracking over the service life. The strain-based approach to crack initiation life evaluation has found widespread use for the following reasons. Vehicles typically experience a large number of small loadings and a small number of large loadings which cause localized plastic straining at blunt notches. Structural components are generally made of low-to-medium strength metals. The strain-based approach was developed for those situations.

Aircraft-type crack propagation analyses have not been utilized because automotive structural components are much smaller than aircraft components, and thus the remaining life after "crack initiation" would be correspondingly reduced. Redundant structure is seldom used, and it is impractical to inspect automotive structure in-service to detect and monitor crack growth. Also, as noted earlier, analysis methods for treating small crack growth within the plastic zone at a notch have not yet been developed to the point that they can be used with confidence in design evaluations.

In order to verify that acceptable crack initiation lives are achieved, prototype vehicles undergo extensive component and durability testing prior to full

production. Durability schedules are selected to simulate field usage through experience gained from millions of miles of proving ground testing. Such comprehensive testing is economically justified since the industry produces an enormous number of vehicles and since durability testing of an automobile is considerably less costly than of aircraft or freight cars and can be conducted in a much shorter period of time.

The previous examples have shown that the use of either conventional crack initiation or crack propagation approaches is influenced mainly by design factors. However, even when the objective is to prevent crack initiation during the service life, a supplementary crack growth analysis can provide useful design information. For example, if predicted initiation life meets a goal at a location, confidence in the design will improve if the life to propagate a crack (for example, 2 mm size) to a dangerous size is substantial. On the other hand, if predicted initiation life just meets a target at a location critical to structural integrity, and if predicted crack propagation life is also very short at that location, then additional efforts either to minimize the chances of crack initiation or to mitigate the consequences of failure would be indicated. As another example, suppose that predicted initiation life at a less critical location nearly meets a goal. If the corresponding crack propagation life puts total life well past the goal, then the time and cost of redesign, retesting, etc., of that structural detail may be saved.

Conclusions

(1) Laboratory data suggest that the fatigue behavior of notched specimens is often governed by crack propagation considerations. In many finite-life situations, most of the life is spent in the growth of small cracks. For long-life, the possibility of nonpropagating or slowly propagating cracks should be checked.

(2) Sharper notches or loadings with a compressive mean bias or the presence of compressive residual stress below the notch root favor the occurrence of nonpropagating cracks or cause virtually all of the structural life to be spent in crack propagation.

(3) A linear elastic fracture mechanics criterion for nonpropagating cracks provided reasonably good predictions for deep edge-notches in round specimens under both tension loading and rotating bending. Use of such a criterion for other types of notches (for example, fillets, holes) needs study.

(4) The growth behavior of small cracks is embedded in the $S-N$ or $\epsilon-N$ data used to predict "initiation" life. While initiation approaches serve their purpose well in many fatigue design evaluations, they are unable to account for a number of influences known to be important in the fatigue behavior of notched structures such as stress/strain gradient and notch size and depth, except by resort to empirical K_f -factors. They are also unable to account for the effect of residual stress distributions below the notch root. A better un-

derstanding of the growth behavior and mechanics of small cracks at notches is needed to provide the analytical framework to account for those effects.

References

- [1] *Fatigue under Complex Loading, Analyses and Experiments*, R. M. Wetzels, Ed., Society of Automotive Engineers, Oct. 1977.
- [2] Topper, T. H., Wetzels, R. M., and Morrow, J., *Journal of Materials*, Vol. 4, No. 1, March 1969, pp. 200-209.
- [3] Stadnak, S. J. and Morrow, J. in *Testing for Prediction of Material Performance in Structures and Components. ASTM STP 515*, American Society for Testing and Materials, 1972, pp. 229-252.
- [4] Schijve, J., *Engineering Fracture Mechanics*, Vol. 11, 1979, pp. 167-221.
- [5] Hoepfner, D. W. and Krupp, W. E., *Engineering Fracture Mechanics*, Vol. 6, 1974, pp. 47-70.
- [6] Nelson, D. V., *Experimental Mechanics*, Vol. 17, No. 2, Feb. 1977, pp. 41-49.
- [7] Wood, H. A. and Engle, R. M., "USAF Damage Tolerant Design Handbook: Guidelines for the Analysis and Design of Damage Tolerant Aircraft," AFFDL-TR-79-3021, Air Force Flight Dynamics Laboratory, Wright-Patterson AFB, Ohio, March 1979.
- [8] Hammouda, M. M. and Miller, K. J. in *Elastic-Plastic Fracture, ASTM STP 668*, American Society for Testing and Materials, 1979, pp. 703-719.
- [9] El Haddad, M. H., Smith, K. N., and Topper, T. H., *Journal of Engineering Materials and Technology*, Vol. 101, 1979, pp. 42-46.
- [10] El Haddad, M. H., Dowling, N. E., and Topper, T. H. *International Journal of Fracture*, Vol. 16, No. 1, 1980, pp. 15-30.
- [11] Frost, N. E. in *Proceedings*, Institution of Mechanical Engineers, Vol. 173, No. 35, 1959, pp. 811-827.
- [12] Frost, N. E., *Journal of Mechanical Engineering Science*, Vol. 2, No. 2, 1960, pp. 109-119.
- [13] Nisitani, H., *Japan Society of Mechanical Engineers Bulletin*, Vol. 11, No. 48, 1968, pp. 947-957.
- [14] Nisitani, H. and Kawano, K., *Japan Society of Mechanical Engineers Bulletin*, Vol. 15, No. 82, 1972, pp. 433-438.
- [15] Nisitani, H. and Kawano, K. in *Proceedings*, 11th Japan Congress on Materials Research (Metallic Materials), 1968, pp. 49-51.
- [16] Dowling, N. E., *Fatigue of Engineering Materials and Structures*, Vol. 2, 1979, pp. 129-138.
- [17] Tada, H., Paris, P. C., and Irwin, G. R., "The Stress Analysis of Cracks Handbook," Del Research Corporation, Hellertown, Pa., 1973.
- [18] Hubbard, R. P., *Journal of Basic Engineering*, Vol. 91, No. 4, 1969, pp. 625-631.
- [19] Saal, H., "Fatigue Crack Growth in Notched Parts with Compressive Mean Stress," ASME Paper No. 71-Met-Z, American Society of Mechanical Engineers, 1971.
- [20] Gerber, T. L. and Fuchs, H. O., *Journal of Materials*, Vol. 3, No. 2, 1968, pp. 359-374.
- [21] Rosenthal, D. and Sines, G. in *Proceedings*, American Society for Testing and Materials, Vol. 51, 1951, pp. 593-610.
- [22] Taira, S. and Murakami, Y., *Japan Society of Mechanical Engineers Bulletin*, Vol. 4, No. 15, 1961, pp. 453-459.
- [23] Dugdale, D. S., *Welding Journal*, Vol. 38, 1959, pp. 455-485.
- [24] Gerber, T. L. and Fuchs, H. O. in *Achievement of High Fatigue Resistance in Metals and Alloys, ASTM STP 467*, American Society for Testing and Materials, 1970, pp. 276-295.
- [25] Underwood, J. H. and Throop, J. F. in *Part-Through Crack Fatigue Life Predictions, ASTM STP 687*, American Society for Testing and Materials, 1979, pp. 195-210.
- [26] Elber, W. in *Fracture Toughness Testing and Slow Stable Cracking, ASTM STP 559*, American Society for Testing and Materials, 1974, pp. 45-58.
- [27] Cathy, W. H. and Grandt, A. F., *Journal of Engineering Materials and Technology*, Vol. 102, 1980, pp. 85-91.

- [28] Liu, A. F., "The Effect of Residual Stress on Crack Growth from a Hole," Report NOR-79-74, Northrop Corporation, Hawthorne, Calif., Aug. 1979.
- [29] Socie, D. F., *Engineering Fracture Mechanics*, Vol. 9, No. 4, 1977, pp. 849-865.
- [30] Kawano, K. and Nisitani, H. in *Proceedings*, 13th Japan Congress on Materials Research (Metallic Materials), 1970, pp. 73-76.
- [31] Hunter, M. S. and Fricke, W. G. in *Proceedings*, American Society for Testing and Materials, Vol. 57, 1957, pp. 643-654.
- [32] Manson, S. S. and Hirschberg, M. H., "Low Cycle Fatigue of Notched Specimens by Consideration of Crack Initiation and Propagation," NASA TN D-3146, June 1967.
- [33] Schijve, J. in *Fatigue Crack Propagation*, ASTM STP 415, American Society for Testing and Materials, 1967, pp. 415-459.
- [34] Dowling, N. E. in *Cyclic Stress-Strain and Plastic Deformation Aspects of Fatigue Crack Growth*, ASTM STP 637, American Society for Testing and Materials, 1978, pp. 97-121.
- [35] Elber, W. in *Damage Tolerance in Aircraft Structures*, ASTM STP 486, American Society for Testing and Materials, 1971, pp. 230-242.
- [36] Walker, E. K., Ekvall, J. C., and Rhodes, J. E., *Journal of Engineering Materials and Technology*, Vol. 102, Jan. 1980, pp. 32-39.
- [37] Manning, S. D. et al, "Durability Methods Development, Vol. 1," AFFDL-TR-79-3118, Air Force Flight Dynamics Laboratory, Wright-Patterson AFB, Ohio, 1979.
- [38] Przybylinski, P. and Halcomb, S., "Interim AAR Guidelines for Fatigue Analysis of Freight Cars," Report R-245, Association of American Railroads, May 1977.
- [39] Reemsnyder, H. S. in *Fatigue Testing of Weldments*, ASTM STP 648, American Society for Testing and Materials, 1978, pp. 3-21.
- [40] Maddox, S. J., *International Journal of Fracture*, Vol. 11, No. 2, 1975, pp. 221-243.
- [41] Lawrence, F. V. and Mainali, P. C., "Fatigue Crack Propagation Life Predictions for Butt and Fillet Welds," FCP Report No. 11, University of Illinois-Urbana, Ill., March 1974.
- [42] Fisher, J. W., Yen, B. T., and Frank, K. H., *Journal of Engineering Materials and Technology*, Vol. 102, Jan. 1980, pp. 20-25.
- [43] El Haddad, M. H., Topper, T. H., and Smith, I. F. C., *Journal of Testing and Evaluation*, Vol. 8, No. 6, Nov. 1980, pp. 301-307.

Durability Design Requirements and Analysis for Metallic Airframes

REFERENCE: Rudd, J. L., Yang, J. N., Manning, S. D. and Garver, W. R., "**Durability Design Requirements and Analysis for Metallic Airframes,**" *Design of Fatigue and Fracture Resistant Structures, ASTM STP 761*, P. R. Abelkis and C. M. Hudson, Eds., American Society for Testing and Materials, 1982, pp. 133-151.

ABSTRACT: Air Force durability design requirements are reviewed and durability analysis methodology capable of satisfying these requirements are presented. The proposed methodology includes (1) durability critical parts, (2) guidelines for economic life criteria, and (3) analytical procedures for quantifying overall structural damage due to fatigue cracking. Two analytical formats for quantifying economic life are proposed: probability of crack exceedance and ratio of repair cost/replacement cost. Although the analytical methodology has been developed and verified using a fastener hole crack as the prototype, the basic concepts and methodology apply to cracks in other structural details as well. The durability analysis methodology is based on a fracture mechanics philosophy, using a probabilistic format but with deterministic crack growth. The methodology accounts for initial quality, crack growth accumulation in a population of details, load spectra, and structural properties. Essential elements of the methodology are presented, including an evaluation and illustration of the analytical methodology using test results for the F-16 full-scale durability test article.

KEY WORDS: durability, fatigue, economic life criteria, crack size distribution, time-to-crack initiation (TTCI), equivalent initial flaw size (EIFS), crack growth, small crack sizes, initial quality, probabilistic fracture mechanics, probability of crack exceedance

Structural integrity requirements for strength, rigidity, durability, and damage tolerance are presented in Military Standard MIL-STD-1530A for ensuring the operational readiness of U.S. Air Force aircraft [1].⁴ This paper addresses the durability portion of structural integrity, which is defined as the ability of the airframe (for example, fuselage, wing, empennage, landing

¹ Aerospace Engineer, Air Force Wright Aeronautical Laboratories, Flight Dynamics Laboratory, Wright-Patterson Air Force Base, Ohio 45433.

² Professor, School of Engineering and Applied Science, George Washington University, Washington, D.C. 20052.

³ Senior Engineering Specialist and Senior Research Scientist, respectively, Materials Research Laboratory, General Dynamics, Fort Worth, Tex. 76101.

⁴ The italic numbers in brackets refer to the list of references appended to this paper.

gear, control systems and surfaces, engine mounts, structural operating mechanisms, etc.) to resist cracking, corrosion, thermal degradation, delamination, wear, and the effects of foreign object damage for a specified period of time. Airframe durability is needed to minimize maintenance and functional (that is, fuel leakage, loss of control effectiveness, etc.) problems which affect the operational readiness of the aircraft. Detailed Air Force analytical and experimental durability design requirements are presented in Military Specifications MIL-A-8866B [2] and MIL-A-8867B [3], respectively. Results of a recent structural survey of the durability problems experienced at Air Force Air Logistics Centers revealed that most aircraft durability problems were the result of cracking [4]. Due to its importance and prevalence, fatigue cracking is the form of degradation considered in this paper.

This paper presents the Air Force durability design requirements as well as a durability analysis methodology [5,6] capable of satisfying these requirements. The analytical methodology includes criteria for identifying durability critical parts, a method for quantifying the initial fatigue quality of the structure and analytical procedures for quantifying overall structural damage due to fatigue cracking in suitable terms for judging fatigue cracking resistance and economic life.

The economic life of a structure is currently defined in qualitative terms: "... the occurrence of widespread damage which is uneconomical to repair and, if not repaired, could cause functional problems affecting operational readiness" [1-3]. The durability analysis methodology presented is evaluated and verified by correlating structural damage predictions obtained using the methodology with the test results of an F-16 full-scale test article. Essential elements of the methodology are presented; details are documented elsewhere [5-12].

Durability Design Requirements

The objective of the Air Force durability design requirements for aircraft structures is to minimize in-service maintenance costs and maximize operational readiness through the proper selection of materials, stress levels, design details, inspections, and protection systems. These design requirements involve both analyses and tests.

Analytical Requirements

Analyses are required to demonstrate that the economic life of the airframe is greater than the design service life when subjected to the design service loads and design chemical/thermal environments. The economic life can be generally characterized by a rapid increase in the number of damage locations or by repair costs as a function of time. The economic life analysis must account for initial quality, environment, load sequence, material property variations, etc. The analysis must be verified by tests.

Experimental Requirements

Design development tests are required to provide an early evaluation of the durability of critical structural components and assemblies and a verification of the durability analysis. A durability test for a full-scale airframe may also be required by the Air Force. A full-scale airframe must be durability tested to one lifetime, and critical structural areas must be inspected before the full production go-ahead decision. Two lifetimes of durability testing plus an inspection of critical structural areas must be completed prior to delivery of the first production airplane. If the economic life of the airframe is reached prior to two lifetimes of durability testing, sufficient inspection and data evaluation must be completed before delivery of the first production airplane to estimate the extent of required production and retrofit changes. If the economic life of the airframe is not reached before two lifetimes of durability testing, a decision will be made to (1) terminate the durability testing and perform a nondestructive inspection (NDI) followed by a destructive tear-down inspection, or (2) terminate the durability testing and perform damage tolerance testing and a nondestructive inspection followed by a destructive teardown inspection, or (3) continue the durability testing for an approved period of time followed by either (1) or (2). In-service nondestructive inspections will also be performed at other intervals specified by the Air Force.

Durability Analysis Criteria

Durability Critical Parts Criteria

Guidelines are needed for selecting durability critical parts. The flow diagram (Fig. 1) can be used to determine if parts are durability and/or damage tolerance critical. Damage tolerance is defined as: "The ability of the airframe to resist failure due to the presence of flaws, cracks, or other damage for a specified period of unrepaired usage" [13]. Further details of the durability critical parts criteria are discussed elsewhere [5].

Economic Life Criteria Guidelines

Quantitative economic life criteria are needed to demonstrate analytical and experimental compliance with Air Force durability design requirements. Such criteria have yet to be defined in quantitative terms. Two promising analytical formats for quantitative economic life criteria are (1) probability of crack exceedance, and (2) cost ratio: repair cost/replacement cost [5, 6, 14-16]. The durability analysis methodology presented in this paper can be used to quantify structural damage in these formats. Thus, for a given *quantitative* economic life criterion [for example, no more than 5 percent of the fastener holes in the lower wing skin can have a crack size ≥ 1.27 mm (0.05 in.)

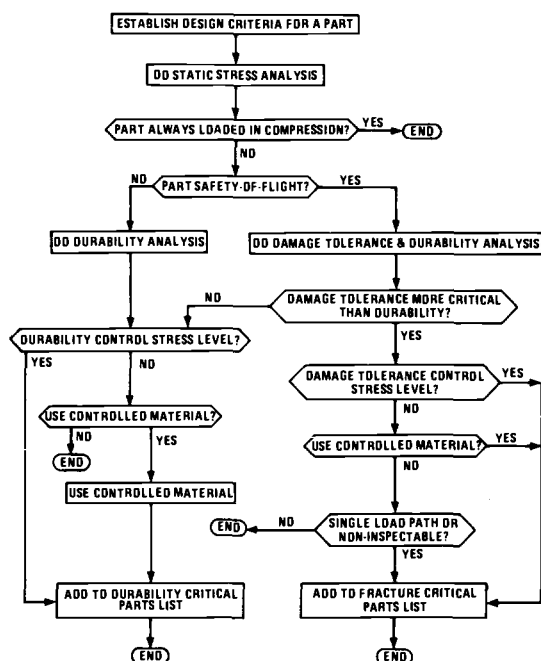


FIG. 1—Flow diagram for selecting durability critical parts.

after 10 000 flight hours], the proposed methodology can be used to analytically demonstrate compliance.

The probability of crack exceedance is a fundamental quantity for defining structural damage and for quantifying economic life criteria in various formats. For example, economic life criteria can be *quantitatively* defined in terms of the percentage or number of fastener holes with a crack size greater than the economic repair crack size a_e or repair cost/replacement cost ratio. One promising format for analytically ensuring economic life is shown in Fig. 2. In this case, structural damage is quantified as a function of time and for different confidence levels. This information could be used to judge the economic life compliance of the structure—given the quantitative criterion for economic life. Economic life criteria guidelines are also discussed elsewhere [5, 6, 14–16].

Durability Analysis Methodology

Analysis Approach

Durability damage is quantified by the length of the dominant fatigue crack emanating from each structural detail (for example, a fastener hole, a

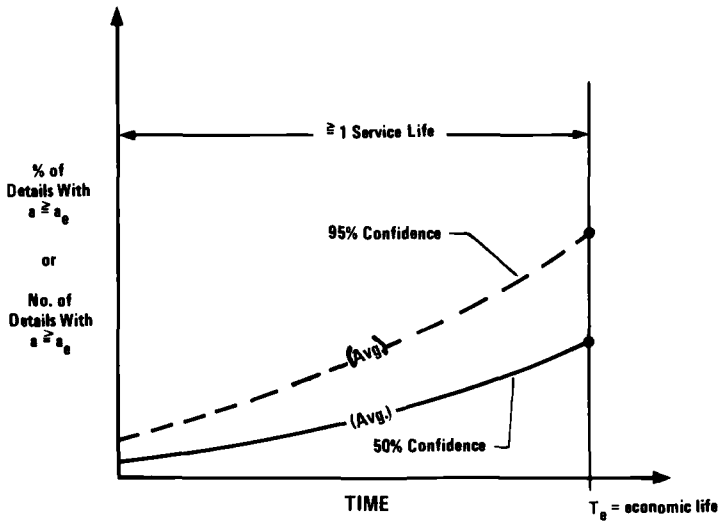


FIG. 2—Economic life analysis format.

fillet, a cutout, or a lug). Durability analysis is concerned with relatively small subcritical crack sizes [for example, ≤ 0.762 -mm (0.03-in.) radial crack in a fastener hole] which may affect structural maintenance requirements but are not an immediate safety hazard. Each fastener hole, for example, is a member of the total population of fastener holes in a part, component, or assembly. Fatigue crack size is considered to be a random variable which is a function of service time. A single time-varying distribution of crack sizes characterizes the durability damage in all fastener holes experiencing a common load history, environment, etc. Calculation of the distribution of crack sizes as a function of service time is the basic object of the present durability analysis methodology. A conceptual description of the durability analysis approach is shown in Fig. 3.

Initial fatigue quality is defined as the initial manufactured state of a structural detail or details with respect to initial flaws in a part, component, or airframe prior to service. The initial fatigue quality for a group of replicate details is represented by an equivalent initial flaw size (EIFS) distribution [5, 6, 14, 17]. An equivalent initial flaw is a hypothetical crack assumed to exist in a detail or group of details prior to service [18–22]. Test results of time-to-crack-initiation and crack growth rates using coupon specimens are employed to define the EIFS distribution. A conceptual description of the initial fatigue quality model is shown in Fig. 4. Once the EIFS distribution (or population) has been defined for a group of details, a deterministic crack growth analysis is used to grow the entire EIFS population to any service time τ ; thus determining the time-varying crack size distribution in service (Fig. 3). The crack growth analysis is performed for the full-scale component using

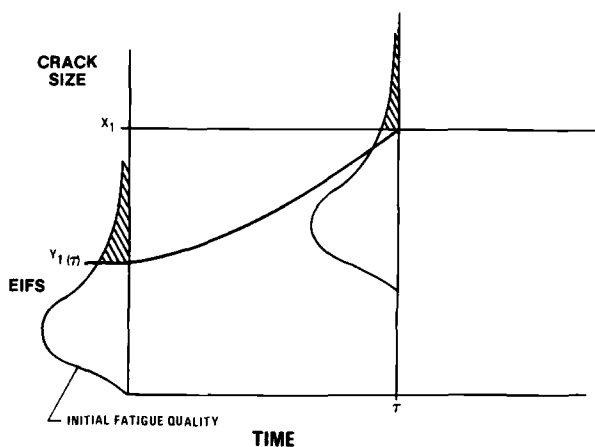


FIG. 3—Durability analysis approach.

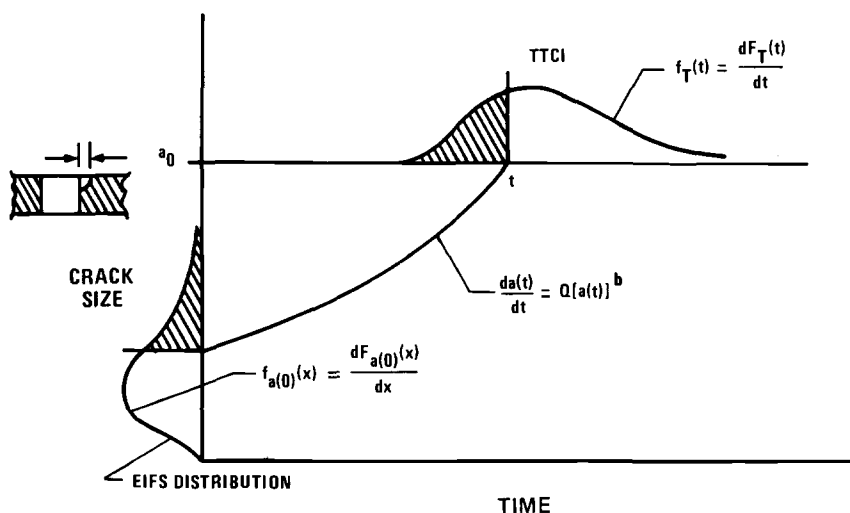


FIG. 4—Initial fatigue quality model.

applicable design conditions (for example, stress level, spectrum, environment) and the user's crack growth analysis computer procedure.

The probability of a crack occurring which is larger than a given crack size, referred to as the "probability of crack exceedance", is the most important information derived from the distribution of crack sizes. For example, in Fig. 3 the probability of exceeding a crack size x_1 at $t = \tau$ is represented by the cross-hatched area under the crack size density function at $t = \tau$. Crack size rankings in the respective distributions for two different times are pre-

served; namely, the crack size x_1 at $t = \tau$ has the same rank (or percentile) as the initial crack size $y_1(\tau)$ at $t = 0$. The probability of crack exceedance is related to the number of expected repairs in a given service interval [5, 6, 14, 17] and provides a basis for judging airframe durability and economic life.

Initial Fatigue Quality Representation

The worst "defect" (whether microstructural constituent, scratch, etc.) in a well-manufactured structural detail cannot be readily detected; this makes direct determination of EIFS unfeasible. However, a model has been developed to derive the initial fatigue quality based on readily observed cracks. An arbitrary crack size, a_0 , is selected which can be readily detected or which can be reliably observed fractographically following testing. The time required for an initial defect, of whatever type, to become a fatigue crack of size a_0 is termed the time-to-crack-initiation (TTCI). In this context, an "initiated" crack of size a_0 is typically larger than normally considered in metallurgical discussions of fatigue crack initiation.

An EIFS distribution for coupon specimens (Fig. 4) has been developed as follows [6, 17]. The time-to-crack initiation (TTCI) distribution for coupon specimens is represented by a three-parameter Weibull distribution, $F_T(t)$,

$$F_T(t) = P[T \leq t] = 1 - \exp \left\{ - \left[\frac{t - \epsilon}{\beta} \right]^\alpha \right\}; \quad t > \epsilon \quad (1)$$

where T is the TTCI, α is the shape parameter, β is the scale parameter, and ϵ is the lower bound. The three Weibull parameters are determined from fractography for coupon specimens or other suitable test results.

The crack growth rate in the small crack size region is assumed to be of the following form:

$$\frac{da(t)}{dt} = Q[a(t)]^b \quad (2)$$

where Q and b are parameters depending on loading spectra, structural and material properties, etc.; $a(t)$ is the crack size at t .

Integrating Eq 2 from $t = 0$ to $t = T$, one obtains the relation between the initial crack size, $a(0)$, and the reference crack size $a_0 = a(T)$ for TTCI (flight hours) as follows:

$$\text{EIFS} = a(0) = [a_0^{-c} + cQT]^{-1/c} \quad (3)$$

where $c = b - 1$.

The EIFS cumulative distribution, $F_{a(0)}(x)$, is obtained by using Eqs 1 and 3 as follows:

$$F_{a(0)}(x) = \exp \left\{ - \left[\frac{x^{-c} - a_0^{-c} - cQ\epsilon}{cQ\beta} \right]^\alpha \right\}; \quad 0 \leq x \leq x_u \quad (4)$$

$$= 1; \quad x > x_u$$

where

$$x_u = [a_0^{-c} + cQ\epsilon]^{-1/c} \quad (5)$$

The five parameters (α , β , ϵ , c , Q) in Eq 4 have been calibrated using crack growth data from Ref 22 for 7475-T7351 aluminum specimens (Fig. 5)

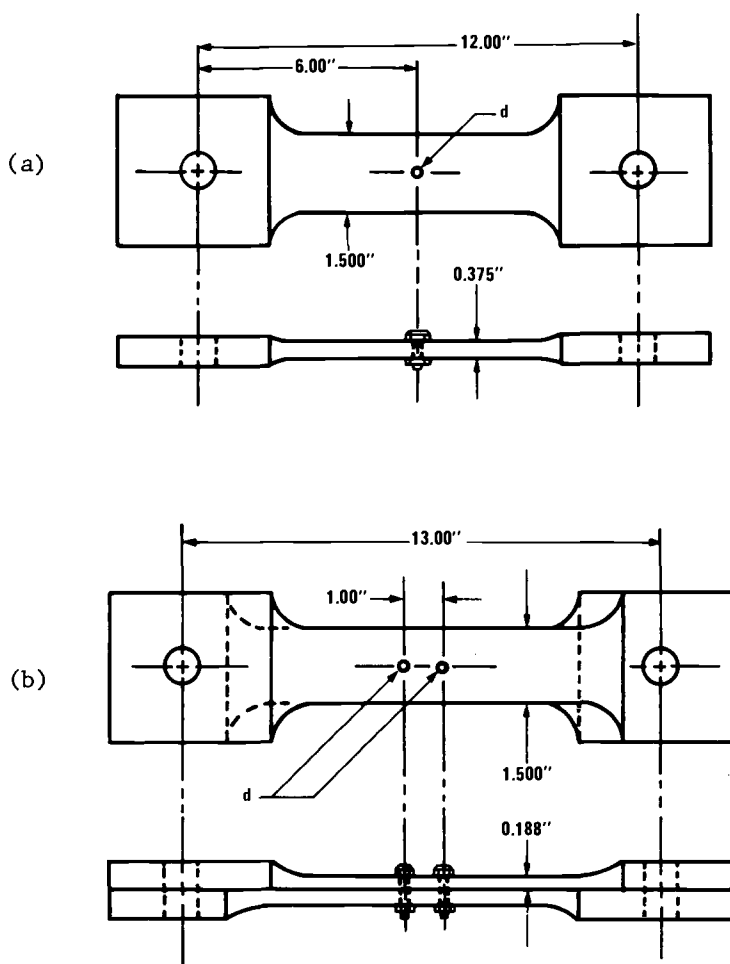


FIG. 5—Fastener hole quality specimens: (a) no load transfer; (b) 15 percent load transfer (XWPF).

for both fighter (F-16) and bomber (B-1) spectra in Refs 6, 10, and 17. It has been shown that (1) the three-parameter Weibull distribution fits observed TTCI test results; (2) Eq 2 is justified for back-extrapolating fractography in the small crack size region for repeating spectra; and (3) the EIFS population, characterized by $F_{a(0)}(x)$, can be transformed (grown) to another service time using a single deterministic crack growth curve [24]. Typical plots of the crack size cumulative distribution versus the crack size are shown in Fig. 6 for the XWPF [15 percent load transfer, F-16 400-h block spectra, gross stress = 234.4 MPa (34 ksi)] data set [22] at $t = 0$, 7200 h, and 10 800 h. It is seen that observed ranked crack sizes (triangles and rectangles) compare very well with predictions (solid and dashed curves).

Analysis Procedure

Durability analysis procedures, described and discussed in detail in Refs 5, 6, 11, and 14, are summarized below.

(1) Divide durability component into m stress regions where the maximum stress in each region may be reasonably assumed to be equal for every location or detail (for example, fastener hole) in a given stress region.

(2) Use the model shown in Fig. 4 and suitable fractography results, if available, to define the EIFS distribution (Eq 4).

(3) For each stress region the crack growth damage accumulation is ex-

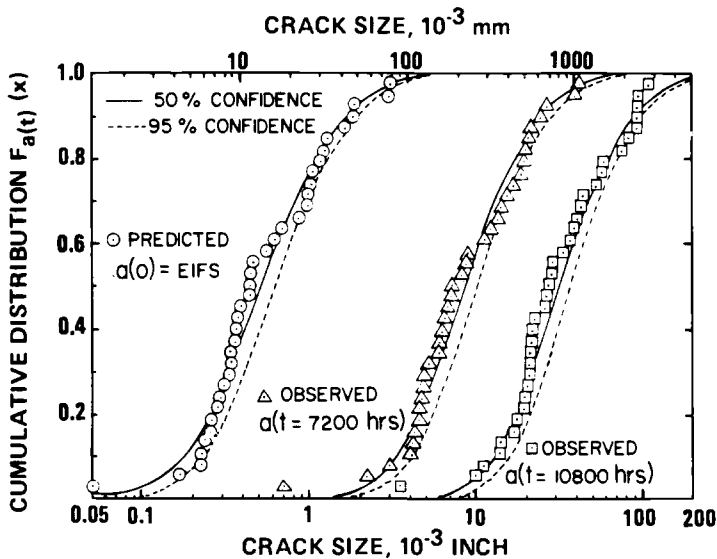


FIG. 6—Crack size versus cumulative distribution $F_{a(t)}(x)$ for XWPF (15 percent load transfer) data set based on fighter spectrum.

pressed either by a curve representing the crack size versus service time, referred to as the "master curve," or by the following equation.

$$\frac{da(t)}{dt} = Q_i [a(t)]^{b_i} \quad (6)$$

The master curve or crack growth parameters Q_i and b_i should be estimated using either applicable fractography results, other test results, or analytical crack growth computer code, such as Ref 23.

(4) In each stress region, determine the cumulative distribution function, $F_{a_i(\tau)}(x_1) = p[a_i(\tau) \leq x_1]$, of the crack size $a_i(\tau)$ at any time τ using Eqs 4 and 6. Then, the probability that the crack size $a_i(\tau)$ will exceed x_1 at τ , denoted by $p(i, \tau)$, is referred to as the probability of crack exceedance. It is computed as $p(i, \tau) = 1 - F_{a_i(\tau)}(x_1)$ in the following [5, 6, 14].

$$\left. \begin{aligned} p(i, \tau) &= 1 - \exp \left\{ - \left[\frac{[y_{1i}(\tau)]^{-c} - a_0^{-c} - cQ_i\epsilon}{cQ_i\beta} \right]^\alpha \right\}; \quad 0 \leq y_{1i}(\tau) \leq x_u \\ &= 1; \quad y_{1i}(\tau) < 0 \\ &= 0; \quad y_{1i}(\tau) > x_u \end{aligned} \right\} \quad (7)$$

where x_u is defined by Eq 5 and

$$y_{1i}(\tau) = [(x_1)^{-c_i} + c_i Q_i \tau]^{-1/c_i} \quad (8)$$

$$c_i = b_i - 1 \quad (9)$$

(5) If the general crack growth master curve is used rather than Eq 6, then Eq 7 still holds except that $y_{1i}(\tau)$ should be obtained from the master curve [5, 6, 14].

(6) The average number of details in the i th stress region with a crack size greater than x_1 at service time τ , $\bar{N}(i, \tau)$, and the corresponding standard deviation, $\sigma_N(i, \tau)$, are determined using the binomial distribution:

$$\bar{N}(i, \tau) = N_i p(i, \tau) \quad (10)$$

$$\sigma_N(i, \tau) = \{N_i p(i, \tau) [1 - p(i, \tau)]\}^{1/2} \quad (11)$$

in which N_i denotes the total number of details in the i th stress region. The average number of details with a crack size exceeding x_1 at the service time τ for m stress regions, $\bar{L}(\tau)$, and its standard deviation, $\sigma_L(\tau)$, can be computed using Eqs 12 and 13, respectively.

$$\bar{L}(\tau) = \sum_{i=1}^m \bar{N}(i, \tau) \quad (12)$$

$$\sigma_L(\tau) = \left[\sum_{i=1}^m \sigma_N^2(i, \tau) \right]^{1/2} \quad (13)$$

Equations 12 and 13 can be used to quantify the extent of damage for a single detail, a group of details, a part, a component, or an airframe. $\bar{L}(\tau)$ approximately corresponds to a 50 percent exceedance probability. Upper and lower bounds for the prediction can be estimated using $\bar{L}(\tau) \pm Z\sigma_L(\tau)$, where Z is the number of standard deviations, $\sigma_L(\tau)$, from the mean, $\bar{L}(\tau)$. Equations 10 to 13 are valid provided that cracks in each detail are relatively small and the growth of the largest crack in each detail is not affected by cracks in neighboring details. Hence the crack growth accumulation for each detail is statistically independent [5,6,14].

Durability Analysis Demonstration

The durability methodology will be illustrated using the lower wing skins of the full-scale F-16 durability test article. Extent of damage predictions for the lower wing skin are compared with observations from the tear-down inspection of the F-16 durability test article. Essential details of the analysis are described, and the results are discussed in quantitative structural durability terms. This demonstration illustrates the durability methodology and the type of output information, but it is not intended to be a final verification of the methodology for full-scale aircraft structure.

The F-16 durability test article was tested to 16 000 flight hours (equivalent to 2 service lives) using the F-16 500-h block spectrum. Each wing received the same loading. Following the test, all fastener holes in the lower wing skins were inspected using the eddy-current technique. Fastener holes with crack indications were confirmed by fractographic evaluation. For conciseness, only resulting crack sizes for the right-hand lower wing skin are shown in Fig. 7.

The durability analysis of the F-16 lower wing skin followed the general procedures previously described. Details of the analysis, including results, are given in Ref 11. Briefly, the analysis was done in the following manner: (1) the lower wing skin was divided into three stress regions (that is, $m = 3$); (2) the initial fatigue quality of all fastener holes in the lower wing skins (Eqs 1, 2, and 4) was quantified using test coupon data from Ref 22 (that is, XWPF data set); (3) the CGR computer program [23] was used to develop crack growth "master curves" and to calibrate Q_i and c_i for the three stress regions; (4) the model parameters (that is, α , β , ϵ , c_i , and Q_i) were calibrated

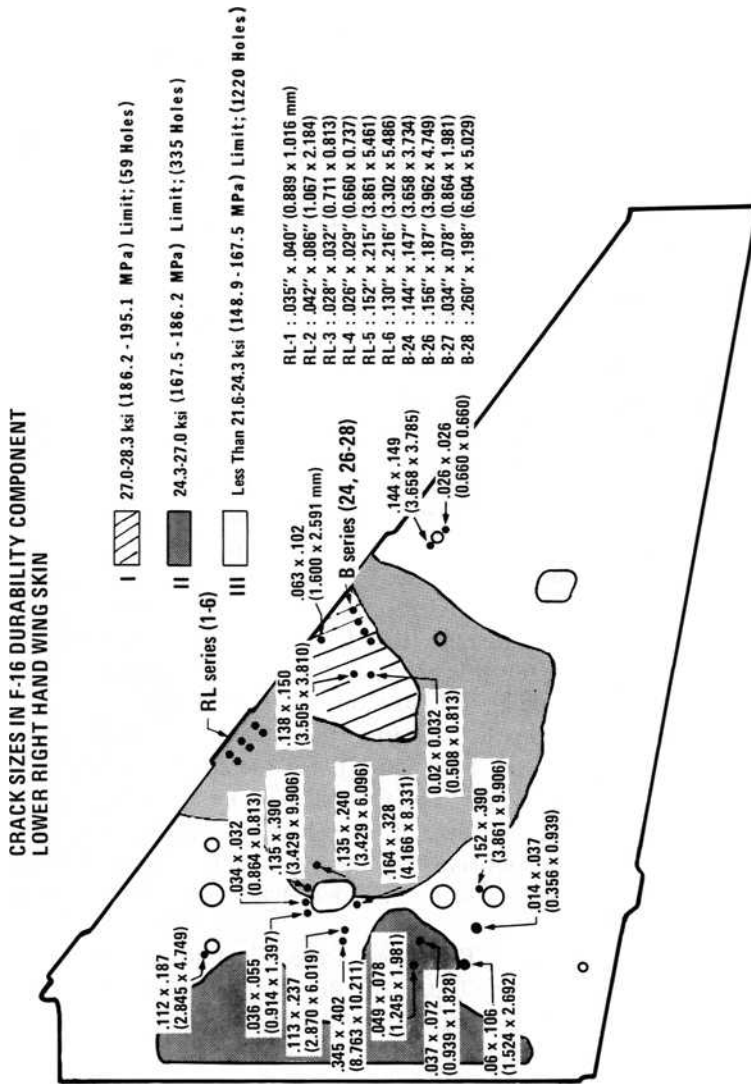


FIG. 7—Observed crack sizes in F-16 durability test component—right-hand lower wing skin after 16 000 flight hours (500-block spectra).

as deterministic values; and (5) Eqs 10 to 13 were used to predict the extent of damage at any service time τ ; in particular, $\tau = 16\,000$ flight hours.

Differences between the coupon test conditions and those in the F-16 lower wing skins are noted. Whereas the lower wing skins on the durability test article were predominantly fastened with countersunk, blind rivets, the XWPF test coupons used protruding head, straight shank, threaded fasteners. The XWPF coupons were tested using the F-16 400-h block spectrum, which is slightly more severe than the full-scale aircraft wing test spectrum used (that is, F-16 500-h block). Load transfer through the fasteners typically ranged from 15 to 20 percent for the full-scale lower wing skins. The XWPF test coupons were designed for a 15 percent load transfer through the fasteners. Other important factors, such as material, manufacturing procedures, load exceedance curves for the test spectra, and maximum spectrum stress level, were similar in the test coupons and durability test aircraft.

Initial fatigue quality model parameters based on the XWPF data set of Ref 22 are summarized in Table 1. In Table 2, crack growth parameters, Q_i and c_i , and pertinent details are presented for the three stress regions.

Results of the durability analysis can be presented in different useful formats for the analytical assurance of economic life. For example, the average percentage of crack exceedance versus crack size plots for the lower wing skin are presented in Fig. 8 for different flight hours. For comparison purposes, ranked observations from the tear-down inspection of the right-hand lower

TABLE 1—Model parameters for defining initial fatigue quality.^a

α	$\beta,^b$ flight hours	ϵ	b	c	$Q \times 10^4$
5.5	14402	0	0.962	-0.038	3.09

^aBased on XWPF data set from Ref 22; 7475-T7351 aluminum; 15 percent load transfer; gross stress = 234.4 MPa (34 ksi); F-16 400-h spectrum; protruding head fastener (NAS 6204-7, $\frac{1}{4}$ diameter).

^b50 percent confidence.

TABLE 2—Crack growth parameters for F-16 lower wing skin.^a

Stress Region	Gross Stress	No. of Holes	b_i	c_i	$Q_i \times 10^4$
I	195.1 MPa (28.3 ksi)	59	1.16	0.16	6.29
II	176.5 MPa (25.6 ksi)	335	1.292	0.292	8.446
III	157.9 MPa (22.9 ksi)	1220	1.266	0.266	4.137

^a7475-T7351 aluminum; F-16 500-h block spectrum; countersunk fastener (MS 90353 type); 15 to 20 percent load transfer; $da(\tau)/d\tau = Q_i[a(\tau)]^{b_i}$

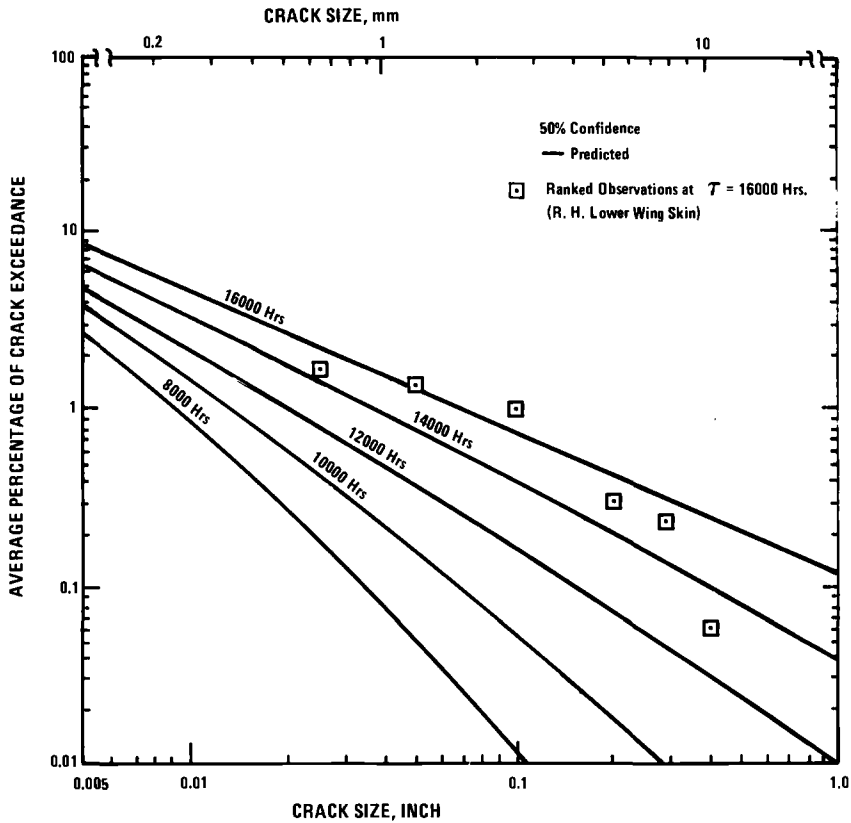


FIG. 8—Crack size versus average percentage of crack exceedance for F-16 lower wing skin in terms of flight hours.

wing skin are also plotted. Note that the average percentage of fastener holes having a crack size exceeding any value x_1 increases with service time. In Fig. 8 the extent of damage predictions for each stress region have been combined for the complete lower wing skin for overall economic life assessment. Similar results have been plotted for individual stress regions [11].

In Fig. 8, for example, approximately 1.8 percent (or $0.018 \times 1614 \cong 29$ fasteners) of the fastener holes in the lower wing skin would be predicted to have a crack size ≥ 0.762 mm (0.03 in.) at 16 000 flight hours. This type of information can be used to judge structural durability and economic life during the design stage. Also, the type of information shown in Fig. 8 could be useful for setting in-service structural maintenance requirements.

Figure 9 illustrates another useful format for presenting the durability analysis results. The percentage of fastener holes having a crack size exceeding any value x_1 at 16 000 flight hours in the first stress region is plotted as a function of exceedance probability. For simplicity, only the exceedance

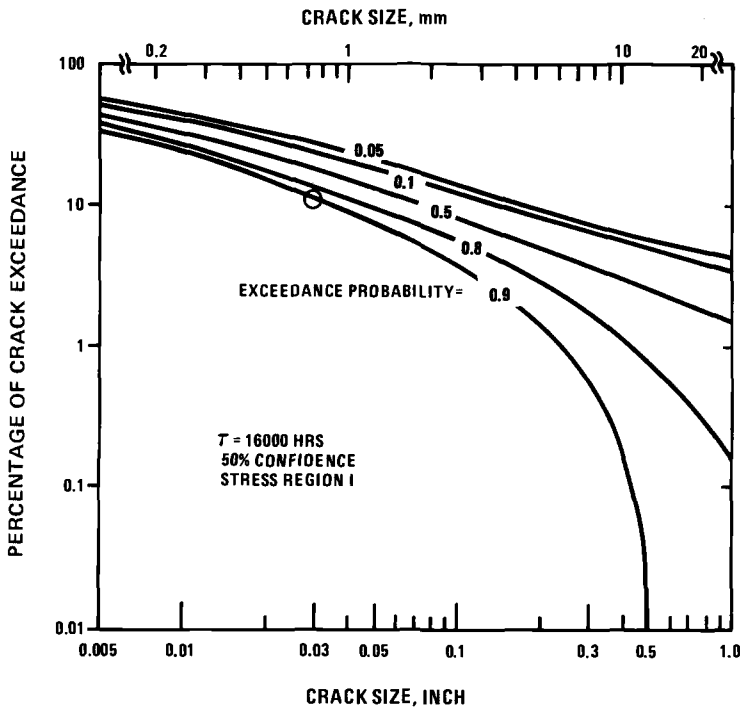


FIG. 9—Crack size versus percentage of crack exceedance for stress region I of F-16 lower wing skin after 16 000 flight hours.

curves associated with exceedance probabilities 0.05, 0.1, 0.5, 0.8, and 0.9 are presented. Test results for the percentage of cracks exceeding 0.762 mm (0.03 in.) in the first stress region of the right-hand lower wing skin are plotted as a circle for comparison. No cracks were observed for the left-hand lower wing skin for this stress region. Plots similar to Figs. 8 and 9 have been made for the second and third stress regions [11]. It was concluded that the correlations between the test results and the predictions based on the present analysis methodology are excellent.

Figure 9 also provides information for estimating the upper and lower bounds for the prediction in terms of arbitrarily selected exceedance probability levels. For example, suppose the upper and lower bounds for the prediction correspond to exceedance probabilities of 0.05 and 0.90, respectively. Then, in Fig. 9, the upper and lower bound prediction for the average percentage of crack exceedance for an 0.762 mm (0.03 in.) crack size at 16 000 flight hours is approximately 22 and 12 percent, respectively.

The total number of details $L(\tau)$ having a crack size larger than the economical repair limit for fastener holes [for example, $a_e = 0.762$ mm (0.03 in.)] in the entire wing skin is a statistical variable. The average value $\bar{L}(\tau)$

and the standard deviation $\sigma_L(\tau)$ of $L(\tau)$ at any service time τ have been computed using Eqs 12 and 13. The average number $\bar{L}(\tau)$ of fastener holes having a crack size larger than 0.762 mm (0.03 in.) in the lower wing skin is plotted in Fig. 10 as Curve 1. Also plotted as Curves 2 and 3 are the results associated with the mean \mp standard deviation; that is, $\bar{L}(\tau) \mp \sigma_L(\tau)$.

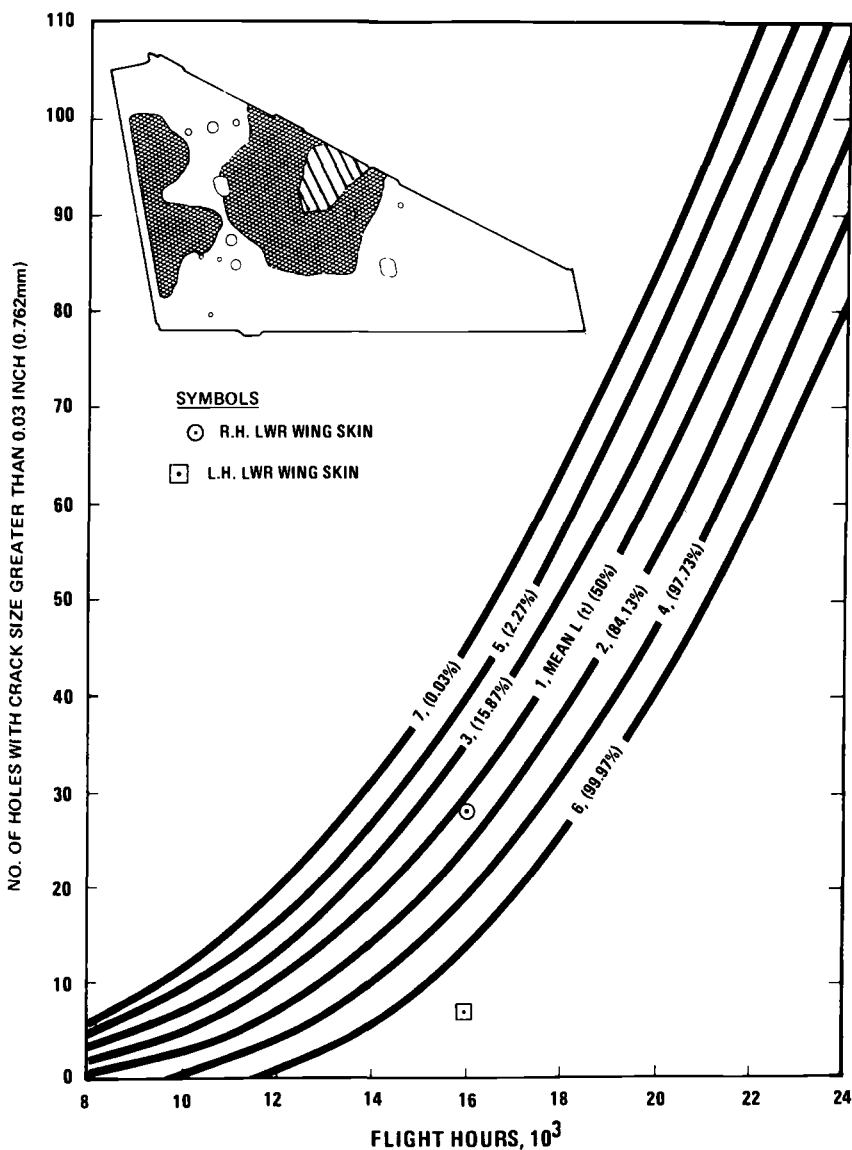


FIG. 10—Flight hours versus number of fastener holes with crack size ≥ 0.762 mm (0.03 in.) for F-16 lower wing skin.

Likewise, Curves 4, 5, 6, and 7 in Fig. 10 correspond to the results of $\bar{L}(\tau) - 2\sigma_L(\tau)$, $\bar{L}(\tau) + 2\sigma_L(\tau)$, $\bar{L}(\tau) - 3\sigma_L(\tau)$, and $\bar{L}(\tau) + 3\sigma_L(\tau)$, respectively. Since the number of details in each stress region is large, it is reasonable to approximate the binomial distribution by the normal distribution. Thus the mean curve $\bar{L}(\tau)$ corresponds to a 50 percent exceedance probability, while other curves correspond to various exceedance probabilities as shown in Fig. 10 in parentheses.

Full-scale test results for the right-hand wing and the left-hand wing at $\tau = 16\,000$ flight hours are plotted in Fig. 10 as a circle and a square, respectively. In addition, the analytical predictions, along with the test results at $\tau = 16\,000$ flight hours in each stress region as well as in the entire lower wing skin, are summarized in Table 3. The durability analysis results shown in Fig. 10 and Table 3 correlate well with observed test results for the right-hand wing, while predictions are conservative [predict more holes with cracks ≥ 0.762 mm (0.03 in.)] for the left-hand wing. One possible explanation for the conservative prediction for the left-hand wing is that there may have been some cracks in the full-scale test article which were not found during NDI.

Conclusions

A durability analysis methodology has been developed for satisfying the Air Force's durability design requirements for airframes. Results of the durability analysis can be used to analytically ensure structural durability. Although quantitative economic life criteria remain to be developed for demonstrating structural design compliance, guidelines and promising analytical formats for such criteria have been presented. Durability analysis methods for quantifying structural damage due to fatigue cracking have been developed and evaluated using test results for coupon specimens and demonstrated for a full-scale airplane test article. Further work is required to test the durability analysis methodology for different spectra, materials, load transfer, and stress levels [24].

TABLE 3—Durability analysis results for F-16 durability test article—lower wing skin.

Stress Region	No. of Holes	Probability that a Crack Will Exceed 0.762 mm (0.03 in.)	No. of Holes Having Crack Size Exceeding $a_e = 0.762$ mm (0.03 in.)			
			Analytical Prediction		Test Results	
			Average	Standard Deviation	Right-Hand Wing ^a	Left-Hand Wing ^a
I	59	0.1760	10.4	2.9	7	0
II	335	0.0408	13.7	3.6	10	2
III	1220	0.0045	5.5	2.3	11	5
Entire wing skin	1614	...	29.6	5.2	28	7

^aAfter 16 000 h of F-16 500-h block spectrum.

Acknowledgments

This research is based on work performed for the on-going "Durability Methods Development" program sponsored by the Air Force Wright Aeronautical Laboratories, Flight Dynamics Laboratory, Wright-Patterson Air Force Base, Ohio (Contract F33615-77-C-3123). Dr. B. G. W. Yee of General Dynamics' Materials Research Laboratory is Program Manager. The authors appreciate the valuable discussions with Dr. B. G. W. Yee, Dr. V. D. Smith, and J. W. Morrow of General Dynamics, and Dr. M. Shinozuka of Modern Analysis Incorporated.

References

- [1] MIL-STD-1530A (11), "Aircraft Structural Integrity Program," 11 Dec. 1975.
- [2] MIL-A-8866B (USAF), "Airplane Strength and Rigidity Reliability Requirements, Repeated Loads and Fatigue," 22 Aug. 1975.
- [3] MIL-A-8867B (USAF), "Airplane Structural Ground Test," Jan. 1975.
- [4] Pendley, B. J., Henslee, S. P., and Manning, S. D., "Durability Methods Development, Volume III-Structural Durability Survey: State-of-the-Art Assessment," AFFDL-TR-79-3118, Sept. 1979.
- [5] Manning, S. D., Yang, J. N., Garver, W. R., Shinozuka, M. et al, "Durability Methods Development, Volume I-Phase I-Summary," AFFDL-TR-79-3118, Sept. 1979.
- [6] Yang, J. N., Manning, S. D., and Garver, W. R., "Durability Methods Development, Volume V-Durability Analysis Methodology Development," AFFDL-TR-79-3118, Sept. 1979.
- [7] Manning, S. D., Flanders, M. A., Garver, W. R., and Kim, Y. H., "Durability Methods Development, Volume II-Durability Analysis: State-of-the-Art Assessment," AFFDL-TR-79-3118, Sept. 1979.
- [8] Shinozuka, M., "Durability Methods Development, Volume IV-Initial Quality Representation," AFFDL-TR-79-3118, Sept. 1979.
- [9] "Durability Methods Development, Interim Technical Quarterly Report," 15 Sept.-15 Dec. 1979, General Dynamics, Fort Worth Division, Report FZM-657-007, 14 Dec. 1979.
- [10] "Durability Methods Development, Interim Technical Quarterly Report," 15 Dec. 1979-15 March 1980, General Dynamics, Fort Worth Division, Report FZM-657-008, 15 March 1980.
- [11] "Durability Methods Development, Interim Technical Quarterly Report," 15 March-15 June 1980, General Dynamics, Fort Worth Division, Report FZM-657-009, 15 June 1980.
- [12] "Durability Methods Development, Interim Technical Quarterly Report," 15 June-15 Sept. 1980, General Dynamics, Fort Worth Division, Report FZM-657-010, 15 Sept. 1980.
- [13] MIL-A-83444 (USAF), "Airplane Damage Tolerance Requirements," July 1974.
- [14] Yang, J. N., "Statistical Estimation of Economic Life for Aircraft Structures," in *Proceedings, AIAA/ASME/ASCE/AHS Structures, Structural Dynamics, and Materials Conference*, St. Louis, 1-6 April 1979, pp. 240-248; *Journal of Aircraft*, Vol. 17, No. 7, 1980, pp. 528-535.
- [15] Yang, J. N., "Statistical Estimation of Service Cracks and Maintenance Cost for Aircraft Structures," *Journal of Aircraft*, Vol. 13, No. 12, 1976, pp. 929-937.
- [16] Manning, S. D. and Smith, V. D., "Economic Life Criteria for Metallic Airframes," in *Proceedings, 21st Structures, Structural Dynamics, and Materials Conference*, Seattle, 12-14 May 1980, pp. 504-511.
- [17] Yang, J. N. and Manning, S. D., "Distribution of Equivalent Initial Flaw Size," in *1980 Proceedings, Annual Reliability and Maintainability Symposium*, San Francisco, 22-24 Jan. 1980, pp. 112-120.
- [18] Wood, H. A., Engle, R. M., Gallagher, J., and Potter, J. M., "Current Practice on Estimating Crack Growth Damage Accumulation with Specific Application to Structural Safety, Durability and Reliability," AFFDL-TR-75-32, 1976.

- [19] Rudd, J. L., "Application of the Equivalent Initial Quality Method," AFFDL-TM-77-58-FBE, July 1977.
- [20] Yang, J. N., "Statistical Approach to Fatigue and Fracture Including Maintenance Procedures," in *Proceedings, Tenth Symposium on Naval Structural Mechanics*, Wash., D.C., Sept. 1978; in *Fracture Mechanics*, edited by Perrone et al., University Press of Virginia, Charlottesville, Va., 1978, pp. 559-577.
- [21] Potter, J. M., "Advances in Fastener Hole Quality Through the Application of Solid Mechanics," paper presented at the Army Symposium on Solid Mechanics, Case Studies on Structural Integrity and Reliability, Cape Cod, Mass., 1978.
- [22] Noronha, P. J. et al, "Fastener Hole Quality," AFFDL TR-78-206, Vols. I & II, Dec. 1978.
- [23] Johnson, W. S. and Spamer, T., "A User's Guide to CGR-GD, A Computerized Crack Growth Prediction Program," Report FZS-241, General Dynamics' Fort Worth Division, Nov. 1976.
- [24] Yang, J. N., "Statistical Crack Growth in Durability and Damage Tolerant Analyses," in *Proceedings, 22nd AIAA/ASME/ASCE/AHS Structures, Structural Dynamics, and Materials Conference*, Atlanta, April 1981, AIAA Paper No. 81-0492, pp. 38-43.

Experimental Evaluation of Initial Flaw Criticality and Analysis Methods for Damage Tolerant Air Force Aircraft

REFERENCE: Rudd, J. L., Brussat, T. R., Chiu, S. T., and Creager, M., "Experimental Evaluation of Initial Flaw Criticality and Analysis Methods for Damage Tolerant Air Force Aircraft," *Design of Fatigue and Fracture Resistant Structures, ASTM STP 761*, P. R. Abelkis and C. M. Hudson, Eds., American Society for Testing and Materials, 1982, pp. 152-171.

ABSTRACT: This paper considers two aspects of the United States Air Force analytical and experimental damage tolerance design requirements for metallic airframes: the locations of initial damage and the accuracy of crack growth analysis. Following a summary of the requirements, an assessment is made of the validity of the initial continuing damage locations specified in the requirements. Guidelines are provided for selecting the initial primary damage location needed but not specified in the requirements. Analyses and test results are presented for typical aircraft structure (that is, chordwise splices, spanwise splices, stringer-reinforced continuous skin, 2-bay wing panels, etc.). The analytical and experimental results are correlated in order to assess the accuracy of the state-of-the-art analytical capability to satisfy the Air Force damage tolerance requirements.

KEY WORDS: damage tolerance, fracture mechanics, fatigue crack growth, residual strength, design criteria, initial damage, aircraft structure, fastener holes, mechanical joints

In order to ensure the operational readiness of United States Air Force aircraft, structural integrity (for example, strength, rigidity, durability, and damage tolerance) requirements exist which are presented in Military Standard MIL-STD-1530A [1].⁴ This paper addresses the damage tolerance por-

¹Aerospace Engineer, Air Force Wright Aeronautical Laboratories, Wright-Patterson Air Force Base, Ohio 45433.

²Senior Research Specialist, Lockheed-California Company, Burbank, Calif. 91520.

³President, Del West Engineering, Chatsworth, Calif. 91311.

⁴The italic numbers in brackets refer to the list of references appended to this paper.

tion of structural integrity, which is defined as the ability of the airframe (for example, fuselage, wing, empennage, etc.) to resist failure due to the presence of flaws, cracks, or other damage for a specified period of unrepaired usage. Damage tolerance of the airframe is needed not only to ensure operational readiness but also safety. The Air Force analytical and experimental damage tolerance design requirements presented in Military Specifications MIL-A-83444 [2] and MIL-A-8867B [3], respectively, are summarized herein for background.

MIL-A-83444 specifies some initial flaw assumptions, such as the types and sizes of initial primary cracks and so-called initial continuing damage flaws. However, the locations of the continuing damage flaws are specified based on engineering judgement and need to be verified. Furthermore, whereas the primary damage is required to be at the "most critical" location, guidelines for selecting the most critical location are not available. Thirdly, the specification requires a fatigue crack growth analysis for aircraft structure, but the accuracy of such an analysis is not well defined. This paper assesses the validity of the initial continuing damage assumptions specified in MIL-A-83444, provides guidelines for selecting the most critical location for primary damage, and assesses the state-of-the-art analytical capability to satisfy MIL-A-83444.

Analytical Damage Tolerance Design Requirements

Flaws, defects, imperfections, or discrepancies exist in aircraft structure due to various material and structural manufacturing and processing operations. The Air Force analytical damage tolerance design requirements of MIL-A-83444 assumes the existence of such flaws in the most unfavorable locations and orientations with respect to the applied stress and material properties. These flaws must meet crack growth and residual strength requirements which are a function of the design concept (that is, slow crack growth and fail safe) and degree of inspectability (that is, noninspectable, depot or base level inspectable, special visual inspectable, walk-around visual inspectable, ground evident inspectable, and in-flight evident inspectable) of the structure. The analytical damage tolerance requirements for each design concept are presented in the following.

Slow Crack Growth Structure

Slow crack growth structure is classified as either (1) noninspectable or (2) depot or base level inspectable. Initial primary damage is assumed to exist in the most critical location of each structural element. The size of the assumed initial primary damage is based upon nondestructive inspection (NDI) capability and the degree of inspectability of the structure.

The initial primary damage sizes and shapes assumed for noninspectable structure are illustrated in Fig. 1. Other surface flaw shapes with initial stress intensity factors equivalent to that of the semicircular surface flaw specified in Fig. 1 may be assumed if appropriate (for example, corner flaws at the edges of structural elements, longer and shallower surface flaws in plates subjected to high bending stresses). Figure 1 indicates that the type of flaw assumed for the initial primary damage is dependent upon the thickness of the material. Smaller initial flaw sizes than those specified in Fig. 1 may be assumed subsequent to a demonstration that all flaws larger than the assumed sizes have at least a 90 percent probability of detection with a 95 percent confidence level. Smaller initial flaw sizes may be also assumed if proof test inspection is used, based on the calculated critical crack size at the proof test stress level. The initial primary damage must not grow to critical size and cause failure of the structure in two (2) design service lifetimes. In addition to this crack growth requirement, a residual strength requirement is specified in MIL-A-83444 for this time period.

For slow crack growth structure that is depot or base level inspectable, the initial primary damage sizes and shapes assumed after completion of the inspection are the same as those previously discussed for noninspectable structure (Fig. 1), provided the component is to be removed from the aircraft and completely inspected with the same NDI procedures that were used during fabrication. Larger initial primary damage sizes must be assumed after completion of the inspection if NDI techniques (that is, penetrant, magnetic particle, and ultrasonics) are used without component or fastener removal (Fig.

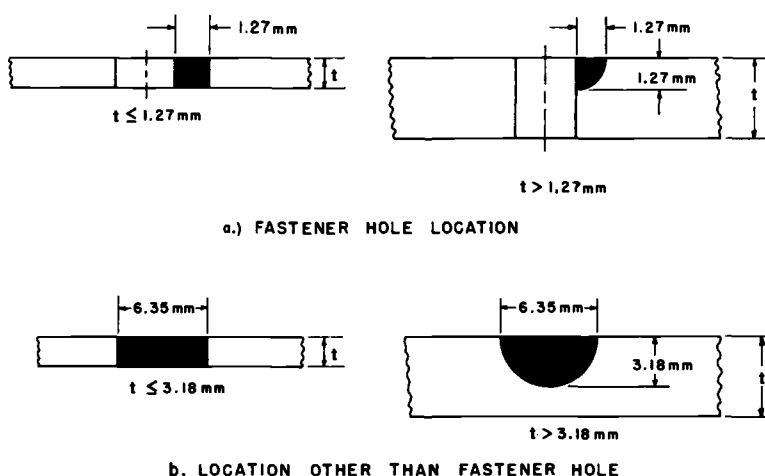


FIG. 1—Initial primary damage for noninspectable and depot or base level inspectable structure with component removal (slow crack growth structure).

2). The crack lengths in Fig. 2 are measured from the edge of the fastener head or nut. Other surface flaw shapes with initial stress intensity factors equivalent to those of the semicircular surface flaws specified in Figs. 1 and 2 may be assumed if appropriate. If close visual inspection techniques are used, a through-the-thickness flaw having at least 50.8 mm (2 in.) of uncovered length must be the minimum assumed damage size. When inaccessibility, paint, sealant, or other factors preclude close visual inspection or the use of NDI techniques, slow crack growth structure must be assumed to be noninspectable. Smaller crack sizes than those specified above may be assumed if proof test inspection is used. The initial primary damage must not grow to critical size and cause failure of the structure in one half ($1/2$) the design service lifetime. In addition to this crack growth requirement, a residual strength requirement is specified in MIL-A-83444 for this time period.

As previously mentioned, the size of the initial primary damage, assumed at the most critical location, is based upon NDI capability. MIL-A-83444 specifies that initial continuing damage must also be assumed at other locations to represent the overall initial quality of the structure. The sizes and shapes of the initial continuing damage to be assumed are specified in Fig. 3. If the contractor has developed initial quality data (for example, fractographic studies which provide a sound basis for determining equivalent ini-

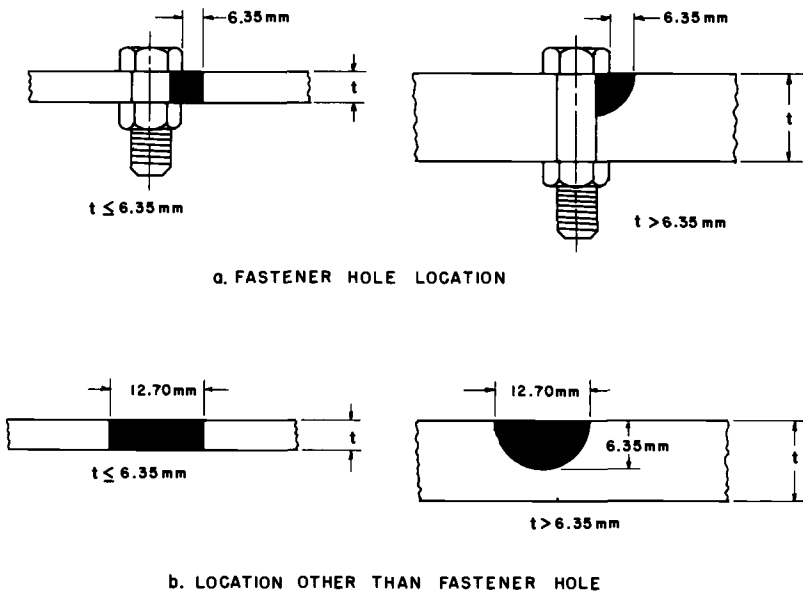


FIG. 2—Initial primary damage for depot or base level inspectable structure without component removal.

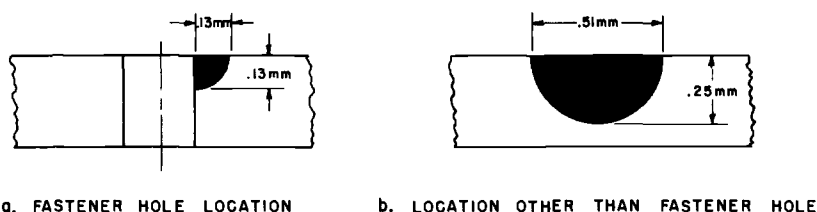


FIG. 3—Initial continuing damage.

tial flaw sizes), these data may be submitted to the procuring activity for review and serve as a basis for negotiating sizes different than those previously specified.

Fail-Safe Structure

Fail-safe structure can be classified as either multiple load path or crack arrest. The degrees of inspectability of fail-safe structure are (1) depot or base level, (2) special visual, (3) walk-around visual, (4) ground evident, and (5) in-flight evident. Because the design requirements and assumptions for multiple load path structure are basically the same as those for crack arrest structure, only the design requirements and assumptions for multiple load path structure will be discussed in this paper.

Two sets of crack growth and residual strength requirements exist for multiple load path structure. The first set applies to intact structure (that is, structure prior to load path failure). The second set applies to the remaining structure subsequent to load path failure. The assumed initial primary damage sizes and shapes after completion of the inspection of intact structure that is depot or base-level inspectable are presented in Fig. 4, provided the component is to be removed from the aircraft and completely inspected with the same NDI procedures used during fabrication. If NDI techniques are used without component or fastener removal, the assumed initial primary damage sizes and shapes are the same as those previously discussed for slow crack growth structure (Fig. 2). The initial primary damage must not grow to critical size and cause failure of the structure in one fourth ($1/4$) the design service lifetime. If the intact structure is not depot or base level inspectable, the assumed initial primary damage sizes and shapes are those presented in Fig. 4. This initial primary damage must not grow to critical size and cause failure in one (1) design service lifetime.

Besides the crack growth requirements specified above, the intact structure and the remaining structure at the time of load path failure must meet residual strength requirements. These requirements are specified in MIL-A-83444 as a function of the degree of inspectability of the structure. Also, subsequent to load path failure, the failed load path plus damage assumed in

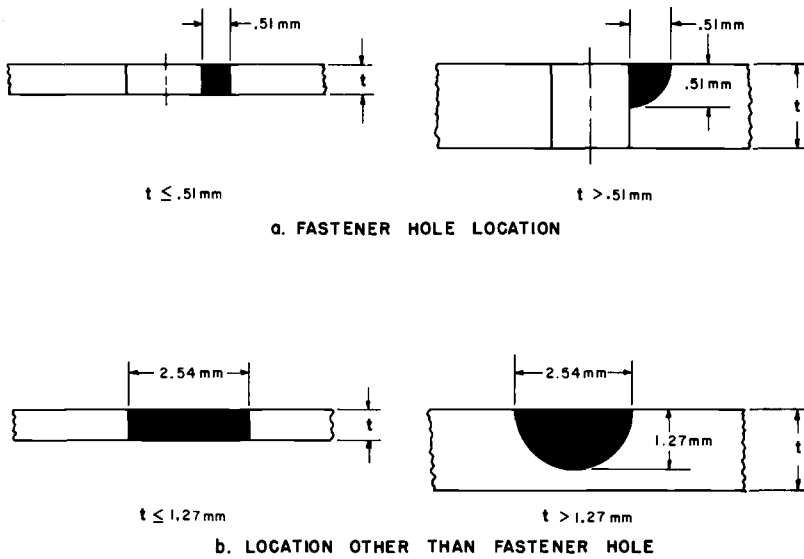


FIG. 4—Initial primary damage for fail-safe, inspectable structure: depot or base level with component removal, special visual, walk-around visual, ground evident, and in-flight evident.

the remaining adjacent structure must meet additional crack growth and residual strength requirements as specified in MIL-A-83444.

Experimental Damage Tolerance Design Requirements

Design development tests [3] are required to provide an early evaluation of the damage tolerance of critical structural components and assemblies. Design development tests are also required to provide an early evaluation or verification of the crack growth and residual strength analyses used to satisfy the analytical damage tolerance design requirements for MIL-A-83444 previously discussed. Specimens used for the design development tests may range from simple coupons and elements to more complex splices, joints, panels, fittings, wing-carry-through structures, etc.

Damage tolerance tests [3] must be performed to demonstrate compliance with the crack growth and residual strength design requirements of MIL-A-83444. The type, number, and duration of tests needed are a function of the design concept and degree of inspectability of the structure. Full-scale damage tolerance testing must be performed if damage tolerance of the airframe is not demonstrated during the design development and full-scale durability tests. Existing hardware must be used for the damage tolerance tests when possible (for example, component and assemblies of the design development tests, full-scale static and durability test articles, etc.). Addi-

tional structural components and assemblies must be fabricated and tested as required.

Inspections are required during damage tolerance testing in accordance with the requirements of MIL-A-83444 for the aircraft in service, as well as any special inspections specified by the Air Force. A destructive teardown inspection must be performed after completion of damage tolerance testing which includes disassembly and laboratory-type inspection of the fracture critical areas. Fractographic examinations are required to obtain crack growth and initial quality data. Inspection proof tests may be performed on components, assemblies, or complete airframes, when approved by the Air Force, in order to establish initial flaw sizes other than those specified in MIL-A-83444 when the use of conventional NDI is impractical or cost ineffective.

Guidelines for Selecting the Most Critical Location of Initial Primary Damage

The Air Force damage tolerance design requirements [2] for metallic airframes specify that initial primary damage must be assumed to exist in the most critical location of each structural element. The most critical locations are not obvious for typical aircraft structure due to the geometric and loading complexities involved. Therefore guidelines are needed for selecting these locations. This paper presents such guidelines for three typical aircraft structural configurations.

A total of 28 tests were conducted to determine the most critical locations of initial primary damage [4]. These tests were conducted for test specimens involving (1) center-stringer-reinforced, continuous skin; (2) center-stringer-reinforced, split skin; and (3) edge-stringer-reinforced, continuous skin. The specimens selected represent typical aircraft structure. A constant amplitude loading was applied with a maximum stress level of 117.21 MPa (17 ksi) and a stress ratio of 0.1. The tests were performed in a controlled laboratory air environment with a temperature of $22 \pm -16^{\circ}\text{C}$ ($72 \pm 3^{\circ}\text{F}$) and a relative humidity of 40 ± 10 percent.

An initial primary fatigue crack was induced into each structural element of the test specimens at the faying surface. This initial primary damage was a 1.27-mm (0.050-in.) quarter-circular corner crack as required by MIL-A-83444 for slow crack growth structure. The precracks were induced prior to assembly using the following procedures. An undersized hole was drilled and a razor notch was made at the corner of the hole. Cyclic fatigue loading was applied until a crack of the desired length was formed from the notch. The hole was redrilled to final size, leaving a 1.27-mm (0.050-in.) corner crack. Since more than one controlled fatigue crack could not be simultaneously induced in each structural element, the initial continuing damage used in the tests was a 0.51-mm (0.020-in.) razor notch. This damage is equivalent in life to the 0.13-mm (0.005-in.) quarter-circular corner crack specified as

the continuing damage in MIL-A-83444. This equivalency was verified by a separate fatigue test program using 35 coupon and small joint specimens. [5,6]

Two different locations were considered for the initial primary damage, referred to as the inside crack and outside crack. The inside crack was directed toward the center of the panel whereas the outside crack faced the panel edge. A clearance-fit, untorqued steel Hi-Lok fastener was inserted into each fastener hole containing initial primary or continuing damage.

Center-Stringer-Reinforced, Continuous-Skin Specimens

Ten specimens were tested for the geometric configuration shown in Fig. 5. Each specimen had an overall nominal length of 1207 mm (47.5 in.) and a test section width of 457 mm (18 in.). The skin and tee section thicknesses were 4.62 mm (0.182 in.) and 4.78 mm (0.188 in.), respectively. Both structural elements contained 6.35-mm (0.25-in.)-diameter fastener holes. Both inside and outside cracks were considered as the initial primary damage.

Three different test cases were considered (Table 1). Test Case I was consistent with the damage tolerance design requirements of MIL-A-83444. This case involved initial continuing damage in the hole (Hole No. 2) adjacent to the one containing the initial primary damage (Hole No. 1), as illustrated in Fig. 5. The holes containing the initial primary and continuing damage were filled with an untorqued, clearance-fit fastener. The fasteners in the nearby

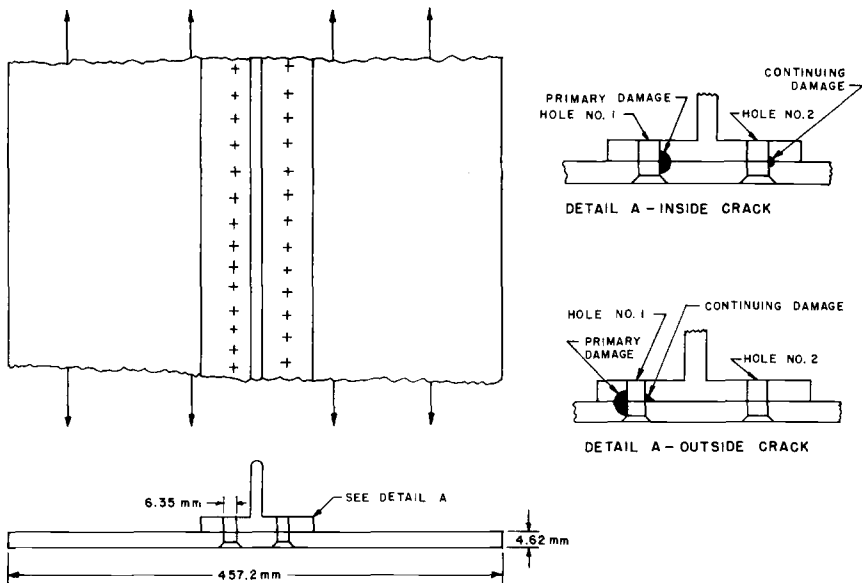


FIG. 5—Center-stringer-reinforced, continuous-skin specimen.

TABLE 1—*Test cases for center-stringer-reinforced, continuous-skin specimen.*

Test Case No.	Fastener for Hole No. 2	Initial Continuing Damage
I	clearance-fit, untorqued	yes
II	clearance-fit, untorqued	no
III	rivet	no

rows were flush-head aluminum rivets, representative of standard design practice for this configuration. Test Case II was identical to Test Case I with the exception that no initial continuing damage flaws were induced in the structure. Test Case III was identical to Test Case II with the exception that Hole No. 2 was filled with a flush-head aluminum rivet rather than an untorqued, clearance-fit fastener.

The total life test results for the ten center-stringer-reinforced, continuous-skin specimens are presented in Table 2. The most critical initial primary damage location (that is, inside or outside crack) for this type of structure can be determined by comparing the lives for the three cases investigated. Test Case I simulates the present Air Force damage tolerant design requirements contained in MIL-A-83444 (that is, continuing damage flaws, clearance-fit fasteners which are finger tight, etc.). A comparison of the mean lives for this case shows that the mean life for the inside crack location is 35 percent greater than that for the outside crack. The mean lives of Test Case II and single lives of Test Case III for the two initial primary damage locations are approximately equal. Therefore the most critical initial primary

TABLE 2—*Test lives for center-stringer-reinforced, continuous-skin specimens.*

	Case I		Case II		Case III	
	Specimen No.	Life, cycles	Specimen No.	Life, cycles	Specimen No.	Life, cycles
Inside crack	4.8-1-1	29 800	4.8-1-3	27 300	4.8-1-5	26 200
	4.8-1-2	26 100	4.8-1-4	27 700		
	mean life = 28 000		mean life = 27 500			
Outside crack	Specimen No.	Life, cycles	Specimen No.	Life, cycles	Specimen No.	Life, cycles
	4.8-1-7	22 600	4.8-1-9	34 000 ^a	4.8-1-11	26 700 ^a
	4.8-1-8	19 000	4.8-1-10	22 200		
	mean life = 20 800		mean life = 28 100			

^aSkin crack stop-drilled in order to obtain further cracking data in stringer.

damage for center-stringer-reinforced, continuous-skin structure is a crack growing away from the stiffener for Test Case I. There is no dominant critical location for Test Cases II and III.

It should be noted that the crack growth in the skin for Specimen Nos. 4.8-1-9 and 4.8-1-11 was intentionally arrested at a crack length of about 40.6 mm (1.6 in.). This crack arrestment occurred after the application of the number of cycles specified in Table 2. The arrestment was accomplished by drilling a 9.53-mm (0.375-in.)-diameter hole at the crack tip and installing a fully torqued Hi-Lok fastener. The purpose of the crack arrestment was to obtain additional cracking data in the stiffener. However, based upon the crack growth behavior of the test specimens without crack arrestment, it is estimated that total specimen failure would have occurred shortly after the number of cycles applied at the time of crack arrestment if the skin crack had been allowed to grow. Therefore the number of cycles applied at the time of crack arrestment was taken as the total life of the specimen.

Center-Stringer-Reinforced, Split-Skin Specimens

The ten center-stringer reinforced, split-skin specimens tested in this program had the same geometry and dimensions as the specimen presented in Fig. 5 with the following exceptions. The hole diameter was 7.92 mm (0.312 in.) and the specimens had two skins rather than one. The two skins were spliced together longitudinally by the tee stringer, simulating a typical aircraft spanwise splice. The splice and the initial damage conditions for these ten specimens are presented in Fig. 6.

The three different test cases investigated for this type of specimen are the same as those specified in Table 1 with the exception that the flush-head aluminum rivets used previously were replaced with interference-fit, flush-head steel fasteners which were fully torqued. These fasteners are representative of standard aircraft design practice for skin-to-skin splices.

The lives for the ten specimens are presented in Table 3. The lives for the inside crack location for Test Cases I, II, and III are 17, 25, and 12 percent higher than the corresponding lives for the outside crack location, respectively. Therefore the most critical initial primary damage for all cases is a

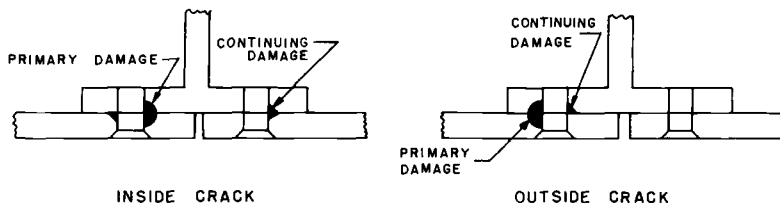


FIG. 6—Initial damage for center-stringer-reinforced, split-skin specimen.

TABLE 3—Test lives for center-stringer-reinforced, split-skin specimens.

	Case I		Case II		Case III	
	Specimen No.	Life, cycles	Specimen No.	Life, cycles	Specimen No.	Life, cycles
Inside crack	4.8-3-13	17 800 ^a	4.8-3-3	24 100	4.8-3-5	25 700
	4.8-3-14	20 100 ^a	4.8-3-4	23 700		
	mean life = 19 000		mean life = 23 900		life = 25 700	
	Specimen No.	Life, cycles	Specimen No.	Life, cycles	Specimen No.	Life, cycles
Outside crack	4.8-3-9	14 500	4.8-3-7	19 100 ^a	4.8-3-11	23 000 ^a
	4.8-3-10	17 900 ^a	4.8-3-8	19 100 ^a		
	mean life = 16 200		mean life = 19 100		life = 23 000	

^aSkin crack stop-drilled in order to obtain further cracking data in stringer.

crack growing away from the stiffener. This result is consistent with that for the center-stringer-reinforced, continuous-skin specimens.

Edge-Stringer-Reinforced, Continuous-Skin Specimens

Eight edge-stringer-reinforced, continuous-skin specimens were tested with the geometric configuration shown in Fig. 7. Each specimen had an overall nominal length of 1130 mm (44.5 in.) and a test section width of 457 mm (18 in.). The skin and angle thicknesses were 4.62 mm (0.182 in.) and 6.35 mm (0.25 in.), respectively. Both structural elements have 7.92-mm (0.312-in.)-diameter fastener holes. The angle stringers simulated spar caps on a wing. A sheet 4.62 mm (0.182 in.) thick and 82.55 mm (3.25 in.) wide was attached to the protruding leg of the angle to simulate a portion of a shear web.

The initial damage conditions are illustrated in Fig. 7. The same three test cases were considered for this type of specimen which were previously described for the center-stringer-reinforced, split-skin specimens. Hence interference-fit, flush-head steel fasteners were used which are representative of standard aircraft design practice for skin-to-spar cap splices.

The test lives for the ten specimens are presented in Table 4. The lives for the outside crack location for Test Cases I, II and III are 16, 17, and 27 per cent higher than the corresponding lives for the inside crack location, respectively. Therefore the most critical initial primary damage for all test cases is a crack growing away from the stiffener. This result is consistent with those for the center-stringer-reinforced, continuous-skin and center-stringer-reinforced, split-skin specimens.

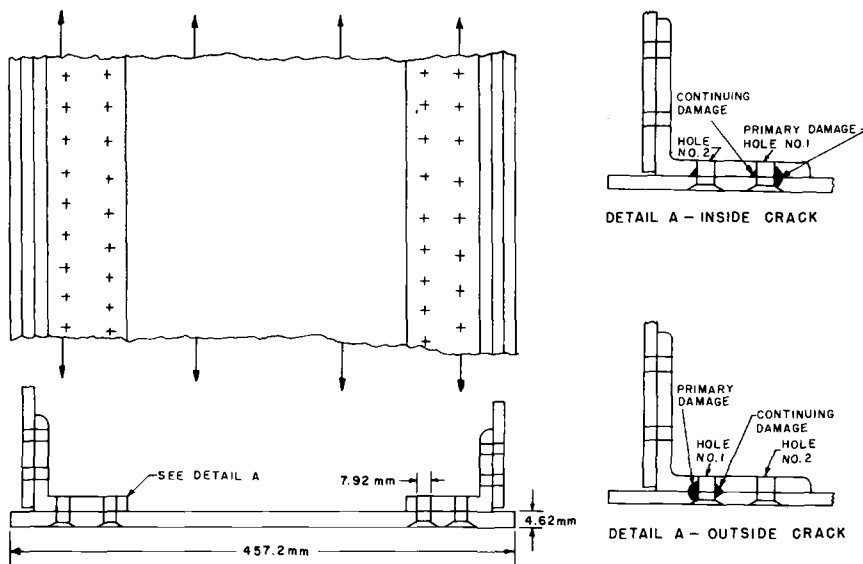


FIG. 7—Edge-stringer-reinforced, continuous-skin specimen.

TABLE 4—Test lives for edge-stringer-reinforced, continuous-skin specimens.

	Case I		Case II		Case III	
	Specimen No.	Life, cycles	Specimen No.	Life, cycles	Specimen No.	Life, cycles
Inside crack	4.9-7	18 300 ^a	4.9-9	18 400 ^a	4.9-11	18 100 ^a
	4.9-8	17 300 ^a				
	mean life = 17 800		life = 18 400		life = 18 100	
Outside crack	4.9-1	19 600	4.9-3	21 500	4.9-5	23 000 ^a
	4.9-2	21 600				
	mean life = 20 600		life = 21 500		life = 23 000	

^aSkin crack stop-drilled in order to obtain further cracking data in stringer.

Assessment of Initial Continuing Damage Location

The Air Force damage tolerance design requirements [2] specify that when the initial primary damage grows into and terminates at an adjacent fastener hole, initial continuing damage must be assumed to exist in the adjacent fastener hole. This initial continuing damage must be assumed to be a

0.13-mm (0.005-in.) quarter-circular corner crack plus the amount of growth which occurs while the primary damage is growing into the adjacent fastener hole. The location of the initial continuing damage is specified as the diametrically opposite side of the adjacent fastener hole at which the primary damage terminated. The specified initial continuing damage is an analysis expedient which is assumed to exist in order to continue the analysis and is based upon a limited amount of test data. This section presents an assessment of the location specified above for the initial continuing damage.

A total of 27 test specimens were used to assess the validity of the initial continuing damage location discussed above. Each specimen contained initial primary damage, but the continuing damage was allowed to initiate naturally during the tests. The structural geometries which were used to determine the most critical initial primary damage locations (for example, center-stringer-reinforced, continuous-skin specimens; center-stringer-reinforced, split-skin specimens; and edge-stringer-reinforced, continuous-skin specimens) were also used in the initial continuing damage assessment. Other structural geometries used for the assessment were 2-bay wing panels [4], single-lap shear joints [5,6], and double lap shear joints [5,6].

The 2-bay wing panel was made up of the center-stringer-reinforced, split-skin specimens and edge-stringer-reinforced, continuous-skin specimens previously presented. The geometry and initial primary damage locations for this specimen are presented in Fig. 8. The tests were conducted for the Test Case II previously discussed.

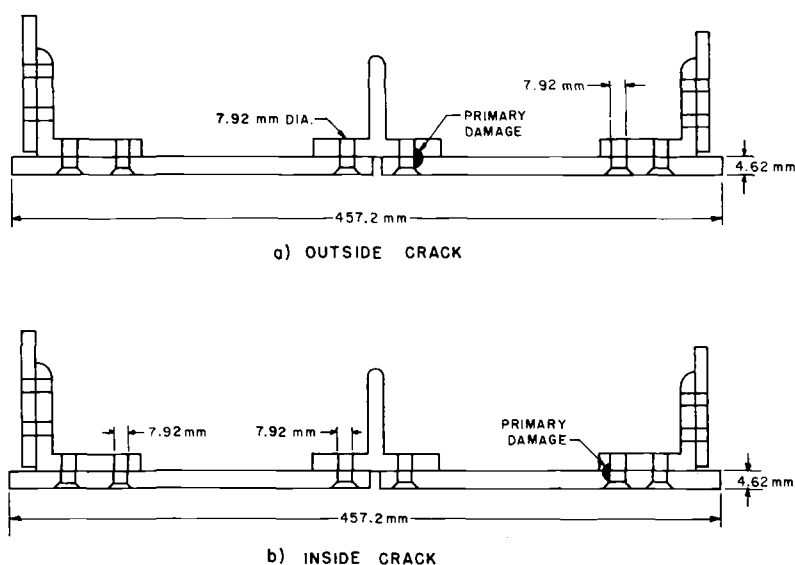


FIG. 8—2-bay wing specimen.

The single-lap shear joint specimen tested is presented in Fig. 9. This specimen is representative of a typical aircraft wing chordwise splice. Three specimens were tested with an overall nominal length of 610 mm (24 in.) and a test section width of 222 mm (8.75 in.). The skin and doubler thickness (Section A-A of Fig. 9) was 4.78 mm (0.188 in.) Both structural elements contained 7.92-mm (0.312-in.)-diameter fastener holes. Test Cases II and III were considered. All fasteners were flush-head steel Hi-Lok fasteners. For Test Case II, all fasteners were installed with clearance fit and without torque. For Test Case III, standard interference fit and standard torque were used in all fastener holes except the one containing the primary damage.

The double-lap shear joint specimen is also representative of an aircraft wing chordwise splice (Fig. 10). Six specimens were tested, four "thick" and two "thin". The skin and doubler thicknesses for the thick specimen were 9.53 mm (0.375 in.) and 4.78 mm (0.188 in.), respectively. The specimen had an overall nominal length of 686 mm (27 in.), test section width of 229 mm (9 in.), and a hole diameter of 9.53 mm (0.375 in.). The thin specimen had a skin thickness of 4.78 mm (0.188 in.), doubler thickness of 2.39 mm (0.094 in.), overall nominal length of 686 mm (27 in.), test section width of 152.4 mm (6 in.), and a hole diameter of 6.35 mm (0.25 in.). The fasteners were protruding-head steel Hi-Lok fasteners. The same test cases (Test Cases II

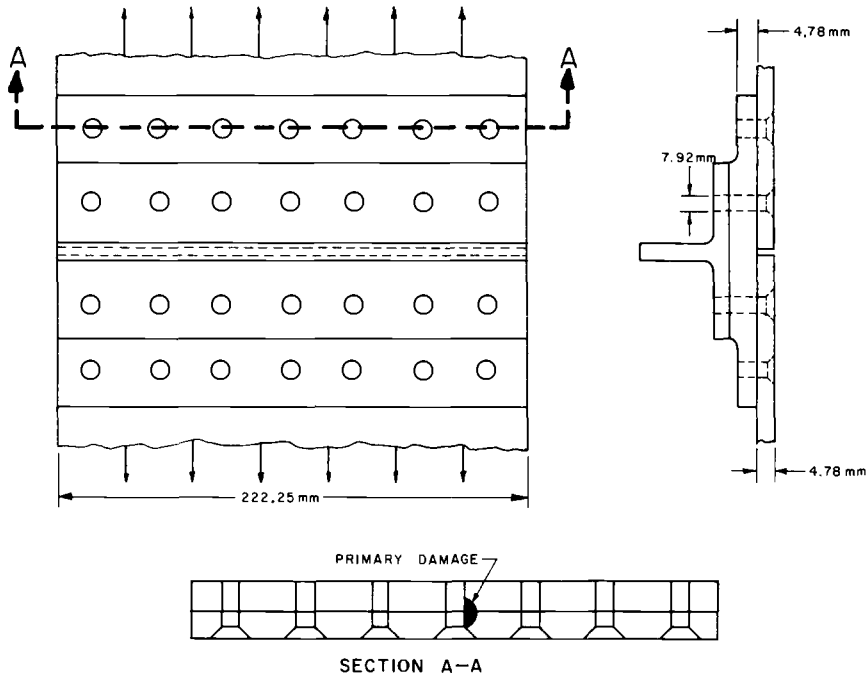


FIG. 9—Single-lap-shear-joint specimen.

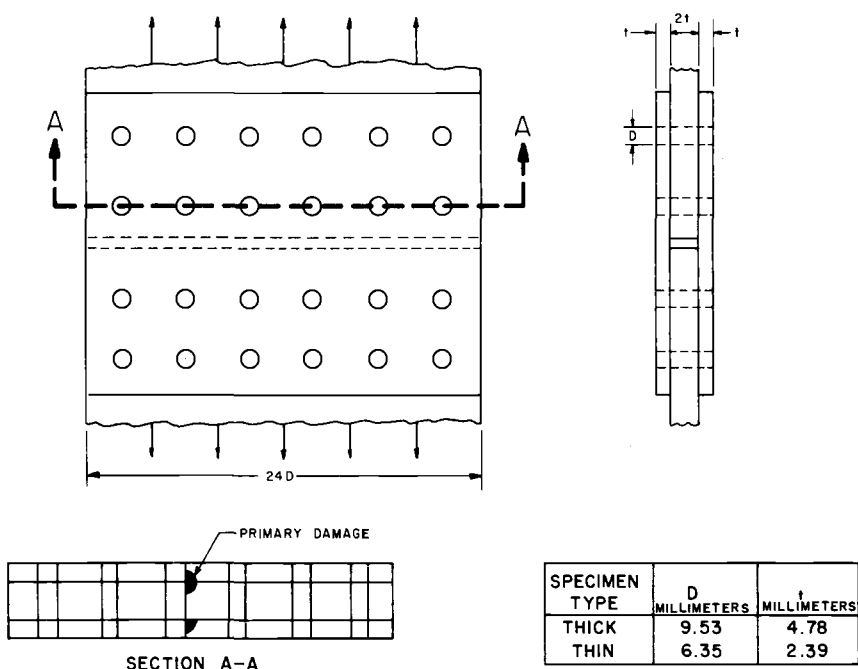


FIG. 10—Double-lap-shear-joint specimen.

and III) were used for the double-lap shear joint specimens that were used for the single-lap shear joint specimens.

A summary of the location where the first continuing damage flaw initiated is presented in Table 5 for all six types of specimens considered. The table indicates that 93 percent of the first cracks initiated in the same fastener hole that contained the primary damage but on the diametrically opposite side. Therefore this location is a more critical continuing damage location than the adjacent fastener hole location specified in the current Air Force damage tolerance design requirements.

Assessment of State-of-the-Art Damage Tolerance Analysis

The Air Force analytical damage tolerance design requirements for aircraft structure were previously discussed. Because of the numerous structural details, initial crack locations, and failure sequences involved in the design of an aircraft, both time and cost must be considered in the selection of a damage tolerance analysis. A crack propagation analysis method which is commonly used and well suited for design is the compounded solution method [7]. This method involves the use of baseline da/dN data and approximate

TABLE 5—Location of first crack reinitiation.

Location	Number of Specimens						Total
	Center-Stringer-Reinforced, Continuous-Skin Specimens	Center-Stringer-Reinforced, Split-Skin Specimens	Edge-Stringer-Reinforced, Continuous-Skin Specimens	3-Bay Wing Panels	Single-Lap Shear Joints	Double-Lap Shear Joints	
Hole Containing Primary Damage	6	6	4	2	2	5	25
Other Holes	0	0	0	0	1	1	2

stress intensity factor expressions for complex configurations obtained by combining known numerical solutions for simpler geometries. Likewise, the reinitiation time of an arrested crack can be predicted from fatigue crack initiation data and stress severity factors estimated by the compounding of known stress concentration factor solutions. Note that this method of predicting crack reinitiation is used in contrast to the initial continuing damage flaw assumptions of MIL-A-83444. An assessment is made of the state-of-the-art damage tolerance analysis capability using the above approaches.

The accuracy of the damage tolerance analysis is assessed by comparing fatigue crack growth predictions made using the analysis with test data for the 39 test specimens previously discussed. The specimens included (1) center-stringer-reinforced, continuous-skin specimens; (2) center-stringer-reinforced, split-skin specimens; (3) edge-stringer-reinforced, continuous-skin specimens; (4) 2-bay wing panels; (5) single-lap shear joints; and (6) double-lap shear joints. All predictions were made prior to testing. The predictions were based upon a number of simplifying assumptions, such as the assumption that the specimen failed when the first member failed. Because of the large amount of details involved and the length limitations of this paper, the specific assumptions and formulas used in the predictions are not discussed here. These details are documented in Refs 4, 5, and 6. Only the analytical/experimental correlations are presented in this paper.

The analytical and experimental lives for each of the 39 specimens are correlated in Tables 6 to 11 and Fig. 11. An analytical/experimental life ratio of one is a perfect correlation (solid line in Fig. 11). Life ratios greater than and less than one indicate unconservative and conservative predictions, respectively. The dashed lines of Fig. 11 represent a factor of two scatter band. The life ratio range (mean \pm standard deviation) for each type of specimen is presented in Fig. 12.

Excellent correlations are obtained for the skin-stringer specimens [4].

TABLE 6—*Analytical/experimental life correlations for center-stringer-reinforced, continuous-skin specimens.*

Specimen No.	Test Life, N_T (cycles)	Predicted Life, N_P (cycles)	Life Ratio, N_P/N_T
4.8-1-1	29 800	26 000	0.87
4.8-1-2	26 100	26 000	1.00
4.8-1-3	27 300	26 200	0.96
4.8-1-4	27 700	26 200	0.95
4.8-1-5	26 200	26 200	1.00
4.8-1-7	22 600	15 700	0.69
4.8-1-8	19 000	15 700	0.83
4.8-1-9	34 000 ^a	24 400	0.72
4.8-1-10	22 200	24 400	1.10
4.8-1-11	26 700 ^a	24 400	0.91
mean life ratio = 0.90; standard deviation = 0.13			

^aSkin crack stop-drilled in order to obtain further cracking data in stringer.

TABLE 7—*Analytical/experimental life correlations for center-stringer-reinforced, split-skin specimens.*

Specimen No.	Test Life, N_T (cycles)	Predicted Life, N_P (cycles)	Life Ratio, N_P/N_T
4.8-3-3	24 100	20 700	0.86
4.8-3-4	23 700	20 700	0.87
4.8-3-5	25 700	20 700	0.81
4.8-3-7	19 100 ^a	18 900	0.99
4.8-3-8	19 100 ^a	18 900	0.99
4.8-3-9	14 500	11 900	0.82
4.8-3-10	17 900 ^a	11 900	0.66
4.8-3-11	23 000 ^a	18 900	0.82
4.8-3-13	17 800 ^a	14 400	0.81
4.8-3-14	20 100 ^a	14 400	0.72
mean life ratio = 0.84; standard deviation = 0.10			

^aSkin crack stop-drilled in order to obtain further cracking data in stringer.

These correlations involved four different types of specimens. All but one of the test lives for the 30 specimens were predicted to within a factor of 1.34. However, the correlations were not as good for the lap joints [8, 9].

The three predictions for the single-lap-shear-joint specimens were unconservative. The stresses used in the analysis of these specimens were less than those which actually occurred during testing because induced transverse bending stresses were neglected in the analysis. Even neglecting bending, the analytical/experimental correlations for the three specimens were approximately within a factor of two.

The six predictions for the double-lap-shear-joint specimens were conser-

TABLE 8—*Analytical/experimental life correlations for edge-stringer-reinforced, continuous-skin specimens.*

Specimen No.	Test Life, N_T (cycles)	Predicted Life, N_P (cycles)	Life Ratio, N_P/N_T
4.9-1	19 600	25 300	1.29
4.9-2	21 600	19 300	0.89
4.9-3	21 500	26 600	1.24
4.9-5	23 000 ^a	30 700	1.33
4.9-7	18 300 ^a	14 100	0.77
4.9-8	17 300 ^a	14 100	0.82
4.9-9	18 400 ^a	23 900	1.30
4.9-11	18 100 ^a	29 700	1.64
mean life ratio = 1.16; standard deviation = 0.30			

^aSkin crack stop-drilled in order to obtain further cracking data in stringer.

TABLE 9—*Analytical/experimental life correlations for 2-bay wing specimens.*

Specimen No.	Test Life, N_T (cycles)	Predicted Life, N_P (cycles)	Life Ratio, N_P/N_T
4.10-2	18 800	18 900	1.01
4.10-4	17 900	23 900	1.34
mean life ratio = 1.18; standard deviation = 0.23			

TABLE 10—*Analytical/experimental life correlations for single-lap-shear-joint specimens.*

Specimen No.	Test Life, N_T (cycles)	Predicted Life, N_P (cycles)	Life Ratio, N_P/N_T
4.7-1	22 500	31 000	1.38
4.7-4	14 900	31 000	2.08
4.7-5	35 200	41 100	1.17
mean life ratio = 1.54; standard deviation = 0.48			

TABLE 11—*Analytical/experimental life correlations for double-lap-shear-joint specimens.*

Specimen No.	Test Life, N_T (cycles)	Predicted Life, N_P (cycles)	Life Ratio, N_P/N_T
4.6A-3	93 400	29 700	0.32
4.6A-4	35 900	29 700	0.83
4.6A-5	165 800	34 600	0.21
4.6A-6	181 100	34 600	0.19
4.6B-2	71 300	38 400	0.54
4.6B-3	217 500	47 300	0.22
mean life ratio = 0.39; standard deviation = 0.25			

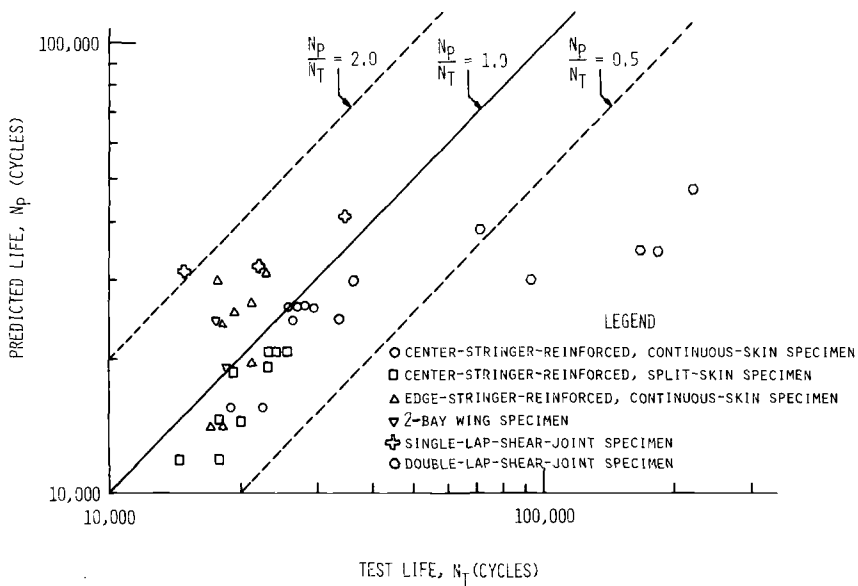


FIG. 11—Summary of accuracy of life predictions.

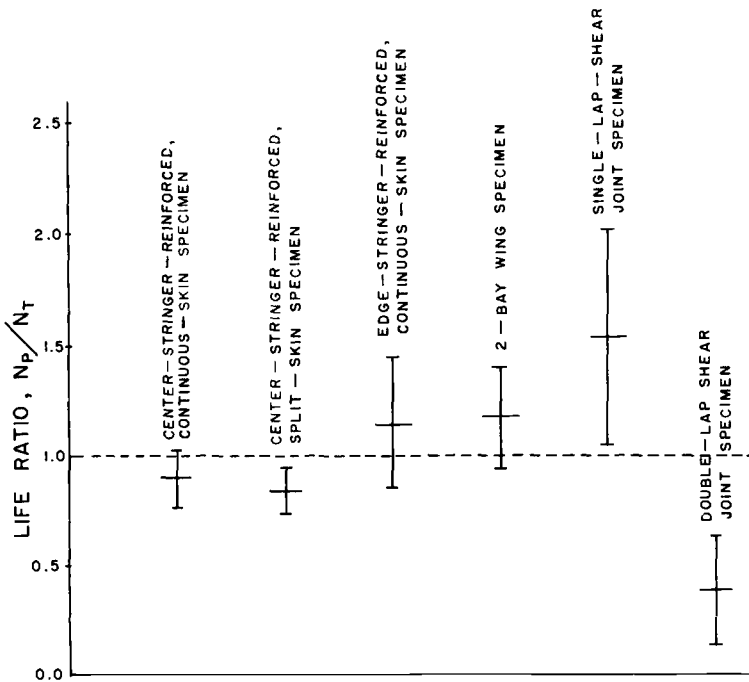


FIG. 12—Accuracy of life predictions for each specimen configuration.

vative. This is owing to the fact that the analysis did not account for the effect of fastener torque and faying surface friction. The actual crack growth rates and crack reinitiation rates were much slower than predicted when the fasteners were fully torqued. Although the load transfer was assumed to be by shear in the fasteners, much of the load was transferred by friction between the doubler and skin at points beyond the plane of cracking. Hence the nominal stress in the plane of cracking was lower than expected. These effects of fastener torque and faying surface friction were neglected in the analysis, which resulted in conservative predictions.

Conclusions

The most critical initial primary damage for skin-stringer structure is a fatigue crack growing away from the influence of the stringer. The most critical location for continuing damage is the same fastener hole containing the primary damage but on the diametrically opposite side. A state-of-the-art damage tolerance analysis based upon the compounded solution method and simplified assumptions is capable of satisfying the Air Force damage tolerance design requirements. However, improvements are needed in the analysis to account for clamp-up and faying surface friction. It should be noted that these conclusions are based upon a single material and constant amplitude stress level. Other materials and flight-simulation spectrum loading should be investigated.

References

- [1] "Aircraft Structural Integrity Program, Airplane Requirements," MIL-STD-1530A, Air Force Aeronautical Systems Division, Dec. 1975.
- [2] "Airplane Damage Tolerance Requirements," MIL-A-83444, Air Force Aeronautical Systems Division, July 1974.
- [3] "Airplane Strength and Rigidity, Ground Tests," MIL-A-8867B, Air Force Aeronautical Systems Division, Aug. 1975.
- [4] Brussat, T. R., Chiu, S. T., Rudd, J. L., and Creager, M., *Engineering Fracture Mechanics*, Vol. 14, No. 4, 1981, pp. 665-683.
- [5] Brussat, T. R., Chiu, S. T., Rudd, J. L. and Creager, M., "Fatigue Crack Growth in Aircraft Joints," *Proceedings for International Conference on Aircraft Fatigue*, May 1979.
- [6] Brussat, T. R., Chiu, S. T., and Creager, M., "Flaw Growth in Complex Structure-Technical Discussion," AFFDL-TR-77-79, Vol. I, Air Force Flight Dynamics Laboratory, Dec. 1977.
- [7] Cartwright, D. J. and Rooke, D. P., *Engineering Fracture Mechanics*, Vol. 6, No. 3, Oct. 1974, pp. 563-571.
- [8] Brussat, T. R., Chiu, S. T., and Creager, M., "Flaw Growth in Complex Structure-Test Data," AFFDL-TR-77-79, Vol. II, Air Force Flight Dynamics Laboratory, Dec. 1977.
- [9] Brussat, T. R. and Chiu, S. T., "Flaw Growth in Complex Structure-Third Interim Report," LR27431, Lockheed-California Company, Dec. 1975.

Maintenance Scheduling Based on Accumulated Crack Growth

REFERENCE: Berens, A. P. and Gallagher, J. P., "Maintenance Scheduling Based on Accumulated Crack Growth," *Design of Fatigue and Fracture Resistant Structures*, ASTM STP 761, P. R. Abelkis and C. M. Hudson, Eds., American Society for Testing and Materials, 1982, pp. 172-187.

ABSTRACT: Currently United States Air Force aircraft structures are inspected and maintained in accordance with a Force Structural Maintenance (FSM) plan. Because actual aircraft mission usage is different for each individual aircraft structure in a force of aircraft, the schedule for individual structural inspections and modifications is adjusted to account for differences in the crack growth accumulation rate. Scheduling adjustments are based on continuous direct or indirect measurements of a potential crack length through individual aircraft tracking.

The purpose of this paper is to describe (1) the logistics/maintenance environment in which the tracking program operates, (2) the crack length projection procedures embedded within the tracking program, and (3) the accuracy requirements for the procedures employed. Accuracy requirements are studied through an analysis of potential errors that are possible in the projections of calendar time to critical crack length. The analysis isolates the effect of potential errors in the estimate of current crack length and compares this component of the total error with those due to the unknown future flying rate and the unknown future stress environment severity. The method permits comparison of prediction precisions for competing tracking systems, and conversely, provides realistic accuracy goals for the development of new systems. Numerical examples are presented based on data from current tracking programs.

KEY WORDS: aircraft structural integrity, aircraft maintenance, damage tolerance, crack growth tracking, error analysis

The United States Air Force preventative maintenance program for airframe structures is based on a Force Structural Maintenance (FSM) plan [1-3].² This plan provides the overriding guidance as to what structural maintenance will be accomplished on all aircraft in a given aircraft force, such as the C-5 force or the F-4 force, in order to ensure that the aircraft are safe to

¹Senior Research Statistician and Group Leader, respectively, Service Life Management, Aerospace Mechanics, University of Dayton Research Institute, Dayton, Ohio, 45469.

²The italic numbers in brackets refer to the list of references appended to this paper.

fly throughout their planned service life. According to Air Force philosophy [4,5] the FSM plan is to contain the when, where, how, and economic impact type information necessary to maintain the structural integrity (safety) for the force of aircraft in the most economic manner possible.

The FSM plan is implemented in practice through the scheduling of individual airplanes for structural maintenance through the Individual Aircraft Tracking (IAT) program [1,3]. The IAT program monitors the historical usage experienced by each aircraft and adjusts the schedule accordingly.

The purpose of this paper is (1) to review the interface that exists between the FSM plan's defined schedule for maintenance and the scheduling of the structural maintenance actions for individual aircraft, (2) to identify some problems that have caused concern about the accuracy of individual aircraft maintenance scheduling, and (3) to suggest several solutions for the identified problems.

Developing the Individual Aircraft's Schedule

The FSM plan defines the schedule for structural maintenance type actions—that is, inspections, modifications, and retirement—through the use of potential crack growth curves. These crack growth curves are derived for specific locations in the structure where crack damage, if allowed to become critical, could impair the safety of the aircraft. One basic feature of the set of FSM plan crack growth curves is that the curves are derived assuming a planned mission usage. Figure 1 shows a typical crack growth curve on which structural maintenance actions are based.

The abscissa, t_{MU} , in Fig. 1 describes the flight hours, or flights accumulated as a result of an aircraft flying according to the planned mission usage. The ordinate is projected crack length, a , that accrues if the airplane flies the

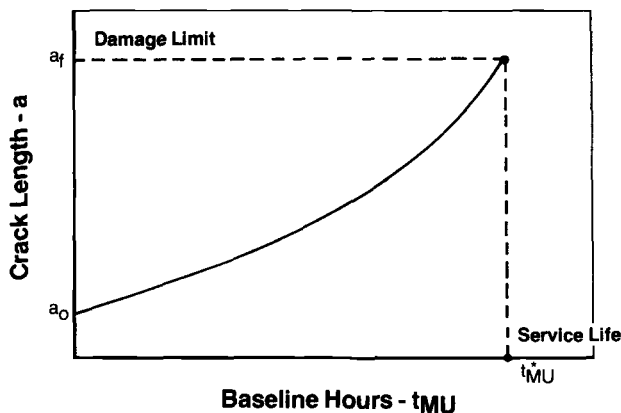


FIG. 1—Typical crack growth curve for specified critical point.

planned pattern of mission usage. The crack grows from the starting crack size and configuration. It is terminated when a critical crack size is reached or an inspection reestablishes the potential crack length at a smaller (predefined) level. Without loss of generality, only the case when the cracks grow monotonically will be considered.

A direct comparison between the crack growths that accrue due to individual aircraft usage is only possible when individual aircraft crack lengths are defined and referenced to the FSM Plan crack length curves for each control point. An example is now outlined to show the manner in which the FSM plan's crack growth curve is used in conjunction with that of the individual aircraft. Figure 2 provides the two curves and shows how the current potential crack length estimate for the individual aircraft relates the individual aircraft's usage, $t_{A/C}$, to that of the FSM planned usage, t_{MU} . The curve in Fig. 2a represents the crack growth through the current quarter of usage for an individual aircraft. The individual aircraft usage, $t_{A/C}$, is measured in the same units—for example, flight hours—that were used to represent the usage for the FSM plan's crack growth curve. Note that the ordinate for the curves in Figs. 2a and 2b are identical with respect to the limits of crack length, and that the shapes of the individual aircraft curve and the FSM plan curve are somewhat similar. These conditions provide the basis for deriving general methods for comparing individual aircraft and for referencing them to some standard.

As illustrated in Fig. 2, the current potential crack length in the individual aircraft defines an equivalent service life used in terms of the FSM plan's defined usage. This level of service life is then used to establish the remaining life

$$t_L = t_{MU}^* - t_{MU} \quad (1)$$

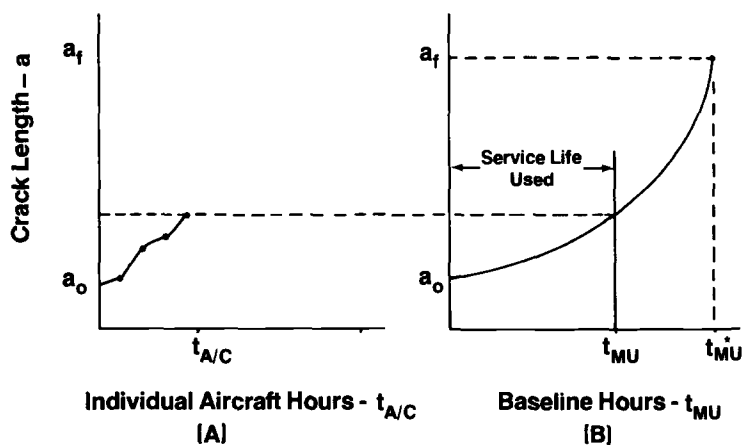


FIG. 2—Relating individual aircraft usage to FSM plan usage for specified critical point.

for the individual aircraft at the specified control point. The projected calendar time, L , associated with the aircraft reaching the crack length limit, a_f , is obtained by dividing the remaining service life by the planned monthly utilization rate, U_p , which is described in terms of the FSM plan's defined usage; that is,

$$L = \frac{t_L}{U_p} \quad (2)$$

The projected calendar date (D_p in years and months) for reaching a critical crack length would then be obtained by adding the calendar time to the current date (D_c):

$$D_p = D_c + L \quad (3)$$

The Air Force utilizes the projected calendar date information in several different ways in order to set the schedule for maintenance actions. For some aircraft forces, the projected dates might be used exactly both for planning in the manner described by Fig. 3 and for accomplishing the structural maintenance according to the defined schedule. For other aircraft forces, the projected dates are used in conjunction with a separately planned depot maintenance schedule. Such aircraft forces are scheduled for reoccurring depot maintenance on a three to four year time period. The separately established depot schedules might result from the need for electronic maintenance or corrosion control. When aircraft are scheduled for periodic depot maintenance

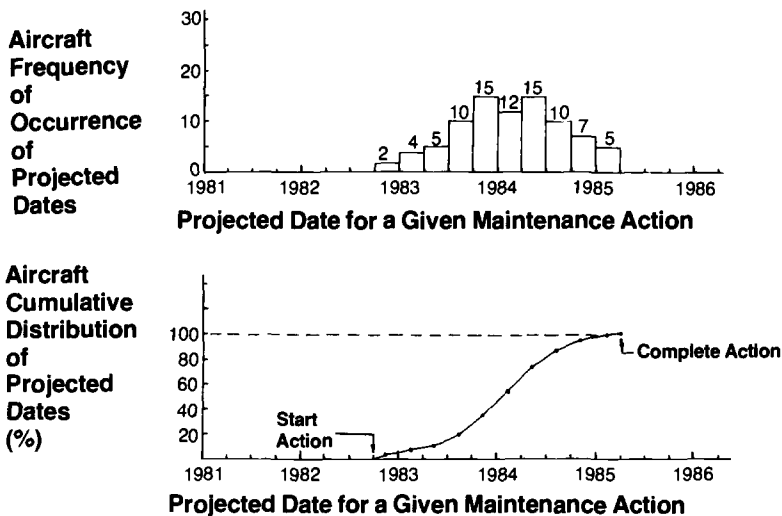


FIG. 3—Distributions of projected calendar dates for given structural maintenance action.

nance, the structural maintenance projected dates then become the indicator which defines the depot period which is the most economically opportune for accomplishing the structural actions for each individual aircraft.

It is the purpose of the remainder of the paper to consider potential errors that can occur in the projected calendar time to a maintenance action (and thus in the projected calendar date) for any given aircraft in a force. We will then interpret the results of the error analysis with respect to economically accomplishing aircraft structural maintenance for safety.

Error Analysis Model

The calculation of months to maintenance action in Eq 2 assumes a one-to-one correlation between planned and actual monthly utilization. In practice, different utilization rates are often realized for well-defined subsets or stratifications of the force; for example, aircraft at a single base. These utilization differences can be monthly flying rates, severity of stress exceedance rates, or both. To account for these differences, the planned utilization rate can be modeled as the ratio of flying rate and severity factor, $U_p = \bar{U}/R$, where \bar{U} represents the monthly flying rate and R is the severity factor which correlates true flight hours with mission usage or baseline hours, $t_{A/C} = Rt_{MU}$. At a tracking update, the projected months to maintenance action and critical crack size are given by

$$L = \frac{(t_{MU}^* - t_{MU})R}{\bar{U}} \quad (4)$$

In a real projection for a particular airplane, t_{MU} will not be known exactly since tracking systems are not capable of determining exact potential crack length at all critical points. Further, future flying rates and severity factors can only be estimated for all the airplanes within the subset; incidentally, these are usually determined from average past experience. Thus the estimate of L from Eq 4 can be considered to be an estimate of the average months to maintenance action for an airplane in the subset. The actual time required for the potential crack to grow to critical will depend on the inaccuracy of its current life estimate, the number of hours actually flown in the forthcoming months, and the aircraft's actual operations that will be encountered.

Assume that t_{MU} , R , and \bar{U} are statistically independent random variables. Then, months to maintenance action, L , is a random variable with average given by Eq 4 and variance estimated by [6]:

$$\sigma_L^2 = \left[\frac{Rt_L}{\bar{U}^2} \right]^2 \sigma_{\bar{U}}^2 + \left[\frac{t_L}{\bar{U}} \right]^2 \sigma_R^2 + \left[\frac{R}{\bar{U}} \right]^2 \sigma_{t_{MU}}^2 \quad (5)$$

$\sigma_{\bar{U}}$ measures the variability (standard deviation) in average flying rates per

month over the projection period; σ_R measures the variability of average usage severity over the projection period; and $\sigma_{t_{MU}}$ measures the variability in the estimate of baseline age due to the inability to exactly calculate the potential crack length at the critical point.

Since averages are used to estimate the months to maintenance action for a particular airplane, the standard deviation, σ_L , provides an estimate of the magnitude of errors (deviations from the average) that could result in the estimate of months to reach critical crack size. Since a complete characterization of possible errors would depend on the distribution of L which is not known, the examples of this paper are expressed in terms of the probable error ($0.67 \sigma_L$). If the distribution of L is normal, the probability of any particular error exceeding the probable error is 0.5.

Usage Parameter Variability

To evaluate the relative importance of the terms of Eq 5, estimates of the variability factors must be obtained. Individual subsections have been prepared to define the procedures, data, and rationale that led to our estimates. The variability estimating subsections have been ordered so that they progress from the factors easiest to estimate to those requiring the most thought and/or assumptions. Estimates of the operational usage variability factors, σ_R and σ_U , were obtained from tracking data collected for A-7 aircraft at one operational base. The reader will note that while the usage variability estimates were obtained from an operational tracking system, the baseline age variability, $\sigma_{t_{MU}}$, estimates are not based on data from any aircraft force.

Variability in Estimate of Flying Rate (\bar{U})

When transforming from flight hours to calendar months, it is customary to assume a constant usage rate per month, \bar{U} , for all aircraft in the stratification of interest. It is recognized that individual aircraft will deviate significantly from \bar{U} for any single month, but it is assumed that over a long period of time, the random deviations will decrease. From the viewpoint of random errors in projected months to critical crack length, the variability due to different usage rates must be modeled, and the model should reflect the fact that there is less variability in average usage over long time periods than there is over short periods. The following model is one approach to this problem.

Let U be the random variable which represents the flight time of a randomly selected aircraft in the subset for a randomly selected month. Let \bar{U} and σ_U denote the mean and standard deviation of the distribution of U . If \bar{U}_m denotes the average flight time of an airplane in the next m -months, then the standard deviation of the average hours per month for this airplane is given by

$$\sigma_{\bar{U}_m} = \frac{\sigma_U}{\sqrt{m}} \quad (6)$$

Data from approximately 75 A-7 airplanes, stationed at a single base over an 18 month period were used to estimate σ_U . Figure 4 displays the cumulative distributions of average flight hours per month for each of three periods. The decreasing trend in the standard deviations of the averages, is in approximate agreement with Eq 6. Figure 5 displays the histogram and a normal distribution fit to the 75 averages over 18 month period. The mean and standard deviation of hours per month calculated from these data are

$$\begin{aligned} \bar{U} &= 25.9 \text{ h/month} \\ \sigma_U &= 22.5 \text{ h/month} \end{aligned}$$

Figure 6 displays the standard deviations of average flight hours per month as a function of time period of projection. This figure is based on the assumption of a flying rate of 25.9 h/month.

Variability in Estimate of Severity Factor (R)

The usage severity factor, R , reflects differences in actual operation from the baseline operation that are expected to be encountered for particular subsets of the force. Individual aircraft within the stratification will experience different severity factors; hence a distribution of R -values can be postulated. The severity factor employed for projections would be the average of this distribution, R . The R -value for a particular stratification of the force

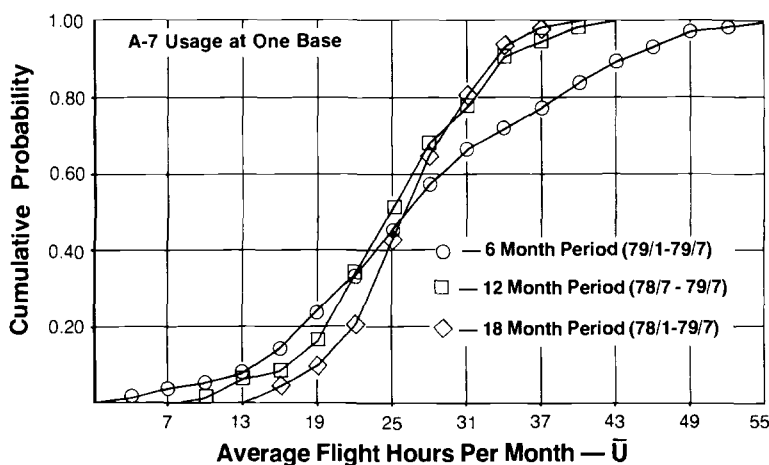


FIG. 4—Cumulative distributions of average flying rates.

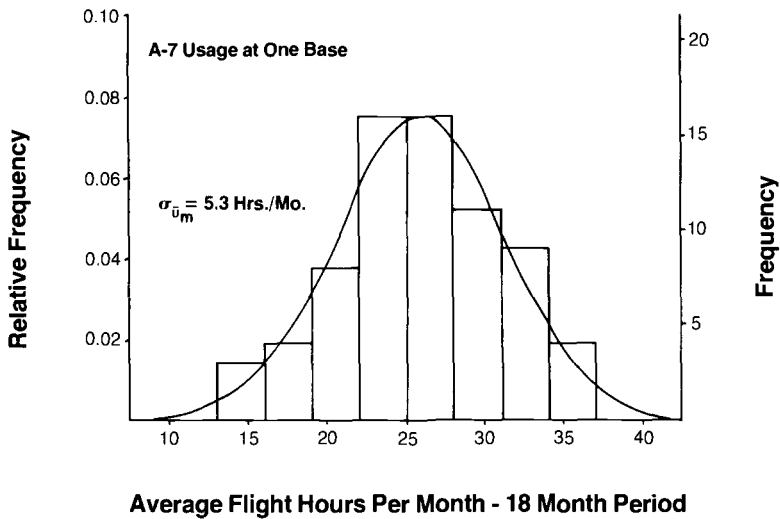


FIG. 5—Probability density function for average flying rates over 18 month period.

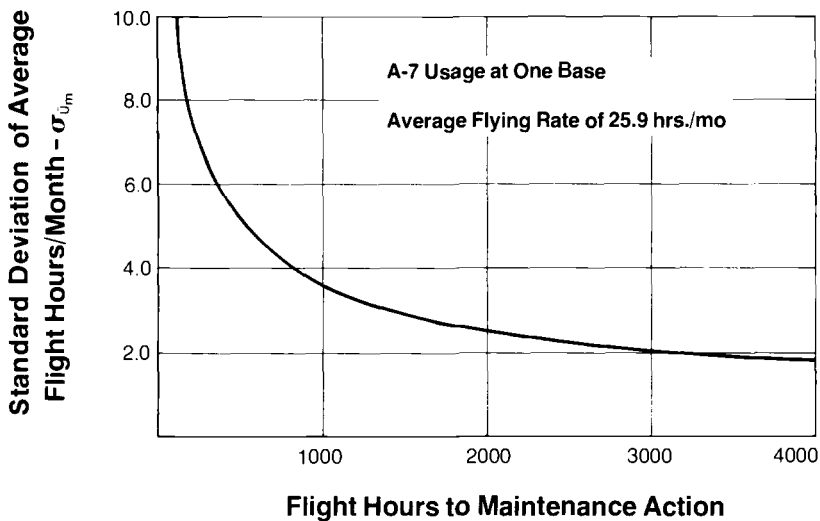


FIG. 6—Standard deviation of average flying rates as a function of length of projection period.

can be estimated from an analysis of detailed stress data for the stratification; however, it is sometimes possible to estimate R from the output of the individual aircraft tracking analysis.

The tracking data output for the A-7 did permit a direct estimation of the severity factor. At each update of the individual aircraft tracking program output, the flight hours and baseline hours were listed for each airplane by

base. The ratio of change in flight hours to change in baseline hours yields the R -value (the random variable) for each airplane over the time period of interest. As in the flying rate description, the period of time over which the changes are calculated influence the variability of the computed R -values about the average. In the example data of this analysis, averages and standard deviations were calculated from the flight and corresponding baseline hours over periods 6, 12, and 18 months and for the total age of each aircraft. Figure 7 presents the observed cumulative distribution functions of the R -values from each of the four time increments. Note the decrease in variability as the averaging period increases. Note also a potential shift in mean severity factor for the last 6 month increment. This shift would indicate that for projection of time to maintenance actions to remain unbiased, it may be necessary to adjust R . In fact for the A-7 force, R -values are updated annually for each base.

The standard deviations of the R -values for the different time periods are shown in Fig. 8. The curve shown in this figure was used to estimate σ_R for the various projection periods where an average flying rate of 25.9 h/month was used to correlate months with flight hours.

Variability in Estimate of Baseline Age

At an update of the individual aircraft tracking analysis, flight data from each airplane are used to estimate the length of a potential crack at each critical point. The type of flight data varies from strain peaks at one or several locations, to counts of normal acceleration peaks at the aircraft cen-

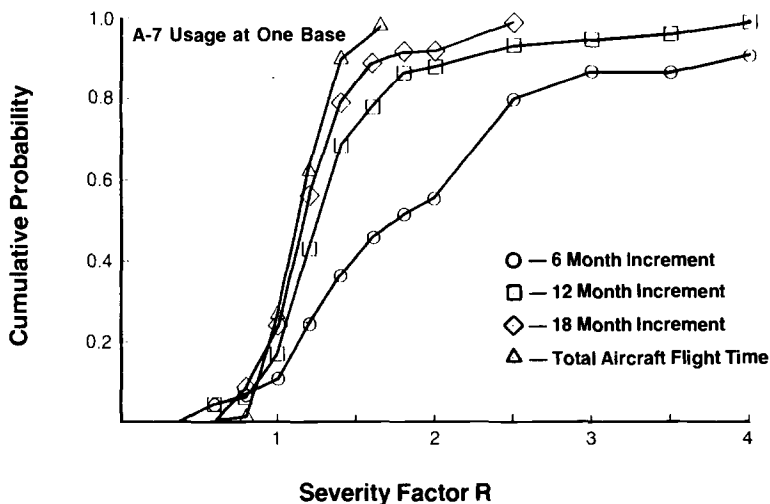


FIG. 7—Cumulative distributions of severity factors.

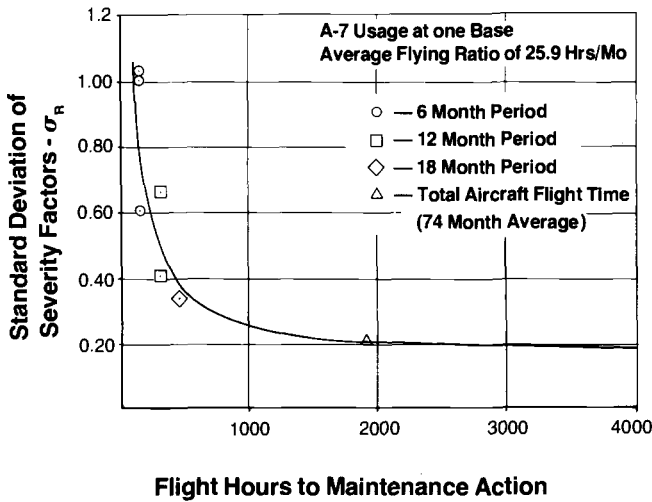


FIG. 8—Standard deviations of severity factors as a function of length of projection period.

ter of gravity, to amount of time in flight conditions or mission segments. The correlation of the flight data with potential crack length at the critical points is not perfect since the estimate will be based on imprecise or incomplete data. To reflect this inaccuracy, a distribution of crack length estimates is postulated and it is assumed that the estimation is unbiased (mean of the estimated crack lengths is the "true" value).

The distribution of errors in estimates of crack length converts to errors in baseline hours as shown in Fig. 9. The standard deviation of baseline hours, t_{MU} , depends on the actual distribution of estimated crack length and the shape of the function which correlates crack length with baseline hours.

For the numerical examples of this paper, it will be assumed that the shape of the correlating function is reasonably approximated by an exponential equation [7]:

$$a = a_o \exp [b t_{MU}] \quad (7)$$

Then [6]:

$$\sigma_{t_{MU}} = \frac{1}{b} \left[\frac{\sigma_a}{a} \right] \quad (8)$$

Since the error in the estimate of potential crack length is expected to increase with time, it will be assumed that the coefficient of variation of crack length estimate, $CV(a) = \sigma_a/a$, will be constant. These assumptions lead to a constant standard deviation in the estimate of baseline hours.

Figure 10 presents probable errors in baseline hour estimates as a function of $CV(a)$ for three separate combinations of critical crack size, a_f , and design

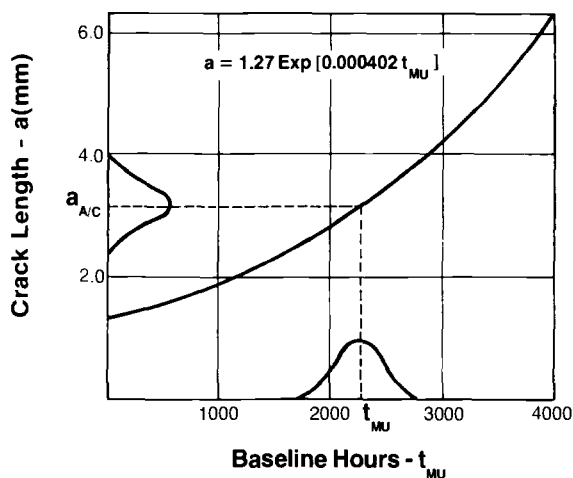


FIG. 9—Transformation of errors in crack length estimates to errors in baseline hours.

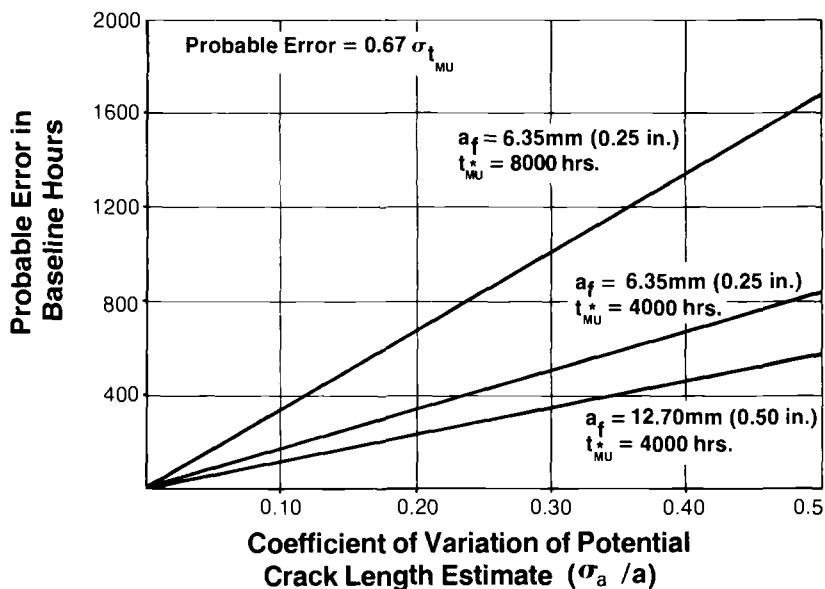


FIG. 10—Probable baseline hour errors as a function of tracking system.

life, t_{MU}^* . All three are based on an initial crack size, a_o , of 1.27 mm (0.05 in.). In the Error Analysis section, baseline $a_f = 6.35$ mm (0.25 in.) with a life of 4000 h is used. The reader is reminded that the example baseline conditions are not related to any specific aircraft force.

During several recent reviews of current tracking systems, it was found

that potential errors in crack length estimates have not been quantified [8, 9]. Tracking systems based on strain recordings in the immediate vicinity of the critical point are generally considered to be "most accurate." However, most existing systems require some form of stress estimation and damage or stress transfer to more remote locations. Further, most existing systems do not use an exact crack growth model to process the stress history data for obtaining the crack length estimation. Rather, they are based on a "statistical" correlation of stress severity with crack length. The tracking programs based on data from pilot logs or aircraft records correlate time in a flight condition with crack growth increments through past determinations of the stress environment for the flight condition and critical point. Although no hard numbers are available, preliminary lower bound estimates of the coefficients of variation for the crack length size of existing or potential tracking systems are presented in Table 1.

A crack growth gage is based on the correlation of observed crack growth in the gage with potential crack growth in the structure, and is currently being studied for implementation. The variability in crack length measurements in the crack growth gages under identical stress environments could be no better than that typically observed in the laboratory. Based on a crack growth variability study of 2024-T3 aluminum specimens at constant load amplitude [10], the coefficients of variation at fixed lives ranged between 0.05 and 0.10. This range represents the near term lower bound for tracking systems based on crack growth gages.

Error Analyses

Equation 5 provides an estimate of the standard deviation of predicted months for a potential crack to reach critical size. This standard deviation measures the random error about the average predicted time and reflects random inaccuracies in the estimate of baseline ages as well as the possibility of errors due to an individual aircraft having a different flying rate or severity factor. It is assumed that no bias is present in the distributions; for if a known bias were present, it would be removed.

The data of the previous section were used in an analysis of the sensitivity

TABLE 1—*Preliminary estimates of minimum tracking system error variabilities.*

Tracking System	Coefficient of Variation of Crack Length Estimate
Cycle-by-cycle analysis with stress history input	0.05
Parametric analysis	0.10 to 0.15
Crack growth gage	0.05 to 0.10

of probable errors (0.67 standard deviations) to the three error sources. The example is based on an average flying rate of 25.9 h/month and a severity factor of 1.15.

The probable error in scheduling an individual aircraft as a function of the projection period is presented in Fig. 11 for coefficients of variation of crack length estimates of 0.0, 0.1, 0.2, and 0.5. Since the objective of individual aircraft tracking is to adjust maintenance schedules to account for differences in usage, the projection periods of prime interest are those less than 5 years. For periods less than 5 years and $CV(a) > 0$, the errors associated with the crack length estimate are noted to be far more important than those due to variations in flying rate or usage severity.

For a coefficient of variation of 0.10, the probable error in the scheduled maintenance date is at least 8 months regardless of the length of the projection. Stated differently, if a time to maintenance action is predicted to be 8 months away, there is approximately a 25 percent chance that the potential critical crack size has already been exceeded. Similarly, if the coefficient of variation of the tracking system is 0.2, the probable error is at least 15 months regardless of the length of the projection period. If the tracking system is perfectly accurate, $CV(a) = 0.0$, projection errors are associated with the uncertainty of future usage and a probable error of about 5 months would result in a 1 year projection.

Since future usage is somewhat controllable, it is of interest to investigate probable errors assuming that flying rates and severity factors are known exactly. Figure 12 displays probable errors for $CV(a) = 0.10$ and 0.20 for combinations of no variation in flying rate and severity factor. This figure demonstrates that the variability of severity factor is a more important contributor

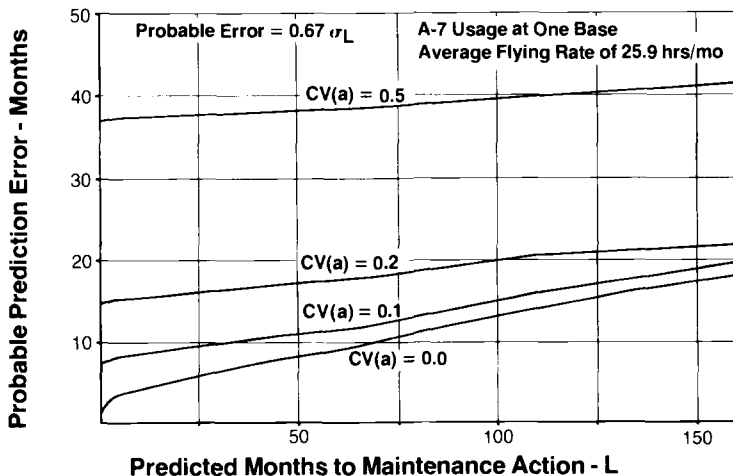


FIG. 11—Probable errors for representative usage and selected tracking system precisions.

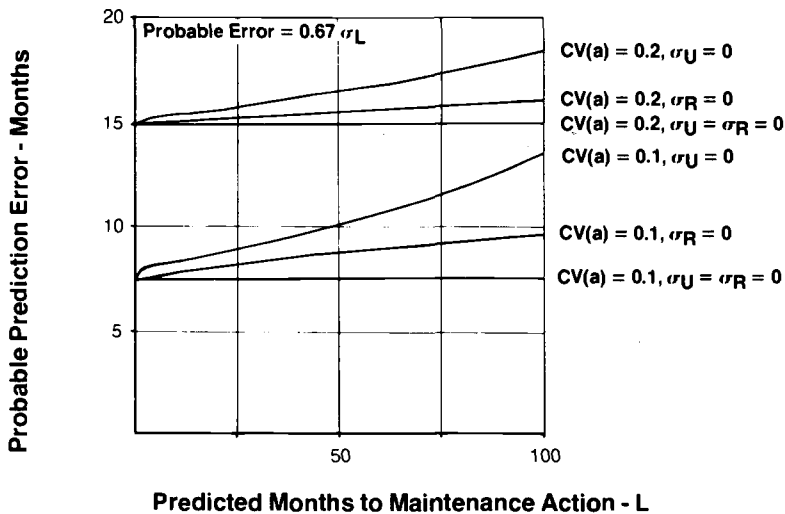


FIG. 12—Probable errors for constant flying rates and usage severities.

to probable error than flying rate. For tracking systems with $CV(a) \geq 0.10$, controlling flying rate to a known constant has no significant effect on the probable error over a two year projection period. Similarly, eliminating severity factor variability has a minor short term effect as compared with variability in the estimate of potential crack length. Note that these comments apply to controlling variability of usage and severity about the predicted values, not to a change in average flying rate or severity.

Figure 13 presents the probable error as a function of coefficient of varia-

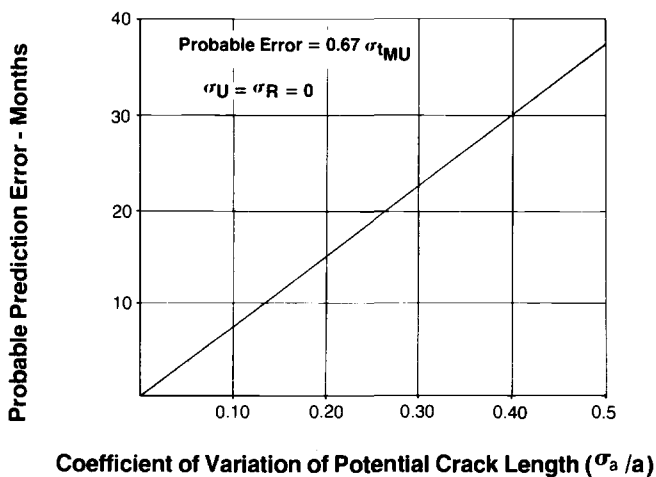


FIG. 13—Probable errors as a function of tracking system precision.

tion of crack length estimate assuming no variation in flying rate and severity factor. These probable errors are independent of the length of the projection period (due to the curve shape assumption), are based on the average flying rate of 25.9 h/month and a severity factor of 1.15, and represent lower-bound probable errors for the tracking system variability.

Discussion

Two basic assumptions inherent in the above analysis are (1) that the FSM plan crack growth curve is given, and (2) that a procedure is available which can estimate changes in crack length exactly for a given crack geometry if the stress history is known exactly. We know that neither assumption is coincident with reality since other crack growth patterns are possible and since crack growth observations are never predicted exactly for variable amplitude load histories. These variabilities should also be considered and described as part of a total analysis of the variability in a tracking system. We have attempted to isolate our attention on the variabilities that directly lead to errors in the projected maintenance schedule of a single aircraft after one accepts the aforementioned defined (usable) assumptions.

The error analysis described in the previous section is, we believe, an essential part of the tracking system data package. The maintenance manager needs information that would permit changes in maintenance schedules to accommodate operational needs. As shown previously, minimizing the variability in usage and in severity of operation minimizes the potential error in the maintenance schedule. Thus the command that operates the aircraft—that is, the using command—should continually be informed about the variability in usage experienced by their aircraft and the impact that this variability has on the maintenance schedule. The using command should also be informed about the variations in schedule that result from “missing data”; for example, unrecorded or obviously inaccurate data.

Figure 3 described the most economically opportune maintenance schedule for a group of aircraft based on tracking data, assuming each of the aircraft crack growth projections was exact. Based on the error analysis, any individual projection could differ by a number of months from the expected. As discussed previously, the error is influenced by variations in aircraft usage, operations, and age (or crack length estimation). Before deciding what level of error is acceptable for a given aircraft and its set of maintenance actions, it is necessary to define the risk associated with not accomplishing the action on time. Realistic accuracy goals for recording usage, operations, or improvements in the crack length predictions in a tracking system can only be set with an understanding of their individual and collective influences on the error in maintenance scheduling and on the risk associated with not accomplishing the required maintenance actions.

Finally, it should be emphasized that the variation in flying rate and usage

severity observed from the A-7 tracking data is typical of that experienced by the attack/fighter/trainer class of aircraft. The error sources identified in Eq 5 will be present in all tracking systems, but their magnitude will depend on both the operational environment and FSM plan for the given aircraft force.

Conclusions

1. Random variation in potential crack length estimates, flying rates, and usage severities can result in significant errors in the estimated date the potential crack will reach critical size. Of the three sources of error, the precision of relating crack length to loading environment is most important.

2. The structural maintenance schedulers should have an estimate of the potential errors, as their magnitude could affect both the safety and economics of the scheduling operation.

3. Quantified error analyses should be performed for the tracking system of each aircraft force. In general, this will require the development of an error analysis model and the processing of existing data to a format required by the model.

References

- [1] "Aircraft Structural Integrity Program, Airplane Requirements," Military Standard MIL STD-1530A, 1975.
- [2] "Airplane Damage Tolerance Requirements," Military Specification MIL-A-83444, 1974.
- [3] Gallagher, J. P., Grandt, A. F., Jr., and Crane, R. L., *Journal of Aircraft*, Vol. 15, July 1978, pp. 435-442.
- [4] Coffin, M. D. and Tiffany, L. C., *Journal of Aircraft*, Vol. 13, Feb. 1976, pp. 93-98.
- [5] Coffin, M. D. and Tiffany, C. F., *Metal Progress*, American Society for Metals, Vol. 109, March 1976, pp. 26-32.
- [6] Deming, W. E., *Statistical Adjustment of Data*, Dover, New York, 1964, p. 39.
- [7] Berens, A. P., "Predicted Crack Repair Costs for Aircraft Structures," ASD-TR-78-39, Aeronautical Systems Division, Wright-Patterson Air Force Base, Ohio, Nov. 1978.
- [8] Clay, L. E. et al., "Force Management Methods Task I Report—Current Methods," AFFDL-TR-78-183, Air Force Flight Dynamics Laboratory, Wright-Patterson Air Force Base, Ohio, Dec. 1978.
- [9] Berens, A. P., "Force Management Methods Task II Report—Volume 1, Summary and Analysis Considerations," AFWAL-TR-80-3120, Air Force Wright Aeronautical Laboratories, Wright-Patterson Air Force Base, Ohio, Aug. 1980.
- [10] Virkler, D. A., Hillberry, B. M., and Goel, P. K., "The Statistical Nature of Fatigue Crack Propagation," AFFDL-TR-78-43, Air Force Flight Dynamics Laboratory, Wright-Patterson Air Force Base, Ohio, April 1978.

Crack Growth

An Investigation of Initial Fatigue Quality

REFERENCE: Wang, D. Y., "An Investigation of Initial Fatigue Quality," *Design of Fatigue and Fracture Resistant Structures*, ASTM STP 761, P. R. Abelkis and C. M. Hudson, Eds., American Society for Testing and Materials, 1982, pp. 191-211.

ABSTRACT: This paper describes an investigation to define statistical fatigue in terms of the initial quality of fastener holes. The objective is to develop and verify equivalent initial flaw size (EIFS) concepts for fatigue durability analysis of typical production quality structures.

A special test procedure was used to obtain a statistically large sample of data under spectrum loading by testing a specimen containing 24 holes. It is possible to obtain a maximum of 96 fatigue data sets in the test of two specimens up to 100 000 flights in a reasonable time. The method involved removing the early cracked holes with a circular saw cutter and continuing the testing of the remaining holes. Marker cycles, which were designed to be an integral part of the spectrum, have served the intended purpose of identifying crack origins and microcrack growth rates using scanning electron microscope (SEM) fractography. The surface mechanical and material defects responsible for the origin of microcracks were examined quite fully.

Through quantitative analysis of a large amount of microcrack growth data and surface macrocrack growth data, many parameters affecting apparent fatigue scatter were resolved. A method was developed to define statistical fatigue quality of fastener holes in terms of EIFS distribution. The EIFS should be a function of initial surface quality and independent of other secondary variables that affect crack growth rate. The procedure involves the use of a master crack growth curve developed from the experimental data of microcrack growth ranging from initial physical flaws as small as 0.005 mm (0.0002 in.). The essential physical defects in 2024-T3 as origins of microfatigue cracking are the tool marks and inclusions.

KEY WORDS: statistical fatigue, fractography, flaws, equivalent initial flaw size, spectrum testing, crack growth, 2024-T3, fastener holes

One of the recent approaches to analyzing fatigue damage accumulation is to consider the entire fatigue process in terms of the growth of cracks from small flaws. This concept forms the basis of the USAF Airplane Damage

¹Senior Engineer, Structural Mechanics, Douglas Aircraft Company, McDonnell Douglas Corporation, Long Beach, Calif. 90846.

Tolerance Requirement, MIL-A-83444, that specifies an initial flaw be assumed to exist in every fastener hole as a result of material and structure manufacturing and processing operations.

The range of a practical equivalent initial flaw size (EIFS) to be used for engineering analysis has been of great interest in the last several years. Several investigations to define the statistical quantity of EIFS distribution have been conducted to assess damage tolerance of military aircraft under the present requirement [1-4].² The procedure to develop EIFS data generally consists of backward extrapolation of the crack growth curve to the zero cycle of loading. The experimental curves have been developed through regressive analysis of fractographic test data. However, it is not an easy task to obtain experimental crack growth curves to zero cycle from a nonpre-cracked specimen. Instead, the experimental curves were correlated to the analytical curves, then the analytical curves were extrapolated to define the EIFS values. It has been shown in the A-7D Quality Assessment Results (/) that EIFS values may be obtainable through regressive analysis of experimental data only. In theory, EIFS should represent a manufactured quality of fastener hole surfaces independent of secondary variables, such as the types of load spectrum, stress level, material, and fastening system. These are the parameters that require further research.

The objective of this research is to assess EIFS distribution for production-quality fastener holes under a relatively long-life transport load spectrum. The statistical distribution has been established by using large quantities of test data developed in this investigation.

Experimental Program

Test Setup

The test was conducted in a 100 000-lb MTS machine under uniaxial cyclic loadings. The loading was controlled by a computer preprogrammed for spectrum loads. Figure 1 shows the overall view of the test setup with specimen. A set of 12.7-mm (1/2-in.) steel plate buckling guides were clamped on both sides of the specimen to prevent buckling during the compressive ground load in the spectrum.

Test Loads Spectrum

The spectrum load tests were chosen for their representation of actual service loading conditions. The sequential loading characteristic also serves as crack growth marker. The basic spectrum for the open hole specimens is a typical, simplified transport spectrum for a lower wing. A detailed descrip-

²The italic numbers in brackets refer to the list of references appended to this paper.

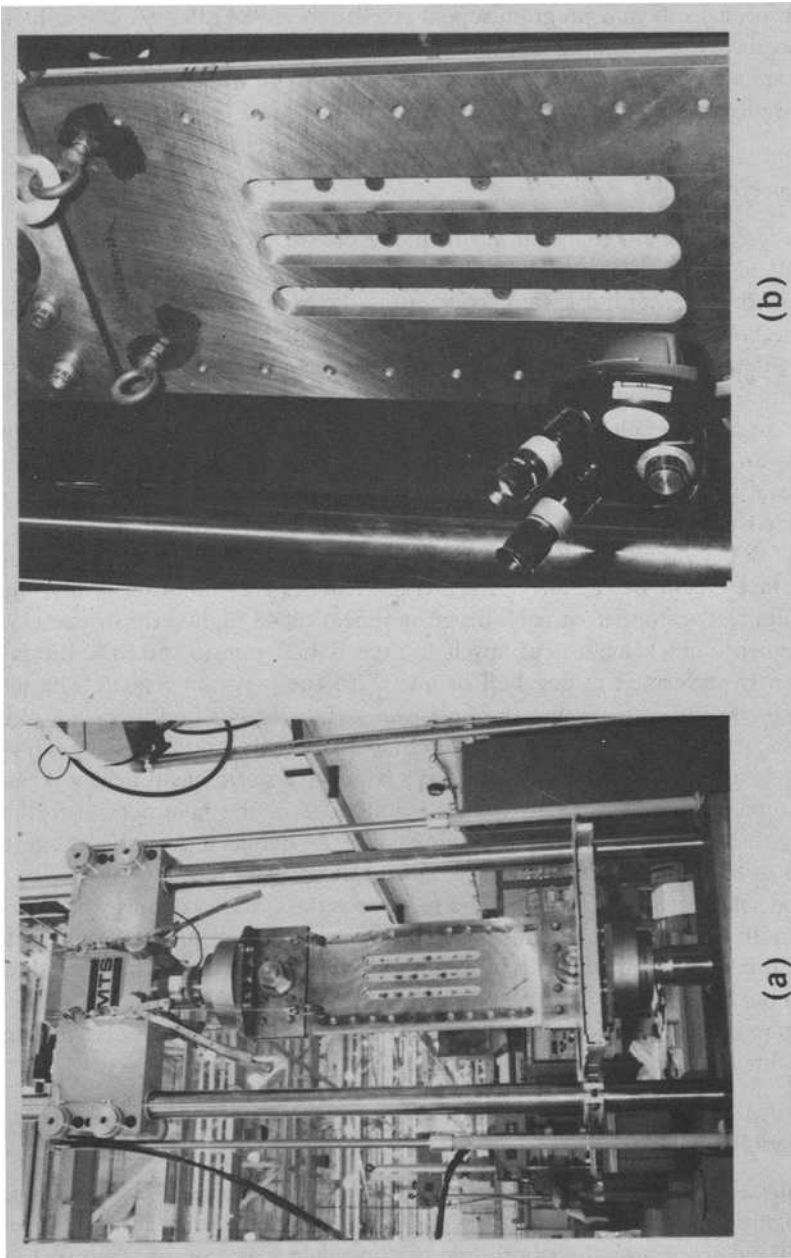


FIG. 1—Spectrum load fatigue test setup for 24 multiple-detail specimens.

tion of the loads spectrum is presented in Ref 5 as BSG Misc 6 Spectrum. Figure 2 presents the loading profile of a flight, and Fig. 3 shows the sequence of high peak loads in a program repeat consisting of 3843 flights. These high peak loads are arranged in such a way that the markers corresponding to the peaks are always identifiable to the accumulated flight number if the fracture surface provides readable markers.

Test Specimens and Procedure

The test specimens reported in this paper consist of three different configurations of 2024-T3 sheet. The descriptions are listed in Table 1. The fabrication of the fastener holes was carried out in the Manufacturing Department, and the holes were representative of production quality.

A 24-detail, multiple-hole, bow-tie specimen detail was selected for the test evaluation. Essentially, the identical 4.8-mm ($\frac{3}{16}$ -in.) open holes are equally spaced in a three column by eight row configuration. This specimen design permits an identical stress level in each detail for a given applied load. This approach is aimed at achieving economy in a time-consuming transport spectrum load test; however, it requires a special test procedure.

Each detail is inspected at a periodic interval depending on the length of the surface crack. Before any surface crack reaches 1.27 mm (0.050 in.), the spectrum test is stopped at each program repeat (3843 flights) for inspection. After surface crack lengths of any hole exceed 1.27 mm (0.050 in.), the inspection is performed at one half or one third the program repeat. The inspection consists of surveying the holes for surface cracks and recording the crack lengths with a pair of X30 stereo binoculars with a built-in scale. During the inspection, the specimen is under a positive static mean load to keep cracks open. Cracking usually occurs at the edge of the hole normal to the loading direction. A complete inspection of the 24 details requires 96 discrete surveys, which include four per hole, two spots on each face.

A special procedure was developed to remove the cracked details when surface lengths exceeded 3.18 mm ($\frac{1}{8}$ -in.). The procedure requires the use of a modified hole saw that makes a 19.05-mm ($\frac{3}{4}$ -in.) cookie cut, symmetrical to the center of the hole. The 19.05-mm ($\frac{3}{4}$ -in.) hole in the specimen is then reamed to remove the rough surface and is fitted with an interference fit plug to prevent cracking during further testing.

Fractography

Application of fractography is an essential part in performing this research. In designing the spectrum loading program, the marker cycles are built in so that fatigue crack growth in both micro- and macroscale can be identified in the fracture surfaces. The marker cycles that register identifiable markings on the fracture surface consist of a sequence of repeatable infrequent high

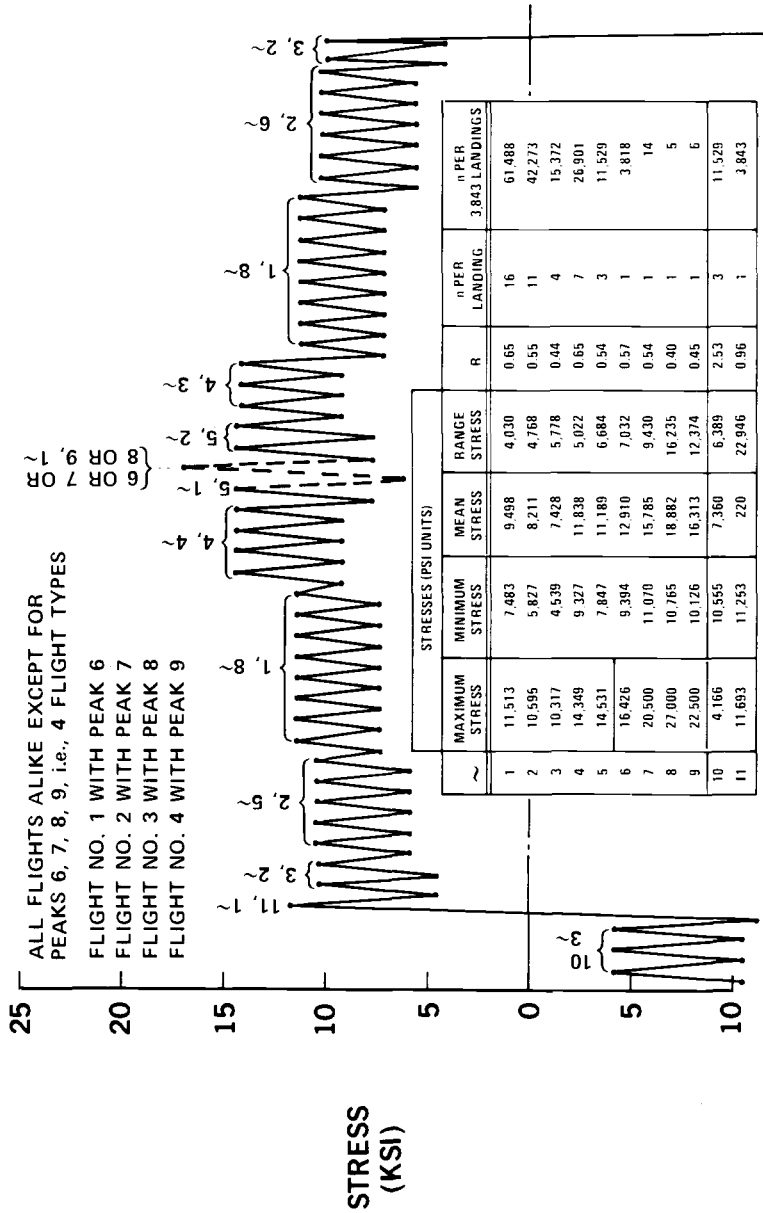


FIG. 2—Flight-by-flight test specimen.

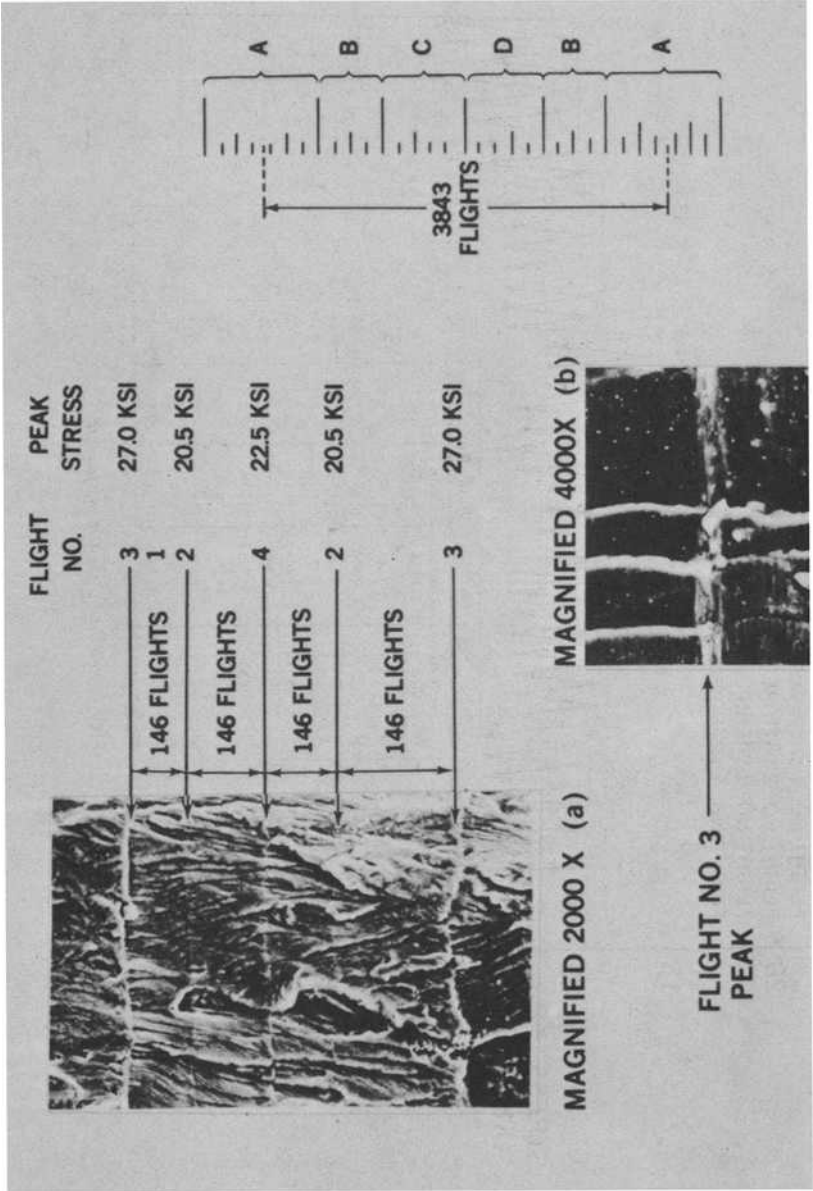


FIG. 3—Sequence of applied marker cycles and an example of corresponding markers on a fracture surface.

TABLE 1—Statistical fatigue life distribution in terms of micro- and macrocrack growth.^a

Specimen Description	No. of Cracks	Total Flights to 0.10 in. Crack		Life in Macrocrack Growth from 0.01 to 0.10 in.		Percent of Life in Microcrack Growth including Crack Initiation $\pm 1\sigma$
		Mean, \bar{X}	Standard Deviation (σ)	Flights	% of Total	
0.071 in. 2024-T3 countersink open holes	48	42 979	5 401	25 000	52 to 67	33 to 48
0.250 in. 2024-T3 countersink open holes	96	48 000	7 998	18 000 to 22 000	32 to 55	45 to 68
0.250 in. 2024-T3 straight open holes	91	77 000	23 760	18 000 to 22 000	18 to 41	59 to 82

^a1 in. = 25.4 mm.

loads. Figure 3 shows a typical sequence of high-peak stress and the corresponding markers on a fracture surface.

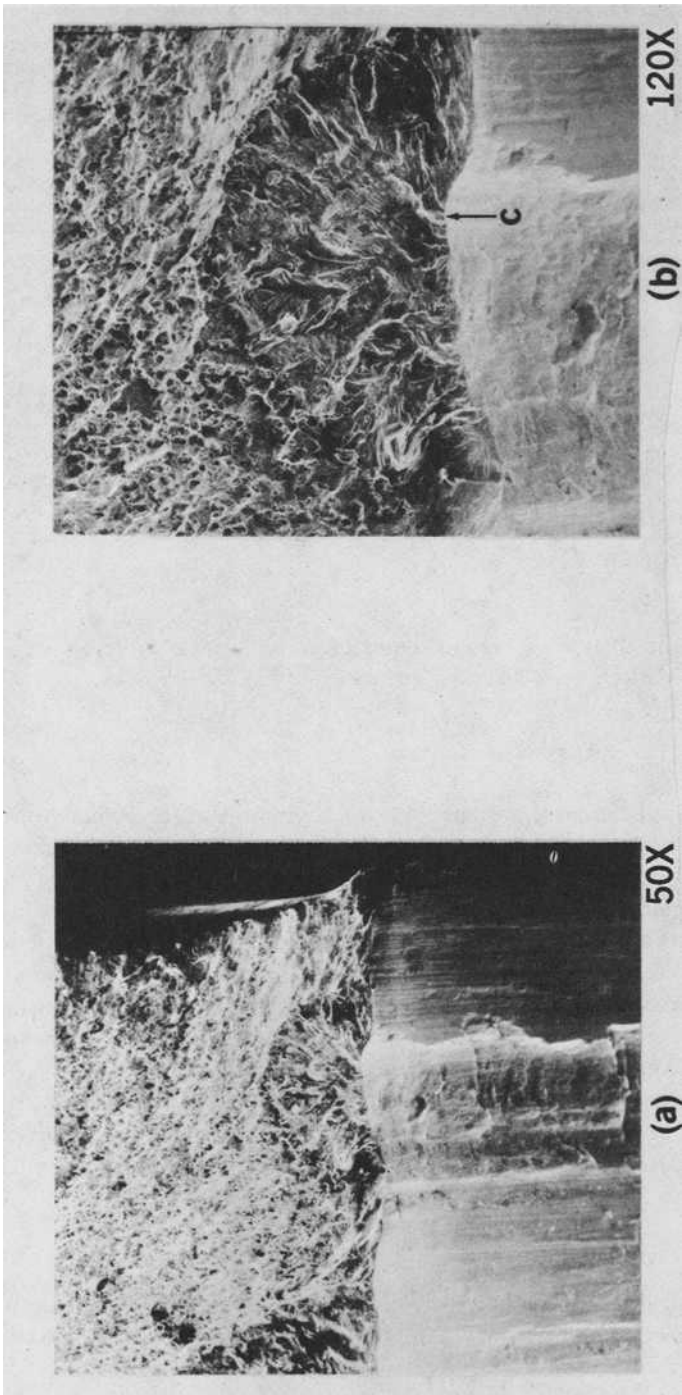
Types of Defects

The identification of various types of common surface defects that result from the manufacture of the hole or from the combination of defect in the material with surface finish imperfections is an important part of defining fatigue quality. Some defects are more sensitive to fatigue cracking than others. Our approach is to examine the defects that associate with cracking. This can be accomplished as a by-product of identifying the origin of the microcracks. The defects are observed along the bore of the hole at the edge of fracture surface and the edge of fracture plane where initiation and slow microcrack growth take place (Fig. 4).

The mechanical defects consist of various forms of tool marks. The material defects in 2024-T3 aluminum alloy are the insoluble constituent particles (inclusions). Descriptions of some typical defects are furnished in Figs. 4 and 5.

Microcrack Growth

The measurements of microcrack growth were accomplished by using a scanning electron microscope (SEM) to record the marker cycles from the



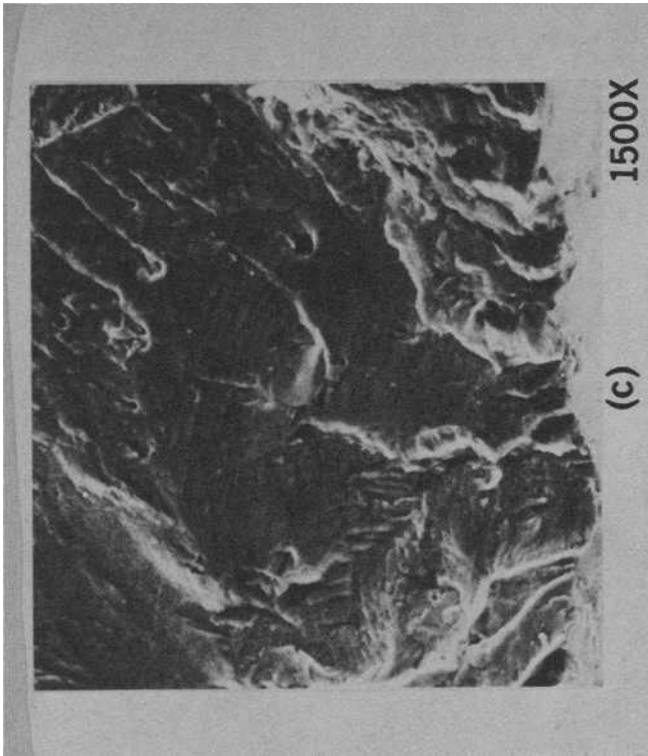
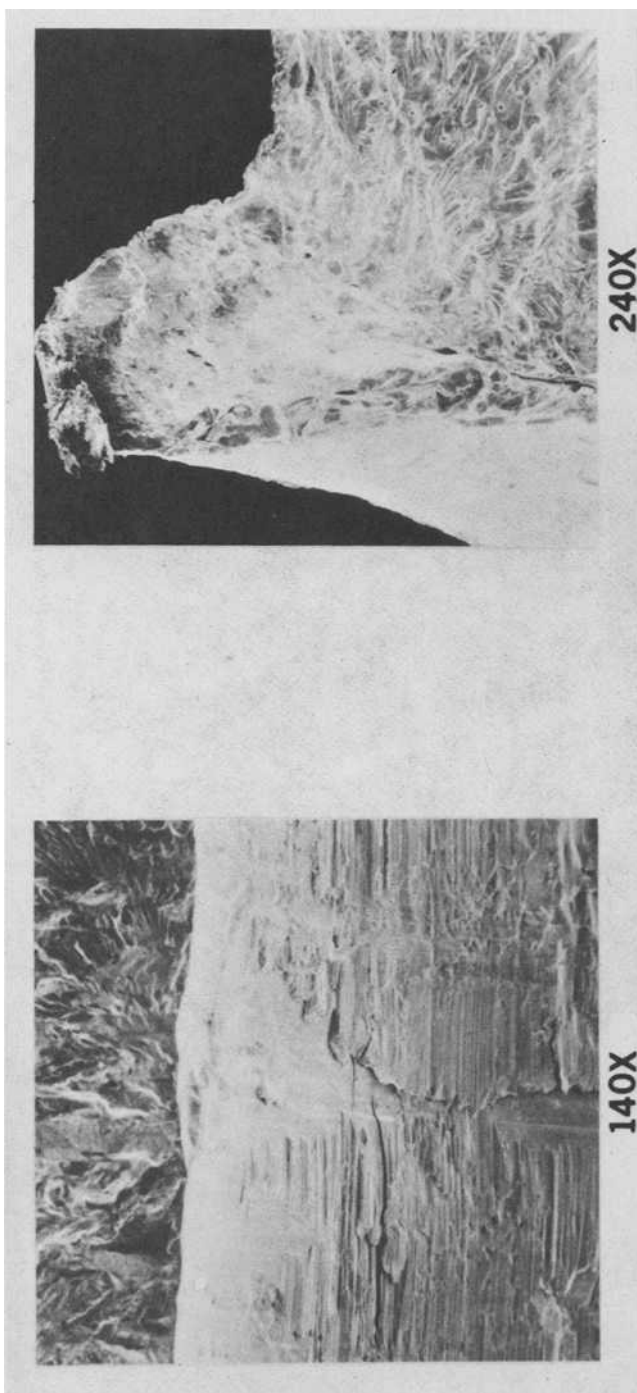


FIG. 4—Three views of differing magnification of an intercepting fatigue crack growth plane and surface of a hole containing $a \approx 0.25\text{-mm}$ ($\approx 0.010\text{-in.}$)-wide tool mark.



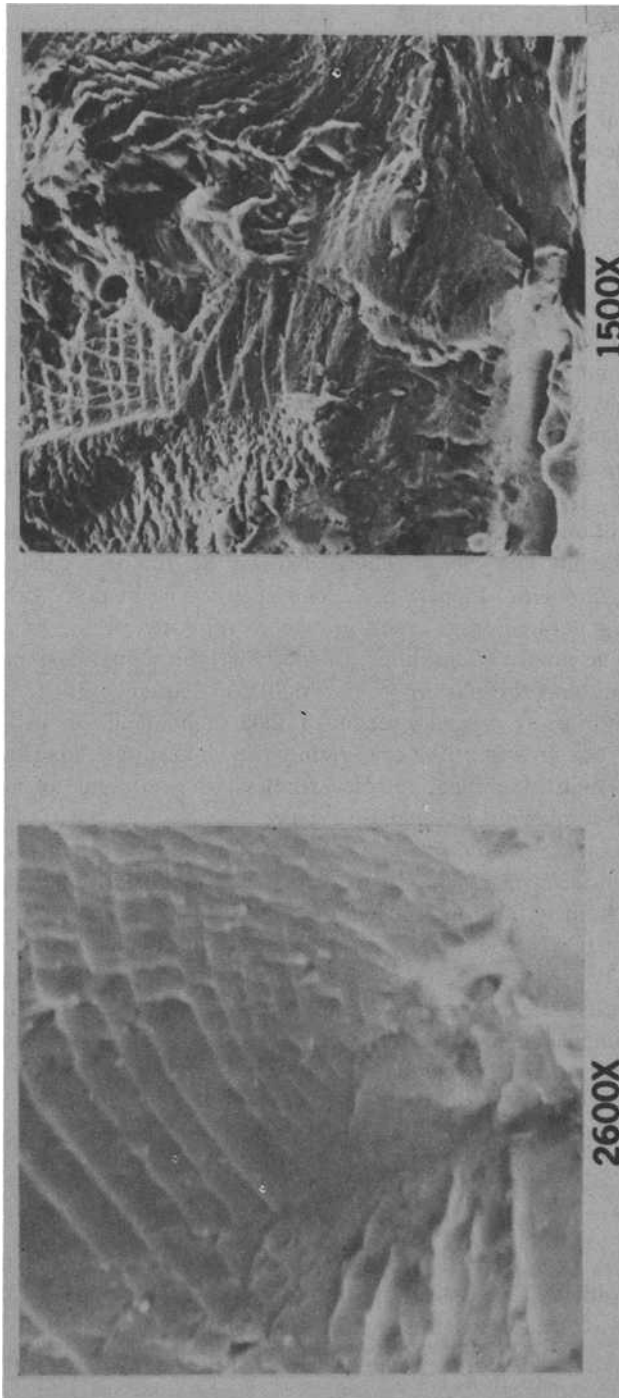


FIG. 5—Views of several microcrack initiation sites.

origin of crack growth. The direction of crack growth on the fracture surface points the way to the origin.

Figures 4a and 4b illustrate a typical surface of microfatigue crack with about 0.25 mm (0.010 in.) depth in a semicircular fan shape. The radiating lines, equivalent to folding lines of a fan, are "fracture traces". They are ridges on the fracture surface reflecting a change in elevations of local planes. These lines converge toward the origin of an expanding crack front. The marker cycles and striations observable under higher magnification are roughly normal to the fracture traces. Figure 4c shows the origin of microcrack growth from an intercepting hole surface. Figure 5 shows some typical microcrack origins. An easily identifiable origin is an inclusion surrounded with rings of markers. In many cases, the inclusions cracked in a very brittle mode, as shown in the flat cleavage plane. However, many of the specimens surveyed do not contain well-defined markers at crack origins. The absence may have been a result of rub out (contact of opposite surfaces) at subsequent cycling.

The rates of microfatigue crack growth were measured by counting the spacing of the marker cycles. These markers do unequivocally represent crack growth under the highest peak load cycles. The distance between the markers was generated from crack growth of repetitive flights of the lower peak loads. The proof can be shown by matching the sequence of alternating marker spacing and the pattern of the high-load sequence in the spectrum, which repeats in every program repeat of 3843 flights (Fig. 3). In the region of very slow crack growth at the origin, only the highest peak loads are resolvable under a high magnification. Nevertheless, the sequence of alternating spacings were similar but on a smaller scale.

The microcrack growth curve may be derived from experimental data. Fig. 6b shows a plot of microcrack growth versus the number of flights for a crack less than 0.04mm (0.0015 in.) in length. Figure 6a shows the corresponding fractograph from which the marker cycle data were taken. In this case, it was quite easy to construct the growth curve by assuming that the surface of the bore, as the reference for the crack length, equaled zero, and that the interior edge of the inclusion at the first marker was the initial data point. As the crack grows away from the origin, the rate appears to increase exponentially. The markers are spaced further apart and become more difficult to locate than where they are situated densely together.

Macrocrack Growth

Separating micro- from macrocrack growth is an arbitrary decision. For convenience, any surface crack length readily measurable with a X30-binocular is defined as a macrocrack, roughly 0.25 mm (0.010 in.) and up. Figure 7 shows an example of a composite plot of micro- and macrocrack growth. Sur-

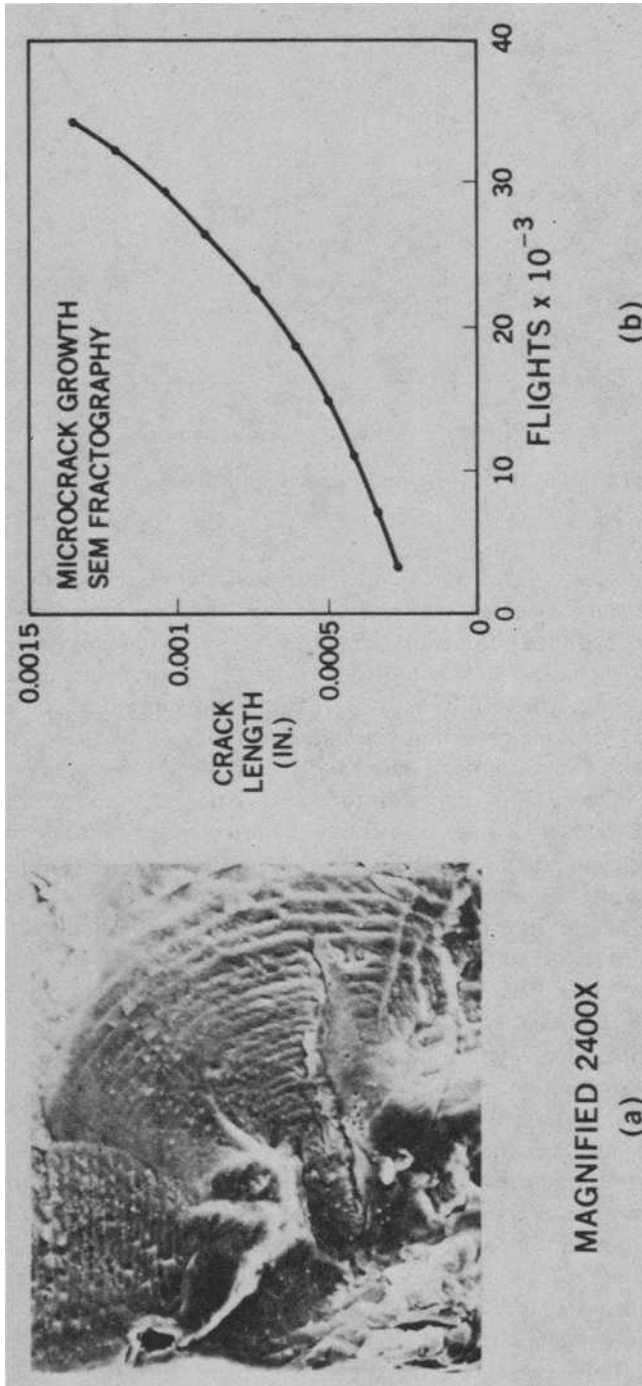


FIG. 6—An example of microcrack growth curve derived from measuring marker spacings in the SEM fractograph.

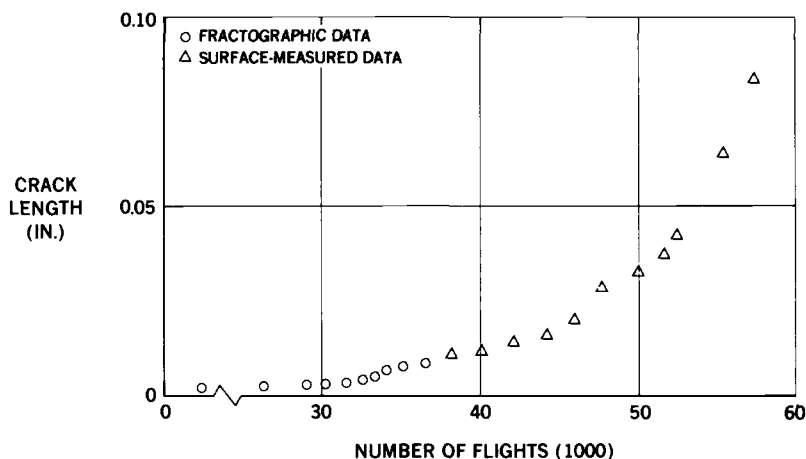


FIG. 7—Results of combined micro- and macro-corner crack growth data for a countersink hole specimen.

face measurements of the microcrack growth curve and the macrocrack growth curve show excellent correlation. In this case, the initial crack starts from the corner of the countersink side and is therefore readily observable on a countersink surface. The maximum crack length is approximately equal to a surface crack length of 0.25 mm (0.01 in.). The continuity of these two crack growth curves suggests that (1) marker cycle counting provided an accurate account of crack growth rate, and (2) relatively few flights were responsible for microcrack initiation in this particular case.

Macrocrack growth results were obtained by making surface measurements of crack lengths during the inspections and by counting the markers with fractography. Quantitative data were recorded from surface measurements of each detail in every specimen, but only a few selected details were subjected to marker counting because it is so time consuming.

The surface crack length rarely coincides with the maximum crack length in the interior. The relationship is dependent on the shape of the crack front, which is, in turn, dependent on the locations of microcracks and the number of microcracks which develop into a dominant macrocrack front.

Figure 8 shows a typical macrocrack progression pattern that was constructed by using the surface crack length data and regressive counting of the markers on the fracture surface along the path of the maximum crack length. The profile of the progressive crack fronts was constructed by connecting the front and back surfaces (both faces) of the crack lengths through appropriate marker locations at the particular flight number. The spacing of the profile lines does not represent crack growth rate, because it was not taken at a fixed interval of flight. However, the marker spacings do reflect crack growth under repeated sequences of spectrum loads (Fig. 3).

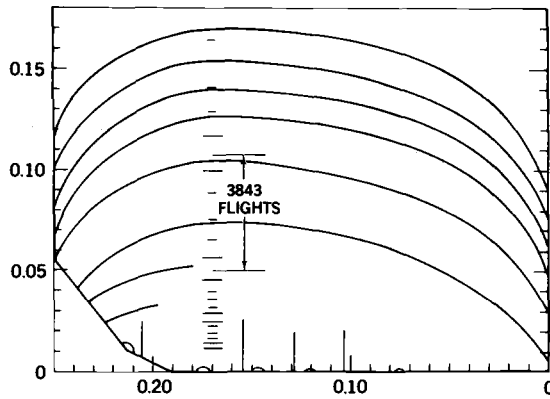


FIG. 8—Plot of a typical interior macrocrack progression pattern.

Data Reduction

Classification of Crack Shape

There appears to be considerable scatter in the rate of crack growth in the surface-measured data. The different crack shapes are the main cause of apparent scatter rather than actual scatter in macrocrack growth rate. The relationship between the maximum crack length (usually not on the surface) and surface crack length is highly dependent on the crack shape, as discussed in the section on macrocrack growth.

In the macrocrack range, interior cracks grow faster than surface corner cracks because of a higher stress intensity factor. For a given surface crack length, the surface rate is proportional to the extent it is trailing the maximum crack length because of the difference in actual maximum crack length. To use the surface crack growth data for analysis, it is necessary to identify the types of crack shapes.

Among all the fracture surfaces of the specimens surveyed, the cracking patterns (shapes) from fastener holes were of two general types: the corner crack and the interior crack. The corner crack emanates from one corner at either the drill entry or exit sides of the hole. The interior crack originates from the interior microcracks, as shown in Fig. 8. It is apparent that the maximum crack length of an interior crack is greater than of a corner crack, for any given surface crack length, until a near straight crack front is achieved. Figure 9 shows a comparison of typical experimental surface crack growth curves for interior and corner crack types.

Distribution of Normalized Fatigue Data

The development of a particular macrocrack type depends on the location of the dominant microcrack and on the number of microcracks. The fatigue

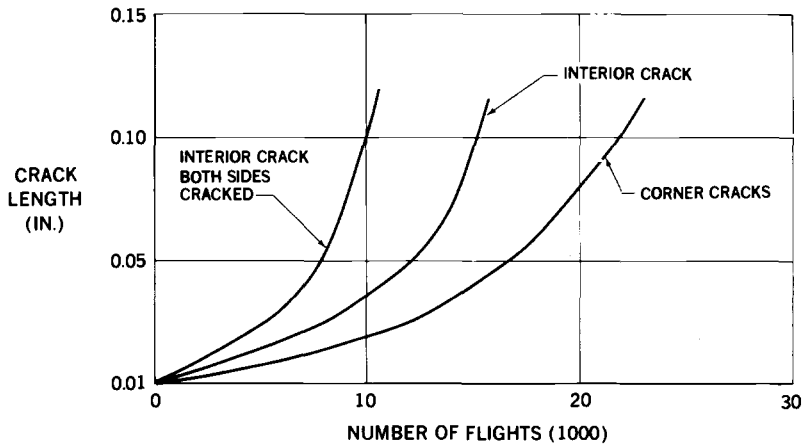


FIG. 9—Comparison of surface-measured crack growth curves of various typical crack profiles for 6.35-mm (0.250-in.) 2024-T3.

life, or the number of flights to propagate the crack to an early stage of macrocrack, is a function of the initial defect size. It is therefore subject to statistical variation, as seen in the fatigue data. In each hole, there are essentially two opposite sites of macrocrack growth at the edge of the hole subject to maximum principal stress. The development of a macrocrack on one site has been shown to influence the crack growth on the other side. Figure 9 shows a typical example of an increasing growth rate of one crack caused by an opposite side crack. Fortunately, most of the fatigue life is consumed in the growth of a microcrack [<0.25 mm (<0.01 in.)], which is quite small, and does not seem to influence cracking on the other side.

To compensate for the effect of opposite side cracks, it is necessary to convert the affected data to values for one-sided cracked only. There are two types of data that require adjustment: (1) when both side cracks are approximately of equal length, and (2) when the side with a short crack is significantly shorter than the side with the long crack.

The hole that is cracked on both sides acts as a center crack. The presence of a longer crack on the opposite side also imposes a higher stress intensity factor on the short crack. A procedure was devised to transform the data that were affected by opposite side cracks to an equivalent life for one-side-cracked only. This is done in two steps: (1) determining the shape of the macrocrack, and (2) adding more flights to the data, which is the difference in the life between one- and both-sides cracked. For example, the difference is about 6000 flights for an interior crack at 2.54 mm (0.10 in.) (Fig. 9).

For those crack details that are less than 2.54 mm (0.10 in.) at the time of removal, the fatigue life at a 2.54-mm (0.10-in.) surface is a projected life for one-side-cracked only. The procedure for projecting the life of 2.54 mm (0.10

in.) consists of (1) determining the appropriate shape of the crack, and (2) adding the macrocrack growth lives from 0.25 to 2.54 mm (0.01 to 0.10 in.) of the appropriate crack shape to the life at 2.54 mm (0.01 in.). Figure 10 shows the statistical fatigue life distribution, in the form of a histogram, for 6.35-mm (0.250-in.)-thick 2024-T3 material with countersink holes.

Equivalent Initial Flaw Size

Master Curve

The purpose of the master curve is to define a full-range crack growth relationship between crack lengths and the number of flights. This curve will provide the reference between the data of a crack length versus fatigue life to an equivalent initial flaw size. Figure 11 exhibits a composite master curve derived from the experimental results for the straight and countersink open holes in 6.35-mm (0.250-in.) 2024-T3. The curve consists of two parts: a microcrack ranging from the smallest practical length 0.25 mm (0.01 in.), and a macro-surface corner crack starting from 0.25 mm (0.01 in.) to more than 2.54 mm (0.10 in.). The scale is expressed in reverse order starting at Flight Zero for a 2.54-mm (0.10-in.) crack length.

Crack growth rate is dependent on crack length, crack shape, and load spectrum. For a given crack shape under a particular load spectrum, the crack growth curve should be identical at any of the 24 details in a specimen. In the microrange, the crack growth curve is influenced by the geometrical factors of a hole. The countersink increases the local stress concentration; therefore the crack growth rate is faster in a countersink hole than in a straight hole. In the macrocrack growth, the difference in rates among hole

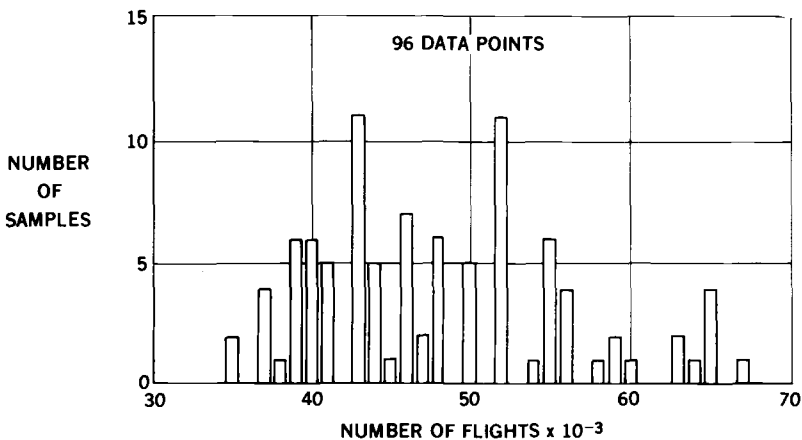


FIG. 10—Fatigue life distribution at 2.54-mm (0.10-in.) surface crack for open-reamed countersink holes.

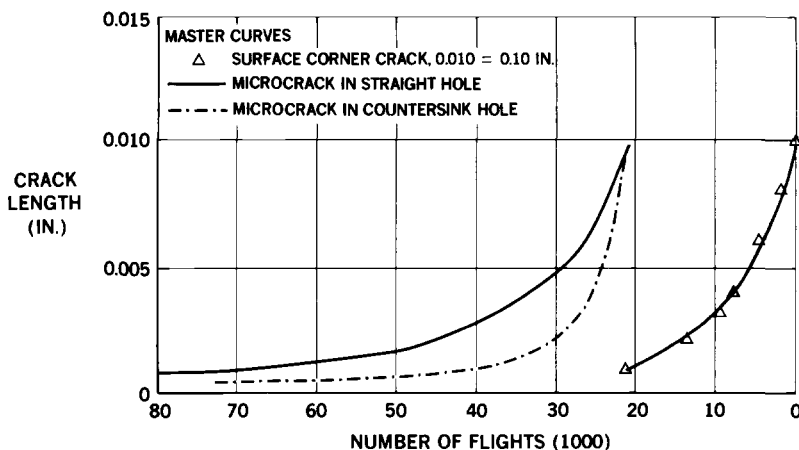


FIG. 11—Relation between number of flights to reach a 2.54-mm (0.10-in.) surface corner crack and initial crack length in straight and countersink holes of 6.35-mm (0.250-in.) 2024-T3.

configurations is not the same as in microcrack growth. In 6.35-mm (0.250-in.)-thick specimens, the rate is essentially the same for a straight or countersink hole. Because of these characteristic differences, it is necessary to establish the particular “master” crack growth curve for a given material thickness and hole configuration combination.

Distribution of EIFS

The fatigue process of a fastener hole consists of (1) the initiation of one or more microcracks, (2) growth of extremely small microcracks to macrocracks, and (3) growth of the dominant macrocrack to failure. As shown in the analysis of experimental results, the major part of the total fatigue life is consumed in the growth of microcracks. The microcrack growth, up to 0.25 mm (0.01 in.), may take 45 to 89 percent of the total life in 6.35-mm (0.250-in.)-thick aluminum with open holes (see Table 1). The microcrack growth period is inversely proportional to the initial flaw size and growth rate. A large initial flaw will result in a smaller percent of the total life for microcrack growth. The growth of a macrocrack from 0.25 to 2.54 mm (0.01 to 0.10 in.) consists of a fixed number of flights, depending on the shape (type) of the crack. The number of flights (cycles) it takes to initiate a microcrack is shown to be quite small in most cases, depending on the severity of the physical defects that become the origin of microcracks. The normalized fatigue-life data at a 2.54-mm (0.10-in.) surface crack, as shown in Fig. 10 and listed in Table 1, includes all three phases.

The concept of equivalent initial flaw size (EIFS) may be applied to defining the fatigue property of a fastener hole. For a given spectrum loading, the

fatigue life is inversely proportional to EIFS and consists of the growth of micro- and macrocracks. The master crack growth curve provides the relationship for transforming the normalized fatigue data to an expression in terms of EIFS. EIFS is the equivalent crack length at zero number of flights. This procedure involves two assumptions: (1) the period for crack initiation is treated as equivalent to additional cycles to propagate a smaller original microcrack than one that does not involve crack initiation, and (2) EIFS is in the form of a singular microcrack that develops into one corner macrocrack, since that was the basis of the master curve derived from experimental results. In reality, many samples involve multiple microcrack and interior macrocrack shapes that result in a faster crack growth than the corner crack. In these cases, the assigned EIFS is a larger value than the physical size of the defect, as a compensation for slower crack growth of the singular corner crack.

Figure 12 shows the statistical distribution of EIFS for the countersink hole specimens in the form of a histogram. Figure 13 shows the comparison of the statistical cumulative probability plots of EIFS for straight and countersink holes, respectively. It should be noted that the mean EIFS value, \bar{x} , of the two groups is quite close, but the standard deviation is twice as great for the straight holes than for the countersink holes. This probably reflects a greater exposure area in the straight hole than in the countersink hole subjected to microcrack initiation.

Statistical Fatigue Life Distribution

The statistical scatter in fatigue life can be analyzed in terms of the EIFS distribution, microcrack growth, and macrocrack growth. As listed in Table

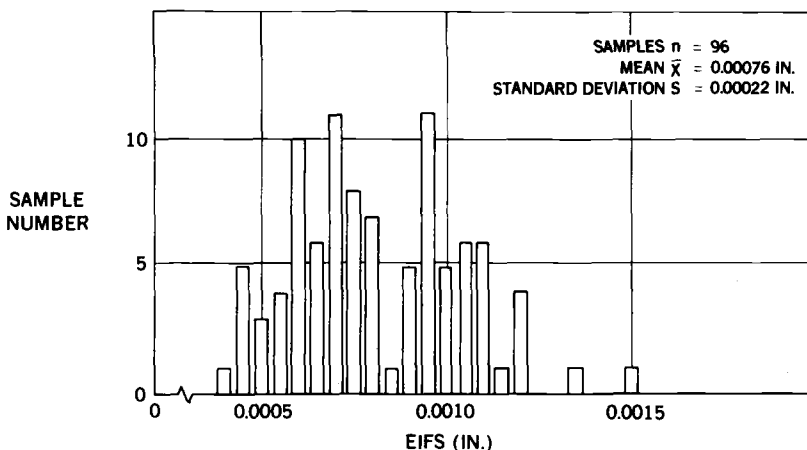


FIG. 12.—Statistical distribution of equivalent initial flow size (EIFS) for 6.35-mm (0.250-in.) 2024-T3 with 4.76-mm ($3/16$)-inch open countersink reamed holes.

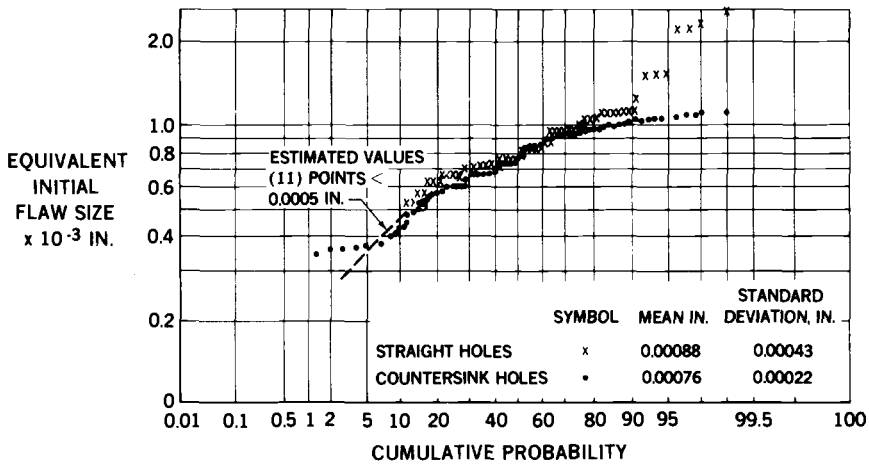


FIG. 13—Cumulative probability plot of EIFS for reamed countersink and straight open holes.

1, the life of macrocrack growth from 0.25 to 2.54 mm (0.01 to 0.10 in.) may be considered as constant. The life of microcrack growth is the principal variable in the scatter. The scatter is proportional to the percentage of life consisting of microcrack growth. For the three open hole configurations in 2024-T3, the increasing order is 1.8-mm (0.071-in.) countersink, 6.35-mm (0.250-in.) countersink, and 6.35-mm (0.250-in.) straight holes, from the minimum of a 33 percent in the 1.8-mm (0.071-in.) countersink holes to an 82 percent maximum total life in the 6.35-mm (0.250-in.) 2024-T3 straight holes.

The scatter in the microcrack growth period is dependent on two variables, namely, the distribution of EIFS and the rate of microcrack growth. For example, the three times greater scatter in the fatigue life of 6.35-mm (0.250-in.) 2024-T3 straight, open holes than in the 6.35-mm (0.250-in.) 2024-T3 countersink holes is caused by the corresponding two times greater scatter in the EIFS, such as that shown in Fig. 13, and by the difference in microcrack growth rate, as shown in Fig. 11. The slow microcrack growth rate will result in a longer life. The 1.8-mm (0.071-in.) countersink holes with the least scatter are the result of a very high microcrack growth rate, and are also the result of the knife-edge effect of the countersink wedge with the least probable exposure area of physical flaws to the maximum stress.

Conclusions

1. Statistical distribution of the equivalent initial flaw size (EIFS) based on quantitative data for the 2024-T3 fastener holes were obtained using the experimental procedure developed in this investigation.

2. The special test procedure using a multiple- (24) detail specimen to obtain statistically large samples of data under spectrum loading is workable for 2024-T3 material.

3. Scatter in the statistical fatigue life distribution can be described in terms of EIFS, microcrack growth life, and macrocrack growth life. The parameters affecting the apparent surface macrocrack growth have been resolved. The most important factors are EIFS distribution and microcrack growth rate.

4. The essential physical defects in 2024-T3 as the origins of microfatigue cracking are the tool marks, burr, and inclusions.

Acknowledgments

The author wishes to express his appreciation to Tom Swift and Paul Abelkis for their technical contributions, to Dennis Brown for his work on fractography, and to E. Hayman and the others in the Mechanical Test Laboratory for their contribution to the test program.

References

- [1] Rudd, J. L. and Gray, T. D., "Quantification of Fastener Hole Quality," presented at the AIAA/ASME 18th Structures, Structural Dynamics and Materials Conference, San Diego, 24-25 March 1977.
- [2] Pinckert, R. E., "Damage Tolerance Assessment of F-4 Aircraft," presented at the AIAA Aircraft System and Technology Meeting, Dallas, 27-29 Sept. 1976.
- [3] Noronha, P. J. et al, "Fastener Hole Quality," Report AFFDL-TR-78-206, Vol. 1, Dec. 1978.
- [4] Manning, S. D. et al, "Durability Methods Development, Vol. 1, Phase I-Summary," AFFDL-TR-79-XXX, June 1979.
- [5] Abelkis, P. R., "Effect of Transport/Bomber Loads Spectrum on Crack Growth," Report AFFDL-TR-78-134, Nov. 1978.

Factors Influencing Propagation of Mode III Fatigue Cracks under Torsional Loading

REFERENCE: Hurd, N. J. and Irving, P. E., "Factors Influencing Propagation of Mode III Fatigue Cracks under Torsional Loading," *Design of Fatigue and Fracture Resistant Structures, ASTM STP 761*, P. R. Abelkis and C. M. Hudson, Eds., American Society for Testing and Materials, 1982, pp. 212-233.

ABSTRACT: Mode III fatigue crack growth rates have been measured in a quenched and tempered low-alloy steel heat treated to a range of strength levels. When compared with Mode I crack growth rates, it is found that Mode III rates are slower than the Mode I by a factor of between 10 and 50. ΔK_T -values in Mode III are believed to be much larger than those of Mode I.

The stability of Mode III cracks compared with those in Mode I is shown to be related to applied ΔK , R -ratio, and the strength level of the steel. Mode III cracks are most stable in tests at $R = -1$, at high values of ΔK , and in the softest material. These conclusions are in part related to the differences between Mode III and Mode I crack growth rates. The results are considered in the light of surface hardening treatments applied to shafts loaded in torsion.

KEY WORDS: torsion, Mode III, Mode I, crack growth, fatigue, thresholds, plasticity, R -ratio

Nomenclature

- a Crack length measured radially from the surface of the bar
- a_{EFF} Effective crack length, with plastic zone correction
- $\Delta K_I, K_{\text{IM}}$ Stress intensity factor range, maximum in stress intensity factor in Mode I
- $\Delta K_{\text{III}}, K_{\text{IIIM}}$ Stress intensity factor range, maximum in stress intensity factor in Mode III
- r Radius of test bar

¹Metallurgist and Section Head, respectively, Materials Engineering Department, GKN Technology Ltd., Wolverhampton, England.

r_m	Maximum plastic zone size
r_r	Reversed plastic zone size
ΔT	Applied torque range
T_{MAX}	Maximum in applied torque
$\Delta\sigma$	Stress range in surface of bar
τ_y	Yield strength in torsion
ΔK_T	Threshold value of ΔK for fatigue crack growth

Torsional loading is extremely important for many components, especially those used in automotive applications. It is particularly relevant for transmission components such as drive shafts and propshafts (where one of the chief roles of the designer is the provision of sufficient fatigue strength to withstand the fluctuating service torques). One aspect of this task which has not been studied in depth, although it can have a considerable effect on the endurance of the component, is the mode of crack growth as influenced by the processing route. A particular example of considerable practical importance is the suppression of Mode I crack growth in components with compressive residual stresses in the surface layers.

As part of a larger program to investigate the mechanism of fatigue failure in torsionally loaded components, factors influencing the growth of fatigue cracks in shear orientations were studied.

It has been widely reported that processes such as induction hardening can improve the fatigue lives of half shafts under torsional loading [1,2].² The separate effects of this process are to raise the strength of the outer layers of the shaft and to introduce compressive residual stresses into these same layers. Observations of failures in induction hardened shafts produced in torsional fatigue show that tensile fatigue cracking at ± 45 deg to the shaft axis is largely eliminated and is replaced by shear cracking. Compressive residual stresses suppress Mode I by promoting crack closure, but will have little effect on shear modes of cracking. An example of this type of failure is shown in Fig. 1. The shear crack is all the more notable if it is considered that the strength level of the outer layers of the bar is approximately 1300 to 1600 MPa, and in normal circumstances such steel would probably fail in torsional fatigue by cleavage or intergranular failure at ± 45 deg to the axis of the bar.

Shear Cracks

When a shaft is subjected to torsion, in addition to the tension-compression stresses at ± 45 deg to the axis of the bar, there are transverse and longitudinal shear planes as shown in Fig. 2. A thumbnail crack in either of

²The italic numbers in brackets refer to the list of references appended to this paper.

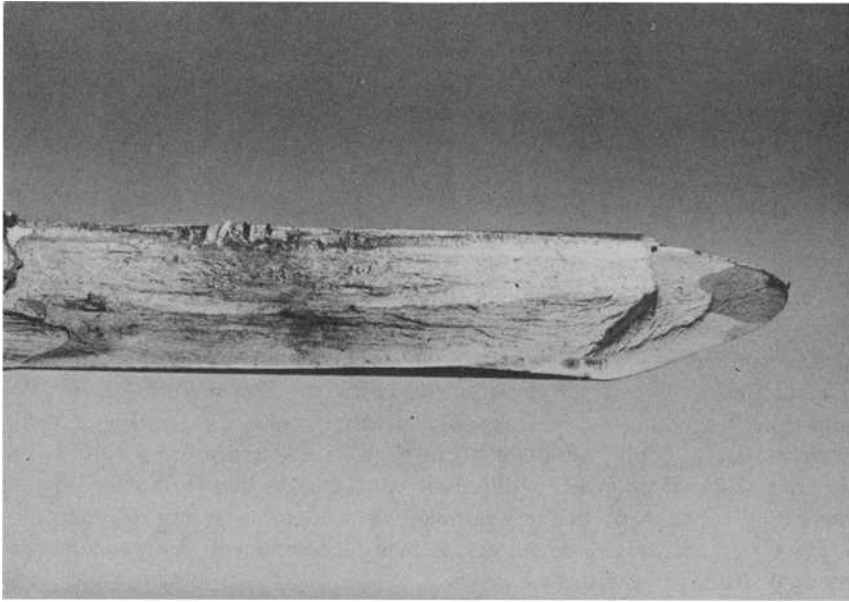


FIG. 1—Example of longitudinal shear fracture of induction hardened shaft, fatigue tested in torsion (X0.78).

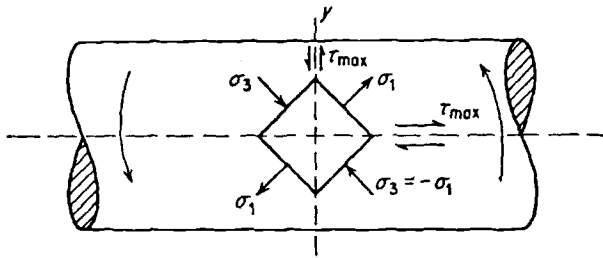


FIG. 2—Stress state in torsion (after Dieter [12]).

these two orientations will be subjected to Mode II displacements where the thumbnail intersects the surface and Mode III displacements at the point of deepest penetration (Fig. 3). As the Mode III crack will be the one which causes complete separation of the bar, this seemed to be the most appropriate one to investigate. This mode has the additional advantage that, unlike Mode II, it is easily produced by a circumferentially notched round bar, subjected to torsion.

Investigations of fatigue crack growth in modes other than Mode I are

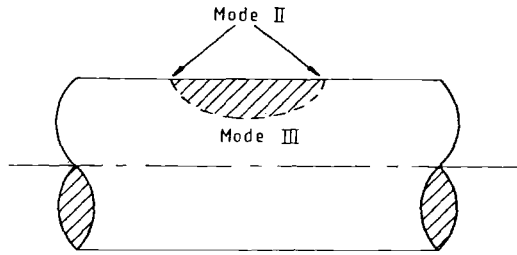


FIG. 3—Thumbnail crack in a torsionally loaded shaft which will be subjected to Mode II at the surface and Mode III at the point of deepest penetration.

relatively few. Much of the research [3-8] has examined Mode I combined with Mode II, this being a commonly encountered crack configuration. Its form is usually that of a slant crack subjected to tensile forces, which thus experiences both Modes I and II. In general, it is observed that the fatigue crack tends to deviate from the original direction to become more nearly perpendicular to the tensile stress. Similar observations have been made by Pook et al [4,5] in their investigation of cracks in Modes II and III. Pook et al find that these orientations are unstable with respect to Mode I. In this context it is of note that Smith [8] has observed that slant cracks subjected to fluctuating compression do extend in Mode II sliding. In this case, the tensile mode is suppressed as the crack faces are closed in compression. However, the sliding mode will still be operative and can evidently result in crack advance. This situation is similar to that in which Mode III cracks are stabilized by residual stresses.

As far as the authors are aware, there are no published measurements of crack growth rates in Mode III. Pook [9] has measured the ΔK_{III} -value at which a Mode I branch crack can form from a Mode III crack. Pook has similarly addressed the problem of branch crack formation from a Mode II crack.

As induction hardened bars are comprised of material with varying strength levels, it was decided to examine the effect of strength level upon crack growth rates in Mode III. The rate of Mode III fatigue crack growth would be correlated with ΔK_{III} . It is thought that such a correlation would be useful for treating problems pertaining to defects in torsionally loaded components where shear crack extension occurs.

In addition to the effect of strength level on these growth rates, the effect of mean torque was assessed. Mean load effects in Mode I are often attributed [10,11] to crack closure. However, Mode III crack growth is unlikely to be influenced by whether or not the crack is closed; the crack tip will experience the entire torque range at all levels of mean torque. Hence it is to be expected

that mean torque effects will be different from the Mode I equivalent. In addition to Mode III, Mode I tests were performed to provide a comparison.

Experimental Procedure

Material

The steel selected for the study was BS 970 605H32 (EN16). This is a quenched and tempered low-alloy steel commonly used for induction hardened shafts. The steel was heat treated by austenitising at 850°C followed by oil quenching. Tempering different samples at 300, 450, and 600°C produced a range of strength levels typical of those encountered in cross sections through an induction hardened shaft. The composition of the steel is shown in Table 1 and the mechanical properties in Table 2. The proof strength in torsion is generally considered to be about half that in tension, assuming the Tresca yield criterion. The microstructure produced by the heat treatment was tempered martensite in each case.

Specimens and Test Procedure

Conventional Mode I fatigue crack growth data were obtained using 25-mm-thick compact tension specimens. The tests were performed in a resonance machine. Both initiation and subsequent crack growth were performed at $R = 0.08$ and at a frequency of 100 Hz. Crack lengths were monitored using a d-c potential drop technique accurate to ± 0.1 mm and sensitive to 0.025 mm. After initiation, the alternating and mean loads were reduced until a suitably low growth rate was achieved. Load reduction was performed in accordance with ASTM recommended practice. After load

TABLE 1—Composition of 605H32 steel.

C	Si	Mn	P	S	Ni	Cr	Mo
0.33	0.2	1.55	0.017	0.029	0.35	0.35	0.23

TABLE 2—Mechanical properties of 605H32 steel.

Tempering Temperature, °C	Proof Strength Tension, MPa	UTS Tension, MPa	% Reduction of Area
600	891	972	63
450	1294	1367	55
300	1556	1696	49

reduction the crack was allowed to grow until an a/w of about 0.7 was reached, when the test was stopped. The crack length-cycles data were analyzed using techniques recommended in ASTM Tentative Test Method for Constant-Load-Amplitude Fatigue Crack Growth Rates Above 10^{-8} m/Cycle (E 647-78 T).

Mode III fatigue crack growth tests were performed on circumferentially notched 25-mm-diameter round bars with a 2.15-mm-deep notch. The bars were subjected to torsional loading in a closed-loop servohydraulic test machine with floating grips to eliminate axial stresses in the bar.

Tests were performed in torque control at two selected R -ratios: 0.08 and -1 . The torque range applied was typically 600 to 800 N·m, but in a few tests at $R = -1$, 1600 N·m was selected. Crack lengths were again monitored using the d-c potential drop technique. Stress intensity values for Mode III were obtained from the expression [13]:

$$\Delta K_{III} = \frac{2\Delta T/r^3}{[1 - (a/r)]^3} \frac{\sqrt{a/\pi}}{\sqrt{[1 + 7.11(a/r)]/(1 - a/r)}}$$

Values of da/dN were obtained from the crack length—cycles data in the same manner as that employed for the Mode I data. After the tests were concluded, the fracture surfaces were examined optically and in the scanning electron microscope.

Results

Initiation and Growth of Cracks in Mode III

At a torque range of 600 N·m, at both the selected R -ratios, fatigue cracks initiated readily at the notch root. This generally occurred within a few hundred cycles of the start of the test. Initiation took place simultaneously all round the bar, and no appreciable crack asymmetry was evident. Crack advance occurred evenly all round the bar, and hence the potential drop reading, which will only be recording local events in the vicinity of the spot welded probes, could be taken as representative of the whole of the crack front.

For the first 2 to 4 mm of crack growth out of the notch, the crack proceeded in a Mode III transverse shear orientation. After this, deviations out of the Mode III plane occurred. When analyzing the crack growth data, only growth rates which were obtained at crack lengths less than this were considered. Similarly, the initial high growth rates obtained as the crack grew from the notch root were also discarded. Deviations occurred most easily in the high-strength steel, where Mode III growth was confined to 1 to 2 mm from the notch, at R -ratios of 0.08. Mode III cracks were most stable in the lowest strength steel. Changing the R -ratio to -1 produced further increases

in Mode III stability relative to Mode I. Scanning electron microscopy showed that the shear fatigue crack surfaces were heavily smeared, and little fractographic information was available.

Examples of the fracture faces which were produced are shown in Figs. 4 and 5. The initial shear crack growth from the notch is followed by deviations out of the Mode III stage on to 45-deg tensile cracking planes.

In some cases propagation of both cracks continued independently, as can be seen in Fig. 6 where 45-deg cracking and the shear plane cracking have both continued. Final failure in all but the highest strength level steel was complex. The highest strength steel used failed by the fast propagation of 45 deg cracks alone. At $R = 0.08$, the two other strength levels failed in a transverse shear mode, with flat facets of slow crack growth preceding the final twist-off. Figures 4 and 7 illustrate the unusual nature of the fracture surfaces produced at $R = -1$ in the lowest strength material.

Initiation of tensile mode branch cracks appeared to depend on the number of cycles to which the specimen was subjected. Attempts to investigate growth rates less than 10^{-9} m/cycle invariably resulted in initiation of Mode I cracks at ± 45 deg to the bar axis, and little propagation of the

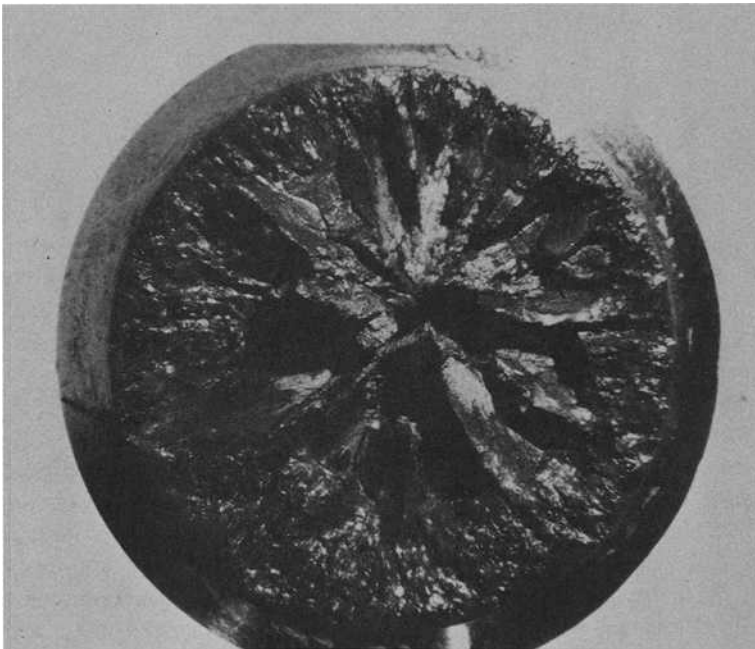


FIG. 4—Fracture face produced by cycling at $\pm 325 \text{ N} \cdot \text{m}$, showing initial growth of Mode III crack from notch, followed by Mode I cracks on ± 45 deg planes (X3.5).



FIG. 5—Closeup of fracture shown in Fig. 4 ($\times 8$).

Mode III crack. At higher values of ΔK , the shear mode was favored relative to the Mode I. Thus reducing the torque amplitude to approach a Mode III threshold always produced Mode I cracking, in the absence of compressive residual stresses.

Figure 7 shows the fracture face produced by testing at $\pm 650 \text{ N} \cdot \text{m}$, which may be compared with Fig. 4 which has been tested at $\pm 325 \text{ N} \cdot \text{m}$, both at $R = -1$. The enhanced out of plane fracture in the case of the smaller torque amplitude is quite evident. This suggests that low ranges of ΔK_{III} favor 45 deg cracking over shear cracking. The differences in morphology which have just been described emphasize the importance of using only true shear crack growth for the Mode III growth rate data, and that achieving such data over a large range of ΔK_{III} is hampered by the incursion of more complicated modes of failure.

Crack growth results for the Mode I tests for three different strength levels

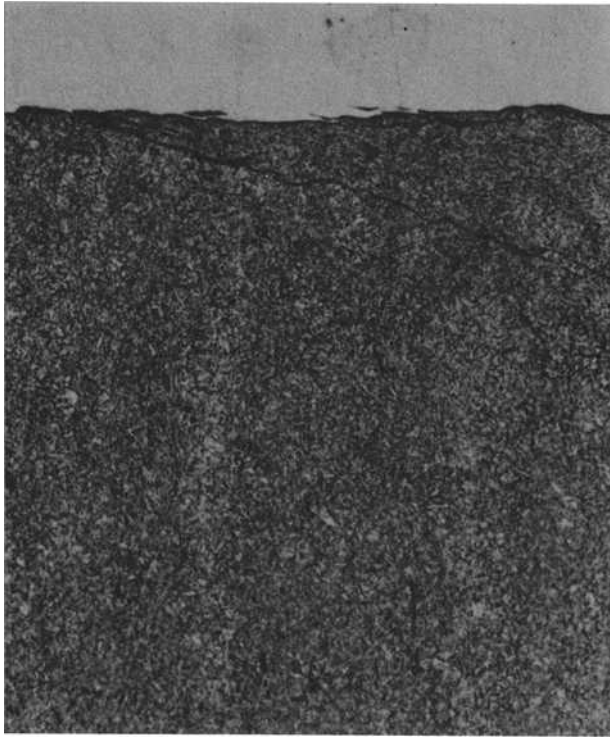


FIG. 6—Section through fracture face showing 45 deg subsidiary cracks branching off the main Mode III crack (X250).

are shown in Fig. 8. As has been observed on previous occasions [14,15], increasing strength level in medium to high strength steels causes an increase in Mode I fatigue crack growth rates. A comparison with Mode III data for each strength level is shown in Figs. 9a, 9b, and 9c.

There are a number of comments which can be made at this stage about these figures. It can be seen that at all strength levels, Mode III crack growth is slower than Mode I growth crack by factors of between 10 and 50. The Mode III curves appear to extrapolate to threshold values in the vicinity of 20 to 25 $\text{MN m}^{-3/2}$, extremely high values in comparison with those obtained in Mode I. It will also be noted that there is little tendency for the highest strength materials to produce faster growth rates and lower thresholds than the lowest strength steel. This behavior is again in contrast to Mode I.

The effect of strength level on Mode III growth rates is shown in Fig. 10. Once more, the effects are different than Mode I. The highest and lowest strength levels have somewhat similar growth rates over the range that they

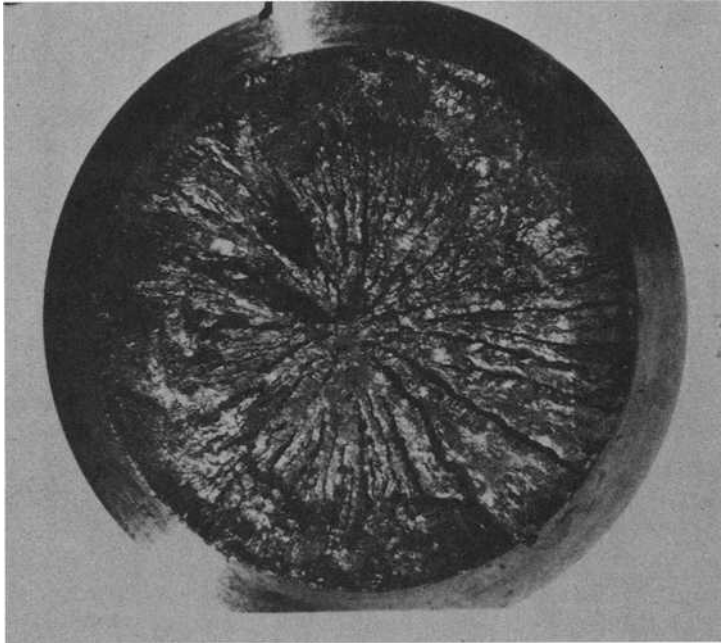


FIG. 7—Fracture face produced by cycling at $\pm 625 \text{ N} \cdot \text{m}$, showing Mode III cracking across the entire section on both longitudinal and transverse planes ($\times 3.5$).

can be compared. However, the intermediate strength level is slower than the other two for similar ΔK -values.

The effect of changing the R -ratio to -1 whilst keeping the torque range the same is shown in Fig. 11. Growth rates for the same value of ΔK for $R = -1$ are somewhat less than those obtained at $R = 0.08$. As noted previously, tests at $R = -1$ could be conducted at lower growth rates, involving larger numbers of cycles than could tests at $R = 0.08$. The latter tended to initiate Mode I cracks more readily and cause premature ending of the test as these grew more rapidly than the Mode III.

The reason for this is illustrated in Fig. 12. Torsional cycling with a cyclic minimum of zero or above will result in a single set of the 45-deg tension planes being subjected to a tensile stress amplitude of $\Delta\sigma$. The other set of 45-deg planes is subjected to compression. If cycling now takes place with a mean of zero, with the same torque range as before, the shear planes will experience the same stress as previously, but the 45-deg planes will individually only experience $\Delta\sigma/2$ in tension and $\Delta\sigma/2$ in compression. Hence the tensile stress on any particular 45-deg plane has been halved, and the propensity to crack growth in this mode relative to the shear mode will be much reduced.

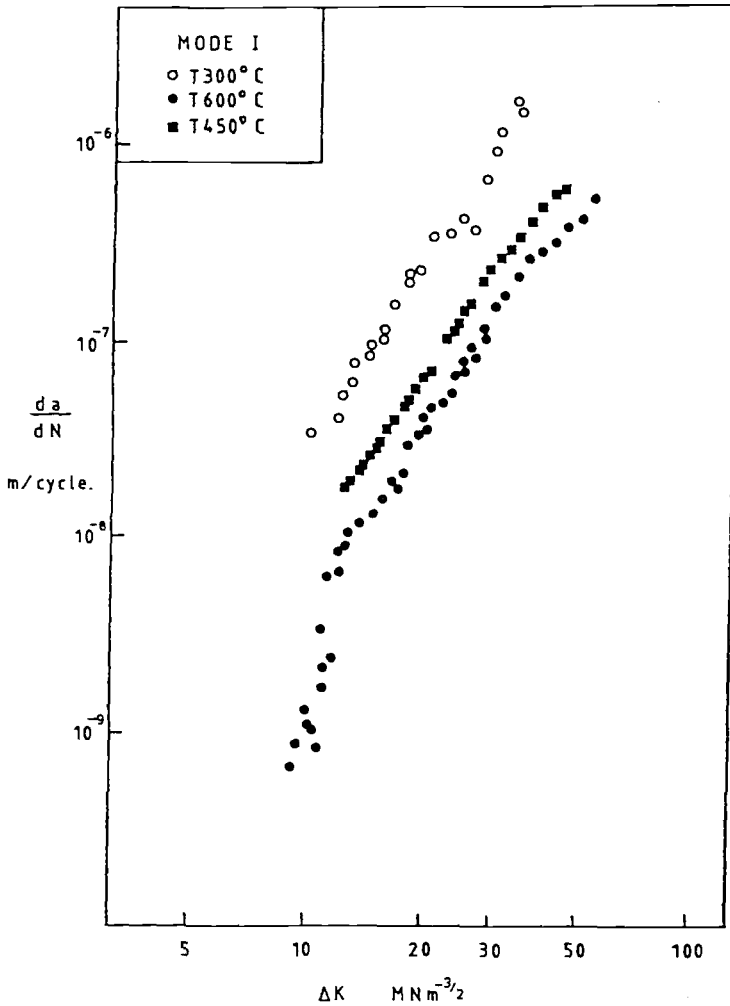


FIG. 8—Plot of $\log \Delta K$ versus $\log da/dN$ for Mode I cracks for the three different strength levels ($R = 0.08$).

As there is no closure effect in Mode III it is to be expected that similar ΔK -values will produce similar growth rates at different R -values, and this is observed. The effects of higher, positive R -values were not investigated as the increased K_{IIM} -values would produce large plastic zones with premature general yield.

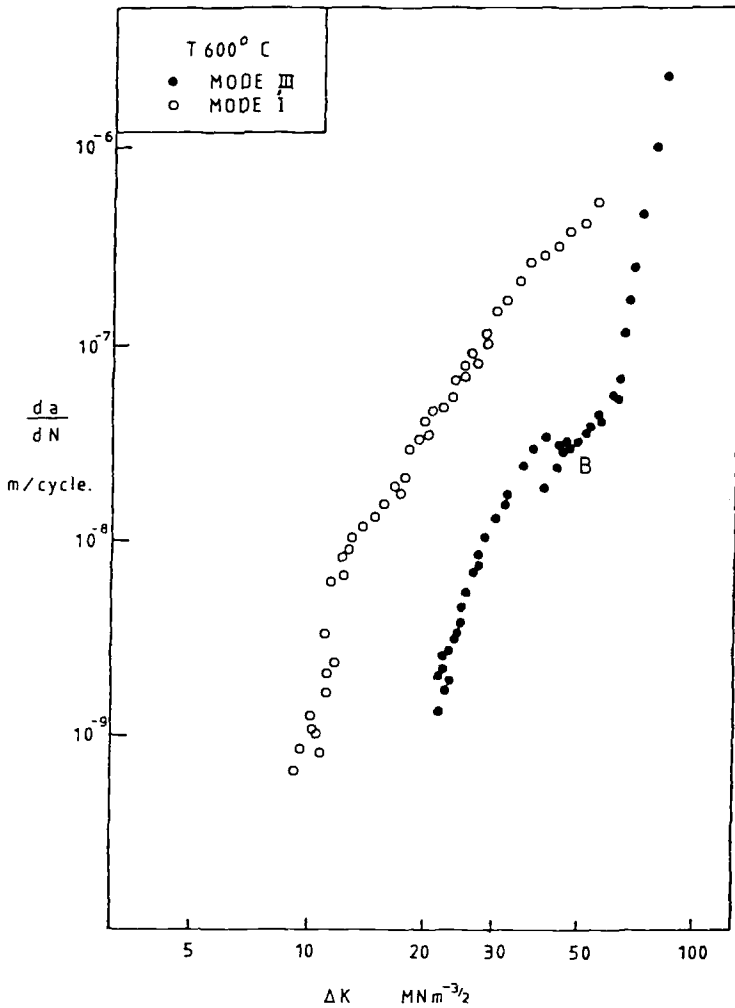


FIG. 9a—Comparison of crack growth rates in Mode I and Mode III for a strength level at $\sigma_y = 891$ MPa ($R = 0.08$).

Discussion

The effects of strength level and R -ratio on Mode I fatigue crack growth rates under tensile loadings in quenched and tempered steels have been noted on many occasions (for example, Refs 15 and 16). The present Mode I results confirm previous observations, and are included here as a yardstick to which the Mode III results may be compared.

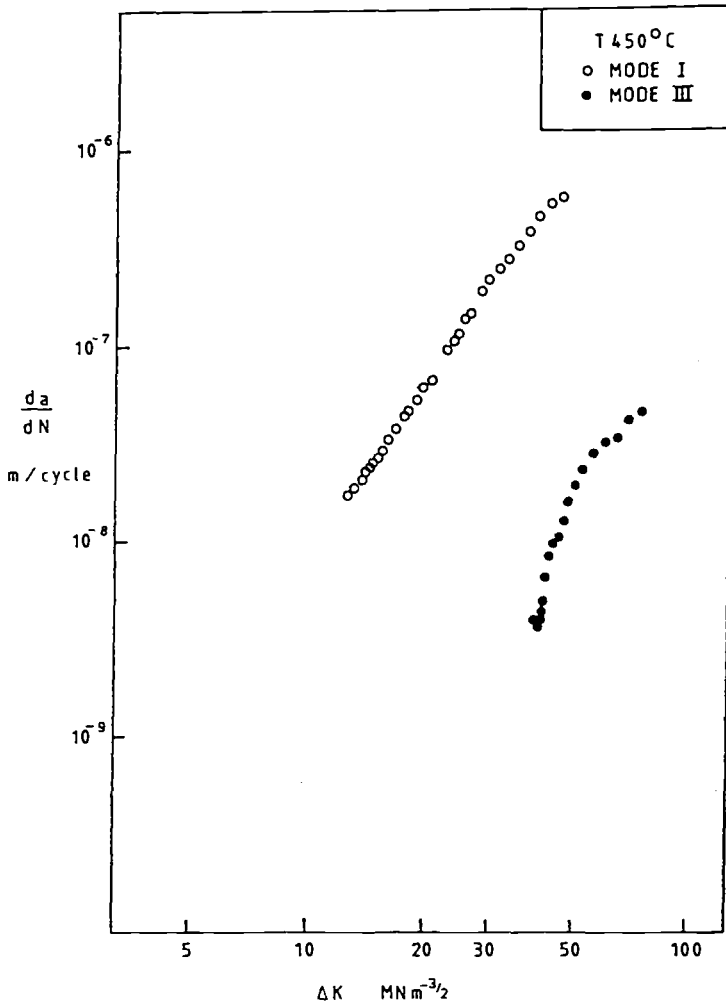


FIG. 9b—Comparison of crack growth rates in Mode I and Mode III for a strength level at $\sigma_y = 1294 \text{ MPa}$ ($R = 0.08$).

The dominating influence on Mode I fatigue crack growth rates is, of course, the stress intensity amplitude ΔK . Over the past 15 years, models of fatigue crack growth have been constructed based on damage accumulation [17,18], cyclic crack-opening displacement (COD), [19,20] or plastic work [21,22]. These models have been successful at predicting the ΔK -dependence of fatigue crack growth rates, but the lesser effects of R -ratio and strength level, especially in the important low-to-intermediate growth rate region, are not predicted. It is becoming clear that both these effects are caused by crack

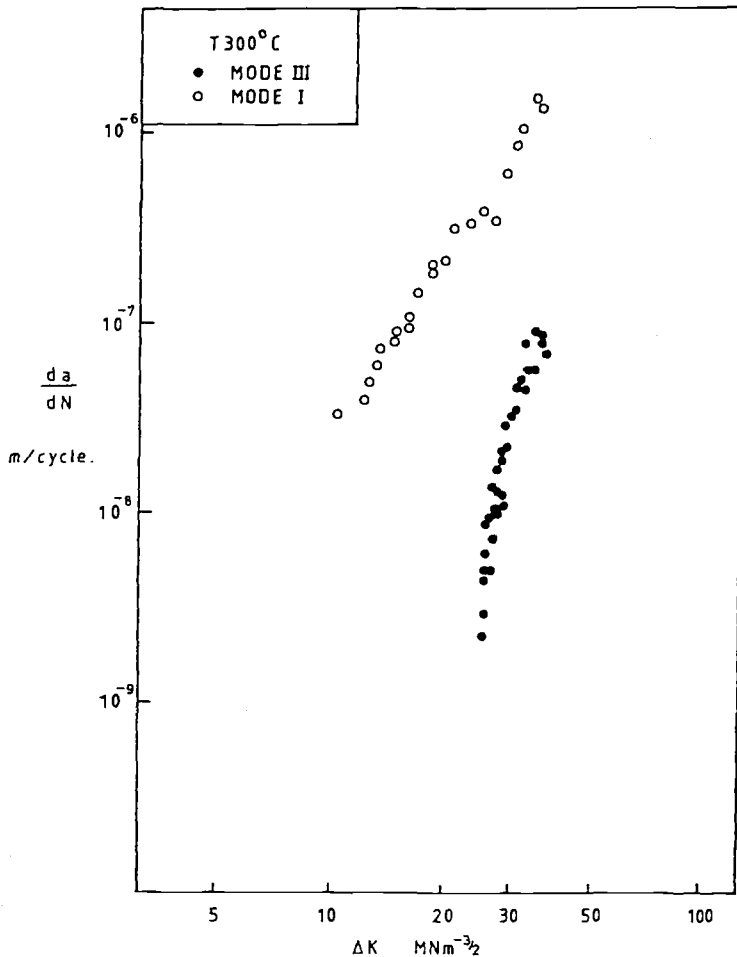


FIG. 9c—Comparison of crack growth rates in Mode I and Mode III for a strength level at $\sigma_y = 1556 \text{ MPa}$ ($R = 0.08$).

closure and environmental interactions [10,11,15,16], neither of which are incorporated into crack growth models.

In the case of sliding modes of crack growth (both Modes II and III), crack closure is not expected to influence the effective ΔK at the crack tip. Furthermore, as the Mode III crack-tip stress field does not contain a hydrostatic tension component [23], it is thought unlikely that hydrogen, derived from water vapor, will have any tendency to diffuse into the crack-tip plastic zone. Both of the sliding modes of crack growth will be subjected to frictional forces between the crack faces, and this will tend to reduce the effective stress intensity factors at the crack tip.

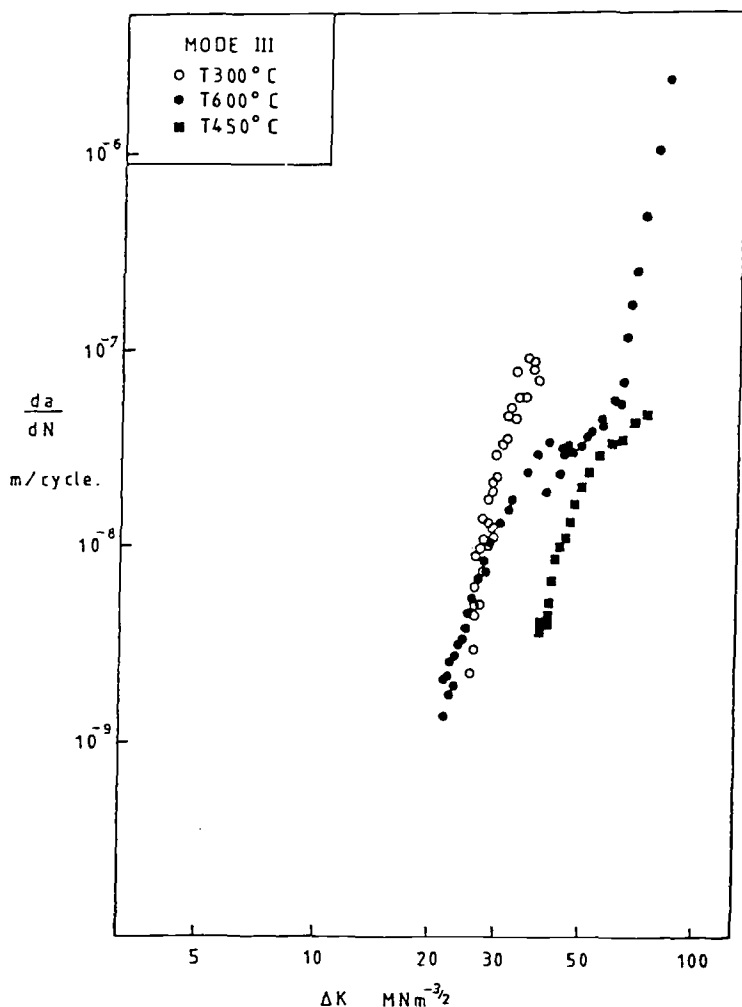


FIG. 10—Comparison of Mode III crack growth rates plotted against ΔK_{III} for the three different strength levels ($R = 0.08$).

A further point of difference between Modes I and II and the Mode III case is that of displacements in the vicinity of the crack tip. The pure Mode III case as theoretically defined does not appear to contain any displacements in the direction of crack growth. If this were strictly true, crack growth in this mode would be impossible. As it does occur, clearly some displacement is possible, but the Mode I maximum growth increment of half the cyclic COD [19,24] is unlikely to be achieved. As the Mode III crack sliding displacement for a given ΔK is some three times that of the Mode I equivalent, it is prob-

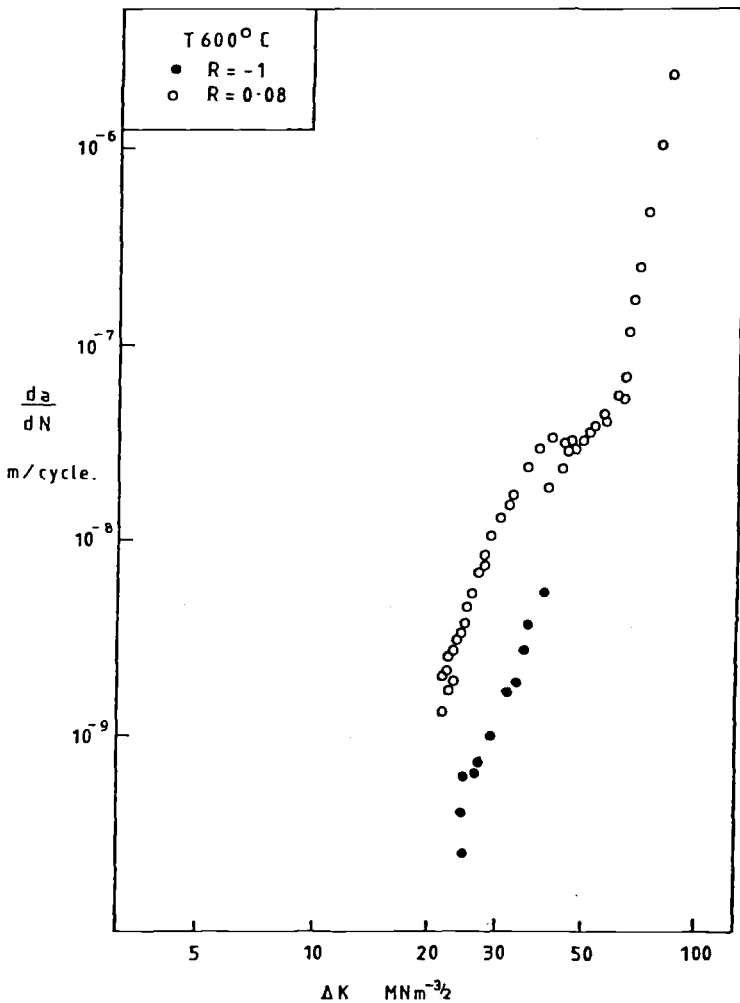


FIG. 11—Effect of R-ratio on crack growth rates for the lowest strength level steel. Data plotted against ΔK_{III} .

able that only a small fraction of the sliding displacement is retained as crack growth. Recent observations [24] have shown that in Mode II, the growth increment is 0.1 of the measured sliding displacement; a considerably smaller fraction than Mode I.

The essential features of Mode III crack growth, as revealed by the data presented here, are that (1) growth rates are much slower than in Mode I; (2) there is no systematic effect of strength level; and (3) thresholds for crack growth are much larger than those in Mode I.

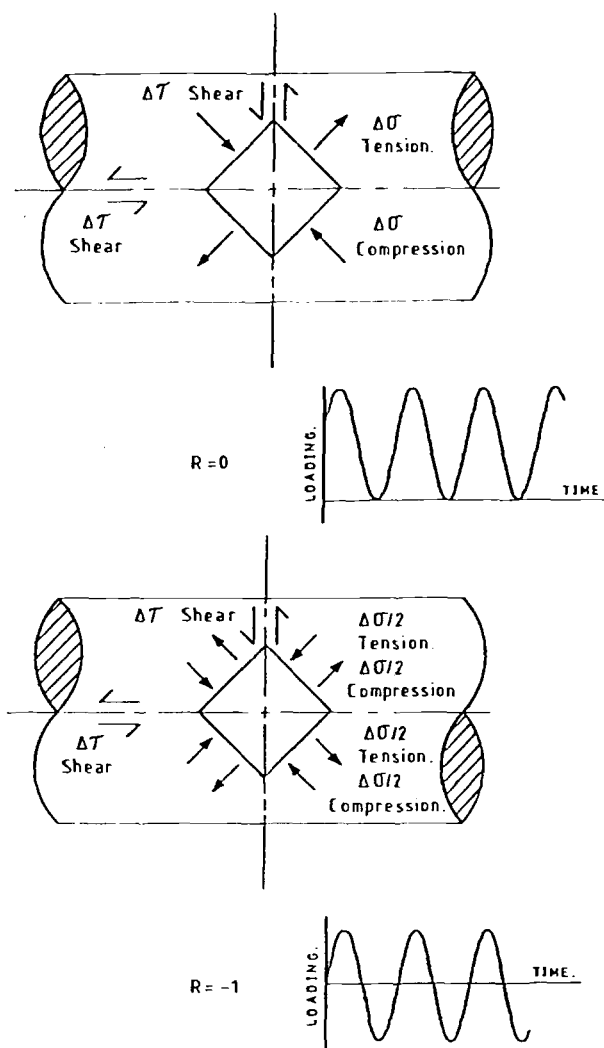


FIG. 12—Difference in stress distribution in torsion produced by changing R-ratio from 0 to -1. Tensile stresses on the 45 deg planes are halved, whilst the shear stresses remain unchanged.

It is probable that the relative difficulty of Mode III growth can be accounted for by the frictional and displacement effects noted above. The effects of strength level are more complex. Mode I type behavior is not observed, but neither is the theoretical inverse relationship of growth rate and proof strength. It is possible that variations in fracture path in the different strength levels are producing different frictional effects and so influencing growth rates. These possibilities are currently under investigation.

Effect of Plasticity

The simple plastic zone sizes (for both monotonic and cyclic loadings) in Mode III are twelve times as great as those for the Mode I, plane strain, equivalent, if the yield stress in shear, τ_y , is taken as one half of the tensile yield stress. The effects of crack-tip plasticity would therefore be expected to be greater in Mode III than in Mode I. All the Mode III growth rate data have hitherto been correlated with the value of ΔK_{III} calculated assuming that linear elastic fracture mechanics is applicable. However, crack-tip plasticity in the Mode III tests is appreciable, and the limits of applicability of this (linear elastic) approach, and the possible use of an elastic-plastic parameter, must be examined.

Consider the Mode III growth rate tests for the lowest strength material tested in this work. At the start of the growth rate test, the plastic zone size, r_m , associated with the maximum stress intensity, K_{IIIM} , in the cycle is

$$r_m = \frac{1}{2\pi} \frac{K_{IIIM}^2}{\tau_y^2} = 0.45 \text{ mm}$$

and the simple reversed plastic zone size, r_r , may be estimated from the following formula although experimental studies [25] suggest that the true reversed plastic zone size may be appreciably different.

$$r_r = \frac{1}{2\pi} \frac{\Delta K_{III}^2}{(2\tau_y)^2} = 0.1 \text{ mm}$$

Crack-tip plasticity is therefore appreciable but contained.

A further assessment of the extent of plasticity may be obtained by considering the ratio of the maximum cyclic torque, T_{MAX} , to the limit torque, T_L , found during the monotonic loading of similar specimens. The ratio of T_{MAX} to T_L is 0.5 at an a/r of 0.22, and this ratio rises to 1 at point B (Fig. 9a) where the Mode III fracture toughness [26] is also approached, and fatigue crack growth becomes extremely rapid. The monotonic and reversed plastic zone sizes at point B are 4.38 and 0.92 mm, respectively, which also indicates that gross yielding of the section occurs here. The values of T_{MAX} , T_L , and r_m over the range of a/r for which growth rate data were obtained for the 300, 450, and 600°C materials are summarized in Table 3 for $R = 0.08$. It is concluded that all growth rate data have therefore been obtained under conditions of appreciable, but contained, yielding.

The simplest correction for plasticity is that based on the plastic zone correction [27]. The cyclic stress intensity range was calculated by evaluating the maximum and minimum stress intensities as those associated with an effective crack length.

$$a_{EFF} = a + \frac{1}{2\pi} \frac{K_{IIIM}^2}{\tau_y^2}$$

TABLE 3—Degree of plasticity in the Mode III tests.

Tempering Temperature, °C	T_{MAX}	r_m , mm
	T_L	
600	0.5 to 1	0.45 to 4.38
450	0.69 to 0.8 ^a	0.71 to 1.1
300	<0.69 ^b	0.2 to 0.4

^aEstimated from the limit torque data for the 600°C material by assuming limit torque proportional to the shear yield stress.

^bObtained from the maximum torque in the toughness test, since fracture occurred before limit torque.

Where K_{IIIM} is the elastically calculated maximum or minimum value of K_{III} . The effect of such a correction is shown in Fig. 13. This correction is thought to give a good approximation for J , provided yielding is contained, in Mode I plane stress and plane strain [28,29], although the limits within which this is true are unclear. The possibility of using another elastic-plastic analysis, if only to verify the above approach, remains a goal of future research. Since the elastic-plastic analysis serves to increase the value of the stress intensity range over that calculated elastically, it may be seen that using an elastic-plastic approach will result in the Mode III growth rates shifting further below those in Mode I at the same ΔK .

For the $R = -1$ tests, the effect due to plasticity is considerably less since the maximum load is greatly reduced for a given range of ΔK_{III} . Over the appropriate range of crack lengths for the 600°C material we have T_{MAX}/T_L in the range of 0.23 to 0.4; the plastic zone sizes associated with maximum torque are 0.14 to 0.32 mm. Using fully reversed cycling therefore allows the effects of plasticity to be greatly reduced, and the conditions are closer to LEFM.

Relevance in Torsionally Loaded Components

The present results provide a rationale for at least some of the observations of fatigue fracture paths in torsionally loaded components. In the absence of compressive residual stresses which promote closure it is clear that the slower crack growth rates and restricted ΔK -range obtained in Mode III will predispose many components to crack growth in Mode I. However, the relative stabilities of the two modes can be altered by both strength level and by the R -ratio. Growth in the shear modes will be most likely to occur in low strength level materials with an R -ratio of -1 .

In the presence of compressive residual stresses, the balance is tilted still further towards shear modes of cracking. In addition to eliminating Mode I opening, as the Mode III threshold is much higher than the Mode I, greatly

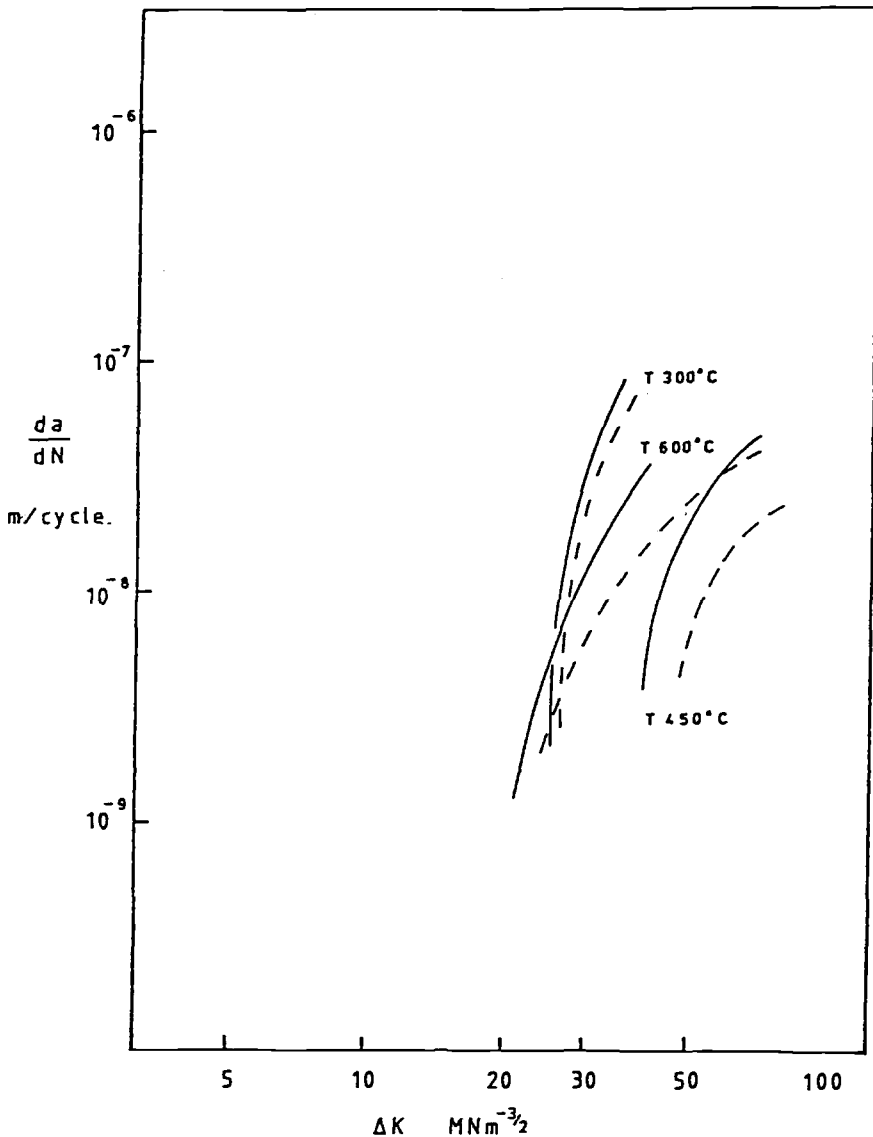


FIG. 13—Plasticity corrected crack growth rate curves compared with uncorrected curves for the three different strength levels (uncorrected: continuous line; corrected: dashed line; $R = 0.08$).

increased torques must be applied in order to achieve ΔK_{III} -values sufficient to grow a Mode III crack. Hence an improvement in fatigue limit caused by compressive residual stress is to be expected.

The threshold values involved are for propagation of a Mode III crack

rather than the initiation of a Mode I branch crack. These latter thresholds, as has been shown by Pook [3,4,5], are much lower, and will dominate the region at ΔK -values less than the true Mode III threshold in the absence of compressive residual stresses.

Conclusions

1. Mode III fatigue crack growth rates have been measured in circumferentially notched specimens of a quenched and tempered steel in a range of strength levels. It is found that crack growth rates are slower by a factor of between 10 and 50 times compared with Mode I data obtained in compact tension specimens.

2. The relative stability of Mode III and Mode I are influenced by the mean stress and by the ΔK -value applied to the crack. This dictates whether a Mode I branch crack is formed or whether the Mode III crack advances.

Acknowledgments

Grateful thanks are due M. S. Starkey and Dr. S. J. Hill for helpful discussions and comments. Thanks are also due many other colleagues who have contributed to the work reported in this paper. The paper is published by permission of Dr. T. L. Johnson, Director, GKN Technology Limited.

References

- [1] Almen, J. O. and Black, P. H., *Residual Stresses and Fatigue in Metals*, McGraw-Hill, New York, 1963.
- [2] Forrest, P. G., *Fatigue of Metals*, Pergamon, 1963.
- [3] Pook, L. P. and Sharples, J. K., *International Journal of Fracture*, Vol. 15, 1979, p. R223.
- [4] Pook, L. P. and Denton, K., *International Journal of Fracture*, Vol. 8, 1972, p. R118.
- [5] Pook, L. P. and Greeman, A. F. in *Fracture Mechanics, ASTM STP 677*, American Society for Testing and Materials, 1979, pp. 23-25.
- [6] Toor, P. M., "Fracture Mechanics under Complex Stress," paper presented at 7th National Symposium on Fracture Mechanics, University of Maryland, 1973.
- [7] Erdogan, F. and Sih, G., *Journal of Basic Engineering*, Vol. 85D, 1963, pp. 519-527.
- [8] Smith, R. A., "Mechanics of Mode II Crack Advance", Session 5J, Conference on Micromechanisms of Crack Extension, Cambridge, 1980.
- [9] Pook, L. P., "The Significance of Mode I Branch Cracks for Combined Modes of Failure," in *Proceedings of ECF3*, J. C. Radon, Ed., Imperial College, London, Sept. 1980, pp. 143-154.
- [10] Elber, W. in *Damage Tolerance in Aircraft Structures, ASTM STP 486*, American Society for Testing and Materials, 1971, pp. 230-242.
- [11] Fuhring, H., *International Journal of Fracture*, Vol. 12, 1976, pp. 917-920.
- [12] Dieter, G. E., *Mechanical Metallurgy*, McGraw-Hill, New York, 1961.
- [13] Rooke, D. P. and Cartwright, D. J., *Stress Intensity Factors*, Her Majesty's Stationery Office, 1976.
- [14] Irving, P. E. and McCartney, L. N., *Metal Science*, Vol. 11, 1977, p. 351.
- [15] Ritchie, R. O., *Metal Science*, Vol. 11, 1977, p. 368.
- [16] Stewart, A. T., *Engineering Fracture Mechanics*, Vol. 13, 1980, pp. 463-478.

- [17] Weertman, J., *International Journal of Fracture Mechanics*, Vol. 5, 1969, p. 13.
- [18] McCartney, L. N. and Gale, B., *Proceedings of the Royal Society*, Vol. A333, 1973, p. 337.
- [19] Tomkins, B., *Philosophical Magazine*, Vol. 18, 1968, p. 1041.
- [20] Pook, L. P. and Frost, N. E., *International Journal of Fracture*, Vol. 9, 1973, p. 53.
- [21] Fine, M. E., *Metallurgical Transactions*, Vol. 11A, 1980, p. 365-379.
- [22] Izumi, Y. and Fine, M. F., *Engineering Fracture Mechanics*, Vol. 11, 1979, p. 791.
- [23] Paris, P. C. and Sih, G. C. in *Fracture Mechanics, ASTM STP 675*, American Society for Testing and Materials, 1979, pp. 243-253.
- [24] Kikukawa, M., Jono, M., and Adochi, M. in *Fracture Mechanics, ASTM STP 675*, American Society for Testing and Materials, 1979, pp. 243-253.
- [25] Lankford, G. and Davidson, D. L., *International Journal of Fracture*, Vol. 14, 1978, p. R87.
- [26] Hurd, N. J. and Irving, P. E., *Proceedings ECF III*, Pergamon, New York, 1980, pp. 239-249.
- [27] McClintock, F. A. and Irwin, G. in *Fracture Toughness Testing and Its Applications, ASTM STP 381*, American Society for Testing and Materials, 1965, pp. 84-113.
- [28] Turner, C. E., *Proceedings ECF III*, Pergamon, New York, 1980, pp. 314-328.
- [29] Sumpter, J. D. G. and Truner, C. E., *International Journal of Fracture*, Vol. 12, 1976, pp. 861-871.

Load-Environment Interaction Effects on Crack Growth in Landing Gear Steels

REFERENCE: Saff, C. R. and Rosenfeld, M. S., "Load-Environment Interaction Effects on Crack Growth in Landing Gear Steels," *Design of Fatigue and Fracture Resistant Structures, ASTM STP 761*, P. R. Abelkis and C. M. Hudson, Eds., American Society for Testing and Materials, 1982, pp. 234-252.

ABSTRACT: Recent research into the crack growth behavior of aircraft landing gear steels shows that combinations of aggressive chemical environment and high sustained loading can cause significant reduction in the fatigue crack growth life of 300M steel. Crack growth behaviors of 300M and HP 9-4-0.30 steels are compared for continuous salt water immersion and alternate immersion in synthetic sea water environments. An analysis approach which sums the crack growth due to cyclic loading in an inert environment is shown to accurately correlate and predict the combined effects of chemical environment and mechanical loading on crack growth. Crack growth behavior under landing gear stress spectra typical of Air Force and Navy usage is compared.

KEY WORDS: crack growth, steels, environmental acceleration, surface flaws, crack growth prediction, landing gear, spectrum loads

Throughout their service lives, aircraft are subjected to a combination of environmental attack and varying loads. The structural integrity of the vehicle can be impaired by surface degradation due to corrosive action or by cracks developed or aggravated by the environment.

A major structural aircraft subsystem which experiences high maintenance cost due to the interactions of high load levels and environmental attack is the landing gear subsystem. This subsystem usually consists of a series of nonredundant structural elements that are exposed to numerous aggressive environments during their lives and yet have to be fabricated, for the most

¹Lead Engineer-Technology, Structural Research Department, McDonnell Aircraft Company, St. Louis, Mo. 63166.

²Aerospace Research Engineer, Structural Research Branch, Naval Air Development Center, Warminster, Pa.

part, from materials which are known to be susceptible to environmentally assisted cracking.

Great care is taken during manufacturing and processing to ensure that these nonredundant structural elements are as flaw-free as possible. However, even with good quality control, minute cracks can develop, for example, during grinding and plating of high-strength steel parts. Also, as with any aircraft structural subsystem, small cracks can be initiated during service life from latent damage sites developed by fretting, pitting, intergranular stress corrosion cracking, and fatigue.

In landing gear structural components, the cracks of principal concern initiate on the surface of the component. Cracks, whether initially present or service developed, can propagate to failure in these highly loaded nonredundant structural subsystems and cause system failure.

Therefore both the Navy and Air Force have sponsored numerous research programs to investigate chemical environment-load interaction effects on crack growth behavior. The objective of recent research has been to determine the sensitivity of landing gear steels to crack growth acceleration in aggressive environments and load spectra typical of fighter aircraft landing gear.

This paper summarizes the results of two of these research programs, one Navy sponsored and one Air Force sponsored [1,2],³ both of which dealt with load-environment interaction effects on crack growth behavior in 300M and HP 9-4-0.30 landing gear steels.

Constant-Amplitude Test Programs

Both research programs included test programs to obtain the experimental data necessary for calibrating and evaluating crack growth prediction algorithms. These test programs are summarized in Table 1. The Navy program used alternate immersion in synthetic sea water [ASTM Specification for Substitute Ocean Water (D 1141-75 (1980))] to simulate the environment to which carrier based aircraft are exposed, while the Air Force program used continuous immersion in 3.5 percent sodium chloride (NaCl) salt water to maximize the influence of an aggressive environment on crack growth.

The tests had three objectives: characterize each material by developing constant-amplitude fatigue crack growth rate data in a dry air environment (Specimens 1 to 3), evaluate a linear summation model of environmentally accelerated crack growth (Specimens 4 to 11), and calibrate the load interaction model for the landing gear stress histories and specimens to be used in the verification test program (Specimens 12 to 14).

300M and HP 9-4-0.30 steels were selected to represent the range of environmental sensitivity found in landing gear steels. Crack growth in 300M

³The italic numbers in brackets refer to the list of references appended to this paper.

TABLE 1—Constant-amplitude test program summary.

Specimen Number	Specimen Type	Environment ¹	Stress Ratio	Frequency (Hz)	Wave Shape	Test Type	Objectives
1	Center Cracked Panel	<10% RH Air	0	10	Sinusoidal	Const-Amp	Develop da/dN and Evaluate Stress Ratio
2			0.5	10			
3			-1	10			
4		Aggressive	0	10			Evaluate Frequency
5			0	1			
6			0	0.1			
7 ²		Aggressive	0	10	Trapezoidal		Evaluate Wave Shape
8			0	1			
9			0	0.1			
10			0.5	0.1			
11			-1	0.1			
12		<10% RH Air	-	10	Sinusoidal	Spectrum	Calibrate Model
13			-	-			
14	Elliptical Flaw	<10% RH Air	0	10	Sinusoidal	Const-Amp	Evaluate K

Notes:



Aggressive environment for the Navy program was alternate immersion in synthetic sea water, for the Air Force program was continuous immersion in 3.5% NaCl salt water



This test was not performed in the Air Force program

3 Test series is identical for both materials

steel was found to be significantly accelerated by exposure to salt water or sea water under loading cycles involving sustained loads. Crack growth in HP 9-4-0.30 steel was shown to be relatively insensitive to immersion in sea or salt water [1,2].

Test specimens are shown in Figs. 1 and 2. 300M steel specimens were heat treated to a 1931 to 2068 MN/m² strength level. HP 9-4-0.30 specimens were heat treated to a 1517 to 1655 MN/m² strength level. Additional material property information is available in Refs 1 and 2.

Specimens were precracked at zero stress ratio and the final stage of precrack growth was obtained at a stress level equal to or less than that at which the subsequent test was performed. For alternate immersion tests, the cracked section of the specimen was immersed during the final stage of precracking to avoid an artificial increase in crack growth rate found to occur when specimens precracked in a laboratory air environment are immersed in salt water for test [2].

Low humidity (<10 percent relative humidity) air was used as a reference environment for both programs. The containment method for this environment was a Mylar case sealed to the specimen by a soft silicone adhesive. Silica jell desiccant was used to obtain low humidity air. For continuous immersion environments the same containment method was used, although the

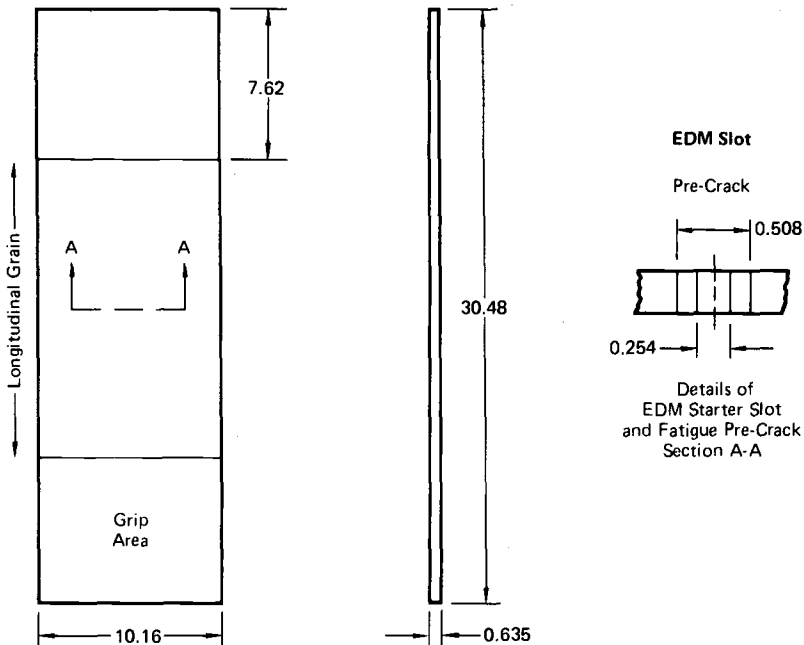


FIG. 1—Center-cracked panel specimen (dimensions in centimetres).

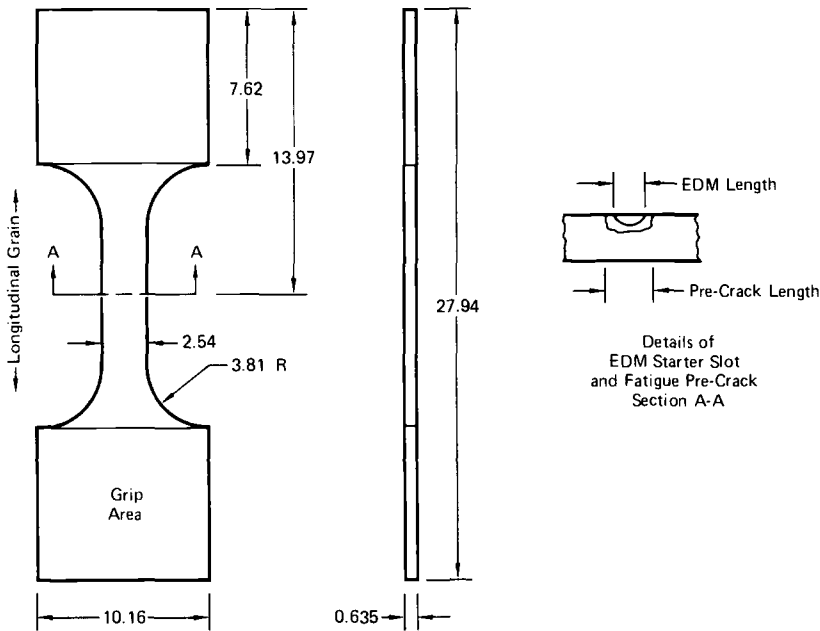


FIG. 2—Surface-flawed panel specimen (dimensions in centimetres).

case was open at the top to replenish the salt water as required. The salt water was periodically replaced to maintain solution chemistry.

The alternate immersion cycle used in the Navy program was 10-min immersion in synthetic sea water followed by 50-min drying by blown, filtered, shop air. The container used for alternate immersion tests is shown in Fig. 3. The Plexiglas container is wide enough to accept the specimen and a nylon tube which encircles the specimen to provide air for the drying cycle. Synthetic sea water was introduced through a plastic tube and stainless steel port and released through a second stainless steel drain port. After immersion, filtered shop air at 10 psia was used to blow the specimen dry. This procedure rapidly dried the specimen surface and container. Rapid drying provided better control of the environment than allowing the specimen and container to dry in laboratory air.

Constant-Amplitude Crack Growth Behavior

Results of constant-amplitude tests in the Air Force program showed that crack growth rates are significantly accelerated by continuous immersion in salt water. Test results for trapezoidal wave loadings at 10 and 0.1 Hz are shown in Fig. 4. The trapezoidal wave was made up of 0.25-s rise and fall

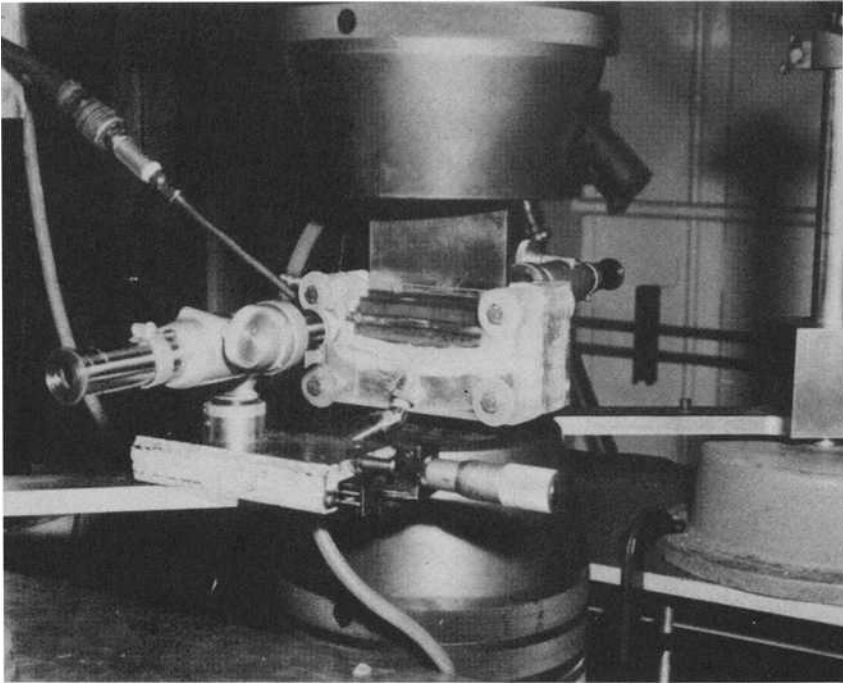


FIG. 3—Container used for alternate immersion tests.

time. For the remainder of the cycle, load was held at maximum. The sustained load time for the 0.1-Hz wave is 9.95 s and for the 10-Hz wave is 0.05 s. The data shown in Fig. 4 indicate that, for 300M steel immersed in salt water, the crack growth rate is almost directly proportional to time at load. Thus the acceleration due to the aggressive environment appears to depend on the sustained load hold time. Some cyclic loading is necessary since crack growth rates in sustained load tests in salt water were an order of magnitude smaller than the rates found in the 0.1-Hz cyclic test.

In contrast, there is little effect of salt water on crack growth in HP 9-4-0.30 steel, as shown in Fig. 5 for 10 and 0.1 Hz trapezoidal wave loading. The 0.1-Hz data show slightly higher crack growth rates than the 10-Hz data at stress intensity factors below $44 \text{ MN/m}^{3/2}$ with no difference shown above that point.

In alternate immersion tests [1], 300M steel again shows considerable crack growth acceleration while immersed (Fig. 6). However, during the drying cycle, crack growth rates rapidly decay toward dry air rates. Crack length measurements in these tests were taken before and after immersion and 25 min into the drying cycle. Thus the crack growth rates shown in Fig. 6 are

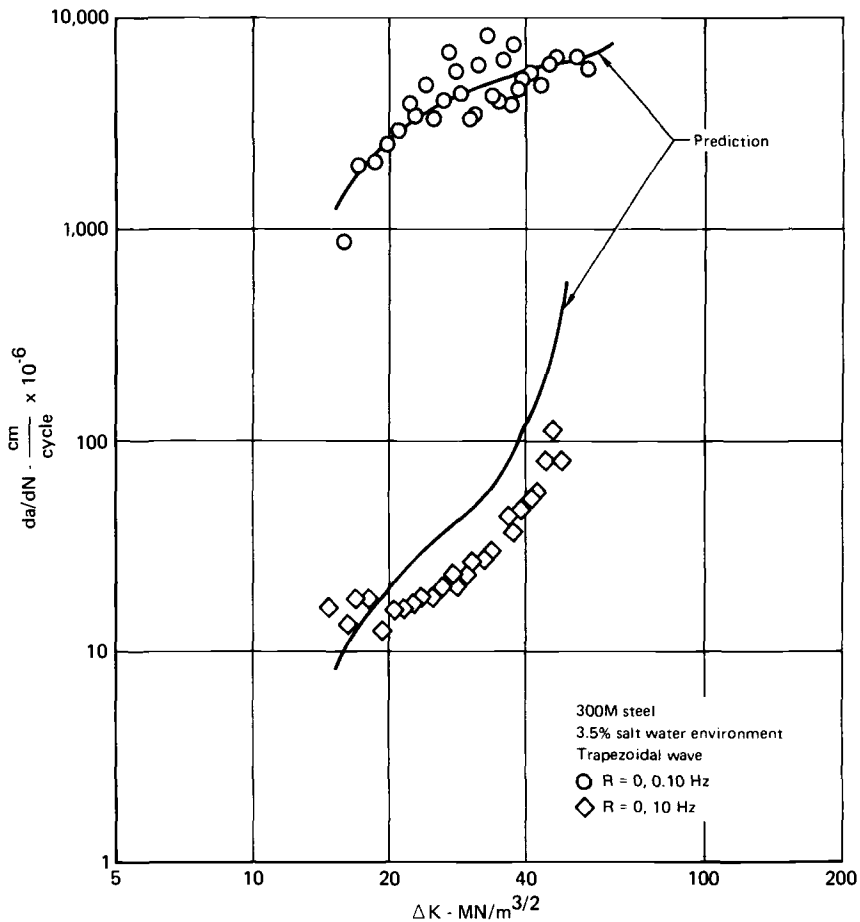


FIG. 4—Acceleration of crack growth rates in 300M steel continuously immersed in 3.5 percent NaCl salt water.

averages for the various time periods, not instantaneous values. The decay of acceleration in the drying cycle results in a regular stair-step pattern in the crack growth curve (Fig. 7).

Alternate immersion was found to increase the apparent threshold stress intensity factor for HP 9-4-0.30 steel [1]. At 10 Hz no effect of the aggressive environment was found. However, at 0.1 Hz the apparent threshold increased to $33 \text{ MN/m}^{3/2}$. Above that value, crack growth rates were nearly the same as in dry air (Fig. 8). Below that value, the crack grew during the first immersion cycle but slowed markedly during drying. Eventually, after several immersion cycles, crack growth stopped entirely. This effect was not evident in continuous immersion tests at any frequency [2].

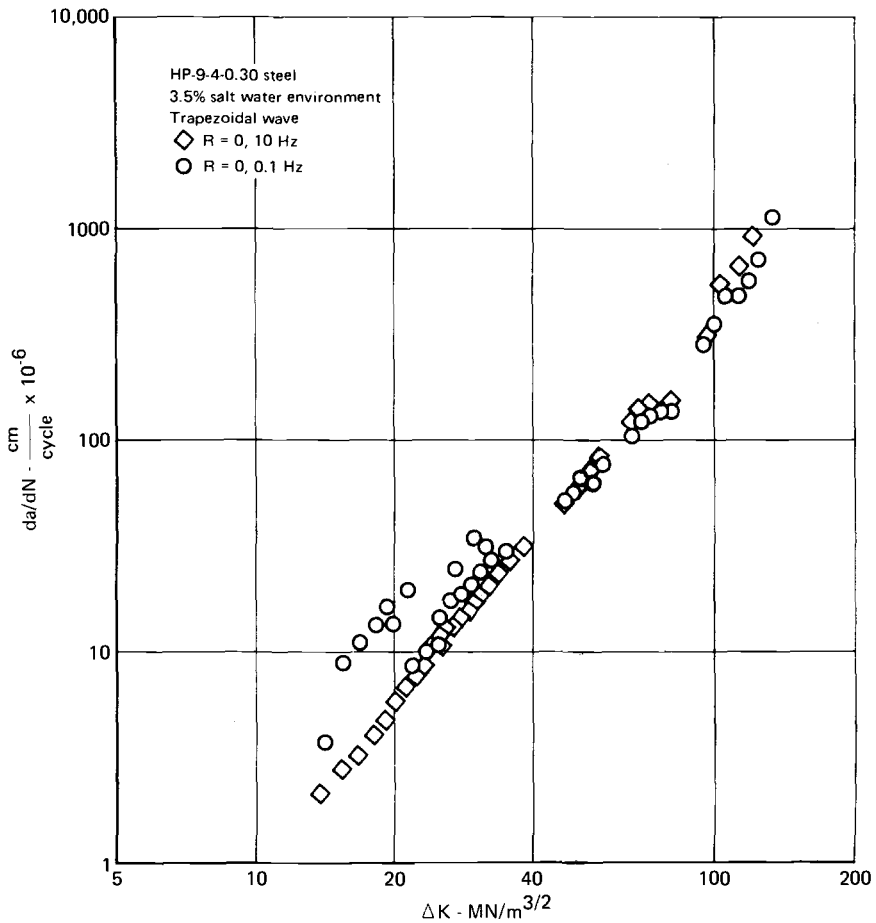


FIG. 5—Effect of continuous immersion in 3.5 percent salt water on crack growth rate in HP 9-4-0.30 steel.

Currently, we conjecture that corrosion products, created on the crack faces during immersion, solidify during drying. These corrosion products reduce the stress intensity factor ranges applied to the crack tip (that is, increasing crack closure), which causes crack growth to slow or stop. However, no measurements of crack-opening displacement (COD) or closure were made to substantiate this conjecture.

Crack Growth Analysis

The Wei-Landes linear summation hypothesis [3,4] suggests that environmentally accelerated crack growth rates can be predicted by adding the

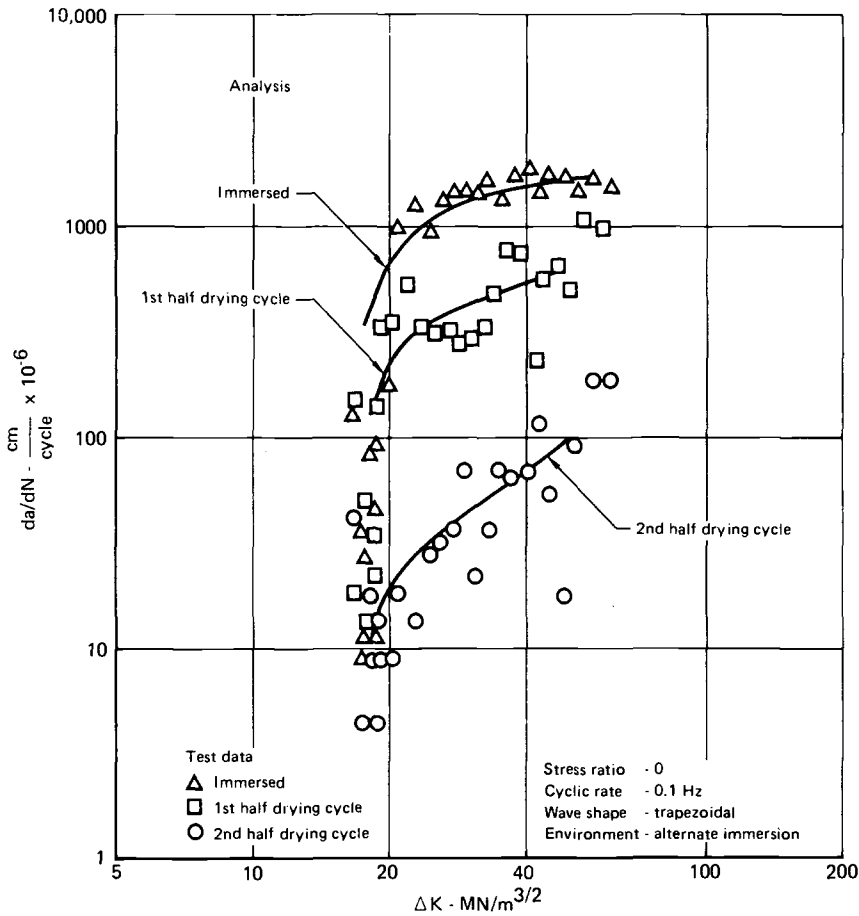


FIG. 6—Acceleration of crack growth rates in 300M steel alternately immersed in synthetic salt water.

crack growth due to the individual mechanisms of environmental attack and cyclic loading. This hypothesis, when used to account for frequency effects, can be expressed as

$$\frac{da}{dN_{total}} = \frac{1}{f} \frac{da}{dt}_{environment} + \frac{da}{dN_{fatigue}} \quad (1)$$

The $da/dt_{environment}$ is obtained from sustained load or low-frequency cyclic tests in the environment, and $da/dN_{fatigue}$ is obtained from cyclic load tests conducted at high frequencies in air or a nonaggressive environment.

The modification of the linear summation hypothesis used in this program

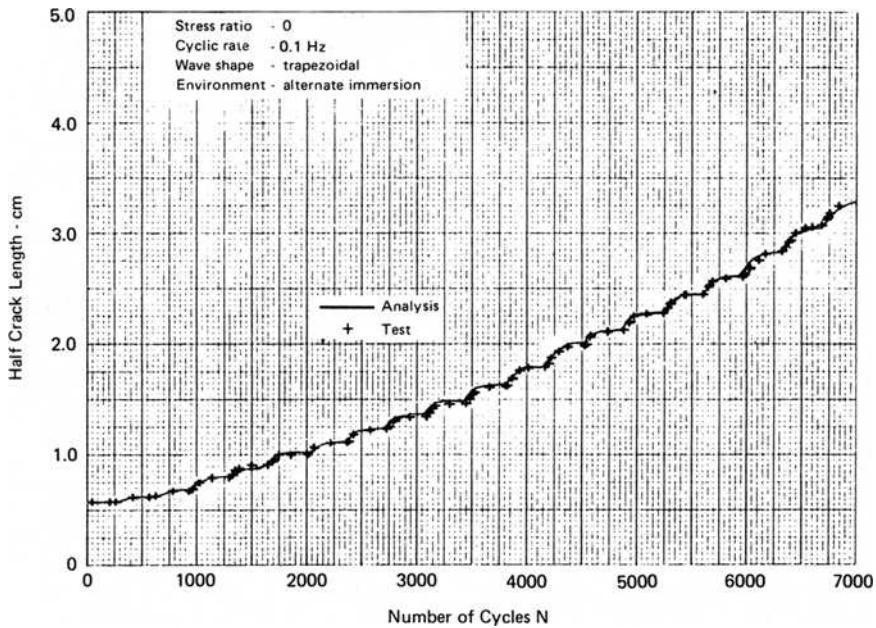


FIG. 7—Crack growth behavior of 300M steel in alternate immersion in sea water at low cycle rates.

is that for any environment the total crack growth rate for any cycle is the sum of two components; one due to mechanical loading in the reference environment (less than 10 percent relative humidity), and one due to sustained load in an aggressive environment. This model is formulated as

$$\frac{da}{dN} = \frac{da}{dN_{\text{ref}}} + \frac{da}{dN_{\text{env}}} \quad (2)$$

where

$$\frac{da}{dN_{\text{env}}} = \int_{t_1}^{t_2} \frac{da}{dt_{\text{immersed}}} dt \quad (\text{during immersion}) \quad (3a)$$

$$= \int_{t_1}^{t_2} \frac{da}{dt_{\text{immersed}}} e^{-\alpha t} dt \quad (\text{during drying}) \quad (3b)$$

where the period of the load cycle is $t_2 - t_1$.

The sustained load crack growth rate, da/dt_{immersed} , was determined by subtracting crack growth rates during immersion at 10 Hz from crack growth

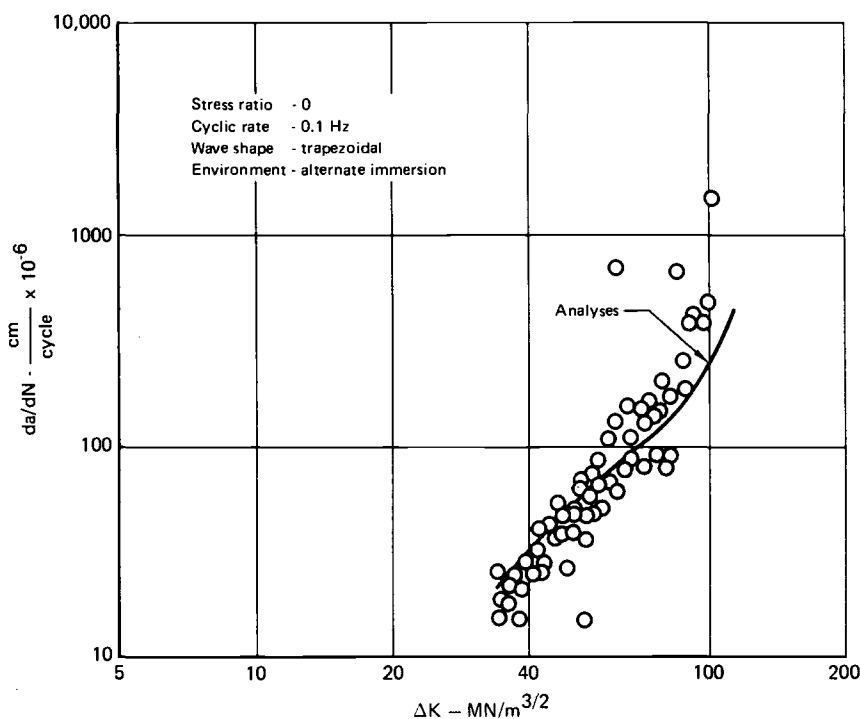


FIG. 8—Effect of alternate immersion in synthetic sea water on crack growth rate in HP 9-4-0.30 steel.

rates during immersion at 0.1 Hz. Trapezoidal waves having the same loading rates are used in each test so that the difference in crack growth rates, if any, is due solely to sustained load in the aggressive environment.

The exponent α in Eq 3b was determined empirically by correlation with the crack growth rates measured during the drying cycle of the trapezoidal wave test using $R = 0$ at 0.1 Hz (Specimen 9). In 300M steel, α was found to be 0.00175. In HP 9-4-0.30, no environmental acceleration was found and α is zero.

Sustained load cracking during immersion is assumed to occur only during the loading and sustained portions of a cycle. When a trapezoidal wave is applied, predicted crack growth is the sum of three components; cyclic growth during loading, sustained load growth during loading, and sustained load growth during the hold time. The unloading portion of a cycle is assumed to produce no crack growth.

The model, summarized by Eq 2, was used for all analyses presented herein. Comparison of analysis and test results for 300M steel (Figs. 4, 6, and 7) indicates the accuracy of the model to describe the crack growth behavior

of 300M steel in the continuous and alternate immersion environments. Predicted and measured lives for all constant-amplitude crack growth tests in 300M steel are summarized in Table 2. Good correlation is evident.

Predicted and measured crack growth lives for HP 9-4-0.30 steel are compared in Table 3. These predictions assume that there is no impact of the aggressive environment. This assumption is confirmed by the test data. However, results from the 0.1-Hz trapezoidal wave shape test in alternate immersion show a significant increase in the apparent threshold stress intensity factor. Plots summarizing the effects of continuous and alternate immersion environments on crack growth life in HP 9-4-0.30 steel are presented in Figs. 5 and 8. These plots indicate the accuracy of the technique.

Under spectrum loadings, da/dN_{ref} and da/dN_{env} are assumed to depend on the effective loading parameters, $K_{\text{max-eff}}$ and $K_{\text{min-eff}}$, computed by the Willenborg model [5].

The following assumptions are also inherent in the analysis:

(1) The unloading portion of the stress cycle produces no crack growth and is ignored in the analysis. The stress intensity range and stress ratio used for analysis are determined by a valley stress and the subsequent peak stress.

(2) In the computation of sustained load crack growth, a cycle has a peak stress intensity factor of $K_{\text{max-eff}}$, as determined by the Willenborg model, and $R_{\text{eff}} = 0$.

(3) Fracture is assumed to occur whenever the stress intensity factor exceeds K_c .

Spectrum Test Programs

In both Navy and Air Force programs, spectrum tests were performed for verification of the crack growth prediction methodology. Test spectra were developed which reflect the primary loadings of landing gear of Navy and Air Force fighter aircraft. Spectrum crack growth analysis parameters were adjusted to best fit the spectrum test results from center-cracked panels tested in the dry air environment. Verification test programs involved three series of tests in each steel (Table 4):

Test Series 1—One surface flawed panel in the dry air environment using the accelerated stress history to evaluate predictions of surface flaw growth in an inert environment.

Test Series 2—One center-cracked panel and one surface flawed panel in salt water and sea water using the accelerated stress history to evaluate the predictions of crack growth in an aggressive environment minimizing sustained load effects.

Test Series 3—One center-cracked panel and one surface flawed panel in salt water and sea water using the sustained load stress history to evaluate

TABLE 2—Constant-amplitude test and analysis results in 300M steel.

Specimen Number	Environment	Stress Ratio	Frequency (Hz)	Wave Shape	Cycles to Grow Crack from 1.27 cm to Failure			
					Navy Program		Air Force Program	
					Test	Analysis	Test	Analysis
1	< 10% RH Air ↓	0	10	Sinusoid ↓	140,000	139,000	83,700	78,200
2		0.5	10		370,000	378,000	717,000	488,000
3		-1.0	10		122,000	126,000	109,200	78,000
4	Aggressive Δ ↓	0	10	Trapezoid ↓	155,000	135,000	64,300	62,400
5		0	1.0		94,000	104,000	13,100	15,600
6		0	0.1		22,900	22,500	2,810	2,040
7	Aggressive Δ ↓	0	10	Trapezoid ↓	140,000	132,000	54,800	35,100
8		0	1.0		62,700	59,300	—	—
9		0	0.1		6,210	6,350	369	400
10		0.5	0.1		7,380	6,630	500	407
11		-1.0	0.1		4,010	6,320	540	400

Notes: Δ Aggressive environment for the Navy program was alternate immersion in synthetic sea water for the Air Force program was continuous immersion in 3.5% NaCl salt water

TABLE 3—Constant-amplitude test and analysis results in HP 9-4-0.30 steel.

Specimen Number	Environment	Stress Ratio	Frequency (Hz)	Wave Shape	Cycles to Grow Crack from 1.27 cm to Failure			
					Navy Program		Air Force Program	
					Test	Analysis	Test	Analysis
1	<10% RH Air ↓	0	10	Sinusoid ↓	137,000	139,000	121,200	114,300
2		0.5	10		390,000	370,000	427,000	402,800
3		-1.0	10		115,800	127,000	94,400	106,100
4	Aggressive Δ ↓	0	10	↓	131,000	139,000	129,500	114,300
5		0	1.0		101,900	139,000	89,500	114,300
6		0	0.1		62,000	56,300	61,100	114,300
7	↓	0	10	Trapezoid ↓	108,500	139,000	131,300	114,300
8		0	1.0		149,400	139,000	—	—
9		0	0.1		54,000	56,500	95,000	114,300
10		0.5	0.1		179,000	136,000	218,000	170,300
11		-1.0	0.1		48,000	52,000	108,900	106,100

Notes: Δ Aggressive environment for the Navy program was alternate immersion in synthetic sea water for the Air Force program was continuous immersion in 3.5% NaCl salt water

TABLE 4—Algorithm verification test program summary.

Specimen Number	Environment	Load Frequency (Hz)	Objective
1	<10% RH Air	~ 10	Evaluate Crack Growth in Inert Environment
2	Aggressive ^①	~ 10	Evaluate Crack Growth in Aggressive Environment
3	Aggressive	~0.1 ^②	Evaluate Crack Growth with Sustained Load in Aggressive Environment

Notes: ^① Aggressive environment for the Navy program was alternate immersion in synthetic sea water, for the Air Force program was continuous immersion in 3.5% NaCl salt water

^② The time sequence of loads is presented in Figure 10

predictions of crack growth under maximum conditions of sustained load and aggressive environment.

The Navy landing gear spectrum is characterized by a few occurrences of high stress levels caused by high sink rate landings and many occurrences of very low stress levels caused by ground handling loadings (taxiing, turning, pivoting, and braking). This stress spectrum differs significantly from the Air Force gear spectrum. Exceedance curves for these spectra are compared in Fig. 9. Ground handling stress levels in the Navy spectrum are no greater than 35 percent of the maximum stress level in the spectrum, while ground handling stress levels in the Air Force spectrum exceed 70 percent of the maximum stress level. This difference in relative stress level due to ground handling loads makes the Navy spectrum much less severe, from a crack growth life point of view, than the Air Force spectrum.

The majority of sustained loads in fighter aircraft landing gear occur during ground handling, especially during braking. Because ground handling stresses in Navy gear are smaller than in Air Force gear, sustained stress levels in Navy gear are much lower than sustained stress levels in Air Force gear. This difference is reflected in the comparison of real time stress histories for Navy and Air Force gear shown in Fig. 10.

The greater severity of the Air Force gear loading as compared with Navy landing gear was verified by comparison of analysis and test lives for surface flawed panels tested to the Air Force and Navy spectra (Table 5). These results indicate that the Air Force landing gear spectrum is significantly more severe than the Navy spectrum for identical initial flaw sizes and maximum stress levels. The initial flaw sizes used in this comparison were selected to provide at least 8000 landings for the Navy spectrum. Even so,

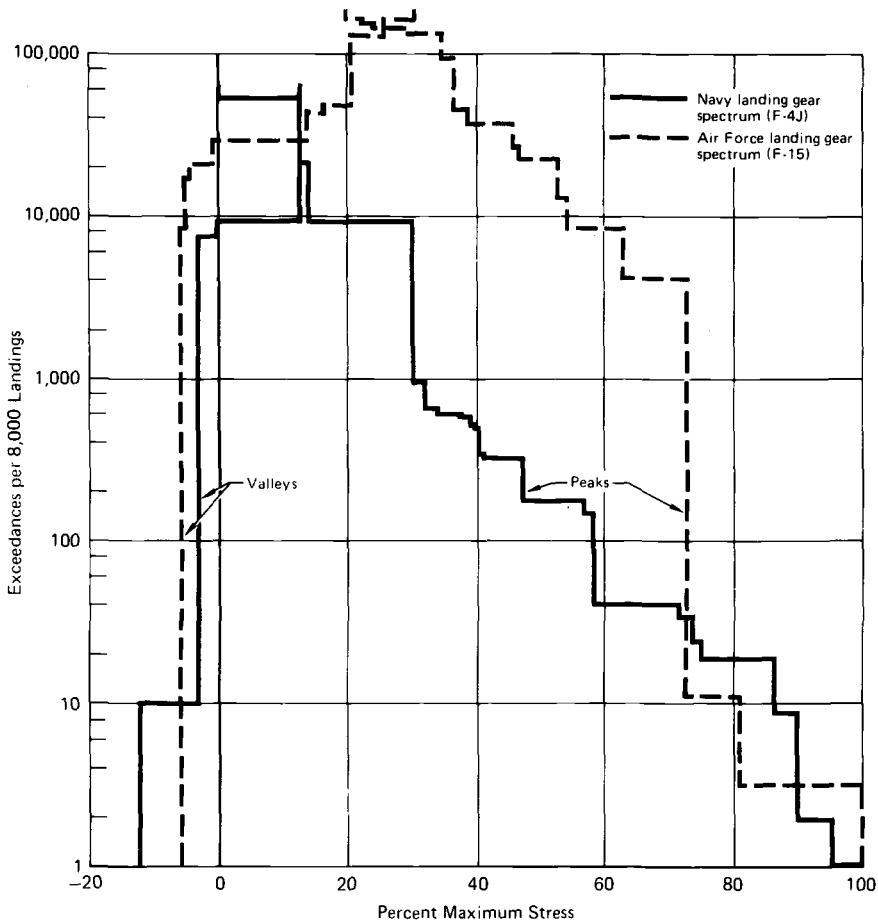


FIG. 9—Comparison of Navy and Air Force main landing gear stress spectra.

these flaw lengths are very close to those at failure; in fact, the crack length at failure in 300M is smaller than the initial flaw length in HP 9-4-0.30.

The maximum stress level used in the HP 9-4-0.30 tests was 85 percent of ultimate strength. This is typical of values used in landing gear components. Consequently, maximum stress levels for 300M steel usually exceed 1276 MN/m^2 in landing gear components. Even so, both test and analysis results show that 300M steel is more sensitive to environment and load variations than is HP 9-4-0.30 steel. The correlation of test and analysis results is good for the range of load spectra and environments used in these studies.

The implication of these data is that cracks will not grow in landing gear of Navy aircraft at stress levels which produce adequate life for Air Force aircraft. However, service experience shows that corrosion cracking is a primary

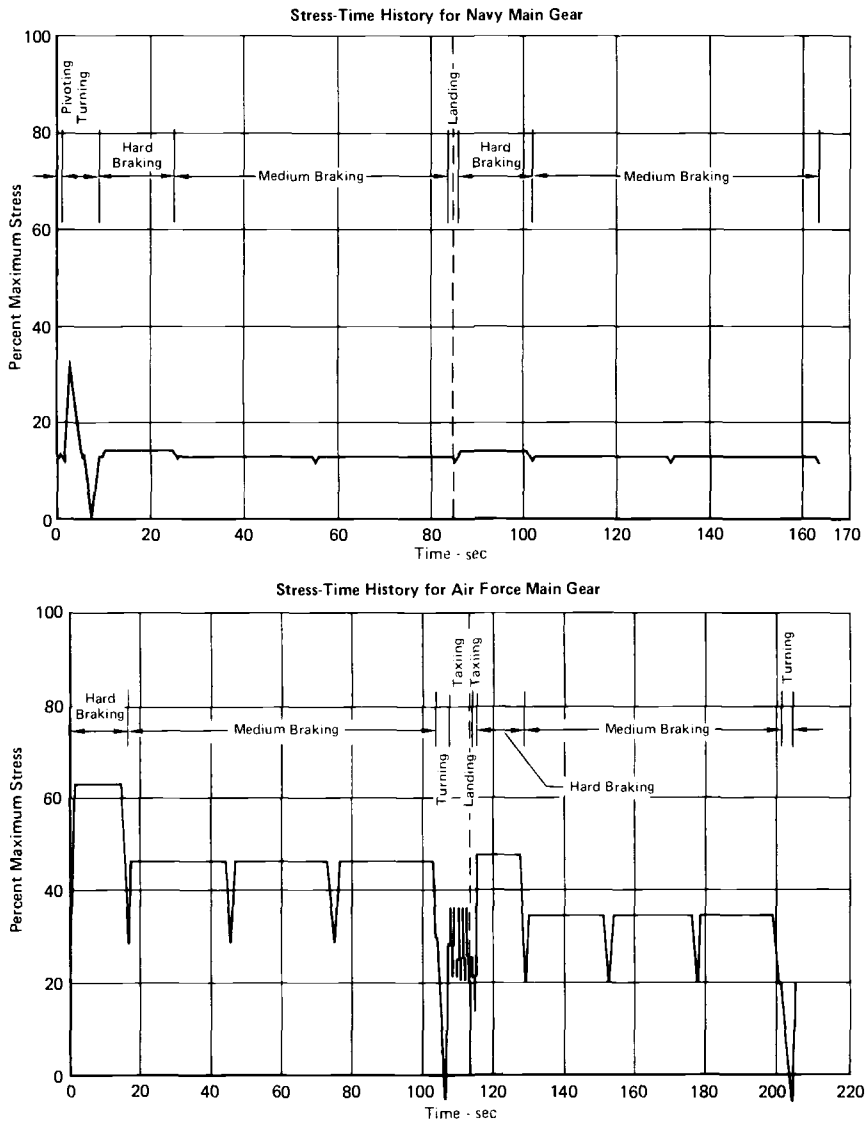


FIG. 10—Comparison of stress-time histories for Navy and Air Force landing gear.

cause for Navy gear replacement in the field [1]. This cracking is caused by high residual tensile stresses in local regions or by actuator loadings or other loadings independent of the primary loading of the gear during landings. To minimize crack growth in Navy gear, residual stresses, actuator loadings, or redundant loads may require more attention during design than stresses caused by primary loading.

TABLE 5—Comparison of spectrum test and analysis lives.

Steel Material	Environment ¹	Sustained Loads	Crack Growth Life - Landings ²			
			Navy Spectrum		Air Force Spectrum	
			Test	Analysis	Test	Analysis
300M	Dry Air	No	10,780	11,780	60	187
	Aggressive	No	11,370	11,780	60	84
	Aggressive	Yes	3,780	3,780	12	4.2
HP9-4-0.30	Dry Air	No	11,370	11,780	500	500
	Aggressive	No	9,370	11,780	510	385
	Aggressive	Yes	7,990	11,780	500	385

Notes: ¹ Aggressive environment for the Navy spectrum is alternate immersion in synthetic sea water, for the Air Force spectrum is continuous immersion in 3.5% NaCl salt water

² Initial flaw lengths are 0.290 cm in 300M steel and 0.706 cm in HP 9-4-0.30. Maximum stress level for both spectra is 1,276 MN/m²

Conclusions

Results of these research programs indicate that immersion in either salt or sea water accelerates crack growth in 300M steel. The acceleration decays with drying time after immersion, which indicates that continuous immersion is a more aggressive environment for crack growth in 300M steel than is alternate immersion.

Immersion in salt or sea water has little impact on crack growth rate in HP 9-4-0.30 steel except at stress intensity factor ranges below 33 MN/m^{3/2}. Alternate immersion at low cycle rates tends to increase apparent threshold stress intensity factor ranges from below 7.7 MN/m^{3/2} at 10 Hz to 33 MN/m^{3/2} at 0.1 Hz. Below these apparent threshold values, crack growth arrests during the drying portion of the immersion cycle and does not reinitiate during subsequent immersions.

Crack growth in alternate immersion environments, such as that applied in this program, can be accurately predicted using linear summation of sustained load crack growth rates derived from cyclic tests in an aggressive environment and cyclic crack growth rates determined from tests in an inert environment. The decay in crack growth rate following removal from an aggressive environment is accurately predicted by a function which decays exponentially with time after removal.

The landing gear stress histories for Navy and Air Force fighter aircraft differ significantly due to the high sink rates to which Navy gear are designed. Sustained stress levels in Navy gear due to primary gear loads are considerably lower than sustained stresses in Air Force gear. This difference makes Navy gear generally less sensitive to crack growth, in any environment, than Air Force gear.

Acknowledgments

These programs were sponsored by the Naval Air Development Center under Contract No. N62269-79-C-0275 and by the Air Force Wright Aeronautical Laboratories under Contract No. F33615-76-C-3133. The excellent laboratory work of K. C. Garland of McDonnell Aircraft Metallurgical Laboratory is gratefully acknowledged.

References

- [1] Saff, C. R., "Environment-Load Interaction Effects on Crack Growth in Landing Gear Steels," NADC-79095-60, Oct. 1980.
- [2] Dill, H. D. and Saff, C. R., "Environment-Load Interaction Effects on Crack Growth," AFFDL-TR-78-137, Nov. 1978.
- [3] Wei, R. P. and Landes, J. D., *Materials Research and Standards*, Vol. 9, No. 7, July 1969, pp. 25-28.
- [4] Pao, P. S., Wei, W., and Wei, R. P., "Effect of Frequency on Fatigue Crack Growth Response of AISI 4340 Steel in Water Vapor," in *Proceedings*, Symposium on Environment Sensitive Fracture of Engineering Materials, Metallurgical Society of AIME, 1977.
- [5] Willenborg, J., Engle, R. M., and Wood, H. A., "A Crack Growth Prediction Model Using an Effective Stress Concept," AFFDL-TM-71-1FBR, 1971.

Analysis Methodology

Prediction of Fatigue Crack Growth under Variable-Amplitude and Spectrum Loading Using a Closure Model

REFERENCE: Newman, J. C., Jr., "Prediction of Fatigue-Crack Growth under Variable-Amplitude and Spectrum Loading Using a Closure Model," *Design of Fatigue and Fracture Resistant Structures, ASTM STP 761*, P. R. Abelkis and C. M. Hudson, Eds., American Society for Testing and Materials, 1982, pp. 255-277.

ABSTRACT: The present paper is concerned with the application of an analytical crack-closure model in the study of crack growth under various load histories. The model was based on a concept like the Dugdale model, but modified to leave plastically deformed material in the wake of the advancing crack tip.

The model was used to correlate crack growth rates under constant-amplitude loading, and to predict crack growth under variable-amplitude and aircraft-spectrum loading on 2219-T851 aluminum alloy sheet material. Predicted crack-growth lives agreed well with experimental data. For 80 crack growth tests subjected to various load histories, the ratio of predicted-to-experimental lives, N_p/N_T , ranged from 0.5 to 1.8. The mean value of N_p/N_T was 0.97 and the standard deviation was 0.27.

KEY WORDS: cracks, crack propagation, stress analysis, fatigue (materials)

Nomenclature

- C_k Material crack growth constants ($k = 1, 5$)
- c Half length of crack, m
- c_f Half length of final crack, m
- c_i Half length of initial crack, m
- c_n Half length of starter notch, m
- d Half length of crack plus tensile plastic zone, m
- F Boundary-correction factor on stress intensity
- K_{\max} Maximum stress-intensity factor, $\text{MPa} \cdot \text{m}^{1/2}$

¹Research Engineer, NASA-Langley Research Center, Hampton, Va. 23665.

K_F	Elastic-plastic fracture toughness, $\text{MPa} \cdot \text{m}^{1/2}$
m	Fracture toughness parameter
N	Number of cycles
N_P	Number of cycles predicted from analysis
N_T	Number of cycles from test specimen
R	Stress ratio (S_{\min}/S_{\max})
S	Applied stress, MPa
S_{\max}	Maximum applied stress, MPa
S_{\min}	Minimum applied stress, MPa
S_o	Crack-opening stress, MPa
t	Specimen thickness, m
W	Specimen width, m
α	Constraint factor, $\alpha = 1$ for plane stress and $\alpha = 3$ for plane strain
ΔK	Stress-intensity factor range, $\text{MPa} \cdot \text{m}^{1/2}$
ΔK_{eff}	Effective stress-intensity factor range, $\text{MPa} \cdot \text{m}^{1/2}$
ΔK_o	Effective threshold stress-intensity factor range, $\text{MPa} \cdot \text{m}^{1/2}$
ΔK_{th}	Threshold stress-intensity factor range, $\text{MPa} \cdot \text{m}^{1/2}$
ΔS_{eff}	Effective stress range, MPa
ρ	Length of tensile plastic zone, m
ρ_{OL}	Plastic-zone size calculated from overload, m
σ_o	Flow stress (average between σ_{ys} and σ_u), MPa
σ_{ys}	Yield stress (0.2 percent offset), MPa
σ_u	Ultimate tensile strength, MPa
ω	Length of compressive plastic zone, m

During fatigue-crack propagation, crack surfaces remain closed during part of a load cycle. Crack closure is caused by residual plastic deformations remaining in the wake of an advancing crack. The crack-closure concept, using the effective stress-intensity factor range, has been used to correlate crack growth rates under constant-amplitude loading [1,2].² Crack closure is also a significant factor in causing load-interaction effects on crack growth rates (retardation and acceleration) under variable-amplitude loading.

The crack-closure phenomenon has been analyzed using two-dimensional, elastic-plastic, finite-element methods [3-6]. The finite-element analyses were shown to be quite accurate, but were very complicated and required large computing facilities. There have also been several attempts to develop simple analytical models of crack closure [3,7-13]. All of these models were based on a concept similar to the Dugdale model [14] or strip-yield model, but modified to leave plastically deformed material in the wake of the crack. Newman [3], Budiansky and Hutchinson [8], and Fühling and Seeger

²The italic numbers in brackets refer to the list of references appended to this paper.

[10,11] studied only the crack-closure behavior. Kanninen and Atkinson [13], using an inclined strip-yield model, studied both residual-stress and crack-closure effects. Dill and Saff [7], Hardrath, et al [9], and Newman [12] used the crack-opening stresses from their models to predict crack growth under spectrum loading.

The purpose of the present paper is to apply an analytical crack-closure model [12], which simulates plane-stress and plane-strain conditions, to crack growth under various load histories. The model was based on the Dugdale model [14], but modified to leave plastically deformed material along the crack surfaces as the crack advances. Plane-stress and plane-strain conditions were simulated by using a "constraint" factor on tensile yielding.

The crack-closure model developed in Ref 12 was for a central crack in a finite-width plate that was subjected to a uniformly applied stress. To calculate Elber's effective stress-intensity factor range [2], crack-opening stresses were calculated from the model under constant-amplitude loading at various applied stress levels and stress ratios. Experimental crack-growth rate data from 2219-T851 aluminum alloy sheet material under constant-amplitude loading [15] were correlated with the effective stress-intensity factor range for a wide range of stress levels and stress ratios. An equation developed in Ref 12 relating crack growth rate to effective stress-intensity factor range, threshold stress-intensity factor range, and fracture toughness was used herein for the complete range of crack growth rates. The closure model was then used to predict crack growth in 2219-T851 aluminum alloy sheet material under variable-amplitude and aircraft-spectrum loading [15].

Analytical Crack-Closure Model

The following section is a brief description of the analytical crack-closure model developed in Ref 12.

To calculate crack-closure and crack-opening stresses during crack propagation, the elastic-plastic solution for stresses and displacements in a cracked body must be known. Because there are no closed-form solutions to elastic-plastic cracked bodies, simple approximations must be used when finite-element solutions are inappropriate. The Dugdale model [14] is one such approximation. The crack-surface displacements, which are used to calculate contact (or closure) stresses under cyclic loading, are influenced by plastic yielding at the crack tip and residual deformations left in the wake of the advancing crack. The applied stress level at which the crack surfaces become fully open (no surface contact) is directly related to contact stresses. This stress is called the "crack-opening stress".

The model was developed for a central crack in a finite-width specimen subjected to uniform applied stress (Fig. 1). The model was based on the Dugdale model, but modified to leave plastically deformed material in the wake of the crack. The primary advantage in using this model is that the

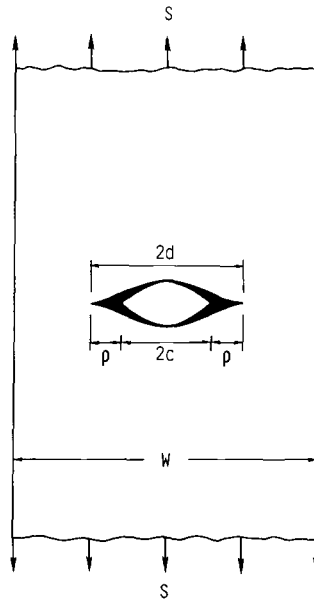


FIG. 1—Center-crack tension specimen with Dugdale plastic zones and residual plastic deformations.

plastic-zone size and crack-surface displacements are obtained by superposition of two elastic problems: a crack in a finite-width plate subjected to (1) a remote uniform stress, S , or (2) a uniform stress, σ , applied over a segment of the crack surface. The stress-intensity factor and crack-surface displacement equations for these loading conditions are given in Ref 12.

Figure 2 shows a schematic of the model at maximum and minimum applied stresses. The model was composed of three regions: (1) a linear elastic region containing a fictitious crack of half-length $c + \rho$, (2) a plastic region of length ρ , and (3) a residual plastic deformation region along the crack surfaces. The physical crack is of half length c . The compressive plastic zone is ω . Region 1 was treated as an elastic continuum; the crack-surface displacements under various loading conditions are given in Ref 12. Regions 2 and 3 were composed of rigid-perfectly plastic (constant stress) bar elements with a flow stress, σ_o , which is the average between the yield stress, σ_{ys} , and the ultimate tensile strength, σ_u . The shaded regions in Figs. 2a and 2b indicate material which is in a plastic state. At any applied stress level, the bar elements are either intact (in the plastic zone) or broken (residual plastic deformation). The broken elements carry compressive loads only, and then only if they are in contact. The elements yield in compression when the contact stress reaches $-\sigma_o$. Those elements that are not in contact do not effect

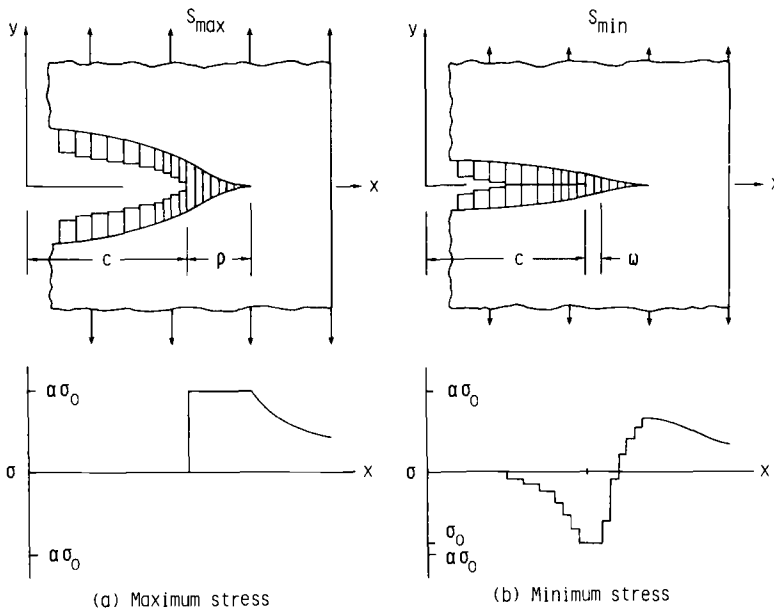


FIG. 2—Crack-surface displacements and stress distributions along crack line.

the calculation of crack-surface displacements. To account for the effects of state of stress on plastic-zone size, a constraint factor α was used to elevate the tensile flow stress for the intact elements in the plastic zone. The effective flow stress $\alpha\sigma_0$ under simulated plane-stress conditions was σ_0 and under simulated plane-strain conditions was $3\sigma_0$. The constraint factor is a lower bound for plane stress and an approximate upper bound for plane strain. These constraint factors were verified using elastic-plastic finite-element analyses of cracked bodies under plane-stress [6] and plane-strain conditions. The procedure used to establish the constraint factor α used herein is discussed later.

The analytical crack-closure model, discussed in detail in Ref 12, was used to calculate crack-opening stresses, S_o , as a function of crack length and load history. In turn, the crack-opening stress was used to calculate the effective stress-intensity factor range, as proposed by Elber, and, consequently, the crack growth rates.

Fatigue Crack Growth Rate Equation

The crack growth equation proposed by Elber [2] states that the crack growth rate is a power function of the effective stress-intensity factor range only. Later, Hardrath et al [9] showed that the power law was inadequate at

high growth rates approaching fracture. The results presented in Ref 12 showed that it was also inadequate at low growth rates approaching threshold. To account for these effects, the power law was modified in Ref 12 to

$$\frac{dc}{dN} = C_1 \Delta K_{\text{eff}}^{C_2} \frac{1 - \left(\frac{\Delta K_o}{\Delta K_{\text{eff}}} \right)^2}{1 - \left(\frac{K_{\text{max}}}{C_5} \right)^2} \quad (1)$$

where

$$\Delta K_o = C_3 \left(1 - C_4 \frac{S_o}{S_{\text{max}}} \right) \quad (2)$$

$$K_{\text{max}} = S_{\text{max}} \sqrt{\pi c} F \quad (3)$$

and

$$\Delta K_{\text{eff}} = (S_{\text{max}} - S_o) \sqrt{\pi c} F \quad (4)$$

The crack-opening stresses, S_o , were calculated from the analytical closure model. Equation 1 gives the "sigmoidal" shape commonly observed when fatigue crack growth rate data is plotted against stress-intensity factor range. In the intermediate range of crack growth rates, Eq 1 is basically Elber's proposed power law, $C_1 \Delta K_{\text{eff}}^{C_2}$. The constants C_1 to C_5 were determined to best fit experimental data under constant-amplitude loading.

The coefficients C_3 and C_4 were determined from threshold data on the 2219-T851 aluminum alloy sheet material from Ref 16. The effective threshold stress-intensity factor range, ΔK_o , was determined from the threshold stress-intensity factor range, ΔK_{th} , as

$$\Delta K_o = U \Delta K_{\text{th}} = \frac{1 - \frac{S_o}{S_{\text{max}}}}{1 - R} \Delta K_{\text{th}} \quad (5)$$

The coefficient C_5 is the elastic stress-intensity factor at failure under cyclic loading or "cyclic" fracture toughness, like the static fracture toughness K_{c} . Of course, toughness computed from an elastic analysis, in general, is not a material constant, but varies with crack length, width, thickness, and specimen type. In the present application, C_5 is the largest value of toughness that can be sustained by a given width, thickness, and specimen type. C_5 was computed to be 77 MPa·m^{1/2} for the 150-mm-wide center-crack tension specimens using the Two-Parameter Fracture Criterion [17] with $K_F = 550$

$\text{MPa} \cdot \text{m}^{1/2}$ and $m = 1$. These values of K_F and m were obtained from final crack lengths and maximum stress levels used in the constant-amplitude crack growth tests from Ref 15 (see Ref 12 for further details).

The coefficients C_1 and C_2 were found from constant-amplitude rate data [15], after C_3 , C_4 , and C_5 were determined, by using a least-squares regression analysis. The constant-amplitude correlations were made using S_o -values computed from the model with various constraint factors. It was found that an α of about 1.9 would give a good correlation under constant-amplitude loading. The procedure used to obtain α will be discussed later. A summary of the coefficients used to correlate the constant-amplitude data with $\alpha = 1.9$ are as follows:

$$\left. \begin{aligned} C_1 &= 2.486 \times 10^{-10} \text{ (} 1.314 \times 10^{-8} \text{)} \\ C_2 &= 3.115 \\ C_3 &= 2.97 \text{ MPa} \cdot \text{m}^{1/2} \text{ (} 2.7 \text{ ksi} \cdot \text{in.}^{1/2} \text{)} \\ C_4 &= 0.8 \\ C_5 &= 77 \text{ MPa} \cdot \text{m}^{1/2} \text{ (} 70 \text{ ksi} \cdot \text{in.}^{1/2} \text{)} \end{aligned} \right\} \quad (6)$$

When SI units are used, ΔK_{eff} and K_{max} are given in $\text{MPa} \cdot \text{m}^{1/2}$ and dc/dN is given in m/cycle . When U.S. Customary units are used, ΔK_{eff} and K_{max} are given in $\text{ksi} \cdot \text{in.}^{1/2}$ and dc/dN is given in $\text{in.}/\text{cycle}$.

Figure 3 shows a plot of ΔK against dc/dN for several R -ratios for 2219-T851 aluminum alloy sheet material to illustrate the sigmoidal shape of Eq 1. The experimental data were obtained from Ref 16 and the curves were calculated from Eq 1. The $R = -1$ data were obtained from a small center-crack tension specimen ($W = 76.2 \text{ mm}$), and the other data were obtained from small compact specimens ($W = 50.8 \text{ mm}$). The crack growth coefficients (C_1 , C_2 , C_3 , and C_4) used to calculate the curves were identical to those shown in Eq 6. However, coefficient C_5 for the small compact specimens was $38.5 \text{ MPa} \cdot \text{m}^{1/2}$ and for the small center-crack specimen was $55 \text{ MPa} \cdot \text{m}^{1/2}$. Again, these coefficients (C_5) were calculated from the Two-Parameter Fracture Criterion [17] using $K_F = 550 \text{ MPa} \cdot \text{m}^{1/2}$ and $m = 1$. The predicted crack growth rate curves in Fig. 3 are in good agreement with the experimental data.

Application of the Crack-Closure Model and Rate Equation

The analytical crack-closure model [12] and crack growth program (FAST-Fatigue Crack Growth Analysis of Structures) was applied to constant-amplitude, variable-amplitude, and aircraft-spectrum loading on 2219-T851 aluminum alloy sheet material.

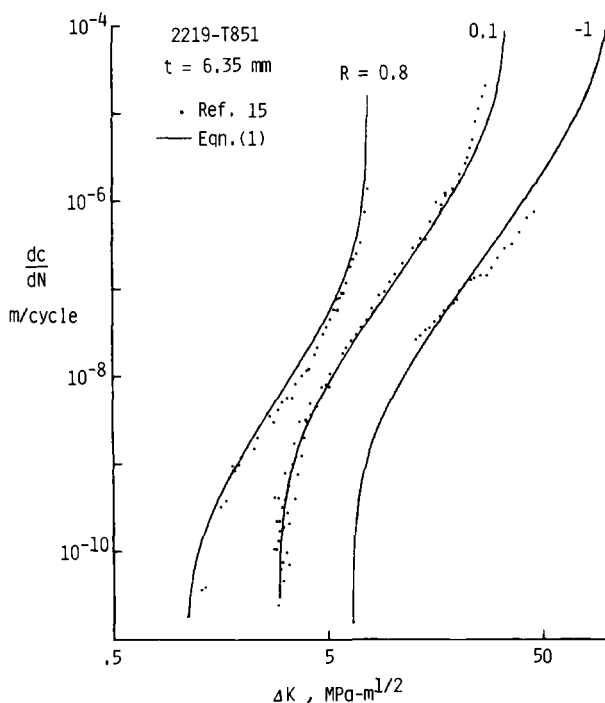


FIG. 3—Comparison of experimental crack growth rates and rate equation for 2219-T851 aluminum alloy at various R -ratios.

Under constant-amplitude loading, the model was exercised under simulated plane stress, plane strain, and conditions between these limits. The particular constraint factor α used herein to approximate the state of stress was obtained from the constant-amplitude crack growth rate data. The crack growth rate equation (Eq 1) was also determined from the constant-amplitude data.

The same constraint factor was also used to predict crack growth under variable-amplitude and aircraft-spectrum loading. Crack-opening stresses were calculated from the model as a function of crack length and load history, and the crack growth rates were predicted from Eq 1. Predicted crack growth lives are compared with experimental data in the following sections.

Constant-Amplitude Loading

Crack-Opening Stresses

Reference 12 showed that the calculated crack-opening stresses under constant-amplitude loading were independent of the constraint factor for

stress ratios, R , greater than about 0.7 and were equal to the minimum applied stress. Thus ΔK_{eff} is equal to ΔK for $R \geq 0.7$. Using crack growth rate data from Refs 15 and 16 for $R \geq 0.7$, the crack growth constants C_1 and C_2 were determined to best fit the high R -value data only. Basically, this crack growth rate equation (Eq 1) depicts the relation between ΔK_{eff} and crack growth rate. If ΔK_{eff} and dc/dN have a unique relationship, then crack growth rates from tests at R -ratios less than 0.7 should determine the experimental ΔK_{eff} and, consequently, the experimental value of S_o . This value of S_o is referred to as the "semi-empirical" crack-opening stress. For each test, the semi-empirical S_o -value was assumed to be constant and was determined from a least-squares regression analysis. These crack-opening stresses, normalized by the maximum applied stress, are shown in Fig. 4 as a function of the R -ratio (symbols). The open symbols and the solid circular symbol are results from center-crack tension (CCT) specimens [15,16]. The solid triangular symbols are results from compact specimens [16]. These results indicate S_o -values that correlate crack growth rate data at various R -ratios with the results at $R \geq 0.7$. The dashed line indicates where S_o is equal to S_{min} or where ΔK_{eff} is equal to ΔK .

For R -ratios less than 0.7, the calculated crack-opening stresses from the closure model are a function of the constraint factor. The semi-empirical results at $R = 0$ were used to estimate the constraint factor. A value of 1.9 was found to give good agreement between the calculated and semi-empirical values. The solid curves show calculations from the closure model with $\alpha = 1.9$ for various applied stress levels. The overall agreement between the calculated and semi-empirical values was considered reasonable.

Crack Growth Calculations

The crack-closure model with $\alpha = 1.9$ was used to calculate the crack growth lives from the initial crack length c_i to the final crack length c_f for the constant-amplitude tests [15] used in Fig. 4. The ratio of predicted-to-experimental lives, N_p/N_T , ranged from 0.6 to 1.8. The mean value of N_p/N_T was 1.01 and the standard deviation was 0.32. These calculations were considered reasonable in view of the scatter that occurs in fatigue crack growth rate tests.

Variable-Amplitude Loading

Crack-Opening Stresses

The closure model ($\alpha = 1.9$) was used to study the crack-opening stresses under various load histories. The calculated crack-opening stresses under single-spike and two-level loading are shown in Fig. 5 as a function of crack length. Under spike loading, S_o takes a sudden drop when the crack-tip

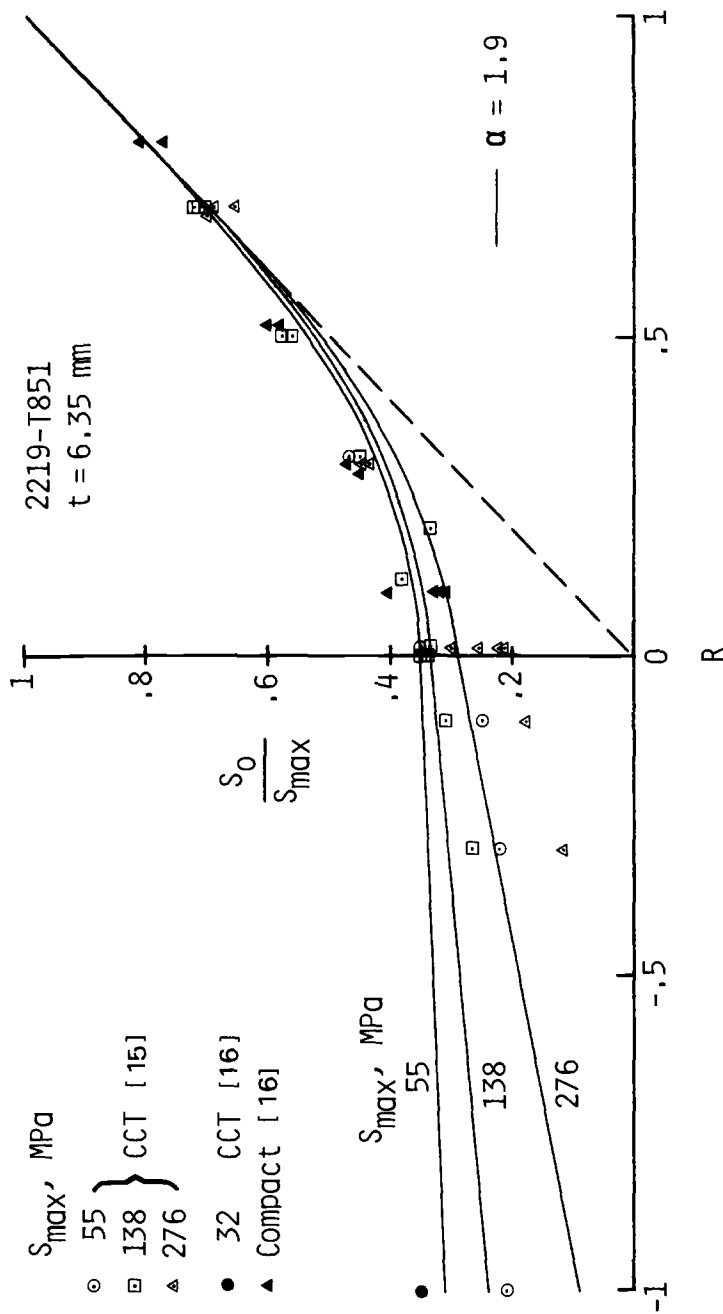


FIG. 4—Comparison of semi-empirical and calculated crack-opening stresses as functions of stress ratio, R , and stress level, S_{max}' .

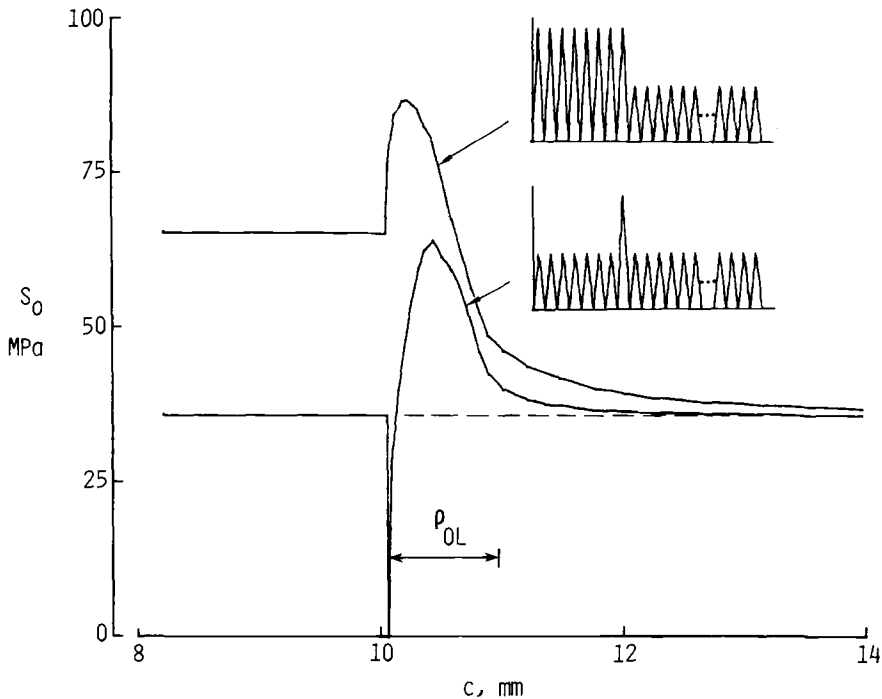


FIG. 5—Comparison of calculated crack-opening stresses during two-level and single-spike loading as a function of crack length.

region blunts due to the spike loading. As the crack grows into the overload plastic zone, ρ_{OL} , the S_o -values rapidly increase until they reach a maximum value at about one half of ρ_{OL} . This is the point of minimum crack growth rate. The S_o -values then drop and approach the stabilized crack-opening stress (dashed line) for the low-level constant-amplitude loading. The retardation effects (S_o greater than dashed line) are nearly eliminated when the crack has grown about one overload plastic-zone size. In contrast, under two-level loading the high load was applied from the initial crack length ($c_i = 3$ mm) for about 2500 cycles. Again, the S_o -values rapidly increase as the crack grows into the overload plastic zone, but they reach higher values than those occurring under the single-spike loading. Thus, retardation effects are much stronger after multi-overloads than after single-spike loading.

The calculated crack-opening stresses under compression-tension and tension-compression spike loading are shown in Fig. 6 as a function of crack length. The horizontal line is the crack-opening stress for the high R -ratio (0.5) constant-amplitude loading. Under compression-tension spike loading, the "compressive underload" (single downward load excursion) had no influence on the subsequent S_o -values. But the tensile overload caused the S_o -

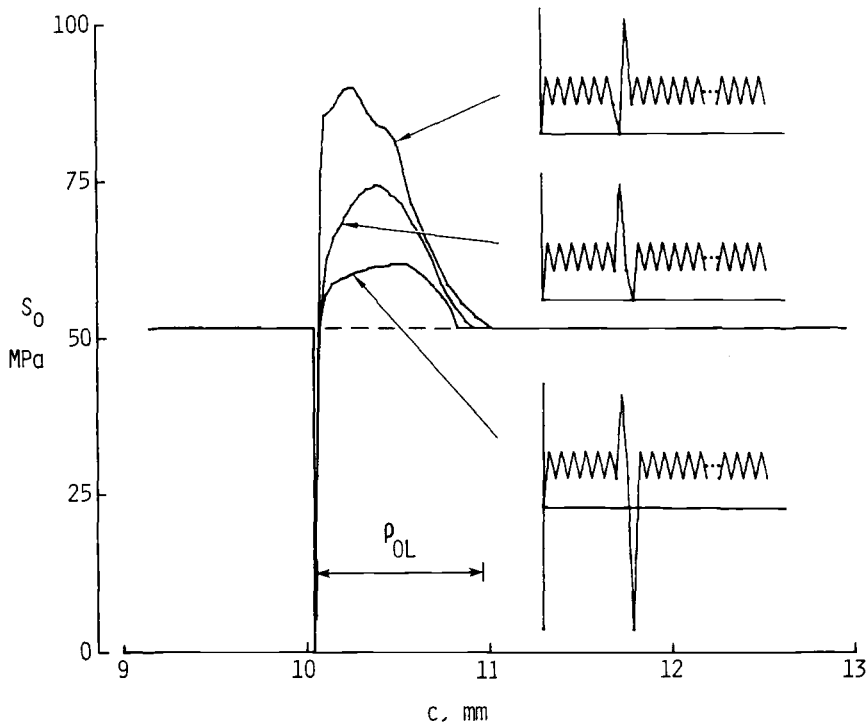


FIG. 6—Comparison of calculated crack-opening stresses during compression-tension and tension-compression spike loading as a function of crack length.

values to be higher than those from the steady-state constant-amplitude loading (dashed line) for about one overload plastic-zone size. If the compressive underload is applied immediately after the tensile overload, the S_o -values are considerably lower than those from the compression-tension spike loading. Thus the compressive underload after the spike eliminates some of the retardation effects due to the tensile overload. A larger compressive underload after the spike causes a larger reduction in the S_o -values, but did not completely eliminate the retardation effect due to the tensile overload.

Figure 7 shows the calculated crack-opening stresses during repeated compression-tension spike loading as a function of crack length. The first load level ($i = 1$) was applied for 2500 cycles. The compression-tension spike ($i = 2$) was then applied. These load sequences were repeated until the specimen failed. The dashed line shows the stabilized crack-opening stress, S_{o1} , for Level 1 only. The dash-dot line shows the stabilized crack-opening stress if only Level 2 were applied. These results show that the interaction between Levels 1 and 2 causes S_o -values to increase slightly during the compressive underload, drop abruptly during the tensile overload, and rapidly

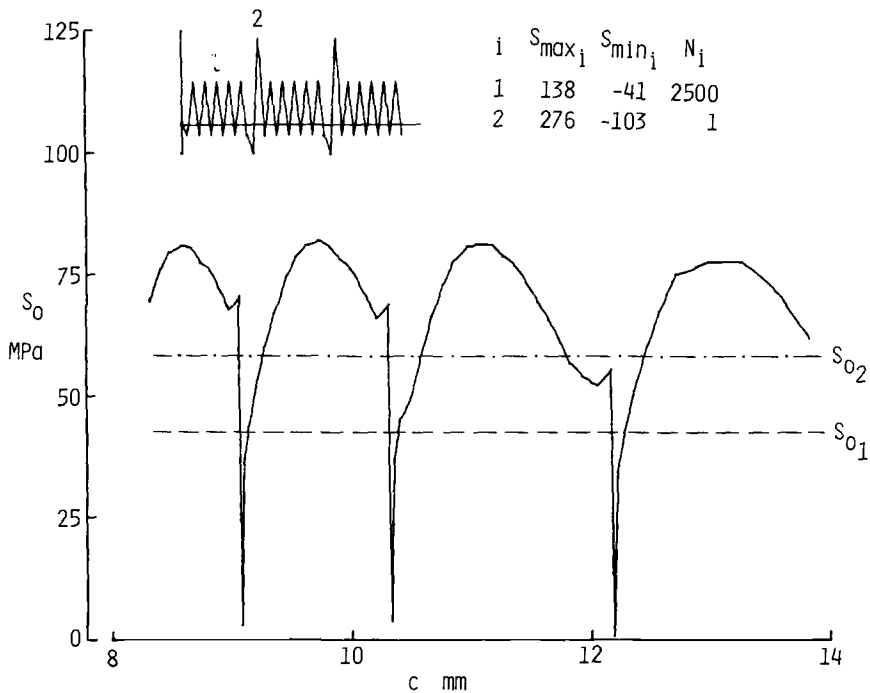


FIG. 7—Calculated crack-opening stresses during repeated spike loading as a function of crack length.

increase during the application of the 2500 cycles. Again, the S_o -values reach a maximum as the crack grows into the plastic zone caused by the tensile overload. The S_o -values would approach S_{o1} if the tensile overload were not repeated.

Crack Growth Predictions

The crack growth rate at each load cycle was computed from Eq 1 using the current values of S_{\max} , S_{\min} , and S_o . Equation 1 predicts retardation (or acceleration) if S_o is larger (or smaller) than the crack-opening stress that would have been produced under constant-amplitude loading at S_{\max} and S_{\min} . To demonstrate how crack growth rates were calculated under variable-amplitude loading, an example is given. Figure 8 shows a typical variable-amplitude load history. The growth rate was computed from Eq 1 using

$$\Delta K_{\text{eff}} = \Delta S_{\text{eff}k} \sqrt{\pi c} F \quad (7)$$

where $\Delta S_{\text{eff}k}$ is the effective stress range of the k th cycle. The growth increment per cycle is

$$\Delta c_k = \left(\frac{dc}{dN} \right)_k \quad (8)$$

On the first and second tensile load excursion, $S_{\min k}$ to $S_{\max k}$,

$$\Delta S_{\text{eff}k} = S_{\max k} - S_o \quad (9)$$

where $k = 1$ or 2 , respectively. This equation was proposed by Elber [2]. However, on the third tensile load excursion $S_{\min 3}$ is greater than S_o . Therefore the effective stress range was assumed to be

$$\Delta S_{\text{eff}k} = [(S_{\max k} - S_o)^{C_2} - (S_{\min k} - S_o)^{C_2}]^{1/C_2} \quad (10)$$

where $k = 3$ and C_2 is the power on the growth law. Thus, the growth increment, $\Delta c_2 + \Delta c_3$, is slightly larger than Δc_1 , if $S_{\max 1} = S_{\max 3}$. The use of Eq 10 was necessary because no crack growth law, when expressed in terms of a power function ($C_2 \neq 1$), would sum to the correct growth increment under variable-amplitude loading. For instance, if the load excursion $S_{\max 2}$ to $S_{\min 3}$ were extremely small, then the sum of growth increments Δc_2 and Δc_3 should be equal to the growth increment Δc_1 . If $S_{\min 3}$ was less than S_o , then the

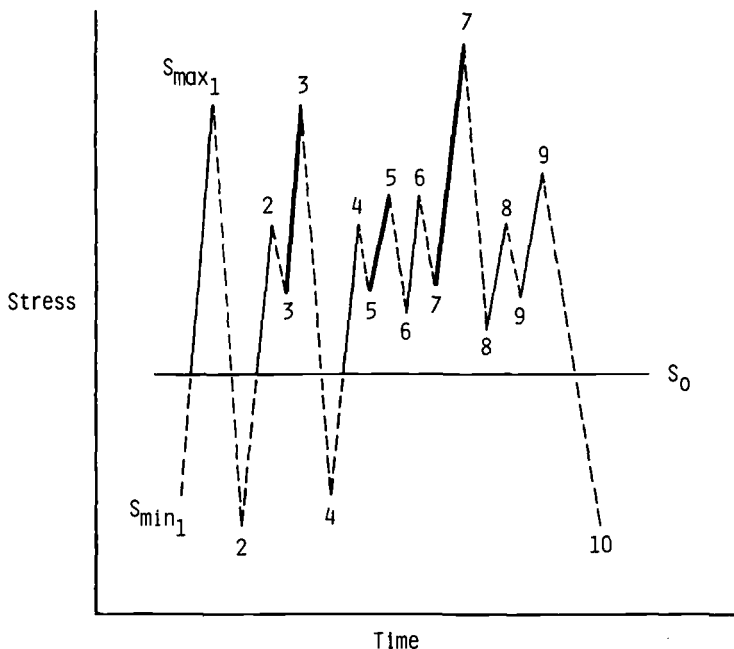


FIG. 8—Variable-amplitude load history.

growth increment Δc_3 should be equal to the growth increment Δc_1 . Equation 10 accounts for these limiting behaviors. Equation 10 is applied only when $S_{\min k}$ is greater than S_o , and only when the current maximum applied stress is higher than the highest maximum stress occurring since a stress excursion crossed S_o . On the fourth excursion, ΔS_{eff} was, again, computed from Eq 9. The effective stress range on the 5th and 7th excursion were, again, computed from Eq 10. But on the 6th, 8th, and 9th excursion,

$$\Delta S_{\text{eff}k} = S_{\max k} - S_{\min k} \quad (11)$$

where $k = 6, 8, \text{ or } 9$, respectively. Note that $S_{\max 6} \leq S_{\max 5}$. Equation 11 was also proposed by Elber [2].

Figure 9 shows the effect of the number of overload cycles on predicted crack growth delay. Crack growth delay is defined as the additional number of cycles required to grow the crack to failure after the overload that is required to grow the crack to failure under constant-amplitude loading only (Level 3). The predicted results (symbols) show that delay or retardation is longer for a larger number of overload cycles. These results are in quantitative agreement with experimental observations [18]. Other retardation

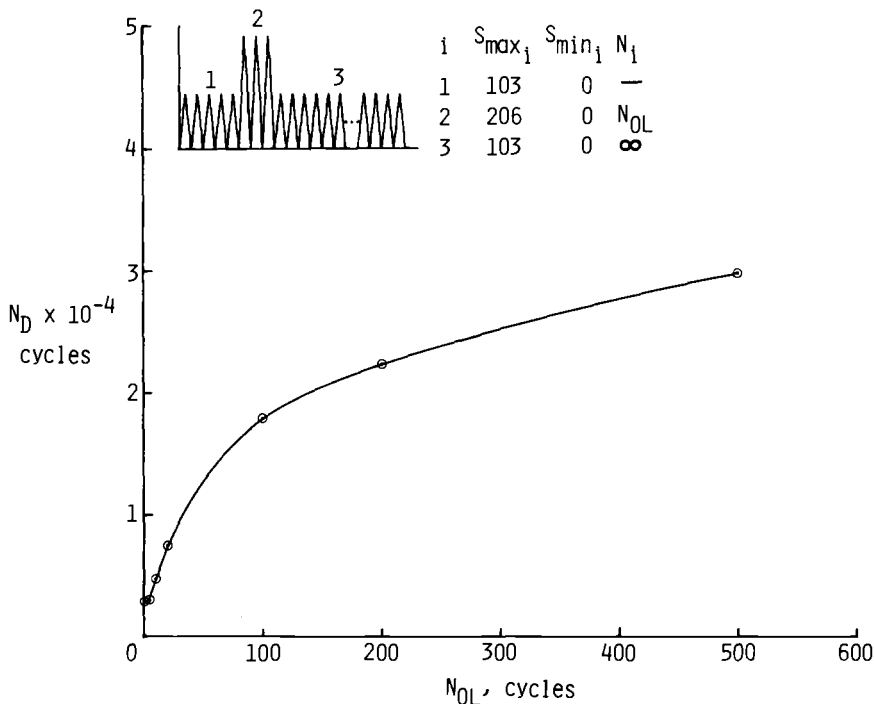


FIG. 9—Effect of the number of overload cycles on predicted crack growth delay.

models [19-21] either do not account for or empirically account for the effect of the number of overload cycles on crack growth retardation.

A comparison between experimental and predicted crack-length-against-cycles curves during two-level loading is shown in Fig. 10. The load sequence is shown in the insert. The high load (Level 1) was a factor-of-2 larger than Level 2. The predicted results (solid curve) were calculated from Eq 1 using the S_o -values computed from the closure model. The maximum computed value of S_o , during the application of Level 2, was about 115 MPa, and the minimum crack growth rate was about 1.4×10^{-7} m/cycle. The predicted results were in fair agreement with the experimental data (symbols). The dash-dot curve shows the predicted results using no load interaction.

Figure 11 shows a comparison of experimental and predicted crack-length-against-cycles curves for repeated tension-compression and compression-tension spike loading. The load sequences applied are shown in the inserts. The experimental results (symbols) and the predicted results (solid curves)

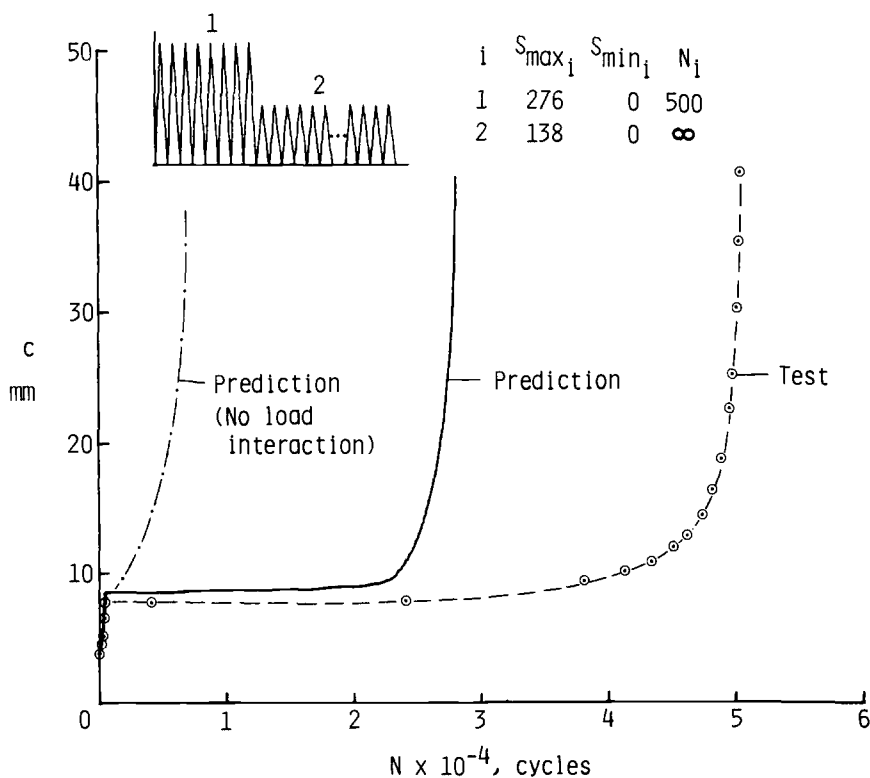


FIG. 10—Comparison of experimental and predicted crack-length-against-cycles curves during two-level loading.

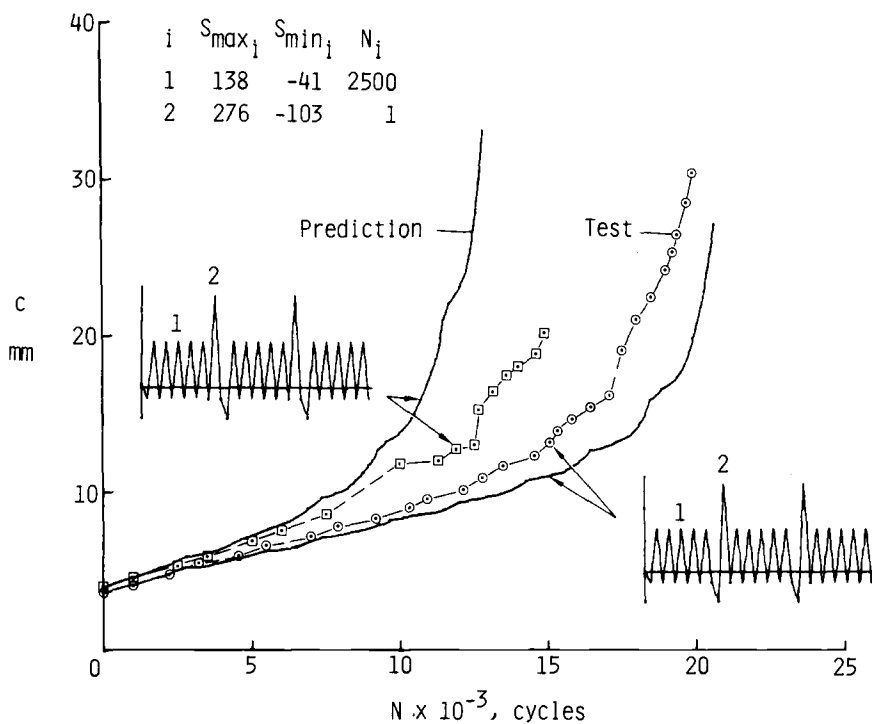


FIG. 11—Comparison of experimental and predicted crack-length-against-cycles curves during repeated tension-compression and compression-tension spike loading.

show that the compressive underload applied after the tensile overload causes the crack to grow faster than when the compressive underload occurs before the tensile overload. Although the predicted results show a stronger effect of the compressive underload than the experimental data, the agreements between the predicted and experimental data are considered good.

A comparison of experimental (symbols) and predicted (solid curve) crack-length-against-cycles curves for a repeated block loading sequence is shown in Fig. 12. The load sequence is shown in the insert. In contrast to the previous case, 50 cycles of the tensile overload were applied before the compressive underload. The predicted results are in good agreement with the experimental data.

Spectrum Loading

Crack-Opening Stresses

The variation of crack-opening stress with crack length for a typical spectrum loading test is shown in Fig. 13. The half length of the elox notch, c_n ,

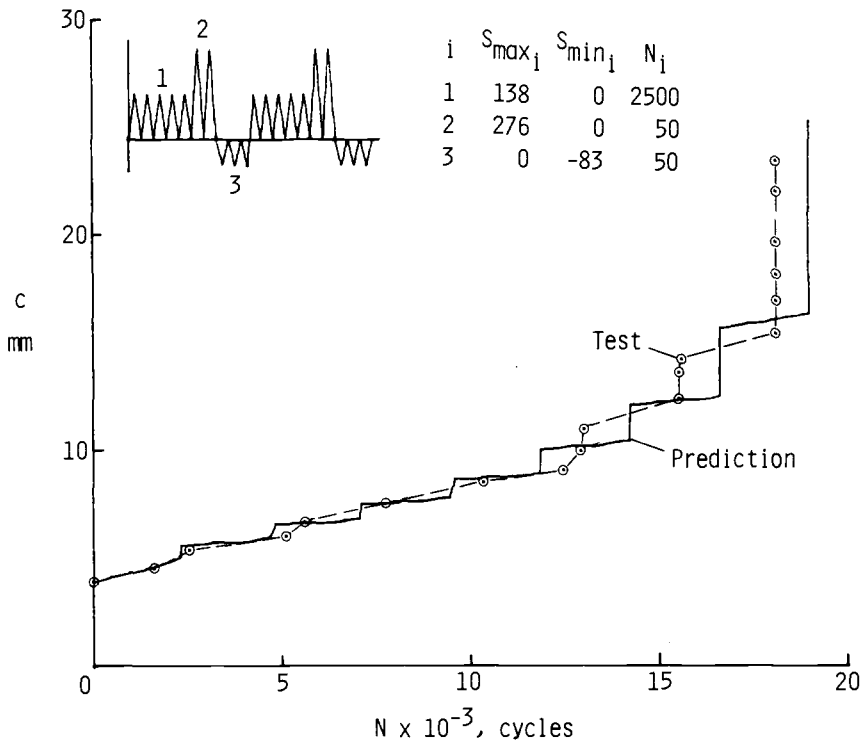


FIG. 12—Comparison of experimental and predicted crack-length-against-cycles curves during repeated block loading.

was 3.2 mm. The specimen was cycled under constant-amplitude loading ($S_{\max} = 69$ MPa) at $R = 0$ until the crack grew to a half length, c_i , of 3.8 mm. Next, a typical fighter-aircraft spectrum was applied to the specimen. The maximum stress was about 183 MPa, and the minimum stress was about -30 MPa. The particular spectrum loads applied are given in Ref 15 under Test M91. The calculated crack-opening stresses plotted in Fig. 13 show only a small fraction of the number of values computed from the model. The crack-opening stresses follow a very irregular pattern while the cyclic loads are applied; even so, they tend to oscillate about a mean value.

The use of an "equivalent" crack-opening stress concept would greatly reduce the computer time required to complete a simulated test. The use of an equivalent stress is justified because, at low to medium stress levels, the crack-opening stresses stabilize under constant-amplitude loading. They also tend to oscillate about a mean value under spectrum loading. The equation for the equivalent crack-opening stress, \bar{S}_o , was

$$\bar{S}_o = \frac{\sum (S_o \Delta c)_k}{\sum \Delta c_k} \quad (12)$$

where the summation was performed over the crack extension increment $c_i + 5 \rho_{\max}$ to $c_i + 10 \rho_{\max}$. The maximum plastic-zone size, ρ_{\max} , was calculated using the maximum stress in the spectrum. (For extremely high stress levels and low R -ratios, where S_o -values do not stabilize, the simulated test specimen may fail before the equivalent crack-opening stress routine is activated.) The dashed line in Fig. 13 shows the calculated equivalent crack-opening stress. The predicted crack growth life using \bar{S}_o was 3.5 percent less than the predicted life using S_o , but the computer time was only about one half as long (2.6 min versus 5.6 min).

Crack Growth Predictions

In Ref 15 crack growth tests were conducted on center-crack tension specimens subjected to five basic aircraft-type load spectra. Three of the spectra were each applied at three different scale factors (same shape spectrum with different scaling of the stresses), and the other two spectra were each applied at two different scale factors. There were 13 different spectrum loading tests.

Figure 14 compares predicted and experimental crack-length-against-

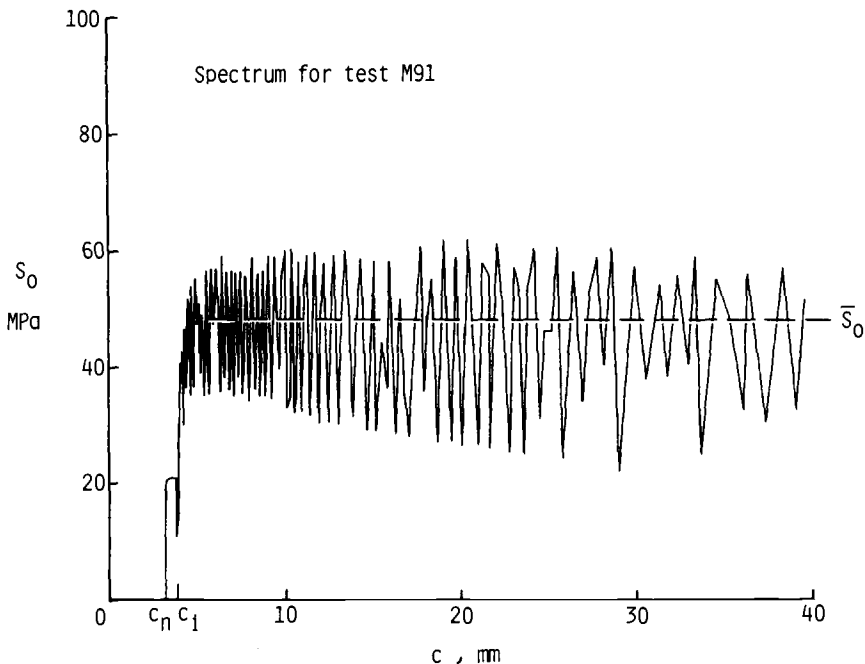


FIG. 13—Calculated crack-opening stresses as a function of crack length under typical aircraft spectrum loading.

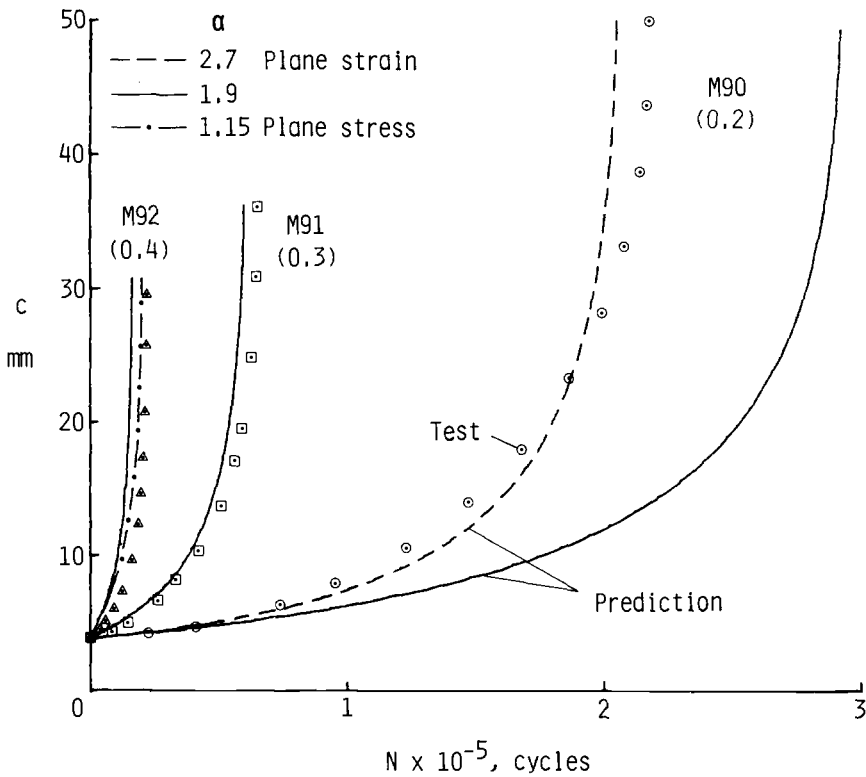


FIG. 14—Comparison of experimental and predicted crack-length-against-cycles curves for spectrum loading.

cycles curves for a typical fighter spectrum. The specimens were subjected to the same spectrum, but with three different scale factors (0.2, 0.3, and 0.4). The predicted results using $\alpha = 1.9$ (solid curves) are in good agreement with the experimental data (symbols). However, for all spectrum tests conducted at a low-stress level (scale factor = 0.2), the predicted results gave longer lives than the experimental data. At the low-stress level, the plastic-zone sizes are small compared with thickness, and plane-strain conditions may prevail. The dashed curve shows calculated results using a constraint factor of 2.7 (plane strain). The results are in excellent agreement with the experimental data, whereas at the high-stress level the predicted results gave shorter lives than the experimental data. At the high-stress level, the plastic-zone sizes are about a factor-of-4 larger than the low-stress level case, and plane-stress conditions may prevail. The dash-dot curve was calculated using $\alpha = 1.15$. The calculated results are in better agreement with the experimental data than the results with $\alpha = 1.9$. These results indicate that the constraint factor may vary with stress level and crack length.

Comparison of Experimental and Predicted Lives

Figure 15 compares experimental, N_T , and predicted, N_P , lives for 18 constant-amplitude load tests, 49 variable-amplitude load tests, and 13 spectrum-load tests. The crack-closure model with $\alpha = 1.9$ was used to predict crack growth lives from the initial crack length c_i to the final crack length c_f . The ratio of predicted-to-experimental lives, N_P/N_T , ranged from 0.5 to 1.8. The mean value of N_P/N_T was 0.97, and the standard deviation was 0.27.

Concluding Remarks

An analytical fatigue crack-closure model was used in a crack growth analysis program (FAST) to predict crack growth under constant-amplitude,

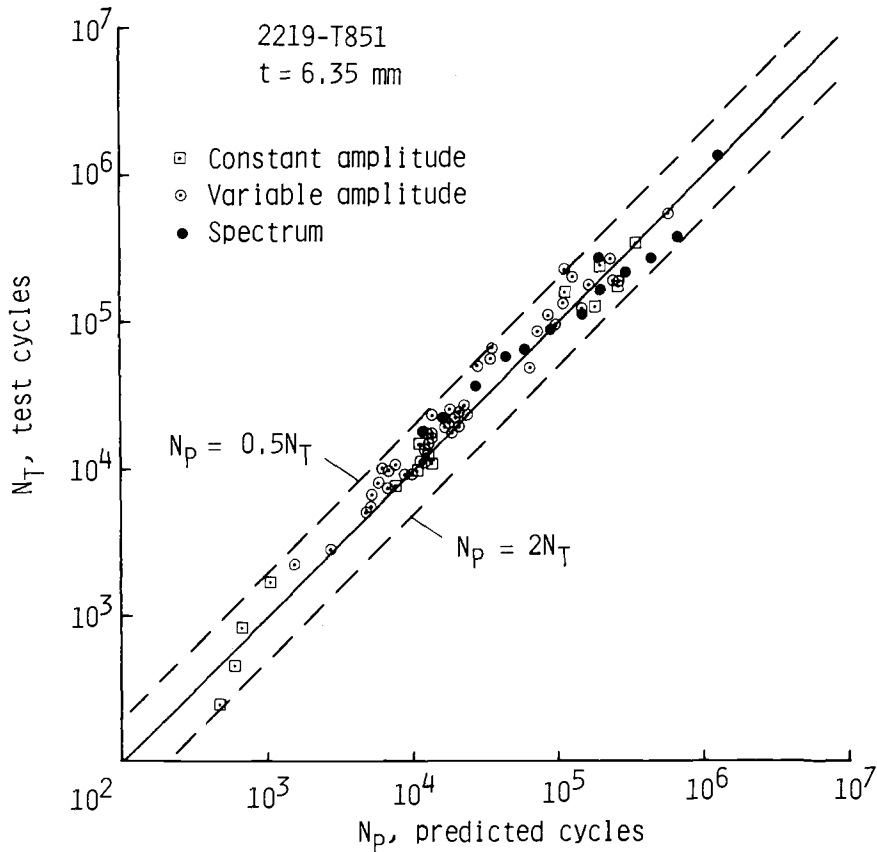


FIG. 15—Comparison of experimental and predicted cycles to failure for 2219-T851 aluminum alloy material under constant-amplitude, variable-amplitude, and spectrum loading.

variable-amplitude, and aircraft-spectrum loading. The model was based on the Dugdale model, but modified to leave plastically deformed material in the wake of the advancing crack tip. The model was used to calculate the crack-opening stresses as a function of crack length and load history under simulated plane-stress and plane-strain conditions.

A crack growth rate equation was developed in terms of Elber's effective stress-intensity factor range, threshold stress-intensity factor range, and fracture toughness to give the "sigmoidal" shape commonly observed when fatigue crack growth rate data are plotted against stress-intensity factor range. The five crack growth constants in this equation were determined from constant-amplitude data on 2219-T851 aluminum alloy sheet material. The equation correlated the constant-amplitude data over a wide range of stress ratios and stress levels quite well.

The analytical closure model with a constraint factor of 1.9 and the rate equation were used to predict crack growth under variable-amplitude and aircraft-spectrum loading on the 2219-T851 aluminum alloy material. The model predicts the effects of load interaction, such as retardation and acceleration. The ratio of predicted-to-experimental crack-growth lives, N_p/N_T , ranged from 0.5 to 1.8 in 62 variable-amplitude and spectrum-load tests. The mean of N_p/N_T was 0.97, and the standard deviation was 0.27. Thus the analytical crack-closure model and the proposed crack growth law predicted crack growth behavior in all tests quite well.

References

- [1] Elber, W., *Engineering Fracture Mechanics*, Vol. 2, No. 1, July 1970, pp. 37-45.
- [2] Elber, W. in *Damage Tolerance in Aircraft Structures*, ASTM STP 486, American Society for Testing and Materials, 1971, pp. 230-242.
- [3] Newman, J. C., Jr., "Finite-Element Analysis of Fatigue Crack Propagation-Including the Effects of Crack Closure," Ph.D. Thesis, VPI & SU, Blacksburg, Va., May 1974.
- [4] Newman, J. C., Jr., and Armen, Harry, Jr., *AIAA Journal*, Vol. 13, No. 8, Aug. 1975, pp. 1017-1023.
- [5] Ohji, K., Ogura, K. and Ohkubo, Y., *Engineering Fracture Mechanics Journal*, Vol. 7, 1975, pp. 457-464.
- [6] Newman, J. C., Jr., in *Mechanics of Crack Growth*, ASTM STP 590, American Society for Testing and Materials, 1976, pp. 281-301.
- [7] Dill, H. D. and Saff, C. R. in *Fatigue Crack Growth under Spectrum Loads*, ASTM STP 595, American Society for Testing and Materials, 1976, pp. 306-319.
- [8] Budiansky, B. and Hutchinson, J. W., "Analysis of Closure in Fatigue Crack Growth," Division of Applied Science, DAS M-1, Harvard University, June 1977.
- [9] Hardrath, H. F., Newman, J. C., Jr., Elber, W., and Poe, C. C., Jr., "Recent Developments in Analysis of Crack Propagation and Fracture of Practical Materials," *Fracture Mechanics*, N. Perrone, Ed., University Press of Virginia, 1978.
- [10] Fühling, H. and Seeger, T., *Engineering Fracture Mechanics Journal*, Vol. 11, 1979, pp. 99-122.
- [11] Fühling, H. and Seeger, T. in *Fracture Mechanics*, ASTM STP 677, C. W. Smith, Ed., American Society for Testing and Materials, 1979, pp. 144-167.
- [12] Newman, J. C., Jr., in *Methods and Models for Predicting Fatigue Crack Growth under Random Loading*, ASTM STP 748, J. B. Chang and C. M. Hudson, Eds., American Society for Testing and Materials, 1981, pp. 53-84.

- [13] Kanninen, M. F. and Atkinson, C., *International Journal of Fracture*, Vol. 16, No. 1, 1980, pp. 53-69.
- [14] Dugdale, D. S., "Yielding of Steel Sheets Containing Slits," *Journal of the Mechanics and Physics of Solids*, Vol. 8, 1960.
- [15] Chang, J. B. and Stolpestad, J. H., "Improved Methods for Predicting Spectrum Loading Effects-Phase I Report," AFFDL-TR-79-3036, Vol. II, March 1978.
- [16] Hudak, S. J., Saxena, A., Bucci, R. J., and Malcolm, R. C., "Development of Standard Methods of Testing and Analyzing Fatigue Crack Growth Rate Data," AFML-TR-78-40, May 1978.
- [17] Newman, J. C., Jr., in *Properties Related to Fracture Toughness*, ASTM STP 605, American Society for Testing and Materials, 1976, pp. 104-123.
- [18] Hudson, C. M. and Raju, K. N., *International Journal of Nondestructive Testing*, Vol. 2, 1970, pp. 189-205.
- [19] Willenborg, J. D., Engle, R. M., Jr., and Wood, H. A., "A Crack Growth Retardation Model Using Effective Stress Concept," AFFDL-TM-71-1-FBR, Jan. 1971.
- [20] Johnson, W. S. in *Methods and Models for Predicting Fatigue Crack Growth under Random Loading*, ASTM STP 748, American Society for Testing and Materials, J. B. Chang and C. M. Hudson, Eds., 1981, pp. 85-102.
- [21] Chang, J. B., Engle, R. M., and Stolpestad, J., "Fatigue Crack Growth Behavior and Life Predictions for 2219-T851 Aluminum Subjected to Variable-Amplitude Loadings," presented at the 13th National Symposium on Fracture Mechanics, June 1980.

Application of an Improved Crack Growth Prediction Methodology on Structure Preliminary Design

REFERENCE: Chang, J. B., Engle, R. M., and Hiyama, R. M., "Application of an Improved Crack Growth Prediction Methodology on Structure Preliminary Design," *Design of Fatigue and Fracture Resistant Structures, ASTM STP 761*, P. R. Abelkis and C. M. Hudson, Eds., American Society for Testing and Materials, 1982, pp. 278-295.

ABSTRACT: An improved crack growth methodology which accounts for load interaction effects was implemented into a computer module, PREGRO, and was subsequently incorporated into an existing preliminary design analysis computer program, APAS. The procedure utilizes the equivalent damage concept, which converts the random spectrum into equivalent constant-amplitude load cycles. By using this improved crack growth prediction module, unnecessary weight penalties can be avoided in the preliminary design of primary structures. Examples are given for the application of this predictive method to wing structures for typical fighter and transport aircraft.

KEY WORDS: crack growth prediction, load interaction effect, preliminary design

Nomenclature

a	Crack length
a_i	Initial crack length
a_f	Final crack length
a_o, a_{oj}	Initial crack length and selected initial crack length
a_{OL}	Crack length immediately following the overload cycle
Δa	Incremental crack growth
δa	Assumed incremental crack growth
C	Growth rate equation coefficient, Eqs 1 and 2
C_f	Growth rate equation coefficient, Eq 19

¹Program Manager/Technical Staff, and Technical Staff, respectively, Rockwell International, North American Aircraft Division, Los Angeles, Calif. 90009.

²Aerospace Engineer, Air Force Wright Aeronautical Laboratory, Wright-Patterson Air Force Base, Ohio 45433.

$da/dF, \Delta a/\Delta F$	Crack growth rate per flight
da/dN	Cyclic crack growth rate
da/dP	Crack growth rate per period
F	Flights
f_{ty}	Material tension yield stress
K_{eff}	Effective stress intensity factor
K_{max}, K_{min}	Maximum and minimum stress intensity factor
$K_{max}^{OL}, K_{min}^{OL}$	Maximum and minimum stress intensity factor associated with overload cycle
$(K_{max})_{eff}, (K_{min})_{eff}$	Maximum and minimum effective stress intensity factor, Eqs 10 and 11
\bar{K}	Measure of the stress intensity factor representing the unitblock spectrum, Eq 18
ΔK	Remote stress intensity factor range
ΔK_{eff}	Effective stress intensity factor range
ΔK_{th}	Threshold stress intensity factor range
m	Walker stress ratio correction exponent
N	Number of cycles
N_A	Number of flights represented in a unitblock spectrum
n	Growth rate equation exponent, Eqs 1 and 2
P	A fixed interval such as a flight or a block of flights
q	Chang acceleration exponent, Eq 2
R	Stress ratio, ratio of minimum stress to maximum stress
R_{eff}	Effective stress ratio
R_{OL}	Stress ratio for the overload cycle
R_{SO}	Shutoff overload ratio, Eq 7
r_i	Plane stress plastic zone radius due to current load cycle
r_{OL}	Plane stress plastic zone radius due to overload
Z_{OL}	Overload plastic zone size
$\lambda(a)$	Stress intensity factor correction factor, geometry dependent parameter
Φ	Gallagher/Hughes proportionality constant, Eq 6
ψ	Growth rate per flight equation exponent, Eq 19
σ	Stress
σ_{eff}	Effective stress
$\sigma_{max}, \sigma_{min}$	Maximum and minimum remote stress
$(\sigma_{max})_{eff}, (\sigma_{min})_{eff}$	Maximum and minimum effective stress, Eqs 8 and 9
σ_{req}	Stress required to break through the overload plastic zone, Eq 5
$(\Delta \bar{\sigma}^2)^{1/2}$	Root mean square of the spectrum stress range history

The evaluation of advanced aircraft configurations requires analytical tools which provide a means for initially sizing and optimizing structural

components. Utility of such analytical tools in the preliminary design environment requires methods and techniques with the ability to function without large amounts of data in a rapid operating mode. This requirement for timely response to requests for design tradeoff data has led to the development of procedures to be used in place of detail design analysis methods. These preliminary design procedures have been integrated into highly sophisticated computer programs which provide sensitivity to advanced materials, construction types, configuration geometry, airloads, missions, and performance. The criteria for alternative method development have been simplicity combined with the ability to provide proper sensitivity to design parameter variations. The rationale employed in these analytical procedures is founded on synthesizing design concepts to detail criteria as set forth in the procuring agency specifications.

The governing document specifying overall requirements for achieving structural integrity of Air Force aircraft is MIL-STD-1530A [1].³ This document defines the applicable specifications, standards, and handbooks to be used on any new system procurement activity. Design to damage tolerance and durability is addressed in military specification MIL-A-83444 [2] and MIL-A-008866B [3] as part of the structural integrity requirements. These latter considerations are fairly new design criteria intended to reduce the number of catastrophic failures due to the presence of undetected cracks and flaws and the overall force management cost.

Detailed crack growth analysis is performed by damage accumulation computer programs such as CRACKS [4] and EFFGRO [5]. These programs perform the crack growth analysis on a cycle-by-cycle basis accounting for stress histories and crack geometries. Application of these programs to preliminary design problems are limited by computer time/cost considerations, since the approach would be used in an iterative mode which converges on a design solution as opposed to point design analysis. In this program operating mode, a more efficient method for predicting crack growth life is required.

One of the initial applications of crack growth prediction methodology to preliminary design computer programs has been the approach employed in the Automated Predesign of Aircraft Structure (APAS III) program [6]. APAS III is a highly modularized program which is the structural synthesis procedure within the Structural Technology Evaluation Program (STEP) [7], developed by General Dynamics Convair Division for the Air Force. Although the crack growth procedure in APAS is considered to be conservative due to not accounting for load interaction effects, it has demonstrated the feasibility of assessing crack growth criteria at the preliminary design level.

Under recent Air Force sponsorship, an improved method has been

³The italic numbers in brackets refer to the list of references appended to this paper.

developed based on a flight-by-flight characterization of crack growth behavior. This method employs a cycle-by-cycle damage accumulation scheme which accounts for retardation and acceleration effects due to tensile overloads and compressive loads to determine an equivalent crack growth rate per flight. A computer program that implements this predicting method was developed and incorporated into APAS.

Typical wing torque box structure for both a transport and a fighter aircraft were analyzed by employing the existing crack growth analysis (PROGRO) module in APAS. Companion solutions were calculated by executing the new crack growth module (PREGRO) to obtain the relative effect of incorporating load interaction effects on the predicted crack growth life.

Crack Growth Module

Past applications of analytical crack growth methodology for use at the preliminary design level have been based on numerical techniques for accumulating damage using crack growth rate per period (da/dP) approaches [8,9]. These methods were developed to provide cost effective means for evaluating crack growth criteria in the early stages of concept formulation. In comparison to cycle-by-cycle methods, significant reduction in computational time has been achieved by coupling efficient integration schemes with the characterization of cycle-by-cycle load history in terms of an equivalent stress over a period of time such as a flight or a block of flights. These methods, based on empirical rate equations derived from constant-amplitude crack growth test data, did not account for the effects of load interaction on crack growth under variable amplitude loading. Application of these equations to variable-amplitude loadings has been shown to result in significant differences between predicted lives and actual test results. Observations by different investigators have shown that tensile overloads retard the crack growth on subsequent load steps, while compressive loads tend to negate the retardation effects. Furthermore, compressive load in a tension-compression cycle tends to accelerate the crack growth.

As a consequence of the foregoing considerations, a task was undertaken to include load interaction effects in a methodology suitable for preliminary design applications. This developmental effort consisted of selecting appropriate load interaction models, compatible constant-amplitude crack growth rate equations, and efficient damage accumulation schemes, which were then incorporated in a crack growth prediction computer program module, PREGRO. A flow chart illustrating the computational processes in PREGRO is shown in Fig. 1.

Crack Growth Rate Equation

Selection of a constant-amplitude crack growth rate equation was made on the following basis:

1. Compatible with the selected load interaction models.
2. Relatively simple with a minimal number of constants characterizing material properties.
3. Commonality with detail design methods to eliminate the need for establishing separate sets of material constants.

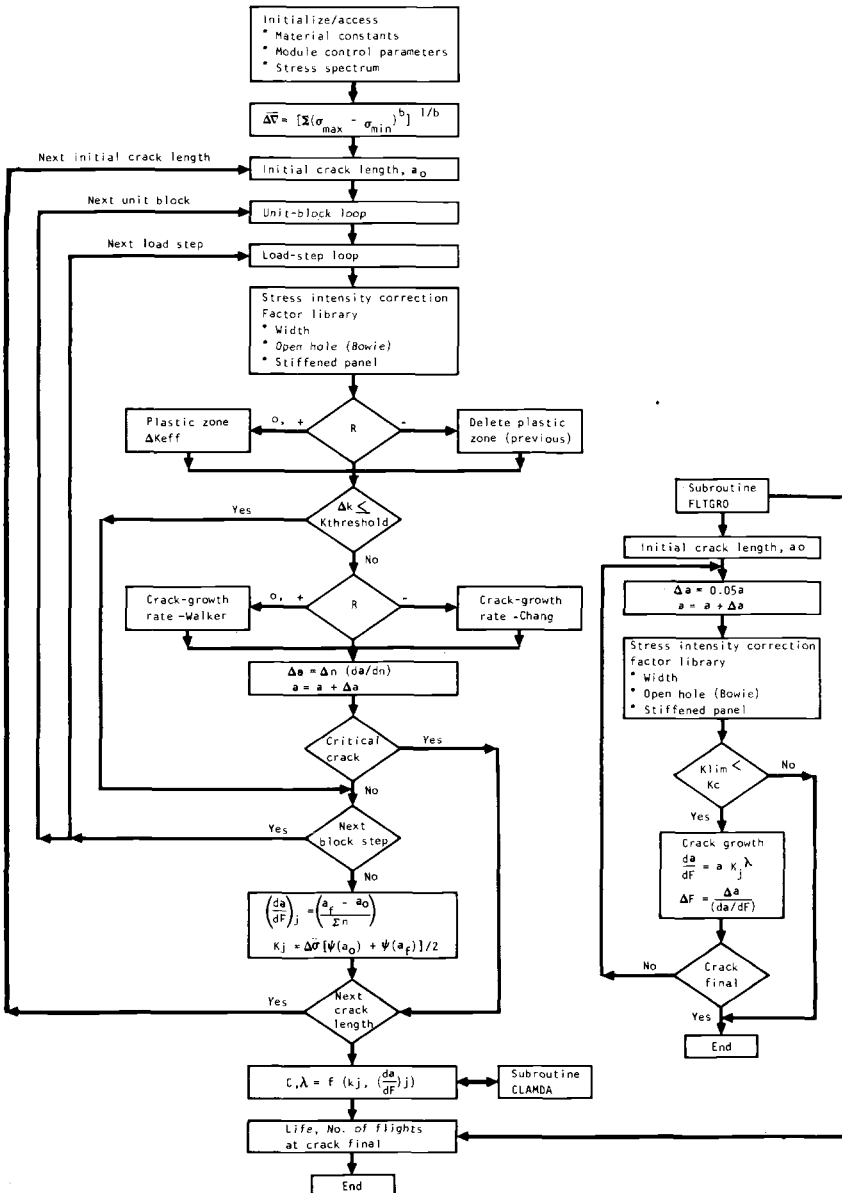


FIG. 1—PREGRO program module flow chart.

Two basic rate equations were employed, one for load cycles with positive stress ratios and the other for negative stress ratio load cycles. The Walker [10] effective stress concept introduced in the Paris rate equation [11] serves as the basis for predicting crack growth rates for positive stress ratio load steps. The Chang [12] compressive load acceleration model is used for negative stress ratio load cycles. Observation of experimental data has shown that at a threshold stress intensity factor range, ΔK_{th} , no discernible growth is observed. This characteristic is accounted for by considering zero growth when the stress intensity factor range is equal to or less than the threshold value. The cyclic growth rate equations incorporating the threshold concept then are as follows:

$$\frac{da}{dN} = C \left[\frac{\Delta K}{(1 - R)^{1-m}} \right]^n \quad \text{for } \begin{matrix} R \geq 0 \\ \Delta K > \Delta K_{th} \end{matrix} \quad (1)$$

$$\frac{da}{dN} = C [(1 - R)^q K_{max}]^n \quad \text{for } \begin{matrix} R < 0 \\ \Delta K > \Delta K_{th} \end{matrix} \quad (2)$$

Load Interaction Models

The generalized Willenborg [13] retardation model in conjunction with the Chang acceleration scheme was selected to account for load interaction effects. This method is based on characterizing time history effects by defining effective stress, σ_{eff} , stress intensity factor, K_{eff} , and stress ratio, R_{eff} , which can then be introduced in the constant-amplitude crack growth rate equations. The plane stress plastic zone, Z_{OL} , at the crack tip due to a tensile overload is given by

$$Z_{OL} = \frac{1}{2\pi} \left[\frac{K_{max}^{OL}}{f_{ty}} \right]^2 \quad \text{for } R_{eff} > 0 \quad (3)$$

When the tensile overload is followed by a compressive load, the Chang scheme considers a reduced effective plastic zone:

$$Z_{OL} = \frac{1}{2\pi} \left[\frac{K_{max}^{OL}}{f_{ty}} \right]^2 (1 + R_{eff}) \quad \text{for } R_{eff} < 0 \quad (4)$$

Following an overload cycle, the half crack length has progressed from a_o to a_{OL} . On any subsequent load step, i , with the crack tip at a_i , crack growth is considered to be affected by the residual plastic zone radius, r_{OL} , if the

plastic zone radius for that step, r_i , lies within that resulting from the previous overload. The original Willenborg model [14] identified an effective stress parameter based on the stress required to break through the overload plastic zone, that is, the stress at which r_i is equal to r_{OL} . The stress required is

$$\sigma_{req} = \frac{f_{ty} \sqrt{2\pi(r_{OL} - a_i)}}{\lambda(a_i) \sqrt{\pi a_i}} \quad (5)$$

Gallagher and Hughes [13] modified the Willenborg effective stress concept by introducing a proportionality constant, Φ , as shown below:

$$\Phi = \frac{1 - \frac{\Delta K_{th}}{K_{max}}}{R_{SO} - 1} \quad (6)$$

R_{SO} in Eq 6 is the shutoff overload ratio, which has been shown to be a material dependent constant. For different levels of K_{max} , corresponding shutoff overloads, K_{max}^{OL} , were observed which resulted in a condition of no crack growth. This material characteristic is given by

$$R_{SO} = K_{max}^{OL} / K_{max} = \text{constant} \quad (7)$$

The effective maximum and minimum stress, stress intensity factors, corresponding effective stress ratio, and stress intensity factor range which incorporate the Gallagher/Hughes modifications are calculated by Eqs 8 to 13:

$$(\sigma_{max})_{eff} = \sigma_{max} - \Phi (\sigma_{req} - \sigma_{max}) \quad (8)$$

$$(\sigma_{min})_{eff} = \sigma_{min} - \Phi (\sigma_{req} - \sigma_{max}) \quad (9)$$

$$(K_{max})_{eff} = (\sigma_{max})_{eff} \lambda(a) \sqrt{\pi a} \quad (10)$$

$$(K_{min})_{eff} = (\sigma_{min})_{eff} \lambda(a) \sqrt{\pi a} \quad (11)$$

$$R_{eff} = (\sigma_{min})_{eff} / (\sigma_{max})_{eff} \quad (12)$$

$$\Delta K_{eff} = (K_{max})_{eff} - (K_{min})_{eff} \quad (13)$$

Damage Accumulation

A three-step procedure was formulated to perform the damage accumulation. The first step consisted of calculating incremental crack growth based

on the cycle-by-cycle growth methodology for a unitblock flight spectrum. The unitblock spectrum consists of all peak and valley loadings which occur for a block of flights representative of the missions flown during the aircraft lifetime.

The Vroman linear approximation method [15] is employed to perform the damage accumulation due to the unitblock spectrum. The approach is based on the assumption that growth rate is a constant throughout a load step in a spectrum such that the crack size is in a linear relationship with the number of load cycles. A load step consists of one or more cycles of constant amplitude loadings. A relatively small incremental change in crack length, δa , is used to calculate the growth rate for a given load step. The number of cycles required to grow the crack through the assumed incremental length is then given by

$$N = \delta a / (da/dN) \quad (14)$$

The value of N is then compared with the cycles in that load step, N_i . If N is greater than N_i , crack growth for that particular step is

$$\Delta a = N_i (da/dN) \quad (15)$$

Crack length is increased by Δa , and the process continues to the next load step. If N is less than or equal to N_i , N is subtracted from N_i , the crack size is increased by δa , and the load step is reconsidered. This process continues with N being compared with the remaining cycles in the step. Computation continues until all load steps in the unitblock are exhausted.

The foregoing cycle-by-cycle crack growth analysis is performed for the unitblock load spectrum for a number of different values of crack size. Crack size, a_j , at the end of the unitblock spectrum is calculated from

$$a_j = a_{oj} + (\Delta a)_j \quad (16)$$

where a_{oj} are the selected values of initial flaw size, and $(\Delta a)_j$ are the incremental changes in the crack size resulting from the unitblock spectrum. Values of the initial crack size, a_{oj} , are selected to cover the expected range of crack sizes, starting at the initial flaw size and continuing through that expected at failure. The crack growth resulting from the unitblock spectrum for a period of N_A -flights is then defined by the following:

$$(\Delta a / \Delta F)_j = (\Delta a)_j / N_A \quad (17)$$

For each of the assumed initial flaw sizes, the corresponding measure of stress intensity factor is defined by

$$\bar{K}_j = \sqrt{(\Delta\bar{\sigma}^2)} [\lambda(a_{oj}) \sqrt{\pi a_{oj}} + \lambda(a_j) \sqrt{\pi a_j}] / 2 \quad (18)$$

where $(\Delta\bar{\sigma}^2)^{1/2}$ is the root mean square of the unitblock spectrum stress range history, and $\lambda(a)$ is a function of crack size a , crack shape, and part geometry.

The second step in the computational procedure consists of characterizing crack growth for the complex flight spectra into an equivalent constant-amplitude loading that will produce the same crack growth life. This method was proposed by Chang et al [12] and is based on the observation of log-log plots of crack growth rate per flight, $(\Delta a/\Delta F)_j$, versus a measure of the stress intensity factor, \bar{K}_j , representing the unitblock spectrum. The foregoing relationship is represented by a nearly straight line when plotted on the log-log scale. The power exponent, ψ , and proportionality constant, C_f , for the crack growth per flight rate equation are calculated by applying a least squares fit procedure to the log $(\Delta a/\Delta F)_j$ versus log (\bar{K}_j) data plot.

$$da/dF = C_f (\bar{K})^\psi \quad (19)$$

Crack growth life is calculated in the third step of the damage accumulation scheme. The linear approximation method is applied to the crack growth rate per flight given by Eq 19 to calculate life over a prescribed crack length interval.

Preliminary Design Process

APAS is a highly modularized program which performs a multistation analysis to synthesize components of box beam structures. Cover panels, spars, and ribs are synthesized in an analytical approach which accounts for the geometric details associated with construction concepts. The program is capable of evaluating any of the 12 different panel constructions shown in Fig. 2. Materials may be selected from a library data bank of properties for aluminum, titanium, and steel alloys or introduced in the input data. Program options provide the user with the choice of either analyzing the structure, based on input element sizing definitions, or performing a redesign optimization within practical constraints of element sizes. The redesign optimization procedure is an iterative approach, starting with user-defined initial size estimates and progressing until a member of each symmetry grouping has a zero margin of safety. This process is initiated for static load strength design, followed by the analysis for fatigue life, crack growth, and residual strength criteria.

Crack growth analysis is performed for each cover panel of the torque box section based on structural geometry, initial flaw size, inspection interval, and stress spectrum. Fracture mechanics material properties are accessed

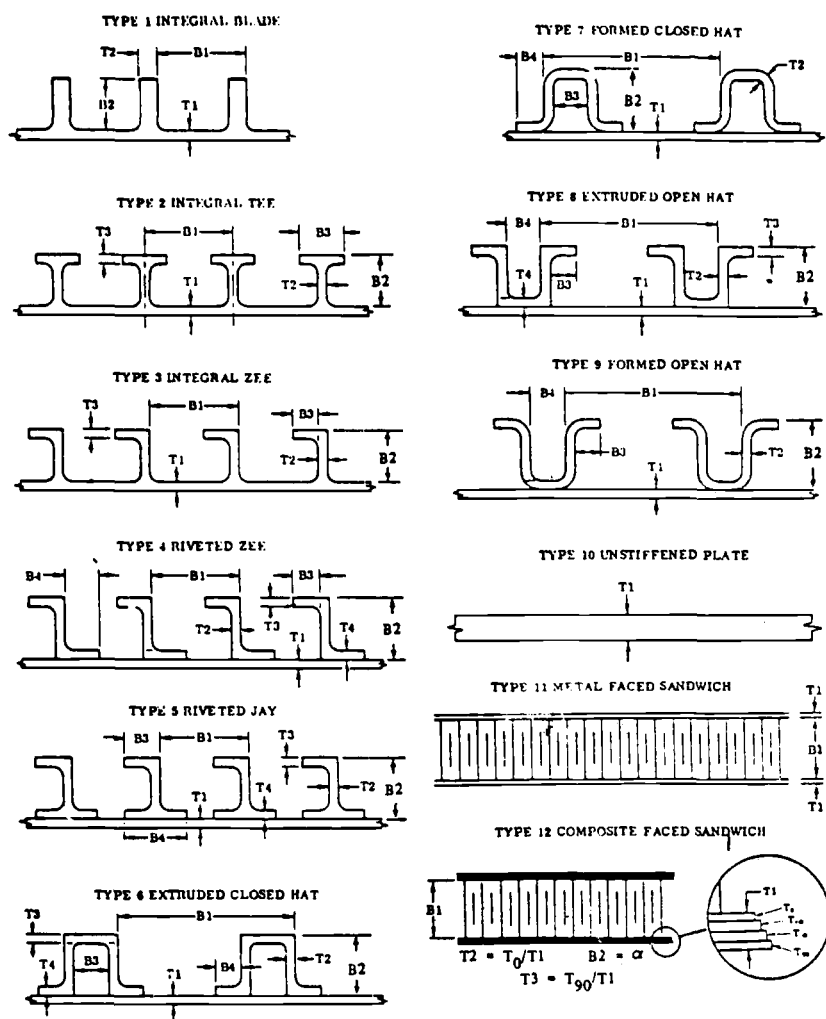


FIG. 2—Skin panel elements.

from a program library. Crack growth characterization parameters employed in the modified Walker rate equation, in conjunction with the generalized Willenborg retardation model, and the Chang acceleration scheme were incorporated in this material data library.

The stress spectrum is generated within APAS based on a prescribed mission profile and load factor/occurrence data together with the element stresses resulting from a set of reference external load conditions. The spectrum is organized according to a predefined sequence and duration of flight segments. Each segment consists of subsegments or steps of minimum and

maximum stresses with the corresponding number of cycles that occur in one block of flights. Ground-air-ground (GAG) cycles are obtained by taking the maximum stress excursions between the peak in flight stresses and the ground condition stresses. Currently, load spectra data for the typical operation of a medium range transport and a lightweight air-to-air fighter are stored in the APAS libraries. Alternative means are provided for modifying these spectra or for defining spectra for other aircraft missions.

Evaluation of the Improved Crack Growth Analysis Module

Within the operating framework of APAS, test cases were executed to compare the results from the initial crack-growth module (PROGRO) with those from the new module (PREGRO). Wing torque box structure for a transport aircraft and for a lightweight fighter were analyzed. These test cases were used to evaluate the predicted results due to spectrum and construction variations with emphasis on the assessment of crack growth load interaction effects.

Transport Case

The wing torque box for a four-engine jet transport aircraft was used to evaluate the impact of the improved crack growth prediction methodology on structural sizing and weight. Construction of the torque box was 2024-T6 aluminum upper and lower covers with riveted 7075-T6 J-stringers and Ti-6Al-4V ribs, spars, and spar caps. Stringer spacing was set at 15.24 cm (6 in.) on the upper cover and 19.05 cm (7.5 in.) on the lower cover. The cross section at wing spanwise station 600 was used for evaluating the effects of strength and stability sizing, flaw growth analysis, and the redesign optimization solution. Station 600 nodal coordinate data, section geometry, and cover element details are shown in Fig. 3.

Four design loading conditions were input to define an envelope of strength requirements. These conditions were as follows: 2.5 *g*, positive maneuver; -1.0 *g*, negative maneuver; 2.0 *g*, taxi; and 1.0 *g*, level flight.

The stress spectrum was derived from the program library flight segment and load factor/occurrence data for the operation of a typical medium-range transport aircraft. Reference load conditions used in the development of this spectrum were as follows: 1.0 *g*, taxi; 1.0 *g*, flight with 1.0 *g* gust; 1.0 *g*, flight with 1.0 *g* maneuver; and 1.0 *g*, landing impact.

Two program operating modes were used to isolate the difference in predicted crack growth life associated with load interaction effects. One approach was taken to obtain a measure of the effect on crack growth life, and the other to obtain the impact on structural sizing and weight.

In order to obtain a measure of the differences in predicted life, APAS was

STATION 600.00 SECTION NODAL GEOMETRY								
NODE	X	Z	NODE	X	Z	NODE	X	Z
1	32.86	14.38	2	57.51	18.13	3	82.16	19.18
4	106.83	18.65	5	131.45	14.38	6	131.45	-7.19
7	106.83	-7.71	8	82.16	-8.69	9	57.51	-8.99
10	32.86	-8.99						

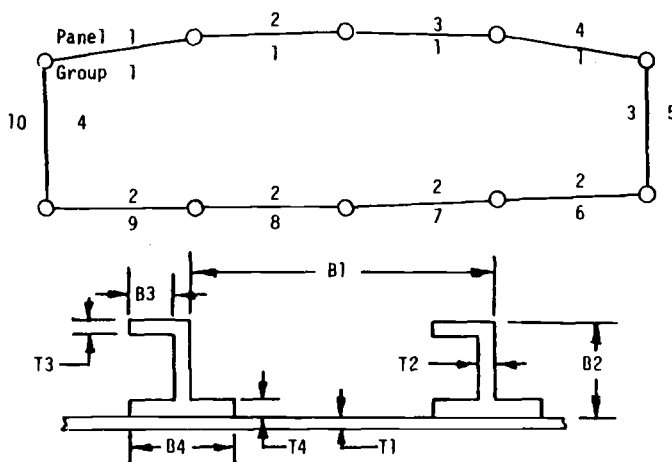


FIG. 3—Sample transport wing geometry.

executed to obtain strength sizing details at Station 600. The strength sizing results were then input data to a second problem case in which only strength and crack growth analyses were performed. Based on this analysis, Panel 9 of the lower cover shown in Fig. 3 was the most critical element with the shortest crack growth life. A comparison of program results for Panel 9 is presented in Fig. 4 in the form of crack length versus flight curves. For those cases where no load interaction effects were considered, there was a negligible difference in predicted life obtained from PROGRO and PREGRO. The incorporation of load interaction effects resulted in an increase of 25 percent in predicted life.

The design to crack growth life requirements was obtained by performing a redesign optimization. A 2.54 cm (1 in.) initial flaw size was chosen, and the inspection interval was set at 20 000 flights. Results of these cases are presented in Table 1. In Fig. 3 and Table 1, Panels 1 to 4 represent the upper cover, Panels 6 to 9 the lower cover, and Panels 5 and 10 the rear and front spars, respectively. Since the spars are primarily designed for shear loadings, no crack growth analysis is performed for Panels 5 and 10 in APAS. Max-

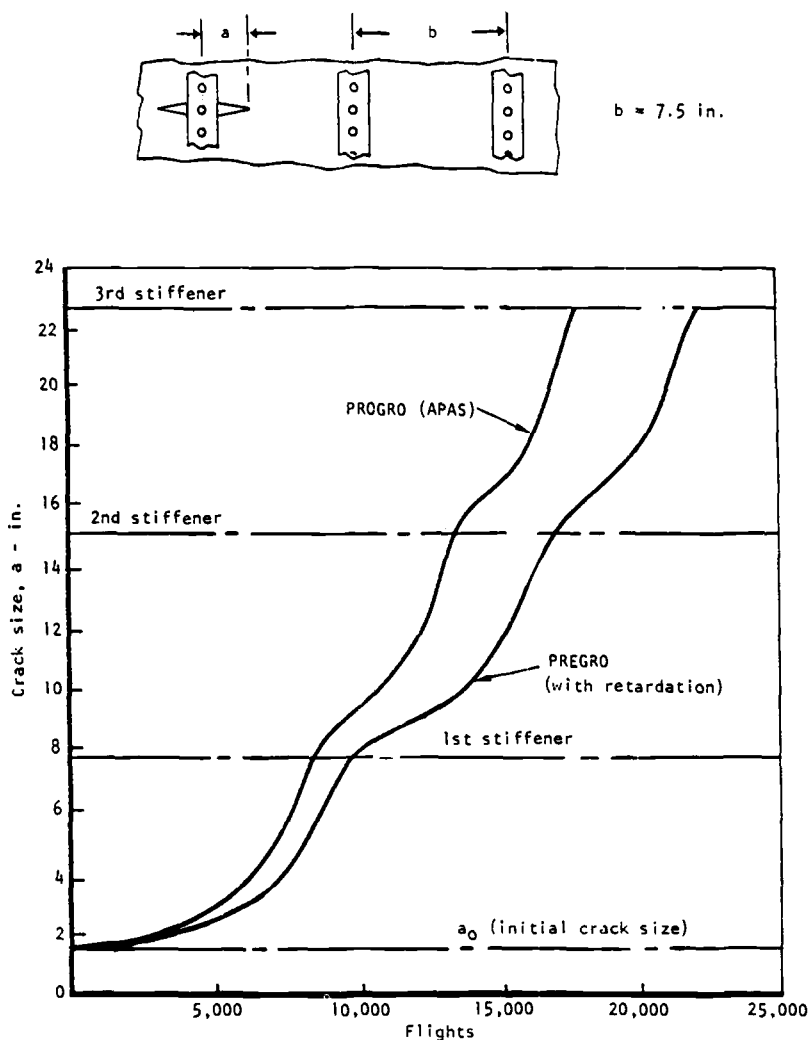


FIG. 4—Crack growth prediction for a transport spectrum, including overload retardation effects.

imum skin and stiffener spectrum stresses, critical initial flaw size, number of safe life flights, and the weight penalty for each of the cover panels are presented in Table 1. A structural weight penalty to the lower cover of 8.56 percent was predicted by the PROGRO module. This penalty was reduced to 1.99 percent as a result of the load interaction effects accounted for by PREGRO.

TABLE 1—Comparison of weight penalties for a sample transport wing design.

STATION 600.00						
INITIAL CRACK SIZE, 2A			2.000 INCHES			
INSPECTION INTERVAL			20000. FLIGHTS			
PANEL NO.	SYMMETRY GROUP	MAXIMUM SPECTRUM STRESS SKIN (PSI)	MAXIMUM SPECTRUM STRESS STIFF. (PSI)	CRITICAL INITIAL FLAW SIZE (2A, IN.)	SAFE LIFE (FLIGHTS)	WEIGHT PENALTY (PERCENT)
FLAW GROWTH ANALYSIS RESULTS USING PROGRO						
1	1	6805.	6872.	29.508	.235E+06	.00
2	1	7781.	7858.	27.205	.137E+06	.00
3	1	7526.	7600.	27.750	.157E+06	.00
4	1	5738.	5744.	32.284	.464E+06	.00
5	3	0.	0.	0.000	0.	0.00
6	2	12118.	12237.	2.178	.205E+05	8.56
7	2	12130.	12249.	2.000	.200E+05	8.56
8	2	12044.	12162.	2.036	.201E+05	8.56
9	2	11528.	11641.	2.999	.234E+05	8.56
10	4	0.	0.	0.000	0.	0.00
FLAW GROWTH ANALYSIS RESULTS USING PREGRO						
1	1	6784.	6846.	29.729	.241E+06	.00
2	1	7786.	7865.	27.247	.138E+06	.00
3	1	7630.	7604.	27.835	.158E+06	.00
4	1	5635.	5751.	32.657	.484E+06	.00
5	3	0.	0.	0.000	0.	0.00
6	2	12731.	12906.	2.182	.205E+05	1.99
7	2	12600.	12925.	2.000	.200E+05	1.99
8	2	12718.	12842.	2.031	.201E+05	1.99
9	2	12193.	12313.	2.959	.233E+05	1.99
10	4	0.	0.	0.000	0.	0.00

Fighter Case

The wing for a contemporary lightweight fighter was selected to evaluate program process results for fighter spectrum and design parameters. The torque box construction for this fighter wing was a multirib design with 2024-T62 integral blade cover panels and transverse angle-stiffened front and rear spars. The cross section at spanwise station 21.64 was used to evaluate the results of the different crack-growth prediction modules. Figure 5 presents the section geometry parameters at station 21.64.

For this sample case, spectrum for a typical fighter air-to-ground mission was input to the program. Spectrum was introduced in the form of a random cycle-by-cycle stress history.

Crack growth analyses were again performed by PROGRO and PREGRO program modules. Crack length versus flight curves resulting from the crack growth analysis of structure sized to strength requirements are presented in Fig. 6. As was the case on the transport wing, the critical crack growth loca-

STATION 21.64
SECTION NODAL GEOMETRY

NODE	X	Z	NODE	X	Z	NODE	X	Z
1	38.48	3.94	2	61.11	4.43	3	83.74	4.20
4	106.37	3.33	5	129.00	2.11	6	129.00	-2.65
7	106.37	-1.50	8	83.74	-2.27	9	61.11	-2.66
10	38.48	-2.42						

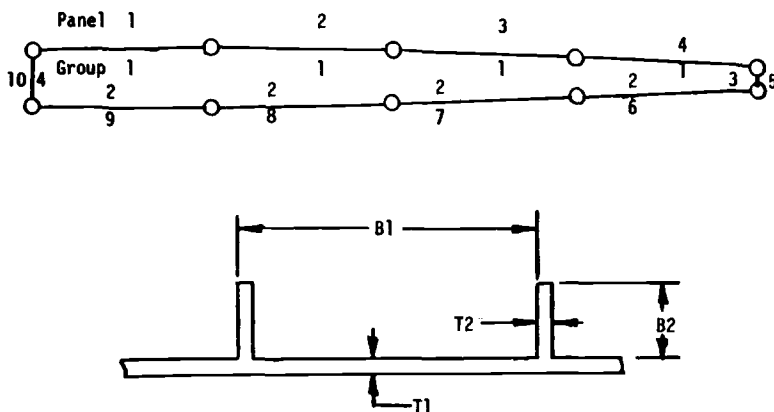


FIG. 5—Sample fighter wing geometry.

tion occurred for the forward panel of the lower cover. Design to crack growth life requirements was based on initial flaw size of 1.27 cm (0.5 in.) with an inspection interval of 4000 flights. APAS results for the fighter wing at station 21.64 are presented in Table 2. The predicted weight penalty of 18.05 percent to the lower cover by PROGRO is reduced to no penalty by PREGRO as a result of including retardation effects.

Concluding Remarks

A crack growth life prediction approach which accounts for load interaction effects can be adapted for use at the preliminary design level in a fully integrated operating mode. An efficient computerized scheme provides a means for including the impact of fracture mechanics requirements early in the preliminary design stage where configuration concept, construction, and material selection trades are made. The approach which accounts for load interaction effects ensures that excessive penalties are not imposed due to the omission of overload retardation effects.

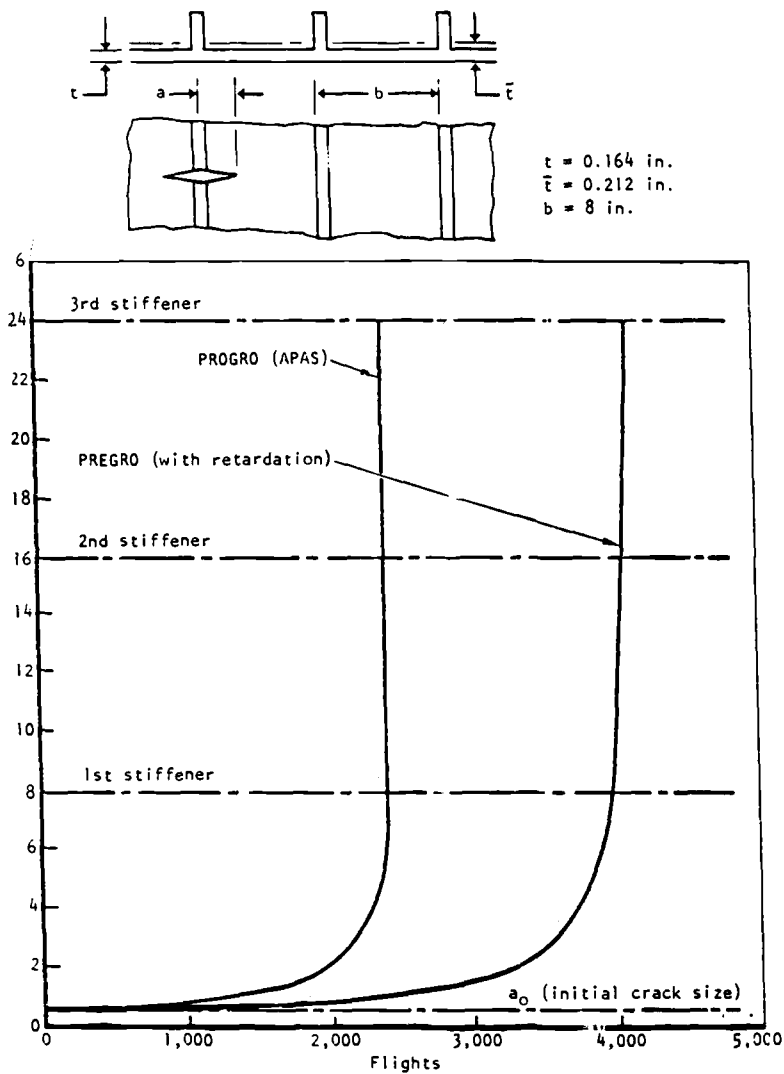


FIG. 6—Crack growth prediction for a fighter spectrum, including overload retardation effects.

Acknowledgments

This report is based on part of the results of a task performed on Contract F33615-77-C-3121, sponsored by the U.S. Air Force Wright Aeronautical Laboratory, Wright-Patterson Air Force Base, Ohio.

TABLE 2—Comparison of weight penalties for a sample fighter wing design.

INITIAL CRACK SIZE, 2A				1.000 INCHES		
INSPECTION INTERVAL				4000. FLIGHTS		
PANEL NO.	SYMMETRY GROUP	MAXIMUM SPECTRUM STRESS SKIN (PSI)	MAXIMUM SPECTRUM STRESS STIFF (PSI)	CRITICAL INITIAL FLAW SIZE (2A, IN.)	SAFE LIFE (FLIGHTS)	WEIGHT PENALTY (PERCENT)
FLAW GROWTH ANALYSIS RESULTS USING PROGRO						
1	1	3349.	3349.	47.632	.241E+08	.00
2	1	3481.	3481.	47.577	.207E+08	.00
3	1	2923.	2923.	47.786	.416E+08	.00
4	1	1863.	1863.	47.965	.252E+09	.00
5	3	0.	0.	0.000	0.	0.00
6	2	10658.	10658.	4.431	.420E+05	18.05
7	2	15064.	15064.	2.679	.13E+05	18.05
8	2	18218.	18218.	1.229	.472E+04	18.05
9	2	18625.	18625.	1.107	.431E+04	18.05
10	4	0.	0.	0.000	0.	0.00

FLAW GROWTH ANALYSIS RESULTS USING PRGRO						
1	1	3291.	3291.	47.772	.418E+08	.00
2	1	3477.	3477.	47.715	.336E+08	.00
3	1	2926.	2926.	47.858	.670E+08	.00
4	1	1837.	1837.	47.978	.432E+09	.00
5	3	0.	0.	0.000	0.	0.00
6	2	12241.	12241.	7.800	.415E+05	.00
7	2	17201.	17201.	2.609	.143E+05	.00
8	2	20822.	20822.	1.206	.465E+04	.00
9	2	21502.	21502.	1.027	.437E+04	.00
10	4	0.	0.	0.000	0.	0.00

References

- [1] "Military Standard, Aircraft Structural Integrity Program, Airplane Refinement," MIL-STD-1530A, Dec. 1975.
- [2] "Airplane Damage Tolerance Requirements," MIL-A-83444, July 1974.
- [3] "Airplane Strength and Rigidity Reliability Requirements, Repeated Loads and Fatigue," MIL-A-8866B, June 1975.
- [4] Engle, R. M., "CRACKS, A Fortran IV Digital Computer Program for Crack Propagation Analysis," AFFDL-TR-70-107, Air Force Flight Dynamics Laboratory, WPAFB, Ohio, 1970.
- [5] Szamossi, M., "Crack Propagation Analysis by Vroman's Model, Program EFFGRO," NA-72-94, Rockwell International, Los Angeles, 1972.
- [6] Kruse, G. S., Tanner, C. J., and Wilson, P. J., "User's Manual for APAS III, Volume 1," CASD-NAS-76-028, General Dynamics Convair Division, San Diego, 1976.
- [7] Oman, B. H., Kruse, G. S., and Reed, T. F., "Structural Technology Evaluation Program (STEP), Vol I-Basic Technical Report," AFFDL-TR-77-110, Air Force Flight Dynamics Laboratory, WPAFB, Ohio, 1978.
- [8] Brussat, T. R. in *Fracture Toughness and Slow Stable Cracking*, ASTM STP 559, American Society for Testing and Materials, 1974, pp. 298-310.
- [9] Chang, J. B. and Cheng, J. S., "Cost Effective Fatigue Crack Growth Analysis for Flight Spectrum Loading," NA-78-629, Rockwell International, North American Aircraft Division, Los Angeles, 1978.
- [10] Walker, K. in *Effects of Environment and Complex Load History on Fatigue Life*, ASTM STP 462, American Society for Testing and Materials, 1970, pp. 1-15.

- [11] Paris, P. C., "The Growth of Fatigue Cracks Due to Variations in Load," Ph.D. thesis, Lehigh University, 1962.
- [12] Chang, J. B., Stolpestad, J. H., Shinozuka, M., and Vaicaitis, R., "Improved Method for Predicting Spectrum Loading Effects-Phase I Report, Volume I, Results and Discussion," AFFDL-TR-79-3036, Vol I, Air Force Flight Dynamics Laboratory, WPAFB, Ohio, 1979.
- [13] Gallagher, J. P. and Hughes, T. F., "Influence of Yield Strength on Overload Affected Fatigue Crack Growth Behavior in 4340 Steel," AFFDL-TR-74-27, WPAFB, Ohio, 1974.
- [14] Willenborg, J., Engle, R. M., and Wood, H. A., "A Crack Growth Retardation Model Using an Effective Stress Concept," AFFDL-TR-71-1, Jan. 1971.
- [15] Chang, J. B., Engle, R. M., and Szamossi, M., "Numerical Techniques in Computer-Aided Fatigue Crack-Growth Analysis," in *Proceedings*, Second International Conference, University of Swansea, United Kingdom, 1980.

Fatigue-Life Prediction for Spotweld Using Neuber's Rule

REFERENCE: Oh, H. L., "Fatigue-Life Prediction for Spotweld Using Neuber's Rule," *Design of Fatigue and Fracture Resistant Structures. ASTM STP 761*, P. R. Abelkis and C. M. Hudson, Eds., American Society for Testing and Materials, 1982, pp. 296-309.

ABSTRACT: Neuber's Rule, which states that the theoretical stress concentration factor is equal to the geometric mean of the actual stress and strain concentration factors, is employed to treat the inelastic behavior of material localized around the spotweld. The stress and strain concentrations estimated by the Rule are compared with published results obtained by the finite-element method. Results show that comparable accuracy of stress-strain estimation can be obtained with Neuber's Rule at a negligible cost and effort. Treating residual stress as a prestressing of the spotweld and using Neuber's Rule to estimate the corresponding stress-strain concentration, fatigue life of a spotweld under constant-amplitude cycling is predicted. The predicted life is in agreement with published results.

KEY WORDS: fatigue, spotweld, Neuber's Rule, stress-strain concentration, residual stress

Sheet metals are frequently joined by spotwelds. These welds are "weak links" in a joined structure because they are sources of stress concentration and because they have undergone severe thermal history during welding. To ensure their fatigue integrity, it is usual to bench test them. This is, of course, costly and time consuming. Analytical methods can reduce the amount of testing by providing a model on which design iterations may be performed, the actual testing serving only as a verification. The purpose of this paper is to provide one such analytical method.

Earlier work showed that the fatigue life of a spotweld is governed principally by the strain concentration localized around the spotweld [1].² It also demonstrated that the finite-element method is capable of estimating the strain concentration and predicting qualitatively the fatigue life. The present

¹Staff Research Scientist, General Motors Research Laboratories, Warren, Mich. 48090.

²The italic numbers in brackets refer to the list of references appended to this paper.

work proposes the application of Neuber's Rule for estimating the strain concentration. The method is much easier to use and estimates strain with comparable accuracy at a negligible cost. By treating residual stress as a pre-stressing of the spotweld, the present work also shows that quantitative life prediction can be obtained.

Analysis

Neuber's Rule

In loading a notched structural member, the highly stressed material is localized around the notch root. If material there remains elastic, the local stress, σ , and the local strain, ϵ , are in direct proportion to each other and to the applied nominal stress, S , and the nominal strain, e . The extent of stress concentration is usually defined in terms of the theoretical elastic stress concentration factor $K_t = \sigma/S = \epsilon/e$. This factor is a constant for a given geometry and loading. When yielding occurs, the stress concentration factor, $K_\sigma (= \sigma/S)$, and the strain concentration factor, $K_\epsilon (= \epsilon/e)$, no longer stay constant. However, as shown by Neuber [2], the product of K_σ and K_ϵ remains a constant. This constant would be K_t^2 since both K_σ and K_ϵ are equal to K_t in the elastic range. Thus the following formula, first proposed by Neuber and which now bears his name, holds:

$$K_\sigma K_\epsilon = K_t^2$$

Neuber's Rule has been used successfully to estimate local stresses and strains at critical locations of notched members. It is now an accepted basis for analytical and experimental fatigue life prediction of notched numbers [3-5].

In applying Neuber's Rule to fatigue problems, K_σ and K_ϵ are written in terms of ranges (that is, peak-to-peak changes) of stress and strain as

$$\left(\frac{\Delta\sigma}{\Delta S} \right) \left(\frac{\Delta\epsilon}{\Delta e} \right) = K_t^2$$

or in an alternative form as

$$(\Delta\sigma\Delta\epsilon)^{1/2} = K_t(\Delta S\Delta e)^{1/2} \quad (1)$$

where a quantity prefixed with the symbol Δ denotes the range of that quantity. Since for a given loading and geometry, the right-hand side of Eq 1 is known, this alternative form of Neuber's Rule provides one relation between the two unknowns $\Delta\sigma$ and $\Delta\epsilon$. Also, $\Delta\epsilon$ is related to $\Delta\sigma$ through the material

stress-strain behavior. The two relations, Neuber's Rule and material stress-strain law, completely determine $\Delta\sigma$ and $\Delta\epsilon$. Thus, using the cyclic stress-strain relation widely accepted for fatigue problems,

$$\Delta\epsilon = \frac{\Delta\sigma}{E} + 2\left(\frac{\Delta\sigma}{2K'}\right)^{1/\eta'} \quad (2)$$

and substituting into Eq 1, one obtains an expression relating local stress range $\Delta\sigma$ to the applied nominal stress range ΔS and K_t from which $\Delta\sigma$ may be solved for

$$(\Delta\sigma)^{1/2} \left[\frac{\Delta\sigma}{E} + 2\left(\frac{\Delta\sigma}{2K'}\right)^{1/\eta'} \right]^{1/2} = K_t (\Delta S)^{1/2} \left[\frac{\Delta S}{E} + 2\left(\frac{\Delta S}{2K'}\right)^{1/\eta'} \right]^{1/2} \quad (3)$$

where E , K' , and η' are material properties. The value of $\Delta\sigma$ so obtained is then substituted back into Eq 2 to solve for $\Delta\epsilon$.

So far, Neuber's Rule has been applied to notch fatigue problems only. And rightly so, because of the predominance of notch problems and because the mathematical basis of the rule derives from an analysis of notch. Whether a mathematical basis exists for applying the rule to spotweld remains to be established. However, critical strain estimated with Neuber's Rule in this work is in close agreement with results obtained by the finite-element method in Ref 1. This close agreement is taken as the basis for applying Neuber's Rule to predict fatigue of spotweld.

Model of the Spotweld

To implement Neuber's Rule, Eq 3, K_t of the spotweld is needed. This is obtained from an elastic stress analysis of the spotweld. For this purpose, the spotweld is modeled as shown in Figs. 1 and 2. Figure 1 shows the spotweld fatigue specimen; Fig. 2 shows the model for one of the two plates. Compared with weld diameter, the specimen plate length is relatively long, and is therefore assumed infinite in the model to simplify the solution. Load is assumed transmitted from one plate to another as a shear force uniformly distributed over the weld area. This shearing force is balanced at one end ($x = -\infty$) by the load. At the other end ($x = +\infty$) and along the two edges, boundary conditions are stress free. This model is and has been purposely kept identical to that in Ref 1 so that a consistent comparison of critical strain can be made. The only difference is that the plate length in Ref 1 is taken as $4/3$ times the plate width. According to Ref 6, this difference would yield less than 1 percent difference in stress.

An elastic stress analysis of the model was performed, details of which may be found in the Appendix. From this analysis, one obtains the K_t of the

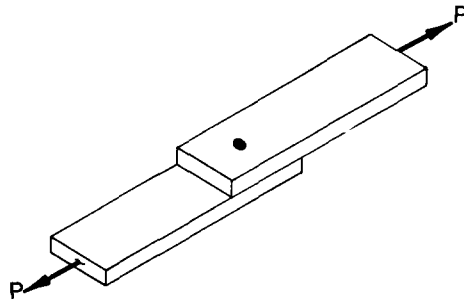


FIG. 1—Spotweld fatigue specimen.

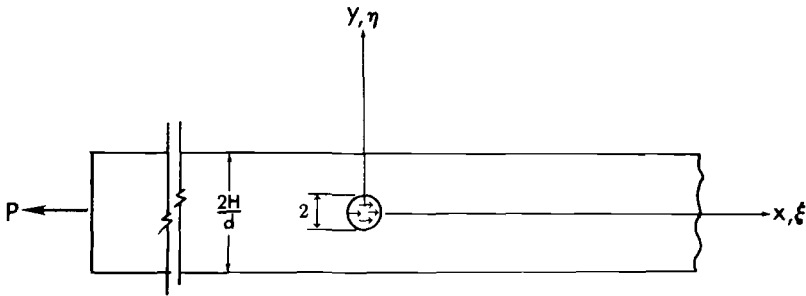


FIG. 2—Mathematical model and coordinate system used in the stress analysis of spotweld. Dimensions are in units of spotweld radius.

spotweld necessary for the implementation of Neuber's Rule, Eq 3. The result depicting the variation of K_t with the ratio of plate width and weld diameter is shown in Fig. 3 for Poisson's ratio = 0.30.

Fatigue-Life Prediction

To predict fatigue life, N_f , the strain-range fatigue-life relation of the material is used:

$$\frac{\Delta\epsilon}{2} = \left(\frac{\sigma_f' - \sigma_o}{E} \right) (2N_f)^b + \epsilon_f' (2N_f)^c \quad (4)$$

where b , c , σ_f' and ϵ_f' are fatigue properties of the material; $\Delta\epsilon$ is the local strain range; and σ_o is the local mean stress. The latter two quantities are estimated as described below.

To estimate the local strain range, $\Delta\epsilon$, the nominal applied stress range, ΔS , is taken as

$$\Delta S = \frac{P}{tH} = \frac{P}{P_0} \cdot \frac{\sigma_{ys}'}{K_t} \quad (5)$$

where for the present study of zero to tension cyclic loading, P is the load amplitude which is also the load range; $P_0 = (tH\sigma_{ys}')/K_t$ is the load level at which incipient yielding occurs at the critical site; and t , H , and σ_{ys}' are as defined in Table 1. Substituting the expression for ΔS into Eq 3 and dividing both sides of the equation by $E^{1/2}$ yields

$$\begin{aligned} \left(\frac{\Delta\sigma}{E}\right)^{1/2} \left[\frac{\Delta\sigma}{E} + 2 \left(\frac{\Delta\sigma}{2K_t'} \right)^{1/\eta'} \right]^{1/2} \\ = \left(\frac{P}{P_0} \frac{\sigma_{ys}'}{E} \right) \left[1 + 2E \left(\frac{P}{P_0} \frac{\sigma_{ys}'}{K_t} \right)^{1/\eta'-1} \left(\frac{1}{2K_t'} \right)^{1/\eta'} \right]^{1/2} \quad (6) \end{aligned}$$

For a known load and geometry, P/P_0 and K_t are known. The preceding equation may therefore be solved for local stress range $\Delta\sigma$ and consequently for local strain range $\Delta\epsilon$ from Eq 2.

In this study, the local mean stress, σ_o , includes the effect of both the nominal applied mean stress and the residual stress from welding. It is known that the residual stress, predominantly tensile, adversely affects the fatigue life of spotweld [7]. This effect is incorporated into σ_o calculation by treating the residual stress as a mechanical prestressing of the material

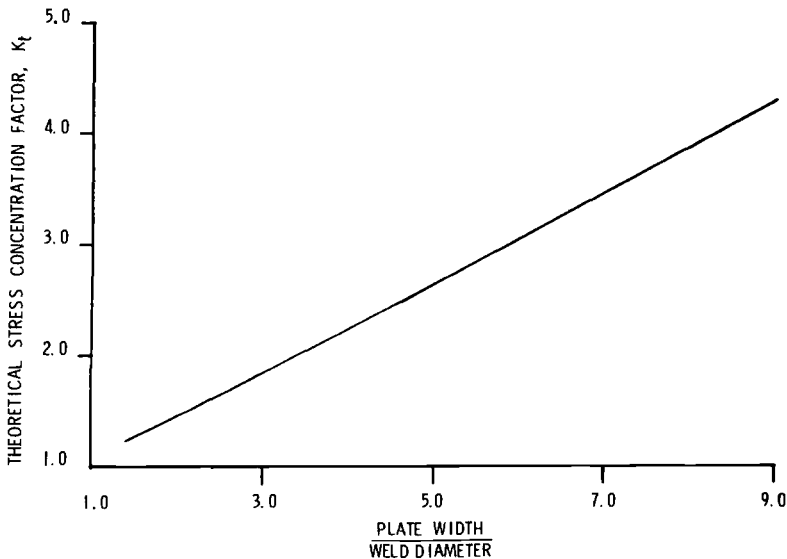


FIG. 3—Variation of K_t with the ratio of plate width and weld diameter.

TABLE 1—Data used in fatigue-life estimate of spotwelds by Neuber's Rule.

Geometry		
Spotweld diameter, d	7.87 mm	
Plate width, H	$3d$	
Plate length, L	infinite ($4d$ in Ref 1)	
Plate thickness, t	1.91 mm	
Theoretical stress concentration factor, K_t	1.86	
Material Properties	HSLA Steel	Mild Steel
Monotonic		
Young's modulus, E	194 GPa	194 GPa
Poisson's ratio, ν	0.3	0.3
Yield strength, σ_{ys}	564 MPa	270 MPa
Cyclic		
Yield strength, 0.2 percent, σ_{ys}'	558.5 MPa	234 MPa
Strain hardening exponent, η'	0.134	0.12
Strength coefficient, K'	1248 MPa	476 MPa
Fatigue		
Fatigue strength coefficient, σ_f'	1055 MPa	607 MPa
Fatigue strength exponent, b	-0.080	-0.099
Fatigue ductility exponent, c	-0.53	-0.40
Fatigue ductility coefficient, ϵ_f'	0.21	0.125

localized around the spotweld. Thus, following the suggestions in Ref 8, the residual stress is taken equal to σ_{ys} , the monotonic yield strength of the base metal, and by elastic superposition, added as an equivalent remote stress, σ_{ys}/K_t , to the remotely applied stress range ΔS ; that is, the nominal applied stress range on the first reversal is taken as

$$\Delta S = \frac{P}{P_0} \cdot \frac{\sigma_{ys}'}{K_t} + \frac{\sigma_{ys}}{K_t} \quad (7)$$

and on subsequent reversals, as that shown in Eq 5. The first reversal establishes the value σ_{\max} , as illustrated in Fig. 4, and subsequent reversals establish the range $\Delta\sigma$. The local mean stress, σ_o , is given by

$$\sigma_o = \sigma_{\max} - \frac{\Delta\sigma}{2} \quad (8)$$

Results

Firstly, we compare the critical local strain at the weld as estimated by Neuber's Rule with that obtained by the finite-element method (FEM). As indicated in Ref 1 and confirmed in the Appendix, the critical point is along the plate centerline, on the weld periphery, and at the trailing end of the shear force at the weld. Strain at this point is estimated through Neuber's

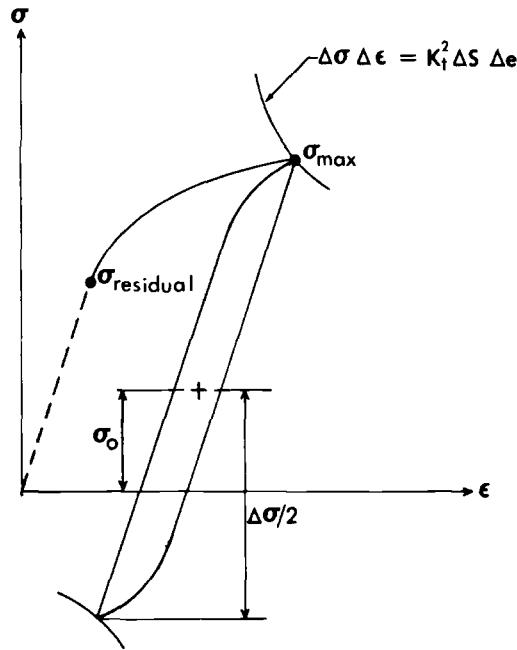


FIG. 4—Schematic of local stress-strain response illustrating the influence of residual stress on local mean stress.

Rule by first solving Eq 6 for $\Delta\sigma$ for a given load level P/P_0 and substituting into the following equations to calculate the various components of strain:

$$\text{elastic} \quad \Delta\epsilon_e = \frac{\Delta\sigma}{E}$$

$$\text{plastic} \quad \Delta\epsilon_p = 2 \left(\frac{\Delta\sigma}{2K'} \right)^{1/\eta'}$$

$$\text{total} \quad \Delta\epsilon = \frac{\Delta\sigma}{E} + 2 \left(\frac{\Delta\sigma}{2K'} \right)^{1/\eta'}$$

$$\text{geometric mean} \quad \left(\Delta\epsilon_e \Delta\epsilon \right)^{1/2} = \left(\frac{\Delta\sigma}{E} \right)^{1/2} \left[\frac{\Delta\sigma}{E} + 2 \left(\frac{\Delta\sigma}{2K'} \right)^{1/\eta'} \right]^{1/2}$$

The geometry and material properties used are listed in Table 1. Except where noted, these are the same data used in the FEM analysis in Ref 1. Comparison of strain estimated by Neuber's Rule and by FEM for the HSLA steel is given in Fig. 5. The curves are FEM results reproduced from Fig. 11

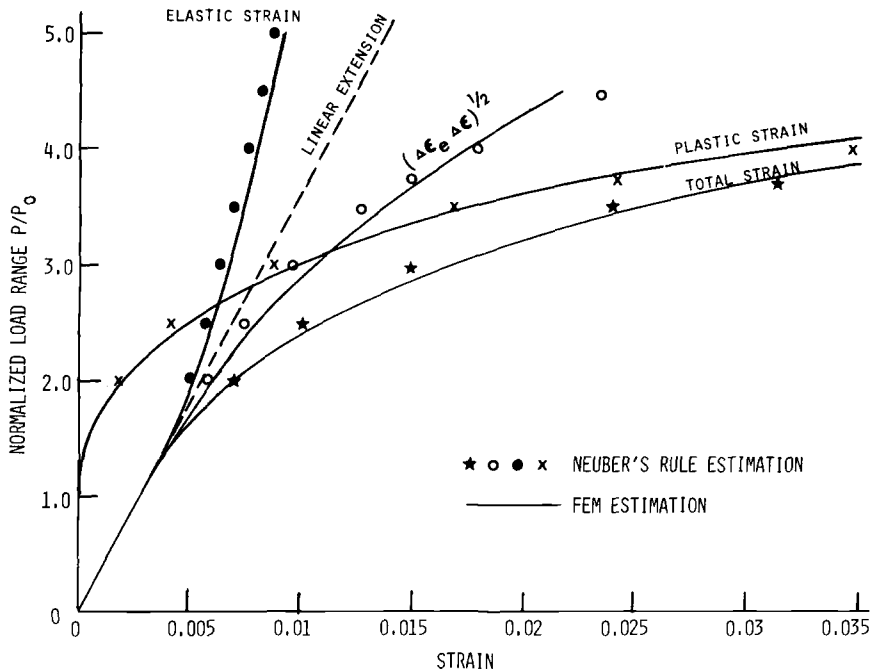


FIG. 5—Elastic, plastic, total, and mean strain at the highest-stressed location.

of Ref 1. The symbols are strain values estimated by Neuber's Rule. Note that from Eq 5, $P/P_0 = 1.0$ corresponds to the load level at which incipient yielding occurs at the critical site; and $P/P_0 = K_t = 1.86$ corresponds to load level at which gross yielding begins. $P/P_0 = 2.7$, which corresponds to 10^3 cycles fatigue life, is about the upper design limit of load. Thus one observes from Fig. 5 that Neuber's Rule coincides with FEM analysis up to gross yielding and differs by at most 6 percent in strain within the load range of interest.

The plotting of load range versus geometric mean strain, P/P_0 versus $(\Delta\epsilon_e \Delta\epsilon)^{1/2}$, was originally intended in Ref 1 to show the limitation of Neuber's Rule. The deviation of the curve from the dotted straight line with increasing load was interpreted as a departure from Neuber's Rule because, if the rule holds, P/P_0 versus $(\Delta\epsilon_e \Delta\epsilon)^{1/2}$ should plot as the dotted straight line. This is, of course, a correct but limited interpretation of Neuber's Rule, as may be seen from Eq 6. The left-hand side of Eq 6 is the expression for geometric mean strain. In the right-hand side, if the nominal applied stress range, ΔS , is limited to the elastic range, the nominal plastic strain is zero and the second term inside the bracket is negligible compared with unity. Thus geometric mean strain would indeed be linearly proportional to load

level P/P_0 . However, as gross yielding begins, the nominal elastic strain decreases with increasing load at the same time the nominal plastic strain increases rapidly. The second term in the bracket becomes comparable to unity, and the geometric mean strain deviates rapidly from linear proportion with load. In other words, the deviation of geometric mean strain from linearity with load should not be taken as a limitation but as a logical extension of Neuber's Rule.

Having demonstrated the accuracy of Neuber's Rule for estimating critical strain, we now show that fatigue life can be predicted accurately as well. Figure 6 shows in symbols the observed fatigue lives of mild steel spotwelds; and Fig. 7, of three HSLA steels. These data, which are reproduced from Ref 1, are observed lives of spotweld specimens pulled cyclically at 25 cycles per minute from zero to a tensile load P with mean load of $0.5 P$. Shown as dotted curves in the figures are predictions by Neuber's Rule with no residual stress. These predictions, which coincide with those obtained by FEM in Ref 1, are consistently higher than the observed values. They were brought into agreement with observations in Ref 1 by multiplying by a reduction factor ($0.174 \pi d t \sigma_f'$). There is no physical basis for the introduction of this factor

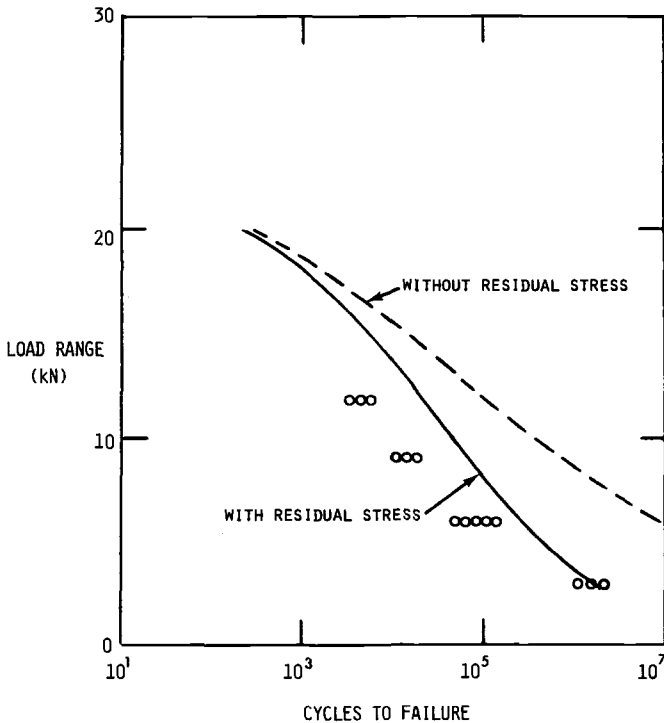


FIG. 6—Predicted and observed fatigue life of mild steel spotweld.

other than that it is dimensionally correct. In this paper, however, the predictions are brought into agreement with observations in a natural way by recognizing the effect of residual stress from welding and treating it as a mechanical prestressing of the spotweld. Thus, incorporating the effect of residual stress into the local mean stress σ_o through Eqs 7 and 8, and substituting into Eq 4, fatigue lives are predicted satisfactorily, as shown by solid curves in Figs. 6 and 7.

Conclusions

(1) Neuber's Rule, widely used for predicting strain in notches, is also applicable to spotwelds.

(2) Compared with FEM, Neuber's Rule is much easier to use for estimating strain concentration. The accuracy is comparable; the cost and effort are negligible.

(3) The roles of factors affecting strain concentration are seen more clearly with Neuber's Rule in a formula than with FEM in numerical values.

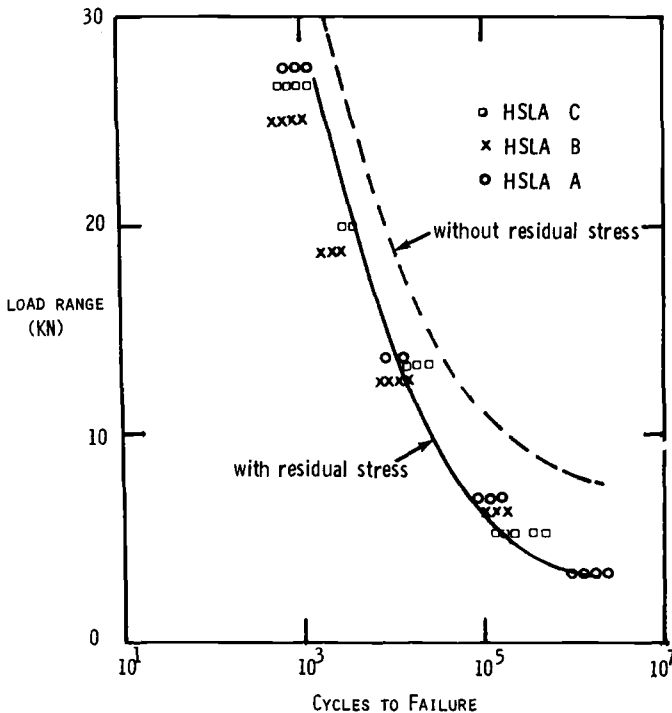


FIG. 7—Predicted and observed fatigue life of HSLA steel spotweld.

(4) Neuber's Rule, used in conjunction with the material strain-range fatigue life relation, can predict the fatigue life of spotweld in the presence of residual stress.

APPENDIX

Determination of the Theoretical Stress Concentration Factor in a Spotweld

The mathematical model of the spotweld is the same as that described in Ref 1, except that the plate length is infinite instead of $4/3$ times the plate width. According to Ref 6, this difference would yield less than 1 percent difference in stresses. Figure 2 shows the model and the coordinate system used in the analysis. Load is transmitted as uniform shear force of intensity, q , over the weld area. This shearing force is balanced at one end ($x = -\infty$) by the load $P = \pi d^2 q/4$. At the other end ($x = +\infty$) and along the two edges, boundary conditions are stress free.

Using the coordinate system shown in Fig. 2, the solution for a force q acting at a point (ξ, η) in an infinite strip was given in Ref 6. Formulae from there pertinent to the present problem are:

$$\chi_0 = \frac{q}{4\pi} [(1 - \nu)(x - \xi) \log r - 2(y - \eta)\theta]$$

$$\chi_5 = \frac{q}{8\pi} (1 + \nu) \int_0^\infty \frac{[mys S - (s + mhc)C]}{m^2(sc + mh)} (B_1 + B_2) \sin m(x - \xi) dm$$

$$\chi_6 = \frac{q}{8\pi} (1 + \nu) \int_0^\infty \frac{(hs C - yc S)}{m(sc + mh)} (B_1' + B_2') \sin m(x - \xi) dm$$

$$\bar{\chi} = \frac{q}{8h^3} y^2(h^2 + \eta y)$$

$$\chi = \chi_0 + \chi_5 + \chi_6 + \bar{\chi}$$

where χ is the stress function which satisfies equations of the system and the boundary conditions. The component χ_0 is the stress function for a point force in an infinite plate, χ_5 and χ_6 are components which annul the stresses along the edges to give the solution for the strip, and $\bar{\chi}$ removes stresses at the end $x = +\infty$ so that the point force is balanced by stresses at $x = -\infty$ alone. In the above equations, the following notations were used:

$$r = [(x - \xi)^2 + (y - \eta)^2]^{1/2}$$

$$\theta = \tan^{-1} \left[\frac{y - \eta}{x - \xi} \right]$$

$$\nu = \text{Poisson's ratio}$$

$$h = \text{strip half-width}$$

$$s = \sinh mh$$

$$c = \cosh mh$$

$$S = \sinh my$$

$$C = \cosh my$$

$$B_1 = \left[m(h - \eta) - \left(\frac{1 - \nu}{1 + \nu} \right) \right] e^{-m(h - \eta)}$$

$$B_2 = \left[m(h + \eta) - \left(\frac{1 - \nu}{1 + \nu} \right) \right] e^{-m(h + \eta)}$$

$$B_1' = -B_1 + e^{-m(h - \eta)}$$

$$B_2' = -B_2 + e^{-m(h + \eta)}$$

m = a dummy variable of integration

Expressions for stresses due to the point force are obtained from χ by differentiation:

$$xx = \frac{\partial^2 \chi}{\partial y^2}; \quad yy = \frac{\partial^2 \chi}{\partial x^2}; \quad xy = \frac{\partial^2 \chi}{\partial x \partial y}$$

Integrating the above expressions with respect to η and ξ over a circular area of unit radius gives the stresses due to a uniform shear force of intensity q over a unit circle. After much simplification, these are:

$$\begin{aligned} \sigma_{xx} &= \int_{-1}^1 \int_{-\sqrt{1-\eta^2}}^{\sqrt{1-\eta^2}} \frac{\partial^2 \chi}{\partial y^2} \partial \xi \partial \eta \\ &= -\frac{qx(5 + \nu)}{8} + \frac{\pi q}{4h} + \frac{q(1 + \nu)}{4} \int_0^\infty (mysS + sC - mhcC) F_1 \sin mx \, dm \\ &\quad - \frac{q(1 + \nu)}{4} \int_0^\infty (mhsC - 2cC - mycS) F_2 \sin mx \, dm \\ \sigma_{yy} &= \int_{-1}^1 \int_{-\sqrt{1-\eta^2}}^{\sqrt{1-\eta^2}} \frac{\partial^2 \chi}{\partial x^2} \partial \xi \, d\eta \\ &= \frac{qx(1 - 3\nu)}{8} + \frac{q(1 + \nu)}{4} \int_0^\infty (sC + mhcC - mysS) F_1 \sin mx \, dm \\ &\quad + \frac{q(1 + \nu)}{4} \int_0^\infty (mhsC - mycS) F_2 \sin mx \, dm \\ \tau_{xy} &= \int_{-1}^1 \int_{-\sqrt{1-\eta^2}}^{\sqrt{1-\eta^2}} \frac{\partial^2 \chi}{\partial x \partial y} \, d\xi \, d\eta \\ &= -\frac{qy(3 - \nu)}{8} + \frac{q(1 + \nu)}{4} \int_0^\infty (mysC - mhcS) F_1 \cos mx \, dm \\ &\quad - \frac{q(1 + \nu)}{4} \int_0^\infty (mhsS - mycC - cs) F_2 \cos mx \, dm \end{aligned}$$

where

$$F_1 = \frac{\left[mh - \frac{(1-\nu)}{(1+\nu)} - \frac{m^2}{4} \right] e^{-mh}}{sc + mh}$$

$$F_2 = F_1 - \frac{e^{-mh}}{sc + mh}$$

Principal stresses σ_1 , σ_2 and effective stress σ_e may now be calculated:

$$\sigma_1, \sigma_2 = \left(\frac{\sigma_x + \sigma_y}{2} \right) \pm \left[\left(\frac{\sigma_x - \sigma_y}{2} \right)^2 + (\tau_{xy})^2 \right]^{1/2}$$

$$\sigma_e = [\sigma_1^2 + \sigma_2^2 - \sigma_1 \sigma_2]^{1/2}$$

Taking the nominal applied stress to be $S = P/2h = \pi q/2h$, Fig. 8 shows the distribution of the normalized stresses σ_1/S , σ_2/S , and σ_e/S on the circumference of the weld for plate width three times the weld diameter. One sees that the critical location

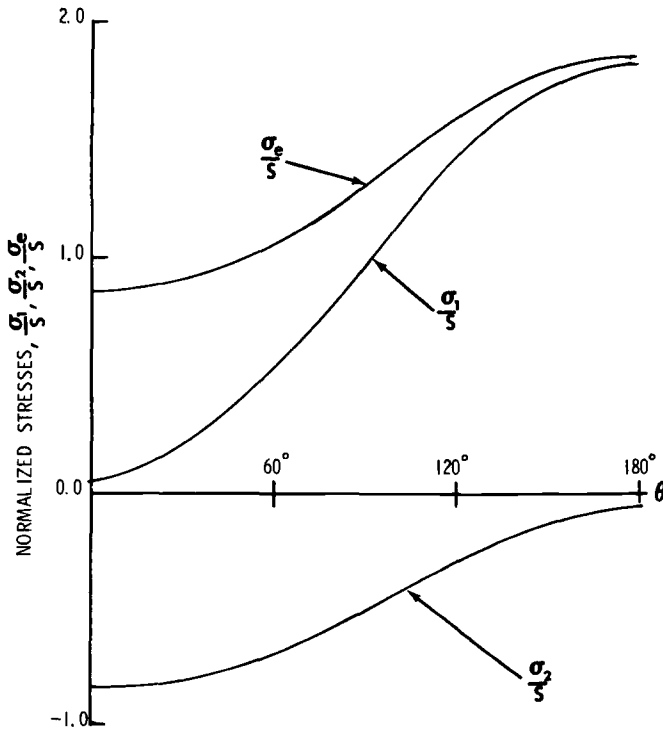


FIG. 8—Stress distribution on the weld circumference.

is at $\theta = 180$ deg; that is, $x = -1.0$, $y = 0$. The theoretical stress concentration factor at this critical point is:

$$K_t = \frac{\sigma_e}{\frac{\pi q}{2h}} = \frac{2h}{\pi} \left[\left(\frac{\sigma_1}{q} \right)^2 + \left(\frac{\sigma_2}{q} \right)^2 - \left(\frac{\sigma_1}{q} \right) \left(\frac{\sigma_2}{q} \right) \right]^{1/2}$$

where

$$\frac{\sigma_1}{q} = \frac{\sigma_{xx}}{q} = \frac{(5+v)}{8} + \frac{\pi}{4h} - \frac{(1+v)}{4} \int_0^\infty [(s - mhc)F_1 - (mhs - 2c)F_2] \sin m \, dm$$

$$\frac{\sigma_2}{q} = \frac{\sigma_{yy}}{q} = -\frac{(1-3v)}{8} - \frac{(1+v)}{4} \int_0^\infty [(s + mhc)F_1 + mhsF_2] \sin m \, dm$$

The variation of K_t as a function of h is shown in Fig. 3.

References

- [1] Kan, Y. R., *Metal Engineering Quarterly*, Nov. 1976, pp. 26-36.
- [2] Neuber, H., *Journal of Applied Mechanics*, Dec. 1961, pp. 544-550.
- [3] Manson, S. S. and Hirschberg, M. H., "Crack Initiation and Propagation in Notched Fatigue Specimens," NASA Technical Memo X-52126, 1965.
- [4] Wetzal, R. M., *Journal of Materials*, Vol. 3, No. 3, 1968, p. 646.
- [5] Topper, T. H., Wetzal, R. M., and Marrow, J., *Journal of Materials*, Vol. 4, No. 1, 1969, p. 200.
- [6] Howland, R. C., *Proceedings of the Royal Society of London*, Series A, Vol. 124, 1929, pp. 89-119.
- [7] Chandel, R. S. and Garber, S., *Metal Technology*, Jan. 1977, pp. 37-44.
- [8] Burk, J. D. and Lawrence, F. V., "The Effect of Residual Stresses on Weld Fatigue Life," FCP Report No. 29, University of Illinois, Urbana, Ill., Jan. 1978.

Critical Failure Modes in Cracked Mechanically Fastened Stiffened Panels

REFERENCE: Gunther, C. K. and Wozumi, J. T., "Critical Failure Modes in Cracked Mechanically Fastened Stiffened Panels," *Design of Fatigue and Fracture Resistant Structures, ASTM STP 761*, P. R. Abelkis and C. M. Hudson, Eds., American Society for Testing and Materials, 1982, pp. 310-327.

ABSTRACT: Conventional residual strength analysis of complex panels is founded on the principles of linear elastic fracture mechanics. Rigorous application of linear analysis techniques combined with failure criteria of ultimate stress capability and critical stress intensity factor results in the conclusion that there exist three potential panel failure modes: (1) skin failure, (2) stringer failures, and (3) fastener failure. Such analysis is in good agreement with test observations for cases involving limited damage. However, for cases where extensive damage exists in the skin element, one or two bay skin crack, linear elastic considerations can result in erroneous conclusions of failure mode and residual strength capability. Elasto-plastic finite-element analysis was conducted; this accounted for the plastic deformation capability of all elements. Crack configurations studied include unstiffened sheet, stringer stiffened sheet with all stringers intact and with center stringer broken. Effects of variations in material, stiffening ratio, and fastener flexibility on failure modes of stiffened panels were investigated. The results show that in all cases skin failure is always the critical failure mode.

KEY WORDS: cracks, elasto-plastic analysis, failure modes, finite element analysis, fracture mechanics, residual strength

Mechanically fastened stiffened skin structure comprises the overwhelming majority of the external surface on existing transport aircraft and gives promise of continued widespread application. Damage tolerance analysis which requires the definition of residual strength capability of such structure has been accorded increased attention under the stimulus of civil and military structural integrity certification requirements.

¹Senior Specialist Engineer and Principal Engineer, respectively, Advanced Airplane Branch, Boeing Military Airplane Company, Seattle, Wash. 98124.

Residual strength analysis of stiffened skin structure is predicated on the principles of linear elastic fracture mechanics. The criterion for failure of a cracked skin is given by

$$K \geq K_{cr} \quad (1)$$

where K_{cr} is the critical stress intensity factor for the skin material, and K is the skin stress intensity factor. The skin stress intensity factor is obtained from

$$K = K_{rem} + K_{stiff} \quad (2)$$

where K_{rem} is the crack driving force due to remote loading, and K_{stiff} is the crack restoring or driving force from the reinforcing elements (stringers).

Closed-form solutions for K_{rem} as a function of remote load, and for K_{stiff} as a function of fastener transfer loads have existed in the literature since 1969 [1].² Thus the problem may be considered solved when fastener transfer loads are defined, and all analytical procedures devolve into attempts at definition of the unknown fastener loads.

Earlier analytical attempts at definition of fastener transfer loads involved modeling of the skin and stringer behavior as purely elastic, with rigid fasteners [1]. As a result, stringer and fastener loads are overstated and the potential for their failure is perceived. Close attention to these results has led observers [2] to predicate three potential primary failure modes: (1) skin failure, (2) stringer failure, and (3) fastener failure. Later analytical attempts incorporate the elasto-plastic behavior of the skin and stringers with elastic fasteners [3]. While this has the result of reducing stringer and fastener loads to more realistic levels, the appreciation of three potential failure modes persists.

Results of tests conducted in-house to define the elasto-plastic behavior of all panel elements (skin, stringer, and fasteners) in conjunction with analysis of panel test results have led to the conclusion that the skin is always the critical element. It will be shown that the inherent plasticity exhibited by aircraft materials used for stringers and fasteners make the potential for their failure remote.

Strain Capability of Stringers

Aluminum alloys used for stringer material exhibit ultimate strain capabilities of 9 to 14 percent in the unnotched condition [4]. While this amount of strain is sufficiently large to preclude stringer failure prior to skin failure, the existence of fastener holes reduces stringer ultimate strain

²The italic numbers in brackets refer to the list of references appended to this paper.

capability to a fraction of the unnotched value. (Typical stringers have 3 to 10 percent "hole-out" for fasteners.)

Vlieger [5] has presented procedures for predicting ultimate strain capability of notched stringers. However, this procedure requires empirical data for solution. A simplified procedure, based on engineering fundamentals and material unnotched stress-strain properties, for the prediction of notched stiffener ultimate strain capability is herein presented.

The stringer is idealized as a strap of width W , with holes of diameter D , at pitch p (Fig. 1). The strain in the cross section not affected by holes is

$$\epsilon_c = \frac{\sigma_g}{E} + \frac{3}{7} \frac{\sigma_o}{E} \left(\frac{\sigma_g}{\sigma_o} \right)^n \quad (3)$$

where σ_g is the remote stringer stress, and σ_o and n are parameters of the Ramberg-Osgood material description (Fig. 2). For the strain in the cross section affected by the holes it is assumed that the remote stress, σ_g , in Eq 3 can be replaced by a constant net section stress expressed as

$$\sigma_{\text{net}} = \sigma_g / (1 - \alpha \cos \theta) \quad (4)$$

where α is the hole-out value defined by

$$\alpha = D/W \quad (5)$$

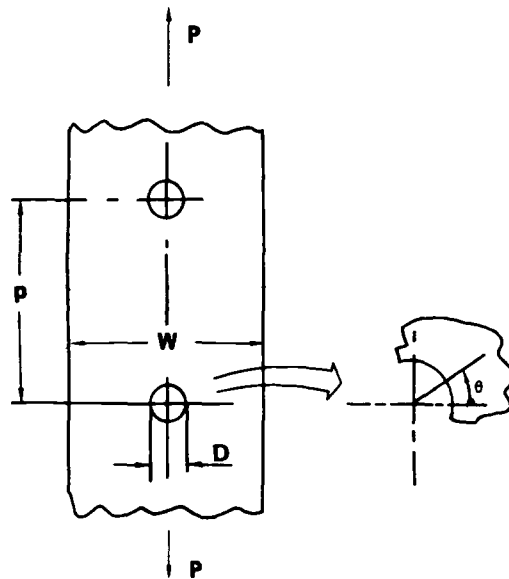


FIG. 1—Stringer geometry.

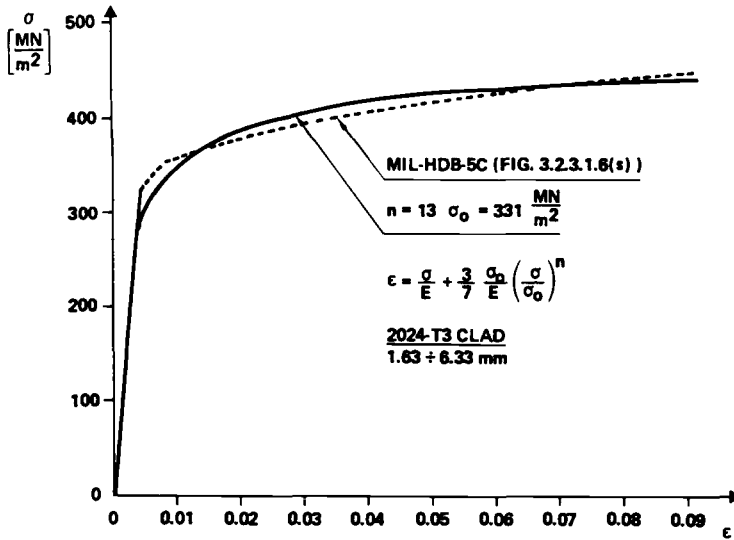


FIG. 2—Example of material stress-strain curve.

and θ is as defined in Fig. 1. Thus the strain in the hole-out affected cross section is expressed as

$$\epsilon_D = \frac{\sigma_{\text{net}}}{E} + \frac{3}{7} \frac{\sigma_o}{E} \left(\frac{\sigma_{\text{net}}}{\sigma_o} \right)^n \quad (6)$$

The stringer displacement, v , over one fastener pitch can now be approximated by

$$v = v_c + 2 v_D \quad (7a)$$

where

$$v_c = (p - D) \epsilon_c \quad (7b)$$

and

$$v_D = \frac{D}{2} \int_0^{\pi/2} \epsilon_D \cos \theta \, d\theta \quad (7c)$$

Strains ϵ_c and ϵ_D are expressed by Eqs 3 and 6.

Finally, stringer strain, ϵ_{STR} , including the effect of hole-out, is given by

$$\epsilon_{\text{STR}} = v/p \quad (8)$$

Tests were conducted on 7075-T651 and 2024-T3511 stringers with hole-out values of 6 to 20 percent. The results of these tests are shown in Table 1.

TABLE 1—Ultimate stringer strains.

Spec. ID	Material	W, cm	D, mm	p, cm	t, mm	Hole-Out, α	Test Results			
							P_{ult} , N	v_{ult} , mm	$\epsilon_{str ult}$	Predicted $\epsilon_{str ult}$
1A	7075-T6S1	3.18	6.35	3.18	4.78	0.20	78498	0.483	0.015	0.024
1B	7075-T6S1	3.18	6.35	3.18	4.88	0.20	80189	0.559	0.018	0.024
2A	7075-T6S1	3.18	6.35	3.18	4.62	0.20	73959	0.686	0.022	0.021
2B	7075-T6S1	3.18	6.35	3.18	4.78	0.20	77341	0.711	0.022	0.023
6B	2024-T3S1	4.14	2.39	0.95	5.64	0.06	96921	0.660	0.069	0.051
6C	2024-T3S1	4.11	6.38	2.54	5.59	0.15	90246	1.346	0.053	0.046

They are compared with predictions made using the developed procedure (Eqs 7 and 8) and typical material properties from MIL-HDBK-5C [4]. The predictions correlate reasonably well with the experimental results. These strain capabilities are not in themselves adequate to preclude stringer failure. They do provide relief, however, and when combined with fastener plastic strain capability effectively preclude stringer failure.

This procedure may also be used to develop the effective moduli for stringers with hole-out. Using the Ramberg-Osgood material description the tangent modulus can be expressed as

$$E_T = \frac{E}{1 + \frac{3}{7} n_e \left(\frac{\sigma}{\sigma_{oe}} \right)^{n_e - 1}} \quad (9)$$

where σ_{oe} and n_e must be derived from the basic material parameters σ_o and n and hole-out α . This can be accomplished using

$$\sigma_{oe} = \left\{ \frac{3 (\sigma_g)^{n_e}}{7 E \left[s(\sigma_g, \alpha) - \frac{\sigma_g}{E} \right]} \right\}^{1/n_e - 1} \quad (10)$$

where

$$s(\sigma_g, \alpha) = \int_0^{\pi/2} \epsilon_D(\sigma_g, \alpha) \cos \theta \, d\theta \quad (11)$$

and ϵ_D is given by Eq 6. Since only two parameters can be determined in Eq 10, it is obvious that a best fit for σ_{oe} and n_e must be obtained.

This procedure was used to develop the effective moduli for the 2024 and 7075 stringers used in the following analyses.

Displacement Capability of Fasteners

Mechanical fasteners provide a source of plastic deformation capability for relief of stringer loads. Early panel residual strength analyses assumed rigid fastener behavior [1]. Later analysis [3,6] included the effects of elastic fastener behavior to failure. Sanga [7] included the effects of fastener plasticity, and Vlioger [5] has presented a procedure for calculating fastener ultimate strain capability with the assistance of empirically derived parameters.

Recently, in-house studies were initiated to define elastic flexibility and ultimate deformation capability of commonly used aluminum and titanium fasteners (rivets and bolts) in aluminum substrate. Specimen geometry is shown in Fig. 3. Flexibilities derived from these tests were in good agreement with the results of predictions made using the equation presented by Swift in

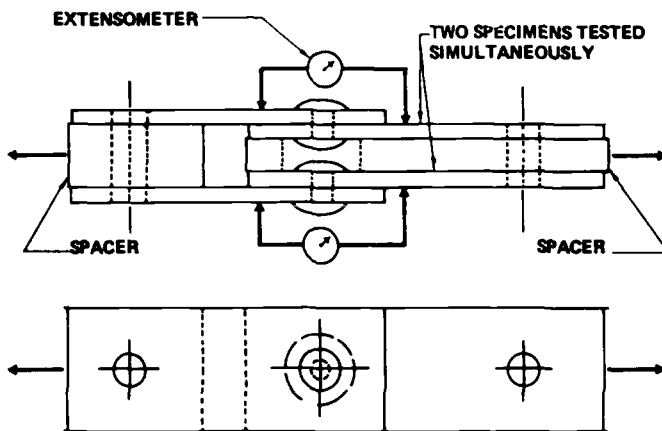


FIG. 3—Fastener flexibility test setup.

Ref 6. No systematic trend could be discerned in these test results, because substrate or fastener material, or both, were varied. Aluminum rivets of 2017, 2024, 2117, and 7050 alloys combined with 2024, 2324, and 7150 substrate produced results with no discernable differences. No explanation for these observations is readily apparent, but they are believed to be at least partially owing to the limited population of data.

Fastener flexibilities used in the analyses described later are as defined by Figs. 4 and 5. The ultimate displacement capabilities of fasteners shown in these figures are not intended as quantitatively definitive. Rather, they are indicative of the order of magnitude of the plastic deformation characteristics of mechanically fastened joints. It may be noted that this deformation is significantly larger than would be anticipated as a result of elastic considerations, and is of sufficient size to significantly reduce the potential for stringer failure.

Sheet Displacements

Sheet displacements in the vicinity of the crack tip have been expressed as (for plane stress):

$$v = \frac{K}{E} \sqrt{\frac{2r}{\pi}} \sin \frac{\theta}{2} \left[2 - (1 + \nu) \cos^2 \frac{\theta}{2} \right] \quad (12)$$

This implies that sheet displacements in the near field are a function of K . It is to be noted that this familiar expression is subject to two important limitations: (1) it is valid only for linearly elastic materials; and (2) it is valid only in the near vicinity of the crack tip.

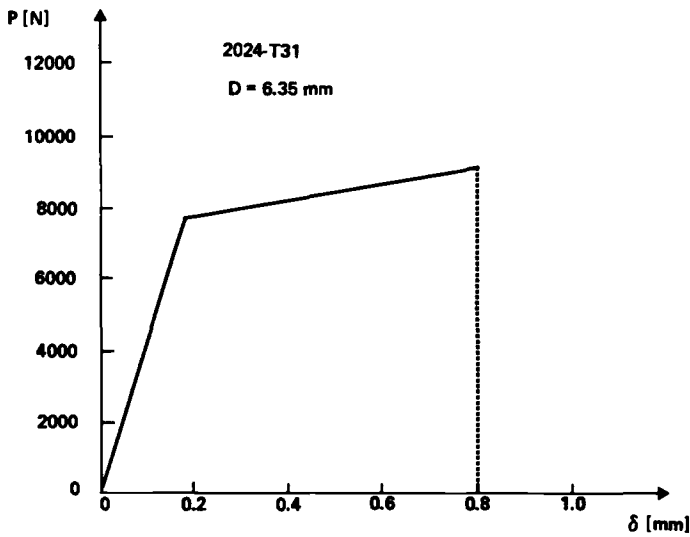


FIG. 4—Aluminum rivet flexibilities.

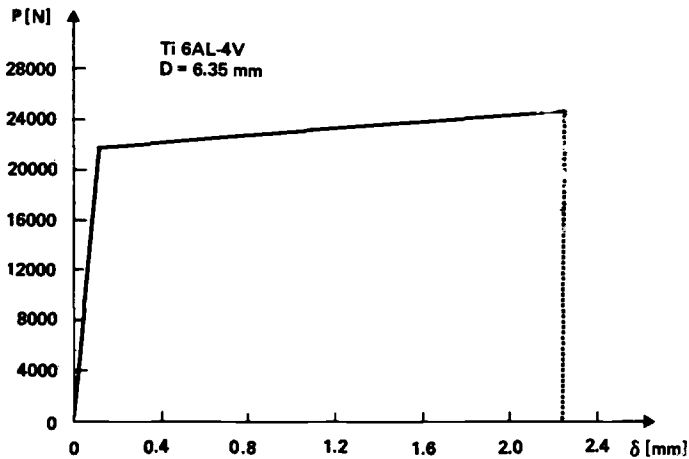


FIG. 5—Titanium bolt flexibilities.

A typical error associated with Eq 12 for

$$r = a/10$$

can be as much as 15 percent depending on θ . However, aircraft metallics exhibit considerable plasticity at applied stress levels considered for residual strength, which negates the utility of Eq 12 for definition of displacements.

In order to define displacements in a cracked sheet, elasto-plastic finite-element analyses for unstiffened sheet were conducted. For these analyses, semicrack lengths of 15.2 and 25.4 cm were selected as representative of cases of interest for transport aircraft with like stringer spacing, and a two bay skin crack centered on a stringer. Two materials were selected for the analyses: 2024-T351 plate and 7075-T651 plate. It is believed that these materials represent the bounds of material properties encountered. The 2024 alloy combines high toughness, K_{cr} , with high ductility (that is, low value of F_{ty}/F_{tu}), whereas the 7075 alloy combines low toughness and low ductility.

Results for the 2024 and 7075 materials are shown in Figs. 6 and 7, respectively. Sheet displacements, v , are shown in the vicinity of the crack tip along a line $y = 2.54$ cm for several levels of stress intensity factor. The rationale for display of the displacement, v , at the location selected follows: Typical fastener pitch, p , for stiffened structure ranges from 1.50 to 3.50 cm. Owing to compatibility considerations, stringer displacements at fastener locations are equal to the difference between sheet displacement and fastener displacement. (Fig. 8). Also, Sanga [7] has shown that fastener displacement within a given stringer location and in the near vicinity of a crack is not strongly dependent on fastener location, y . Thus it is reasoned the most critical case for stringer failure would be that of a crack running through a fastener location with an active crack tip. This condition may be envisioned as arising as a consequence of a skin crack propagating into a fastener hole under the in-

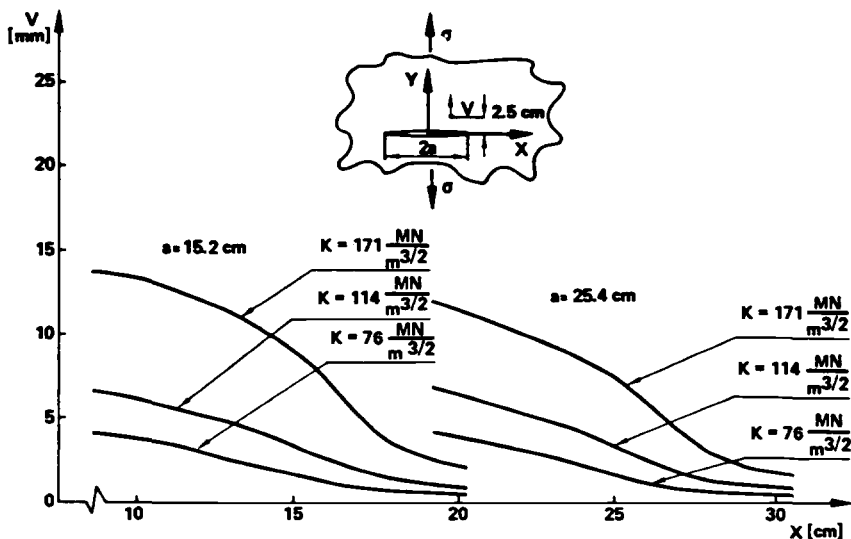


FIG. 6—Unstiffened sheet displacements (2024-T3).

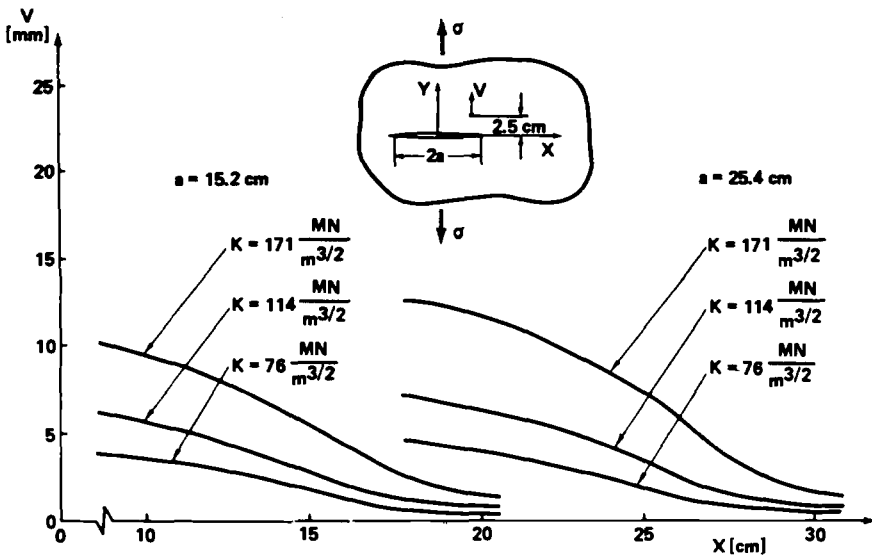


FIG. 7—Unstiffened sheet displacements (7075-T6).

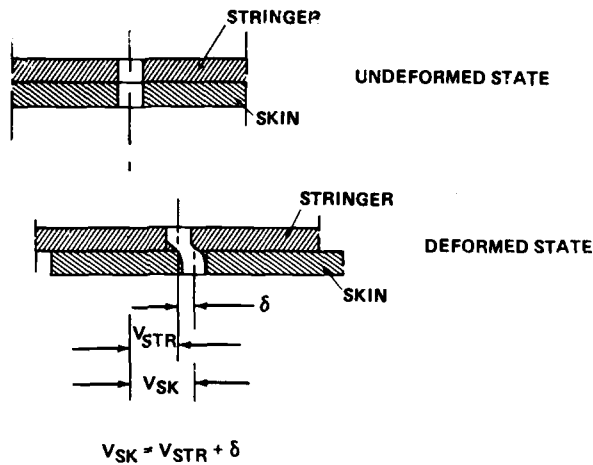


FIG. 8—Compatibility of displacements.

fluence of flight loads, and reinitiating at the far side of the hole prior to application of residual strength load.

It may be observed from Figs. 6 and 7 that the ultimate strain capability of stringers with hole-out is insufficient to lead to the conclusion that stringers will remain intact at loading conditions leading to skin criticality. In order to

appraise the potential for stringer failure it is necessary to address fastener displacement and crack closing action in the sheet due to transfer of loads from skin to stringer. This can only be accomplished by elasto-plastic analysis involving all elements of the structure. Figure 6 shows that the shorter crack length configuration in 2024-T3 material produces larger displacements in the vicinity of the crack tip for the same levels of stress intensity factor. The opposite is true for the 7075-T6 material (Fig. 7). Further analysis is conducted using the shorter crack configuration, since it presents a more widely used stringer spacing.

Analysis of Stiffened Skin Structure

As mentioned previously, elasto-plastic analysis of stiffened skin structure was conducted only for a stringer spacing corresponding to the 15.2 cm semicrack length. These analyses utilized a two-dimensional fine grid finite-element model (no out-of-plane bending) to determine fastener transfer loads and deflections and stringer loads and deflections. Finally, sheet stress intensity factor, K , was determined using

$$K = \sigma\sqrt{\pi a} = \sum_{i,j} C_{ij} P_{ij} \quad (13)$$

where

- C_{ij} = influence coefficients (for example, Ref 1),
- P_{ij} = fastener loads from finite-element analysis,
- i = 1, 2, 3, . . . , stringer number, and
- j = 1, 2, 3, . . . , fastener location.

In all cases skin cracks were centered at a stringer location and cases involving intact and fractured central stringers were addressed.

Intact Central Stringer Case

Analyses of two bay skin cracks centered over intact central stringers were conducted using the following structural parameters: (1) 2024 and 7075 material, (2) 0 and 10 percent hole-out in stringer, (3) 100 percent stiffening ratio, and (4) aluminum fasteners.

Stiffening ratio is defined by

$$\mu = \frac{\text{area of stringer}}{\text{skin gage} \times \text{stringer spacing}} \quad (14)$$

The results of these analyses are shown in Fig. 9. Superimposed on the plots of stringer strain as a function of K are levels of stringer ultimate strain capability (Fig. 10), which were determined using the procedure developed.

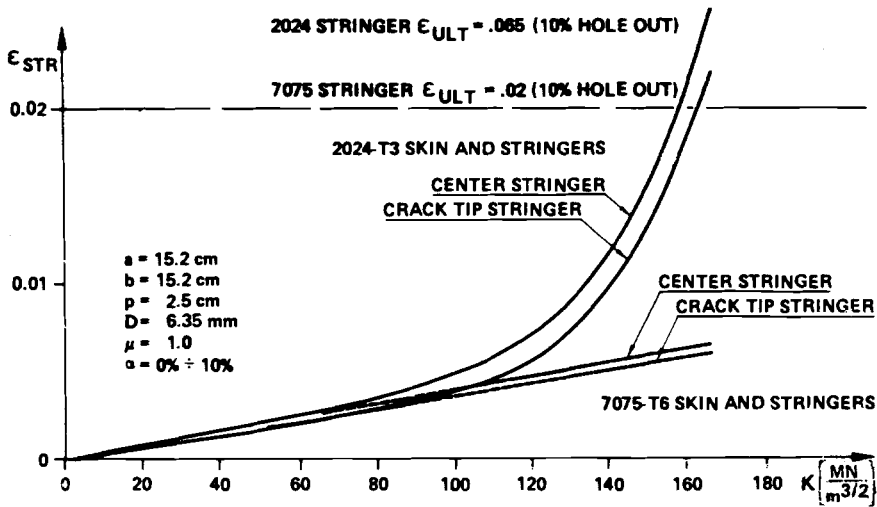


FIG. 9—Maximum stringer strain; all stringers intact.

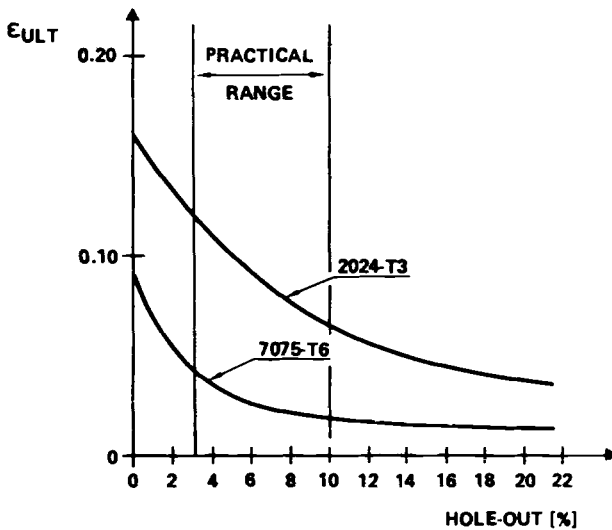


FIG. 10—Ultimate stringer strain.

One surprising result of these studies is the insensitivity of stringer displacements (strain) to stiffener hole-out. These differences were so small that strains are shown as a single value in Fig. 9 for both hole-out values. An explanation for this lies in the fact that hole-out has an insignificant impact on stringer stiffness throughout the elastic range and only a small influence

from yield to failure. However, hole-out has a significant impact on stringer ultimate strain capability (Fig. 10).

It can be seen that within the range of structural parameters normally encountered in aircraft structure, similar skin and stringer material, stringer failure is improbable. One could also infer that a combination of very tough 2024 skin material ($K_{cr} = 165 \text{ MN/m}^{3/2}$) with 7075 stringers and 10 percent hole-out could result in central stringer failure. Such combinations are not used in-house, but should be investigated further.

It is reasonable to question the conclusion that the potential for initially perfect stringers to fail is remote, since other stiffening ratios (lower) or use of stiffer fasteners (steel or titanium) could increase stringer strains relative to sheet displacements and enhance the potential for stringer failure. However, further analysis was not deemed warranted for the intact stringer case. The reasoning was as follows:

The rigorous application of military and commercial damage tolerance specifications, MIL-A-83444 [8] and FAR 25.571 [9], require the consideration of damage at multiple sites. If a skin crack has propagated to a semilength equal to a stringer spacing, a stringer crack originating at the same location will propagate to a length sufficient to cause stringer fatigue failure under normally encountered flight loads. Thus, it is reasonable to consider the case of a two bay skin crack centered over a broken central stringer as the condition of real concern.

Fractured Central Stringer Case

Analysis of two bay skin cracks centered over a fractured central stringer were conducted to assess the potential for crack tip stringer failure under various panel configuration variables. The variables studied were: (1) 2024 and 7075 material, (2) crack tip stringer location, (3) stiffening ratio, (4) fastener material, and (5) 0 and 10 percent hole-out in stringer. The crack tip stringer is considered as critical for this crack configuration, since stringer failure would certainly lead to panel failure.

To constrain the analytical effort to reasonable levels the following hierarchy of studies and variables was established:

(1) The impact of crack tip stringer location was assessed. For these studies a stiffening ratio of 100 percent, aluminum fasteners, and hole-out values of 0 and 10 percent were used. The two tip crack stringer locations addressed were $x = a$ and $x = 0.857a$, since these locations are variously reported to result in the highest panel residual strength.

(2) After selecting the most critical crack tip stringer location ($x = 0.857a$) from (1) above, the impact of a change in stiffening ratio from 100 to 50 percent was assessed. It was anticipated that the lower stiffening ratio

would result in a greater tendency to stringer criticality, and 50 percent stiffening was selected as the minimum reasonably encountered.

(3) After selecting the most critical crack tip stringer location ($x = 0.857a$) and a stiffening ratio of 50 percent, analyses were conducted to assess the impact of fastener material on stringer criticality. Aluminum and titanium fasteners were addressed.

In all analyses the impact of stringer hole-out was investigated. As stated previously, this had negligible impact on stringer strains; however, it does have a significant impact on stringer ultimate strain capability and panel K required for stringer failure.

The results of all three studies for the 2024 skin and stringer combination are shown in Fig. 11, and the results for the 7075 combination are shown in Fig. 12. Superimposed on each figure are the stringer ultimate strain capabilities for a 10 percent hole-out value. It may be seen that even at the more optimistic levels of critical stress intensity factors for the two sheet materials studied (for example, $K_{cr} = 165 \text{ MN/m}^{3/2}$ for 2024 and $K_{cr} = 82 \text{ MN/m}^{3/2}$ for 7075) stringer failure is not possible.

In the event that it is desired to assess the potential for failure of a 7075 stringer on 2024 sheet it would be possible to transfer the stringer strain cutoff value ($\epsilon_{ult} = 0.020$) from the 7075 material combination plot to the

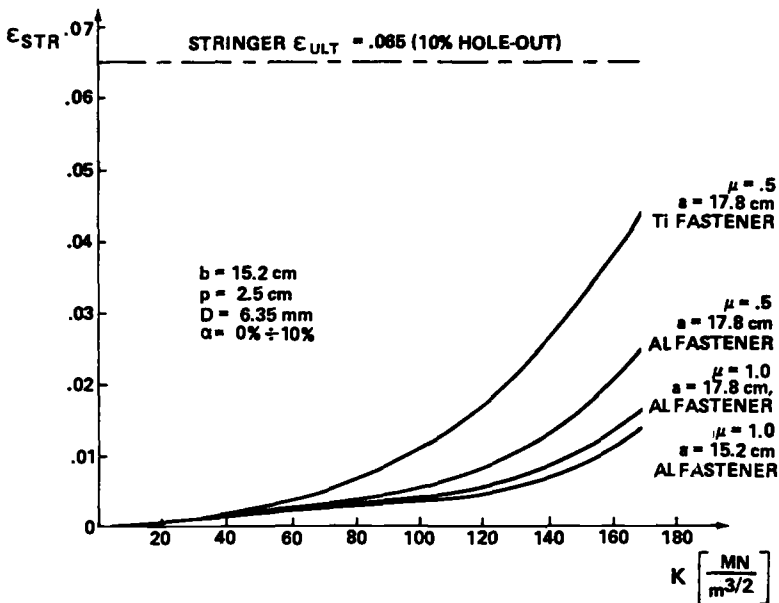


FIG. 11—Maximum stringer strain-broken stringer (2024-T3).

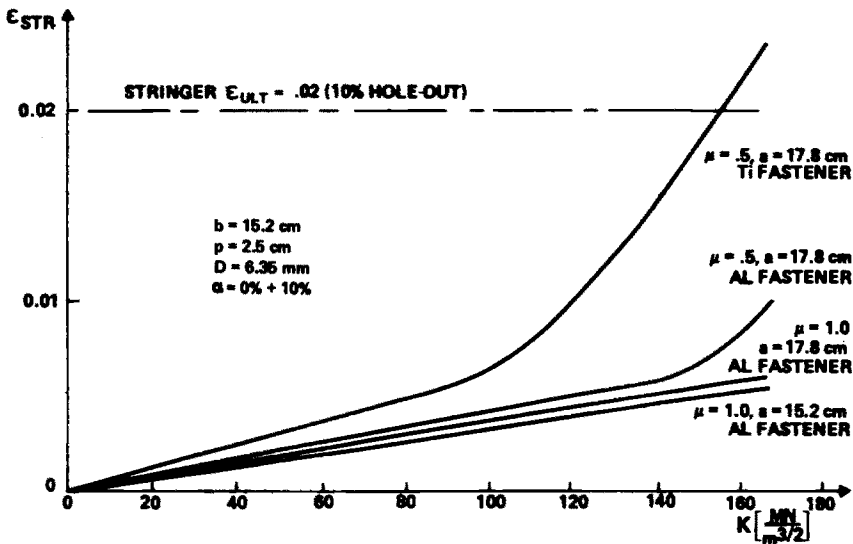


FIG. 12—Maximum stringer strain—broken center stringer (7075-T6).

2024 plot. This procedure introduces a degree of error in that strains of 7075 stringers would be smaller than those shown for 2024 stringers. However, the error is conservative. It is not recommended that a reverse procedure be applied, 2024 ultimate strain cutoff on 7075 curves, as an unconservative error of undefined magnitude is introduced.

In all cases the 7075 curves have been extended to sheet K_{cr} -values far higher than normally encountered. This has been done to cover the newer 7000 series alloys, 7050 and 7475, which exhibit static properties similar to 7075 with considerably higher fracture properties.

Conclusions and Recommendations

It has been shown that, for typical aircraft structure, fastener or stringer failure is not the critical failure mode. For all cases analyzed, the skin provides the critical failure path for materials presently in widespread use. It has also been shown that under certain conditions—that is, combinations of high toughness skin (2024) and low ductility stringers (7075)—stringer failure can be the predominant failure mode.

An interesting observation on the impact of the variables investigated is that stiffening ratio has little influence on stringer criticality. Also, fastener material behavior is one of the more important variables in affecting stringer strains. The extreme sensitivity of stringer strains to fastener material properties leads naturally to the question of potential criticality of stringers where steel fasteners are employed. No analyses were conducted using steel

fasteners, because their elasto-plastic behavior is not at present fully defined. It is surmised, upon evaluation of results with aluminum and titanium fasteners, that use of steel fasteners with 7075 stringers would increase the probability of stringer failure, especially when used in conjunction with high-toughness sheet. When test data defining the elasto-plastic behavior of steel fasteners become available, further analyses should be conducted to assess their impact on possible stringer criticality.

Additionally, a method for determining effective stringer moduli and ultimate strain capability has been determined from basic material properties.

These conclusions pertain to cases where the crack-tip stringer is in an initially perfect condition. More parametric analysis should be conducted to provide procedures for quickly determining the level of strain in the crack tip-stringer. Corresponding stresses may then be used to evaluate the criticality of a cracked crack-tip stringer.

All analyses were conducted without consideration of eccentricity. To the knowledge of the authors only one work is reported in which controlled tests [2] have been conducted to determine the effect of eccentricity on stiffened panel residual strength. Vlieger presented test results of nominally identical panels with the exception that some were stiffened by a pair of straps, one riveted to each surface of the skin material, and some had zee-stiffeners attached to one surface only. In these tests no significant difference in failure load was observed. These results indicate that eccentricity is of secondary importance and may be ignored. More work is recommended to fully define the importance of eccentricity in cracked stiffened panel behavior.

Acknowledgments

The contribution of R. V. Sanga, Boeing Commercial Airplane Company, to this publication by providing the fastener flexibility data is acknowledged.

References

- [1] Poe, C. C., "Stress-Intensity Factor for a Cracked Sheet with Riveted and Uniformly Spaced Stringers," NASA Technical Report, NASA TR R-358, May 1971.
- [2] Vlieger, H., "Residual Strength of Cracked Stiffened Panels," National Aerospace Laboratory, NLR-TR71004 U, Netherlands, Jan. 1971.
- [3] Swift, T. in *Damage Tolerance in Aircraft Structures, ASTM STP 486*, American Society for Testing and Materials, 1971, pp. 164-214.
- [4] *Military Standardization Handbook*, Metallic Materials and Elements for Aerospace Vehicle Structures, MIL-HDBK-5C, Vol. 2, 15 Dec. 1978.
- [5] Vlieger, H., "Fail Safe Characteristics of Built Up Structures," in *Proceedings, 9th Congress of the International Council of the Aeronautical Sciences*, Aug. 1974.
- [6] Swift, T., "The Effects of Fastener Flexibility and Stiffener Geometry on the Stress Intensity in Stiffened Cracked Sheet," *Prospects of Fracture Mechanics*, Noordhoff, 1974.

- [7] Sanga, R. V., "The 747 Fail-Safe Structural Program," *Fail Safe Aircraft Structures*, Vol. II, ICAF Symposium 1973, RAF TR 73183, 1974.
- [8] "Airplane Damage Tolerance Requirements," Military Specification MIL-A-83444, United States Air Force, 2 July 1974.
- [9] "Federal Aviation Administration Advisory Circular AC 25.571-1," 28 Sept. 1978.

DISCUSSION

*T. Swift*¹ (written discussion)—Two statements made in the subject paper require comment. These statements are (1) skin is always the critical element; and (2) the effects of stiffener eccentricity are of secondary importance and may be ignored. Consider Statement 1: It has been shown by elastic-plastic analysis supported by tests that for some geometrical configurations stiffened panel failure can be precipitated by fastener failure. Swift² cites a case where the residual strength of a panel containing a two-bay crack with a broken central stiffener was limited by outer stiffener to skin fastener failure. In this test the fasteners in the two outer stiffeners failed in shear over the entire length of the panel, thus precipitating panel failure. Elastic-plastic analysis based on the displacement compatibility approach, which accounts for fastener nonlinear shear displacement and stiffener eccentricity (bending), predicted this failure mode and stress level. This result is also published in Swift.³ A certain degree of caution should therefore be exercised before discounting fastener failure as an important mode.

Consider Statement 2: It is noted that stiffener eccentricity was not included in analysis in the subject paper and yet it was concluded to be unimportant. Tests of Vlieger⁴ were cited as evidence but Vlieger himself, in this reference, states "that the load carrying capacity of the eccentrically stiffened sheet is clearly lower than that of a sheet with symmetric strip stiffeners with the same cross sectional area". It is also noted that the stiffeners in Vlieger's tests were closely spaced, thus minimizing load transfer effects. Stiffener bending caused by eccentricity was considered by Swift and Wang⁵ using finite-element analysis for both longitudinal and circumferential crack conditions in fuselage structure. Figure 14 of this reference illustrates that considerable bending exists in the two outer stiffeners for a two-bay crack condi-

¹National Resource Specialist, Fracture Mechanics/Metallurgy, Federal Aviation Administration, Washington, D.C.

²Swift, T., "Damage Tolerance Analysis of Redundant Structures," in *Fracture Mechanics Design Methodology*, AGARD-LS-97, 1979.

³Swift, T., "The Effects of Rivet Yielding on Residual Strength of Stiffened Structure Containing Cracks," in *Practical Applications of Fracture Mechanics*, AGARD-AG-257.

⁴Vlieger, H., "Residual Strength of Cracked Stiffened Panels," NLR Report NLR-TR-71004U, 1971.

⁵Swift, T. and Wang, D. Y., "Damage Tolerance Design-Analysis Methods and Test Verification of Fuselage Structure," AFFDL-TR-70-144, 1970.

tion. Figure 51 of the same reference shows strain gage data correlated with analysis which illustrates the effects of stiffener eccentricity. Figure 33 in Swift⁶ also shows strain gage data correlated with analysis illustrating considerable bending due to stiffener eccentricity. The results of analysis on several configurations, shown in Tables 2, 3, and 4 in Swift,⁶ all indicate high bending in stiffeners as a function of crack length. In addition to this finite-element analysis, stiffener eccentricity has also been considered using displacement compatibility analysis methods. The results of this analysis, contained in Swift,⁷ also illustrate the importance of considering stiffener eccentricity. Analysis throughout the work by Swift² considers stiffener eccentricity, and Tables 3 to 7 of this reference contain inner and outer fiber stresses as a function of crack length resulting from a parametric study. Here again, considerable stiffener bending exists. The test correlation in Swift⁸ would not have been possible without consideration being given to stiffener eccentricity. Therefore, although stiffener eccentricity may not be of prime importance for some configurations, it should not be ignored, as was suggested in the subject paper.

C. K. Gunther and J. T. Wozumi (authors' closure)—Response to Statement 1: Our statements concerning critical failure modes were made for typical aircraft materials. The upper bound of fracture toughness is considered to be 180 ksi $\sqrt{\text{in.}}$, with typical values of presently used materials somewhat lower. The use of no more than 160 ksi $\sqrt{\text{in.}}$, is recommended for residual strength analysis. Close investigation of the work by Swift² shows that fastener failure is not the critical failure mode until the stress intensity factor values exceed 180 ksi $\sqrt{\text{in.}}$. The authors agree that, if such high fracture toughness values are to be considered, the probability of fastener or stringer failure as primary failure mode should be investigated.

Response to Statement 2: The experimental data of Vlieger⁴ do not support the claim that eccentricity is an important consideration. We agree that stiffener bending theoretically should have the effect of reducing the effective stiffness of the skin-reinforcing element, resulting in lower residual strength. Until further experimental evidence shows conclusively that eccentricity has a significant influence on the reinforcing capability of the stringer, such effects will be believed to be small. In any event, consideration of eccentricity increases the potential for skin failure as primary failure mode.

⁶Swift, T. in *Damage Tolerance in Aircraft Structures, ASTM STP 486*, American Society for Testing and Materials, 1971, pp. 164-214.

⁷Swift, T., "The Effects of Fastener Flexibility and Stiffener Geometry on the Stress Intensity in Stiffened Crack Sheet," in *Prospects of Fracture Mechanics*, Noordhoff International Publishing, 1974.

⁸Swift, T., "Design of Redundant Structures," in *Fracture Mechanics Design Methodology, AGARD-LS-97*, 1979.

Methodology for Evaluating Weight Savings from Basic Material Properties

REFERENCE: Ekvall, J. C., Rhodes, J. E., and Wald, G. G., "Methodology for Evaluating Weight Savings from Basic Material Properties," *Design of Fatigue and Fracture Resistant Structures, ASTM STP 761*, P. R. Abelkis and C. M. Hudson, Eds., American Society for Testing and Materials, 1982, pp. 328-341.

ABSTRACT: Major payoffs of new aerospace structures in terms of weight savings, performance, and life-cycle cost are anticipated from successful development of advanced materials. To aid in development of new alloy systems a method has been developed for predicting weight savings resulting from material (property set) improvements for specific failure modes in aircraft structures. Material properties include density, modulus of elasticity, strength, fatigue, crack growth, fracture toughness, and stress corrosion resistance. Weight savings analysis includes consideration of the margins of safety for various failure modes that could affect the size of the aircraft structure. Results of analysis applicable to a carrier-based patrol aircraft and an advanced tactical fighter indicate a weight savings potential of up to 16 percent for advanced aluminum alloys.

KEY WORDS: weight saving, aircraft structure, aluminum alloys, durability, damage tolerance, material properties, strength-weight relationships, margins of safety

Nomenclature

da/dN	Crack growth rate
E	Modulus of elasticity
E_s	Secant modulus
E_t	Tangent modulus
F	Allowable stress
F_{cy}	Compressive yield strength
F_{max}	Maximum stress in constant-amplitude fatigue cycle
F_{tu}	Ultimate tensile strength

¹Staff Scientist, Senior Research and Development Engineer, and Research and Development Engineer, respectively, Lockheed-California Company, Burbank, Calif. 91520.

K_c	Critical plane stress fracture toughness
K_{Ic}	Plane strain fracture toughness
K_{max}	Stress intensity for maximum tension stress
K_t	Theoretical geometric stress concentration factor
ΔK	Stress intensity for stress range
$\overline{\Delta K}$	$(\Delta K)^m (K_{max})^{(1-m)}$ effective stress intensity
m	Material constant
N	Cycles to failure
t	Material thickness
W	Weight
δ	Density
1, 2, ...	Material designation and failure mode category
MS	Margin of safety = $\frac{\text{allowable stress or load}}{\text{design stress or load}} - 1$

In recent years research studies have shown a potential for developing aluminum alloys with improved material properties by combinations of alloy modifications, thermal mechanical treatments, powder metallurgy techniques, and rapid solidification rate (RSR) process [1-4].² These metallurgical developments permit the formulation of new alloy systems which previously could not be made by conventional manufacturing methods. Preliminary testing of some experimental alloys indicates increases in strength and modulus, decreases in density, and improved fatigue, crack growth, and fracture toughness properties compared with currently available aluminum alloys [5,6]. However, the dilemma for the alloy development researchers is to determine what combination of material properties will provide the most significant weight reduction in aircraft structures.

Research is being conducted to develop advanced aluminum alloys from rapidly solidified powders for aerospace applications [7-9]. To aid in the development of the new alloy systems, a methodology has been developed to evaluate weight saving potential for aircraft structures. This methodology provides relationships between specific material properties and weight savings for an entire aircraft. By use of Lockheed systems analysis program (ASSET), the calculated weight savings can be translated into aircraft performance parameters, such as increased payload, range, fuel savings, and other factors, for both constant mission and weight choices [3].

The method of evaluating structural weight reduction for these advanced aluminum alloys is illustrated in Fig. 1. An aircraft design with currently available aluminum alloys is used as a baseline for comparison. Aircraft structural weight is subdivided according to primary failure modes which are used to size the structure. Equations for each failure mode relate changes in

²The italic numbers in brackets refer to the list of references appended to this paper.

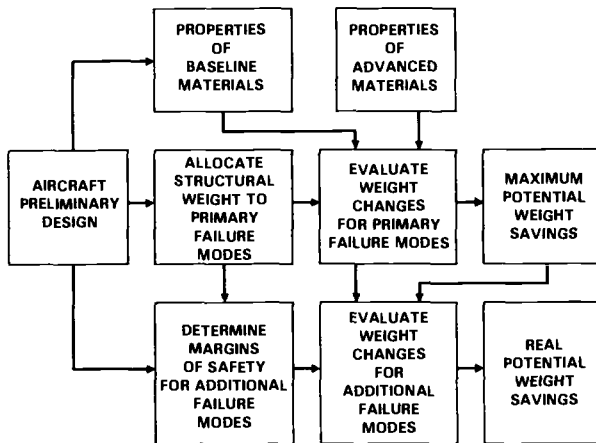


FIG. 1—Aircraft structural weight evaluation of new material.

weight to the basic material properties. Then the maximum potential weight savings is evaluated with improved material properties assuming that the primary failure modes do not change. To determine the “real” weight reduction, the effect of other potential failure modes on structural weight must be considered. The “real” weight savings will depend on the margin of safety associated with each failure mode as well as reduction in weight from improved properties.

Model for Predicting Weight Savings

Seven basic failure modes are considered as an initial first step for a weight saving evaluation. The equations for evaluating the weight saving potential were developed in Ref 7 and are summarized in Table 1. These relationships were developed using weight-strength analysis procedures given in Ref 10. The relationship between the structural weight, W_2 , for the advanced material and the structural weight for the basic material, W_1 , is obtained by substituting the appropriate material properties into the weight ratio equation. The potential weight savings is then given by the following equation:

$$\% \text{ of weight savings} = \left[1 - \frac{W_2}{W_1} \right] 100 \quad (1)$$

To evaluate any potential failure mode not shown for the baseline structure, the ratio W_2/W_1 is multiplied by the margin of safety correction factors given in Table 1 to obtain the “real” weight savings. Then for any given com-

TABLE 1—Weight ratios and margin of safety factors according to aircraft structure failure mode criteria.

Category	Failure Mode	Weight Ratio (W_2/W_1)	Margin of Safety Factors
1	tensile strength	$\frac{\delta_2}{\delta_1} \frac{F_{tu1}}{F_{tu2}}$	$\frac{1}{(1 + MS)}$
2	compressive strength	$\frac{\delta_2}{\delta_1} \frac{F_{cy1}}{F_{cy2}}$	$\frac{1}{(1 + MS)}$
3	crippling	$\frac{\delta_2}{\delta_1} \left[\frac{E_{s1}}{E_{s2}} \frac{F_{cy1}}{F_{cy2}} \right]^{0.25}$	$\left[\frac{1}{1 + MS} \right]^{0.5}$
4	compression surface column and crippling	$\frac{\delta_2}{\delta_1} \left[\frac{E_{s1} E_{t1} F_{cy1}}{E_{s2} E_{t2} F_{cy2}} \right]^{0.2}$	$\frac{1}{(1 + MS)}$
5	buckling compression or shear	$\frac{\delta_2}{\delta_1} \left[\frac{E_1}{E_2} \right]^{0.33}$	$\left[\frac{1}{1 + MS} \right]^{0.33}$
6	aeroelastic stiffness	$\frac{\delta_2}{\delta_1} \frac{E_1}{E_2}$	$\frac{1}{(1 + MS)}$
7	durability and damage tolerance allowable (DADTA)	$\frac{\delta_2}{\delta_1} \frac{F_1}{F_2}$	$\frac{1}{(1 + MS)}$

ponent, the failure mode yielding the lowest value of W_2/W_1 , including the effect of margins of safety, is substituted into Eq 1 to obtain the "real" weight savings.

The material properties required for evaluation of failure modes 1 to 6 are illustrated in Fig. 2. These properties include the modulus of elasticity, secant modulus, tangent modulus, and compressive yield strength. In addition, the tensile ultimate strength and density are required. Except for density, these properties can be determined from the tensile stress-strain curve of the material. For most materials the tension and compression stress-strain curve is approximately equal up to the yield strength.

To evaluate the durability and damage tolerance allowable (DADTA), the material properties shown in Fig. 3 are required. To acquire these data the following types of coupon tests are necessary: $S-N$ or spectrum fatigue, constant-amplitude crack growth, fracture toughness (K_{Ic} and K_{Ic}), and stress corrosion. Normally this amount of testing would only be conducted on alloys that show a definite promise of significant weight savings.

Refinements can be made in the seven categories to provide a more accurate assessment of structural weight. A category could be added to cover

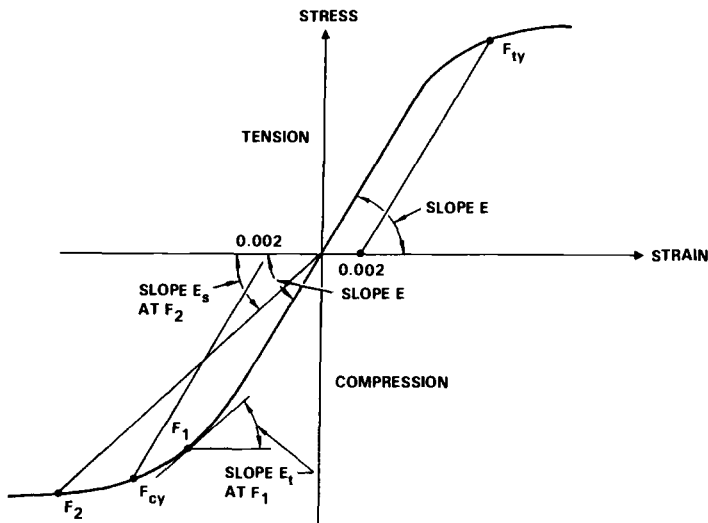


FIG. 2—Material properties stress-strain curve.

structure sized by minimum gage requirements. Also, the structure in Category 4 could be subdivided to cover several ranges of structural loading indices or stress levels. As shown in Table 1 and Fig. 2, the weight ratio is a function of the tangent and secant moduli at a given stress level. To simplify the calculations, the elastic modulus of elasticity can be used for both secant and tangent modulus in Category 3 and 4 failure modes. This implies that the tangent and secant moduli will vary in the same proportion as the elastic moduli for the advanced and baseline aluminum alloy. This simplification should still provide reasonable preliminary estimates of weight saving potential of new alloys.

Material Properties

For the weight saving evaluations given in this paper, 7075-T76 extrusion is used as the baseline material. The baseline minimum and typical properties for this material are summarized in Table 2. This material is used for the skin of the wing lower surface of the S-3A aircraft where good fatigue, crack growth, and fracture toughness properties are required. The static strength properties are about 5 percent lower than 7075-T6 material and about 8 percent higher than 2024-T4 material. An advanced aluminum alloy should have an improvement in some of the properties given in Table 2; otherwise it would not be selected for new aircraft design.

To provide some guidance for alloy development, analyses were conducted

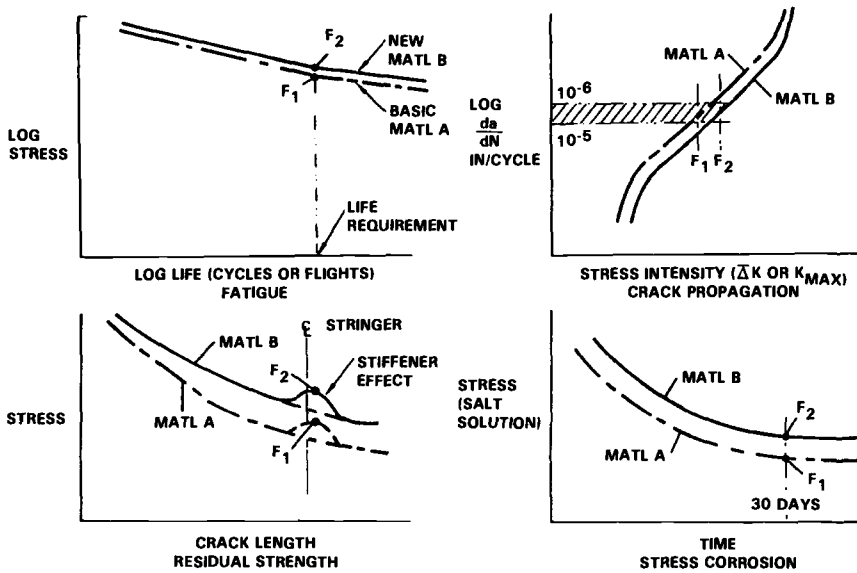


FIG. 3—Stress ratio for durability and damage tolerance allowable.

TABLE 2—7075-T76 extrusion baseline properties.

Property	Test Direction	Minimum ^a	Typical
Tensile ultimate (F_{tu}), MPa (ksi)	L	510 (75)	522 (80)
Tensile yield (F_{ty}), MPa (ksi)	L	448 (65)	483 (70)
Compression yield (F_{cy}), MPa (ksi)	L	448 (65)	483 (70)
Shear ultimate (F_{su}), MPa (ksi)	L	283 (41)	303 (44)
Elongation, % in 4D	L	7	10
Tensile modulus, GPa (10^3 ksi)	L	72 (10.4)	...
Compression modulus, GPa (10^3 ksi)	L	74 (10.7)	...
Shear modulus, GPa (10^3 ksi)	L	28 (4.0)	...
Poisson's ratio	...	0.33	...
Density, kg m^{-3} (lb in.^{-3})		2796 (0.101)	...
Fatigue (F_{max}), MPa (ksi) (net)			
For $K_t = 2.7$, $R = 0.1$, $N = 1.4 \times 10^5$	L	...	152 (22)
Plane strain fracture toughness	LT	...	33 (30)
(K_{Ic}), $\text{MPa m}^{1/2}$ ($\text{ksi } \sqrt{\text{in.}}$)	TL	...	27 (25)
Fatigue crack growth (ΔK), $\text{MPa m}^{1/2}$ ($\text{ksi } \sqrt{\text{in.}}$)			
For $da/dN = 10^{-5}$ in./cycle, 90 to 95 % RH	LT	...	11 (10)
$\Delta K = 25$ ksi, $\text{MPa m}^{1/2}$ ($\text{ksi } \sqrt{\text{in.}}$)			
For $da/dN = 2.5 \times 10^{-4}$ in./cycle, 90 to 95 % RH			27 (25)
Stress corrosion threshold, $\text{MPa m}^{1/2}$ ($\text{ksi } \sqrt{\text{in.}}$)	ST	27 (25) ^b	...
Exfoliation corrosion resistance		$> B^b$...

^aA-values from MIL-Handbook-5 unless otherwise specified.^bSpecification values, exfoliation corrosion per EXCO.

to determine the fatigue and crack growth properties required for structural areas not DADTA critical [8]. For this analysis DADTA properties required for wing upper surface structures, which are primarily loaded in compression, were evaluated and compared with the wing lower surface DADTA properties. Results of the analysis are presented in Table 3, which shows the permissible percent increase in tension stress, without weight penalty, for wing upper surface structures. This indicates that the margin of safety for Category 7 failure mode on compression critical structure is from 0.21 to more than 0.3 for three different types of aircraft.

The requirements for fracture toughness properties were also evaluated for aircraft structure [8]. Currently there is no design requirement regarding plane strain fracture toughness. However, some minimum value of K_{Ic} is desired so that the structure will not be critical for manufacturing defects or material flaws. Structural members where this property is of interest include stiffeners, spar caps, rib truss members, etc. If it is assumed that these members must support ultimate loads with a 1.27-mm (0.050-in.) crack at the edge of a fastener hole, the following plane strain fracture toughness properties are required:

$$K_{Ic} = 0.31 F_{tu} \text{ for DADTA critical structure} \quad (2)$$

$$K_{Ic} = 0.21 F_{tu} \text{ for compression critical structure} \quad (3)$$

The plane strain fracture toughness for 7075-T76 material given in Table 2 exceeds the requirements of Eq 2 in the LT direction and is equal to this requirement in the TL direction. Equation 3 is in general agreement with the minimum K_{Ic} -values for aluminum alloys used in the past for aircraft structures.

Advanced aluminum alloys are being developed in a program sponsored by the Defense Advanced Research Project Agency [7-9]. The goals for this program are (1) a 30 percent increase in specific stiffness (E/δ), and (2) a 20

TABLE 3—Permissible increase in tension stress without weight penalty for compression critical structure.

Type of Aircraft	% Increase in Tension Stress ^a	
	Fatigue	Crack Growth
Fighter w/o stores	> 30	> 30
Fighter w/stores	23	...
Patrol	21	22
Transport	29	> 30

^aTo make upper-wing surface structure as critical as lower-wing surface structure.

percent increase in specific stiffness and strength (F_{tu}/δ) with the other properties equivalent to 7075-T76. Some alloys that meet these goals, with the exception of DADTA properties, are shown in Table 4. Alloy A is a lithium-aluminum alloy meeting Goal 1. Alloy B, an aluminum-lithium alloy with a reduced density, and Alloy C, a nonlithium-aluminum alloy with an increased density, both meet Goal 2. The strength, modulus, and density properties of Alloys A and B appear achievable based on preliminary testing. No DADTA type properties have been obtained to date for Alloys A, B, and C. The values given in Table 4 were only selected to illustrate the impact of the DADTA properties on the "real" weight savings discussed later. Alloy D represents a modified aluminum alloy with improved strength and DADTA properties based on the results presented in Ref 11.

Potential Weight Savings for Primary Failure Modes

To provide some guidance to materials development, the S-3A Viking airplane (Fig. 4) and a preliminary design of an advanced tactical fighter (ATF) were evaluated for the effect of material property improvements on structural weight [7,12]. The S-3A is a carrier based ASW type aircraft which has a fold joint in the wing. The ATF aircraft is a single engine Mach 2 class fighter with a delta wing and a vertical tail on each wing tip. Examples of S-3A structure designed to various failure criteria are shown in Fig. 4.

The allocation of structural weight by failure mode is shown in Table 5. The percent of aircraft weight for the S-3A was obtained from a detailed review of stress analyses of the structural components. Only the wing, tail, body, and strake were considered for the ATF aircraft, since the landing gear, nacelle, and air induction systems are primarily steel and titanium. Allocation of weight for the ATF structure was made by reviewing available loads and drawings, combined with prior applicable experience. The weight breakdown of both aircraft is similar in terms of percent weight affected by strength (51.3 and 52.5) or modulus (56.2 and 58.9). Weight savings in the ATF aircraft is more dependent on Category 7 material properties, 19 percent versus 13.7 percent for the S-3A.

TABLE 4—Potential advanced aluminum alloy properties relative to 7075-T76 aluminum.

Material	% Change in Material Properties				
	Tensile Strength	Compression Yield	Elastic Modulus	Density	DADTA
A	0	0	+18	-9	-20
B	+14	+14	+14	-5	-10
C	+27	+27	+27	+6	0
D	+10	+10	0	0	+20

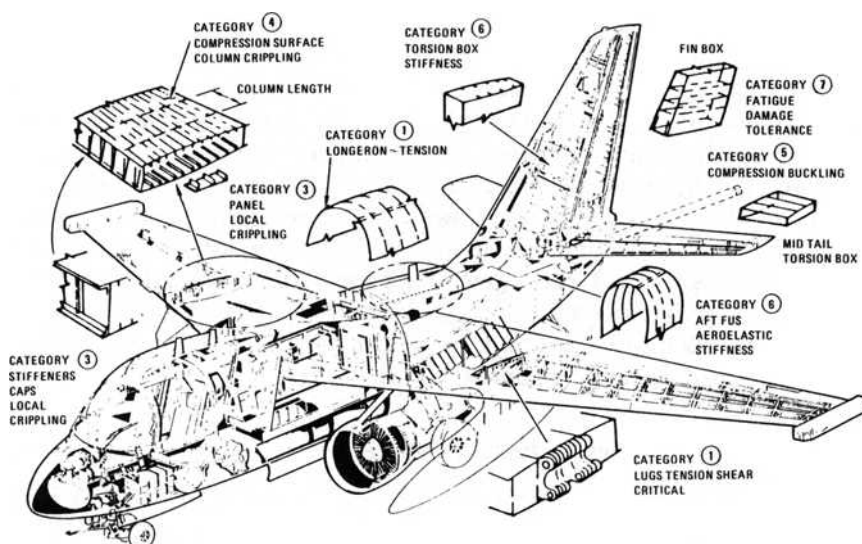


FIG. 4—Typical criteria category areas for S-3A aircraft.

TABLE 5—Allocation of weight by failure criteria.

Category No.	Failure Mode	% A/C Weight	
		S-3A	ATF
1	tensile strength	30.1	18.6
2	compressive strength	0	3.5
3	crippling	14.3	19.5
4	column and crippling (compression surface)	8.1	9.7
5	buckling (compression or shear)	19.7	18.1
6	aeroelastic stiffness	14.1	11.6
7	DADTA	13.7	19.0
		100.0	100.0

Using 7075-T76 aluminum alloy as a baseline material, weight savings were evaluated for those alloy systems with the assumed material property variations given in Table 4. Material properties for Alloys A to D were applied to weight ratio equations given in Table 1 for each of the seven failure modes. The percentage change in structural weight for each category and each alloy was determined from Eq 1. Results are summarized in Table 6 for each failure mode. The percent weight change for each failure mode apply to any structure. The maximum weight saving for an individual component is 22.9 percent for Alloy A, Failure Mode 6. Components with negative weight savings would not be substituted for the baseline material.

To obtain the total weight savings for the S-3A and ATF aircraft, the percentages given in Table 6 for each failure mode are multiplied by the percentages in Table 5 for the S-3A and ATF structure. In calculating aircraft weight savings, zero percent weight change was assumed for Alloys A, B, and C in Category 7.

In Table 6, Alloy A shows the biggest weight saving, 11.7 percent and 10.7 percent for the S-3A and ATF aircraft, respectively. This is primarily due to the lower density which affects the structural weight for all failure mode categories. If the best alloy were used for each category, the percent weight savings are increased by about five percent to 16.3 percent and 15.9 percent, respectively, for the two aircraft. The potential weight savings for both aircraft are about the same for each material or combination of materials.

The significance of various material properties on weight savings for the S-3A aircraft is illustrated in Fig. 5. The weight savings for the ATF aircraft are approximately the same as that shown in Fig. 5 except the DADTA curve would be slightly higher. Since density affects all failure modes, the structural weight saving is directly proportional to the improvements in density. Improvements in strength or stiffness are about equal and reduce structural weight about 2.5 to 3.5 percent per 10 percent property improvement. The DADTA property improvements have the least impact on overall structural weight savings because of the low percentage of structure in Category 7.

Consideration of Different Failure Modes

The effect alternative failure modes have on structural weight is illustrated in Fig. 6 for two failure mode categories (5 and 6). The equations from Table 1 were used to plot the curves for each failure mode. For the baseline properties, $E_2/E_1 = 1.0$, the aeroelastic failure mode (6) is critical with a zero per-

TABLE 6—Potential weight saving by failure mode category.

Category	% Weight Saving				Best Alloy in Each Category
	Alloy A	Alloy B	Alloy C	Alloy D	
1	+9	+16.7	+16.5	+9.1	+16.7
2	+9	+16.7	+16.5	+9.1	+16.7
3	+12.7	+11.0	+5.9	+2.4	+12.7
4	+14.8	+12.2	+8.2	+1.9	+14.8
5	+13.8	+9.0	+2.0	0	+13.8
6	+22.9	+16.7	+16.5	0	+22.9
7	-13.8	-5.6	-6.0	+16.7	+16.7
Totals for S-3A	+11.7	+11.7	+9.2	+5.5	+16.3
Totals for ATF	+10.7	+10.6	+7.9	+5.8	+15.9

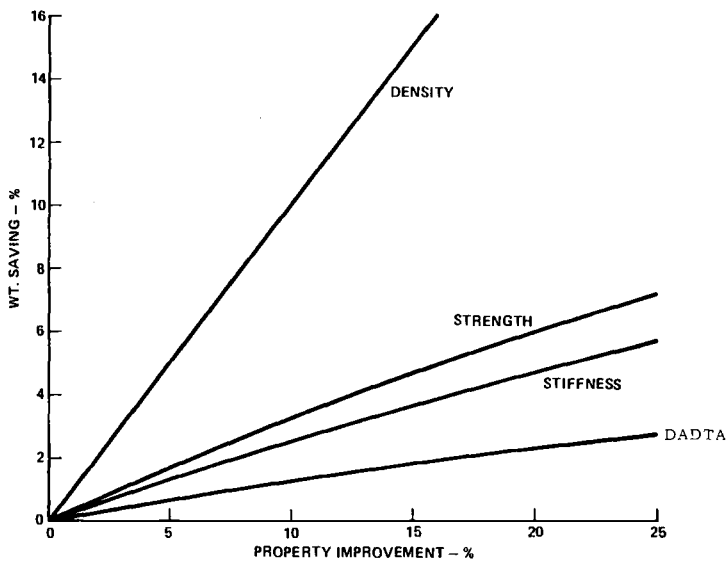


FIG. 5—Effect of property improvement on S-3A weight savings.

cent margin of safety whereas the buckling mode is assumed to have a 20 percent margin. However, with increase in modulus, the weight saving for the buckling mode (5) increases at a slower rate than for failure mode 6. For a modulus increase of about 10 percent, both failure modes are equally critical. With further improvements in modulus, the buckling mode is more critical and limits the potential weight savings that can be achieved for aeroelastic critical structure indicated by the shaded area. Additional failure modes could be plotted on the figure in a similar manner if the margins of safety are known. The minimum envelop for all failure modes would then be the "real" potential weight savings.

Figure 7 also illustrates the effect additional failure modes have on structural weight savings for a hypothetical new material. The bars in the figure show the relative material thickness or structural weights required to meet four failure mode criteria. The baseline material in this example is strength critical with margins of safety projected for DADTA, aeroelastic, and buckling failure modes. The new material has improved strength and modulus with no improvement in DADTA properties. Therefore weight savings would be limited to the thickness required to meet the DADTA requirements as the other failure mode criteria require less thickness with the new hypothetical material.

The "real" weight savings potential for Alloys A to D in Table 4 were calculated for the S-3A and ATF aircraft. It was assumed that in each case the next most critical failure mode is Category 7 with margins of safety of 10,

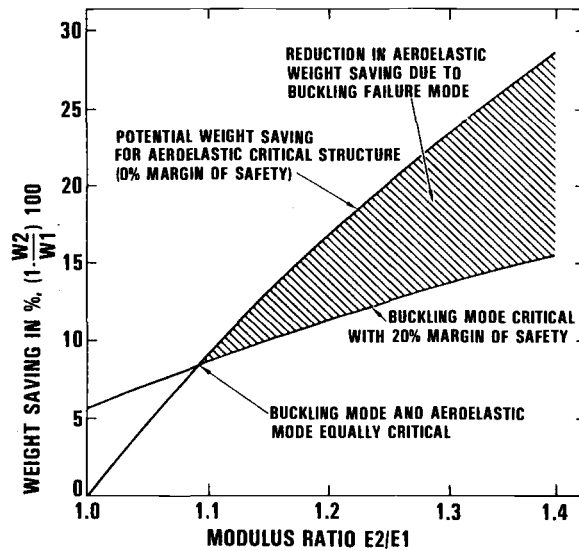


FIG. 6—Interaction of two failure modes with material property improvements.

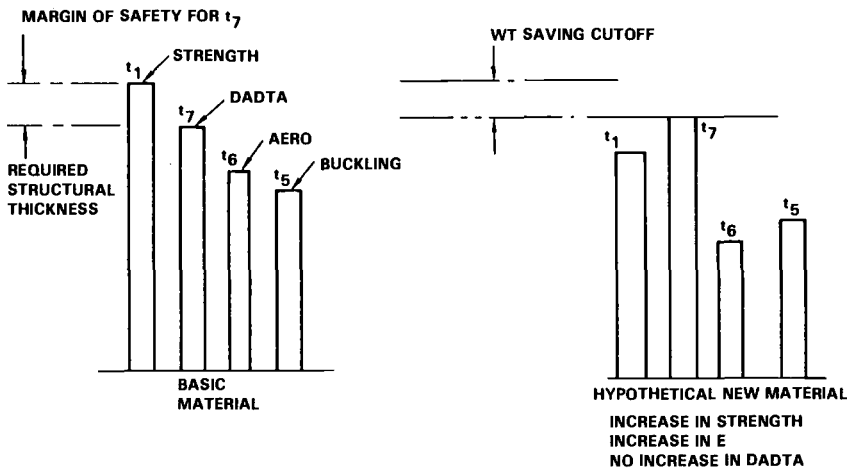


FIG. 7—Potential weight savings considering additional failure modes.

20, and 30 percent for Categories 1, 2 to 4, and 5 to 6, respectively. The percent weight change was calculated using the weight ratio equations given in Table 1, including the effect of the margin of safety correction factor. The values given in Table 7 for each category are the same as those given in Table 6 except where Category 7 becomes more critical than the primary failure mode. The “real” weight savings for each aircraft are reduced significantly

TABLE 7—*Real^a weight saving by failure mode category.*

Category	% Weight Saving				Best Alloy in Each Category
	Alloy A	Alloy B	Alloy C	Alloy D	
1	-3.41	+4.04	+3.64	+9.1	+4.04
2	+5.21	+12.04	+11.7	+9.1	+12.04
3	+5.21	+11.0	+5.9	+2.4	+11.0
4	+5.21	-12.04	+8.2	+1.9	+12.04
5	+12.5	+9.0	+2.0	0	+12.5
6	+12.5	+16.7	+16.5	0	+16.7
7	-13.8	-5.6	-6.0	+16.7	+16.7
Totals for S-3A	+5.4	+7.9	+5.3	+5.5	+12.8
Totals for ATF	+5.4	+8.1	+5.3	+5.8	+12.4

^aAssuming DADTA is alternative failure mode with 10, 20, and 30 percent margins of safety for failure modes 1, 2 to 4, and 5 to 6, respectively.

for Alloys A, B, and C, but are not affected for Alloy D. Alloy B is now the best alloy with an indicated weight saving of approximately 8 percent. If the best alloy is used for each category, the weight savings are increased to 12.8 and 12.4 percent, respectively, for the two aircraft.

These results indicate the importance of considering secondary failure modes on projecting weight savings for new alloys. Also, since Category 7 is often the next most critical failure mode when considering Categories 1 to 6, its impact on weight savings is considerably more significant than indicated in Fig. 5.

To achieve maximum weight savings for aircraft structures several advanced aluminum alloys need to be developed; that is, a high-strength low-density alloy for failure modes 1 and 2, a high-modulus low-density alloy for failure modes 5 and 6, and a combination of strength and stiffness with low density for failure modes 3 and 4. Finally, improvement in durability and damage tolerance properties are needed for failure mode 7. A combination of advanced materials with improved properties shows a weight saving potential of 4 to 11 percent higher than the weight saving achieved by the use of a single alloy. However, the properties for these new alloys should be achieved without significant reductions in the other mechanical properties or secondary failure modes would become critical and limit the weight savings.

Acknowledgments

Technical data presented in this paper were obtained in whole or in part in a program under the following Agency sponsorship: Defense Advanced Research Projects Agency (DOD), DARPA Order #3417, 1400 Wilson Blvd.,

Arlington, Va. 22209, and Air Force Materials Laboratory, Air Force Systems Command, U.S. Air Force, Wright-Patterson Air Force Base, Ohio 45433.

References

- [1] *Proceedings of the Second International Conference on Rapidly Quenched Metals*, N. J. Grant and B. C. Giessen, Eds., MIT Press, Cambridge, Mass., 1976, Section I.
- [2] *Proceedings of the Second International Conference on Rapidly Quenched Metals*, N. J. Grant and B. C. Giessen, Eds., MIT Press, Cambridge, Mass., Section II.
- [3] Lewis, R. E., Webster, D., and Palmer, I. G., "A Feasibility Study for Development of Structural Aluminum Alloys from Rapidly Solidified Powders for Aerospace Structural Applications," AFML-TR-78-102, July 1978.
- [4] Simenz, R. F. and Guess, M. K., *Journal of Aircraft*, Vol. 17, No. 17, July 1980, pp. 514-520.
- [5] Sanders, T. H. and Balmuth, E. S., "Aluminum-Lithium Alloys: Low Density and High Stiffness," *Metal Progress*, March 1978.
- [6] Lebo, M. and Grant, N. J., "Structure and Properties of a Splat Cooled 2024 Al Alloy," *Metallurgical Transactions*, Vol. 5, 1974, p. 1547.
- [7] Lewis, R. E. et al, "Development of Advanced Aluminum Alloys from Rapidly Solidified Powders for Aerospace Applications," LMSC-D674504, March 1979.
- [8] Lewis, R. E. et al, "Development of Advanced Aluminum Alloys from Rapidly Solidified Powders for Aerospace Structural Applications," LMSC-D678772, Sept. 1979.
- [9] Lewis, R. E. et al, "Development of Advanced Aluminum Alloys from Rapidly Solidified Powders for Aerospace Structural Applications," LMSC-D686125, March 1980.
- [10] Shanley, F., *Weight-Strength Analysis of Aircraft Structure*, McGraw-Hill, New York, 1952.
- [11] Cebulak, W. S., "Program to Develop High Strength Aluminum Powder Metallurgy Mill Products, Phase IVB-Scale-Up to 1545 kg (3400 lb) Billet," FA-TR-76067, 25 April 1977.
- [12] Walter, R. W., Mooney, J. E., Hamm, R. A., and June, R. R., "Wing Fuselage Critical Components Development," AFFDL-TR-78-146, Nov. 1978.

Experimental and Analytical Evaluation of Structures

Fatigue Crack Growth in Stiffened Panels under Pressure Loading

REFERENCE: Chu, H. P., Hauser, J. A., and Sikora, J. P., "Fatigue Crack Growth in Stiffened Panels under Pressure Loading," *Design of Fatigue and Fracture Resistant Structures*, ASTM STP 761, P. R. Abelkis and C. M. Hudson, Eds., American Society for Testing and Materials, 1982, pp. 345-372.

ABSTRACT: An experimental study was conducted to characterize the fatigue crack growth behavior of stiffened panels under uniform lateral pressure loading. The panels were made of standard 5456 aluminum alloy and fabricated by weldbonding. Fatigue failure of the panels consisted of cracking of the stiffeners, followed by cracking of the skin. Crack growth rate data showed a maximum value in the stiffeners and a constant value in the skin before failure. A weldbonded stiffened panel could endure more fatigue cycles than a gas metal arc welded panel under similar pressure loading. The panel data were correlated with base line materials data and represented by either of two simple equations in terms of fatigue crack growth rate versus stress intensity factor range. The stress intensity analysis for the panels was made by an approximation method which considered the combined effects of tension and bending stresses. Accuracy of this method was verified by photoelastic measurements.

KEY WORDS: fatigue, aluminum alloy, fracture mechanics, stiffened panels, crack growth, weldbonding

Nomenclature

a	Crack length (half crack length for center-cracked panel)
c, m, n	Constants (used in Eqs 6 and 7)
F_1, F_2, F_3	Correction factors (used in Eqs 2, 3, and 4)
h	Plate thickness
K	Stress intensity factor
K_c	Critical value of stress intensity factor (fracture toughness)
\bar{K}_j	Component of K due to Q_j
M	Bending moment

¹Metallurgist, Structural Engineer, and Physicist, respectively, David W. Taylor Naval Ship Research and Development Center, Bethesda, Md. 20084.

Q_j	Rivet forces
R	Stress ratio
r, ϕ, θ	Polar coordinates
S_b	Bending stress
S_t	Tensile stress
ΔK	Stress Intensity factor range
ΔK_{th}	Fatigue threshold of ΔK
σ_o	Far-field stress
τ_{max}	Maximum shear stress

Stiffened panels are extensively used as structural elements in the construction of high-performance ships. Previous work on stiffened panels was limited to uniaxial tensile loading. For example, Poe and Vlieger [1,2]² studied their fatigue crack growth and residual strength characteristics under simple tension. This work was different from others in that the panels were tested in bending. The purpose was to investigate fatigue crack growth in aluminum alloy stiffened panels under uniform lateral loading similar to the water pressure experienced by ship structures, such that the data would be useful for controlling fatigue and fracture in modern ships as discussed by Sorkin, Wolfe, Vanderveldt, and others [3,4]. The technical approach was based on the fracture mechanics concept that fatigue crack propagation in structural elements can be predicted from base line materials data in terms of the linear elastic stress intensity factor range, ΔK , versus crack growth rate, da/dN , as shown by Paris and Wei [5,6]

Experimental Procedure

Materials

The stiffened panels tested were made of a standard aluminum-magnesium alloy. The skin material was 5456-H343 sheet, and the stiffeners were 5456-H111 extrusions. All the materials were 3.2 mm (0.125 in.) thick and tested in the as-received condition. Chemical composition and mechanical properties are listed in Table 1.

Stiffened Panel Fabrication and Testing

Three aluminum alloy stiffened panels were fabricated by weldbonding. Figures 1a and 1b show the dimensions of the panels, which were designed to have the necessary details of a structural element in a simple configuration [7]. The weldbonding process used an adhesive and spot welded the flanges

²The italic numbers in brackets refer to the list of references appended to this paper.

of the inverted tee stiffeners to the base plate. Two of the weldbonded panels had 1.27-mm (0.05-in.)-deep notches cut by a jeweler's saw at the midpoint of the free edge of the stiffeners. The third panel was not prenotched so that fatigue cracks could follow their natural courses of initiation and propagation.

A special fatigue machine was used to provide lateral loading by compressed air from zero to preselected gage pressures ($R = 0$) at a speed of 0.2 Hz with the panel supported and constrained along the two edges perpendicular to the stiffeners (Fig. 1b). The operation and loading method of a

TABLE 1—Chemical composition and mechanical properties of 5456 aluminum alloy.

Temper	Chemical Composition, weight %								Mechanical Properties	
	Mg	Mn	Fe	Cr	Ti	Zn	Si	Al	0.2% Yield Strength, MPa (ksi)	Tensile Strength, MPa (ksi)
H343	6.0	0.91	0.33	0.13	0.06	0.05	0.01	bal	278 (40.3)	389 (56.4)
H111	5.4	1.0	0.32	0.13	0.07	0.02	0.01	bal	179 (26.0)	290 (42.1)

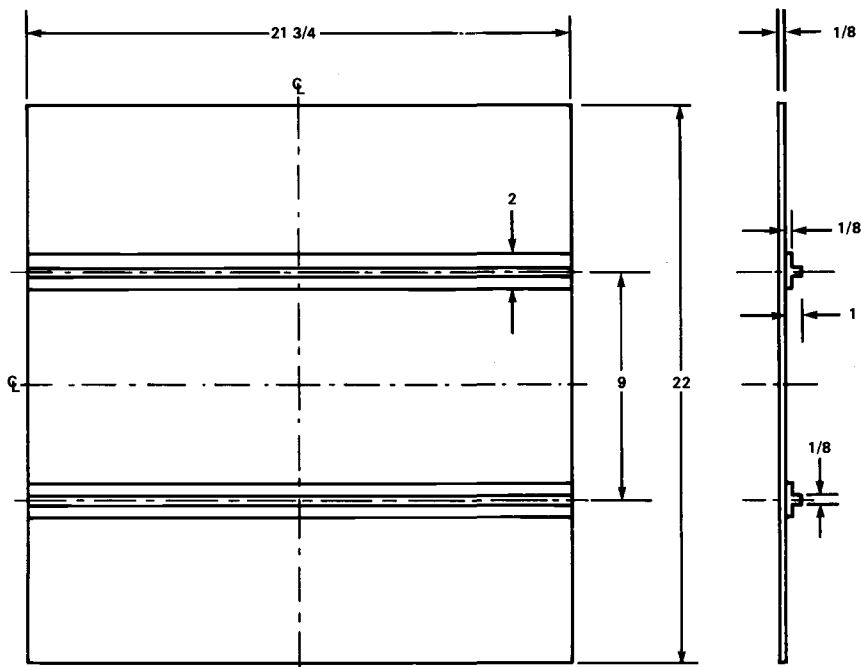


FIG. 1a—Weldbonded stiffened panel (all dimensions in inches; 1 in. = 25.4 mm).

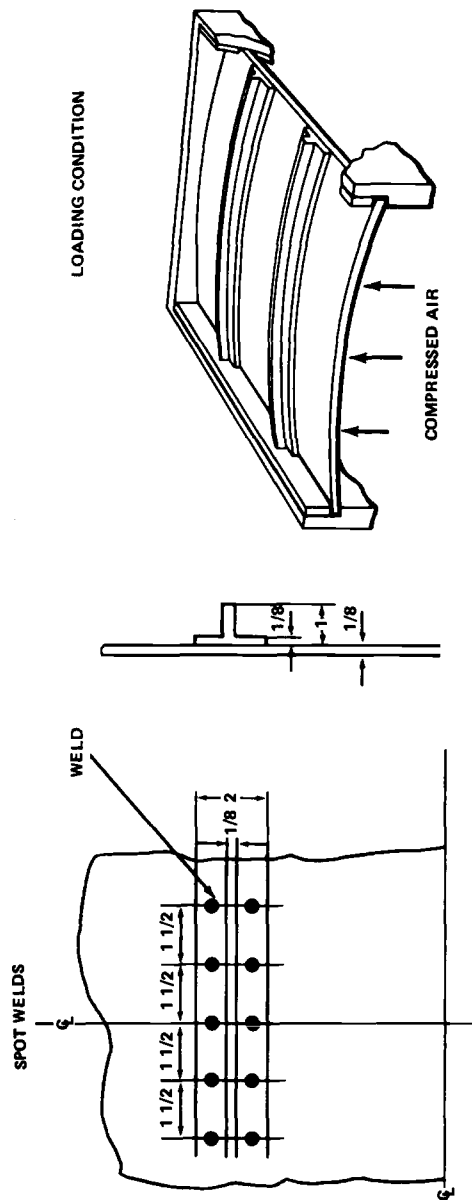


FIG. 1b—Spot weld location in weldbonded stiffened panel and loading conditions (all dimensions in inches; 1 in. = 25.4 mm).

similar machine have been described previously by Cordiano [8]. Before testing, rectangular rosette strain gages were placed on the top and bottom surfaces in the center of all the panels to measure strains from which the applied stresses were calculated. Crack length measurements were taken with a $\times 10$ microscope.

The pressure and the initial stresses for the panels are listed in Table 2. Included in this table are the data of two additional panels of the same materials and configuration, which were made by conventional gas metal arc (GMA) welding of two bar stiffeners using 5356 aluminum wire (Fig. 2). The GMA panels were tested previously [9] in the same way as the weldbonded panels, and the results are included here for comparison.

Photoelastic Stress Intensity Measurements

Another GMA welded panel similar to that shown in Fig. 2 was used for photoelastic measurements of stress intensity factors. A photoelastic coating was cemented to the top center portion of the panel and also to the sides of the stiffeners. The panel was mounted on a load frame, with the two edges perpendicular to the stiffeners supported and constrained by bolts. To simulate crack growth in fatigue testing, notches were cut in small increments with a hacksaw blade and then sharpened by a knife edge. The cuts started from the free edges of both stiffeners at the midpoint, extended to the base, and then continued through the skin material along the transverse center line of the panel. The load was applied normal to the central area of the bottom surface of the panel. Photoelastic and strain gage readings as well as

TABLE 2—Summary of stiffened panel cyclic pressure loads and initial stresses.

Panel No.	Panel Type	Initial Stress					
		Cyclic Pressure		Tension		Compression	
		MPa	(psi)	MPa	(ksi)	MPa	(ksi)
I	weld	0 to 0.138	(0 to 20)	138.6	(20.1)	-48.3	(-7.0)
II ^a	bond	0 to 0.138	(0 to 20)	137.9	(20.0)	-48.3	(-7.0)
III ^a	weld	0 to 0.055	(0 to 8)	78.6	(11.4)	-38.6	(-5.6)
IV	bond	0 to 0.138	(0 to 20)	183.4	(26.6)	-56.5	(-8.2)
V	GMA ^b	0 to 0.138	(0 to 20)	124.8	(18.1)	-85.1	(-12.3)
	weld	0 to 0.055	(0 to 8)				
	GMA						
	weld						

^a Panel with prenotched stiffeners.

^b GMA = Gas metal arc.

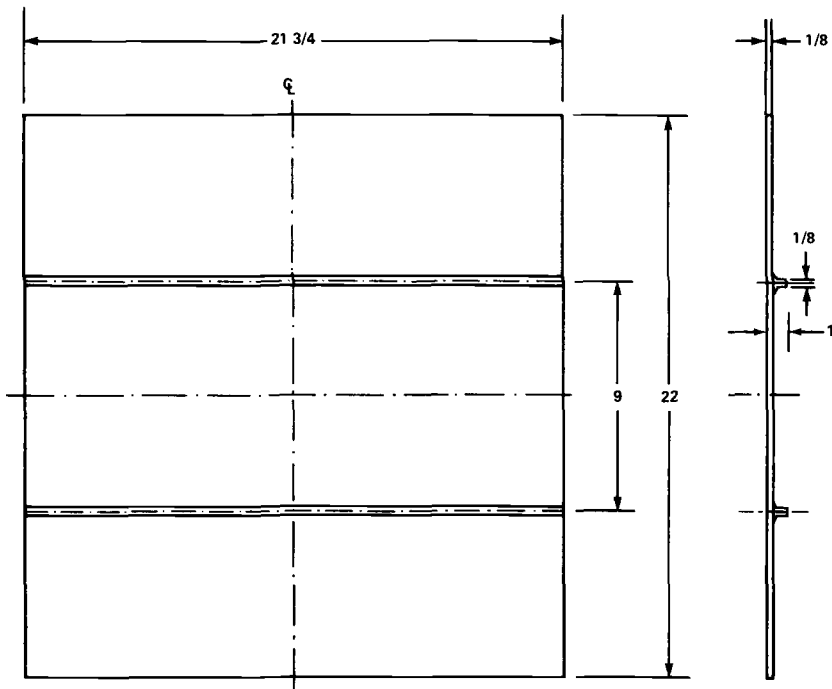


FIG. 2—Gas metal arc welded stiffened panel (all dimensions in inches; 1 in. = 25.4 mm).

dial-gage deflection measurements at the center of the panel were taken at each increment of the notching process.

Results and Discussion

Fatigue Cracking in Stiffened Panels

The manner in which the stiffened panels failed in the fatigue tests depended on the fabrication process. The three cracked weldbonded panels are shown in Figs. 3a, 3b, 4a, 4b, 5a, and 5b. Two photographs are provided for each panel, one for the top and the other for the bottom side. The unique feature is that, after the stiffeners had broken through the flanges, new cracks initiated and propagated in the skin material. In all cases, the cracks in the skin ran through two neighboring weld spots and were not aligned with the cracks in the stiffeners. Also, cracks branched from the spot welds in Panel III (Fig. 5b). Irwin [10] has pointed out that many instances of crack branching have been observed and that the branching appears to be related to the attainment of a limiting crack speed in dynamic fracturing. In the present case, crack branching occurred at relatively low speed in the fatigue

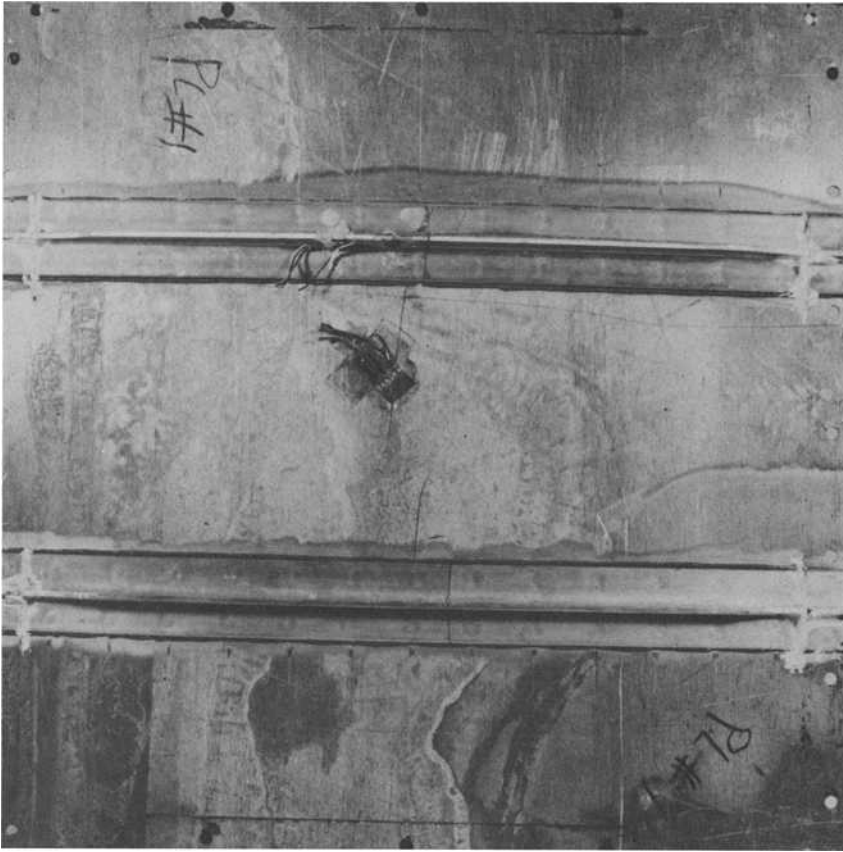


FIG. 3a—Panel I after fatigue testing: top (tension) side.

test, since this particular panel was cycled under 0 to 0.055 MPa (0 to 8 psi), which was the lower pressure load used in the experiment with an initial stress of 78.6 MPa (11.4 ksi). In the case of the GMA welded panels, a crack would start, as expected, at the free edge of each stiffener and propagate into the skin material on both sides of the stiffener. The panels gradually failed as the two central cracks grew toward each other. A photograph of a fatigue cracked GMA welded panel is shown in Fig. 6, where the central cracks are labeled by letters B and C. Notice that, as with the weldbonded panels, all the cracks initiated and propagated in the general area along the center line of the panels where the stresses were the highest.

An example of crack growth measurements in prenotched stiffeners is presented in Fig. 7. The data show a stage of slowdown in crack propagation in the stiffeners as the crack approaches the base plate. The phenomenon can

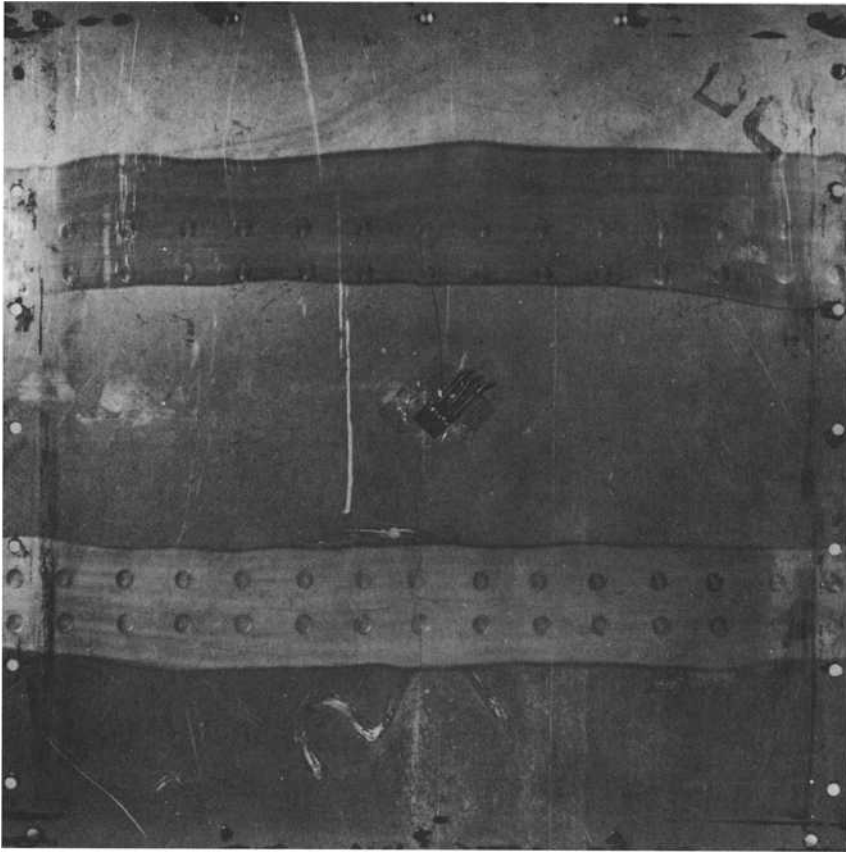


FIG. 3b—Panel I after fatigue testing: bottom (compression) side.

be better seen in terms of fatigue crack growth rate (FCGR) computed by the ASTM recommended method [11]. In Fig. 8 the da/dN values increase continually from the beginning and reach a peak when the crack is about halfway through the stiffener. Thereafter the crack growth rate decreases as the crack approaches the flange of the stiffener. Although this kind of retardation in crack growth can be readily attributed to the presence of the skin material and the flange of the stiffener, no similar data have been found in the technical literature.

Examples of crack growth data in the skin of the panels are given in Fig. 9. The initial part of the data points could be faired into straight lines. This is a unique feature which has been observed in all of the five stiffened panels. Thus the data indicate that the cracks at first grew at practically constant

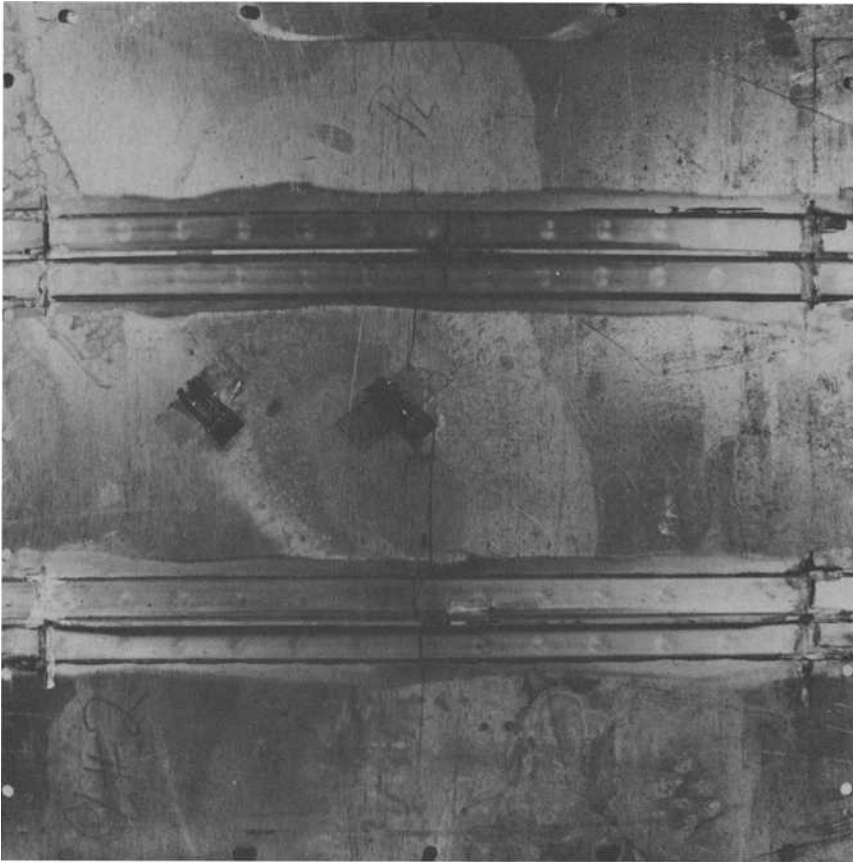


FIG. 4a—Panel II after fatigue testing: top (tension) side.

rates. Afterwards, the cracks grew at increased rates as they approached the central region of the panel. The crack growth behavior is a consequence of load transfer in the stiffeners and the skin during crack extension under the present loading condition. Figure 9 also shows that under identical pressure loading the weldbonded panel sustained almost three times as many pressure cycles as the GMA welded panel. This is simply illustrated by the fact that, when a crack grew to 76 mm (3 in.), the GMA welded panel had endured a total of 24 000 cycles, whereas the weldbonded panel had seen about 67 000 cycles. Previous investigations have shown that the weldbond process is superior to riveting or other conventional welding in both static and fatigue tests [12, 13]. It should be noted, however, the difference in fatigue life between Panel I (weldbond) and Panel IV (GMA) is mainly in crack initiation

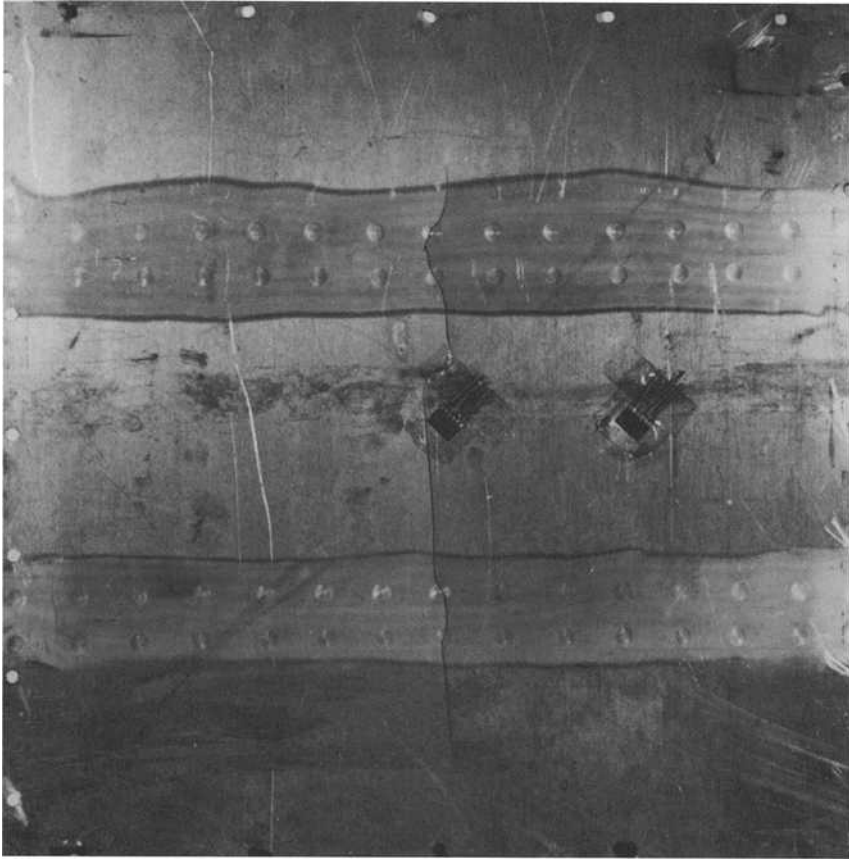


FIG. 4b—Panel II after fatigue testing: bottom (compression) side.

because, once cracking starts, the crack growth rate behavior becomes the same in both types of panels in terms of da/dN versus ΔK . Table 2 shows that the measured stress in Panel I was lower than in Panel IV, most likely due to the additional material of the inverted tee flanges necessary for the weldbonding process. The lower stress should account for part of the longer fatigue life of the weldbonded panel.

Stress Intensity Factor

Analytical Method—In order to predict fatigue crack growth in the stiffened panels from base line materials data according to fracture mechanics theory, a stress intensity expression for the panels is needed. Since math-

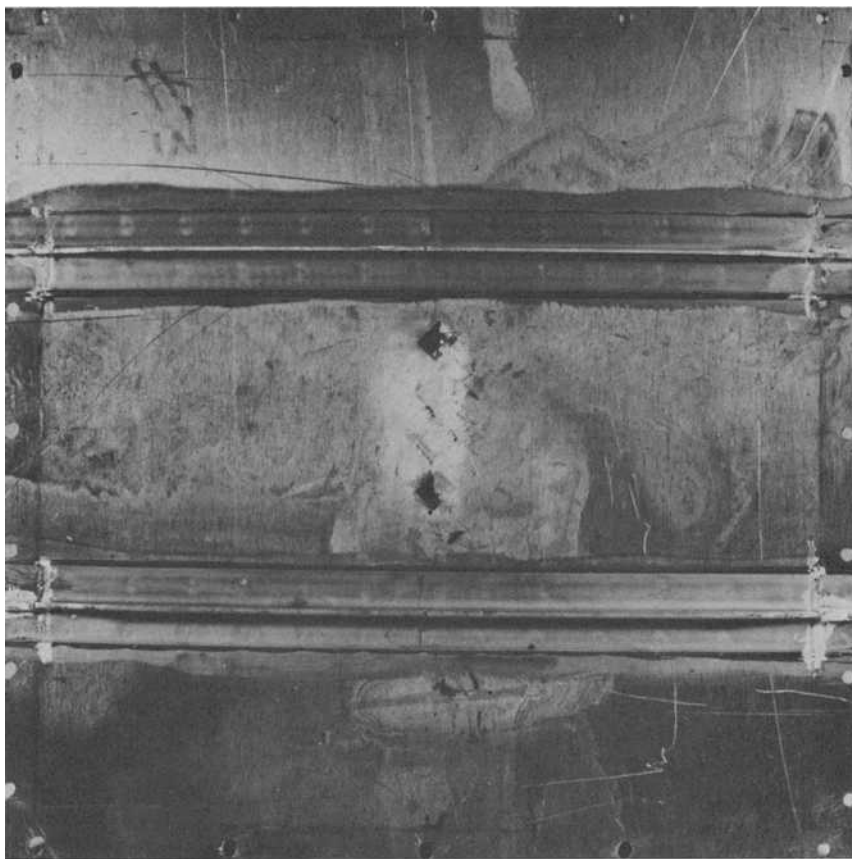


FIG. 5a—Panel III after fatigue testing: top (tension) side.

emational solutions are not available for the crack problem of the stiffened panels tested under the present loading condition, an approximate analysis has to be made. This is accomplished by considering the panel skin under combined loading of tension (membrane) and bending stresses. The stress intensity contributions from these stresses are added to obtain the total value of ΔK such that

$$\Delta K_{\text{total}} = \Delta K_{\text{tension}} + \Delta K_{\text{bending}} \quad (1)$$

The tension contribution to ΔK is as follows:

$$\Delta K_{\text{tension}} = F_1 F_2 (S_t \sqrt{\pi a} + \sum_j \bar{K}_j Q_j) \quad (2)$$

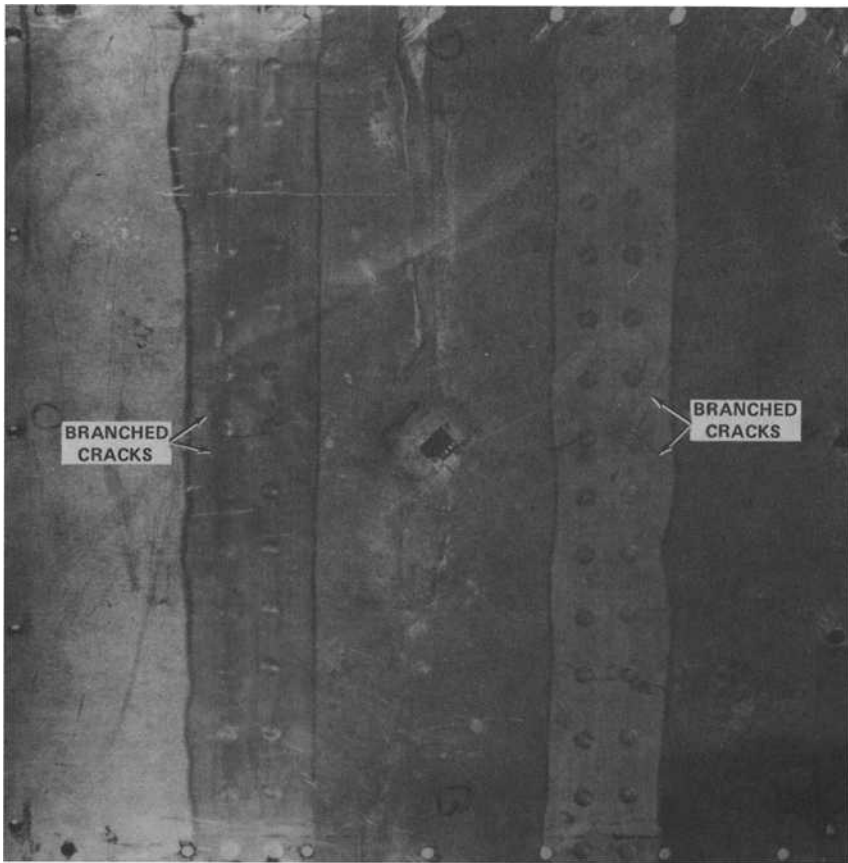


FIG. 5b—Panel III after fatigue testing: bottom (compression) side.

where F_1 and F_2 are correction factors for a pair of collinear cracks [14] and for a crack in a plate of finite width [15], respectively. Inside the brackets is the formula from Poe for a stiffened panel with broken stringers [1, 16]. The term $S_t\sqrt{\pi a}$ is the familiar K -expression for a wide plate with a transverse center crack of length $2a$ subjected to a uniform tensile stress S_t , and $\bar{K}_i Q_j$ is the component of K due to the rivet forces Q_j . For the present work, a continuous weld is modeled by closely spacing the rivets.

According to Sih [14], the stress intensity factor for a cracked plate under uniform bending is

$$\Delta K_{\text{bending}} = F_3 M \sqrt{\pi a} \quad (3)$$

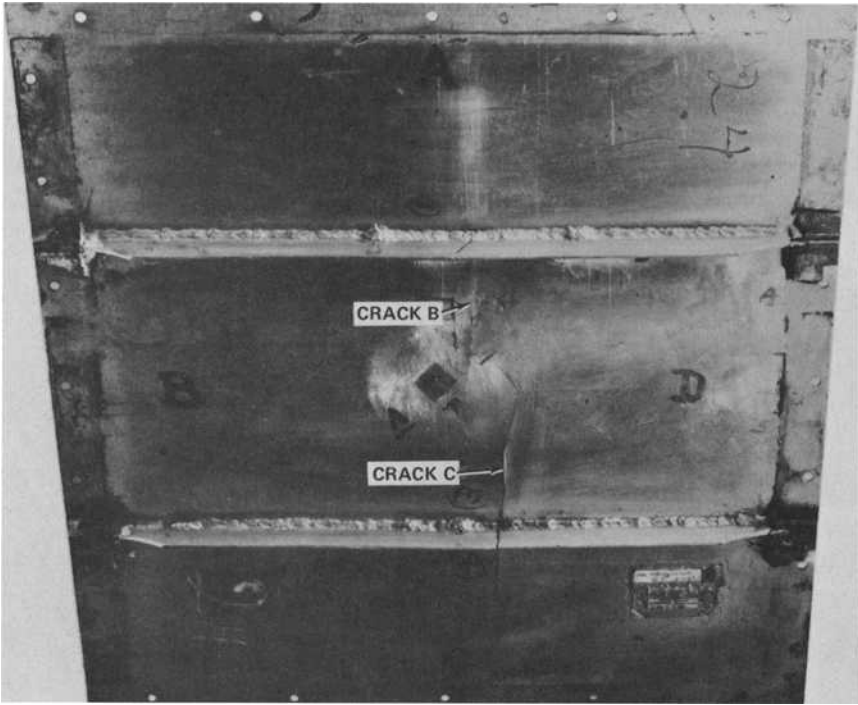


FIG. 6—Panel IV after fatigue testing.

The bending moment is

$$M = \frac{S_b h^2}{6}$$

Therefore

$$\Delta K_{\text{bending}} = F_3 \left(\frac{S_b h^2}{6} \right) \sqrt{\pi a} \quad (4)$$

where S_b is bending stress, h is plate thickness, and F_3 is a function of crack length, plate thickness, and Poisson's ratio. The values of S_b and S_t for Eqs 2 and 4 are obtained from the measured stresses by assuming a linear stress distribution through the thickness of the panel (Fig. 10).

It should be noted that a solution for the stiffeners is not formulated here and that the present solution for the panel skin involves simplifications. For example, Sih's formula is only for a smooth plate, and the effect of broken stringers on bending has to be neglected. Also, because mathematical solutions are unavailable, the presence of two cracks in one plate and the finite

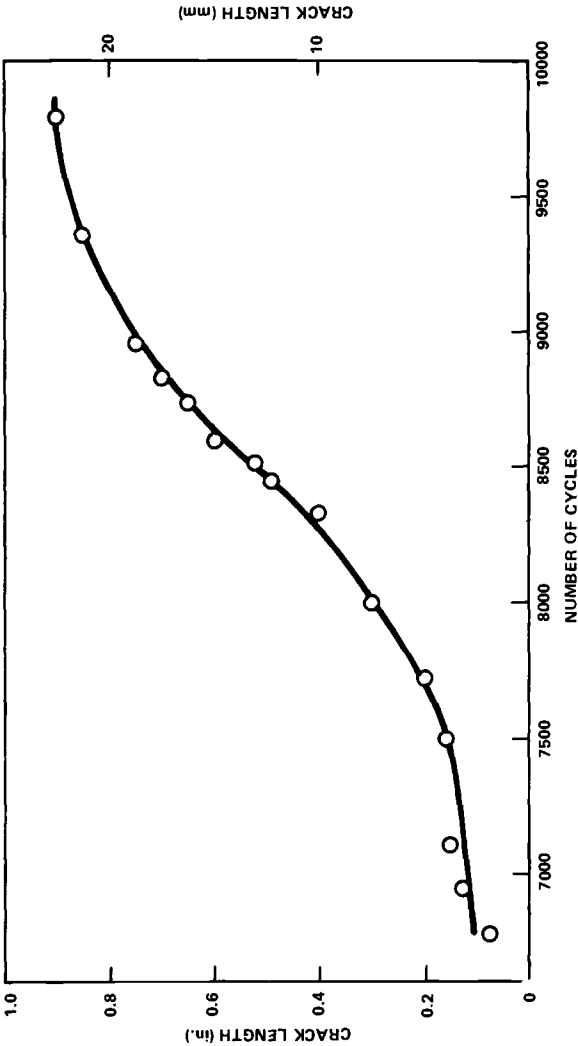


FIG. 7—Fatigue crack growth measurements in a prenotched stiffener of Panel III.

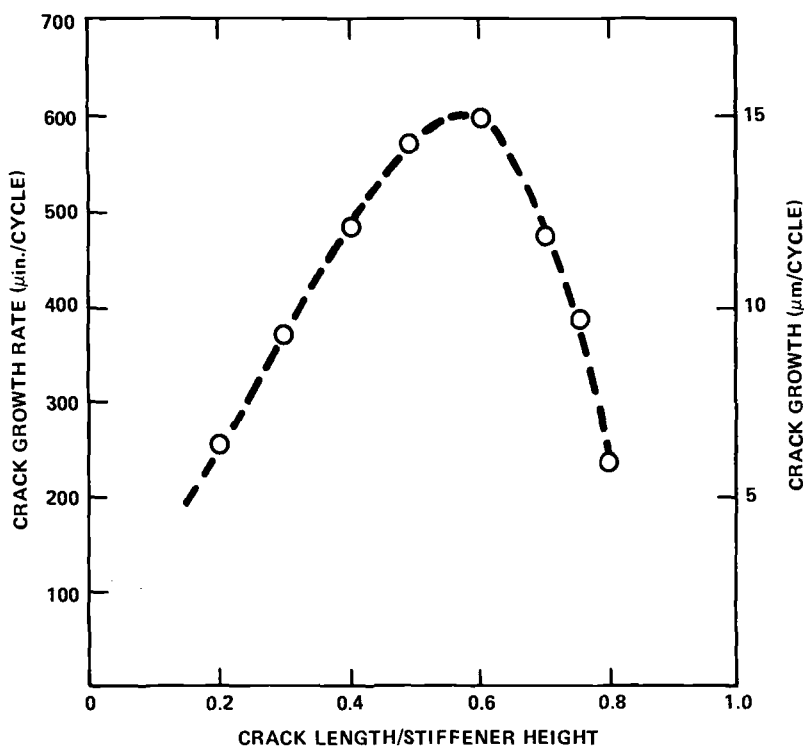


FIG. 8—Crack growth rate da/dN computed from data in Fig. 7 in a prenotched stiffener of Panel III.

width of the plate are not considered in the bending analysis. As shown below, the consequences of these simplifications, which are unavoidable at the present time, can be reconciled, and the method of analysis does provide a close correlation between the stiffened panel and the materials data.

Experimental Method—In the photoelastic experiment, the load was scaled to produce deformation in the panel equivalent to that produced in Panel V under 0.055 MPa (8 psi) uniform pressure used in stiffened panel testing. A typical isochromatic fringe pattern at the tip of a sharp notch in the stiffener is illustrated in Fig. 11. Similar patterns were also observed in the panel skin. The stress intensity factor K was computed by means of Irwin's equation [17]:

$$4\tau_{\max}^2 = \left(\frac{K}{2\pi r} \sin \theta + \sigma_o \sin \frac{3\theta}{2} \right)^2 + \left(\sigma_o \cos \frac{3\theta}{2} \right)^2 \quad (5)$$

where r and θ are polar coordinates at the crack tip (Fig. 11). The far-field stress σ_o and the maximum shear stress τ_{\max} were determined by strain gage readings and photoelastic measurements.

Figure 12 shows the photoelastically determined stress intensity factor in the stiffener. The interesting feature is that, as the notch becomes deeper, the stress intensity increases to a maximum and then drops to lower values. A comparison of Figs. 8 and 12 shows that there is a correspondence between the crack growth rate and the stress intensity factor values as a function of crack length in the stiffener.

The stress intensity factors for a cracked stiffened panel determined from the photoelastic results are presented in Fig. 13. Included in the graph are the analytical results calculated by Eq 1 for Panel V. It can be seen that the analytical method gives higher K -values than the photoelastic method when the crack length is short. As the crack grows into the central region of the panel, the results from both methods are practically equal. This is reasonable since the stiffener effect, which is neglected in $\Delta K_{\text{bending}}$ in Eq 1, should di-

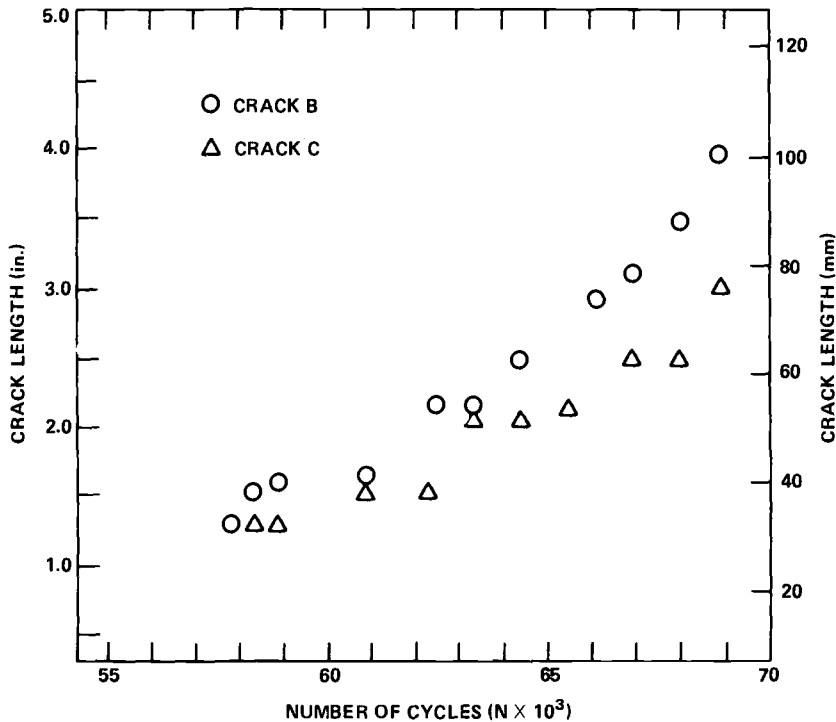


FIG. 9a—Crack growth measurements in the skin of Panel I (weldbonded) under pressure loading of 0 to 0.138 MPa (0 to 20 psi).

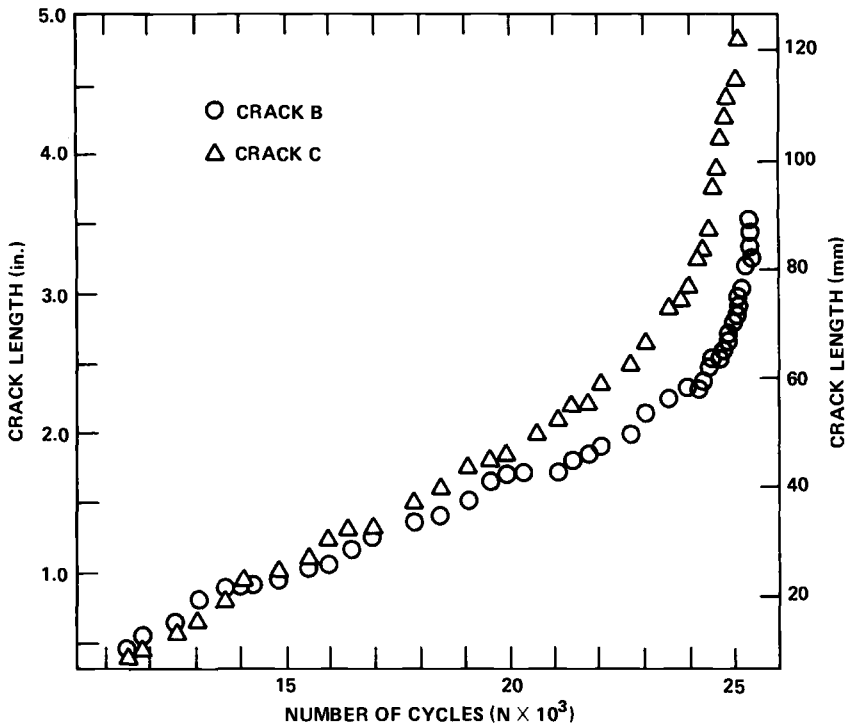


FIG. 9b—Crack growth measurements in the skin of Panel IV (gas metal arc welded) under pressure loading of 0 to 0.138 MPa (0 to 20 psi).

minish as the crack grows away from the stiffeners. For crack length between 30 and 64 mm (1.2 to 2.5 in.), the photoelastic method gives, within the scatter of data, an approximately constant value of $K = 20 \text{ MPa}\sqrt{\text{m}}$ (18 $\text{ksi}\sqrt{\text{in.}}$), which is in agreement with the constant crack growth rate observed previously in Fig. 9. On the other hand, the analytical method produces a gradual increase in K -values from 17 to 22 $\text{MPa}\sqrt{\text{m}}$ (15 to 20 $\text{ksi}\sqrt{\text{in.}}$) in the same range of crack length. Since the difference in the above K -values obtained from the two methods is small, it is considered that, in spite of the simplifications, the analytical method provides adequate results for a correlation of the fatigue crack growth data.

Correlation of Data

Because failure of the stiffened panels is dependent primarily on the two central cracks growing toward each other, the ΔK_{total} and the da/dN values are computed only for these cracks in the present work. Results for the weld-

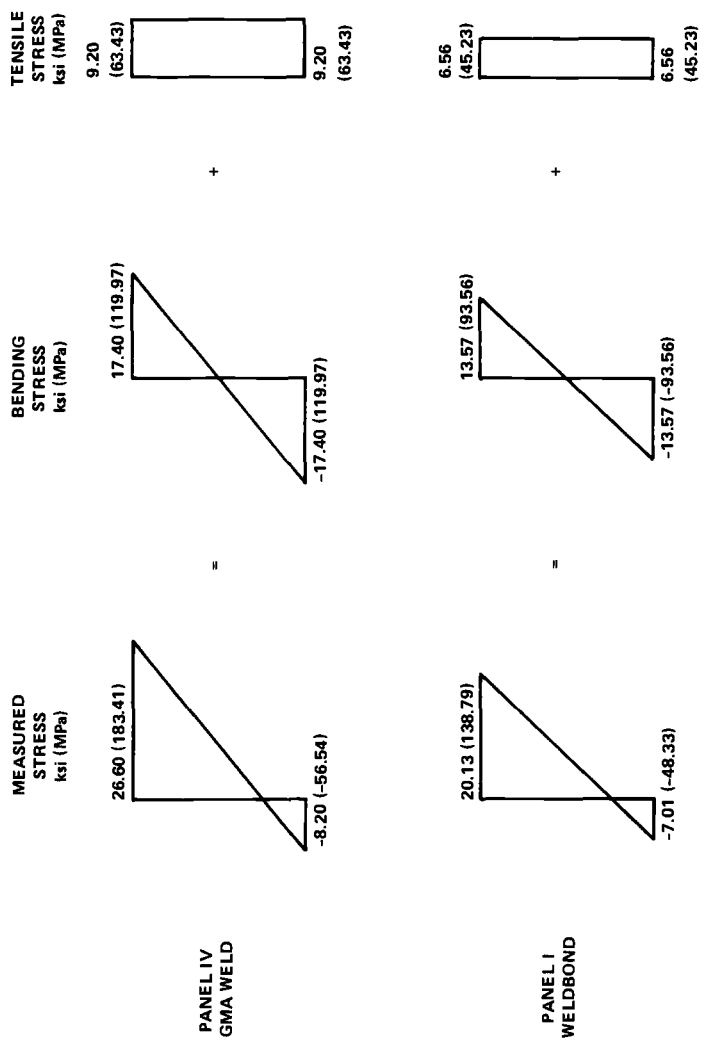


FIG. 10—Examples of tensile and bending stress computations from measured stresses.

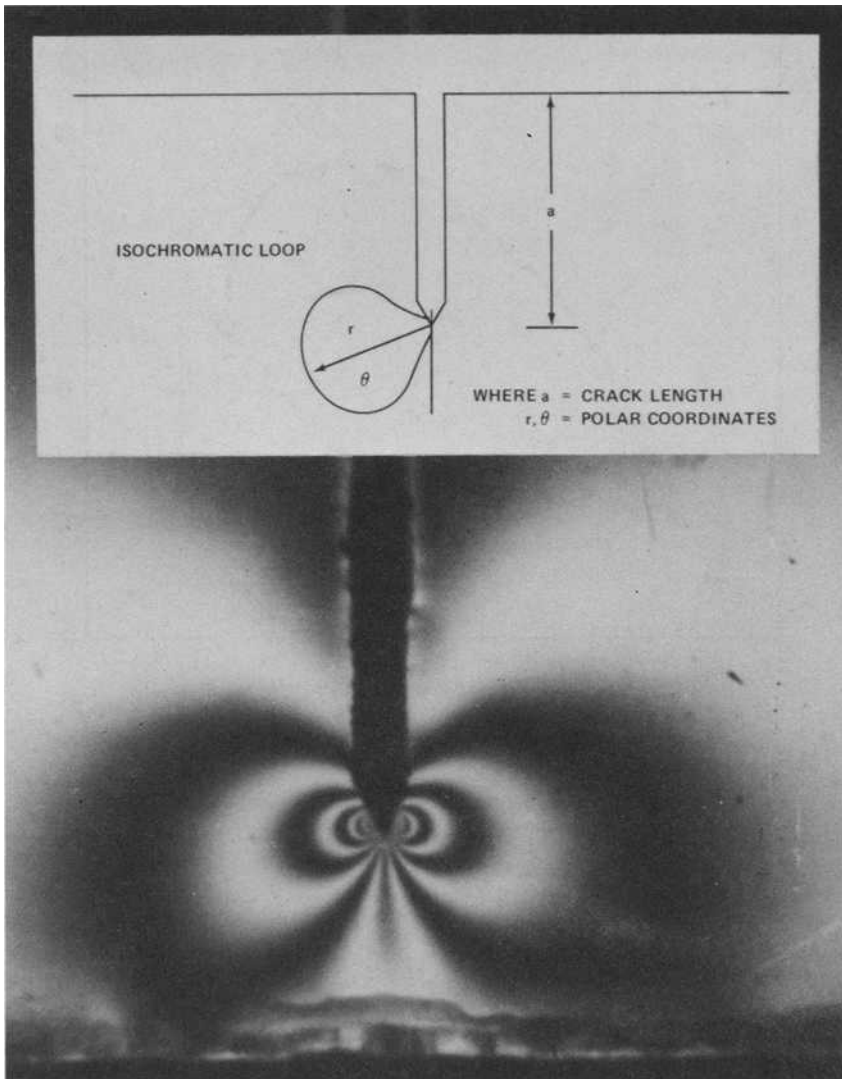


FIG. 11—Typical isochromatic fringe pattern of crack in stiffener.

bonded panels are plotted in Fig. 14. It is interesting to note that the data points representing the two cracks in Panel III cover a relatively wider scatter band. These were the cracks which branched during fatigue testing under a pressure of 0 to 0.055 MPa (0 to 8 psi). In general, the da/dN versus ΔK results have an acceptable scatter of data and a high degree of agreement for the three welded bonded panels tested.

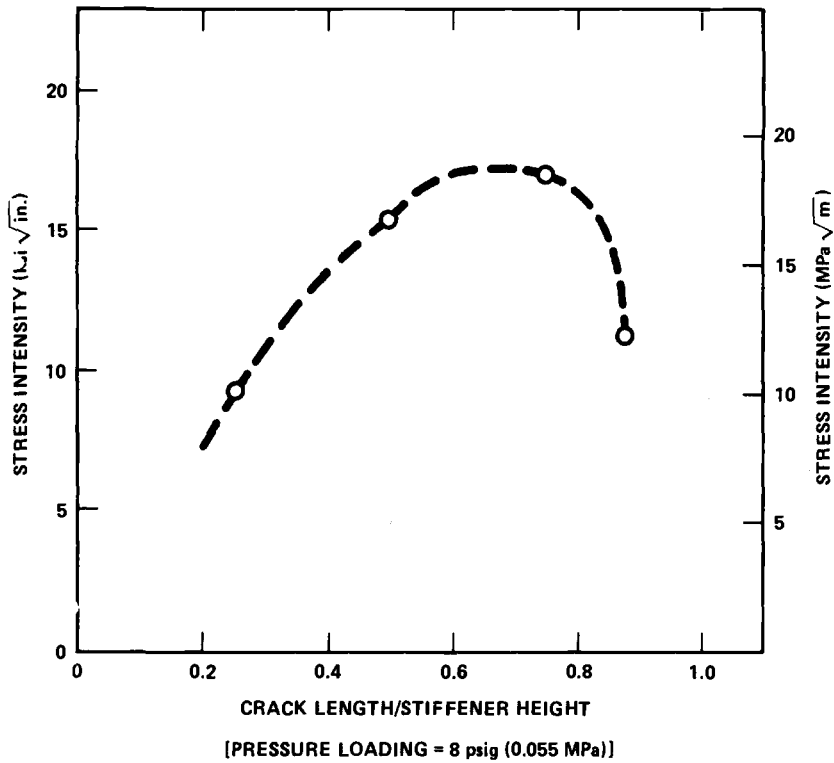


FIG. 12—Stress intensity factor K of a cracked stiffener from photoelastic measurements.

The base line materials data on 5456-H343 aluminum alloy, which were obtained in a previous investigation [18], are plotted together with the data on all five stiffened panels in Fig. 15. It is evident that, on the basis of total stress intensity by Eq 1, a correlation of the two sets of data has been achieved as they join each other and form a continuous curve. Thus the present analytical method has been shown to be adequate for predicting fatigue crack propagation in stiffened panels from materials data which were obtained by testing simple specimens, namely compact tension specimens [18]. The materials data occupy the lower portion of the curve in Fig. 15 because crack length measurements were not taken up to the point of rupture of the compact tension specimens; the panel data are situated at the upper portion since the cracks grew in the skin material at relatively high rates prior to fast crack propagation. The stiffened panels did not separate into two parts, and the crack lengths could be measured until the end of the tests.

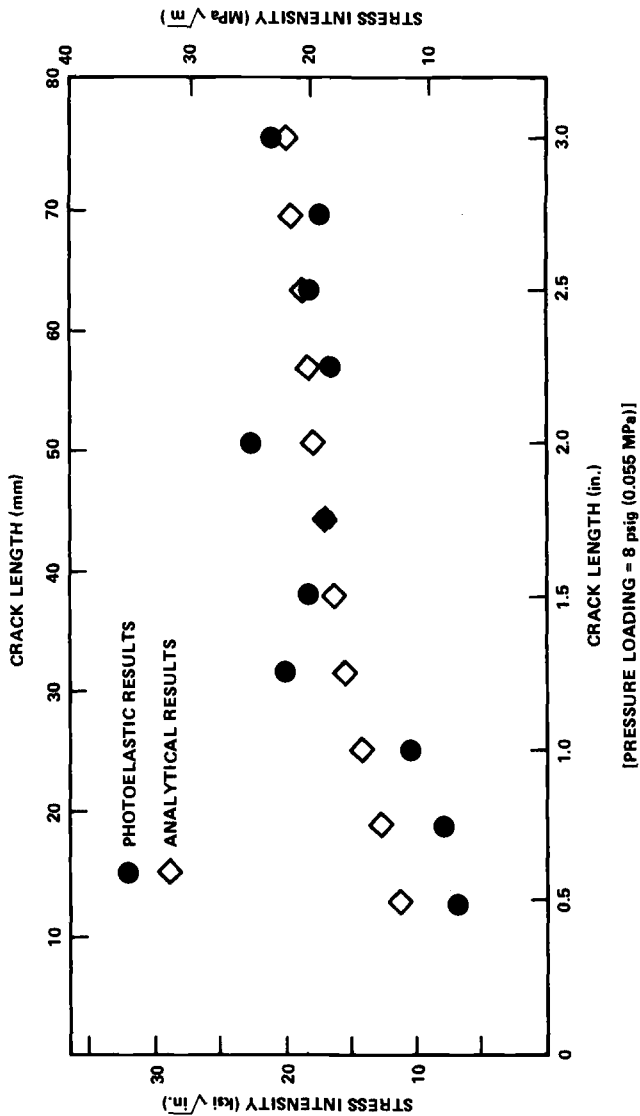


FIG. 13—Stress intensity factor K along center line in the central region of a cracked stiffened panel.

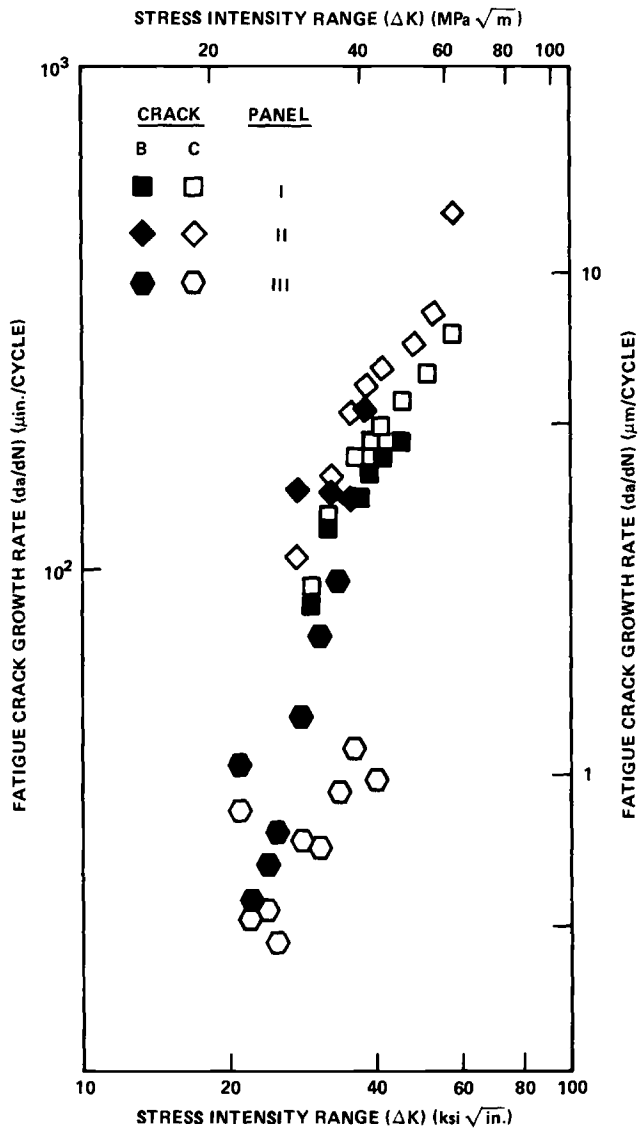


FIG. 14—FCGR versus stress intensity range of weldbonded stiffened panels.

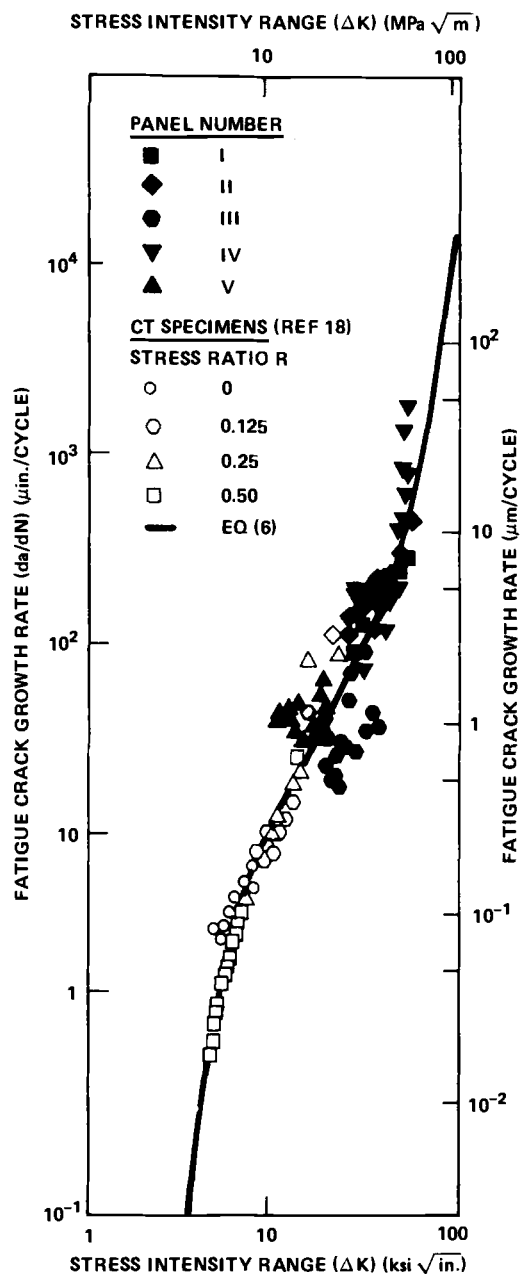


FIG. 15—Correlation of FCGR results of stiffened panels and base line materials data of compact tension specimens.

Representation of Data

The fracture mechanics method of characterizing fatigue crack growth behavior is to establish a relationship between da/dN and ΔK . Two equations have been developed by Chu [19]:

$$\frac{da}{dN} = \frac{C(\Delta K - \Delta K_{th})^n}{[(1 - R)K_c - \Delta K]^m} \quad (6)$$

and

$$\frac{da}{dN} = \frac{C(\Delta K^n - \Delta K_{th}^n)}{[(1 - R)K_c - \Delta K]^m} \quad (7)$$

where ΔK_{th} is the fatigue threshold under which cracks will cease to grow, and K_c is the critical value of K for unstable crack propagation. The coefficients c , n , and m are empirically determined constants.

Since the materials data in Fig. 15 indicate that the 5456-H343 alloy was insensitive to the effect of mean stresses [18], Eqs 6 and 7 may be evaluated for $R = 0$. This is also consistent with the loading condition of the stiffened panels. The constant ΔK_{th} may be estimated as $4 \text{ MPa}\sqrt{\text{m}}$ ($3.6 \text{ ksi}\sqrt{\text{in.}}$) from Fig. 15. The value of K_c is estimated as $117.3 \text{ MPa}\sqrt{\text{m}}$ ($106.8 \text{ ksi}\sqrt{\text{in.}}$) from test results of a 381-mm (15-in.)-wide center-cracked specimen (see Appendix). Figures 15 and 16 illustrate that the test data can be adequately represented by either Eq 6 or 7. The empirical constants are presented in Table 3.

Conclusions

The results of the stiffened panels tested under cyclic lateral pressure loading warrant the following conclusions:

1. In testing of weldbonded panels the stiffeners broke first. After the stiffeners broke completely, new cracks initiated and propagated in the skin. When tested without prenotches in the stiffeners, a weldbonded panel could endure more fatigue cycles than a GMA welded panel under the same pressure loading.

2. There was a stage of crack growth at approximately constant rates in the skin followed by fast crack propagation and final failure. The crack growth rate in the stiffeners increased to a peak value at about halfway through the stiffeners, and then decreased as the crack progressed toward the skin.

3. Fatigue crack growth data on stiffened panels could be correlated with base line materials data based on the approximation method of stress intensity analysis of the panels by considering the contributions due to tension and bending stresses. This method was verified by photoelastic measurements.

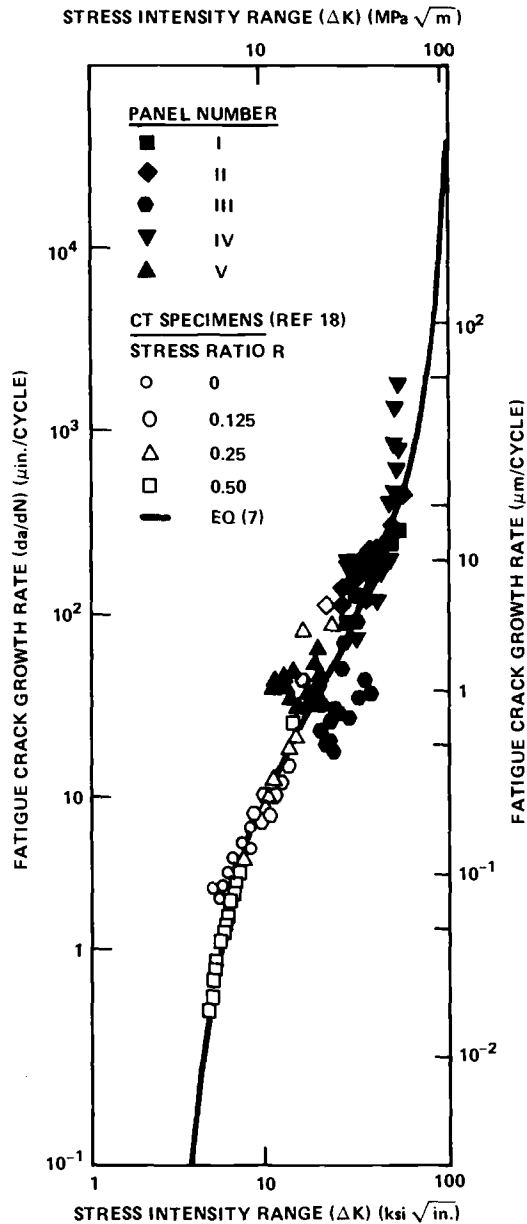


FIG. 16—Correlation of FCGR results of stiffened panels and base line materials data of compact tension specimens.

TABLE 3—Crack growth equation constants.

Equation	C			
	SI	U.S. Customary	m	n
6	245	(8948)	2.0	1.24
7	108	(4045)	2.0	1.50

4. The crack growth data could be represented by the two simple equations relating da/dN and ΔK . These equations should be useful for the prediction of fatigue life of stiffened panels.

Acknowledgments

The support of this work by the Naval Sea Systems Command is gratefully acknowledged. Thanks are due Dr. H. H. Vanderveldt and C. H. Pohler for their initiation and guidance of the project, C. C. Poe for providing his computer program, Dr. W. E. Lukens and J. G. Macco for technical consultation and assistance, and N. V. Marchica for his contribution to this work.

APPENDIX

Estimation of K_{Ic} of the 5456-H343 Sheet Aluminum Alloy

The fracture toughness K_{Ic} -value of the 5456-H343 aluminum alloy was needed for Eqs 6 and 7, so that crack growth in the stiffened panels could be predicted up to unstable crack propagation. The K_{Ic} -value was measured by testing a 381-mm (15-in.)-wide specimen with a center notch of 114.3 mm (4.50 in.), which was oriented in the rolling direction of the sheet alloy. After fatigue precracking, the specimen was tested in an MTS machine at a strain rate of 0.2 percent per minute. A load versus crack-opening displacement curve was recorded, and the effective crack length was determined from this curve in accordance with ASTM Recommended Practice for *R*-Curve Determination (E 561-80).

The crack extension behavior of the specimen under tensile loading followed a typical pattern observed by Sullivan et al [20]. As shown in Fig. 17, the crack, at first, maintained its initial length under rising load (Region I). Slow stable crack growth occurred as the load was further raised (Region II). In this region, if the load were held constant, the crack would cease to grow. Finally, the load reached the maximum and stayed at a constant level, while the crack grew at an accelerating rate until rupture (Region III). Sullivan et al suggested that the starting point of Region III is the limit of structural integrity, and the effective crack length at this location and the maximum load should be used to calculate fracture toughness K_{Ic} of the material. The fracture

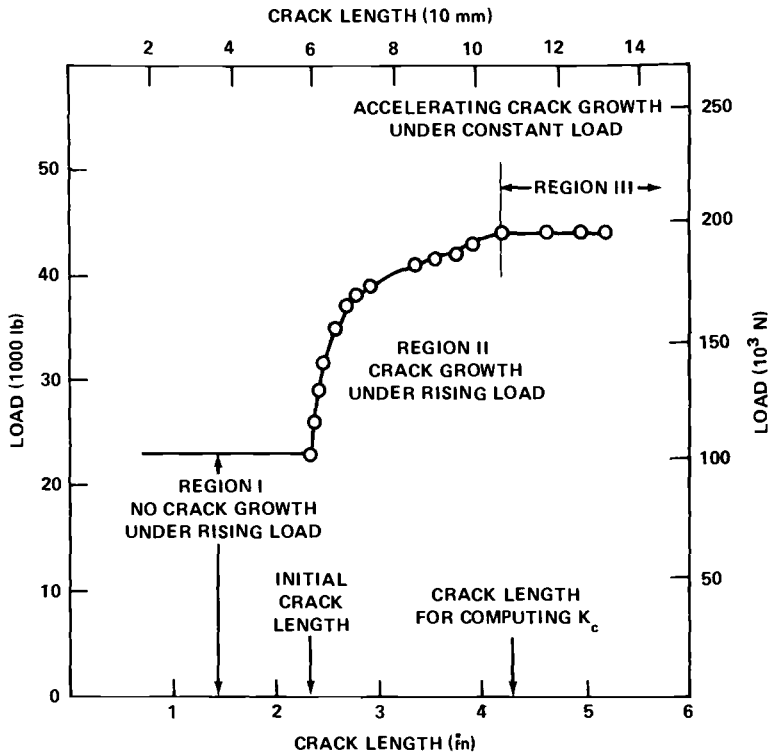


FIG. 17—Crack extension in the center-notched tension specimen.

toughness was computed by this method as $K_{Ic} = 117.3 \text{ MPa}\sqrt{\text{m}}$ ($106.8 \text{ ksi}\sqrt{\text{in.}}$) by the use of Feddersen's formula for center-notched specimens [21].

It should be noted that this was an estimation of the K_{Ic} -value and that the 5456-H343 aluminum alloy was apparently a tough material. A simple calculation revealed that the net section stress of the specimen at failure was 367.7 MPa (53.3 ksi), which was about equal to the tensile strength of the alloy. It indicates that the 381-mm (15-in.)-wide specimen sustained a considerable amount of plastic deformation before rupture.

References

- [1] Poe, C. C. in *Damage Tolerance in Aircraft Structures*. ASTM STP 486, American Society for Testing and Materials, 1971, pp. 79-97.
- [2] Vlieger, H., *Engineering Fracture Mechanics*, Vol. 5, No. 2, June 1973, pp. 447-477.
- [3] Sorkin, G. et al, *Engineering Fracture Mechanics*, Vol. 5, No. 2, Sept. 1975, pp. 307-352.
- [4] Wolfe, R. J. et al, *Engineering Fracture Mechanics*, Vol. 7, No. 3, Sept. 1975, pp. 565-581.
- [5] Paris, P. C. in *Proceedings*, 10th Sagamore Army Materials Research Conference, Syracuse University Press, 1964, pp. 107-132.

- [6] Wei, R. P., *Journal of Engineering Materials and Technology*, Vol. 100, April 1978, pp. 113-120.
- [7] Lukens, W. E., "Fatigue Behavior of Aluminum Alloy Weldments and Panels," presented at the Golden Gate Welding and Metals Conference, San Francisco, Calif., Jan. 1975.
- [8] Cordiano, H. V., *Journal of Engineering for Industry*, Vol. 92, No. 1, Feb. 1970, pp. 86-92.
- [9] Chu, H. P. et al, "Fatigue Crack Propagation in Aluminum Alloy Stiffened Panels Under Uniform Lateral Loading," SESA Paper D-23, Society for Experimental Stress Analysis, presented at SESA spring meeting, Dallas, Tex., May 1977.
- [10] Irwin, G. R. in *Fast Fracture and Crack Arrest*, ASTM STP 627, American Society for Testing and Materials, 1977, pp. 7-18.
- [11] "A Digest of Tentative Standard Methods of Test for Fatigue Crack Growth Rate in Metallic Materials," ASTM Task Group E24.04.01, July 1975.
- [12] Craddock, J. M., "Weldbonding/Rivetbonding: Application Testing of Thin Gauge Aircraft Components," AIAA Paper No. 73-805, American Institute of Aeronautics and Astronautics, 1973.
- [13] Haughey, V. A., "Improved Approach to Structural Integrity of Spacecraft Shrouds by Use of Skin-Corrugated Weldbond," AIAA Paper No. 74-381, American Institute of Aeronautics and Astronautics, 1974.
- [14] Sih, G. C., *Handbook of Stress Intensity Factors*, Lehigh University Press, 1973.
- [15] Tada, H. et al, *The Stress Analysis of Cracks Handbook*, Del Research Corporation, 1973.
- [16] Poe, C. C., "The Effect of Broken Stringers on the Stress Intensity Factor for a Uniformly Stiffened Sheet Containing a Crack," presented at the 10th Anniversary Meeting of the Society of Engineering Science, Raleigh, N.C., Nov. 1973.
- [17] Irwin, G. R., "The Dynamic Stress Distribution Surrounding a Running Crack-A Photoelastic Analysis," *SESA Proceedings*, Society for Experimental Stress Analysis, Vol. 16, No. 1, 1958.
- [18] Chu, H. P. et al, "Fatigue Crack Growth in S456-H343 Aluminum Alloy," presented at the AIME Annual Meeting, American Institute of Metallurgical and Petroleum Engineers, Denver, Colo., 26 Feb.-2 March 1978.
- [19] Chu, H. P. in *Fracture Toughness and Slow-Stable Cracking*, ASTM STP 559, American Society for Testing and Materials, 1974, pp. 245-260.
- [20] Sullivan, A. M., Freed, C. N., and Stoop, J. in *Fracture Toughness Evaluation by R-Curve Methods*, ASTM STP 527, American Society for Testing and Materials, 1973, pp. 85-101.
- [21] Feddersen, C. E. in *Plane Strain Crack Toughness Testing of High Strength Metallic Materials*, ASTM STP 410, American Society for Testing and Materials, 1967, pp. 77-79.

Durability and Damage Tolerance Behavior of Adhesively Bonded Primary Structure

REFERENCE: Potter, D. L., "Durability and Damage Tolerance Behavior of Adhesively Bonded Primary Structure," *Design of Fatigue and Fracture Resistant Structures. ASTM STP 761*, P. R. Abelkis and C. M. Hudson, Eds., American Society for Testing and Materials, 1982, pp. 373-407.

ABSTRACT: The Primary Adhesively Bonded Structure Technology (PABST) program was a U.S. Air Force sponsored program started in Feb. 1975 for the purpose of validating the use of adhesive bonding to join primary aircraft fuselage structural members. This paper will report on the analysis and component testing performed during the design development phase of the program, and the successful full-scale fuselage durability and damage tolerance test that was performed to four design lives. The goal of the program was to provide a savings of 20 percent on the acquisition and maintenance cost relative to mechanically fastened primary structure. Such effects as manufacturing quality, environment exposure, and a unique design criterion for bonded structure have significant impact on analysis methods. The initial development test program and results led to new testing techniques required for bonded joints to gain early design information. This is shown to be especially true for pressurized structure due to the unique behavior of metal crack propagation in this type structure. The full-scale fuselage test results and analysis correlation will be discussed as will the expanded purpose of the damage tolerance phase of this test and resulting demonstrations of crack containment within a stiffened skin panel under full cabin pressure.

KEY WORDS: adhesive bonding, primary structure, crack propagation, bond flaw, durability, environmental exposure

The application of adhesively bonded joints to primary aircraft structure has been a viable option to mechanically fastened joints for many years. In Europe, aircraft have been produced using this joining concept dating back to the 1940s; for example, the Fokker F-27 and F-28, the DeHaviland Comet, and Hawker-Siddeley Trident III B, all using Redux as the adhesive to join the wing and fuselage longerons to the skin. There are essentially no

¹Chief Engineer, PABST Program, Douglas Aircraft Company, Long Beach, Calif. 90845.

primary aircraft structures of U.S. design in commercial service today which rely on an adhesive to carry all of the structural loads.

In recent years the technological advancements in surface treatment and adhesives have indicated that the new 120°C (250°F) cure adhesive systems offer not only less metal degradation owing to the lower cure temperatures, but greatly increased durability and environmental resistance.

In 1972, the U.S. Air Force began a cost reduction study in view of the rapidly increasing costs of conventional mechanical fastened structure, maintenance costs, and fuel costs [1,2].² These studies indicated that there was a potential 20 percent acquisition cost savings and a 15 percent weight savings if the primary structure of the aircraft were adhesively bonded; in addition, a significant improvement in structural durability and integrity could be achieved.

In February of 1975, the Air Force awarded Douglas Aircraft the Primary Adhesively Bonded Structure Technology (PABST) program, with the objectives to demonstrate and validate the application of adhesive bonding to primary structure. The timing of the program coincided with the start of the development of the Air Force Advanced Medium STOL Transport (AMST) program, and the Douglas candidate, the YC-15 fuselage, was selected as the baseline demonstrator.

The PABST program is a multi-disciplined approach to the validation of bonding primary structures. The general procedure was to define the utilization of the aircraft, followed by developing the criteria, selecting a surface treatment and adhesive, performing a development test program, and finally, a full-scale fuselage test. This paper will describe this sequence and the resulting conclusions.

Design Criteria

The criteria for the PABST program contain the requirements of the applicable military aircraft specifications with appropriate modifications consistent with the scope of the PABST program [3]. These specifications include the MIL-A-008860 series, MIL-STD-1530 (USAF), and MIL-A-83444 (USAF) documents. The intent was that the implementation of these criteria in the bonded fuselage design would result in a structural integrity equivalent to that required for airworthiness. The implementation was demonstrated by test and analysis.

Durability considerations in bonded structures required that the environmental spectrum must be defined owing to the effects on the adhesive. For the 11 percent of the airframe life spent in flight, the environmental conditions are fairly well defined as noted earlier, but for the remaining 89 percent of its life the aircraft will be parked outside exposed to the elements and sub-

²The italic numbers in brackets refer to the list of references appended to this paper.

ject to the local atmospheric environment. The anticipated utilization must be considered and the aircraft designed to the extremes of the environment within the geographic areas of the projected utilization.

In recent years, a considerable body of data on the surface temperature of various items of equipment in open air storage has been accumulated. These data are presented in Ref 4 to 6.

An example of how a spectrum of atmospheric environment which an airplane can be expected to experience is shown in Fig. 1. This is a composite of the ambient air humidity and surface temperature developed based on the YC-15 design utilization. The upper limit of 60°C (140°F) and 100 percent relative humidity was selected as the ground exposure environment for test and analysis purposes on the PABST program.

For damage tolerance, the metallic structure was designed to the slow crack growth section of MIL-A-83444 such that the possibility of catastrophic failure was extremely remote. In addition to the military requirements, a fail-safe capability comparable to that of a commercial airplane fuselage, as defined in Federal Aviation Regulation 25, was imposed as follows:

The structure shall be capable of withstanding: (1) limit load with a two-bay crack, and (2) the maximum average internal member load occurring in 20 lifetimes, or limit load, whichever is less, for the foreign object damage. For these loads the structure shall withstand: (1) a two-bay skin crack or skin-to-stiffener disbond and the center stiffener (or splice) intact, and (2) a 38-cm (15-in.)-long foreign object damage skin crack with both the center

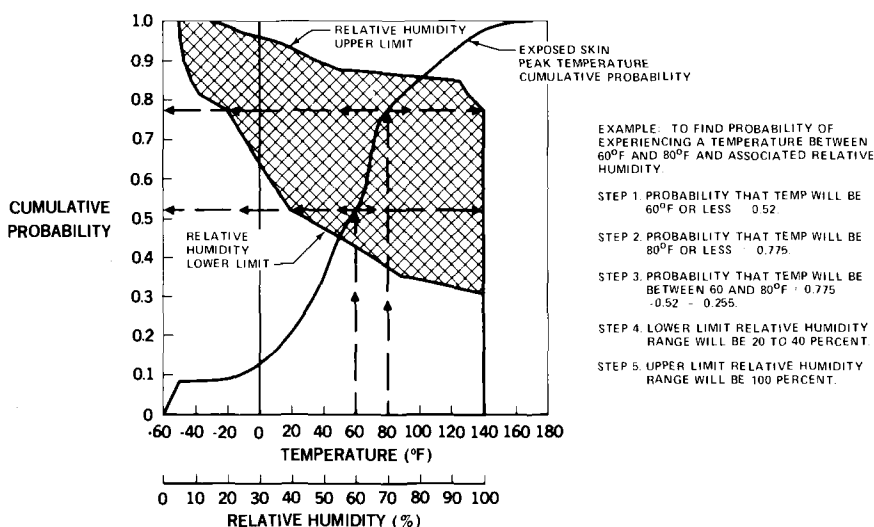


FIG. 1—Composite thermal and humidity environment [$t_c = (t_F - 32)/1.8$].

stiffener (or splice) and crack arrest member (if present) failed. All cracks considered shall be assumed to propagate in both directions.

The damage tolerance criterion for bonded joints is presently not addressed in either the military or civil specifications, so the following supplemental requirements were imposed (accounting for environmental effects):

An initial flaw shall be assumed to exist in each and every bond in its most critical location, including those highly stressed areas resulting from variable bondline thickness. The size of the flaw shall be the greater of: (1) the minimum detectable size for the nondestructive inspection (NDI) technique used on the bond, or (2) the smallest flaw remaining after a larger flaw has been repaired. Each flaw shall be evaluated for residual strength independently of all other flaws, either in the bond or metal. Initial flaws shall be located so there is no interaction between them.

The fail-safe capability of the bonded structure shall be capable of withstanding:

- (1) Limit load with each of the following two-bay disbond configurations:
 - (a) A two-bay disbond in only one side of a double strap butt splice.
 - (b) A two-bay disbond in a single strap butt splice, or single lap splice.
 - (c) A two-bay longeron-to-skin disbond.
 - (d) A two-bay shear-tee-to-skin or crack-arrest-member-to-skin disbond.
- (2) The maximum average internal member load occurring in 20 life-times, or limit load, whichever is less, for the foreign object damage specified as:
 - (a) A 38-cm (15-in.) disbond on both sides of a splice.
 - (b) A 38-cm (15-in.)-long foreign object damage skin crack with both the center frame (or splice) and the crack arrest member failed or with both the longeron (or splice) and crack arrest member failed as applicable.

Surface Treatment Selection

Implementation of the criteria requires that for bonded primary structure an extensive surface preparation and adhesive selection program be performed [7]. The selection process treats each of the elements of the adhesive joint (Fig. 2), and the evaluation of the results may directly affect the eventual structural arrangement and sizing.

In the PABST program, the surface preparation and processing evaluation was performed on three candidate surface treatments: phosphoric acid anodize (Spec BAC-5555, Boeing Company), chromic acid anodize (Spec BPS FW4352, Rev. G, Bell Helicopter Company), and chromic acid anodize

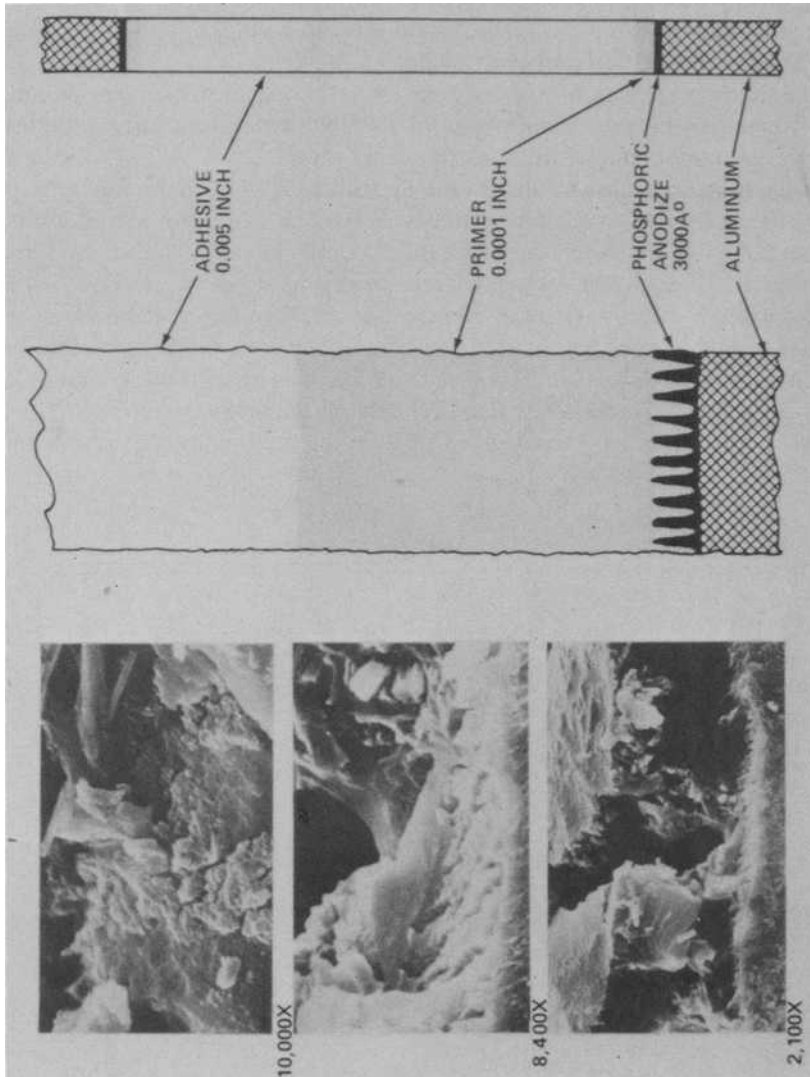


FIG. 2—Metal adhesive bonding interfaces.

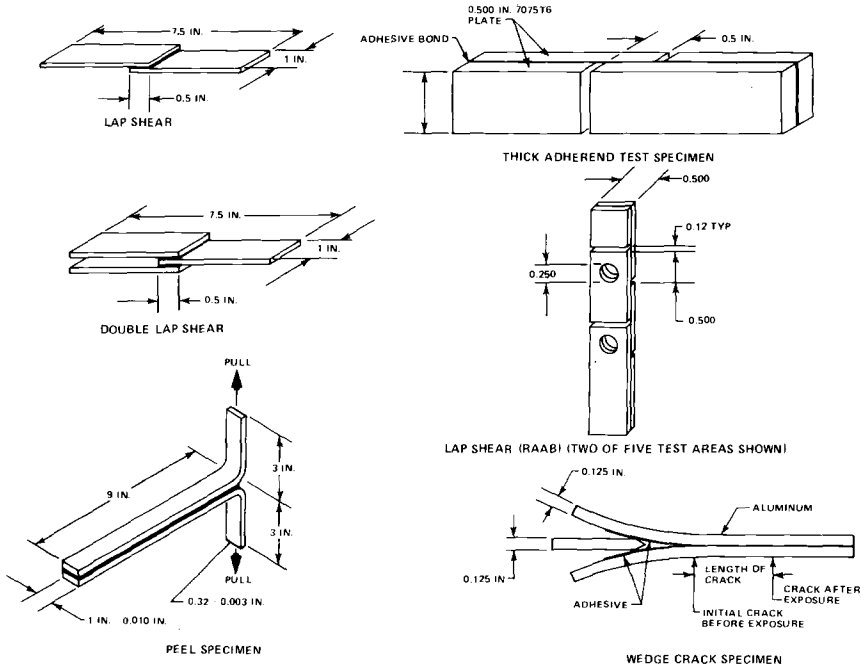
(Spec PS13201, McDonnell Douglas Corporation). The FPL etch, Spec BAC-5514, Boeing Company, was used as a reference standard.

The test method of evaluating surface treatments was proposed by Bethune in 1975 [8] and uses as a test article the wedge crack specimen (Fig. 3). All surface treatments tested arbitrarily used the same primer (American Cynamid BR-127) and adhesive (American Cynamid FM73) to provide a common basis for comparison. No adhesive could be evaluated until the surface treatment selection had been made.

The crack propagation values within a test matrix measured the production processing tolerance interaction of the solution concentration, applied voltage, solution temperature, and anodizing time.

Five wedge crack test specimens for each alloy, 2024-T3 bare and 7075-T6 bare, were prepared for each test matrix. Wedge crack growth was measured after a 1-h exposure to 60°C (140°F) and 95 to 100 percent relative humidity. Then each specimen was completely separated so that the failure mode could be evaluated. Acceptability of a failure mode was based on visual evidence of an unacceptable adhesive failure (occurring other than within the adhesive) or an acceptable cohesive failure (occurring completely within the adhesive).

These comparative tests revealed that only phosphoric acid anodize had no adhesive failures and low crack growth within the full range of the test matrix



after more than 10 000 wedge crack tests, and was therefore the most acceptable when considering the practical aspects of a production environment. However, it was found that phosphoric acid anodize surfaces experienced strength degradation when contaminated by handling—whether with clean cotton gloves, kraft paper, or bare hands—prior to the application of the primer. Therefore in all subsequent program fabrication it was required that the parts not be touched after being anodized and before priming. Parts were primed before removal from the anodizing racks.

In addition to these short-term environmental exposure tests, long-term wedge crack tests were performed at the Douglas Aircraft Company, El Segundo Sea Atmosphere Test Station. Both clad and nonclad, 2024-T3 and 7075-T6, alloys were simultaneously evaluated for their effect on surface treatment. The test site, approximately 46 m (50 yd) from the Pacific Ocean, is located within the boundaries of an oil refinery and is adjacent to a sewage disposal plant. Corrosive agents deposited on test specimens remain for long periods and are not subject to frequent removal by rainfall. The results to date are shown in Fig. 4. Note that clad 7075-T6 does not have any durability on any of the candidate surface treatments. The crack growth in the phosphoric acid anodize showed comparatively the least crack growth for both alloys.

Adhesive Selection

In the PABST program four candidate film adhesive and corrosion resistant primers of the new generation of environment-resistant 121°C (250°F) cure type were selected for evaluation. The selection of these four systems was based on data from the adhesive manufacturer and available industrial test data. These were: (1) American Cyanamid, FM-73/BR-127 Mat Carrier, (2) Hysol Division, The Dexter Corporation, EA9628/9202 Woven Carrier, (3) 3M Company, AF55/XA3950 Woven Carrier, and (4) Narmco Material, Inc., M1133/6740 Woven Carrier.

These adhesives were extensively evaluated by the matrix of specimens and environments shown in Fig. 5. The phosphoric acid anodize previously selected was used on all test specimens, and the manufacturer's recommended procedures were used for the priming and curing. Within this test matrix an evaluation was made of processing tolerances such as primer thickness, primer cure temperature, adhesive out-time, and adhesive heat-up rate.

Lap shear tests showed comparative data while T-peel tests showed the effect of the adhesive carrier. Although the failures were all of the desired cohesive mode, subsequent long-term durability tests revealed that adhesive material selection based on static T-peel or lap shear performance would have been incorrect.

Reduced Area Adhesive Bond (RAAB) specimens provide the most envi-

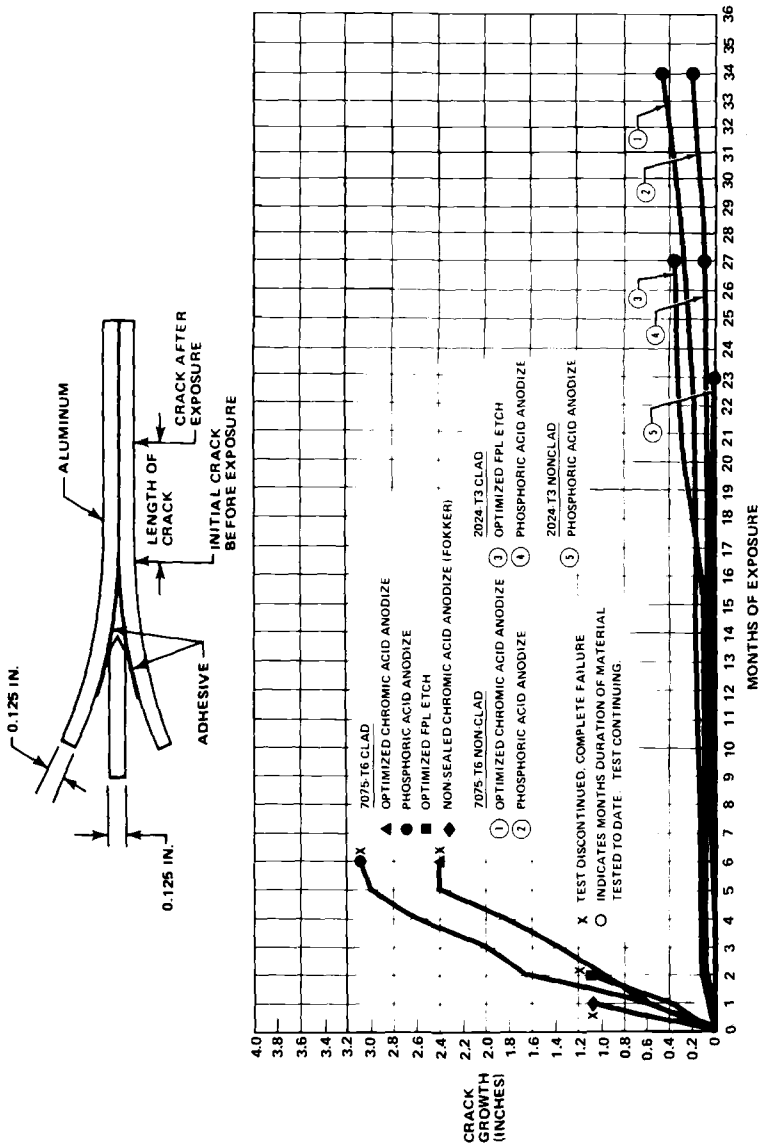


FIG. 4—Beach exposure test (1 in. = 2.54 cm).

	SPECIMEN TYPE	MECHANICAL PROPERTIES			ENVIRONMENTAL EXPOSURES										
		70°F	RT	+180°F	TT-S 735	JP-4	MIL-H 5606	140°F 100% RH	SALT SPRAY	CHEM MILL	BILGE FLUID	MIL-C 25769	IMMER CORR	FIRE EXT	BEACH EXPOS
METAL TO METAL	LAP SHEAR	X	X	X	X	X	X	X	X				X		X
	DOUBLE LAP SHEAR	X	X	X											
	STRESSED LAP SHEAR				X	X	X								X
	T-PEEL	X	X	X	X	X	X	X	X				X		
	CREEP		X	X											
	THICK ADHEREND	X	X	X											
	WEDGE CRACK				X	X	X	X	X	X	X	X	X	X	X
	DOUBLE CANTILEVER		X					X							X
	NAPKIN RING TEST		X												
	RAAB SUSTAINED LOAD							X							
	RAAB CYCLIC LOAD	X						X							
SANDWICH	CLIMBING DRUM	X	X	X											
	OPEN FACED CLIMBING DRUM				X	X	X	X	X						
	FLATWISE TENSION		X	X											
	BEAM SHEAR		X												

FIG. 5—Adhesive property tests [$t_c = (t_F - 32)/1.8$].

ronmental exposure of the bond line and are good for comparing the resistance of similar adhesives in stressed and cycle-stressed environments. The RAAB test results in Figs. 6 and 7 show that cycle stressed specimens fail in fewer hours than specimens with a constant stress, even at a lower stress level. Again in these tests, the mat carrier performs better in both the constant stress and cycle-stressed tests. The RAAB specimens were also used to indicate the presence of moisture in the uncured (as received) adhesive. Static shear tests performed at 121°C (250°F) will indicate by lower shear values the presence of moisture. Table 1 shows how drastically the durability can be reduced by small amounts of moisture in the adhesive.

Thick adherend test specimens were used early in the program to evaluate the cyclic durability of the adhesive system. These tests were performed at a cyclic rate of 30 Hz (1800 cpm) and no failures occurred after 10^6 cycles. Later, data from Boeing showed a greatly reduced cycle life when tested at slow cyclic rate (Fig. 8). The 1-hour loaded and 15 min at no load test point is a realistic loading rate when considering the baseline YC-15 average flight time was 1 h. Thick adherend specimen tests for shear stress-strain data also showed a higher failing stress and lower strain for fast test cycle rates. These results demonstrated the importance of cycle testing adhesive systems at a loading rate equivalent to the actual service usage.

The results of the surface treatment and adhesive testing phase of the pro-

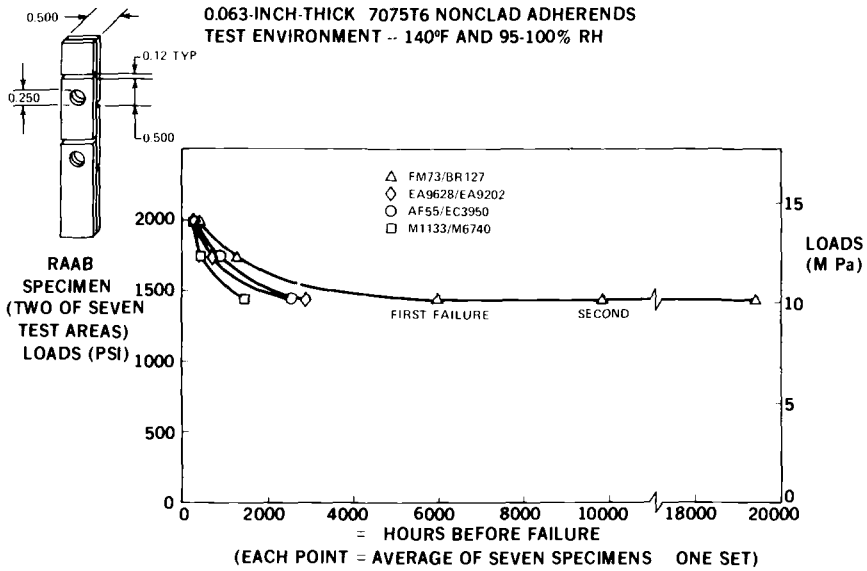


FIG. 6—RAAB sustained loads (1 in. = 2.54 cm).

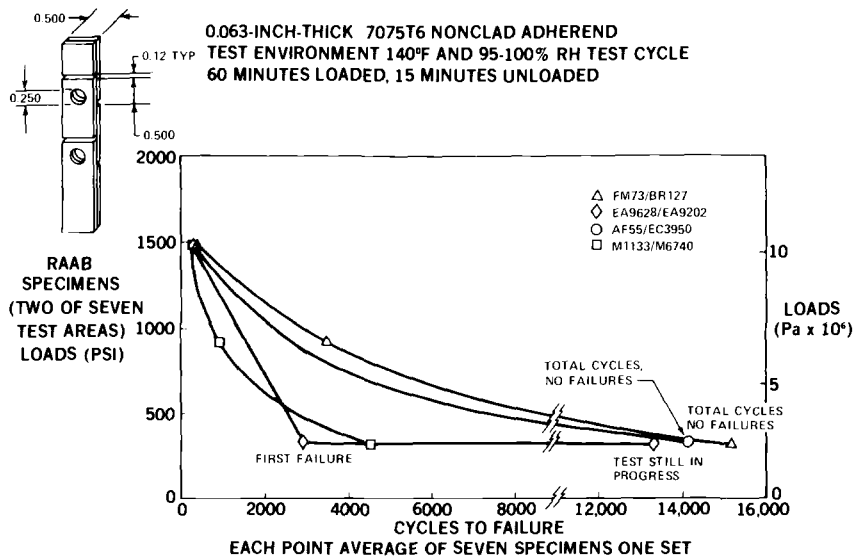


FIG. 7—RAAB specimen cyclic load (1 in. = 2.54 cm).

TABLE 1—Cycle stress durability of FM73 (cycles to failure).

SPECIMEN NUMBER	VARIATION OF CHEMICAL COMPOSITION										STANDARD FORMULATION
	CURING AGENT (PERCENT)				EPOXY (PERCENT)		ELASTOMER (PERCENT)		WATER ⁽³⁾ (PERCENT)		
	+ 50	- 50	+ 10	- 10	- 30	+ 36	+ 30	- 30	+ 1 30	+ 1 03	
1	77	578	363	521	213	454	133	512	8	60	578
2	88	605	367	548	213	478	208	526	9	63	717
3	95	606	394	609	214	563	219	527	10	64	739
4	97	626	428	615	215	599	257	530	11	65	791
5	150	675	434	649	216	621	382	541	12	66	804
6	(1)	724	476	653	217	730	517	543	13	67	810
7	(1)	734	(1)	672	(1)	(1)	(1)	547	14	68	855
AVG	101	650	410	610	215	574	286	532	11	65	756

- NOTES (1) INADVERTENTLY FAILED DURING LOAD ADJUSTMENT
 (2) TEST CONDITIONS
 140°F. 100% R.H.
 1200 PSI
 CYCLIC LOADING, 1 HOUR ON, 15 MINUTES OFF.
 (3) STANDARD ADHESIVE WITH WATER ADDED AT ROOM
 TEMPERATURE, 100% R.H.

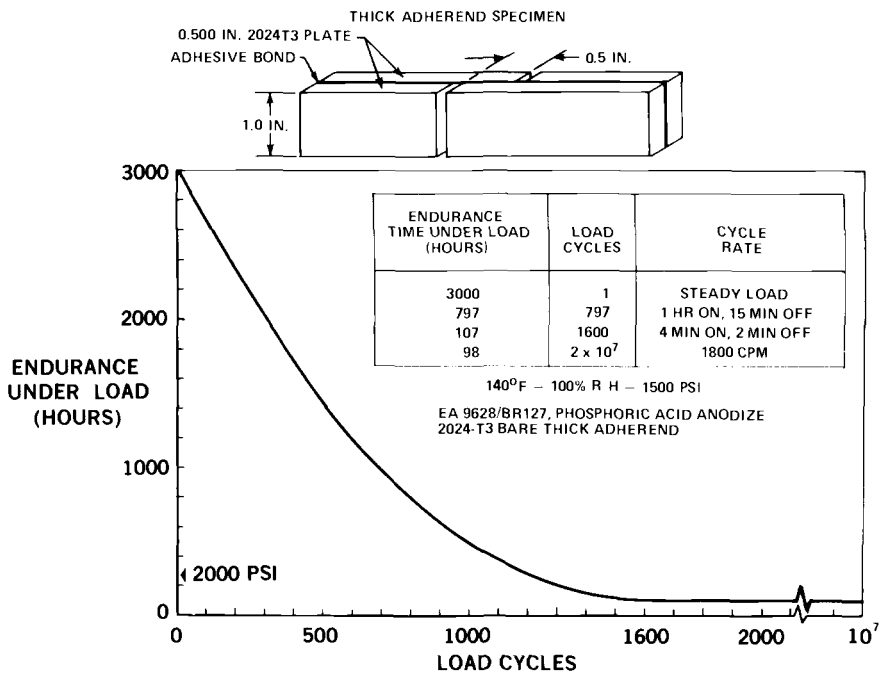


FIG. 8—Effect of cycle rate on endurance (1 in. = 2.54 cm).

gram did not reveal that any one test specimen type would clearly discriminate for all loading conditions and environments. It was also evident that no one adhesive system contained markedly superior qualities over the remainder of the candidates. The FM-73 adhesive (mat carrier with BR127 primer) and the phosphoric acid anodize were selected as the adhesive system to be used during the remainder of the program. This choice was based primarily on its wide processing tolerances being best suited for a production environment.

Component Test Program

This phase of the PABST program was directed toward demonstrating that the static, fatigue, damage tolerance, and fail-safe requirements (previously defined in the design criteria) had been met for the various candidate structural configurations. The test specimens are summarized in Fig. 9.

A basic criterion established at the beginning of the program was that the design must permit any metal element to be broken at any location without causing the adhesive bond to fast-fracture catastrophically. Skin splices were of particular concern since they had no backup fasteners. The bonded joint analysis method [9-12] determined the required skin overlap length. For other failure modes in bonded joints, such as skin buckling due to shear, or compression and skin pillowing due to cabin pressure, there were no analysis methods known and the component test plan was aimed at providing the evaluation.

The tension tee tests demonstrated the ability of a frame-to-skin bonded joint to react to the ultimate design cabin pressure load of 98.6 kPa (14.3 psi). The test results (Fig. 10) showed a large margin compared with the design loads.

The static shear combined with compression or tension tests demonstrated the bonded longerons and frame shear tees ability to resist the peeling action of skin wrinkles. The results of this series of tests are summarized in Table 2. The failure prediction analysis values were based on mechanical attachment analysis methods and test results from previous programs. It is significant to note that these bonded panels exceeded the predicted values, but even more significantly, the mode of failure was always initially in the metal stiffeners and not in the bond, as shown in Fig. 11 where the base leg of the longeron remained bonded to the skin despite severe wrinkling of the skin.

The next test was conducted to examine the effect of static frame bending where the skin is in compression. The specimen consisted of three equally loaded frame segments bonded to the skin. The initial failure was observed to originate in the bond, over a 2.5 cm (1-in.) length, starting at the edge of the central frame shear tee (Fig. 12). This was followed immediately by the complete disbond of the shear tee between two longerons. This bond failure ini-

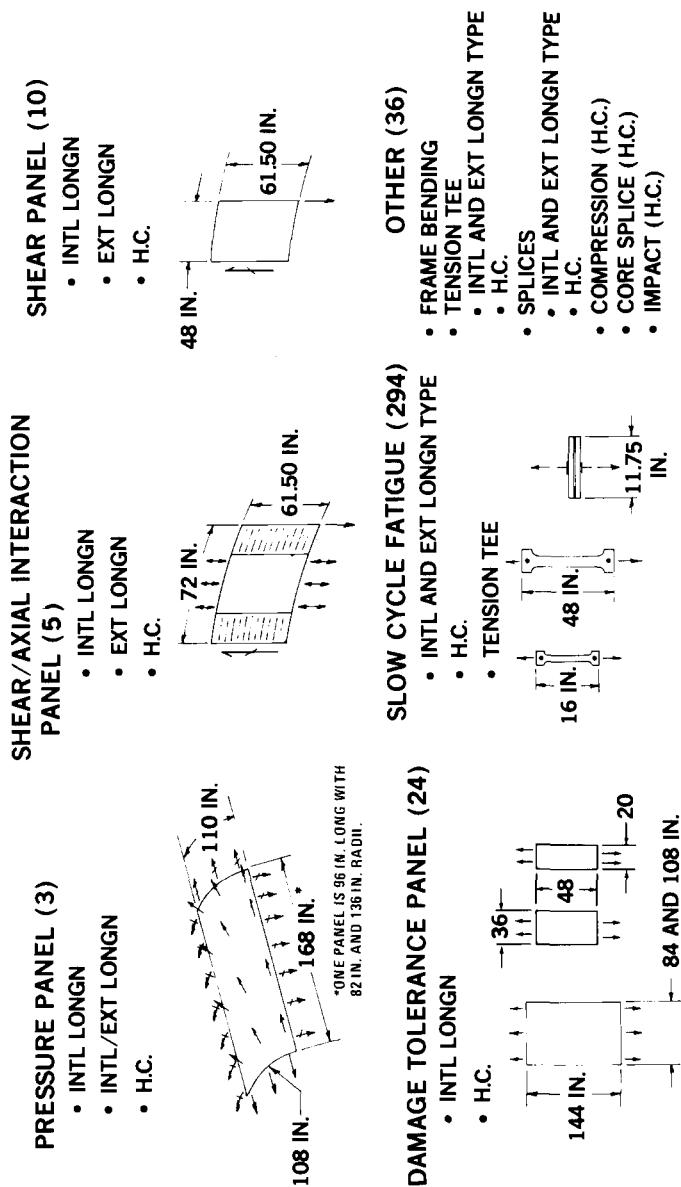


FIG. 9.—Summary of test articles (1 in. = 2.54 cm).

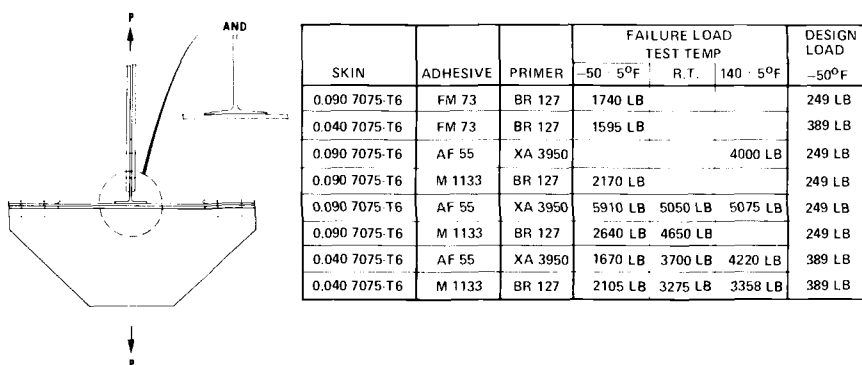


FIG. 10—Tension tee test specimen for testing tension in the bond joint between the skin and the frame/shear-tee [$t_c = (t_F - 32)/1.8$].

tiating at the edge of the bonded frame shear tee demonstrated the importance in the design of bonded structure of avoiding abruptly ending a bonded member on unreinforced skin. Subsequent PABST program fatigue testing further demonstrated this point, and correction design measures were taken before fabricating the full-scale test article.





An initial concern of a bonded primary structure was how the bonded joint would retard a growing metal crack compared with a riveted design. To assess this effect a group of cyclic tests were performed on flat and subsequently on curved panels. The first of these tests was performed on small flat panels with a single central stiffener with a small metal flaw introduced at a rivet hole on one panel and on another similar, but bonded, panel in the skin under the bonded joint. It took considerably longer for the skin flaw to propagate to a 8 cm (3 in.) length in the bonded panel (230 000 cycles) than in the riveted panel (140 000 cycles).

A second set of small flat panels with two stiffeners and a skin flaw midway between them were cycle tested until the crack had propagated to 3.8 cm (1.5 in.) beyond each stiffener edge and then a static residual strength load applied. The results showed that not only did the bonded panel retard the crack more than the riveted panel as it passed over the stiffener area (11 000 cycles for the bonded panel compared with 1000 cycles for the riveted panel), but the bonded panel failing load for residual strength was 13.5 percent higher. These encouraging results led to the testing of large flat panels which resembled more closely the complete configuration and which were less influenced by boundary conditions that would affect crack propagation results.

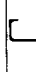


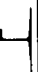


One of the large flat panels tested for crack propagation data had 0.51-cm (0.20-in.) flaws sawcut at Points 1 and 2 as shown in Fig. 13. Constant amplitude cyclic loads representing the hoop tension resulting from 49.29 kPa (7.15 psi) cabin pressure were applied at a 1-Hz rate.

TABLE 2—Shear compression/tension interaction static test panel.

ADHESIVE FM73, PRIMER BR127, TEST TEMP - 140°F

SKIN 7075T6	LONGERON	TEST		DESIGN		ANALYSIS PREDICTION	
		SHEAR (KSI)	AXIAL (KSI)	SHEAR (KSI)	AXIAL (KSI)	SHEAR (KSI)	AXIAL (KSI)
0.05		18.1	-29.2	17.8	14.0	18.1	-21.1
0.05		23.0	56.5	13.4	55.4	23.0	35.0
0.09	NONE	16.9	8.7	16.3	-8.4	16.9	5.4
0.05		30.6	67.9	13.4	55.4	12.5	67.9
0.05		18.0	-18.2	17.8	14.0	18.0	-13.5

PRIMER BR127

SKIN 7075T6	LONGERON	ADHESIVE	TEST TEMP	TEST SHEAR (KSI)	DESIGN SHEAR (KSI)	ANALYSIS FAILURE PREDICTION (KSI)
0.04		FM73	-50°F	19.8	13.0	18.3
0.09		RIVETED	R.T.	24.6	20.0	21.8
0.09		FM73	R.T.	26.5	20.0	21.8
0.04		M1133	-50°F	27.5	13.0	18.3
0.04		M1133	140°F	25.3	13.0	18.3
0.09	NONE	FM73	140°F	19.6	20.0	10.6
0.09*	NONE	FM73	140°F	23.8	20.0	12.6
0.0434		FM73	140°F	30.7	13.0	23.3

NOTE: $P_a = 0.145 \times 10^{-3}$ psi
 $t_c = (t_F - 32)/1.8$
 cm = 0.394 IN.

*12 IN. FRAME SPACING

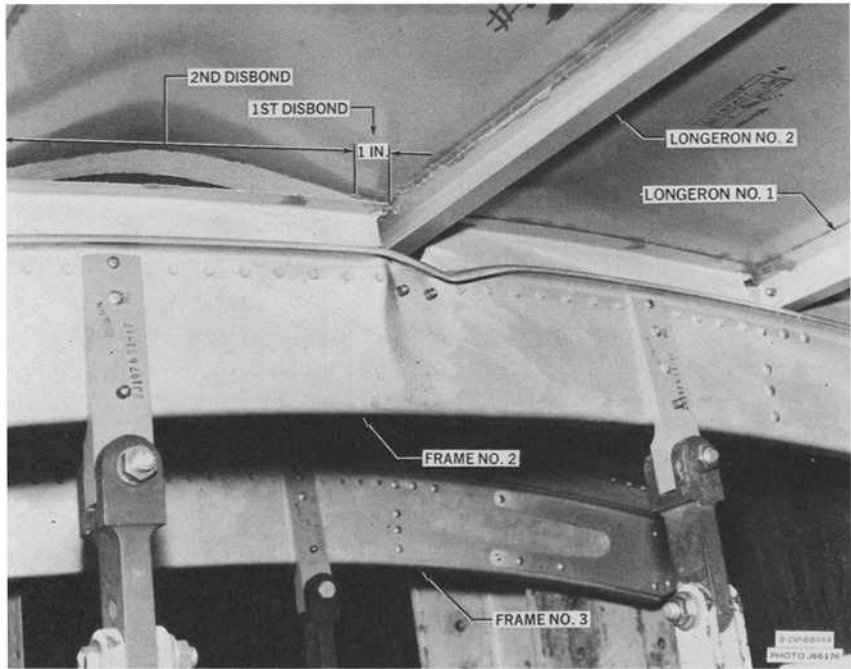
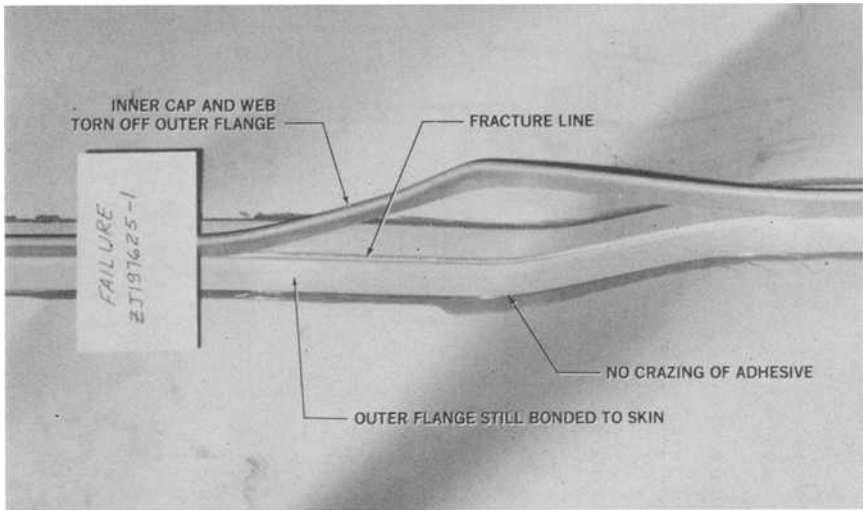


FIG. 12—Frame bending test—frame failure.

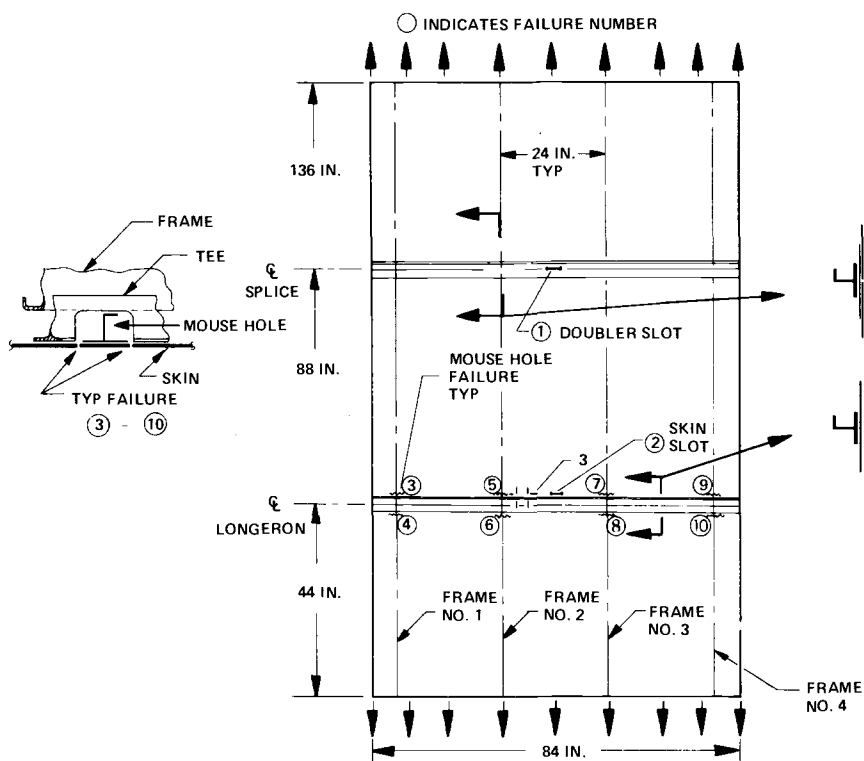


FIG. 13—Internal longeron test—failure locations (1 in. = 2.54 cm).

It is known from our experience with riveted design that the intersection of the longeron and the frame has been a critical area for crack initiation. The cutout in the frame shear tee at this intersection is referred to by the designers as a "mouse hole." During an inspection at 31 270 cycles, a 10.8-cm (4.2-in.) crack was discovered at one of the longeron mouse holes. After 35 070 cycles, four of the possible eight mouse hole locations where the shear tee stopped on the skin were cracked. The panel was tested through 36 803 cycles when a complete panel failure occurred through the mouse hole cracks. After the test, it was determined that all eight similar locations had developed fatigue cracks prior to the failure, demonstrating again the importance of not ending a stiffener on unreinforced skin. It should be noted that the mouse hole cutouts at the splice area developed no fatigue cracks owing to the splice doublers reducing the stress concentration in the skin at the shear tee end.

The next test effort was performed on curved pressurized panels subjected to biaxial stresses and evaluated the fatigue life and damage tolerance com-

pliance with the criteria. One of these test specimens represented one of the highest loaded panels on the YC-15 fuselage. The overall dimensions are shown and the structural arrangements are detailed in Fig. 14. All the frame shear tees are bonded to the 0.127-cm skin (0.050-in. 7475-T761) as well as the bonded splice and longeron No. 2.

The specimen was mounted in a test fixture which applied vacuum pressure to the outer skin surface to simulate cabin pressure. Whiffle trees and hydraulic jacks supplied the hoop and longitudinal loads respectively. The panel was cycle tested at a rate of one pressure cycle each four seconds. The panel successfully withstood 38 028 pressure cycles with no fatigue cracks or disbonds. Subsequent to this, six damage tolerance flaws were cut in the structure and the panel was again cycled for an additional 38 028 cycles (two lifetimes). Other than the propagation of the damage tolerance flaws, no fatigue cracks were encountered in the participating structure. The longest flaw propagation was 4.95 cm (1.95 in.).

The next phase of testing on this panel was to cut the fail-safe flaws and test for residual strength. Two flaws were planned for this test, but each was tested separately.

The first fail-safe flaw, was a two-bay crack with the centerline frame intact. This flaw length was successively extended in three steps until the full two-bay crack was reached. In each step full pressure (vacuum) was applied before applying the fail-safe longitudinal load. No flaw growth was noted on the application of the pressure loading alone, but as the longitudinal load

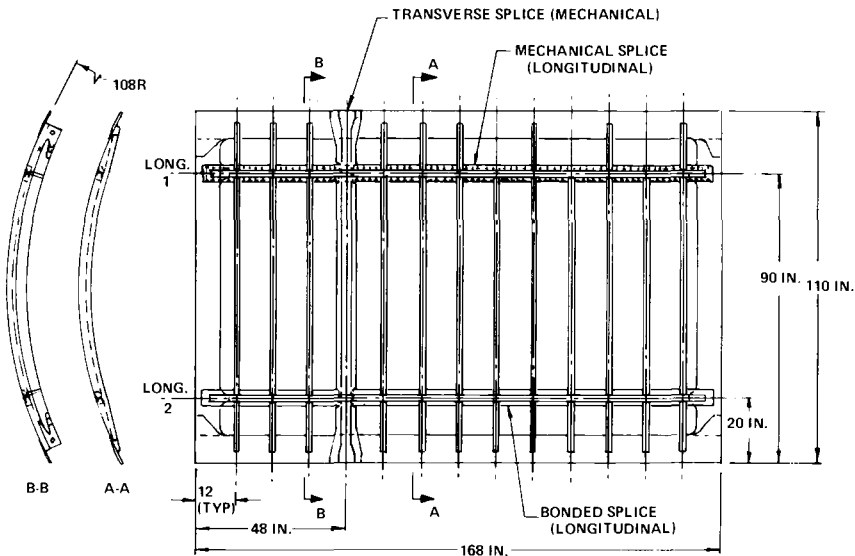


FIG. 14—Structural arrangement of test panel (1 in. = 2.54 cm).

was applied, the crack tips grew and turned 90 deg to the sawcut direction on each of the first two flaw length steps. On the third flaw length step, and during the application of the longitudinal load, the crack tips propagated to the adjacent frame shear tee bond lines and each turned circumferentially. The crack was successfully arrested by the bonded shear tees.

The second test represented the foreign object damage and was made by sawing 38 cm (15 in.) through a frame and the skin longitudinally. The fail-safe load was applied in the same sequence as before. At a pressure of 47.6 kPa (6.9 psi) and no longitudinal load, the flaw propagated to the adjacent frames and was again arrested at the frame shear tee bondline.

After the residual strength tests, an additional 37 000 cycles, almost two lifetimes, were imposed on the specimen and still there were no fatigue failures. The specimen was therefore subjected to a total of almost six lifetimes (113 246 cycles) without experiencing any fatigue failures or disbonds in the participating structure.

A second test specimen similar to the panel discussed above, except representing the structural area around the crew's entrance door, was installed in the same test fixture.

The test plan was also the same, including the installation of flaws in the metal. One of these flaws was extended to 15 cm (6 in.) after the initial 0.64-cm (0.25-in.) flaw had not propagated significantly in two design lives of cycling. The intent was to determine the behavior of the crack as it entered the bonded joint for comparison with the earlier small flat panel test previously discussed. This flaw propagated rapidly to the bonded frame shear tees, but turned parallel to the frames at the bondlines (Fig. 15) forming a "window" opening in the panel bounded by the stiffening elements. This behavior of cyclic crack propagation and the residual strength crack arrest of the first test panel is more representative of an actual full-scale structure than the results from the earlier flat panel tests where cracks propagated straight across the bondline. Also, these two curved pressure panel specimens revealed that cracks are completely contained within the bonded boundaries of the initial cracked panel.

It is significant to note that in past experience with an all riveted specimens tested in this same test fixture, the cracks turned at the frame riveted joint, but further cycling resulted in the crack working out of the rivet line and continuing in the same original direction until a catastrophic failure occurred (Fig. 16). This behavior agrees that reported incidences on actual flight aircraft where skin cracks have developed and passed across riveted frames to lengths of 2 to 3 m (75 to 130 in.) before detection or decompression occurred.

In the early phase of the PABST program, the effects of environment and cycle rate on bonded joints were determined to be important in representing real-life aircraft durability. However, the small coupons tested then were not

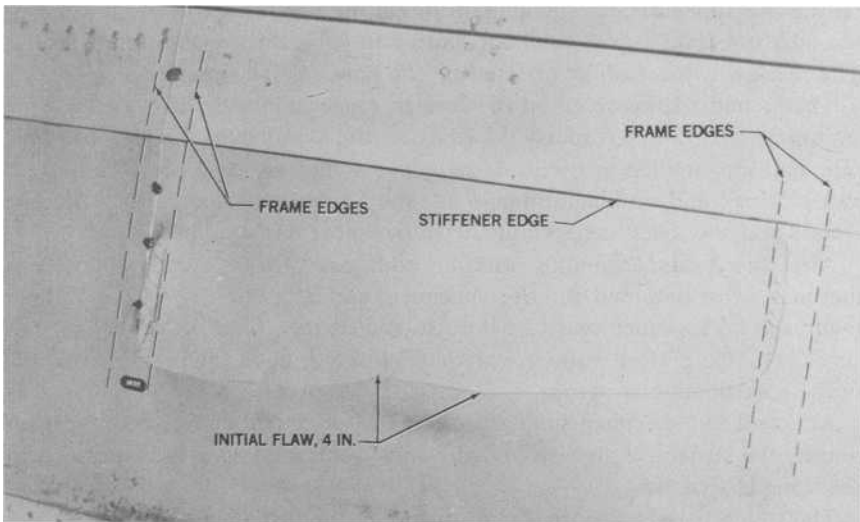


FIG. 15—*Bonded, curved panel crack propagation (1 in. = 2.54 cm).*

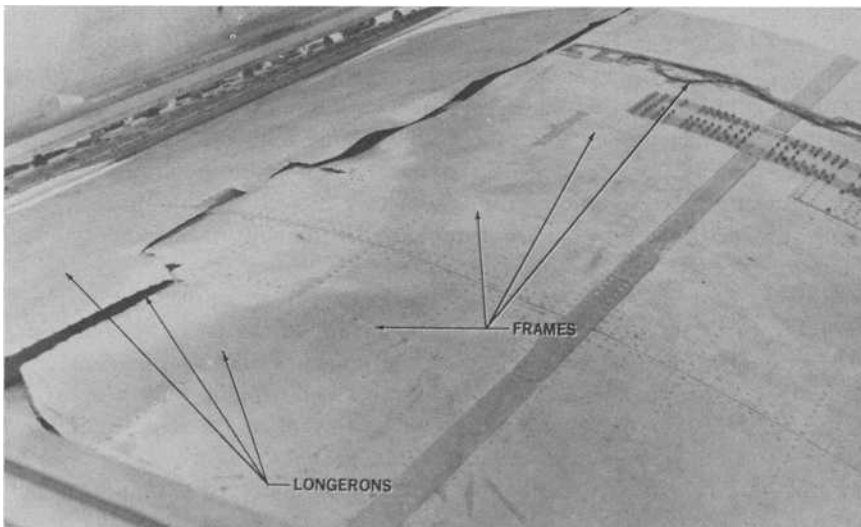


FIG. 16—*Riveted, curved panel crack propagation after fast fracture.*

representative of an actual configured aircraft structure. The full-scale test article was to be tested in laboratory environment and at a fairly high cycle rate, which leads to the dilemma of how to relate the full-scale test to actual aircraft utilization. To solve the problem, two identical panels were built to represent the structure of the fuselage.

The first panel was tested in laboratory air like the full-scale test article and was subjected to shear and axial loads plus an external vacuum. The spectrum was equivalent to the one used on the full-scale test article. Each spectrum contained two pressurized flights and one nonpressurized low-level flight and took 60 s to apply.

The panel successfully withstood 45 600 cycle spectrums (91 200 pressure cycles) or 4.8 lifetimes. No bondline flaws grew in size and only two of the four metal flaws showed slight growth. No metal fatigue failure or disbond developed.

The second shear panel was placed in the same jig, but with two changes. The laboratory air environment was changed to apply 60°C (140°F) at 100 percent relative humidity when the flight was in the taxi mode, and the temperature was raised to ambient for low-level flight and then lowered to -45°C (-50°F) to represent the high-altitude flight case. The other major change over the previous test was the cycle rate. The time to complete one spectrum was 90 min. The environmental equipment was able to change specimen temperature from +60°C (+140°F) to -45°C (-50°F). Figure 17 shows the complete spectrum and the relationships of loads and temperatures. This panel successfully withstood one design life of 9500 spectra with no bondline flaw growth or metal flaw growth. There was also no evidence of corrosion or metal fatigue.

Since both panels demonstrated identical durability and damage tolerance characteristics, it was concluded that a bonded YC-15 would achieve at least one design life of trouble-free service if exposed to real-life environments and loading rates.

Full-Scale Test Program

The main structural component that was intended to validate adhesive bonding for primary structure was a full-scale section of the YC-15 fuselage. This Full Scale Demonstration Component (FSDC) was 38 m (42 ft) long and extended from the forward part of the cargo compartment to a station 61 cm (24 in.) aft of the main fuselage frame which supports the landing gear and the wing rear spar (Figs. 18, 19, and 20). The structural members and assemblies that make up the FSDC were designed to the static, fatigue, and damage tolerance criteria noted earlier.

All skins and doublers were bonded to one another and to the stiffening elements. The remainder of the structure was mechanically fastened. The

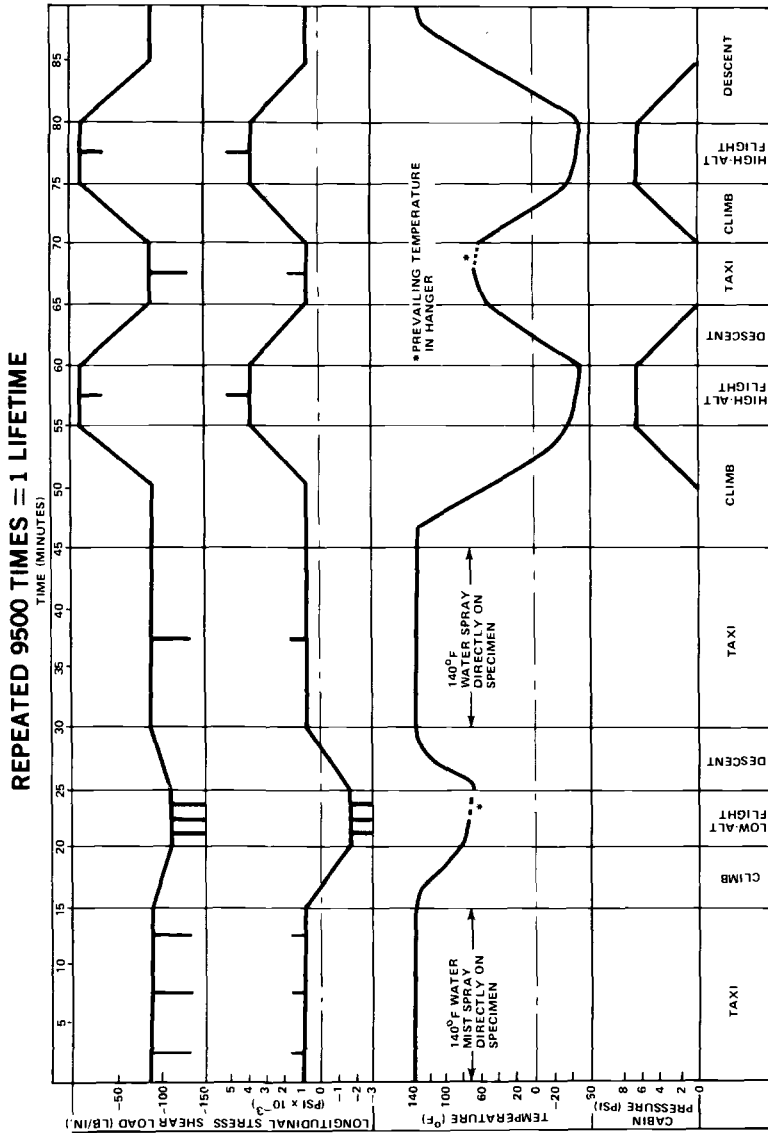


FIG. 17—Interaction fatigue test slow cycle spectrum [$N/m = 17.6 \text{ lb/in.}$; $PA = 0.145 \times 10^{-3} \text{ psi}$; $t_c = (t_F - 32)1.8$].

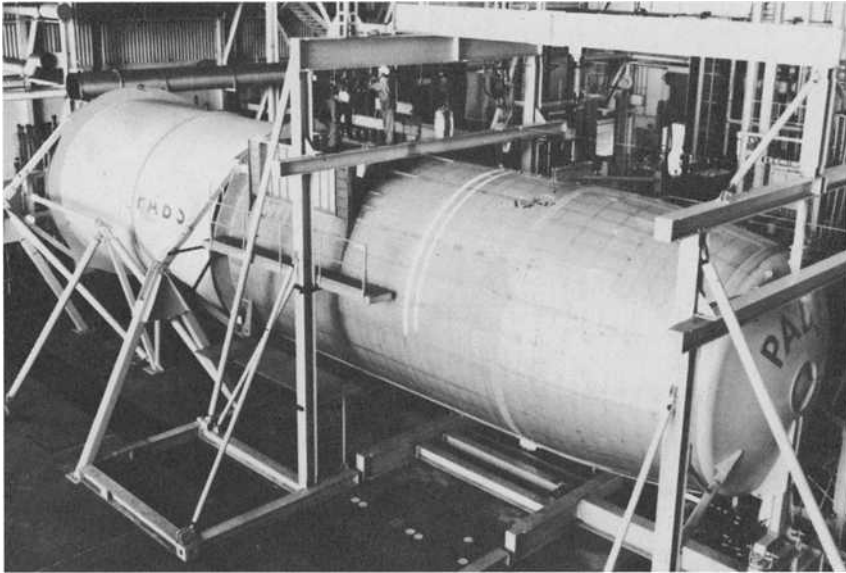


FIG. 18—Full-scale demonstration component test setup.

minimum skin thickness was set at 0.127 cm (0.05 in., 2024-T3 bare) based on foreign object damage criteria.

The “mouse hole” in the shear tees was designed with bonded doublers under the internal longerons, and shear tees joggled over these doublers to minimize skin cracking as was experienced earlier on the large flat panel tests (Fig. 21).

Tear stoppers (7475-T761 bare material) were located in a longitudinal direction along the fuselage sides (wide-spaced longeron area) to satisfy the slow crack growth and residual strength requirements of the criteria. The close-spaced longeron upper and lower skin panels did not require tear stoppers because the panel dimensions were such that the criteria flaw did not attain critical dimensions in the transverse direction. Cracks in the longitudinal direction were stopped by the bonded frame shear tees.

Before beginning the test, 18 damage tolerance flaws (DT's) were sawcut in the FSDC. The flaws were 0.635-cm (0.250-in.) sawcuts with finite radius tips. Crack growth time histories were measured from the time that fatigue cracks nucleated at the sawcut tips. The location of the metal flaws was determined from the damage tolerance analysis. In addition to the metal flaws, there were 844 bond flaws that resulted from the manufacturing phase. These discrepant bond flaw areas were purposely left unrepaired so the maximum data could be collected on the behavior of bond flaw propagation under full-scale test conditions. It should be noted that during the

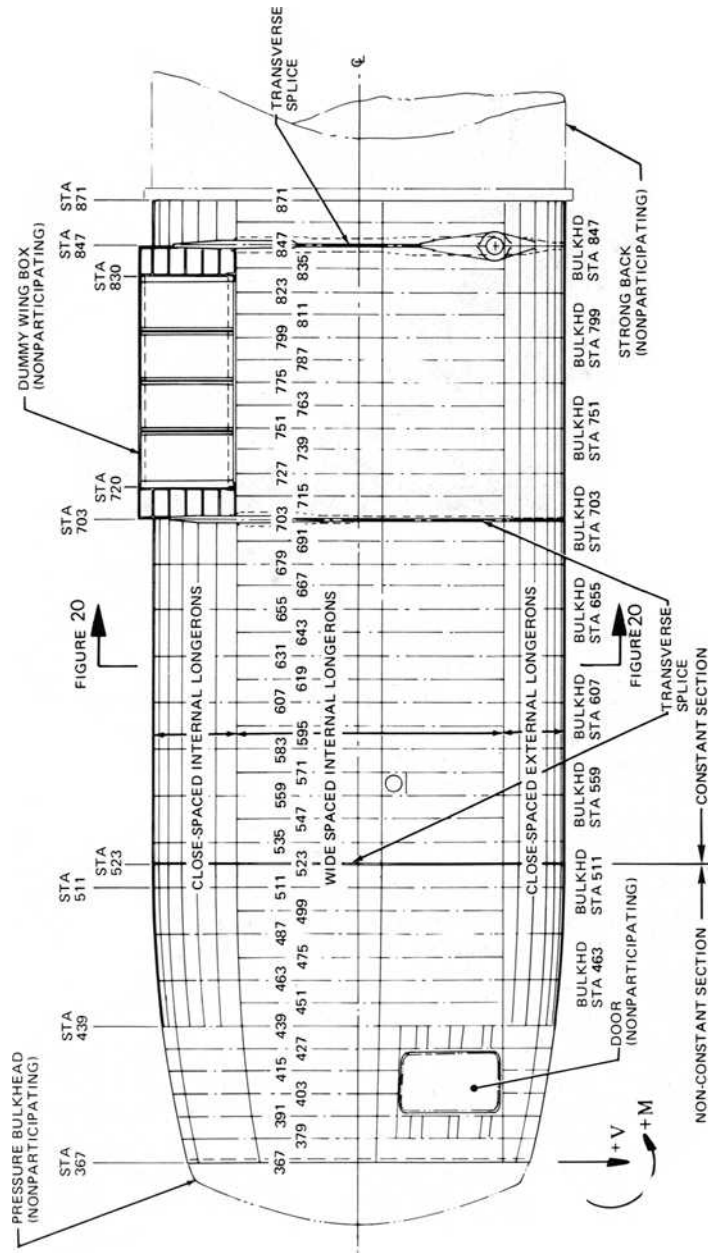


FIG. 19—Full-scale demonstration component.

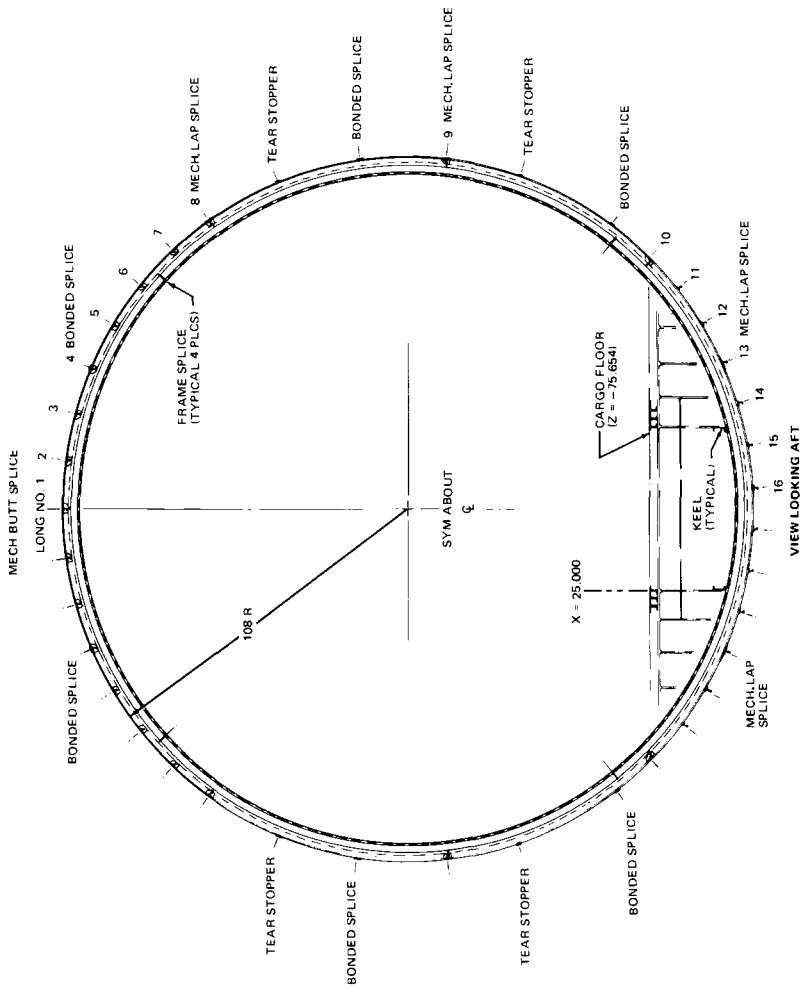


FIG. 20—Full-scale demonstration component—typical constant section frame.

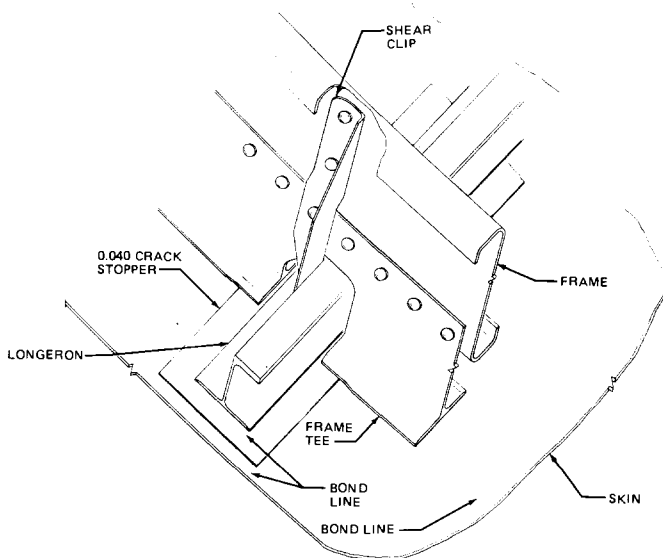


FIG. 21—Typical frame/longeron intersection (1 in. = 2.54 cm).

manufacturing phase of this program, a primary purpose was to investigate different tooling and bonding techniques and to determine their relative merit. This resulted in the variations in bond quality from panel-to-panel on the FSDC.

Prior to the start of any testing, the FSDC was subjected to a static proof pressure of 65.79 kPa (9.53 psi) as required by MIL-A-8867A for a flight article. After removing the proof pressure, there was no evidence of permanent set or disbond.

Dynamic cycling started at a rate of one flight per minute, but this rate was improved to one flight per thirty-five seconds for the majority of the test period. The cycling rate was found to have no dynamic effect on the structural response. The temperature and humidity inside the FSDC reached a peak temperature of 56.11°C (133°F) (and 51 percent relative humidity) and a peak relative humidity of 81 percent [and 17°C (63°F)] during the 10-month testing period. The loading spectrum was based on an analysis of projected military utilization for turbulence, maneuvers, ground taxi, and landing impact and would result in the equivalent damage. Hydraulic jacks applied the test loads at the test article nose, through a whiffing system distributed across the cargo floor, and at the wing. Cabin pressure was supplied by pneumatic pumps.

None of the 18 damage tolerance skin flaws propagated through a bonded joint after 76 230 flight cycles. The largest propagating flaw is shown in Fig. 22 (DT 17) after propagating from a 0.635-cm (.250-in.) initial flaw. A true

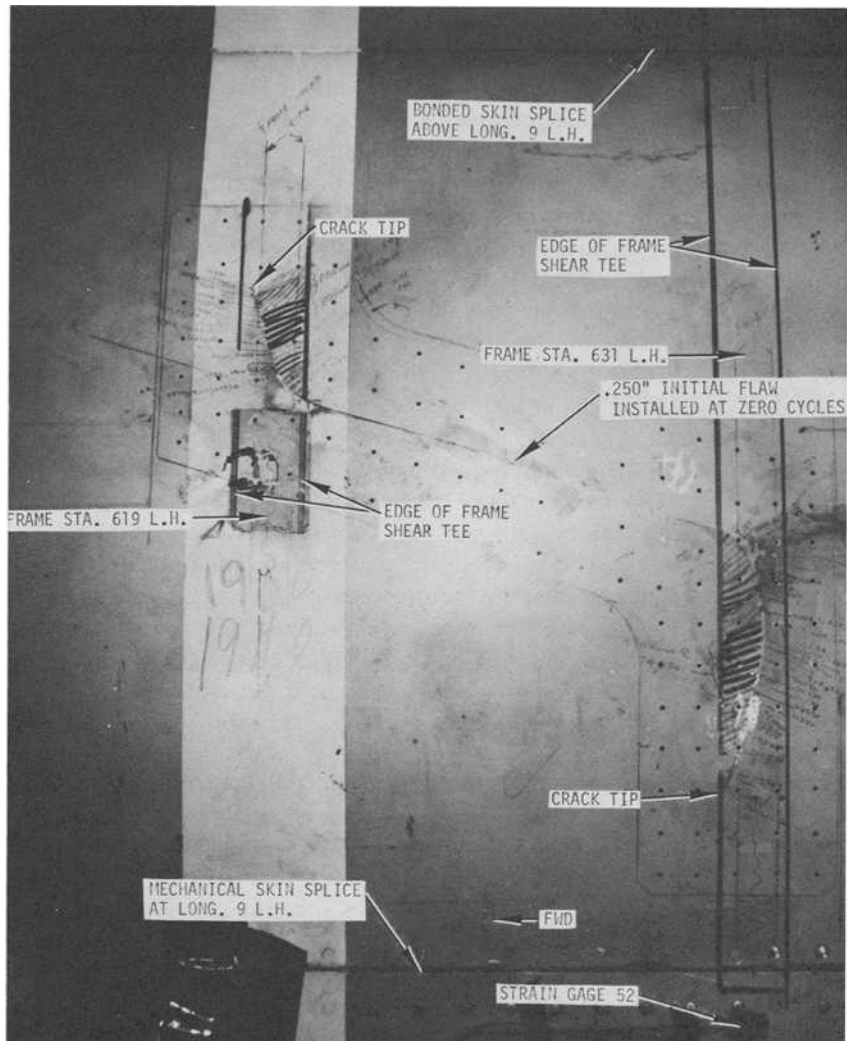


FIG. 22—76 230 cycles; DT 17 flaw propagation prior to repair completion.

crack initiated at each end of this flaw at 16 550 cycles, and each true crack propagated to the edge of the bondlines, 12.7 cm (5.0 in.) at 65 830 cycles, the last 10.2 cm (4.0 in.) of propagation occurring in only 2300 cycles. During this last 2300 cycles and continuing to the end of the test at 76 230 cycles, visual and aural observations revealed that the pressurized air escaping through the crack set up a high-frequency fluttering of the free edge of the skin such that for each pressure cycle additional fatigue damage accumulated at the crack tip caused by this high-frequency "scissoring" action.

As the crack progressed into the bondline, one side of the crack remained bonded while the other side disbonded, a condition that further increased the "scissoring" action at the tip. The crack at station 631 propagated 18.9 cm (7.5 in.) down the bondline compared with 8.9 cm (3.5 in.) at station 619 in the 10 400 cycles from the time the crack reached the bondline edge. The station 619 frame is an intermediate frame and lighter, and because of its relative softness does not pinch in the pressurized skin as much as station 631, a full depth frame. This results in the skin hoop stresses being more pronounced compared with station 631 where the stiffer frame pinches the skin such that the longitudinal pressure induced stresses exceed the hoop stresses, thus causing the crack to turn and run down the frame. The crack at station 631 continued to turn and approach the panel from which it started and is typical behavior of cracks in bonded structure.

Of the 18 metal skin flaws installed at the beginning of the durability test, all of the midbay flaws showed good correlation with analysis (Fig. 23). Of the remaining 14 metal skin flaws located adjacent to a stiffening element, only one propagated and all showed poor correlation with analysis.

Two conclusions were made from the crack propagation behavior. Firstly, all of the skin flaws exceeded the requirements of slow crack growth required from MIL-A-83444 damage tolerance specification; secondly, the present method of analysis for predicting crack growth is accurate for midbay flaws where the stress field is primarily biaxial, but near a stiffener, with the additional complexity of pressure pillowing stresses, the analysis method is conservative, but not as accurate.

At the conclusion of the durability test (76 230 flight cycles or 4 design lives), inspections revealed no instances of a metal crack initiating as a result of a bonded joint. Further, there was no significant bond flaw propagation from the initial 844 flaws nor initiation of any new bond flaws. This performance is compared with a similar sized all-mechanically-fastened fuselage test from an earlier aircraft development program in Fig. 24.

At about three design lives, it became evident that the damage tolerance requirements of MIL-A-83444 had been satisfied, and an opportunity existed for investigating the behavior of metal flaw propagation into bondlines during the remainder of the test. DT8 was extended to 20 cm (8 in.) and immediately propagated away from the longeron into an arc shape. This behavior is the result of the hoop stress and the shear stress (resulting from the redistribution of hoop load around the sawcut) combining at the sawcut tip and rotating the principal stress plane away from the longitudinal axis. There is also the additional longitudinal stress that acts only on the unstiffened sawcut edge and is a result of the cabin pressure pillowing the sawcut skin edge, setting up a catenary type reaction that further rotates the principal stress plane. The unstiffened sawcut edge, opposite to the longeron, began to flutter in the same manner as that previously described for DT17. Continued test cycling resulted in the propagation and final fast fracture and

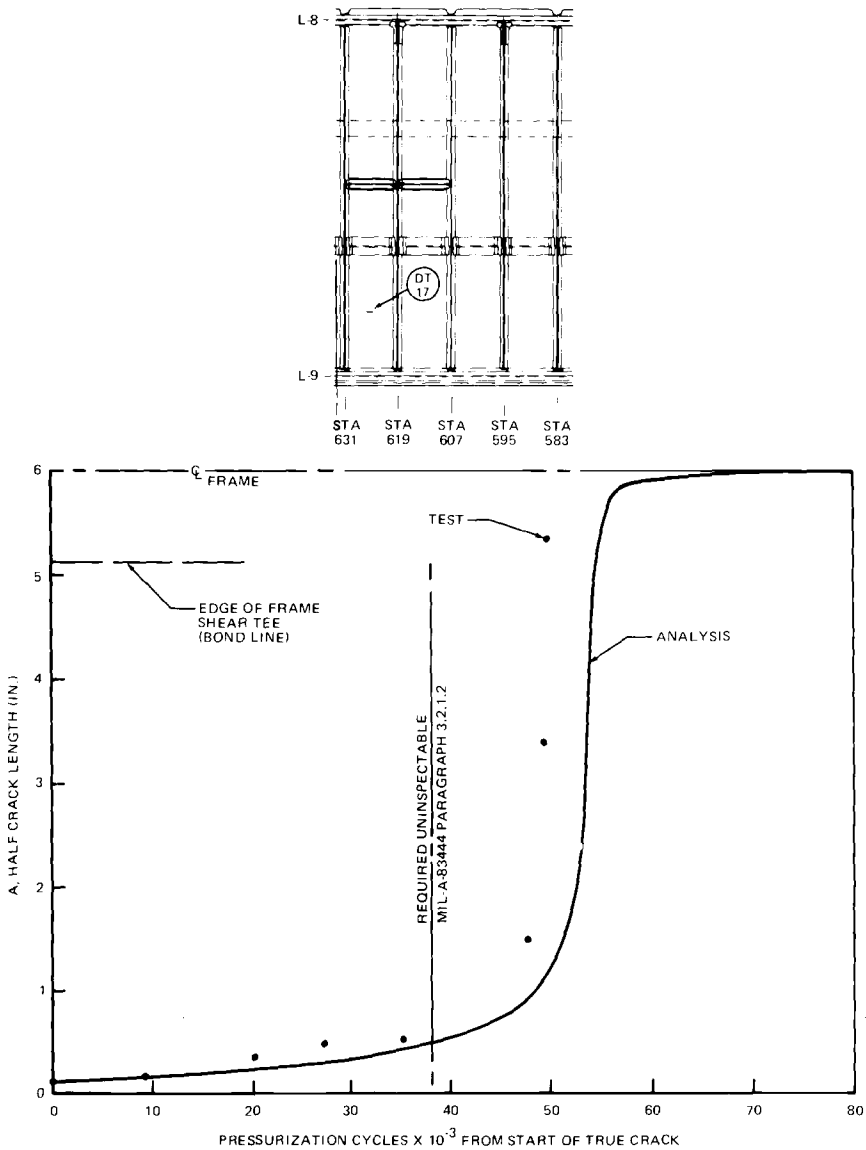


FIG. 23—DT 17 crack growth.

arrest shown in Fig. 25, 7828 cycles after the 20-cm (8-in.) sawcut. At the longeron 3-bonded doublers, the crack turned running about 0.93 cm (0.38 in.) parallel to the longeron without penetrating the bondline. Subsequent NDI in the area of the final crack tip location found no evidence of disbond despite the dynamic metal peeling action.

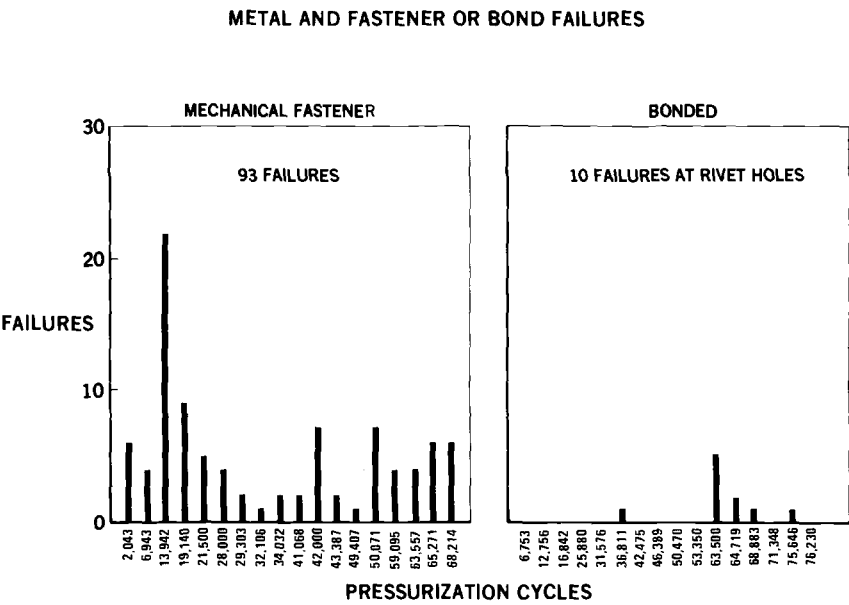


FIG. 24—Full-scale fuselage test results.

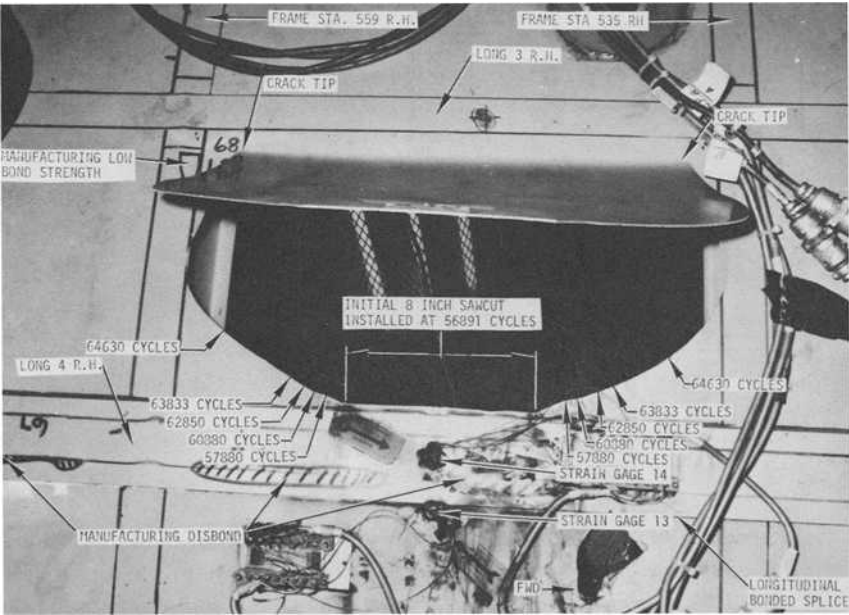


FIG. 25—64 719 cycles, DT 8 final failure (Panel 11, outboard surface) (1 in. = 2.54 cm).

The 49.30 kPa (7.15 psi) cabin pressure was maintained for a number of seconds after this failure without any effect to the structure adjacent to the failure area. It is significant to note that the pneumatic test system air supply capability is 1370 m³ (60 000 ft³)/min, and it was only because of this that cabin pressure could be maintained during the last 200 test cycles. In contrast, the YC-15 baseline aircraft has a capability of 6 m³ (200 ft³)/min with both air-conditioning packs operating; this capability precludes any possibility of an actual aircraft ever having a crack reach this length before inability to pressurize, visual warnings, and aural warnings would be known by the flight crew. The final decompression of the 339 m³ (12 000 ft³) volume of 49.30 kPa (7.15 psi) air through the failure area took 5 s, well within acceptable human tolerances, and certainly would not result in secondary structural damage.

The behavior of DT 8 with an initial metal flaw adjacent to a stiffener gave rise to the question as to what would be the behavior for a metal flaw located at the midbay of a stiffened panel. To answer this question, at 64 719 cycles an additional 21-cm (8-in.) flaw, DT 20, was sawed into the midbay of the panel on the exact opposite side of the test specimen from DT 8. This selection of flaw location eliminated any variable due to stress field intensity for comparison with DT 8 behavior.

The cracks at both ends of the sawcut propagated in a straight line into the bondline at the frames and immediately turned. The forming of a "Z"-shaped crack is in contrast with DT 8 which immediately propagated into an oval shape. The difference in crack shape is explained by considering that DT 20, centrally located between longerons, followed the maximum stress in the hoop direction until it reached the frame bondline where the hoop stress is reduced due to the frame pinching effect and the longitudinal stress becomes the maximum stress causing the crack to turn and run parallel to the frame.

At about 68 000 cycles the DT 20 crack path at frame station 559 developed a branch crack running up the frame and slowly turning back into the skin bay. This allowed a flap to form between the frame stations bounding the major crack propagation, and subsequent flap opening and decompression at 68 206 cycles, when at full cabin pressure (Fig. 26).

The behavior of the bonded structure to contain the final failure, as demonstrated by DT 8 and DT 20, was subsequently shown by three additional crack propagation tests with the same results; that is, all final failures were contained within the original panel, and the final decompression was benign in that it did not result in a catastrophic failure as is frequently the case for a mechanically fastened panel (Fig. 16).

The final test performed on the FSDC was the static ultimate load condition representing a two-point STOL landing. After applying test loads to 66 percent of ultimate (100 percent limit load), the FSDC was inspected and data reviewed. There was no failure or permanent set despite the severe compression buckling in the bottom fuselage between stations 727 and 823 and



FIG. 26—68 206 cycles: DT 20 final failure (Panel 12, outboard surface) (1 in. = 2.54 cm).

the shear wrinkles along the fuselage side. At about 135 percent limit load the longerons on the bottom failed locally in the area between stations 727 and 823. Figure 27 shows that the longeron failures tore the upstanding leg, but the base leg remained bonded to the skin.

The initial failure appeared to occur at station 763 in the transition area between the typical bonded structure and the test support fixture. This transition area was "beefed up" with additional longerons and doubled up longerons in order to withstand the loads induced by the stiffness of the steel test support fixture.

In retrospect, the "beef up" caused an increase in longeron stiffness that attracted a disproportionate load increase which without the "beef up" would have redistributed into the adjacent cargo floor structure before the longerons completely failed. It became apparent after increasing test loads to 141 percent of limit load that there was no change in the failure area, so the test was stopped. This concluded the test phase for the FSDC Test Article.

Conclusions

(1) Initial NDI detected adhesive flaws in the FSDC structure were destructively exposed after completion of the test program and showed excellent correlation using the Fokker Bondtester Model 70.

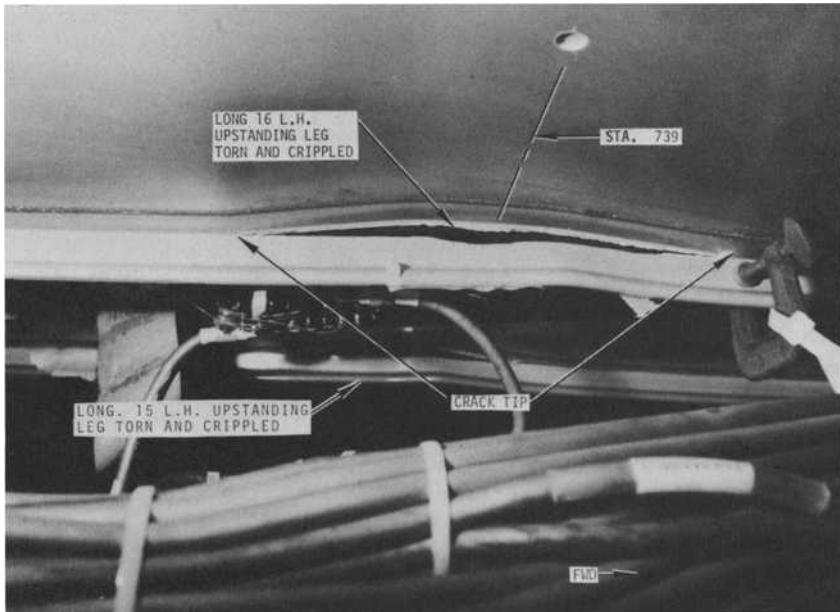


FIG. 27—Ultimate test; longeron 16 L.H. cracked upstanding leg (outboard surface).

(2) Mylar release film or contaminants such as hydraulic fluid in the bondline that fill an adhesive void can act as an ultrasonic coupling agent which prevents accurately detecting voids and disbonds with NDI.

(3) Durability tests of bonded structure should be performed at a cycle rate and environment similar to that of actual service usage. The phosphoric acid anodize and FM73 adhesive system successfully sustained all real-life service test conditions.

(4) Durability tests of bonded structure should be performed at a cycle rate and environment similar to that of actual service usage. The phosphoric acid anodize and FM73 adhesive system successfully sustained all real-life service test conditions.

(5) Metal crack propagation is contained within the stiffened boundaries of pressurized panels. Midbay cracks propagate in a straight line to the adjacent bonded joint and then turn. Cracks located off the midbay begin to turn immediately. All cracks eventually form a "window" which will be obviously detectable either because of a benign depressurization or inability to pressurize.

(6) The PABST program has clearly demonstrated that the new 121°C (250°F) cure modified epoxy adhesives have environmental resistance and strength characteristics necessary for primary aircraft structure.

(7) The damage tolerances and durability of bonded primary structure has

been demonstrated as markedly superior to mechanically fastened structure even with the wide latitude in fabrication quality allowed on the PABST program.

(8) The potential weight and cost savings of bonded primary structure was validated based on manufacturing cost analysis and FSDC test performance.

Acknowledgments

This work was sponsored by the Air Force Wright Aeronautical Laboratories (AFWAL) under the joint management and technical direction of Flight Dynamics Laboratory (AFWAL/FDL) and the Materials Laboratory (AFWAL/ML), Wright-Patterson Air Force Base, Ohio. This contract is administered as part of the Advanced Metallic Structures, Advanced Development Programs (AMS/ADP), Program Element Number 63211F, Project 486U. Mr. F. D. Boensch is the Program Manager and Mr. W. L. Shelton is the Project Engineer (AFWAL/FBA) for the PABST program. The author wishes to express his appreciation to Dr. L. J. Hart-Smith for his work on bonded joints, Mr. T. R. Lall for his work on the criteria, and Mrs. M. B. Harmon for her work on the damage tolerance analysis.

References

- [1] "Summary of Air Force/Industry Manufacturing Cost Reduction Study," AFML-TM-LT-73-1, 28 Aug.-1 Sept. 1972.
- [2] "Summary Report on the Low Cost Manufacturing/Design Seminar," AFML-TM-LT-74-3, 22-24 May 1973.
- [3] Potter, D. L. et al., "Primary Adhesively Bonded Structure Technology (PABST) Design Handbook for Adhesive Bonding," AFFDL-TR-79-3129, Douglas Aircraft Company, McDonnell Douglas Corporation, Aug. 1979.
- [4] Military Standard, "Climatic Extremes for Military Equipment," MIL-STD-210B, 15 Dec. 1973.
- [5] Ulrich, R. D. and Schafer, H., "Application and Evaluation of Thermal Standard in the Field," NWPTP 4834, Part 3, May 1977.
- [6] Schafer, H., "A Summary of Measured Temperature Exposure Data of Aircraft Rocket Catapults and Cockpit Equipment," NWC TP 5969, July 1977.
- [7] Shannon, R. W. et al., "Primary Adhesively Bonded Structure Technology (PABST) General Material Property Data," AFFDL-TR-77-107, Douglas Aircraft Company, McDonnell Douglas Corporation, Feb. 1975-Sept. 1978.
- [8] Bethune, A. W., "Durability of Bonded Aluminum Structure," *Society for the Advancement of Material and Process Engineering (SAMPE) Journal*, Vol. II, No. 3, July-Sept. 1975.
- [9] Hart-Smith, L. J., "Further Developments in the Design and Analysis of Adhesive-Bonded Structural Joints," Douglas Paper 6922, Douglas Aircraft Company, Symposium on Joining of Composite Materials, American Society for Testing and Materials, Minneapolis, Minn., 16 April 1980.
- [10] Hart-Smith, L. J., "Analysis and Design of Advanced Composite Bonded Joints," Douglas Aircraft Company, McDonnell Douglas Corporation, NASA-Langley Research Center Contract Report, NASA CR-2218, Jan. 1973.
- [11] Hart-Smith, L. J., "Adhesive-Bonded Double-Lap Joints," Douglas Aircraft Company,

McDonnell Douglas Corporation, NASA-Langley Research Center Contract Report, NASA CR-112235, Jan. 1973.

- [12] Hart-Smith, L. J., "Adhesive Bond Stresses and Strains at Discontinuities and Cracks in Bonded Structures," Douglas Aircraft Company, Report No. MDC-J6068, Sept. 1976.

Bibliography

Swift, T., "The Effects of Adhesive and Stiffener Yielding on the Fracture Strength of Adhesive Bonded Cracked Panels," Douglas Aircraft Company, McDonnell Douglas Corporation, IRAD Technical Report MDC-J7233, May 1976.

Thrall, E. W., Jr., "Failure in Adhesively Bonded Structures," Douglas Aircraft Company, McDonnell Douglas Corporation, AGARD-NATO Lecture Series 102, Bonded Joints and Preparation for Bonding, Oslo, Norway, The Hague, Netherlands, 2-6 April 1979.

Thrall, E. W., Jr., "The Primary Adhesively Bonded Structure Technology Program (PABST)," Douglas Aircraft Company, McDonnell Douglas Corporation, 17th Annual Conference on Adhesion and Adhesives, The City University, London, 17-28 March 1979.

Thrall, E. W., Jr., "Prospects for Bonding Primary Aircraft Structure in the 80's," Douglas Aircraft Company, McDonnell Douglas Corporation, 25th National SAMPE Symposium/Exhibition, San Diego, 6-8 May 1980.

M. Zako,¹ T. Kawashima,² H. Aono,³ K. Jimboh,⁴
H. Ohnabe,⁵ and T. Miyoshi⁶

Residual Life Prediction of Jet Engine Rotor Disks

REFERENCE: Zako, M., Kawashima, T., Aono, H., Jimboh, K., Ohnabe, H., and Miyoshi, T., "Residual Life Prediction of Jet Engine Rotor Disks," *Design of Fatigue and Fracture Resistant Structures, ASTM STP 761*, P. R. Abelkis and C. M. Hudson, Eds., American Society for Testing and Materials, 1982, pp. 408-423.

ABSTRACT: For the application of this study, an aircraft jet engine rotor disk under constant temperature (room temperature) is selected. Assuming crack initiation to occur at the rim slot of an aircraft jet engine rotor disk under constant temperature (room temperature) for the application of this study, and converting the three-dimensional stress into a two-dimensional one, their life prediction is analyzed. The life prediction system was predicated on stress analysis, nondestructive testing, and material properties. The stress at the cracked part of the rim slot is calculated by the finite-element method, and the crack propagation is calculated by Paris's rule. Assuming K_{Ic} and the difference between K_{Ic} and calculated K —that is, $(K_{Ic} - K)$ —to be a Gaussian distribution, safety is estimated by the relationship between fracture probability, P_f , and standard deviation.

In the numerical examples, assuming an elliptic surface crack at four different parts of the rim slot, the crack propagation after 2000 cycles is calculated. The safety factor of rotor disks is judged by the value of $(K_{Ic} - K)$.

KEY WORDS: fracture, fatigue life, crack propagation, structural analysis, reliability, failure probability, retirement for cause, decision analysis, turbine rotors, rotating machine, elements, jet engine

¹Senior Research Engineer, Aseismic Development, Research Institute, Ishikawajima-Harima Heavy Industries Co., Tokyo, Japan.

²Research Engineer, Research and Development Department, Aero-Engine and Space Operations, Ishikawajima-Harima Heavy Industries Co., Tokyo, Japan.

³Manager, Structural Integrity Section, Research and Development Department, Aero-Engine and Space Operations, Ishikawajima-Harima Heavy Industries Co., Tokyo, Japan.

⁴Manager, Research and Development Department, Aero-Engine and Space Operations, Ishikawajima-Harima Heavy Industries Co., Tokyo, Japan.

⁵Chief Research Engineer, Engineering Development Department, Aero-Engine and Space Operations, Ishikawajima-Harima Heavy Industries Co., Tokyo, Japan.

⁶Associate Professor, Department of Precision Machinery Engineering, University of Tokyo, Tokyo, Japan.

Traditionally, life prediction of aircraft jet engine rotor disks is decided by crack initiation criteria. For example, useful life is defined as the number of cycles needed to produce a 0.8-mm-long crack on the surface with a probability of 0.1 percent. In this way of thinking, useful life is statistically based on the number of the population of disks which have minimum strength properties, although this is conservative for real materials. For example, Inconel 718, a typical nickel-based superalloy, has a large scatter in crack initiation at 538°C (1000°F).

Recently, in the development of fracture mechanics, the concepts of Damage Tolerant Design and Retirement-for-Cause have been applied to the design and maintenance of aircraft jet engine rotor disks in order to reduce the life cycle cost of disks.

Retirement-for-Cause is a life extension procedure based on fracture mechanics analysis of crack propagation intended to retire the individual cracked disk from service rather than necessitate removal of all the disks from service after a specified time and to optimize the overall service life and thereby minimize maintenance costs. Recently, this methodology has been extensively studied by many researchers [1-6].⁷ Also, a Damage Tolerant Design System for fan disks has been reported by Meece and Spaeth [7] in 1979.

The present investigation offers an outline of an evaluation system for the residual life of rotor disks [4], consisting of stress analysis, nondestructive testing, and material properties. The two-dimensional stress analysis of the rim slot of turbine disks was conducted by the finite-element method. For the actual three-dimensional crack, the two-dimensional stress around the crack was converted to a quasi-three-dimensional stress.

Crack propagation was calculated by Paris's rule. Assuming K_{Ic} and the difference between K_{Ic} and calculated K —that is, $(K_{Ic} - K)$ —to be a Gaussian distribution, the probability of failure, P_f , is calculated and then the reliability of rotor disks is analyzed. These investigations were conducted for four different critical parts of the rim slot of the turbine disks as numerical examples.

Outline of the Evaluation System

In order to evaluate the residual life of a rotor disk under constant temperature as numerical example, information on material testing results, stress analysis of the disk, and size of the crack or relative damage is necessary. The material properties and stress distribution of the disk can be obtained by material tests and the finite-element method by computer. The crack information can be obtained by using nondestructive tests. The

⁷The italic numbers in brackets refer to the list of references appended to this paper.

residual life can be evaluated by this information, and the flow chart of the system for residual life prediction is shown in Fig. 1 [4].

The central part of Fig. 1 shows the stress analysis for a disk and the stress map. The loading of the engine can be determined from past operation or design data. The residual life is calculated by these parameters. For instance, if damage such as a crack is found on the rotor disk when it is inspected, its position and amount of damage will be measured and the stress around the crack tip will be calculated by the stress map. As the mechanical properties are determined from the material testing data, the rates of progression of damage for a certain load history until the next inspection are calculated. Hence a probability judgement as to whether the disk has to be changed immediately or not can be made.

Stress Analysis

The mesh of the rim slot of the rotor disk for the finite-element method is shown in Figs. 2a and 2b. The mechanical properties and the parameters used for calculation are shown in Table 1.

The computational results for the stress distribution of the rotor disk under the constant temperature (room temperature) were input to a computer to enable such further calculations as might be needed. Therefore, if a crack is observed, stress analysis of the crack and evaluation of residual life can be done immediately by using the map.

The stress map of the rim slot is shown in Fig. 3. It must be noted, however, that the actual crack is three-dimensional, and it is very difficult to analyze rotor disk stress three-dimensionally. As it is very convenient for design to analyze two-dimensionally, this paper will analyze stress as a two-

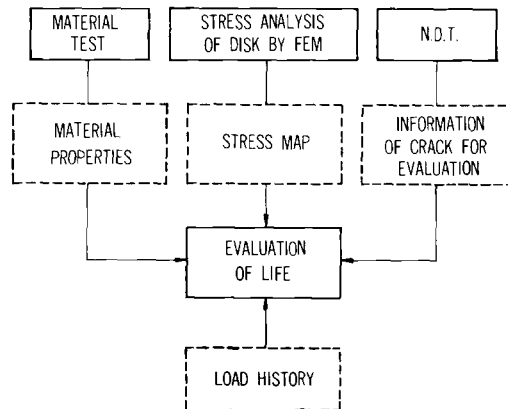


FIG. 1—Flow chart of evaluation system for residual life of machine components.

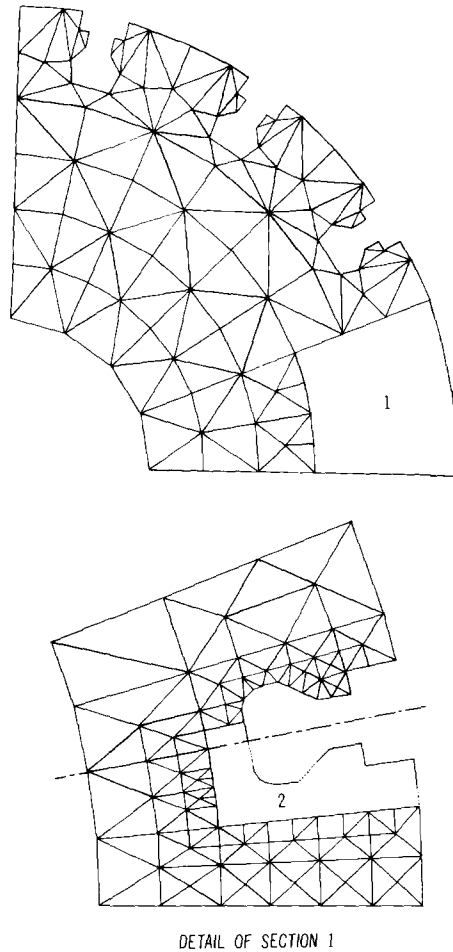


FIG. 2a—Finite-element mesh of rim slot of rotor disk.

dimensional problem. Thus, to determine stress around the crack, the actual crack in three dimensions must be changed to a two-dimensional one. Therefore, and consonant with the geometric shape of the crack, actual stress on the rotor disk is calculated by translation to two-dimensional stress with the stress map.

The geometric shape of a crack for translation to two-dimension is shown in Fig. 4, where a is actual crack length and $a\sqrt{\cos^2\theta + \sin^2\theta\cos^2\alpha}$ is the observed crack length on the surface of the disk.

The following equations are derived from Fig. 4:

$$\sigma = \sigma_1 \cos^2\phi + \sigma_2 \sin^2\phi$$

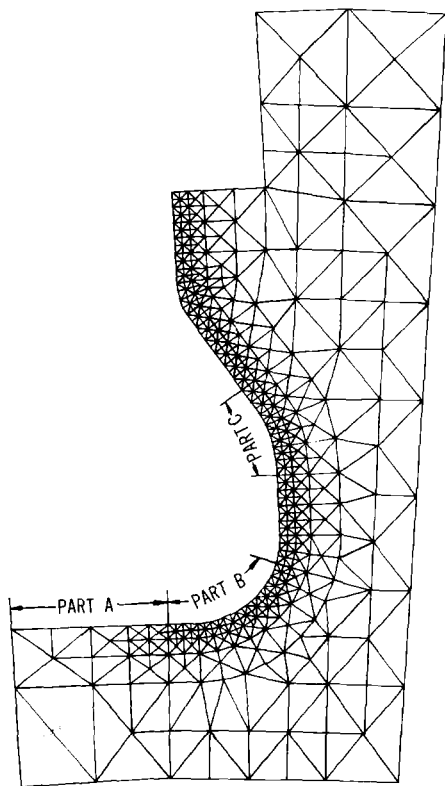
$$\sigma'' = \sigma_1 \sin^2 \phi' + \sigma_2 \cos^2 \phi' \quad (1)$$

$$\sigma = \sigma' \cos^2 \alpha \cos^2 \theta + \sigma'' \sin^2 \theta$$

where, σ_1 and σ_2 are the calculated stress in two dimensions, and σ is the applied stress on the actual crack. Therefore, if the data on the angles and crack length can be measured in two dimensions, the stress around the crack will be calculated as quasi-three-dimensional.

Fracture Toughness

Two specimen types were prepared for the fracture toughness test: Ti-6Al-4V(IMI 318), and Ti-6Al-4V-Zr(IMI 685). Crack initiation was electrically measured. Figure 5 outlines the measurement method for a three-point-



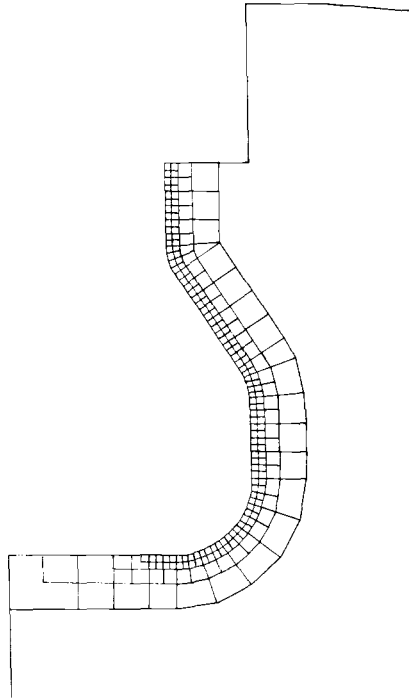
DETAIL OF SECTION 2

FIG. 2b—Finite-element mesh of rim slot of rotor disk.

TABLE 1—*Mechanical properties and parameters for analysis.*^a

Number of blades	16
Mass of one blade	0.95 kg
Outside diameter	250 mm
Inside diameter	80 mm
Rotational speed	5800 rpm
Density	4.68 g/cm ³
Young's modulus	108 853 MPa
Poisson's ratio	0.34
Crack propagation factors	
Value of <i>C</i>	2.197×10^{-3}
Value of <i>m</i>	4

^aMaterial = IMI318; test temperature = room temperature (20°C).

FIG. 3—*Division-of-stress map.*

bending test to the point of unstable crack propagation. In order to obtain fracture toughness, the precracked bend-bars and compact tension specimens were used. Figure 6 is a typical testing result of the relations of crack-opening displacement (COD) versus load and voltage difference versus COD,

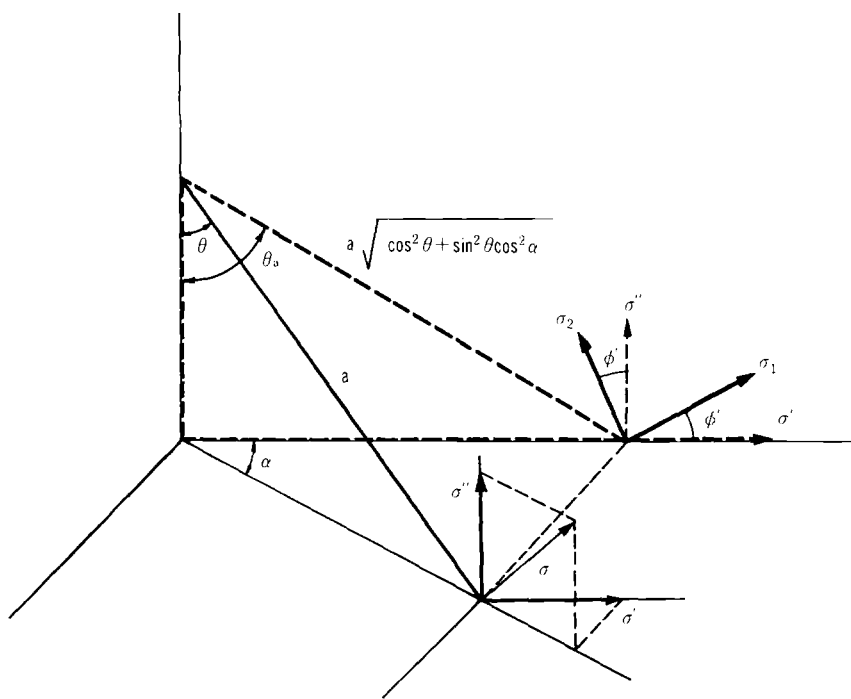


FIG. 4—Geometric relation of crack in two dimensions and three dimensions.

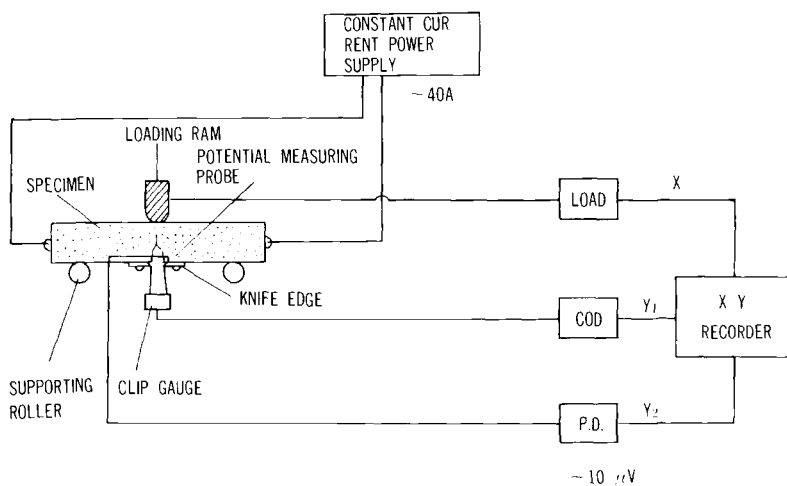


FIG. 5—Scheme of electricity measurement for crack initiation.

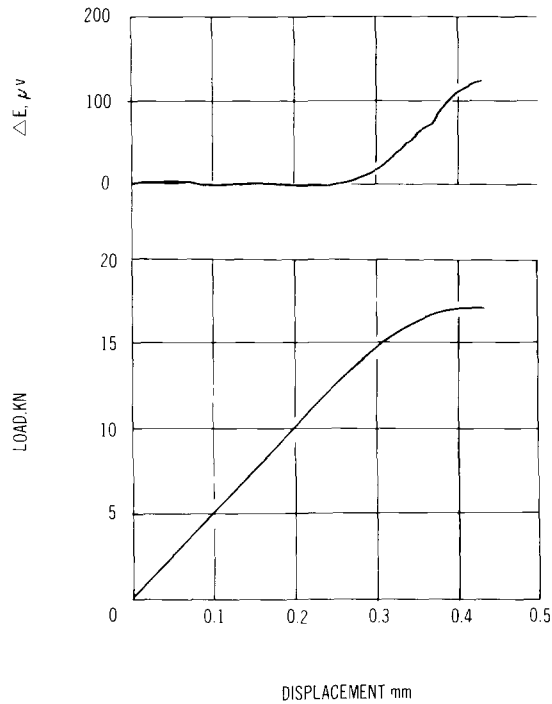


FIG. 6—Typical testing result of ΔE versus COD and load versus COD.

in order to determine the initiation point of unstable crack propagation. The experimental results of fracture toughness are shown in Table 2.

Calculation Procedure of Residual Life

The progression rate of a crack can be calculated by Paris's rule. If a crack is found in a periodic inspection, it will progress till the next periodic inspection by the following equation:

$$A = A_0 + \int_0^N C(\Delta k)^m dn \quad (2)$$

where A_0 , N , and A represent crack length in the first periodic inspection, the number of cycles until the next periodic inspection, and the crack length then, respectively. Thus, the crack propagation rate is calculated for each number of cycles, and the stress intensity factor, K_I , due to the propagated crack length for each cycle is analyzed. Therefore, as the fracture toughness K_{Ic} was already obtained by the fracture toughness tests, the value of $(K_{Ic} -$

TABLE 2—Test result of fracture toughness.^a

Specimen No.	Material	Type	K_{Ic} , MPa·m ^{1/2}	Crack Length, mm
1	IM1685	BB	49.62	12.25
2	IM1685	BB	50.55	12.90
3	IM1318	BB	42.18	12.45
4	IM1318	BB	44.66	12.75
5	IM1318	BB	42.18	12.80
6	IM1685	CT	52.72	12.25
7	IM1318	CT	42.18	12.95
8	IM1318	CT	39.38	12.60

^aTest temperature = room temperature (20°C).

K_I) for each arbitrary cycle can be calculated. From this value, rotor disk usability can be judged. For instance, when the inspection interval is 2000 h, the K_I -value after 2000 h from prior inspection is calculated, and if the value of $(K_{Ic} - K_I)$ is greater than zero, the rotor disk can be used until the next inspection. However, if the value of $(K_{Ic} - K_I)$ is less than zero, the rotor disk must be changed.

Despite these findings, the problem arises that true reliability has not been fully considered by these values. For the actual state, it will be very important to calculate reliability based on the stress intensity factor.

Applications

For practical application, a few examples are analyzed. The state of an observed crack after a spin test is shown in Fig. 7. Most cracks appear in the rim slot, as in this figure, and the important positions for strength of a rotor disk are the rim slot, the bolt hole connecting the disk and the shell, and the bore. Therefore cracks occurring in the rim slot have been analyzed as applications of the method presented in this paper.

In calculating the probability of failure, P_f , the distributions of K_I and K_{Ic} must be considered. As a typical example, when the distribution of K_{Ic} -values is Gaussian, the difference of K_{Ic} from the K_I -value is also Gaussian because the calculated K_I is definite. Figure 8 shows the definition of probability of fracture.

If many cracks occur on the rotor disk, the probability of failure, P_f^i is

$$P_f^i = 1 - \prod_{i=1}^n (1 - P_f^i). \quad (3)$$

where P_f^i is the probability of failure for each disk, and i is the number of cracks. When P_f^i is extremely smaller than 1, we can obtain

$$P_f' = \sum_{i=1}^n P_f^i \quad (4)$$

When each crack is considered independently, Eq 4 becomes

$$P_f' \leq n(P_f^i)_{\max} \quad (5)$$

In this paper only a single crack is considered on the rim slot, because many cracks do not ordinarily occur at the same time.

As the rim slot is separated into three parts (Fig. 2), it is necessary to calculate the probability of failure for cracks occurring in each part, so the input data shown in Table 1 are used. The shape of the crack is assumed to be a half ellipse (Fig. 9). The input data used to calculate failure probability are X_1 , X_2 , θ , and α , the former showing the coordinate points of crack initiation and the latter being the crack orientation.

Example 1

Because crack propagation clearly depends on flight time, one hour has been chosen as the flight time cycle for these examples, as one flight hour corresponds to the approximate distance from Tokyo to Osaka. Two thousand hours were set as the interval for periodic inspection.

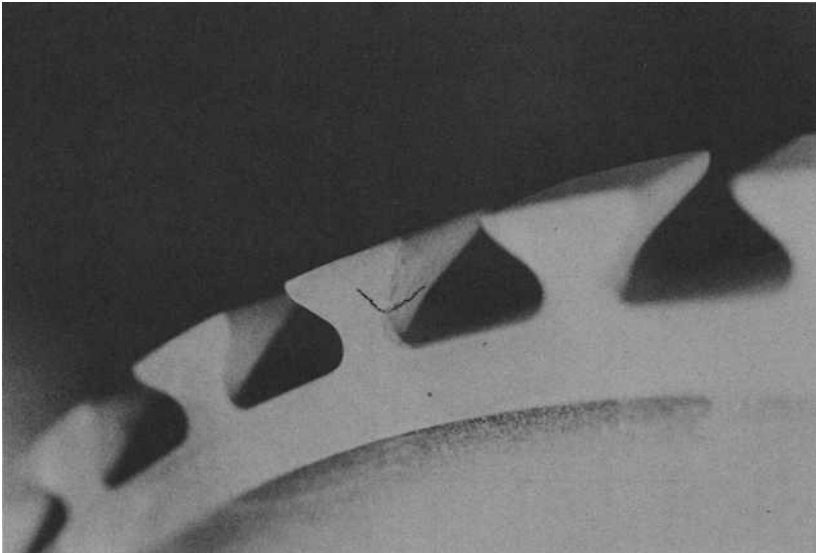


FIG. 7—Crack on rim slot of rotor disk.

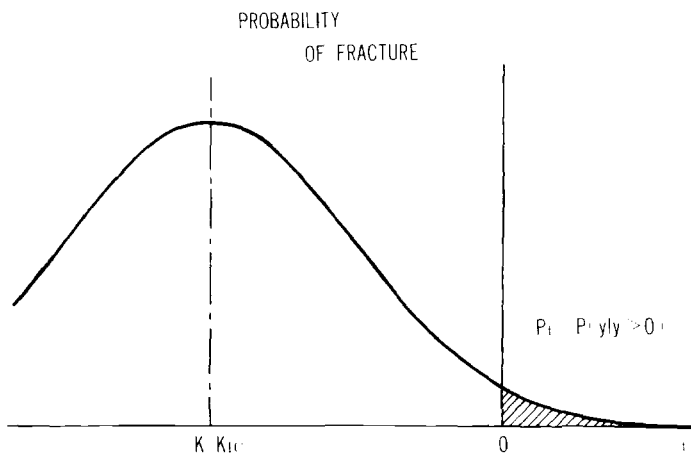


FIG. 8—Definition of probability of fracture.

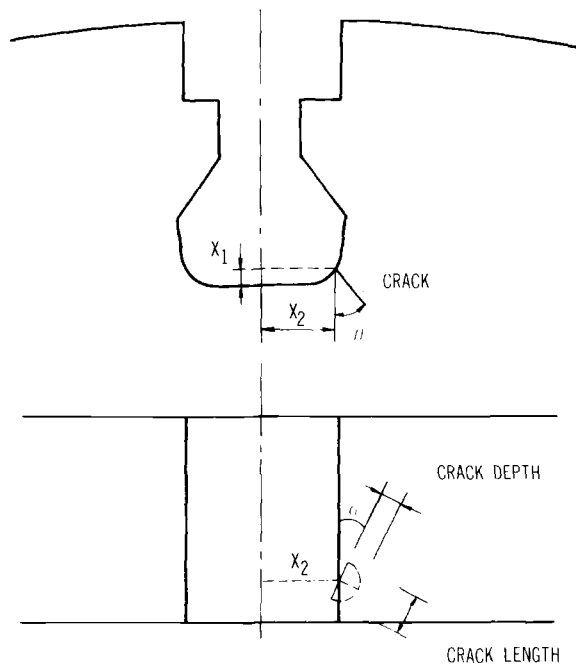


FIG. 9—Input data for calculation of residual life of semi-elliptical crack.

For the semi-elliptical crack of 4.0 mm depth and 8.0 mm length in Part A as shown in Fig. 2, where X_1 and X_2 are 0 and 2.0 mm, respectively, the computed results are shown in Table 3, as derived from the input and output computer sheets. In input, Angle 1 and Angle 2 mean θ and α . In the output, the crack length is recorded every 100 h, and the crack length when the flight time reaches 2000 h is shown in the last line.

According to this result, the difference K_{Ic} from K_I is

$$(K_{Ic} - K_I) \doteq 5.9\sigma$$

where σ is standard variation. The probability of failure for this value becomes 10^{-8} because the Gaussian is considered as the distribution for the value of K_{Ic} .

Under actual conditions, it is considered that the probability of failure

TABLE 3—Example 1.

```

INPUT CRACK DATA LENGTH X1 AND X2
FORMAT 2F10.0
0.0 2.0
INPUT CRACK DATA CRACK LENGTH AND DEPTH
FORMAT 2F10.0
8.0 4.0
INPUT CRACK DATA ANGLE1 AND ANGLE2
FORMAT 2F10.0
0.0 0.0

0.4000066241320683D 01
0.4000132484835357D 01
0.4000198730544131D 01
0.4000264978447114D 01
0.4000331228544415D 01
0.4000397480836143D 01
0.4000463735322406D 01
0.4000529992003315D 01
0.4000596250878977D 01
0.40006662511949503D 01
0.4000728775215001D 01
0.4000795040675580D 01
0.4000861308331348D 01
0.4000927578182416D 01
0.4000993850228893D 01
0.4001060124470888D 01
0.4001126400908509D 01
0.4001192679541865D 01
0.4001258960371067D 01
0.4001325243396222D 01

THETA= 0.3249978E 01
(KIC-K)/SIGMA = 5.90501

IT IS DANGER

```

must be greater than 6.7σ for safety, meaning that in this example the crack is dangerous because the value of $(K_{Ic} - K_I)$ is smaller than 6.7σ .

Example 2

For the semi-elliptical crack of 4.5 mm depth and 9.0 mm length which occurred in Part B where X_1 and X_2 are 1.0 and 10.2 mm, respectively, the computed result is shown in Table 4. In this example, the value of $(K_{Ic} - K_I)$ is approximately 11.8σ . It is probable that this crack is safe until the next inspection because the value of $(K_{Ic} - K_I)$ is greater than 6.7σ . The probability of failure is about 10^{-29} .

TABLE 4—Example 2.

```

INPUT CRACK DATA LENGTH X1 AND X2
FORMAT 2F10.0
1.0    10.2
INPUT CRACK DATA CRACK LENGTH AND DEPTH
FORMAT 2F10.0
9.0    4.5
INPUT CRACK DATA ANGLE1 AND ANGLE2
FORMAT 2F10.0
0.0    0.0

```

```

0.4500018800410217D 01
0.4500037600977526D 01
0.4500056401701929D 01
0.4500075202583428D 01
0.4500094003622025D 01
0.4500112804817722D 01
0.4500131606170520D 01
0.4500150407680422D 01
0.4500169209347430D 01
0.4500188011171546D 01
0.4500206813152770D 01
0.4500225615291107D 01
0.4500244417586558D 01
0.4500263220039124D 01
0.4500282022648807D 01
0.4500300825415609D 01
0.450031962839534D 01
0.4500338431420581D 01
0.4500357234658755D 01
0.4500376038054055D 01

```

```

TETA= 0.3249998E 01
(KIC-K)/SIGMA = 11.87471

```

```

IT IS SAFE

```

Example 3

For the semi-elliptical crack of 4.0 mm depth and 8.0 mm length which occurred in the boundary point Part A and Part B where X_1 and X_2 are 0 and 4.0 mm, respectively, the computed result is shown in Table 5. In this example the value of $(K_{Ic} - K_I)$ is approximately 6.6σ . It is recognized that this crack is dangerous because the value is smaller than 6.7σ .

Example 4

For the semi-elliptical crack of 4.0 mm depth and 8.0 mm length which occurred in Part C where X_1 and X_2 are 9.0 and 12.5 mm, respectively, the

TABLE 5—*Example 3.*

```

INPUT CRACK DATA LENGTH X1 AND X2
FORMAT 2F10.0
0.0      4.0
INPUT CRACK DATA CRACK LENGTH AND DEPTH
FORMAT 2F10.0
8.0      4.0
INPUT CRACK DATA ANGLE1 AND ANGLE2
FORMAT 2F10.0
0.0      0.0

```

```

0.40000574666793120 01
0.40001152950202170 01
0.40001729450227850 01
0.40002305966870910 01
0.40002882500132050 01
0.40003459050011980 01
0.40004035616511430 01
0.40004612199631120 01
0.40005188799371770 01
0.40005765415734090 01
0.40006342048718800 01
0.40006918698326630 01
0.40007495364558280 01
0.40008072047414490 01
0.40008648746895960 01
0.40009225463003420 01
0.40009802195737580 01
0.40010378945099170 01
0.40010955711088910 01
0.40011532493707500 01

```

```

THETA= 0.3249998F 01
(KIC-K)/SIGMA = 6.65989
IT IS DANGER

```

computed result is shown in Table 6. In this example the value of $(K_{Ic} - K_I)$ is approximately 26.5σ . It is recognized that this crack is safe because the value is greater than 6.7σ .

Conclusion

A system to calculate the residual life of machine components has been established, and a few examples for aircraft jet engine rotor disks under constant temperature (room temperature) have been solved in this paper by using the system. Though this system is not perfect because heat, creep phenomena, and other physical deviations have not been considered, it is still very effective in determining residual life.

TABLE 6—Example 4.

```

INPUT CRACK DATA LENGTH X1 AND X2
FORMAT 2F10.0
  9.0    12.5
INPUT CRACK DATA CRACK LENGTH AND DEPTH
FORMAT 2F10.0
  6.0    4.0
INPUT CRACK DATA ANGLE1 AND ANGLE2
FORMAT 2F10.0
 120.0   0.0

```

```

0.4000000001339079D 01
0.40000000002678159D 01
0.40000000004017239D 01
0.40000000005356319D 01
0.40000000006695399D 01
0.40000000008034479D 01
0.40000000009373559D 01
0.40000000010712639D 01
0.40000000012051719D 01
0.40000000013390799D 01
0.40000000014729879D 01
0.40000000016068959D 01
0.40000000017408039D 01
0.40000000018747119D 01
0.40000000020086199D 01
0.40000000021425279D 01
0.40000000022764359D 01
0.40000000024103439D 01
0.40000000025442518D 01
0.40000000026781599D 01

```

```

THETA= 0.1232446E 03
(KIC-K)/SIGMA    = 26.51779

```

```

IT IS SAFE

```

Especially since residual life can be calculated when the rotor disk is checked in inspection, the compiling of practical data for rotor disks should lend itself to establishment of a useful system.

References

- [1] Besuner, P. M. and Sorenson, K. G., "Retirement-for-Cause: A Workable Approach for Structural Life Extension and Response to In-Service Problems," Technical Report EPRI NP-855, Aug. 1978.
- [2] Hill, R. J., Reimann, W. H., and Ogg, J. S., "A Retirement-for-Cause Study of an Engine Turbine Disk," AIAA/SAE/ASME 15th Joint Propulsion Conference, Las Vegas, 18-20 June 1979.
- [3] Annis, C. G., Van Wanderham, M. C., Harris, J. A., and Sims, D. L., "Gas Turbine Engine Disk Retirement-for-Cause: An Application of Fracture Mechanics and NDE," ASME 80-GT-127, Gas Turbine Conference and Products Show, New Orleans, 10-13 March 1980.
- [4] Wells, C. H., "Quantitative Lifetime Assurance of Turbine Rotors," private communication.
- [5] Rau, C. A. and Besuner, P. M., *Transactions*, American Society of Mechanical Engineers, Vol. 102, 1980, pp. 56-63.
- [6] Wells, C. H., "Reliability of Steam Turbine Rotors," Technical Report EPRI NP-923-SY, Oct. 1978.
- [7] Meece, C. E. and Spaeth, C. E., "Damage Tolerant Design: An Approach to Reduce the Life Cycle Cost of Gas Turbine Engine Disks," AIAA/SAE/ASME 15th Joint Propulsion Conference, Las Vegas, 18-20 June 1979.

Fatigue and Fracture Tolerance Evaluation of Tall Loran Tower Eyebolts

REFERENCE: Rice, R. C. and Smith, C. E., "Fatigue and Fracture Tolerance Evaluation of Tall Loran Tower Eyebolts," *Design of Fatigue and Fracture Resistant Structures, ASTM STP 761*, P. R. Abelkis and C. M. Hudson, Eds., American Society for Testing and Materials, 1982, pp. 424-444.

ABSTRACT: Laboratory and analytical fatigue studies were undertaken to assess the criticality of flaws found within several 63.5-mm-diameter communication tower eyebolts. Fatigue-fracture mechanics analyses provided fatigue life predictions which compared closely with subsequent fatigue experiments on the eyebolts subjected to particular load histories. Results of the study provided the basis for continued usage of many of the used eyebolts and gave specific guidelines on flaw size/location/criticality that were important in setting nondestructive inspection intervals and sensitivity limits.

KEY WORDS: fatigue, fracture, damage tolerance, lugs, guyed towers, fatigue life prediction

Nomenclature

a	Crack length or depth
a_i	Initial crack length
a_f	Final crack length
A_1, A_2	Intercepts defining positions of log-linear segments of strain-life curve
c	One half the surface crack length
C	Crack growth rate intercept
da/dN	Crack growth rate
E	Young's modulus
K_ϵ	Strain concentration factor

¹Principal Research Scientist, Battelle Columbus Laboratories, Columbus, Ohio 43201.

²Chief, Engineering Section, Construction and Engineering Branch, United States Coast Guard, Washington, D.C. 20591.

ΔK	Stress intensity factor range
ΔK_{eff}	Effective stress intensity range
ΔK_f	Final stress intensity range
ΔK_i	Initial stress intensity range
K_{max}	Maximum stress intensity
ΔK_{th}	Threshold stress intensity range
m	Exponent in equivalent strain parameter
M_k	Back face stress magnification factor
n	Crack growth rate exponent
n_1, n_2	Exponents defining slopes of log-linear segments of strain-life curve
N	Fatigue cycles
N_f	Fatigue cycles to failure
N_i	Fatigue cycles to crack initiation
N_p	Fatigue cycles from crack initiation to failure
P_{max}	Maximum eyebolt load
P_{min}	Minimum eyebolt load
R	Ratio of minimum to maximum stress
ΔS	Nominal stress range
t	Product thickness
TUS	Typical ultimate strength
TYS	Typical yield strength
ϵ_{eq}	Equivalent strain parameter
ϵ_{max}	Local maximum strain
σ_{max}	Local maximum stress
Φ	Flaw shape parameter

During inspection of the guyline hardware of the 410-m Loran tower on Iwo Jima in 1976, magnetic-particle indications of cracks in eyebolts of the second-level guylines were discovered. These indications were found at the head and eye fillets of AISI 1045 eyebolts. Because the tower structures are compressively loaded through tensile preload on the guylines and a single eyebolt failure will result in destruction of the tower by buckling, serious concern existed over the remaining service life of the damaged eyebolts in this tower and in other high towers operated by the U.S. Coast Guard. A 410-m loran tower collapsed at the U.S. Coast Guard Station at Angissoq, Greenland in 1964 because of an eyebolt failure. Concern over the observed damage in the eyebolts of the Iwo Jima tower prompted the present study to (1) investigate the extent and cause of the observed damage in the eyebolts, and (2) estimate the remaining life in the damaged eyebolts.

This paper begins with a description of the experimental work and a discussion of the fatigue test results on both unused and damaged eyebolts. Next, the fatigue and fracture tolerance analyses are described, and the cor-

relation between experiment and analysis is presented for the investigated eyebolt design. Further details regarding the overall study, including specific details on the metallographic and nondestructive examination of the eyebolts can be found in Rice et al [1].³

Experimental Work

The goal of the experimental program was to evaluate the extent of damage in the used AISI 1045 steel eyebolts. Because of time and cost constraints, actual field loads and environments were not used in the laboratory for the fatigue testing of new and used eyebolts. Constant-amplitude cyclic loading was chosen, along with an environment of room temperature, laboratory air (at 293 K and 50 percent relative humidity). The ambient environment was considered acceptable since neither corrosion nor corrosion-assisted cracking was found to be of significance in the damaged areas of the used eyebolts [1]. Constant-amplitude cycling was employed with the realization that the locations of the fatigue failure within the eyebolts tested in the laboratory might differ from those experienced in the field, especially if the degree of field damage was modest and had not created appreciable localized damage (that is, cracking).

The minimum and maximum eyebolt loads were based on the design preload for the 63.5-mm-diameter eyebolts in the second-level guylines (102 kN) and a percentage of the maximum static design load for the eyebolts (587 kN), respectively. The experiments were completed on a 2200 kN capacity, electro-hydraulic, servocontrolled test system. Cyclic frequencies of 10 to 15 Hz (cycles per second) were used in all experiments.

The eyebolt-fatigue tests fall into three categories: (1) unused eyebolt tests, (2) flawed eyebolt experiments, and (3) eyebolt strain-gage experiments.

Unused Eyebolt Experiments

Three unused AISI 1045 steel eyebolts were fatigued tested to failure employing maximum stress levels equivalent to 133, 100, and 70 percent of the maximum eyebolt design load. The two most severe experiments were conducted using the same stress ratio as the design load ratio of 0.174 (102 kN/587 kN). The least severe experiment was conducted using a minimum load equivalent to the design preload, which produced a slightly higher stress ratio of 0.248. The results of those experiments are listed in Table 1.

The unused eyebolt fatigue experiments provided a basis of comparison with data obtained from fatigue tests on used eyebolts in the next phase of the experimental work. The eye web failures which resulted were of significance because no service failures had ever occurred in that location. The dif-

³The italic numbers in brackets refer to the list of references appended to this paper.

TABLE 1—*Experimental results from fatigue tests on 63.5-mm-diameter eyebolts.*

Test Type	Identification	Loading Conditions			Fatigue Life, cycles	Failure Site	Initial Condition
		Maximum Load, kN	Minimum Load, kN				
Unused-eyebolt tests	S-1	778	135		49 300	eye web	unused
	S-3	587	102		324 000	eye web	unused
	S-2	411	102		3 320 000	eye web	unused
Flawed-eyebolt tests	2A1-1C	411	102		13 500 000 ^a		
		587	102		269 000	eye web	used, two long flaws in eye fillet
	2A2-2C	411	102		5 970 000 ^a		
		587	102		334 000	head fillet	used, two flaws in head fillet
	2A1-3C	411	102		6 020 000 ^a		
		587	102		265 000	eye web	used, one small flaw in head fillet

^aNo failure; the load was increased and the test was continued.

ferences in loading between the laboratory and the field undoubtedly contributed to this result.

It is also of importance to note that the unused eyebolt experiments were completed with unused rockers installed,⁴ just as they are typically used in most of the critical eyebolt placements in the field. The rockers, which were made of Alloy 718, saw the same load history as the eyebolts and they consistently failed at very short lives compared to the eyebolts. In fact, the rockers consistently failed at less than 2 percent of the eyebolt fatigue lives.

It became apparent that the rockers were the weak link in the guyline system. If it were not for the fact that rocker failures are typically noncritical (that is, rocker failures do not cause collapse of the guyline and subsequent collapse of the tower), the emphasis of the study on the eyebolts rather than the rockers would have been questionable. Even in the infrequent cases where rocker failures have occurred, they have been detected soon afterward with a high-power telescope during guyline inspections, and the necessary rocker replacements have been made without damage to the tower.

In contrast, the progressive degradation of an eyebolt is not visible with a high-power telescope and failure of an eyebolt does invariably cause collapse of the tower. Therefore the focus of the study on the remaining service life potential of the eyebolts did seem warranted.

The short fatigue lives of laboratory-tested rockers were important in another way. It became apparent that maximum guyline loads must generally be below 50 percent of the eyebolt design load; otherwise, rocker failures would have been occurring regularly in the field. In reality, many of the rockers have remained in service for 10 years and endured over 10^7 guyline load oscillations without failure. The high maximum loads employed in the laboratory were only used to allow the development of eyebolt fatigue failures in a realistic time frame.

Flawed Eyebolt Tests

The second series of fatigue tests involved evaluations of eyebolts taken from service. The three eyebolts had been removed from service because they were considered to be significantly damaged, as evidenced by sizeable surface flaws detected in the head- and eye-fillet regions during on-site, magnetic-particle inspections.

The first experiment was done on Eyebolt 2A1-1C because it contained two very long, parallel, transverse surface flaws in the eye-fillet area. Strain gages were applied to this eyebolt prior to fatigue testing (Fig. 1). In addition to strain gages in the eyehole and head-fillet regions, several gages were placed

⁴A rocker is a universal-ring assembly that nests between the eyebolt head and the insulator cap recess. It permits the eyebolt head to pivot under lateral loads, thereby reducing bending stresses at the eyebolt head fillet.

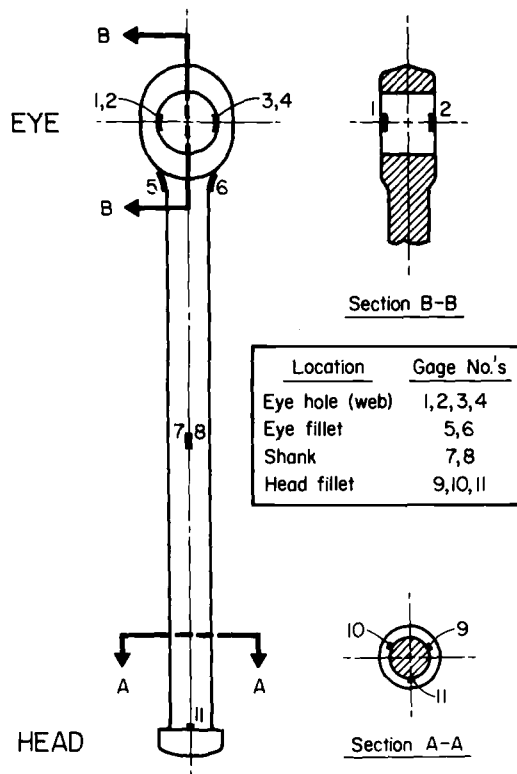


FIG. 1—Strain gage locations for Specimen S-2.

over the flaws in the eye fillet, so that any growth of these flaws could be identified readily.

After the cyclic loads were selected, initial strain-gage readings were made during a static application of the maximum load level. The test was then begun and continuous cycling was maintained except for occasional strain-gage checks under static maximum load. No significant variations in strain-gage output were observed, a condition that indicated no accumulation of damage within the eyebolt at these locations. Cycling was continued through 13 500 000 cycles, and no damage was evident. Then the maximum load was increased to the design level and the test was restarted. At this higher load, the eyebolt failed in 269 000 cycles, a value that was only slightly below the fatigue life found with the unused eyebolt at the same load level. The flaws in the eye fillet did not grow during the test; the failure occurred in the eye web. This result was very significant because it showed that the flaws in the eye fillet, originally thought to be quite damaging, were really insignificant factors in determining the remaining service life of the used eyebolt. A destruc-

tive examination of these eye-fillet flaws after completion of the fatigue test proved them to be fabrication flaws less than 1.2 mm deep.

The second flawed eyebolt selected for the test was identified as 2A2-2C. It was chosen because it had been examined nondestructively and was found to contain two flaws in the head-fillet region, the area thought to be most critical from the standpoint of actual eyebolt fatigue performance in service.

Again, no significant damage (or increase in existing flaw sizes) was observed on the eyebolt at the initial load range. The maximum load was therefore increased and at the higher load range, the eyebolt did fail in an additional 334 000 cycles. Significantly, the failure did occur at the head fillet and grew from one of the flaws that had been identified during nondestructive inspection. Subsequent fractographic examination of the failure surface also revealed that the initial flaw leading to failure had been a fatigue crack, rather than a fabrication flaw. Despite the size and initiation mechanism of the failure, the fatigue performance of this eyebolt was slightly superior to both of the others tested previously at that load level. The meaning of these results will be discussed further in a later section.

The final flawed eyebolt that was fatigue tested was Eyebolt 2A1-3C. In nondestructive inspections, it had been found to contain a single flaw in the head fillet region. This experiment had the same cyclic loads as the previous two flawed eyebolts. There was no discernible damage after 6 020 000 cycles at that load level, so the maximum load was increased to the design limit load for the rest of the test. After 265 000 additional cycles at this higher load range, this flawed eyebolt failed. It did not fail in the head fillet; instead, it failed across the eye web where most of the earlier eyebolt failures had occurred. Metallographic examinations of the head fillet after the test failed to reveal this defect. It is possible that the flaw was quite shallow, which might partially explain why the head-fillet location of this eyebolt was noncritical.

For purposes of comparison, all of the eyebolt-fatigue-test results are listed in Table 1. The meaning of these results from an analytical standpoint is reviewed in the Discussion.

Eyebolt Strain-Gage Measurements

To understand more about the actual local strains within the eyebolts for uniaxial-loading conditions, a series of small metal-foil strain gages was placed on two unused eyebolts (S-2 and S-3) and one flawed eyebolt (2A1-2C) before fatigue testing, and records were made of the resultant local strains. The locations of the gages used on S-2 are shown schematically in Fig. 1. The size of the gages varied from about 0.8 to 6 mm, depending on the strain gradients in the region being monitored; for example, strains at the head-fillet (which had a root radius slightly under 5 mm) were monitored with the smallest available, carefully positioned gages. Results of the strain-gage data

are summarized in Fig. 2. The strain-gage readings showed three things. Firstly, shank readings were exactly of the magnitude predicted from applied loads, shank cross-sectional area-estimates, and modulus estimates; that is, the shank strain-concentration values were close to unity. Secondly, the eye-fillet strains were slightly more than twice as high as the shank strains, which indicated that the effective eye-fillet strain-concentration factor was 2.1. Thirdly, the eyehole strains, as measured on the interior hole surface at the outside edges, were of practically the same magnitude as the head-fillet strains and of a magnitude approximately three times the shank strains. Although some variation was evident in the measurements, it was conservative to approximate both the head-fillet and eyehole strain-concentration factors with a value of 3.0.

Discussion

Some tentative conclusions regarding the objectives of this eyebolt-fatigue-evaluation program could be made after all of the fatigue tests were completed, but further support for these conclusions was desirable, so analyses were performed to develop fatigue-life estimates under other loading conditions and to attempt to answer some of the questions that arose during the testing program.

Fatigue-life estimates were made by considering the potentially critical

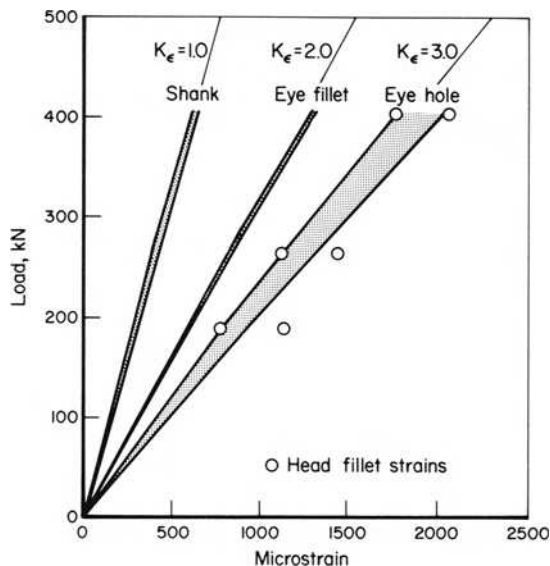


FIG. 2—Strain measurements during cyclic loading of Eyebolt S-2.

sites within the eyebolt and assessing the probable number of fatigue cycles that would be required to initiate a crack in those areas. The two phases of crack initiation and propagation are first dealt with separately in the following subsections, then they are treated jointly to develop the overall-fatigue-life estimates.

Crack-Initiation-Life Estimation

The estimation of crack-initiation life in a component subjected to fatigue loading can be handled in several ways, but all methods must rely on sound material-property information and realistic information regarding the deformation response of the component in critical areas. For the analysis described here, it was important to know: (1) baseline fatigue properties for the eyebolt material; (2) the cyclic stress-strain response of the material; (3) the maximum load, load ratio, and cross-sectional area of the eyebolt; and (4) the local strain-concentration factors for the eyebolt at critical locations.

A fatigue-life curve for unnotched SAE 1045 steel under fully reversed loading was obtained from Landgraf [2] for a strength level (TYS, 630 MN/m²; TUS, 725 MN/m²) very nearly the same as that estimated for the eyebolts. Since this curve was developed from tests on small, 6.35-mm-diameter unnotched laboratory specimens, cycles to failure, N_f were considered nearly coincident with cycles to initiation, N_i .

Along with the fatigue information, Landgraf [2] also reported the monotonic and cyclic stress-strain response for this material. This information was important because it was needed to make a realistic estimate of the local stresses in critical regions of the eyebolt when those regions were subjected to large strain amplitudes that induced significant cyclic plasticity.

Information on the local strain-concentration factors in the critical areas of the eyebolt was developed in the course of the laboratory work in this program. The results of those measurements were presented in Fig. 2.

With all of the necessary background information ascertained, it was then possible to proceed with the prediction of crack-initiation lives for the AISI 1045 steel eyebolts subjected to various hypothetical axial-load magnitudes. The first step was to compute the nominal stress range, ΔS . Then the local strain amplitude, ϵ_a , was estimated from ΔS and the local strain-concentration factor, K_ϵ , as follows:

$$\epsilon_a = \frac{K_\epsilon \Delta S}{2E} \quad (1)$$

where E = the elastic modulus.

From Eq 1, the maximum local strain, ϵ_{\max} , was then estimated:

$$\epsilon_{\max} = \frac{2\epsilon_a}{1 - R} \quad (2)$$

and the local maximum stress, σ_{\max} , was approximated from ϵ_{\max} using the cyclic stress-strain curve. After computing all of the local stress and strain components, the only important step remaining was to combine those parameters into an equivalent strain factor that properly accounted for the stress-ratio differences between the eyebolt loadings and the fully reversed ($R = -1.0$) baseline fatigue data that were available in the literature [1]. Previous work [3] showed that for a variety of materials, this stress-ratio difference could be accounted for through use of an equivalent-strain parameter, ϵ_{eq} , computed as follows:

$$\epsilon_{\text{eq}} = (2\epsilon_a)^m (\sigma_{\max}/E)^{1-m} \quad (3)$$

The exponent m was chosen to be 0.40 based on earlier optimization studies [3]. Using Eq 3 and the available fully reversed fatigue data, it was then possible to construct an expression relating anticipated crack initiation life with equivalent strain as follows:

$$N_f = A_1 \epsilon_{\text{eq}}^{n_1} + A_2 \epsilon_{\text{eq}}^{n_2} \quad (4)$$

where the A and n values were graphically determined constants. Equation 4 represents a curve similar in shape to that of the commonly used Basquin/Coffin-Manson relationship [4-6], except that equivalent strain, rather than fatigue life, was the independent variable, and fatigue life, rather than strain amplitude, was the dependent variable.

Employing the aforementioned analysis procedure, it was possible to construct estimated fatigue crack initiation life curves for a range of maximum eyebolt loads, as shown in Fig. 3. Several points concerning Fig. 3 and the analytical estimates of crack-initiation life are worthy of note. Firstly, the crack-initiation-life estimates for the eyehole and head-fillet were the same, because all the input parameters defining ϵ_{eq} were the same. This means that for a particular constant-amplitude, uniaxial load, the cycles to initiate a crack in either critical region would be essentially the same. Why is it then that no fatigue cracks have ever been found in the eyehole, whereas three have been found in the head-fillet area of three different eyebolts (for example, Eyebolt 2A2-2C)? The most plausible explanation seems to be that substantial bending stresses were introduced in the head-fillets of certain eyebolts during service, either because no rocker was present (as in the cluster eyebolts at the top of the guyline), or because the rocker did not completely remove bending moments caused by cable dynamics. These bending stresses probably aggravated local stresses in the head-fillet area to the extent that

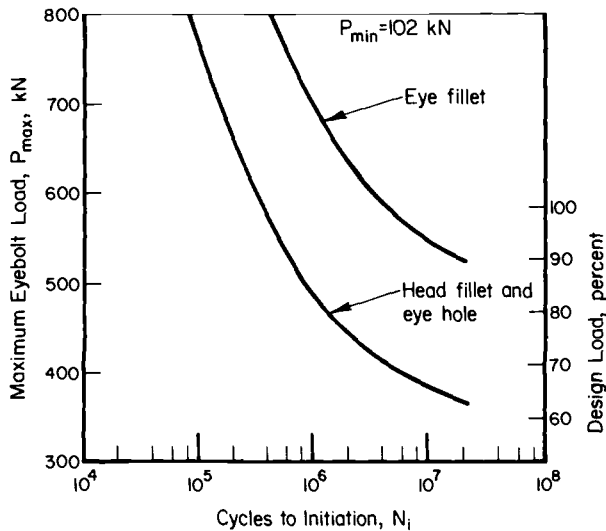


FIG. 3—Projected crack-initiation cycles for the eyebolt head-fillet, the eye-hole, and the eye-fillet.

fatigue cracks eventually formed. The analytical prediction still remains, however, that for purely uniaxial loads, there appears to be nearly equal probability of crack initiation in the eyehole and head-fillet. This is, of course, based on the assumption that normal dimensional tolerances are maintained for the eyebolt and eyepin.

The second point regarding Fig. 3 is that the eye-fillet region is predicted to be far less critical than the eyehole or head-fillet in terms of crack initiation. In fact, for maximum loads below 85 percent of static design load, these areas within the eyebolt differ by more than two orders of magnitude in crack-initiation life. This result simply means that, unless a crack is already present in the eye fillet of a new eyebolt, there is little chance that one will develop there before a crack initiates either in the eyehole or the head-fillet.

Crack-Propagation-Life Estimation

Crack growth data on a family of steels similar to the AISI 1045 steel used in the eyebolt have been developed by Barsom [7]. A logarithmically linear band was formed between crack growth rate and crack-tip stress intensity over an intermediate range in ΔK , and the mean line of this band can be expressed as

$$da/dN = C \cdot \Delta K^n \text{ (mm/cycle)} \quad (5)$$

where

C = a constant, defined by the intercept in da/dN at $\Delta K = 1 \text{ MN}/\text{n}^{3/2}$,
and

n = an exponent (usually in the range of 3 to 5).

In this particular case, C had a value of 4.9×10^{-9} and n had a value of about 3.0, based on stress ratios of 0.00 to 0.25.

Although outside the range of Barsom's data, it is generally agreed that the logarithmically linear relationship between da/dN and ΔK does not remain valid for very high and very low values of ΔK . The deviation in crack growth rate from the linear relationship for low stress intensities is generally modeled by an asymptote designated as a threshold stress intensity, ΔK_{th} , and the comparable deviation from linear at high stress intensities is modeled by an asymptote called a critical stress intensity or ΔK_c level. The lower asymptote, or threshold stress intensity, is of greatest concern in this analysis because it identifies a ΔK -level below which crack growth would not be expected to occur.

The stress intensity range, ΔK , for a semi-elliptical crack growing into a component can be defined by the following expression:

$$\Delta K = 1.1 M_k \Delta S \frac{\sqrt{\pi a}}{\Phi}$$

$$M_k = 1 + \frac{\pi}{4} \left(\frac{a}{t} \right)^2 \left(\frac{\Phi}{1.1\sqrt{a/c}} - 1 \right) \quad (6)$$

$$\Phi = \sqrt{1 + 4.6 \left(\frac{a}{2c} \right)^{1.65}}$$

where

a = the crack depth, and

$2c$ = the surface crack length.

If the ratio of a to $2c$ is constant, the expression for Φ also is a constant, which simplifies the expression for ΔK . A transverse crack growing in a homogeneous material through a uniform tensile-stress field usually will maintain an $a/2c$ ratio of about 0.50, in which case Φ has a value of 1.57. The parameter M_k is a back-face stress-magnification factor that is essentially unity in value for a crack less than one half as deep as the thickness of the component through which it is passing. In cases where Φ can be considered to have a constant value of 1.57 and M_k is essentially unity, the expression for ΔK simplifies to

$$\Delta K = 0.7 \Delta S \sqrt{\pi a} \quad (7)$$

For flaws less than about 25 mm deep in the head-fillet and less than about 5 mm deep in the eyeweb, Eq 7 has reasonable validity. Cracks of greater depth in either area of the eyebolt would almost certainly decrease in crack-aspect ratio ($a/2c$), and the more complex expression given in Eq 6 should be used.

With the basic stress intensity expressions defined and crack growth characteristics of the AISI 1045 steel estimated, it was then possible to proceed to a detailed crack-propagation-life estimate for the eyeweb and head fillet.

Eyebolt-Head-Fillet Crack Growth Predictions—The conditions of stress through the eyebolt cross section at the head-fillet are nonuniform because of the stress magnification that is caused by the geometrical stress concentration. The pattern of those stresses was estimated from data presented by Grover for circumferentially notched bars [8], and those stresses were taken into account when considering a hypothetical small flaw propagating from the eyebolt head-fillet into the shank cross section.

The significant result of the head-fillet crack-tip stress magnification was a nonlinear pattern of stress intensity versus crack depth. This trend is shown in Fig. 4 for two levels of maximum load. According to this result, it would be expected that a crack initiating in the head fillet would grow faster initially than it would after extending to a depth of 3 to 4 mm. After passing through this region of minimum stress intensity, the crack would begin to accelerate its growth until a critical stress intensity was reached and failure of the eyebolt occurred. Of course, this pattern would occur only if cyclic loads were nearly of constant magnitude, as they were in the BCL laboratory tests. The same stress pattern of intensity versus crack depth pattern would exist for variable-amplitude loading, but a whole series of curves like those presented in Fig. 4 would be required to describe the instantaneous crack-tip stress intensities for particular crack depths.

Tentative verification of the behavior predicted in Fig. 4 was obtained through microscopic examination of the head-fillet fracture surface of Eyebolt 2A1-2C [1]. Examination at magnifications of X5000 with a scanning electron microscope revealed fatigue striations in the first 5 mm of crack growth that had nearly constant spacing and were of a length that corresponded to a macroscopic crack growth of about 1×10^{-4} mm/cycle. Assuming one striation per cycle, that rate of growth would be predicted on the basis of a stress intensity range of about $27 \text{ MN/m}^{3/2}$. This value is in reasonable agreement with the predicted stress intensities of 22 to $26 \text{ MN/m}^{3/2}$ for a 587 kN maximum load and cracks up to 5 mm deep.

Another important consideration in the prediction of head-fillet crack-tip stress intensities and crack growth rates was the threshold stress intensity for crack growth. Threshold information developed for a steel of similar strength [8] indicated ΔK_{th} -values of 9 to $13 \text{ MN/m}^{3/2}$ for stress ratios of 0.10 to 0.25.

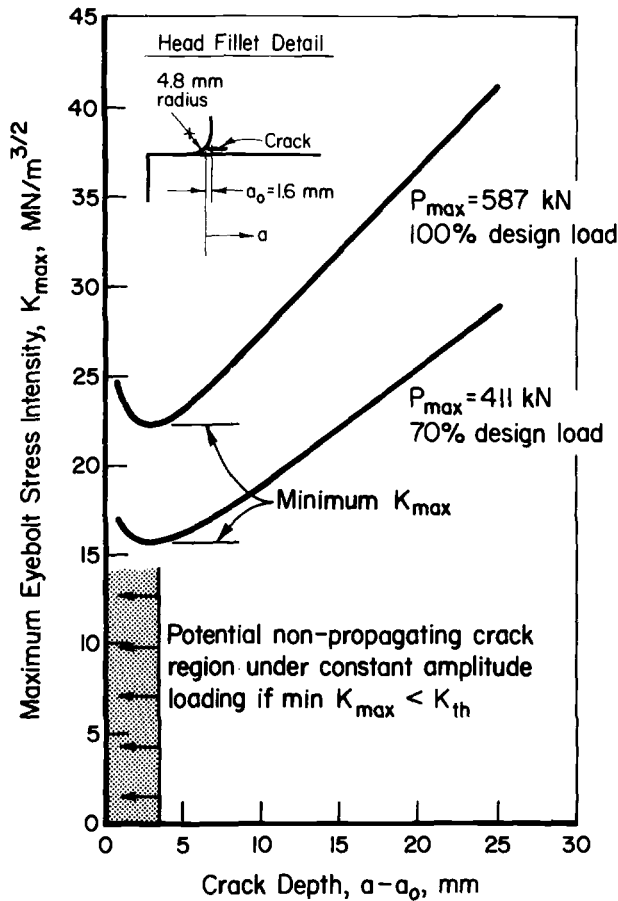


FIG. 4—Maximum stress intensity versus crack depth in the eyebolt-head-fillet region for two maximum-load levels.

Assumed threshold-stress-intensity values of 9, 11, and 13 $\text{MN}/\text{m}^{3/2}$ were used to compute maximum load levels below which crack propagation would not be expected to occur. The results of these computations are shown in Fig. 5 for a range of crack depths. The most significant conclusion drawn from this figure was that small cracks (less than 2.5 mm deep) would stop growing after they were initiated if the load magnitudes were less than 300 kN for an assumed threshold stress intensity of 9 $\text{MN}/\text{m}^{3/2}$, less than 370 kN for an assumed threshold value of 11 $\text{MN}/\text{m}^{3/2}$, and less than 430 kN for an assumed threshold of 13 $\text{MN}/\text{m}^{3/2}$.

Direct evidence of this nonpropagating crack phenomenon was seen in the fatigue test of Eyebolt 2A2-2C. A maximum eyebolt load of 411 kN did not

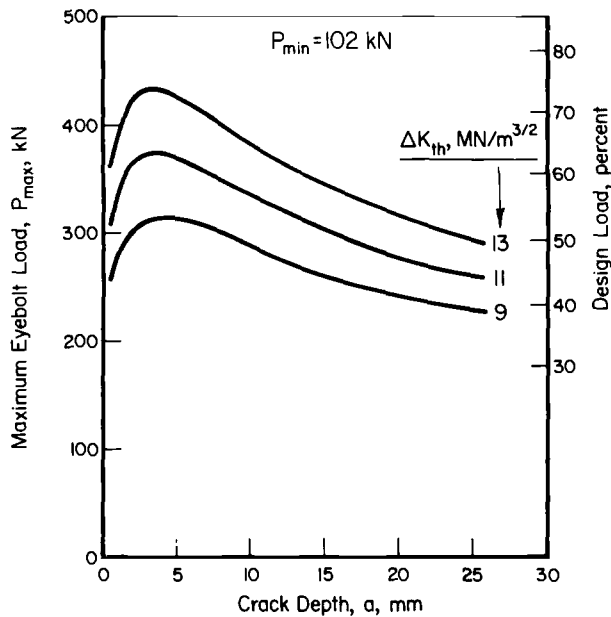


FIG. 5—Maximum load levels below which crack propagation would not be expected to occur in the eyebolt-head-fillet region, for several possible threshold-stress-intensity levels and a range of crack depths.

extend a 1.5 mm-deep head-fillet crack, but an increased load of 587 kN caused it to grow and ultimately cause failure. This test provided evidence that the threshold stress intensity for this eyebolt material was in the range of 11 to 13 $\text{MN}/\text{m}^{3/2}$.

After considering all of these factors that affect the growth characteristics of cracks in the eyebolt-head-fillet, it was possible to develop estimates of crack propagation life for specific eyebolt-loading conditions. Starting from the basic crack growth rate expression given in Eq 5, it was possible to construct an estimate of the fatigue cycles, ΔN , that an eyebolt could withstand during the progression of a fatigue crack from an initial depth, a_i , to a final depth at failure, a_f . This expression is as follows:

$$\Delta N = \frac{1}{C \Delta K_{eff}^n} (a_f - a_i) \quad (8)$$

where $\Delta K_{eff} = [(\Delta K_f^n + \Delta K_i^n)/n]^{1/n}$, and C and n are constants for the material from Eq 5. The information necessary to solve Eq 8 is basically:

(1) What initial crack depth, a_i , is physically realistic and of concern from the standpoint of eyebolt integrity?

- (2) What final crack depth, a_f , is realistically associated with failure of the eyebolt at the head?
- (3) What stress intensity ranges are associated with a_i and a_f ?
- (4) What values of C and n define the crack growth characteristics of the material?

An initial crack depth of 1 to 6 mm was considered physically meaningful for these 63.5 mm-diameter eyebolts, and a final critical crack length of 38 mm was chosen. Stress intensity levels associated with these crack sizes were determined from Eqs 6 and 7. The resultant estimates of crack-propagation cycles to failure for the eye-fillet region for a range of maximum-load levels are shown in Fig. 6. The runout levels associated with ΔK_{th} -values of 9, 11, and 13 $\text{MN}/\text{m}^{3/2}$ also are shown. The correlation of these predictions with actual experimental data is discussed later.

Eyebolt-Eyeweb Crack Growth Predictions—A flaw on the inner diameter of the eyebolt-eyehole propagates in a substantially different manner than does a flaw in the head-fillet region of the Loran-tower eyebolts. One of the major reasons for differences in crack growth rates is the sizeable difference in the associated stress fields through which the cracks propagate. The combined tensile and bending stresses that are generated in the eyeweb when the eyebolt is loaded cause the high inner-diameter tensile stresses that decrease nearly linearly to form compressive stresses on the outer eye diameter. This

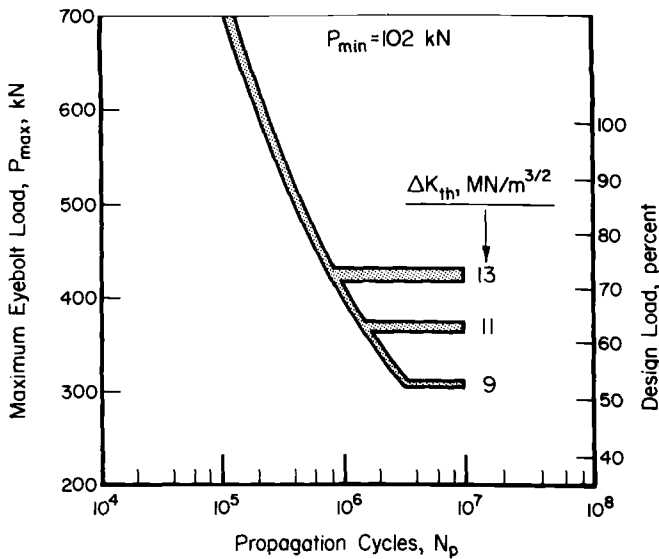


FIG. 6—Expected crack-propagation cycles to failure at various load levels and various crack-tip threshold stress intensities for the eyebolt-head-fillet region, assuming an initial crack depth of 1 to 6 mm.

pattern of stresses was considered in analyzing the probable growth patterns of cracks in the eyeweb.

Both corner cracks and midsection surface flaws in the eyehole were considered. A semicircular crack shape was predicted for crack depths up to about 6 mm, but beyond that point, it was assumed that actual flaws within the web would become increasingly elliptical, a condition which would lead to higher stress intensities at the base of the crack front. The exact shape of the flaw in this region was not particularly important, however, because web failure was imminent at this point.

The rapid increase in crack-tip stress intensities with increasing crack depth can be seen in Fig. 7 in which maximum stress intensities are plotted as a function of flaw depth within the eyeweb for two maximum-load levels. This pattern is in sharp contrast to the one seen in the head-fillet region (Fig. 4) where cracks 6-mm deep displayed approximately the same stress intensities as flaws less than 1 mm deep. The net result of this difference in ΔK versus crack depth is increased flaw criticality in the eyeweb region. An important factor that has offset this criticality in the field is simply that, in service, operating loads have apparently not been sufficiently high to generate fatigue cracks in the eyehole.

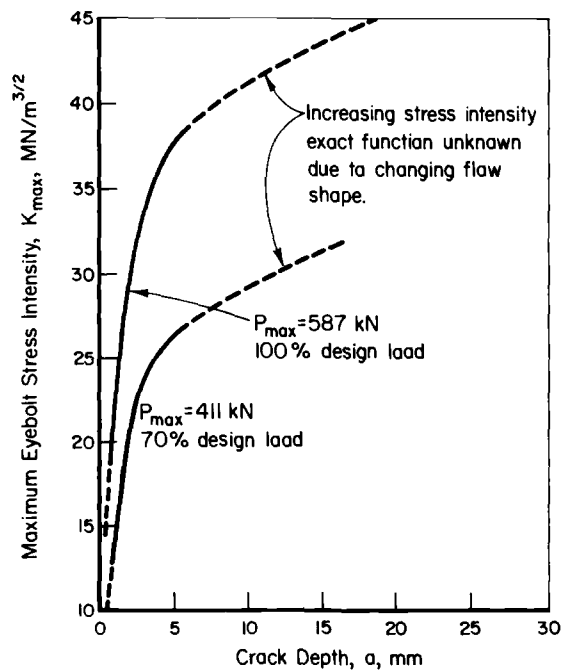


FIG. 7—Maximum stress intensity versus crack depth in the eyebolt-eyehole region for two maximum-load levels.

To illustrate the effect of a flaw in the eyeweb on service life, the number of cycles of loading that the eyebolt would withstand before failure was calculated for a 0.75-mm-deep flaw initiated in the eyeweb. This result is shown in Fig. 8 for a large range of potential maximum eyebolt loads. The potential threshold-stress-intensity levels also are shown for the 0.75-mm-deep assumed flaw. Here it is quite evident that even a relatively high cyclic load with a maximum of 70 percent of static design load would not propagate that initial flaw unless the threshold stress intensity for the eyebolt was below approximately $12 \text{ MN/m}^{3/2}$. It is certainly true, however, that large loads, causing stress intensities above the threshold level, are predicted to cause eyebolt failure in the eyeweb in a relatively small number of cycles ($\sim 100\,000$) if a crack is initiated there. This conclusion is supported by the fact that five out of six eyebolts tested in this experimental program did fail in the eyeweb. The extent of the correlation between analytical predictions and experimental results is discussed further in the following section.

Correlation of Analytical and Experimental Results—Two eyebolt-fatigue-life estimates result from the analyses just presented—one of the head-fillet and the other for the eye-hole. Estimates for crack initiation in both areas were the same (ignoring potential effects of bending stresses at the head fillet), but the predicted propagation cycles to failure at the head fillet were substantially higher than at the eyeweb.

The total-life prediction for the head fillet is shown in Fig. 9. Cycles to crack initiation, N_i , cycles of crack propagation, N_p , and total cycles to fail-

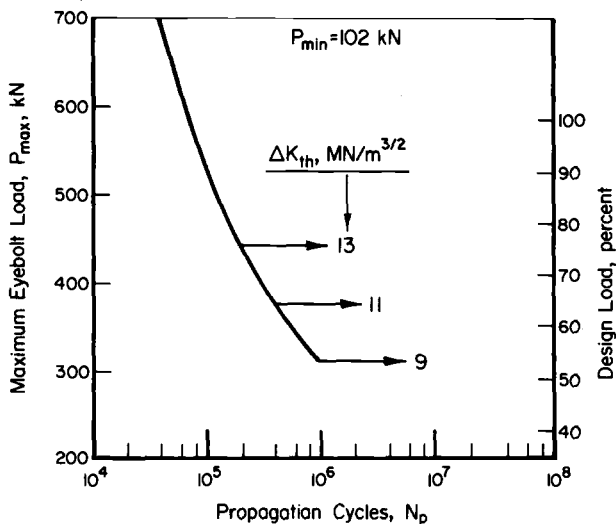


FIG. 8—Expected crack propagation cycles to failure at various load levels for the eyebolt-eyeweb, assuming an initial flaw of 0.75 mm.

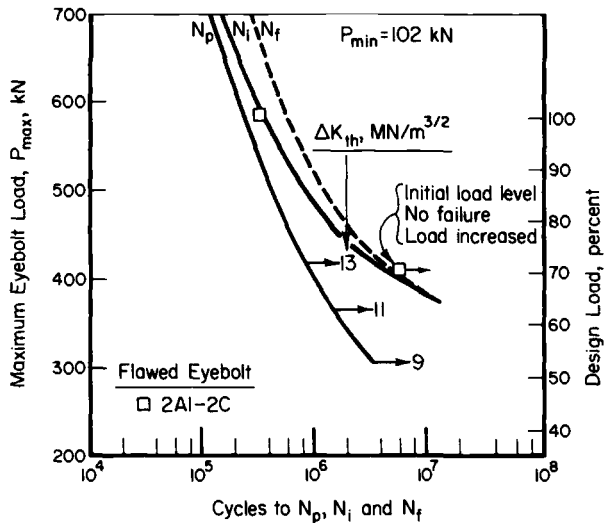


FIG. 9—Total-fatigue-life estimate and experimental results for the eyebolt-head-fillet region.

ure ($N_i + N_p = N_f$) are shown for a range of maximum eyebolt loads. The only valid experimental result to compare with the head-fillet analytical estimates is the single head-fillet failure (Eyebolt 2A2-2C). As was mentioned earlier, this eyebolt was found to have an initial 1.5-mm-deep fatigue crack in the head fillet. When tested in the laboratory under cyclic conditions with a maximum load of 411 kN, no crack extension was observed through 6 000 000 cycles. At this maximum load, threshold crack-tip stress intensities ($\sim 12.5 \text{ MN/m}^{3/2}$) were not exceeded, and it was not until the load was increased to 587 kN that the crack propagated and ultimately caused failure in 334 000 additional cycles. This crack propagation life at 587 kN corresponds reasonably well with the predicted value of 250 000 cycles for N_p . Thus the correlation between analysis and experiment was quite good.

Total-life predictions for the eyehole are shown in Fig. 10. Again, N_i , N_p , and N_f cycles are shown, along with comparative experimental data on the five eyebolts tested that failed in the eyehole. The test results at 411 kN show somewhat mixed trends, although there does appear to be a logical explanation based on the analysis. The unused eyebolt failed at almost exactly the number of cycles predicted (3 320 000 cycles actual versus 4 000 000 cycles predicted), assuming that the actual threshold stress intensity for this unused eyebolt material was below about $12 \text{ MN/m}^{3/2}$. The two used eyebolts tested at this load level did not show signs of damage through 6 000 000 and 13 000 000 cycles, respectively. The analysis predicts that small cracks would initiate in the eyehole after this number of cycles of that load magnitude, but

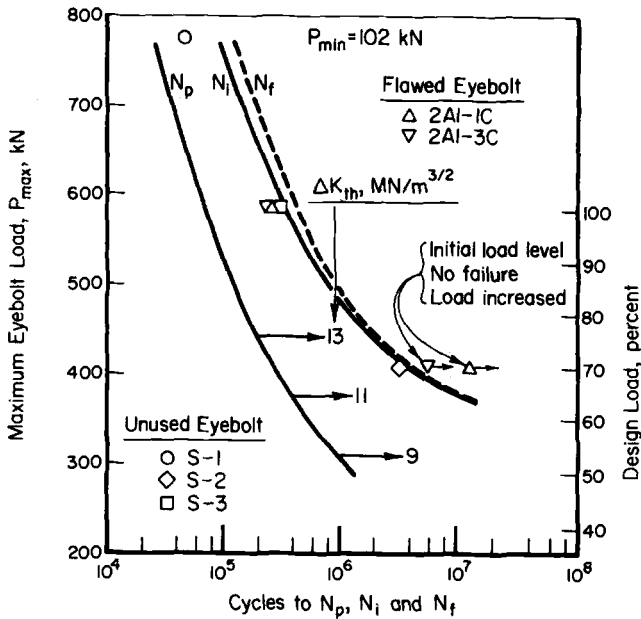


FIG. 10—Total-fatigue-life estimate and experimental results for the eyebolt-eyehole region.

it also predicts that they would not grow if actual threshold stress intensities for the used eyebolt material not only slightly exceeded $12 \text{ MN/m}^{3/2}$. At the higher load level of 587 kN, all of the eyebolts that failed at the eye did so in from 265 000 to 332 000 cycles, results that compare reasonably well with the predicted result of 450 000 cycles. Analytical predictions were that the effects of threshold levels on crack propagation would be insignificant at this higher load level, and that result was evident in the actual laboratory data.

Conclusions

Several important conclusions appear to be valid based on the analytical and experimental work described in this paper:

(1) Flaws observed in the used eyebolts taken from service were not significantly damaging to the eyebolts, and they did not significantly reduce the remaining service-fatigue-life potential.

(2) Cracks less than 2.5 mm deep at the head fillet are not imminently hazardous unless extremely high service loads (above 50 percent of the design load) occur for a sustained period of time.

(3) Cracks over 1.5 mm deep at the eyeweb are potentially hazardous, but the probable service loads are such that cracks of this depth are not likely to develop by fatigue in the eyeweb.

Acknowledgments

This research was sponsored by the United States Coast Guard under Contract No. C.G.65.034A. Numerous Battelle personnel contributed to this study, and this paper is indirectly a result of their efforts. Specifically, the following engineers were instrumental in this study: C. E. Jaske, R. P. Meister, Jay Mitchell, E. S. Bartlett, and in particular, D. B. Roach.

References

- [1] Rice, R. C., Jaske, C. E., Mitchell, J., Meister, R. P., Bartlett, E. S., and Roach, D. B., "A Study to Conduct Testing of Tall Loran Tower Eyebolts," Summary Report submitted by Battelle's Columbus Laboratories to the United States Coast Guard under Contract No. C.G.65.034A., 30 Sept. 1977.
- [2] Landgraf, R. W., "Cyclic Deformation and Fatigue of Hardened Steels," Theoretical and Applied Mechanics Report 320, University of Illinois, Urbana, Ill., 1968.
- [3] Rice, R. C., Davies, K. B., Jaske, C. E., and Feddersen, C. E., "Consolidation of Fatigue and Fatigue-Crack Propagation Data for Design Use," Contractor Report prepared by Battelle's Columbus Laboratories for Langley Research Center, NASA CR-2586, Oct. 1975.
- [4] Basquin, O. H. in *Proceedings*, American Society for Testing and Materials, Vol. 10, Part II, 1910, pp. 625-630.
- [5] Manson, S. S., "Behavior of Materials Under Conditions of Thermal Stress", in *Heat Transfer Symposium*, University of Michigan Engineering Research Institute, 1953, pp. 9-75.
- [6] Coffin, L. F., Jr., *Transactions of the American Society of Mechanical Engineers*, Vol. 76, 1954, pp. 931-950.
- [7] Barsom, J. M., "Fatigue Behavior of Pressure-Vessel Steels," Welding Research Council Bulletin, No. 194, May 1974.
- [8] Grover, H. J., *Fatigue of Aircraft Structures*, NAVAIR 01-1A-13, prepared by Battelle's Columbus Laboratories for the Naval Air Systems Command, 1966, pp. 58-59.
- [9] Broek, D. and Rice, R. C., "Fatigue Crack Growth Properties of Rail Steels", Final Report (Part I), submitted by Battelle's Columbus Laboratories to the U.S. Department of Transportation under Contract No. DOT-TSC-1076, July 1977.

S. H. Smith,¹ N. D. Ghadiali,¹ Akram Zahoor,¹
and M. R. Wilson²

Fracture Tolerance Analysis of the Solid Rocket Booster Servo-Actuator for the Space Shuttle

REFERENCE: Smith, S. H., Ghadiali, N. D., Zahoor, Akram, and Wilson, M. R., "Fracture Tolerance Analysis of the Solid Rocket Booster Servo-Actuator for the Space Shuttle," *Design of Fatigue and Fracture Resistant Structures, ASTM STP 761*, P. R. Abelkis and C. M. Hudson, Eds., American Society for Testing and Materials, 1982, pp. 445-474.

ABSTRACT: The results of an evaluation of the fracture tolerance of three components of the thrust vector control servo-actuator for the solid rocket booster of the space shuttle are described. These components were considered as being potentially fracture critical and therefore having the potential to fall short of a desired service life of 80 missions (that is, a service life factor of 4.0 on a basic service life of 20 missions). Detailed stress analysis of the rod end, cylinder, and feedback link components was accomplished by three-dimensional finite-element stress analysis methods. A dynamic structural model of the feedback system was used to determine the dynamic inertia loads and reactions to apply to the finite-element model of the feedback link. Twenty mission stress spectra consisting of lift-off, boost, re-entry, and water impact mission segments were developed for each component based on dynamic loadings. Experimental fracture response data da/dN , K_{Ic} , and K_c were used for the structural alloys of the actuator components. These alloys were Inconel 718, 17-4 PH (H1025), 6061-T651, 2024-T851 (T351), and A286. Linear fatigue crack growth life and residual strength analyses were performed on the component critical locations using the Forman da/dN equation and CRACKS III computer code. Most components were determined to have the potential of reaching a service life of 80 missions or service life factor of 4.0.

KEY WORDS: stress analysis, fracture mechanics, stress intensity factors, mission spectra, dynamic loads, finite element models, fatigue crack growth life, residual strength, service life factor

¹Principal Research Scientist, Principal Research Scientist, and Research Scientist, respectively, Battelle Columbus Laboratories, Columbus, Ohio 43201.

²Senior Design Engineer, Moog Incorporated, East Aurora, N.Y.

The application of linear elastic fracture mechanics to the fatigue crack growth life prediction of engineering structures is becoming increasingly important as a means of fracture control and damage tolerance assessment of structures. Because of the limitations in nondestructive inspection techniques in detecting small crack-like defects and damage which could occur during the operational life of the structure, fatigue crack growth life analysis is usually conducted to determine the service life of the structure.

The thrust vector control servo-actuator for the solid rocket booster (SRB) of the space shuttle was designed and subjected to dynamic development tests at NASA's George C. Marshall Space Flight Center. Upon review of the actuator design, NASA selected 14 components as being potentially fracture critical. The actuator and components are shown in Fig. 1, and this paper presents the results of the rod end, cylinder, and feedback link analysis. Initial crack sizes assumed at the critical locations in the components and the service life factor analysis based on fatigue crack growth were based on the criteria defined in the SRB fracture control plan [1].³ The solid rocket booster was designed as a reusable structure for a basic service life of 20 missions.

The complex geometry and applied loadings of the actuator components

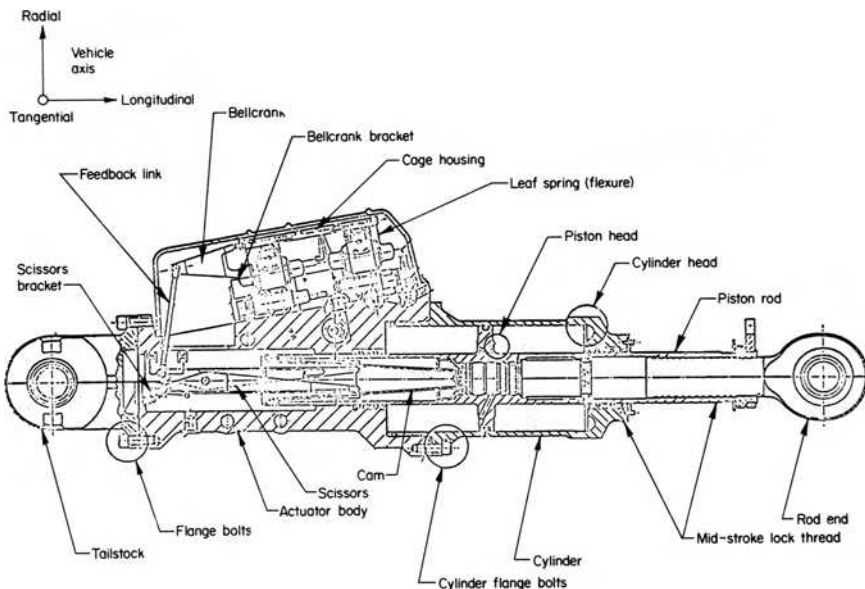


FIG. 1—Structural component identification—SRB actuator.

³The italic numbers in brackets refer to the list of references appended to this paper.

selected for stress and fracture mechanics analyses resulted in using finite-element methods to determine the peak stresses and distributions at critical locations in the components. Also, the objective of the fracture tolerance analysis was to use state-of-the-art linear elastic fracture mechanics methods in the fatigue crack growth life and residual strength analyses of the components.

The following sections of the paper describe the fracture mechanics analysis methods used, the initial damage size and fatigue crack growth assumptions, mission stress spectra development, and the fatigue crack growth and residual strength results of the actuator components.

Fracture Mechanics Analysis Methods

Each of the actuator components defined as being potentially fracture critical was analyzed for its service life factor based on spectrum loading fatigue crack growth behavior. This has been accomplished via linear elastic fracture mechanics (LEFM) analysis. LEFM applied in this context involves several aspects: finite-element stress analysis, use of stress intensity factor solutions, mission stress spectra development, and fatigue crack growth and residual strength predictions. All of these, when applied to structures, provide a damage or fracture tolerance evaluation of the structure [2,3]. Each will be discussed in turn in the next several sections.

Stress Intensity Factor Solutions

The types of cracks considered in the fracture-mechanics analyses of the components were either surface cracks, corner cracks at holes, or through-the-thickness cracks. Stress intensity solutions were available for treating each of the types of cracks located in infinite, semi-infinite, or finite simple geometries. Stress intensity factors for cracks emanating at the edge of lug holes were derived based on method of superposition of stress intensity factors.

Elliptical Surface Cracks—The surface crack solution most commonly used in fracture mechanics analysis is the solution developed by Irwin [4] and Shah and Kobayashi [5] for a plate with finite thickness under uniform tension stress; that is,

$$K_I = \frac{1.12\sigma\sqrt{\pi a}}{(Q)^{1/2}} M_k \alpha \quad (1)$$

$$Q = \phi^2 - 0.212 \left(\frac{\sigma}{\sigma_{ys}} \right)^2 \quad (2)$$

where

- Q = flaw shape parameter, $f(a/2c)$,
- a = surface crack depth,
- $2c$ = surface crack length,
- σ = applied uniform tension stress,
- σ_{ys} = yield stress,
- ϕ = complete elliptical integral of second kind,
- M_k = back surface magnification factor, and
- α = finite width correction factor.

Corner Cracks at Holes—A corner crack can be handled as a special case of surface crack. The corner crack at the edge of an open hole was determined by using superposition of the Bowie solution [6] and modifying the solution for a corner crack. This approach has been shown to provide a stress intensity solution in the small crack length range which is as accurate as the solutions of other investigators [7, 8]. Based on this approach, the solution becomes

$$K_I = \frac{1.12\sigma\sqrt{\pi a}}{(Q)^{1/2}} F\left(\frac{a}{R}\right) M_k \alpha \quad (3)$$

where $F(a/R)$ is the Bowie factor, which accounts for the stress concentration of the hole, and R is hole radius.

Cracks Emanating at Lug Holes—Structural lugs can be treated as loaded holes. However, the stress intensity factor solution can be determined by using superposition of stress intensity solution for a crack emanating at an open hole in a plate under uniform tension stress and a crack subjected to wedge force opening loads. This approach was used in arriving at a stress intensity solution for the analysis of cracks in the actuator lugs.

With reference to Fig. 2, the solution of K_{Ih} for one crack emanating at an open hole is [6]:

$$K_{Ih} = \sigma\sqrt{\pi a} F\left(\frac{a}{R}\right) \alpha \quad (4)$$

where α is a finite width correction factor and is a function of a/w .

The solution of K_{IP} for a pair of concentrated forces acting on a crack is [9]:

$$K_{IP} = \frac{P\sqrt{a_2}}{2t\sqrt{\pi}} \left[\frac{(3 + \mu)R^2 + 2a_2^2}{(R^2 + a_2^2)^{3/2}} \right] \left[\frac{a_2 - x}{a_2 + x} \right]^{1/2} \alpha \quad (5)$$

where

$$\begin{aligned} a_2 &= (a + 2R)/2, \\ x &= a_2 - R, \\ t &= \text{plate thickness,} \\ \mu &= \text{Poisson's ratio, and} \\ P &= \sigma(Wt). \end{aligned}$$

The K_I -solution for the lug geometry using superposition and for application to a corner crack emanating at a lug hole is [9]:

$$K_I = \frac{1.12(K_{Ih} + K_{IP})}{2(Q)^{1/2}} M_k \quad (6)$$

A literature search revealed another solution for lugs, that of Impellizzeri and Rich [10], involving the use of Buechner's weight function method. The solution is summarized and presented as follows for a single crack emanating at a lug hole:

$$K_I = 1.12\beta\sigma \frac{\sqrt{\pi a}}{(Q)^{1/2}} M_k \quad (7)$$

where $\beta = f(x, a) = m_b \phi_1 \phi_2$, where

x = distance from edge of lug hole,
 m_b = Bueckner's weight function,
 ϕ_1 = geometry correction factor, and
 ϕ_2 = finite width correction factor.

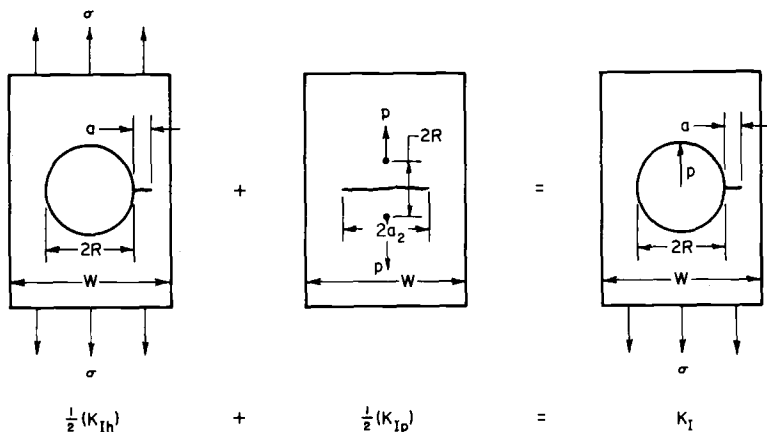


FIG. 2—Superposition of K-solutions for lugs.

Cracks at Stress Concentrations—Stress intensity factors for cracks assumed to emanate at points of high stress concentration and to propagate under an applied stress field set up by that concentration were handled by β -factors. The results of the finite-element stress analysis provided the peak stress and distribution of stress away from the stress concentration. For these cases

$$K_I = \beta\sigma\sqrt{\pi a} \quad (8)$$

where

$$\beta = \sigma_a/\sigma,$$

σ_a = stress level at a distance equal to a away from the edge of the stress concentration, and

σ = average applied uniform gross area stress.

Fatigue Crack Growth Rate Behavior

Several fatigue crack growth rate equations are available for analysis of constant-amplitude loading rate data and for use in spectrum loading fatigue crack growth predictions. The equation selected was the rate equation derived by Forman [11]:

$$\frac{da}{dN} = \frac{C(\Delta K)^n}{(1-R)K_c - \Delta K} \quad (9)$$

where

da/dN = fatigue crack growth rate,

ΔK = cyclic stress intensity factor range,

K_c = fracture toughness for data fitting,

C = material parameter,

n = material parameter, and

R = stress ratio.

The basic constant-amplitude fatigue crack growth data extracted from the literature [12] were reduced and analyzed to the Forman da/dN equation, and the parameters C and n were determined. Additional experimental data generated for this analysis were also fitted to the Forman da/dN equation.

The C and n values in the Forman da/dN equation are dependent on the cyclic stress ratio R . The spectrum loadings were made up of blocks of loading cycles of various R -ratios. Therefore, in order to apply a fatigue crack growth rate equation to make crack growth life predictions, a weighted C and n analysis was conducted based on a normalized da/dN behavior. Equation 9 can be rewritten as

$$\log \left(\frac{da}{dN} \{ (1-R)K_C - \Delta K \} \right) = \log C + n \log \Delta K \quad (10)$$

This equation is linear on a log-log plot with n as the slope and C the intercept. When da/dN versus ΔK data are plotted in accordance with Eq 10, the data consolidate and are independent of R [13]. All the material da/dN data for the actuator components were analyzed on a normalized basis, and the weighted C and n values were determined. Figure 3 shows a typical plot of normalized fatigue crack growth rate behavior for 17-4 PH stainless steel.

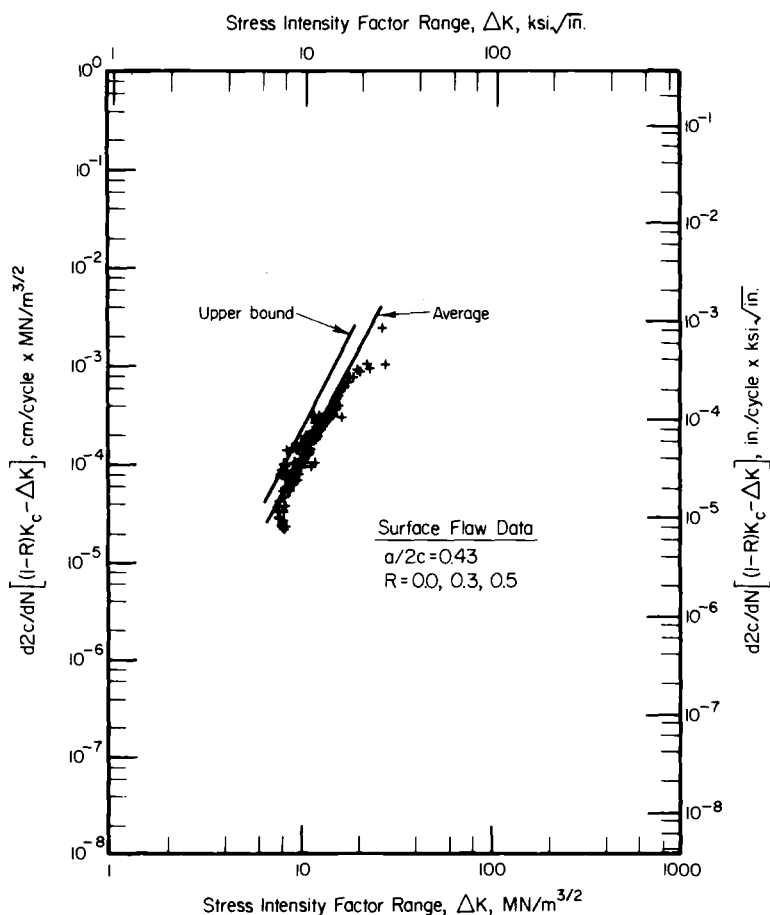


FIG. 3—Normalized fatigue crack growth rate behavior for 17-4 PH stainless steel in laboratory air.

Fracture Response Data for Structural Alloys

A summary of the da/dN data analysis of the data extracted from the literature and experimentally generated for this study is shown in Table 1. Normalized upper bound C and n values are shown for various environments which were used depending upon the environmental exposure of the assumed crack in the critical location of the actuator. The selected fracture toughness values of K_c and K_{Ic} were lower bound valid values of the alloys to reflect minimum toughness and heat-to-heat variation.

Mission Stress Spectra

The mission loads data were provided by NASA and were segmented into various parts of the basic mission spectrum for the 20 missions. The vibration g -levels were those resulting from the dynamic developmental testing of the

TABLE 1—Forman C and n values and fracture toughness values for structural alloys of components.

Alloy and Heat Treatment	da/dN Normalized Behavior		Fracture Toughness, K_c , K_{Ic} MN/m ^{3/2} , (ksi√in.)
	C , in./cycle/ (psi√in.) ^{$n-1$}	n	
Inconel 718 STA	8.532×10^{-13} (laboratory air)	2.790	$K_{Ic} = 132.0$ (120.0)
	9.693×10^{-19} (wet air)	3.821	
17-4 PH (H1025)	7.237×10^{-13} (laboratory air)	2.650	$K_c = 131.9$ (120.0)
	9.813×10^{-17} (seawater)	3.590	$K_{Ic} = 54.9$ (50.0)
6061-T6/T651	1.636×10^{-12} (laboratory air)	2.705	$K_{Ic} = 25.2$ (22.9)
	1.048×10^{-11} (seawater)	2.588	
	6.129×10^{-10} (hydraulic fluid)	2.140	
2024-T851	5.988×10^{-14} (wet)	3.241	$K_{Ic} = 27.5$ (25.0) $K_c = 65.9$ (60.0)
2024-T351	1.51×10^{-16} (laboratory air)	3.789	$K_{Ic} = 60.4$ (55.0)
	5.421×10^{-14} (wet)	3.189	$K_c = 132.0$ (120)
A286	3.274×10^{-6} (laboratory air)	1.120	$K_{Ic} = 193.4$ (176)
	3.256×10^{-10} (seawater)	1.198	

actuator. The g -level data were converted into load levels assuming that the g -levels were acting at the actuator's center of gravity.

Figure 4 shows a schematic diagram of the mission load segments and the loading sources. The basic mission sequence consisted of lift-off, boost, and re-entry segments. For the various 20 missions, these loading segments were the same. However, for water impact loads, the last segment of each mission, different load levels were used for each of the 20 missions.

The loading sources for lift-off and boost were low frequency vibration, random vibration, and engine gimbel. These load sources were alternating loads for three axes. Low frequency and random vibration were considered with a steady-state longitudinal load. Re-entry load sources consisted of random vibration with a steady-state load for each axis. Hydraulic fluid pressure levels for liftoff and boost segments of the mission were used for those components subjected to pressure.

The load spectra, consisting of several different segments, were converted to stress spectra for spectra fatigue crack propagation analysis based on the

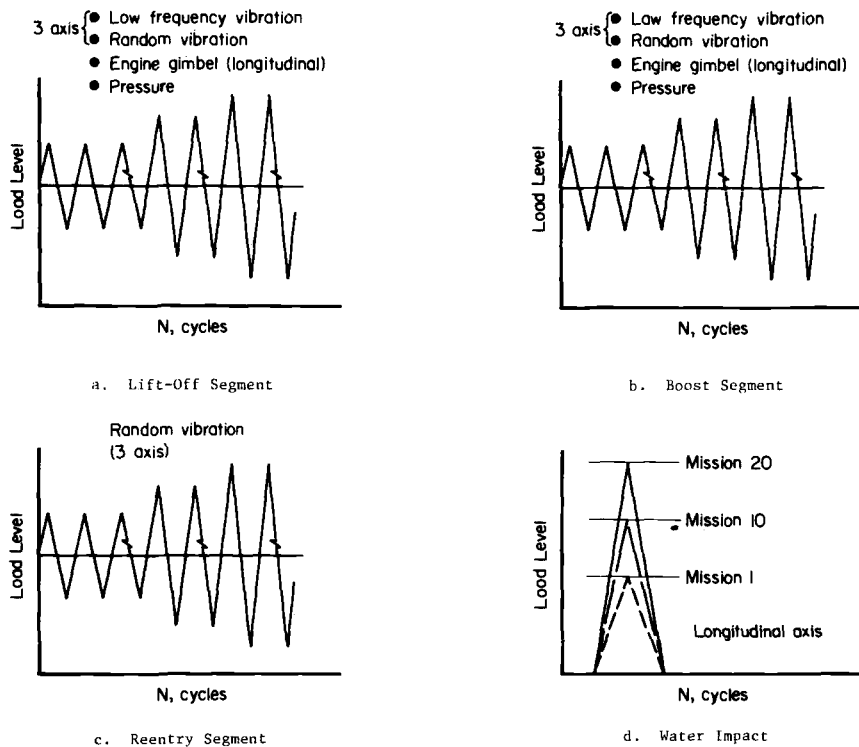


FIG. 4—Mission load segments for 20 mission stress spectra.

results of the stress analysis for each component. Usually only two directions of loading were considered in causing crack growth. These were radial and longitudinal which were superimposed to provide a total normal stress. The loading spectra discussed above were applied to the actuator rod end and cylinder components.

The mission stress spectra applied to the feedback link were spectra generated from strain gage data taken during the dynamic response developmental testing on the actuator. The details of the spectrum development techniques are discussed under the fracture mechanics analysis results of the feedback link.

Initial Damage Size and Fatigue Crack Growth

The initial damage (crack) sizes assumed in the spectrum loading fatigue crack growth analysis were based on the fracture control criteria defined in Ref 1. Initial crack sizes assumed depended on the structural location and geometry of the component. In general, the following initial sizes were assumed based on the criteria of the SRB Fracture Control Plan: (1) a 0.127-cm (0.05-in.)-radius corner crack at the edge of holes; (2) surface cracks with $a_o = 0.318$ cm (0.125 in.) and $2c_o = 0.636$ cm (0.250 in.) at structural locations of high stress concentration; and (3) $a = 0.127$ cm (0.05 in.) through-the-thickness edge crack in parts where thickness was less than 0.254 cm (0.10 in.).

Spectrum loading fatigue crack growth life predictions were performed based on linear cumulative crack growth analysis. The numerical integration computer program used in the analysis was "CRACKS III" computer code [14]. In order for a potentially fracture critical location in a component to qualify as nonfracture critical, the resulting fatigue crack growth life had to be equal to or greater than 80 missions. This is equivalent to a service life factor of 4.0 applied to the basic 20 mission desired life.

Fatigue Crack Growth and Residual Strength Results of Actuator Components

Fourteen of the SRB actuator components shown in Fig. 1 were selected as being potentially fracture critical. All of these components were analyzed, and the results for three of these components are presented in the following. These are the actuator rod end, cylinder, and feedback link of the feedback system. Several potentially fracture critical locations were considered in each of the three components analyzed.

Actuator Rod End Component

The rod end of the actuator, shown in Fig. 5a, was a main load-carrying component designed for longitudinal, radial, tangential, and combined

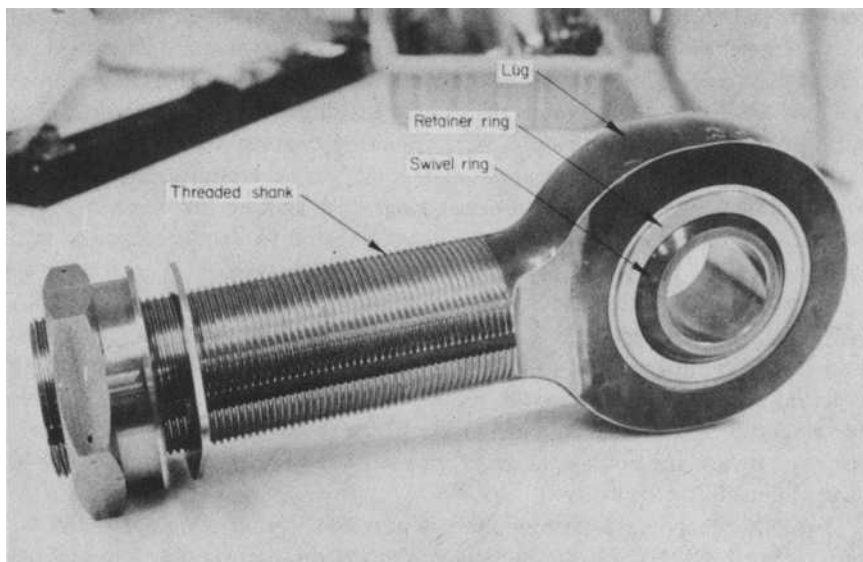


FIG. 5a—Finite-element model of rod end component—photograph of rod end.

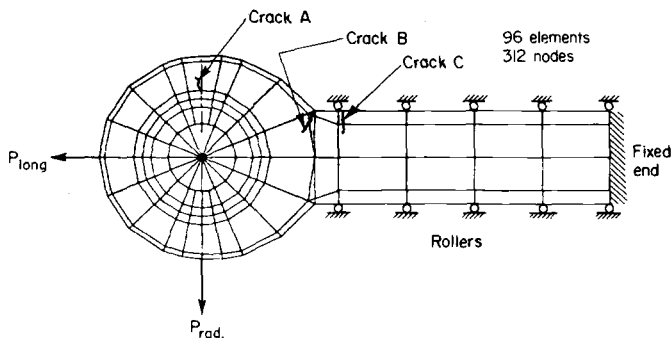


FIG. 5b—Finite-element model of rod end component—plane view of finite-element model.

loads. The lug structural alloy was Inconel 718 [solution-treated and aged (STA)], the retainer ring was Inconel 718 (solution treated), and the loading pin was Ti-6Al-4V (mill anneal).

Stress Analysis—A detailed three-dimensional finite-element model was developed for the rod end structural component (Fig. 5b). The model contained 96 isoparametric three-dimensional solid elements and 312 nodal points. Because of geometrical symmetry, only one half of the rod end component was modeled. The retainer ring and the loading pin were modeled as

separate structures and connected to the rod end lug through common double nodes which were elastic spring elements. This was done to provide a means of satisfying the boundary contact problem between the circumferential surface of the lug, retainer ring, and loading pin during loading. The spring elements were used only on the loading bearing side of the lug, retainer, and loading pin interfaces (that is, 180 deg). Under either radial or longitudinal loading the lug, retainer ring, and loading pin contact nodal points with spring elements were rigidly connected to displace equally in a radial direction, but rotate in a circumferential direction.

Finite-element stress analysis was performed using the program ADINA [15]. The lug net-section stress distribution (Crack A location) was determined for longitudinal and radial loadings of 4448 N (1000 lb). The resulting nominal normal stress across the lug net-section was 2.16 MN/m^2 (313 psi) for longitudinal and 0.86 MN/m^2 (125 psi) for radial loading. For these net-section stresses, the equivalent gross area stresses were determined for use in stress intensity factor analysis.

Two other locations for stress analysis purposes were the lug eye-shank intersection (Crack B) and the lug shank shaft (Crack C). Under longitudinal loading, the lug eye-shank intersection showed a stress concentration factor of 2.24 for a gross stress of 1.157 MN/m^2 (167.87 psi). Under radial loading, the elevation in stress at this point was in the same proportion as for longitudinal loading. Therefore a constant factor was used in developing the mission stress spectra under longitudinal and radial loadings. The shank was analyzed for longitudinal (axial) and radial (bending) loads both by the finite-element model and conventional stress analysis [16]. These results showed a normal stress of 1.173 MN/m^2 (168 psi) for longitudinal loading and 13.514 MN/m^2 (1960 psi) bending stress for radial loading.

The shank or shaft of the rod end was threaded for connection to the piston rod (Fig. 5a). The threaded grooves around the shank diameter and along the shank length developed a stress concentration factor which was considered in the stress intensity factor analysis. The notch root geometry of the threads was U-shaped and handled as a stress concentration considering the root radius. From Ref 17, with $D/d = 1.039$ and $r/d = 0.022$, the K_t for a single groove was taken as 2.55. For multiple grooves, the K_t dropped to 1.36 for the end groove.

The effect of tangential applied loadings on fatigue crack propagation at the three crack locations was rationalized. The lug net-section crack location (Crack A) and propagation direction was selected based on the assumption that the primary loadings produced during lift-off and boost of the actuator would be longitudinal and therefore perpendicular to the assumed crack propagation direction. Radial loadings would produce a normal stress component perpendicular to this crack propagation direction. Tangential loadings would not produce any bending moment across the cracked section and therefore were neglected. For the rod lug eye-shank intersection (Crack B)

and the shank shaft (Crack C), the original surface crack locations were selected as perpendicular to the longitudinal loading direction for the same reasons as mentioned above. The normal stress components, due to the radial loadings, were analyzed as a result of the bending. Tangential loadings at these two locations would also produce bending stresses; however, at the shaft peripheral locations selected, these locations would be at the neutral axis and the assumed surface crack depth would be unstressed. Therefore tangential loading as contributing to crack growth was neglected.

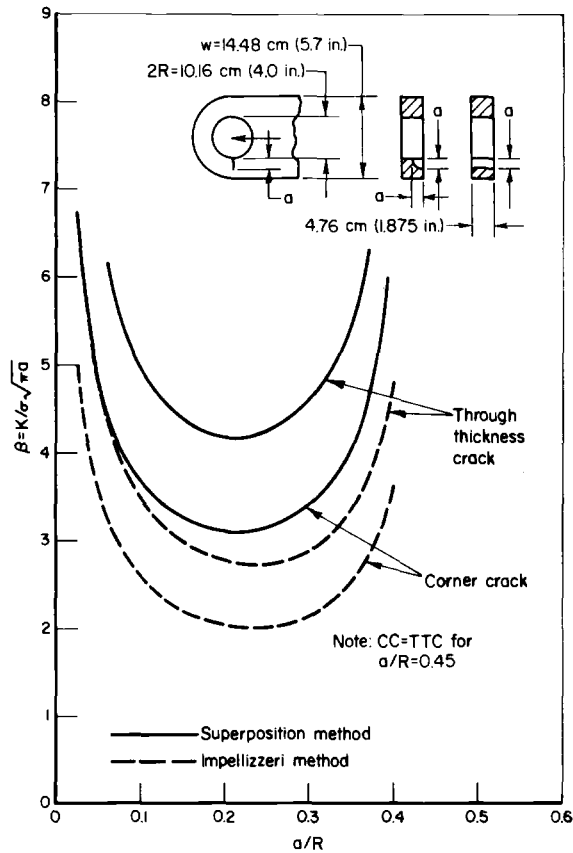
Stress Intensity Factor Analysis—The potentially critical locations of the rod end component selected for fracture mechanics and service life analyses because of high stresses were (1) the lug net-section (Crack A), (2) the lug eye-shank intersection (Crack B), and (3) the threaded shank (Crack C). The variation of stress intensity factor level with crack size was determined for the lug net-section. Superposition techniques as presented in Eq 6 and application of the Impellizzeri approach, Eq 7, were used in the lug stress intensity factor analysis. Figure 6 shows a plot of the variation of beta ($\beta = K/\sigma\sqrt{\pi a}$) with a/R for a quarter-circle corner crack and through-the-thickness crack emanating on one side of the lug hole. The beta parameter is $K/\sigma\sqrt{\pi a}$ where σ is the equivalent gross area stress on the lug. A comparison of the two methods in Fig. 6 showed that the superposition technique resulted in higher stress intensity levels than the Impellizzeri approach. As expected, the through-the-thickness crack situation resulted in higher stress intensity levels than the corner crack case. The corner crack becomes a through-the-thickness crack at $a/R = 0.45$. The beta factors for use in the fatigue crack growth analysis were the results from the application of the superposition technique, since it resulted in the more conservative solution.

The lug eye-shank intersection (Crack B) and the shank (Crack C) were analyzed for surface cracks emanating on the surface of the structure. Stress intensity formulations for the surface crack configuration were given in Eqs 1 and 2.

Fatigue Crack Growth and Residual Strength—Stress spectra for each of the 20 missions were developed for the three rod end locations based on the results of the stress analysis. Each mission stress history consisted of the sequential segments of lift-off, boost, re-entry, and water impact. For fatigue crack growth analysis, all compression stresses were truncated to zero.

The analytical results of the spectrum loading fatigue crack growth behavior for the rod end lug net-section (Crack A) is shown in Fig. 7. In this analysis, the initial assumed damage size was a 0.127-cm (0.05-in.)-radius corner crack emanating at the edge of the lug hole. The results show that the fatigue crack growth life was greater than 220 mission spectra, which was beyond the 80 spectra required to attain a service life factor of 4.

Spectrum loading fatigue crack growth behavior for the rod end eye-shank intersection (Crack B) is also shown in Fig. 7. The analytical growth behavior was determined from an initial surface crack of $a_o = 0.318$ cm (0.125 in.)

FIG. 6—Variation of beta with a/R for rod end lug.

and $2c_o = 0.636$ cm (0.250 in.). Based on this initial surface crack size for this location, the crack growth life was 85.0 spectra or a service life factor of 4.25, which satisfied the required crack growth life criterion.

A spectrum loading fatigue crack growth analysis of a surface crack emanating at the base of the end thread of the rod and shaft (Crack C) was conducted. These results are also shown in Fig. 7. Based on the same initial surface crack size as the Crack B location, fatigue crack growth life was greater than 220 missions, which satisfies the crack growth life requirement of 80 missions for a service life factor of 4.

Figure 8 shows a residual strength diagram for the three locations in the rod end component. From the results of the stress analysis and the use of the stress intensity factor solutions, the critical applied gross stress levels for various assumed crack sizes is represented in this diagram for $K_{Ic} = 132$ MN/m^{3/2} (120 ksi√in.). For Crack A location, the maximum applied oper-

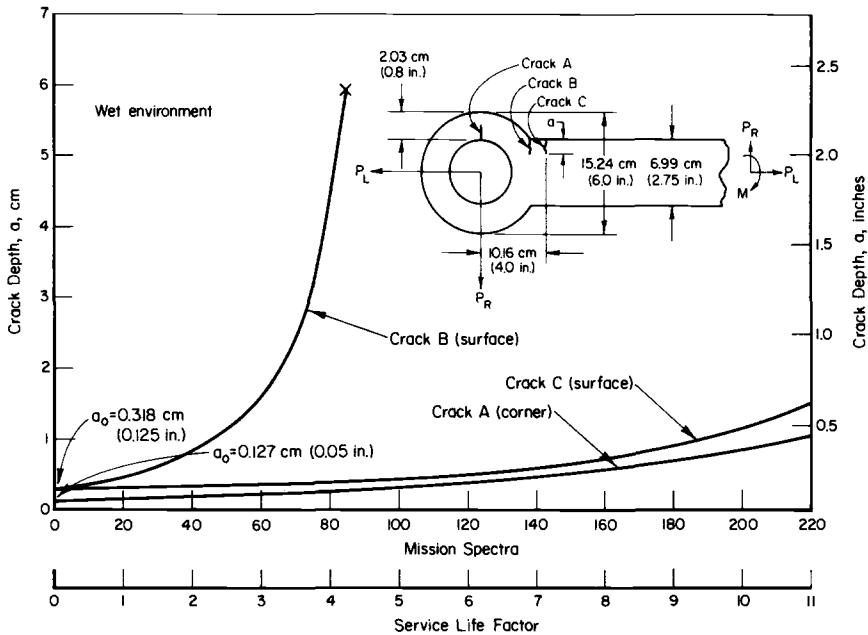


FIG. 7—Spectrum loading fatigue crack growth behavior of rod end component (Inconel 718 STA).

ational gross stress level in the 20 mission spectra was 117.2 MN/m^2 (17.0 ksi). The critical crack size at this stress level would be 1.85 cm (0.73 in.). The lug eye-shank intersection was subjected to a maximum operational stress level of 242.7 MN/m^2 (35.2 ksi). At this applied stress level, the critical surface crack size would be $a_{cr} = 3.56 \text{ cm}$ (1.40 in.) and $2c_{cr} = 7.12 \text{ cm}$ (2.80 in.). For the rod end shank crack located at the first thread, the maximum applied operational stress level was 200.6 MN/m^2 (29.1 ksi). The critical crack size for this stress level was well below the curve.

Actuator Cylinder Component

The main structural purpose of the actuator cylinder was to provide the housing of the piston rod and head. The cylinder housing was mainly subjected to internal pressure and radial bending. The structural alloy of the cylinder was stainless steel 17-4 PH (H1025). The cylinder flange was attached to the actuator body by eighteen A286 steel bolts.

Stress Analyses—The cylinder component was analyzed by an axisymmetric finite-element model developed for the cylinder flange, cylinder wall housing, and built-up end section. The model consisted of 80 isoparametric elements and 300 nodal points. Figure 9 shows the model and the constraints

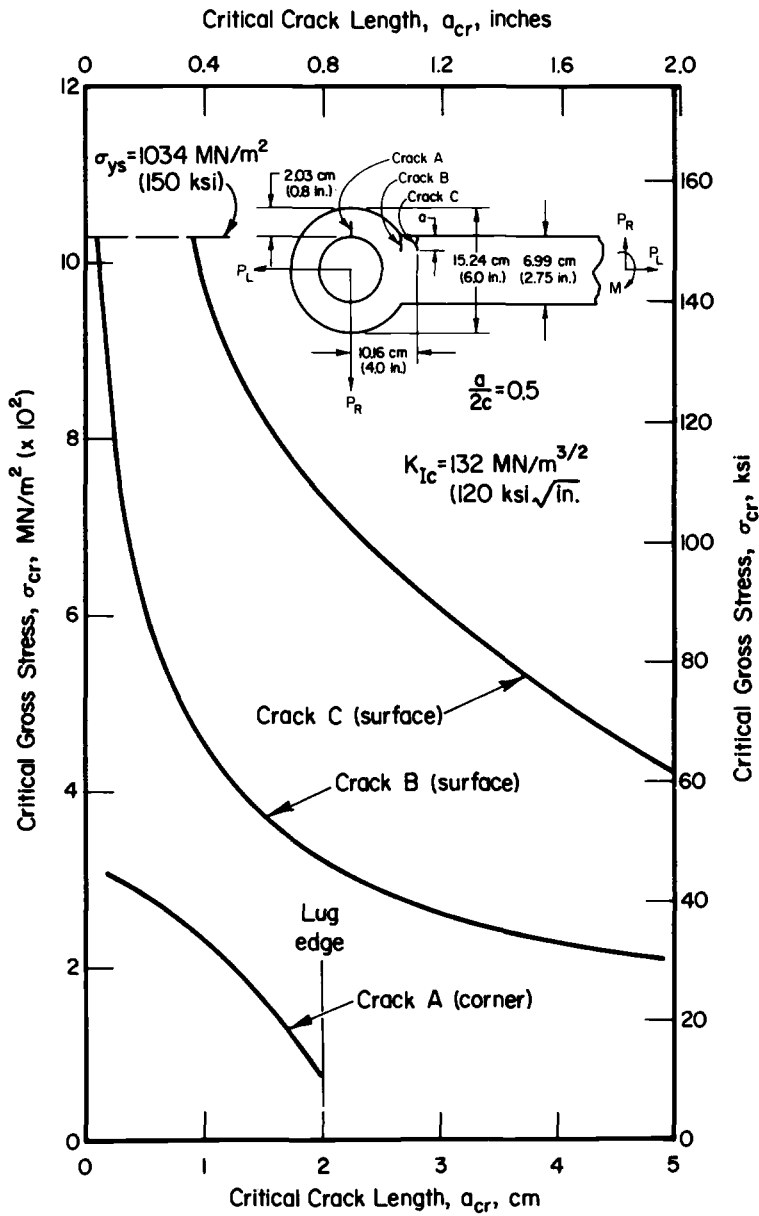


FIG. 8—Residual strength diagram for rod end component (Inconel 718 STA).

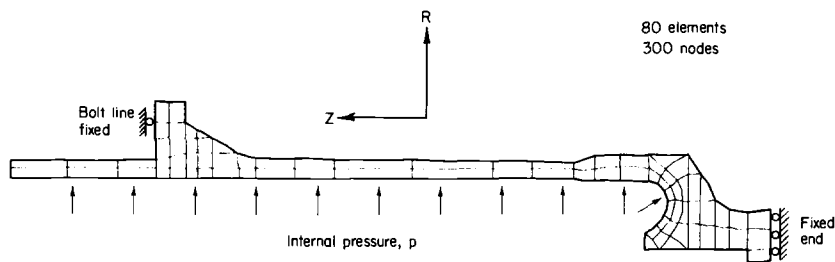


FIG. 9—Axisymmetrical finite-element model of cylinder.

applied for stress analysis. The attachment bolt line was fixed to restrain bending in the flange section. The built-up end was fixed along the edge. Stress analysis was conducted for an internal pressure of 6.895 MN/m^2 (1000 psi).

The distribution of longitudinal and hoop stresses at two high-stressed points in the bulb and built-up area of the cylinder head wall was determined by the finite-element analysis. The results (without the piston) showed that the cylinder wall (thin section) exhibited the nominal hoop stress, PR/t , and longitudinal stress, $PR/2t$, levels of 82.74 MN/m^2 (12.0 ksi) and 41.37 MN/m^2 (6.0 ksi). If the piston were to be included in the stress analysis, the longitudinal stresses in the cylinder would be lower than $PR/2t$. Using $PR/2t$ stresses resulted in a conservative analysis of fatigue crack growth life. The flange area of the cylinder wall showed a peak stress of 68.95 MN/m^2 (10.0 ksi) with the bolt line constrained. The axisymmetric model could not be used to determine the bending stresses due to flange bending. Therefore the stress analysis reported in Ref 16, which showed a 295.8 MN/m^2 (42.9 ksi) maximum combined stress in the flange, was used. The results of the stress analysis and consideration of structural geometry showed that four locations of the cylinder could be fracture critical.

These potentially critical locations of the cylinder selected for analysis, as shown in Fig. 10, were (1) the cylinder head bulb under hoop stress (Crack Location A), (2) the cylinder head cutout (for end pressure plate) under longitudinal stress (Crack Location B), (3) the cylinder wall thin section (Crack Location C), and (4) the flange corner area next to the body section (Crack Location D).

The distribution of stresses away from the inside diameter of the cylinder wall was used to determine the variation of beta with surface crack depth (Crack A) in the cylinder head area. The cutout for the pressure end plate was assumed to have a stress concentration factor of 3.0 applied to the longitudinal stress (Crack B). The cylinder wall flaw (Crack C) was assumed to initiate on the outside surface and propagate under applied hoop stress. The flange flaw (Crack D) was assumed to initiate in the corner and propagate

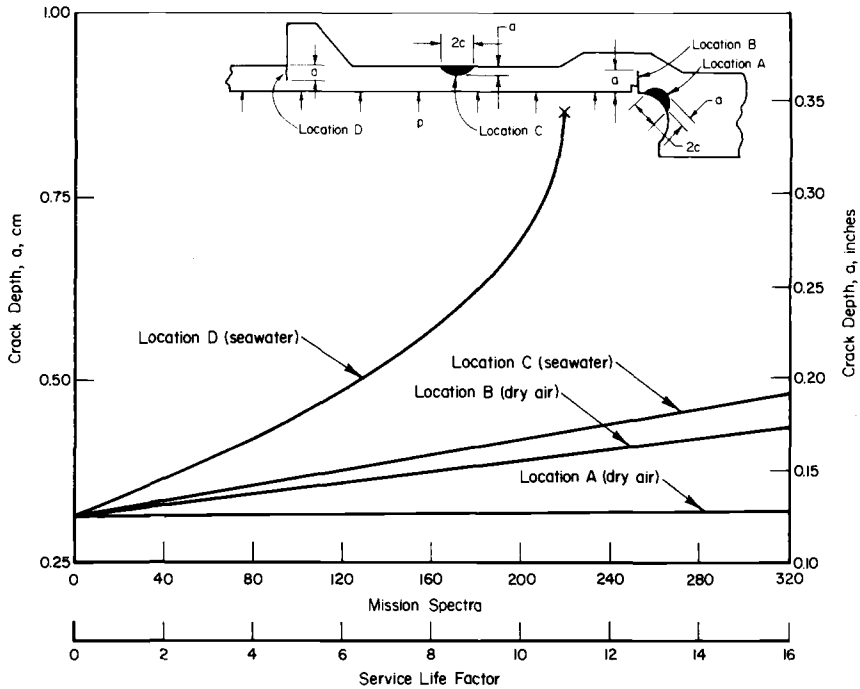


FIG. 10—Spectrum loading fatigue crack growth behavior of cylinder critical locations [17-4 PH (H1025)].

under longitudinal stresses. For this location, the bolts were assumed as a reaction point only without load transfer in accordance with the loose fit bolt criteria defined in Ref 1. All of the surface cracks were treated as part-through cracks in the cylinder wall without curvature correction. The stress intensity solution given in Eq 1 was used. For through-the-thickness cracks, the Folias [18] curvature correction factor was considered.

Fatigue Crack Growth and Residual Strength—Stress spectra equivalent to the 20 missions were developed for each of the four locations analyzed for fatigue crack growth life. The assumed initial flaw size at each location was a surface crack with $a_o = 0.318$ cm (0.125 in.) and $2c_o = 0.636$ cm (0.250 in.). The spectrum loading fatigue crack growth behavior for the actuator cylinder head and wall is shown in Fig. 10. The analysis assumed that the surface cracks at Locations A and B would be environmentally protected, and dry air environment was used as the da/dN behavior. If Locations A and B were to be exposed to hydraulic fluid, the life would be longer since da/dN is slower in hydraulic fluid than dry air. Location C was assumed to be exposed to seawater environment and the growth behavior (utilized in the analysis) was based on seawater da/dN data. If Location C was assumed on the inside and

exposed to hydraulic fluid, the life would have been longer because of slower da/dN . The spectrum fatigue crack growth analysis was conducted for these three locations up to 320 missions. The results showed that Location C was the most critical of the three, but stable crack growth resulted up to a surface crack depth of 0.457 cm (0.180 in.) in 320 missions. Each of the cracks at Locations A, B, and C were shown to be contained in the wall without pressure leakage.

Spectrum loading fatigue crack growth behavior for the surface crack (Crack D) in the flange corner is also shown in Fig. 10. The analysis results shows this location to be the most critical in the cylinder. The fatigue crack growth life of this location was 220 missions, resulting in a service life factor of 11.0. The predicted fatigue crack growth behavior of Location D surface crack would result in pressure leakage of the cylinder.

The residual strength diagram for each of the cylinder critical locations is shown in Fig. 11. Critical applied stress and surface crack depth analysis was based on a plane strain fracture toughness level of $54.9 \text{ MN/m}^{3/2}$ ($50 \text{ ksi}\sqrt{\text{in.}}$). Maximum operational stress levels applied to Locations A, B, C, and D were respectively 51.6 MN/m^2 (7.48 ksi), 44.8 MN/m^2 (6.50 ksi), 251.0 MN/m^2 (36.4 ksi), and 342.0 MN/m^2 (49.6 ksi). The critical surface crack depths for each of these applied stress levels result in surface crack depths greater than the cylinder wall thickness at each location. Therefore each location would result in a through-the-thickness crack and pressure leakages would occur.

Feedback Link (Push Rod) Component

The feedback link (push rod) was a small structural member that was connected from the scissors upper arm to the bellcrank in the feedback system (Fig. 1). The feedback link was fabricated from either 2024-T851 or T351. The fracture mechanics analysis was concentrated on evaluating the fatigue crack growth behavior and residual strength of 2024-T851 aluminum alloy. Other aluminum alloys and A286 steel were also considered in the fracture mechanics analysis because of their slower fatigue crack growth rate.

Stress Analysis and Mission Spectrum—The stress analysis and mission spectrum development for the feedback link was performed by different techniques and methods than those of the other two components. A dynamic vibration and loads model of the entire feedback system was developed to define inertia and component reaction loads as well as system natural frequencies. A NASTRAN [19,20] model was developed for the dynamic analysis. The resulting dynamic loads and boundary conditions were applied to three-dimensional finite-element models of each of the feedback components to define peak stresses and stress distributions at critical locations in the components.

The feedback link is symmetrical about two planes, namely a plane along the length of the link and a plane cutting the link into half. Hence, a quarter-

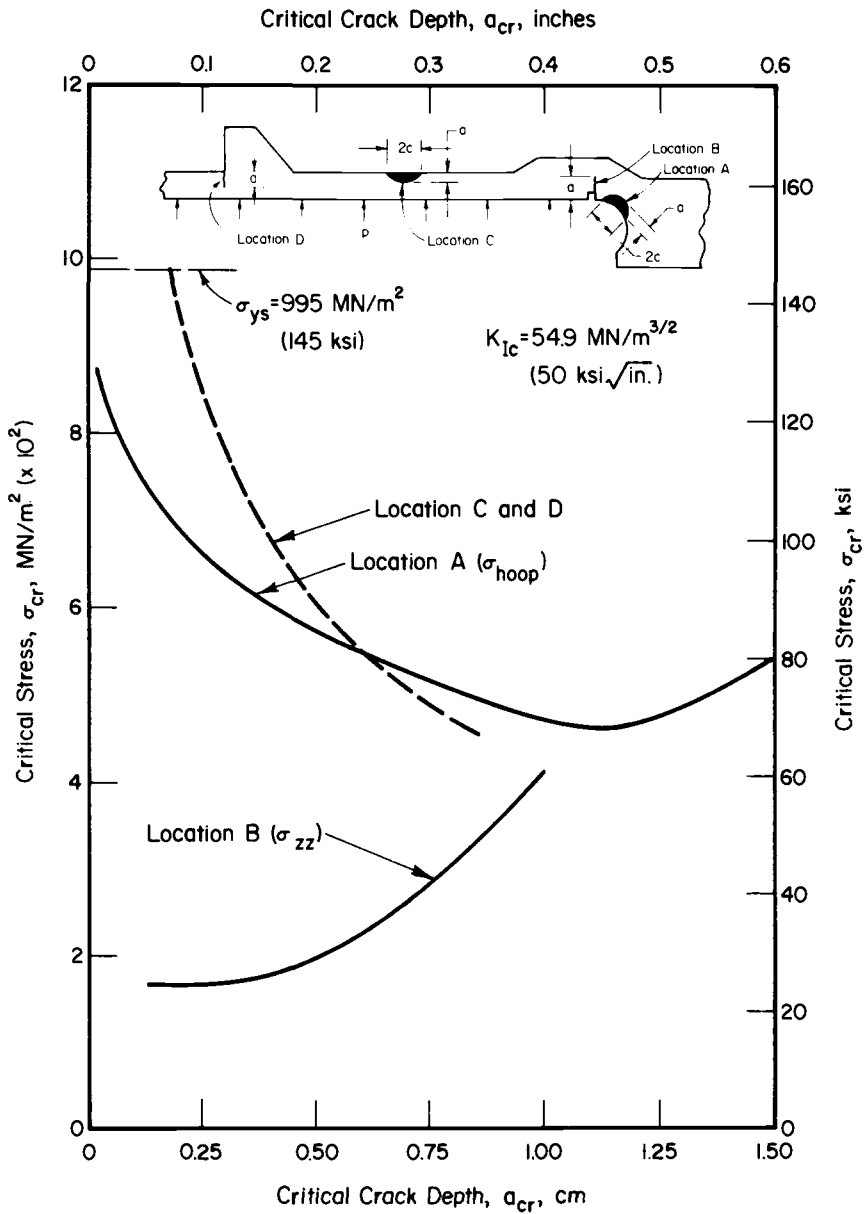


FIG. 11—Residual strength diagram for cylinder critical locations [17-4 PH (H1025)].

section three-dimensional finite-element model was developed for the feed-back link. The finite-element model consisted of 268 isoparametric elements and 502 grid points. Figure 12 shows the quarter-section finite-element model. The stresses calculated using program ADINA were very low at and

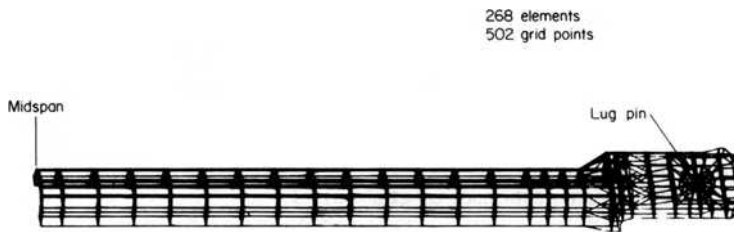


FIG. 12—Detailed finite-element model of the feedback link.

near the lug sections for the imposed dynamic reaction loads. The maximum stress occurred at the midspan of the feedback link for longitudinal dynamic vibration.

The mission stress spectrum for fatigue crack growth analysis was generated based on the results of dynamic vibration response tests conducted on the SRB actuator by NASA structural dynamics personnel. Components in the feedback system were subjected to various excitation inputs which were random loadings produced by the generation of "white-noise." The dynamic conditions which were considered in the testing are shown in Table 2. This dynamic testing included excitation inputs to the rod end (nozzle end) and the tailstock (skirt end) of the actuator. Dynamic response testing was also conducted under combined nozzle and skirt end inputs. Certain mission segments of the basic flight mission were simulated by various intensity levels of the random input loading.

Strain gages were mounted on the components of the feedback system to measure the strain response of the components when subjected to the various input axis loadings as described in Table 2. The dynamic strain responses were taken in the form of power spectral density (PSD) plots with an analog computer. The strain response PSD curves in the form of $\log [(\text{micro-strain})^2/\text{Hz}]$ versus $\log f$, Hz, were for stress spectrum loading analysis. Figure 13a shows an example of the feedback link PSD strain response curve for longitudinal vibration from the nozzle end. Random load-time history analysis and PSD concepts are further defined in Refs [21] and [22].

The natural frequency, f_n , for all the excitation responses of each component to the inputs, either nozzle end or skirt end, were assumed as constant for each axis of response: longitudinal (X), radial (Y), and tangential (Z). The first mode natural frequency of the feedback link component as determined from all the PSD plots was 475 Hz. The cyclic content of each of the mission segments of lift-off, boost, and re-entry were determined by $f_n \times \text{flight time}$ divided by 10.0. This criterion was imposed by NASA based on the vibration test data. Each axis of response contained the same number of cycles.

Root-mean-square (RMS) stress levels for each dynamic test condition were determined from the power spectral density (PSD) strain response plots. The RMS strain (ϵ_{rms}) was calculated as

$$\epsilon_{\text{rms}} = [\Delta f_{\text{hp}} \cdot \epsilon_{\text{peak}}]^{1/2} \quad (11)$$

where

Δf_{hp} = half-power bandwidth, Hz, and
 ϵ_{peak} = peak strain response, $(\mu \text{ cm/cm})^2/\text{Hz}$.

Secondary peak responses were not included as additional peak responses if their peak values were at least one-half magnitude or lower than the primary peak strain PSD value. All 3σ stress/strain values were calculated as 3 RMS strain, 1σ = RMS level, and used in a Rayleigh probability distribution of stresses. Table 2 shows the 3σ stress levels for the midspan critical location of the feedback link. The probability density function for the Rayleigh distribution is [21, 22]:

$$P(\sigma_{\text{max}}) = \frac{\sigma_{\text{max}}}{\sigma^2} \exp\left(\frac{-\sigma_{\text{max}}^2}{2\sigma^2}\right) \quad (12)$$

where σ = RMS stress level and σ_{max} is the maximum stress. Figure 13b shows a parametric plot of the Rayleigh distribution function for stress maxima as normalized to the RMS stress. The stresses and cycles were clipped (truncated and ignored) at the high and low level ends of the stress distribution. The high stresses were clipped at 3σ and the low level at 0.75σ (25 percent low-level stresses). Stress layers were generated at 0.1σ intervals. The final stresses for a given axis and flight segment were ordered in a low-high-low sequence to simulate narrow band random response history shape. The sequence of stresses within a given mission segment were highest stress axis response first, second highest stress axis response second, and lowest stress axis response last.

Stress Intensity Factor Analysis—The initial crack geometry that was applied to the feedback link critical bending section was a surface crack with $a_o = 0.318 \text{ cm}$ (0.125 in.) and $2c_o = 0.636 \text{ cm}$ (0.250 in.). Since the thickness of the tube wall of the feedback link was only 0.167 cm (0.066 in.), an initial surface crack of this size would automatically be a through-thickness crack. This crack would be a circumferential crack subjected to bending stresses. The stress intensity factor is magnified due to the curvature effect of the tube surface of the feedback link. At long crack lengths, the stress intensity is magnified even more. The stress-intensity factor of a circumferential through crack is [18]:

$$K_I = \beta_c \sigma_g \sqrt{\pi a} \quad (13)$$

TABLE 2—Combined dynamic excitation conditions for mission spectrum development for feedback link (push rod) critical location
(Gages 10 and 11) longitudinal response.

Spectrum Segment	Excitation End	Axis	Flight Time, s	fn, Hz	Applied Cycles, Total ^a	Strain Gage (ϵ_{rms}), $\mu\text{cm/cm}$	Critical Location Nominal 3σ Stress, MN/m ² (ksi)
Liftoff	nozzle + skirt	longitudinal (X)	10	475	475	253.37	52.4 (7.60)
		radial (Y)	10	475	475	277.53	57.4 (8.33)
	nozzle	tangential (Z)	10	475	475	380.29	78.7 (11.41)
		longitudinal (X)	14	475	665	200.10	41.4 (6.00)
		radial (Y)	14	475	665	231.05	47.8 (6.93)
Boost	nozzle + skirt	tangential (Z)	14	475	665	355.00	73.4 (10.65)
		longitudinal (X)	40	475	1900	276.12	57.2 (8.28)
	nozzle	radial (Y)	40	475	1900	297.38	61.5 (8.92)
		tangential (Z)	40	475	1900	398.64	82.5 (11.96)
		longitudinal (X)	56	475	2660	200.10	41.4 (6.00)
Re-entry	nozzle + skirt	radial (Y)	56	475	2660	231.05	47.8 (6.93)
		tangential (Z)	56	475	2660	355.00	73.4 (10.65)
	nozzle	longitudinal (X)	30	475	1425	454.76	94.1 (13.64)
		radial (Y)	30	475	1425	217.62	45.0 (6.53)
		tangential (Z)	30	475	1425	250.73	51.9 (7.52)

^a Cycles before truncation.

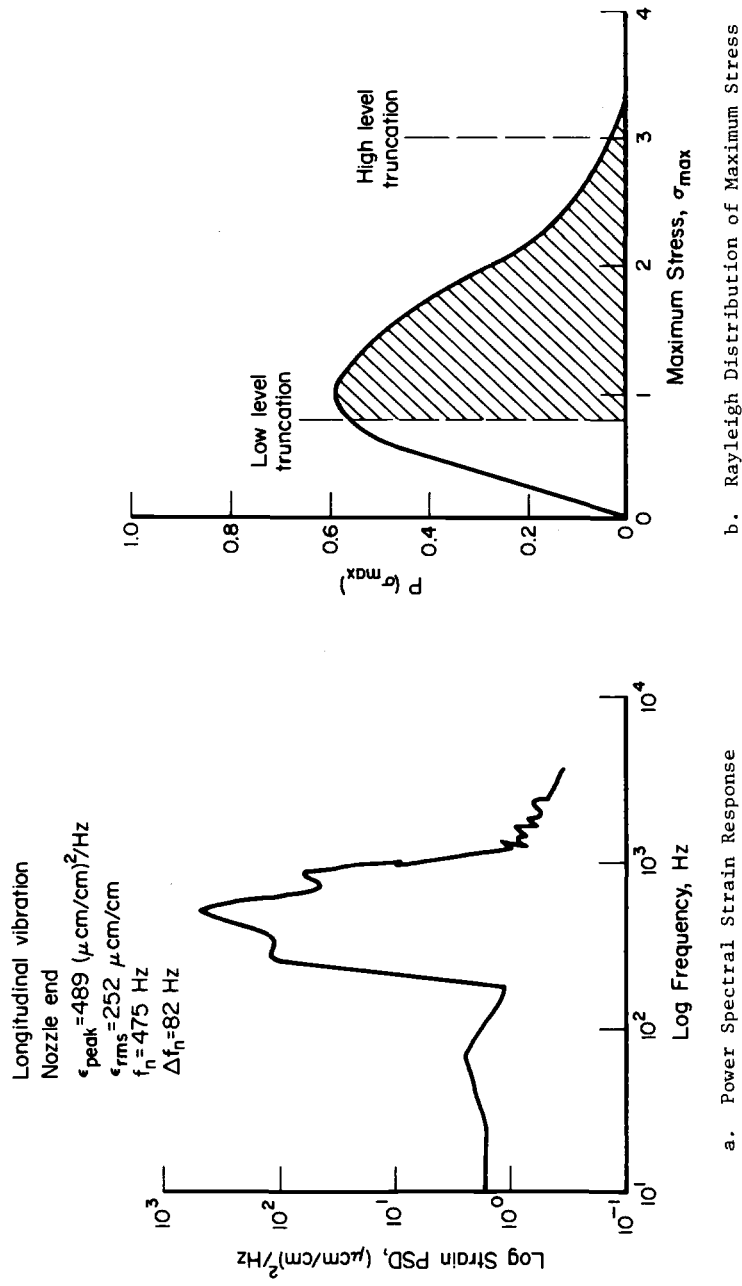


FIG. 13—Feedback link strain response and stress peak distribution.

where

σ_g = applied stress,

a = half-crack length,

$\beta_c = f(\lambda)$, the Folias correction factor for a thin cylinder,

and the normalized crack length parameter, λ , is given by

$$\lambda = [12(1 - \mu^2)]^{1/4} a / \sqrt{Rt} \quad (14)$$

where

R = cylinder radius,

t = tube thickness, and

μ = Poisson's ratio.

Iterative fatigue crack growth analysis was performed to smaller crack sizes. When the iteration involved the assumption of a small surface crack less than the feedback link wall thickness, then the stress intensity solution utilized was that for a surface crack. However, if during the propagation the surface crack broke through the feedback wall, then the stress intensity solution was changed to that described above.

Fatigue Crack Growth Results—The initially assumed crack located in the feedback link critical bending section when subjected to longitudinal vibration was a surface crack with $a_o = 0.318$ cm (0.125 in.) and $2c_o = 0.636$ cm (0.250 in.). This crack size assumption automatically makes the initial crack a through-the-thickness crack with $2c_o = 0.636$ cm (0.250 in.) at an equivalent ΔK -level. Figure 14 shows the resulting predicted fatigue crack growth life of 11 missions based on this initial crack size. Successive iterations were performed to smaller initially assumed crack sizes. The second analysis assumed that the initial surface crack size was just through-the-thickness with $a_o = t = 0.168$ cm (0.066 in.) and $2c_o = 0.336$ cm (0.132 in.). The resulting predicted fatigue crack growth life was 30 missions based on this assumed crack size, as shown in Fig. 14. Additional fatigue crack growth life predictions were made to determine what initial surface crack size would qualify the structure for 40 missions and 80 missions. These initial surface crack sizes were $a_o = 0.155$ cm (0.061 in.), $2c_o = 0.310$ cm (0.122 in.) and $a_o = 0.121$ cm (0.048 in.), $2c_o = 0.242$ cm (0.0956 in.), respectively. The corresponding initial through-the-thickness crack sizes that resulted in an equivalent initial ΔK to reach 40 and 80 missions, respectively, were $2a_o = 0.310$ cm and 0.244 cm (0.122 and 0.096 in.).

The inspection of the feedback link at these small flaw sizes was somewhat difficult. This was owing to the fact that the cracks could initiate and propagate along the inside surface of the tube. Therefore cracks were not visible on the outside until the crack front had broken through the tube wall and was visible on the outside surface.

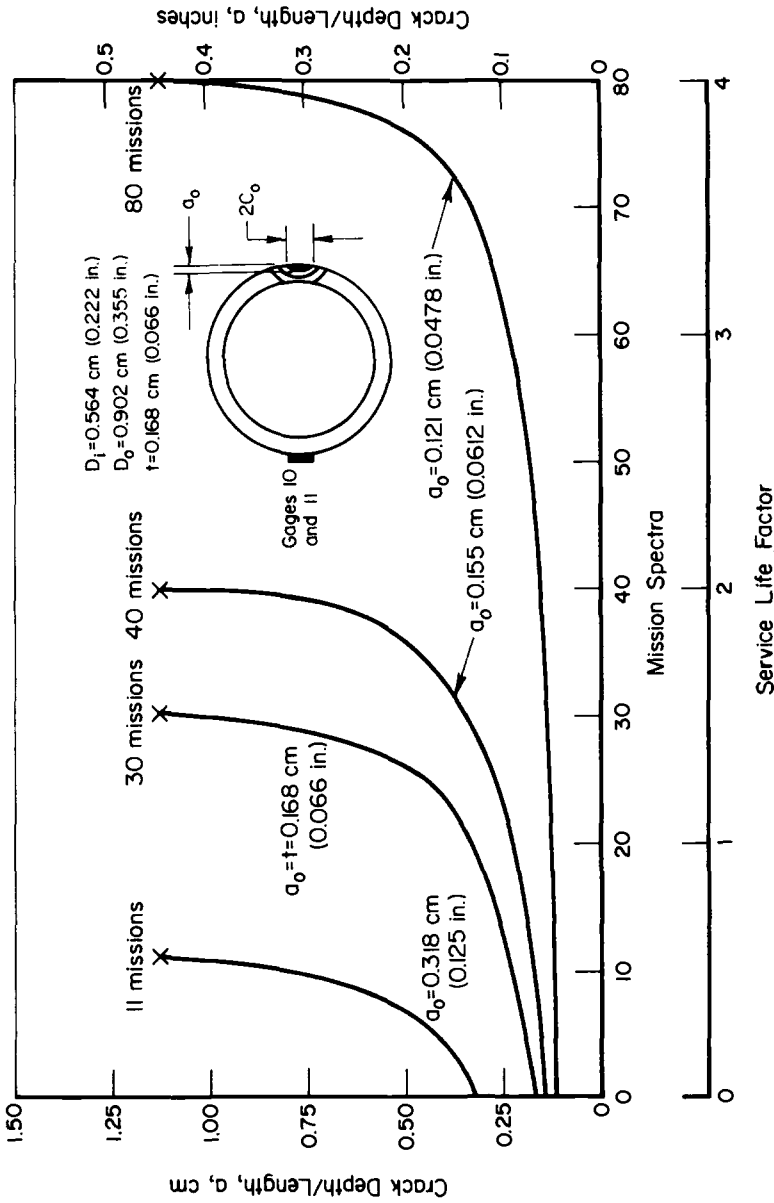


FIG. 14—Spectrum loading fatigue crack growth behavior of feedback link from various initial flaw sizes, longitudinal vibration (2024-T851).

It was desirable to conduct fatigue crack growth life analysis for 6061-T651 and 2024-T351 aluminum alloys and A286 steel alloy to determine if another material would be more suitable. The results of these fatigue crack growth life predictions are shown in Fig. 15. Each of these material substitutes shows improved fatigue crack growth life over the life obtained with 2024-T851.

The results of the fatigue crack growth life analysis of the feedback link showed that special inspection procedures had to be applied to the feedback link. Surface cracks no longer than $a_o = 0.127$ cm (0.05 in.) and $2c_o = 0.254$ cm (0.10 in.) would be screened by nondestructive inspection to qualify the 2024-T851 feedback link for a service life factor of 4.0 or 80 missions.

Summary and Discussion

Stress analysis of complex structural components by finite-element methods provides results as to the locations which are highly stressed and can be assumed as potentially fracture critical. Applying damage tolerance or fracture control criteria provides results that can be used to determine if the structural component could fall short of its intended service life.

Linear elastic fracture mechanics analysis has been applied in predicting the service life of three components of the actuator based on fatigue crack growth from initially assumed cracks at critical locations. These results were considered valid, since the applied stress levels due to the mission loadings were low with respect to the yield stress and the cracks in the components were subjected to elastic stress fields.

The use of upper bound da/dN and lower bound K_c and K_{Ic} was another assumption which led to conservative fatigue crack growth life prediction. This was a valid assumption, since in some cases where limited data were available some consideration was needed with respect to heat-to-heat variation and scatter.

Conclusions

Based on the finite-element stress analysis results and application of the fracture mechanics methods described, the following conclusions are given:

- (1) The Inconel 718 rod end lug component showed an analytical spectrum fatigue crack growth life of at least 220 missions (SLF = 11.0) for the lug shank and lug net-section and 85 missions (SLF = 4.25) for the lug eye-shank intersection.
- (2) Spectrum loading fatigue crack growth analysis of the four surface cracks located in the 17-4PH (H1025) cylinder wall and subjected to pressure and longitudinal bending stresses showed a service life of 220 missions (SLF = 11.0) or greater.
- (3) The 2024-T851 feedback link with an initial through-the-thickness

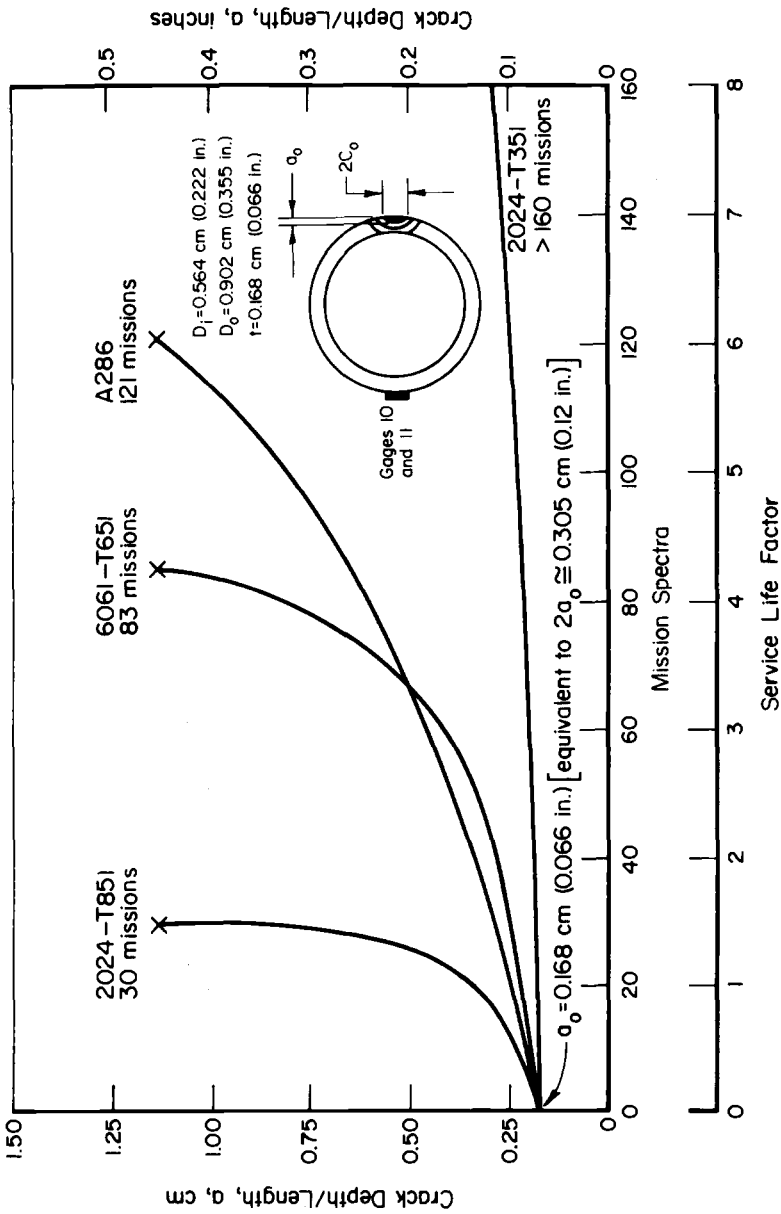


FIG. 15—Spectrum loading fatigue crack growth behavior of feedback link with various alloys, longitudinal vibration.

crack of $2a_o = 0.336$ cm (0.132 in.) showed a 20 mission service life and less than $SLF = 4.0$.

(4) As a means of fracture control, special nondestructive inspection of the feedback link was recommended to eliminate any possible surface cracks larger than $a_o = 0.127$ cm (0.050 in.) and $2c_o = 1.254$ cm (0.100 in.) to achieve the $SLF = 4.0$ criteria. A structural alloy substitute to 6061-T651, 2024-T351, or A286 steel would also result in $SLF > 4.0$.

Acknowledgments

The research work presented in this paper was conducted under NASA Contract NAS-8031720 with W. W. Jackson of NASA/MSFC and T. E. Riffin of Moog, Incorporated as the project managers. Assistance in the dynamic loads area by Dr. J. C. Kennedy of the Applied Dynamics and Acoustics Section at Battelle is appreciated.

References

- [1] Horton, W. P. and Hardy, G. B., "SRB Fracture Control Plan," George C. Marshall Space Flight Center, NASA, SE-020-002-2H, June 1974.
- [2] Smith, S. H. and Simonen, F. A., "Damage Tolerance Analysis of an Aircraft Structural Joint," in *Advances in Joining Technology*. Brook Hill Publishing Company, Chestnut Hill, Mass., 1976.
- [3] Smith, S. H., Forte, T. P., Malik, H. J., and Ghadiali, N. D., "Analytical and Experimental Fatigue-Crack-Growth Behavior of an Aircraft Horizontal Stabilizer," presented at 1978 SESA Spring Meeting, Wichita, Kan.
- [4] Irwin, G. R., *Journal of Applied Mechanics*, Dec. 1962, pp. 651-654.
- [5] Shah, R. C. and Kobayashi, A. S., "Stress-Intensity Factors for an Elliptical Crack Approaching the Surface of a Semi-Infinite Solid," *International Journal on Fracture Mechanics*, Vol. 9, No. 2, 1973.
- [6] Bowie, O. L., *Journal of Mathematics and Physics*, Vol. 35, 1956, pp. 60-71.
- [7] Smith, S. H., "Fatigue-Crack-Growth Behavior of C-5A Wing Control Points," Battelle's Columbus Laboratories, ASD-TR-74-18, May 1974.
- [8] Sova, J. A., Crews, J. H., Jr., and Exton, R. S., "Fatigue-Crack-Initiation and Growth in Notched 2024-T3 Specimens Monitored by a Videotape System," NASA Technical Note, TN D-8224, Aug. 1976.
- [9] Wood, H. A. and Engle, R. M., "USAF Damage Tolerant Design Handbook: Guidelines for the Analysis and Design of Damage Tolerant Aircraft," AFFDL-TR-79-3021, March 1979.
- [10] Impellizzeri, L. F. and Rich, D. L., "Spectrum Fatigue Crack Growth in Lugs," McDonnell Aircraft Company Report, MCAIR-75-006.
- [11] Forman, R. J., Kearney, B. E., and Engle, R. M., "Numerical Analysis of Crack Propagation in a Cyclic-Loaded Structure," *Journal of Basic Engineering*, Vol. 84D, 1967.
- [12] "Damage Tolerant Design Handbook, A Compilation of Fracture and Crack Growth Data of High Strength Alloys," Parts 1 and 2, MCIC-HB-1, Jan. 1975.
- [13] Broek, D. and Smith, S. H., "Spectrum Loading Fatigue Crack Growth Predictions and Safety-Factor Analysis," Battelle Final Report to Naval Air Development Center, NADC-76232-30, Sept. 1976.
- [14] Engle, R. M., Jr., "CRACKS III User's Manual," AFFDL-TM-74-173, 1975.
- [15] Bathe, Klaue-Jurgen, "ADINA-A Finite Element Program for Automatic Dynamic Incremental Nonlinear Analysis," Massachusetts Institute of Technology, Cambridge, Mass., Report 82448-1, Sept. 1975.

- [16] Chormann, G. G., Jr., Dalton, G. M., and Wilson, M. R., "Stress Analysis Report-SRB Servoactuator Moog Model No. 17-310," Moog, Inc., Report No. MRE-2266, 16 July 1976.
- [17] Peterson, R. E., *Stress Concentration Factors*, Wiley, New York, 1974.
- [18] Folias, E. S., *International Journal of Fracture Mechanics*, Vol. 2, 1967, pp. 1-11.
- [19] McCormick, C. W., "The NASTRAN User's Manual," NASA SP-222(01), May 1973.
- [20] MacNeal, R. H., "The NASTRAN Theoretical Manual," NASA SP-221(01), Dec. 1972.
- [21] Smith, S. H., "Fatigue Crack Growth Under Axial Narrow and Broad-Band Random Loading," in *Acoustical Fatigue in Aerospace Structures*, Syracuse University Press, Syracuse, N.Y., 1965.
- [22] Smith, S. H. in *Structural Fatigue in Aircraft*, ASTM STP 404, American Society for Testing and Materials, 1966, pp. 74-100.

Summary

Summary

The goal of this symposium was to present current fatigue and damage-fracture tolerance design criteria, practices, methodology, and technology necessary to attain a safe and economic operation of all types of structures during their projected lifetimes. What are the requirements? How are they satisfied? What methods are used in materials selection, detail design, analysis, testing, and manufacturing? New innovations? This volume, through the seventeen papers presented at the symposium and four others, attempts to answer some of these questions. Aircraft, ground vehicle, ship, offshore, nuclear power, and other structures are covered. The papers are grouped into five sections: (1) Overview, (2) Design and Criteria, (3) Crack Growth, (4) Analysis Methodology, and (5) Experimental and Analytical Evaluation of Structures.

The following sections summarize the papers from each of the five groups.

Overview

This section contains three papers covering fatigue and fracture resistance design approaches in three different fields of structures: ground vehicles, nuclear power, and transport aircraft. In the ground vehicle field, *Watson and Hill* present an extensive historical review of fatigue knowledge development and accentuate service loads measurement, stress analysis, and materials and component testing. The local elastic-plastic stress-strain cumulative damage approach is identified as the most often used current method to predict fatigue life in ground vehicles. *Jones et al* cover the codes and concepts used in the nuclear power industry. Fatigue life is usually evaluated using elastic stress-strain history and linear damage rule. Damage tolerance evaluation is based on linear elastic fracture mechanics (LEFM) and crack growth analysis, starting with in-service detectable flaws. Environmental effects are significant. Great emphasis is given to codes (ASME, Federal Regulations) and NRC guidelines for fatigue and fracture resistance design, materials, construction, operation, and in-service inspection. The approach taken to attain safe and economic structure life of transport aircraft, as seen through the eyes of one manufacturer, is presented by *Goranson et al*. It is assumed that this is similar to the approaches taken by other manufacturers. Broad guidelines that all manufacturers must follow are given in Federal Regulations. Current approaches emphasize good durability, damage

tolerance, and in-service inspections. Use of LEFM in crack growth and residual strength analysis is extensive. Of interest is the Damage Tolerance Rating (DTR) system, which utilizes past service experience and statistics to rate structures for design and inspections.

Design and Criteria

Hartt describes the approach taken with offshore welded steel structures in designing for fatigue resistance. Mechanical, material, and environmental variables are discussed with attention focused on cathodic protection. Design of offshore structures requires the application of 10^7 to 10^8 low-stress amplitude cycles. Thus it is a high-cycle fatigue problem complicated by the variation in weld properties and effects of sea water. Linear elastic fracture mechanics and crack growth analysis are being introduced to enhance design procedures and improve scheduling of inspections. *Nelson and Socie* review crack initiation and propagation behavior in notched laboratory specimens, and show by example how practical considerations dictate whether crack initiation or crack propagation analysis is used in design. For example, crack propagation analysis is extensively used in aircraft structure design, whereas crack initiation analysis is the main approach in the automotive field. In two papers, *Rudd et al* describe the Air Force durability and damage tolerance design requirements and analysis methodology. Durability is defined as the ability of the structure to operate within established economic limits; that is, cracking and other degradation during service lifetime should not exceed acceptable economic limits or affect the operational readiness of the aircraft. The durability analysis is based on the statistical definition of the equivalent initial flaw size (EIFS) distribution and crack growth analysis. This procedure is illustrated by an example from the F-16 program. In their second paper the Air Force damage tolerance design requirements are reviewed with emphasis on the location of initial damage and the accuracy of crack growth analysis. A test program of 28 skin-stringer specimens was conducted to determine the most critical locations of initial primary damage. Results reflect only one material and constant-amplitude loading. *Berens and Gallagher* present a description of the Air Force maintenance-tracking program based on crack growth. Maintenance schedule accuracy requirements are studied through an analysis of potential errors that are possible in the projections of calendar time to critical crack length.

Crack Growth

Wang describes an investigation to define the equivalent initial flaw size (EIFS) distribution of fastener holes. Through quantitative analysis of a large amount of microcrack growth data and surface macrocrack growth data

he produced EIFS statistical distributions for 2024-T3 aluminum sheet. The essential physical defects of cracking origins are tool marks and inclusions. Mode III fatigue cracking is covered by *Hurd and Irving*. They performed torsion loading tests on round low-alloy steel specimens, typical of automotive transmission components. Mode III rates are significantly lower than Mode I, by a factor of between 10 and 50. *Saff and Rosenfeld* present results of an experimental program in which they investigated crack growth of aircraft landing gear steels 300M and HP 9-4-.30, with emphasis on loading-environment effects. Immersion in salt or sea water accelerates crack growth in 300M, but has a less pronounced effect on HP 9-4-.30. The authors present an analysis that predicts the effect of alternative immersion environments. Tests were performed with Air Force and Navy fighter landing gear loads spectra.

Analysis Methodology

Analysis methodology is covered by five papers, which range from crack growth to weight savings calculations from materials properties. *Newman* applies an analytical crack closure model which simulates plane-stress and plane-strain conditions to predict crack growth under various load histories. The model considers plastically deformed material in the wake of the advancing crack tip, and accounts for retardation and acceleration load interaction effects. The model was checked against 2219-T851 aluminum test data. N_P to N_T ratios varied from 0.5 to 1.8. A crack growth analysis method for use in preliminary design is outlined by *Chang et al.* The procedure utilizes the equivalent damage concept to convert the random spectrum into equivalent constant-amplitude loads and accounts for load interaction effects. *Oh* illustrates the use of Neuber's Rule for stress concentrations to predict the fatigue life of spotwelds. Good correlation between test and analysis is obtained for steel spotwelds under constant-amplitude loading. *Gunther and Wozumi* present residual strength analysis and failure modes of cracked mechanically fastened stiffened panels. Elasto-plastic finite-element analysis accounts for the plastic deformation capability of all elements. The authors conclude that in all cases skin failure is always the critical failure mode. In a discussion appended to the paper, Swift disagrees with this conclusion by stating that for some geometrical configurations stiffened panel failure can be precipitated by fastener failure. He also points out that stiffener eccentricity was not included in analysis. *Ekvall et al* present an interesting methodology for evaluating weight savings from basic material properties. The properties considered include density, elasticity, static strength, fatigue, crack growth, fracture toughness, and stress corrosion. Analysis results are shown for two different aircraft.

Experimental and Analytical Evaluation of Structures

Chu et al describe an experimental study to characterize fatigue crack growth behavior of weld-bonded stiffened panels typical in ship construction. The panels are subjected to lateral pressure loading. The crack growth data were correlated with base line materials data. *Potter* presents the results of an extensive program on the durability and damage tolerance behavior of adhesively bonded aircraft primary structure. The program involved analysis and development testing culminating in a full-scale fuselage durability and damage tolerance test. Real and accelerated time environmental effects were evaluated. The program demonstrated that bonding of primary structure produces durability and damage tolerance superior to that of mechanically fastened structure. *Zako et al* present an interesting treatment of the damage tolerance problem of jet engine rotor disk. The crack growth analysis is based on material properties and two-dimensional finite-element stress analysis. The problem in the end is handled from probability of failure point of view, with respect to K_{IC} -values. The last two papers deal with practical examples with fatigue and fracture evaluation of structural components. *Rice and Smith* present an evaluation of communication tower eyebolts. Fatigue tests were performed on unused eyebolts and eyebolts taken from service. Fatigue-fracture mechanics analyses results compared favorably with experimental results. Crack initiation lives were predicted using local stress-strain analysis approach. Standard analysis procedures were used for crack growth prediction. The evaluation of the other structural component, solid rocket booster servoactuator, as described by *Smith et al*, consisted of crack growth and residual strength analysis in three areas of the component. Three-dimensional finite-element analysis was performed to support the calculation of stress intensity factors. Fatigue life estimation was based on crack growth analysis starting with an initial flaw. A nondestructive inspection plan was defined on the basis of this analysis for one area of the component.

Final Remarks

The overall impression of the symposium and this publication is the predominant use of crack growth—residual strength linear elastic fracture mechanics approaches as opposed to the so-called fatigue life prediction to crack initiation using nominal or local stress-strain and $S-N$ or $\epsilon-N$ allowables. Only in the ground vehicle field does the latter approach appear to be the primary method of design and evaluation. However, the structures designer and analyst should always remember that in most cases the optimum design should have a combination of good durability and damage tolerance, where durability is the ability of the structure to operate and to be maintained during the planned service life within acceptable economic

limits, and damage tolerance is the ability of damaged (due to fatigue, corrosion, or accidental damage) structure to operate safely between inspections.

P. R. Abelkis

Douglas Aircraft Company, McDonnell Douglas Corporation, Long Beach, California; symposium co-chairman and co-editor

C. M. Hudson

NASA-Langley Research Center, Hampton, Virginia; symposium co-chairman and co-editor

Index

A

Adhesives, 379
 Allowable damage, 51
 ASME Boiler and Pressure Vessel
 Code, 28

B

Bauschinger effect, 14, 15
 Block loading, 18

C

Charpy impact energy, 37
 Closure model, 255, 261
 Component testing, 16, 18, 384
 Constant amplitude loading, 235,
 262
 Corrosion, 96
 Crack initiation, 111, 217, 432
 Crack opening displacement (COD),
 224, 226
 Cycle counting
 Level crossing, 19
 Peak distribution, 19
 Peaks, 19
 Rainfall method, 20
 Range counting, 20
 Range mean analysis, 20
 Range-pair counting, 20

D

Damage accumulation, 284
 Damage detection, 75

Damage growth period, 51
 Damage tolerance, 31, 51, 63, 153
 Design criteria, 49, 127, 134, 286,
 374
 Durability, 51, 55, 134, 143

E

Error analysis, 176, 183

F

Failure modes, 65, 335
 Fasteners, 315
 Fatigue, 15, 19
 Fatigue analysis, 20, 30, 54, 57, 101,
 229
 Fatigue crack growth analysis, 36,
 101, 112, 127, 217, 241, 259,
 267, 281, 288, 434, 454
 Fatigue crack growth data
 A553 GR.B steel, 41
 BS4360 GR.50D steel, 98
 BS605 H32 steel, 222
 HP 9-4-0.30 steel, 241
 300 M steel, 240, 242
 17-4 PH stainless steel, 451
 5456 aluminum alloy, 367, 369
 Fatigue life calculation, 415
 Fractography, 194
 Fracture tolerant design, 32
 Fracture toughness, 34, 35, 333, 412,
 416, 452
 Full scale test program, 393

- | | |
|--|---|
| <p style="text-align: center;">G</p> <p>Gerber diagram, 13</p> <p>Goodman diagram, 13</p>
<p style="text-align: center;">I</p> <p>Initial flaw size, 139, 158, 197, 207, 454</p>
<p style="text-align: center;">L</p> <p>Linear elastic fracture mechanics, 15, 66, 447</p>
<p style="text-align: center;">M</p> <p>Material properties, 13, 216, 301, 333, 347</p> <p>Miner's rule, 93</p> <p>Mode III cracks, 215</p>
<p style="text-align: center;">N</p> <p>Neuber's rule, 13, 296</p> <p>Nonpropagating cracks, 115</p>
<p style="text-align: center;">P</p> <p>Plasticity, 229</p> <p>Power spectral density, 19</p>
<p style="text-align: center;">R</p> <p>Random loading, 18</p> <p>Residual strength, 65, 454</p> | <p><i>R</i>-ratio, 40</p> <p><i>RT</i>_{NDT}, 33</p>
<p style="text-align: center;">S</p> <p>Service life, 6</p> <p>Skin-stringer construction, 69, 159, 289, 310, 346, 389</p> <p><i>S-N</i> curves, 13, 30, 56, 94</p> <p>Spectrum loading, 192, 245, 255, 271, 452</p> <p>Strain life, 15, 111, 129</p> <p>Stress analysis, 11, 410</p> <p>Stress concentration factors, 12, 21</p> <p>Stress history, 23, 93, 126</p> <p>Stress intensity factor, 67, 101, 349, 354, 447, 466</p> <p>Stress-life, 128</p> <p>Stress-strain relationship, 15, 23</p> <p>Structural integrity, 133</p> <p>Supplemental inspection documents, 49</p> <p>Surface treatment, 376</p>
<p style="text-align: center;">V</p> <p>Variable amplitude loading, 255, 263</p>
<p style="text-align: center;">W</p> <p>Weight savings model, 330</p> <p>Welds, 95, 298</p> <p>Wöhler curves, 13, 14</p> |
|--|---|

